AD-A286 731

PROCEEDINGS

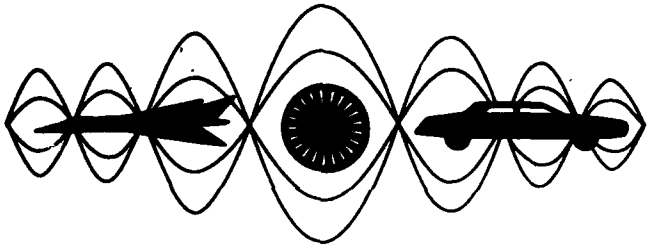

SECOND INTERNATIONAL CONGRESS ON RECENT DEVELOPMENTS IN AIR- AND STRUCTURE-BORNE SOUND AND VIBRATION

MARCH 4-6, 1992 AUBURN UNIVERSITY, USA

95-01104

DTIC
ELECTE
FEB 28 1995
S G D

Edited by

Malcolm J. Crocker

P. K. Raju

DISTRIBUTION STATEMENT A
Approved for public release;
Distribution Unlimited

Volume 2

PROCEEDINGS

DTIC
ELECTE
FEB 2 8 1995
S G D

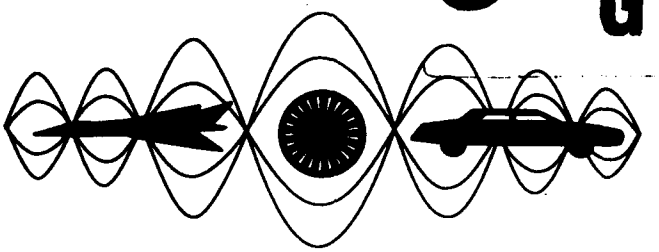

SECOND INTERNATIONAL CONGRESS ON RECENT DEVELOPMENTS IN AIR- AND STRUCTURE-BORNE SOUND AND VIBRATION

MARCH 4-6, 1992 AUBURN UNIVERSITY, USA

N00014-92-J-1525
ONR

Accesion For
NTIS CRA&I
DTIC TAB
Unannounced
Justification
By
Distribution /
Availability Codes
Dist | Avail and / or Special
A-1

Edited by
Malcolm J. Crocker
P. K. Raju

Volume 2

DISTRIBUTION STATEMENT A
Approved for public release;
Distribution Unlimited

Copyright © 1992, Mechanical Engineering Department, Auburn University, AL, USA
Printed in the United States of America
Cover design by Malcolm J. Crocker and Wally Ridgeway

Copies may be ordered from:
International Sound & Vibration Congress Editors
Mechanical Engineering Department
202 Ross Hall
Auburn University, AL 36849-5331, USA

Available only as a set of three volumes at the price of $125 each plus $30 each set for airmail.

Permission is hereby granted for any person to reproduce a fractional part of any paper herein, provided that permission is obtained from its author(s) and credit is given to the author(s) and these Proceedings. Notification to the Editors of these Proceedings at Auburn University is also required. An author, or his research sponsor, may reproduce his paper in full, crediting these proceedings; this permission is not assignable.

SECOND INTERNATIONAL CONGRESS ON RECENT DEVELOPMENTS IN AIR- & STRUCTURE-BORNE SOUND AND VIBRATION

MARCH 4-6, 1992

Auburn University
USA

Sponsored by **AUBURN UNIVERSITY** in cooperation with
THE INTERNATIONAL COMMISSION ON ACOUSTICS OF IUPAP
and with the following professional societies:

ACOUSTICAL SOCIETY OF AMERICA
ACOUSTICAL SOCIETY OF THE NETHERLANDS
ACOUSTICAL SOCIETY OF THE RUSSIAN FEDERATION
AMERICAN HELICOPTER SOCIETY
AMERICAN SOCIETY OF MECHANICAL ENGINEERS
ASSOCIATION BELGE DES ACOUSTICIENS
ASSOCIAZIONE ITALIANA di ACUSTICA
AUSTRALIAN ACOUSTICAL SOCIETY
THE CANADIAN SOCIETY FOR MECHANICAL ENGINEERING
DEUTSCHE ARBEITSGEMEINSCHAFT FÜR AKUSTIK (DAGA)
INSTITUTE OF ACOUSTICS, UNITED KINGDOM
INSTITUTE OF NOISE CONTROL ENGINEERING/JAPAN
INSTITUTE OF NOISE CONTROL ENGINEERING/USA
INSTITUTION FOR MECHANICAL ENGINEERS, UNITED KINGDOM
THE AMERICAN SOCIETY FOR NONDESTRUCTIVE TESTING, INC.
VEREIN DEUTSCHER INGENIEURE (VDI-EDV), GERMANY
THE SOUTH AFRICAN ACOUSTICS INSTITUTE
SOCIÉTÉ FRANÇAISE D'ACOUSTIQUE
SOVIET ACOUSTICAL ASSOCIATION
ACOUSTICAL COMMISSION OF THE HUNGARIAN ACADEMY OF SCIENCES

General Chairman—Malcolm J. Crocker, Mechanical Engineering Department
Program Chairman—P. K. Raju, Mechanical Engineering Department

DTIC QUALITY INSPECTED 4

Scientific Committee

Adnan Akay, Wayne State University, Michigan
Michael Bockhoff, Centre Techniques Des Industries Mecaniques, France
Brian L. Clarkson, University College of Swansea, United Kingdom
J. E. Ffowcs-Williams, University of Cambridge, United Kingdom
Robert Hickling, National Center for Physical Acoustics, Mississippi
G. Krishnappa, National Research Council of Canada
Leonid M. Lyamshev, Andreev Acoustics Institute, Moscow
Richard H. Lyon, Massachusetts Institute of Technology, Massachusetts
Gideon Maidanik, David Taylor Research Center, Maryland
M. L. Munjal, Indian Institute of Science, India
Alan Powell, University of Houston, Texas
Clemans A. Powell, NASA Langley Research Center, Virginia
J. N. Reddy, Virginia Polytechnic Institute & State University, Virginia
Herbert Überall, Catholic University of America, D.C.
Eric Ungar, Bolt Beranek and Newman, Massachusetts
V. V. Varadan, Pennsylvania State University, Pennsylvania
R. G. White, Institute of Sound and Vibration Research, United Kingdom

Organizing Committee

John E. Cochran, Auburn University (Aerospace Engineering)
Robert D. Collier, Tufts University (Mechanical Engineering)
Malcolm J. Crocker, Auburn University (Mechanical Engineering)
Malcolm A. Cutchins, Auburn University (Aerospace Engineering)
Ken Hsueh, Ford Motor Co., Allen Park, Michigan
Gopal Mathur, McDonnell Douglas, Long Beach, California
M. G. Prasad, Stevens Institute of Technology (Mechanical Engineering)
P. K. Raju, Auburn University (Mechanical Engineering)
Mohan Rao, Michigan Technological University (Mechanical Engineering)
Uday Shirahatti, Old Dominion University (Mechanical Engineering)

Financial Support

Financial support for these international congresses has been provided by:

National Science Foundation
Office of Naval Research
Office of Naval Research—Europe
Alabama Space Grant Consortium
National Aeronautics and Space Administration
College of Engineering (Auburn University)
Department of Mechanical Engineering (Auburn University)

FOREWORD

This three-volume book of proceedings includes the written versions of the papers presented at the Second International Congress on Recent Developments in Air- and Structure-Borne Sound and Vibration held at Auburn University March 4-6, 1992. The Congress was sponsored by Auburn University in cooperation with the International Commission on Acoustics of IUPAP and the 20 professional societies in 14 countries listed at the beginning of each volume. The support of this Commission and the professional societies has been invaluable in ensuring a truly international congress with participation from 30 countries. This support is gratefully acknowledged. In addition, the organizing committee would like to thank the National Science Foundation, the Office of Naval Research, the Office of Naval Research—Europe, the Alabama Space Grant Consortium, NASA, the College of Engineering and the Department of Mechanical Engineering of Auburn University for financial assistance.

Topics covered in the Proceedings include Sound Intensity, Structural Intensity, Modal Analysis and Synthesis, Statistical Energy Analysis and Energy Methods, Passive and Active Damping, Boundary Element Methods, Diagnostics and Condition Monitoring, Material Characterization and Non-Destructive Evaluation, Active Noise and Vibration Control, Sound Radiation and Scattering, and Finite Element Analysis.

The order in which the 217 papers appear in these volumes is roughly the same as they were presented at the Congress although the order is modified somewhat so they can be grouped in the topics above. There are also six keynote papers, including Professor Sir James Lighthill on Aeroacoustics and Atmospheric Sound, Professor Frank J. Fahy on Engineering Applications of Vibro-Acoustic Reciprocity; Dr. Louis Dragonette on Underwater Acoustic Scattering, Professor Robert E. Green on Overview of Acoustical Technology for Non-Destructive Evaluation, Professor David Brown on Future Trends in Modal Testing Technology and Professor Lothar Gaul on Calculation and Measurement of Structure-borne Sound. The papers in this book cover all major topics of interest to those concerned with engineering acoustics and vibration problems in machines, aircraft, spacecraft, other vehicles and buildings.

In the last 30 years, improvements in computers have allowed rapid developments in both theoretical and experimental analysis of acoustics and vibration problems. In the early 1960s statistical energy analysis (SEA) was first applied to coupled sound and vibration problems. In the early 1970s the finite element method (FEM) was first used in acoustics problems. In recent years considerable progress has been made with the boundary element method (BEM) in which discretization is confined to two-dimensional surfaces instead of three-dimensional fields. Some of these approaches have been combined for instance in SEA-FEM. The 1980s, which have also seen rapid advances in improved measurement techniques, could be called the decade of sound intensity, as it can now be used for rapid measurements of the in-situ sound power of a machine, to rank noise sources and determine transmission loss of structural partitions. Power flow in structures also now can be determined with the use of structural intensity measurements. Sound

and vibration signals are being used increasingly to diagnose the condition of machinery and to detect faults or to determine the properties of materials through non-destructive evaluation. There is also increased knowledge in sound radiation and scattering; in particular advances have occurred in scattering theory and in numerical solution techniques.

The organization and hosting of a conference is a considerable undertaking, and this Congress is no different. We would firstly like to thank all the authors who submitted their contributions promptly making publication of this book before the Congress possible. We would also like to acknowledge the assistance of the scientific committee and organizing committee who helped to completely organize some sessions. The staff of the Mechanical Engineering Department of Auburn University also provided valuable assistance. Our special thanks are extended to Rose-Marie Zuk who worked untiringly and efficiently on all aspects of the Congress program and this book, to Julia Shvetz who provided invaluable expert assistance in all areas of Congress planning in particular with travel arrangements for foreign guests, and to Olga Riabova for her hard work on Congress communications.

Malcolm J. Crocker, General Chairman
P.K. Raju, Program Chairman

TABLE OF CONTENTS

	Page
FOREWORD	v
DISTINGUISHED LECTURE SERIES	1
KEYNOTE ADDRESS	3
A GENERAL INTRODUCTION TO AEROACOUSTICS AND ATMOSPHERIC SOUND Sir James Lighthill, University College London, United Kingdom	5
AEROACOUSTICS	35
VORTEX SOUND INTERACTION Ann Dowling, University of Cambridge, United Kingdom	37
NUMERICAL PREDICTIONS IN ACOUSTICS Jay C. Hardin, NASA Langley Research Center, Virginia	51
THE BROADBAND NOISE GENERATED BY VERY HIGH TEMPERATURE, HIGH VELOCITY EXHAUSTS S.A. McInerny, California State University, California	59
FLOW-INDUCED NOISE AND VIBRATION OF CONFINED JETS Kam W. Ng, Office of Naval Research, Virginia	67
STRUCTURAL-ACOUSTIC COUPLING IN AIRCRAFT FUSELAGE STRUCTURES Gopal P. Mathur and Myles A. Simpson, Douglas Aircraft Company, California	81
RESPONSE VARIABILITY OBSERVED IN A REVERBERANT ACOUSTIC TEST OF A MODEL AEROSPACE STRUCTURE Robert E. Powell, Cambridge Collaborative Inc., Massachusetts	89
RESPONSE OF LAUNCH PAD STRUCTURES TO RANDOM ACOUSTIC EXCITATION Ravi Margasahayam and Valentin Sepcenko, Boeing Aerospace Operations, Inc. Raoul Caimi, NASA Engineering Development, Florida	97
SONIC BOOM MINIMIZATION: MYTH OR REALITY? Kenneth J. Plotkin, Wyle Laboratories, Virginia	105
CONTROL OF SUPERSONIC THROUGHFLOW TURBOMACHINES DISCRETE FREQUENCY NOISE GENERATION BY AERODYNAMIC DETUNING Sanford Fleeter, Purdue University, Indiana	113
COMPARISON OF RADIATED NOISE FROM SHROUDED AND UNSHROUDED PROPELLERS Walter Eversman, University of Missouri-Rolla, Missouri	121

NOISE AND VIBRATION ANALYSIS IN PROPELLER AIRCRAFT BY ADVANCED EXPERIMENTAL MODELING TECHNIQUES 129
Herman Van der Auweraer and Dirk Otte. LMS International, Belgium

AERODYNAMIC NOISE GENERATED BY CASCADED AIRFOILS 137
Gerald C. Lauchle and Lori Ann Perry, The Pennsylvania State University, Pennsylvania

VIBRATION ISOLATION OF AVIATION POWER PLANTS TAKING INTO ACCOUNT REAL DYNAMIC CHARACTERISTICS OF ENGINE AND AIRCRAFT 143
V.S. Baklanov and V.M. Vul, A.N. Tupolev Aviation Science and Technical Complex, Moscow, Russia

PASSIVE DAMPING 149

ANALYSIS OF CONSTRAINED-LAYER DAMPING OF FLEXURAL AND EXTENSIONAL WAVES IN INFINITE, FLUID-LOADED PLATES 151
Pieter S. Dubbelday, Naval Research Laboratory, Florida

EFFECT OF PARTIAL COVERAGE ON THE EFFECTIVENESS OF A CONSTRAINED LAYER DAMPER ON A PLATE 157
M.R. Garrison, R.N. Miles, J.Q. Sun, and W. Bao, State University of New York, New York

REDUCTION OF NOISE AT STEEL SHELLS WORKING BY USING VIBRODAMPING COVERS OF MULTIPLE USE 165
Victor F. Asminin, Sergey I. Chotelev, and Yury P. Chepulsky, Voronezhsky Lesotechnichesky Institute, Russia

SIMULTANEOUS DESIGN OF ACTIVE VIBRATION CONTROL AND PASSIVE VISCOELASTIC DAMPING 169
Michele L.D. Gaudreault, Ronald L. Bagley, and Brad S. Liebst, Air Force Institute of Technology, Ohio

A SUBRESONANT METHOD FOR MEASURING MATERIAL DAMPING IN LOW FREQUENCY UNIAXIAL VIBRATION 177
George A. Lesieutre and Kiran M. Govindswamy, The Pennsylvania State University, Pennsylvania

PASSIVE DAMPING TECHNOLOGY 181
Eric M. Austin and Conor D. Johnson, CSA Engineering, Inc., California

RECENT APPLICATION OF THE PASSIVE DAMPING TECHNOLOGY 189
Ahid D. Nashif, Anatrol Corporation, California

MATERIAL AND STRUCTURAL DYNAMIC PROPERTIES OF WOOD AND WOOD COMPOSITE PROFESSIONAL BASEBALL BATS 197
Robert D. Collier, Tufts University, Massachusetts

THE DAMPING EFFICIENCY OF METAL AND COMPOSITE PANELS 205
Richard M. Weyer, The Pennsylvania State University, Pennsylvania
Richard P. Szwerc, David Taylor Research Center, Maryland

DAMAGE INDUCED DAMPING CHARACTERISTICS OF GLASS REINFORCED EPOXY COMPOSITES 217
Max A. Gibbs and Mohan D. Rao, Michigan Technological University, Michigan
Anne B. Doucet, Louisiana State University, Louisiana

ON THE FLEXURAL DAMPING OF TWO MAGNESIUM ALLOYS AND A MAGNESIUM ALLOYS AND A MAGNESIUM METAL-MATRIX COMPOSITE 223
Graeme G. Wren, Royal Australian Air Force, Australia
Vikram K. Kinra, Texas A&M University, Texas

DAMPING IN AEROSPACE COMPOSITE MATERIALS 237
A. Agneni, L. Balis Crema, and A. Castellani, University of Rome, Italy

TRANSVERSE VIBRATION AND DAMPING ANALYSIS OF DOUBLE-STRAP JOINTS 249
Mohan D. Rao and Shulin He, Michigan Technological University, Michigan

DAMPED ADVANCED COMPOSITE PARTS 257
David John Barrett, Naval Air Development Center, Pennsylvania
Christopher A. Rotz, Brigham Young University, Utah

DAMPING OF LAMINATED COMPOSITE BEAMS WITH MULTIPLE VISCOELASTIC LAYERS 265
Shulin He and Mohan D. Rao, Michigan Technological University, Michigan

FUNDAMENTAL STUDY ON DEVELOPMENT OF HIGH-DAMPING STRUCTURAL CABLE 271
Hiroki Yamaguchi and Rajesh Adhikari, Asian Institute of Technology, Thailand

VISCOUS DAMPING OF LAYERED BEAMS WITH MIXED BOUNDARY CONDITIONS 279
Eugene T. Cottle, ASD/YZEE, Ohio

PASSIVE DAMPING APPLIED TO AIRCRAFT WING SKIN 287
Vincent J. Levraea, Jr. and Lynn C. Rogers, Wright-Patterson AFB, Ohio

MEASUREMENT OF DAMPING OF CONCRETE BEAMS: PASSIVE CONTROL OF PROPERTIES 295
Richard Kohoutek, University of Wollongong, Australia

ACTIVE CONTROL AND DAMPING 303

EXPERIMENTS ON THE ACTIVE CONTROL OF TRANSITIONAL BOUNDARY LAYERS 305
P.A. Nelson, J.-L. Rioual, and M.J. Fisher, Institute of Sound and Vibration Research, United Kingdom

RECENT ADVANCES IN ACTIVE NOISE CONTROL 313
D. Guicking, University of Göttingen, Germany

STOCHASTIC ACTIVE NOISE CONTROL 321
A.J. Efron and D. Graupe, University of Illinois at Chicago, Illinois

ACTIVE NOISE CONTROL WITH INDOOR POSITIONING SYSTEM 329
Kenji Fukumizu, Hiroo Kitagawa, and Masahide Yoneyama, RICOH Co, Ltd., Japan

A NEW TECHNIQUE FOR THE ACTIVE CANCELLATION OF WIDE-BAND NOISE USING MULTIPLE SENSORS 337
Felix Rosenthal, Naval Research Laboratory, Washington, D.C.

A GENERAL MULTI-CHANNEL FILTERED LMS ALGORITHM FOR 3-D ACTIVE NOISE CONTROL SYSTEMS 345
Sen M. Kuo and Brian M. Finn, Northern Illinois University, Illinois

TIME AND FREQUENCY DOMAIN X-BLOCK LMS ALGORITHMS FOR SINGLE CHANNEL ACTIVE NOISE CONTROL 353
Qun Shen, Active Noise and Vibration Technologies, Arizona
Andreas Spanias, Arizona State University, Arizona

ENERGY BASED CONTROL OF THE SOUND FIELD IN ENCLOSURES 361
Scott D. Sommerfeldt and Peter J. Nashif, The Pennsylvania State University, Pennsylvania

A PID CONTROLLER FOR FLEXIBLE SYSTEMS 369
A. Subbarao, University of Wisconsin - Parkside, Wisconsin
N.G. Creamer, Swales and Associates, Inc., Maryland
M. Levenson, Naval Research Laboratory, Washington, D.C.

NUMERICAL SIMULATION OF ACTIVE STRUCTURAL-ACOUSTIC CONTROL FOR A FLUID-LOADED SPHERICAL SHELL 377
C.E. Ruckman and C.R. Fuller, Virginia Polytechnic Institute and State University, Virginia

OPTIMUM LOCATION AND CONFIGURATION OF AN INTRA-STRUCTURAL FORCE ACTUATOR FOR MODAL CONTROL 387
Jeffrey S. Turcotte, Steven G. Webb, and Daniel J. Stech,
U.S. Air Force Academy, Colorado

DEVELOPMENT OF AN ACTIVE VIBRATION CONTROLLER FOR AN ELASTIC STRUCTURE 395
Douglas R. Browning and Raymond S. Medaugh, AT&T Bell Laboratories, New Jersey

ACTIVE VIBRATION CONTROL OF FLEXIBLE STRUCTURES USING THE SENUATOR 405
Shin Joon, Hahn Chang-Su, and Oh Jae-Eung, Hanyang University, Korea
Kim Do-Weon, Samsung Electronics, Korea

STRUCTURAL VIBRATION 411

RADIAL IMPULSIVE EXCITATION OF FLUID-FILLED ELASTIC CYLINDRICAL SHELLS 413
C.R. Fuller and B. Brévart, Virginia Polytechnic Institute and State University, Virginia

ROTOR DYNAMIC IMPACT DAMPER TEST RESULTS FOR SYNCHRONOUS AND SUBSYNCHRONOUS VIBRATION 425
Tim A. Nale and Steven A. Klusman, General Motors Corporation, Indiana

VIBRATION DESIGN OF SHAKERS LABORATORY OF THE NEW HONG KONG UNIVERSITY OF SCIENCE AND TECHNOLOGY 435
Westwood K.W. Hong and Nicholas J. Boulter, Arup Acoustics, Hong Kong

KEYNOTE ADDRESS 443
PROGRESS IN BOUNDARY ELEMENT CALCULATION AND OPTOELECTRONIC MEASUREMENT OF STRUCTUREBORNE SOUND 445
Lothar Gaul and Martin Schanz, University of the Federal Armed Forces Hamburg, Germany
Michael Plenge, JAFO Technology, Germany

SOUND-STRUCTURE INTERACTION AND TRANSMISSION OF SOUND AND VIBRATION 459

PLATE CHARACTERISTIC FUNCTIONS TO STUDY SOUND TRANSMISSION LOSS THROUGH PANELS 461
R.B. Bhat and G. Mundkur, Concordia University, Montreal, Canada

SOUND TRANSMISSION LOSS OF WALLBOARD PARTITIONS 469
Junichi Yoshimura, Kobayasi Institute of Physical Research, Japan

SOUND TRANSMISSION ANALYSIS BY COMPUTATIONAL MECHANICS USING CHARACTERISTIC IMPEDANCE DERIVED THROUGH A FINITE ELEMENTAL PROCEDURE 477
Toru Otsuru, Oita University, Japan

NEW METHOD FOR CALCULATION AND DESIGN NOISE ISOLATING ENCLOSURES 485
Ludmila Ph. Drozdova, Institute of Mechanics, Russia

EXPERIMENTAL RESEARCHES OF AIR- AND STRUCTURE-BORNE SOUND OF AGRICULTURAL MACHINES AND TRACTORS 493
Moissei A. Trakhtenbroit, VISKHOM Acoustic Laboratory, Russia

TIME DOMAIN APPROACH OF FLUID STRUCTURE INTERACTION PHENOMENA APPLICATION TO SATELLITE STRUCTURES 499
D. Vaucher de la Croix and C. Clerc, METRAVIB R.D.S., France
J.M. Parot, IMDYS, France

ACOUSTICS OF SHELLS WITH INTERNAL STRUCTURAL LOADING 507
Y.P. Guo, Massachusetts Institute of Technology, Massachusetts

LOW-FREQUENCY SOUND RADIATION AND INSULATION OF LIGHT PARTITIONS FILLING OPENINGS IN MASSIVE WALLS 515
Roman Y. Vinokur, Lasko Metal Products, Inc., Pennsylvania

THE TRANSMISSION OF VIBRATION WAVES THROUGH STRUCTURAL JUNCTIONS 523
Yan Tso, Defence Science and Technology Organization, Australia

THE SPATIAL-FREQUENCY CHARACTERISTICS OF SOUND INSULATION OF LAMINATED SHELLS 533
G.M. Avilova, N.N. Andreev Acoustics Institute, Russia

STATISTICAL ENERGY ANALYSIS AND ENERGY METHODS 539

MODELING AND ESTIMATING THE ENERGETICS OF COMPLEX STRUCTURAL SYSTEMS 541
G. Maidanik and J. Dickey, David Taylor Research Center, Maryland

AN ASSESSMENT OF THE MICROGRAVITY AND ACOUSTIC ENVIRONMENTS IN SPACE STATION FREEDOM USING VAPEPS 543
Thomas F. Bergen and Terry D. Scharton, Jet Propulsion Laboratory, California
Gloria A. Badilla, SYSCON Corporation, California

APPLICATION OF VAPEPS TO A NON-STATIONARY PROBLEM 551
L.K. St-Cyr and J.T. Chon, Rockwell International, California

DEVELOPMENT OF ENERGY METHODS APPLIED FOR CALCULATIONS OF VIBRATIONS OF ENGINEERING STRUCTURES 555
Sergei V. Budrin and Alexei S. Nikiforov, Krylov Shipbuilding Research Institute, Russia

THE STATISTICAL ENERGY ANALYSIS OF A CYLINDRICAL STRUCTURE 561
M. Blakemore and R.J.M. Myers, Topexpress Limited, United Kingdom
J. Woodhouse, University of Cambridge, United Kingdom

PREDICTION OF TRACKED VEHICLE NOISE USING SEA AND FINITE ELEMENTS 569
David C. Rennison and Paul G. Bremner, Vibro-Acoustic Sciences Limited, Australia

MEASUREMENT OF ENERGY FLOW ALONG PIPES 577
C.A.F. de Jong and J.W. Verheij, TNO Institute of Applied Physics, The Netherlands

COMPARISON OF MODE-TO-MODE POWER FLOW APPROXIMATION WITH GLOBAL SOLUTION FOR STEPPED BEAMS 585
Wu Qunli, Nanyang Technological University, Singapore

RECIPROCITY METHOD FOR QUANTIFICATION OF AIRBORNE SOUND TRANSFER FROM MACHINERY 591
Jan W. Verheij, TNO Institute of Applied Physics, The Netherlands

VIBRATIONAL RESPONSE OF COUPLED COMPOSITE BEAMS 599
C. Nataraj, Villanova University, Pennsylvania
P.K. Raju, Auburn University, Alabama

KEYNOTE ADDRESS 609
THE RECIPROCITY PRINCIPLE AND APPLICATIONS IN VIBRO-ACOUSTICS 611
F.J. Fahy, Institute of Sound and Vibration, United Kingdom

GENERAL SOUND AND VIBRATION PROBLEMS 619

FLOW-INDUCED VIBRATION PROBLEMS IN THE OIL, GAS AND POWER GENERATION INDUSTRIES - IDENTIFICATION AND DIAGNOSIS 621
M.P. Norton, University of Western Australia, Western Australia

IMPEDANCE OF A VISCOUS FLUID LAYER BETWEEN TWO PLATES 633
Michael A. Latcha, Oakland University, Michigan
Adnan Akay, Wayne State University, Michigan

VIBRATION SUPPRESSION IN THE BUILDING FLOORS BY THE SYSTEMS WITH OXIDE-MAGNETS 641
Villen P. Khomenko, Research Institute of Building Structures, Ukraine
Leonid N. Tulchinsky, Institute for Material Science Problems of AS of the Ukraine, Ukraine

RECIPROCAL DETERMINATION OF VOLUME VELOCITY OF A SOURCE IN AN ENCLOSURE 645
Bong-Ki Kim, Jin-Yeon Kim, and Jeong-Guon Ih, Korea Advanced Institute of Science & Technology, Korea

ANALYSIS OF FORCED ACOUSTIC FIELDS INSIDE STRUCTURALLY COUPLED CAVITIES 651
Arzu Gönenç and Mehmet Çalişkan, Middle East Technical University, Turkey

THEORETICAL AND EXPERIMENTAL ASPECTS OF ACOUSTIC MODELING OF ENGINE EXHAUST SYSTEMS WITH APPLICATIONS TO A VACUUM PUMP 659
B.S. Sridhara, Middle Tennessee State University, Tennessee
Malcolm J. Crocker, Auburn University, Alabama

RUSSIAN CHURCH BELL 667
Boris N. Njunin and Alexander S. Larucow, Moscow Automobile Plant (ZIL) Russia

A COMPARISON OF MEMBRANE, VACUUM, AND FLUID LOADED SPHERICAL SHELL MODELS WITH EXACT RESULTS 675
Cleon E. Dean, Stennis Space Center, Mississippi

EXPERIMENTAL STUDIES OF WAVE PROPAGATION IN A SUBMERGED, CAPPED CYLINDRICAL SHELL 683
Earl G. Williams, Naval Research Laboratory, Washington, D.C.

SOUND ABSORBING DUCTS 689
Alan Cummings, University of Hull, United Kingdom

DUCT ACOUSTICS: JUNCTIONS AND LATTICES, APPLICATION TO PERFORATED TUBE MUFFLERS 697
Jean Kergomard, Laboratoire d'acoustique de l'Université du Maine, France

EFFECTIVENESS OF IMPROVED METHOD AND TECHNIQUES FOR HVA DUCT SOUND ANALYSIS AND PREDICTION 703
Michihito Terao, Kanagawa University, Japan

FLOW DUCT SILENCER PERFORMANCE 711
J.L. Bento Coelho, CAPS-Instituto Superior Técnico, Portugal

MATRICES FOR PIPING ELEMENTS WITH FLOW 717
K.K. Botros, NOVA HUSKY Research Corporation, Calgary, Canada

RESONANT FREQUENCIES OF THE LONG PIPES 725
L.N. Kljachko, I.I. Novikov, and I.I. Ustelencev, Noise and Vibration Control Laboratory, Russia

GENERIC BUCKLING ANALYSIS OF ORTHOTROPIC PLATES WITH CLAMPED AND SIMPLY SUPPORTED EDGES 729
S.D. Yu and W.L. Cleghorn, University of Toronto, Canada

SOUND AND VIBRATION MEASUREMENTS 737

A FREQUENCY DOMAIN IDENTIFICATION SCHEME FOR DAMPED DISTRIBUTED PARAMETER SYSTEMS 739
R. Chander, Aerostructures, Inc., Virginia
M. Meyyappa, McDonnell Douglas Helicopter Co., Arizona
S. Hanagud, Georgia Institute of Technology, Georgia

ELASTIC BEHAVIOR OF MIXED Li-Zn AND Li-Cd FERRITES 745
D. Ravinder, Osmania University, India

OBSERVATION OF ELASTIC WAVE LOCALIZATION 753
Ling Ye, George Cody, Minyao Zhou, and Ping Sheng,
Exxon Research & Engineering Co., New Jersey
Andrew Norris, Rutgers University, New Jersey

FREE FIELD MEASUREMENT AT HIGH FREQUENCIES OF THE IMPEDANCE OF POROUS LAYERS 759
Jean F. Allard and Denis Lafarge, Université du Maine, France

EVALUATION OF A DYNAMIC MECHANICAL APPARATUS 763
Gilbert F. Lee, Naval Surface Warfare Center, Maryland

DETERMINING THE AMPLITUDE OF PROPAGATING WAVES AS A FUNCTION OF PHASE SPEED AND ARRIVAL TIME 771
J. Adin Mann III, Iowa State University, Iowa
Earl G. Williams, Naval Research Laboratory, Washington, D.C.

ISOLATING BUILDINGS FROM VIBRATION 779
David E. Newland, University of Cambridge, United Kingdom

LINEAR DYNAMIC BEHAVIOR OF VISCOUS COMPRESSIBLE FLUID LAYERS: APPLICATION OF A COMPLEX SQUEEZE NUMBER 787
T. Önsay, Michigan State University, Michigan

FUZZY COMPREHENSIVE EVALUATION OF SHOCK INTENSITY OF WARSHIP PROPULSIVE SYSTEM 795
Pang Jian, Wuhan Ship Development and Design Institute, China
Shen Rongying, Jiao Tong University, China

ON THE EVALUATION OF NOISE OF THE CAM TYPE MECHANISMS 803
A.J. Chistiakov and N.L. Suhanov, S.M. Kirov Institute of Textile and Light Industry, Russia

MULTIFUNCTIONAL CEILINGS 807
T.I. Galaktionova, Central Research and Design Institute of School Buildings, Russia

PHASE FEATURES OF MAN AND ANIMALS REACTION TO INFRASOUND EFFECT 811
B.J. Fraiman, Voronezh Electronics Plant, Voronezh
A.S. Faustov, Voronezh Medical Institute, Voronezh
A.N. Ivannikov and V.I. Pavlov, Moscow State University, Russia

MEASURING OF THE TURBULENCE AND SOUND ABOVE THE OCEAN 815
A.N. Ivannikov, S.V. Makeev, and V.I. Paviov, Moscow State University, Russia

COMPARISON TESTS BETWEEN ACOUSTIC EMISSION TRANSDUCERS
FOR INDUSTRIAL APPLICATIONS 821
S.C. Kerkyras, P.A. Drakatos and K.L. Tzanetos, University of Patras, Greece
W.K.D. Borthwick, CEC Brite Directorate
R.L. Reuben, Heriot-Watt University, United Kingdom

USING A CIRCUMFERENTIAL TRANSDUCER TO MEASURE INTERNAL
PRESSURES WITHIN A PIPE 829
R.J. Pinnington and A. Briscoe, University of Southampton, England

CONDITION OF OLD MACHINES IN THE LIGHT OF
VARIOUS VIBRATION STANDARDS 837
R.L. Murty, Regional Engineering College, India

PHOTOACOUSTIC METHOD OF THE DETERMINATION OF AMPLITUDE
NON-RECIPROCALNESS IN GYROTROPIC MEDIA 845
G.S. Mityurich, V.P. Zelyony, V.V. Sviridova, and A.N. Serdyukov,
Gomel State University, The Republic of Byelorus

A SOLUTION TO THE NOISE PREDICTION PROBLEM AT LOW FREQUENCIES 847
Yurii I. Bobrovnitskii, Blagonravov Institute of Engineering Research, Russia

A PARALLEL PATH DIFFERENCE ON-LINE MODELLING ALGORITHM FOR
ACTIVE NOISE CANCELLATION 851
Yong Yan and Sen M. Kuo, Northern Illinois University, Illinois

STUDIES OF THE BUILDING CONSTRUCTIONS BY MEANS OF
NONLINEAR DIAGNOSTICS 859
A.E. Ekimov, I.I. Kolodieva, and P.I. Korotin, Academy of Sciences of the USSR, Russia

MEASUREMENT OF ACOUSTIC POWER OF FANS UNDER CONDITIONS OF
REVERBERANT NOISE OF AERODYNAMIC TEST RIG 863
V.M. Kazarov, V.G. Karadgi, and A.S. Mirskov,
Central Aerohydrodynamics Institute (TSAGI), Russia

STATISTICS OF REVERBERANT TRANSFER FUNCTIONS 869
Mikio Tohyama and Tsunehiko Koike, NTT Human Interface Laboratories, Japan
Richard H. Lyon, Massachusetts Institute of Technology, Massachusetts

KEYNOTE ADDRESS 877
OVERVIEW OF ACOUSTICAL TECHNOLOGY FOR NONDESTRUCTIVE EVALUATION 879
Robert E. Green, Jr., The Johns Hopkins University, Maryland

MATERIAL CHARACTERIZATION AND NON-DESTRUCTIVE EVALUATION 887

ANALYTICAL DETERMINATION OF DYNAMIC STRESS ON PRACTICAL CEMENT
MILLS USING RANDOM VIBRATION CONCEPT 889
V. Ramamurti, University of Toledo, Ohio
C. Sujatha, Indian Institute of Technology, India

EVALUATION OF ACOUSTIC EMISSION SOURCE LOCATION FOR DIFFERENT THREE-SENSOR ARRAY CONFIGURATIONS 897
Vasisht Venkatesh and J.R. Houghton, Tennessee Technological University, Tennessee

DEFECTS DETECTION IN STRUCTURES AND CONSTRUCTIONS BY NOISE SIGNALS DIAGNOSTICS METHODS 905
Vadim A. Robsman, Union "Electronics of Russia," Russia

TOOL FAILURE DETECTION USING VIBRATION DATA 909
T.N. Moore, Queen's University, Kingston, Canada
J. Pei, Stelco, Hamilton, Canada

PHOTOACOUSTIC METHOD APPLICATION QUALITY CONTROL OF ULTRACLEAN WATER 917
Alekxei M. Brodnikovskii and Vladimir A. Sivovolov, Institute of Electronic Machinery, Russia

ULTRASONIC MEASUREMENTS 919
Vinay Dayal, Iowa State University, Iowa

EVALUATION OF LAMINATED COMPOSITE STRUCTURES USING ULTRASONIC ATTENUATION MEASUREMENT 927
Peitao Shen and J. Richard Houghton, Tennessee Technological University, Tennessee

EXPERT SYSTEM FOR ULTRASONIC FLAW DETECTOR 935
A.N. Agarwal, S.C. Suri, and M.S. Bageshwar, Central Scientific Instruments Organization, India

BOUNDARY ELEMENTS AND FINITE ELEMENTS 943

RECENT APPLICATIONS OF BOUNDARY ELEMENT MODELING IN ACOUSTICS 945
A.F. Seybert, T.W. Wu, and G.C. Wan, University of Kentucky, Kentucky

NUMERICAL MODELING OF PERFORATED REACTIVE MUFFLERS 957
S.H. Jia, A.R. Mohanty, and A.F. Seybert, University of Kentucky, Kentucky

ON SELECTING CHIEF POINTS TO OVERCOME THE NONUNIQUENESS PROBLEM IN BOUNDARY ELEMENT METHODS 965
Peter M. Juhl, Technical University of Denmark, Denmark

IMPLEMENTATION OF BOUNDARY ELEMENT METHOD FOR SOLVING ACOUSTIC PROBLEMS ON A MASSIVELY PARALLEL MACHINE 973
A. Dubey, M. Zubair, and U.S. Shirahatti, Old Dominion University, Virginia

SOUND RADIATION OF HEAVY-LOADED COMPLEX VIBRATORY STRUCTURES USING BOUNDARY INTEGRAL EQUATION METHOD 983
Michael V. Bernblit, St. Petersburg Ocean Technology University, Russia

OBTAINING OF UNIQUE SOLUTION OF A SOUND RADIATION AND SCATTERING PROBLEM USING A BEM BASED OF THE HELMHOLTZ'S INTEGRAL 989
I.E. Tsukernikov, Scientific and Industry Amalgamation "MIR," Russia

ISOPARAMETRIC BOUNDARY ELEMENT MODELING OF ACOUSTICAL CRACKS 993
T.W. Wu and G.C. Wan, University of Kentucky, Kentucky

A SOLUTION METHOD FOR ACOUSTIC BOUNDARY ELEMENT EIGENPROBLEM WITH SOUND ABSORPTION USING LANCZOS ALGORITHM 1001
C. Rajakumar and Ashraf Ali, Swanson Analysis Systems, Inc., Pennsylvania

THEORETICAL AND PRACTICAL CONSTRAINTS ON THE IMPLEMENTATION OF ACTIVE ACOUSTIC BOUNDARY ELEMENTS 1011
P. Darlington and G.C. Nicholson, University of Salford, United Kingdom

BOUNDARY ELEMENT FORMULATIONS FOR ACOUSTIC SENSITIVITIES WITH RESPECT TO STRUCTURAL DESIGN VARIABLES AND ACOUSTIC IMPEDANCE 1019
Nickolas Vlahopoulos, Automated Analysis Corporation, Michigan

MODELLING RADIATION FROM SUBMERGED STRUCTURES: A COMPARISON OF BOUNDARY ELEMENT AND FINITE ELEMENT TECHNIQUES 1027
Jean-Pierre G. Coyette, Numerical Integration Technologies, N.V., Belgium

FINITE ELEMENT MODELING OF VISCOELASTIC DAMPERS 1037
A. Gupta, M.J. Kim, and A.H. Marchertas, Northern Illinois University, Illinois

THE METHOD OF MODAL PARAMETERS TO DETERMINE THE BOUNDARY CONDITION OF FINITE ELEMENT MODEL 1045
Wang Fengquan and Chen Shiyu, Southeast University, China

VIBRATION AND EIGENVALUE ANALYSIS USING FINITE ELEMENTS 1053
Tirupathi R. Chandrupatla, GMI Engineering and Management Institute, Michigan
Ashok D. Belegundu, The Pennsylvania State University, Pennsylvania

DYNAMIC ANALYSIS OF PRACTICAL BLADED DISKS USING FEM AND CYCLIC SYMMETRY TECHNIQUES 1061
A.S. Panwalkar and A. Rajamani, Bharat Heavy Electricals Limited, India
V. Ramamurti, Indian Institute of Technology, India

KEYNOTE ADDRESS 1073
UNDERWATER ACOUSTIC SCATTERING 1075
Louis R. Dragonette, Naval Research Laboratory, Washington, D.C.

SOUND PROPAGATION, RADIATION AND SCATTERING 1085

SOUND BACKSCATTERING FROM OCEAN BOTTOM 1087
Anatoly N. Ivakin, N. N. Andreev Acoustics Institute, Russia

LABORATORY SIMULATION OF POINT MONOPOLE AND POINT DIPOLE SOUND SOURCES 1093
K. K. Ahuja, Georgia Institute of Technology, Georgia

RECONSTRUCTION OF SURFACE ACOUSTIC FIELD FROM MEASUREMENTS OF PRESSURE OVER A LIMITED SURFACE 1103
Angie Sarkissian, Charles F. Gaumond, Earl G. Williams, and Brian H. Houston, Naval Research Laboratory, Washington, D.C.

SCATTERING OF SOUND BY STRONG TURBULENCE AND CONDITIONS OF CHERENKOV RADIATION 1111
Vadim I. Pavlov and Oleg A. Kharin, Moscow State University, Russia

RECOGNITION OF UNDERWATER TARGETS BY MEANS OF RESONANCES IN THEIR SONAR ECHOES 1117
Guillermo C. Gaunaurd, Naval Surface Warfare Center, Maryland
Hans C. Strifors, National Defense Research Establishment, Sweden

HIGH-FREQUENCY ELASTIC WAVES EXCITED WITHIN THE STRUCTURE OF A SPHERICAL SHELL BY INCIDENT SOUND IN WATER 1125
Robert Hickling and James F. Ball, University of Mississippi, Mississippi

ELEMENTS, EIGENFUNCTIONS AND INTEGRAL EQUATIONS IN FLUID-STRUCTURE INTERACTION PROBLEMS 1133
Richard P. Shaw, S.U.N.Y. at Buffalo, New York

FAR-FIELD RADIATION FROM A LINE-DRIVEN FLUID-LOADED INFINITE FLAT PLATE WITH ATTACHED RIB STIFFENERS HAVING ADJUSTABLE ATTACHMENT LOCATIONS 1141
Benjamin A. Cray, Naval Underwater Systems Center, Connecticut

THE EFFICIENCY OF LAYERED HOUSING WITH ARBITRARY SHAPE 1149
Samual A. Rybak, N. N. Andreev Acoustics Institute, Russia

SOUND RADIATION BY STRUCTURES WITH DISCONTINUITIES 1151
P.I. Korotin and A.V. Lebedev, Academy of Sciences of the USSR, Russia

A NEW APPROACH TO THE ANALYSIS OF SOUND RADIATION FROM FORCED VIBRATING STRUCTURES 1157
T.M. Tomilina, Blagonravov Institute of Engineering Research, Russia

THE ASYMPTOTIC METHOD FOR PREDICTING ACOUSTIC RADIATION FROM A CYLINDRICAL SHELL OF FINITE LENGTH 1163
A. V. Lebedev, Academy of Sciences of the USSR, Russia

STRUCTURAL RESPONSE AND RADIATION OF FLUID-LOADED STRUCTURES DUE TO POINT-LOADS 1171
Chafic M. Hammoud and Per G. Reinhall, University of Washington, Washington

ACOUSTICAL IMAGES OF SCATTERING MECHANISMS FROM A CYLINDRICAL SHELL 1179
Charles F. Gaumond and Angie Sarkissian, Naval Research Laboratory, Washington, D.C.

CALCULATION OF SOUND RADIATION FROM COMPLEX STRUCTURES USING THE MULTIPOLE RADIATOR SYNTHESIS WITH OPTIMIZED SOURCE LOCATIONS 1187
Martin Ochmann, Technische Fachhochschule Berlin, Germany

RADIATION AND SCATTERING AT OBLIQUE INCIDENCE FROM SUBMERGED OBLONG ELASTIC BODIES 1195
Herbert Überall and X. L. Bao, Catholic University of America, Washington, D.C.
Russel D. Miller, NKF Engineering, Virginia
Michael F. Werby, Stennis Space Center, Mississippi

RAY REPRESENTATIONS OF THE BACKSCATTERING OF TONE BURSTS BY SHELLS IN WATER: CALCULATIONS AND RELATED EXPERIMENTS 1203
Philip L. Marston, Ligang Zhang, Naihua Sun, Greg Kaduchak, and David H. Hughes, Washington State University, Washington

VIBRATIONS, SOUND RADIATION AND SCATTERING BY SHELLS WITH ARBITRARY SHAPE 1211
Vadim V. Muzychenko, N. N. Andreev Acoustics Institute, Russia

SOUND RADIATION AND PROPAGATION IN CENTRIFUGAL MACHINE PIPING 1219
Danielius Guzhas, Vilnius Technical University, Lithuania

SOUND RADIATION BY A SUBMERGED CYLINDRICAL SHELL CONTAINING INHOMOGENEITIES 1227
Aleksander Klauson and Jaan Metsaveer, Tallinn Technical University, Estonia

SPACE TIME ANALYSIS OF SOUND RADIATION AND SCATTERING 1235
C. Clerc and D. Vaucher de la Croix, METRAVIB R.D.S., France

VIBRATIONAL AND ACOUSTIC RESPONSE OF A RIBBED INFINITE PLATE EXCITED BY A FORCE APPLIED TO THE RIB 1243
Ten-Bin Juang, Anna L. Pate, and Alison B. Flatau, Iowa State University, Iowa

ANALYTICAL AND EXPERIMENTAL DETERMINATION OF THE VIBRATION AND PRESSURE RADIATION FROM A SUBMERGED, STIFFENED CYLINDRICAL SHELL WITH TWO END PLATES 1253
A. Harari and B.E. Sandman, Naval Undersea Warfare Center Division, Rhode Island
J.A. Zaldonis, Westinghouse Corporation, Pennsylvania

SPREADING LOSSES IN OUTDOOR SOUND PROPAGATION 1255
Louis C. Sutherland, Rancho Palos Verdes, California

SOUND PROPAGATION 1261
Marinus M. Boone, Delft University of Technology, The Netherlands

WEATHER EFFECTS ON SOUND PROPAGATION NEAR THE GROUND 1269
Conny Larsson, Uppsala University, Sweden

PROPAGATION OF SOUND THROUGH THE FLUCTUATING ATMOSPHERE 1277
D. Keith Wilson, The Pennsylvania State University, Pennsylvania

SOUND SHIELDING BY BARRIERS WITH CERTAIN SPECIAL TREATMENTS 1285
Kyoji Fujiwara, Kyushu Institute of Design, Japan

SOUND INTENSITY, STRUCTURAL INTENSITY AND SOUND FIELD SPATIAL TRANSFORMATION 1291

SOUND POWER DETERMINATION BY MANUAL SCANNING OF ACOUSTIC INTENSITY 1293
Michael Bockhoff, CETIM, France
Ondreij Jiricek, Technical University Prague, Czechoslovakia

THE INFLUENCE OF ELECTRICAL NOISE OF MEASUREMENT OF SOUND INTENSITY 1299
Finn Jacobsen, Technical University of Denmark, Denmark

INTERFERENCE EFFECTS IN SOUND INTENSITY FIELD OF SIMPLE SOURCES 1307
M.G. Prasad and W.S. Kim, Stevens Institute of Technology, New Jersey

EXPERIMENTAL STUDY ON THE APPLICATION OF UNDERWATER ACOUSTIC INTENSITY MEASUREMENTS 1315
Eric Stusnick and Michael J. Lucas, Wyle Laboratories, Virginia

INTENSITY MEASUREMENTS USING 4-MICROPHONE PROBE 1327
I.V. Lebedeva and S.P. Dragan, Moscow State University, Russia

USE OF REFERENCES FOR INCLUSION AND EXCLUSION OF PARTIAL SOUND SOURCES WITH THE STSF TECHNIQUE 1331
Jørgen Hald, Brüel & Kjær Industri A/S, Denmark

IMPEDANCE-RELATED MEASUREMENTS USING INTENSITY TECHNIQUES 1337
Tapio Lahti, Finnish Acoustics Centre Ltd., Finland

ENERGETIC DESCRIPTION OF THE SOUND FIELD AND DETERMINATION OF THE SOURCE'S PARAMETERS BY THE SPACE INTENSITY SENSOR 1345
A.N. Ivannikov, V.I. Pavlov, and S.V. Holodova, Moscow State University, Russia

MEASUREMENT OF STRUCTURAL INTENSITY IN THIN PLATES USING A FAR FIELD PROBE 1353
A. Mitjavila, S. Pauzin, and D. Biron, CERT ONERA DERMES, France

FREQUENCY-WAVENUMBER ANALYSIS OF STRUCTURAL INTENSITY 1361
J.M. Cuschieri, Florida Atlantic University, Florida

SOUND AND VIBRATION ANALYSIS 1369

SEPARATION OF MULTIPLE DISPERSIVE STRUCTUREBORNE TRANSMISSION PATHS USING TIME RECOMPRESSION 1371
Eric Hoenes and Alan Sorensen, Tracor Applied Sciences, Texas

DYNAMIC MECHANICAL PROPERTIES OF VISCOELASTIC MATERIALS 1379
Surendra N. Ganeriwala, Philip Morris Research Center, Virginia

A NEW APPROACH TO LOW FREQUENCY AEROACOUSTIC PROBLEM DECISIONS BASED ON THE VECTOR-PHASE METHODS 1387
V.A. Gordienko, B.I. Goncharenko, and A.A. Koropchenko, Moscow State University, Russia

VIBRATION OF STEEL SHEETS OF THE SHEET-PILER 1395
L.N. Kljachko and I.I. Novikov, VNIITBchernet, Russia

VIBRATION REDUCTION IN INDEXABLE DRILLING 1399
W. Xue and V.C. Venkatesh, Tennessee Technological University, Tennessee

FREE ASYMMETRIC VIBRATIONS OF LAYERED CONICAL SHELLS BY COLLOCATION WITH SPLINES 1405
P.V. Navaneethakrishnan, Anna University, India

ONE OF THE METHODS OF EXPRESS-CONTROL OF THE SOUND-CAPACITY MACHINES 1413
V. Didkovsky and P. Markelov, Kiev Politechnics, Ukraine

AUTOMOBILE DIAGNOSTIC EXPERT SYSTEM BY NOISE AND VIBRATION 1419
Joon Shin and Jae-Eung Oh, Hanyang University, Korea

NOISE AND VIBRATION PROTECTION AT SOVIET COAL MINING ENTERPRISES 1425
V.B. Pavelyev and Yu V. Flavitsky, Skochinsky Institute of Mining, Russia

ADVANCED TECHNIQUES FOR PUMP ACOUSTIC AND VIBRATIONAL PERFORMANCE OPTIMIZATION 1429
E. Carletti and G. Miccoli, National Research Council of Italy, Italy

STATISTICAL ACOUSTICS THEORY APPLICATIONS FOR NOISE ANALYSIS IN TRANSPORT VEHICLES 1437
Nickolay I. Ivanov and Georgiy M. Kurtzev, The Institute of Mechanics, Russia

AUTOMATED SYSTEM FOR CALCULATING THE LIMIT OF ADMISSIBLE NOISE CHARACTERISTICS OF INDUSTRIAL EQUIPMENT 1445
I.E. Tsukernikov and B.A. Seliverstov, Scientific and Industry Amalgamation "MIR," Russia

CALCULATION OF NOISE REDUCTION PROVIDED BY FLEXIBLE SCREENS (BARRIERS) FOR PRINTING MACHINES 1449
Boris I. Klimov and Natalia V. Sizova, Scientific - Research Institute of Printing Machinery, Russia

ECONOMIC EVALUATION OF INDUSTRIAL NOISE SILENCERS 1455
Olga A. Afonina and Natalya V. Dalmatova, Moscow Aviation Institute, Russia

SPECTRUM VARIATIONS DUE TO ARCHITECTURAL TREATMENT AND ITS RELATION TO NOISE CONTROL 1459
O.A. Alim and N.A. Zaki, Alexandria University, Egypt

INTERNAL COMBUSTION ENGINE STRUCTURE NOISE DECREASE OWING TO THE COEFFICIENT CHANGE OF NOISE RADIATION OF ITS ELEMENTS 1465
Rudolf N. Starobinsky, Polytechnical Institute, Russia
Michael I. Fessina, Volga Automobile Associated Works, Russia

FORMULATION OF THE INTERIOR ACOUSTIC FIELDS FOR PASSENGER VEHICLE COMPARTMENTS 1475
Şadi Kopuz, Y. Samim Ünlüsoy, and Mehmet Çalişkan, Middle East Technical University, Turkey

NOISE FROM LARGE WIND TURBINES: SOME RECENT SWEDISH DEVELOPMENTS 1481
Sten Ljunggren, DNV INGEMANSSON AB, Sweden

NOISE FROM WIND TURBINES, A REVIEW 1489
H.W. Jones, Hugh Jones & Associates Limited, Tantallon, Canada

SOUND POWER DETERMINATION OF FANS BY TWO SURFACE METHOD 1497
Kalman Szabó, Gyula Hetenyi, and Laszlo Schmidt, Ventilation Works, Hungary

ACOUSTIC RADIATION FROM FLAT PLATES WITH CUTOUT THROUGH FE ANALYSIS 1505
PV Ramana Murti, JNTU University, India
V Bhujanga Rao and PVS Ganesh Kumar, N.S.T.L., India

ILLUSTRATIONS OF NUMERICAL PREDICTION OF SOUND FIELDS 1513
G. Rosenhouse, Technion-Israel Institute of Technology, Haifa

ASPECTS REGARDING CAVITATION OCCURRENCE DURING THE NORMAL OPERATION OF CENTRIFUGAL PUMPS 1521
L. Comănescu, INCERC-Acoustic Laboratory, Romania
A. Stan, Academia Română, Romania

A SIMPLE LASER DEVICE FOR NONCONTACT VIBRATIONAL AMPLITUDE MEASUREMENT OF SOLIDS 1525
Alexei M. Brodnikovskii, R&D Center "Praktik," Russia

THE OPTIMIZATION OF NONLINEAR VEHICLE SYSTEMS USING RANDOM ANALYSIS 1527
Fangning Sun, Chengde Li, Jianjun Gao, and Pamela Banks-Lee, North Carolina State University, North Carolina

THE TRANSMISSION OF AERODYNAMICALLY-GENERATED NOISE THROUGH PANELS IN AUTOMOBILES 1535
John R. Callister, General Motors Proving Ground, Michigan
Albert R. George, Cornell University, New York

EXPERIMENTAL STUDY OF TRANSFER FUNCTION MEASUREMENTS USING LEAST-MEAN-SQUARE ADAPTIVE APPROACH 1543
Jiawei Lu, United Technologies Carrier, New York
Malcolm J. Crocker and P.K. Raju, Auburn University, Alabama

KEYNOTE ADDRESS 1553
FUTURE DEVELOPMENTS IN EXPERIMENTAL MODAL ANALYSIS 1555
David Brown, University of Cincinnati, Ohio

MODAL ANALYSIS AND SYNTHESIS 1565

DIRECT UPDATING OF NONCONSERVATIVE FINITE ELEMENT MODELS USING MEASURED INPUT-OUTPUT 1567
S.R. Ibrahim, Old Dominion University, Virginia
W. D'Ambrogio, P. Salvini, and A. Sestieri, Universitá di Roma, Italy

CURVATURE EFFECTS ON STRUCTURAL VIBRATION: MODAL LATTICE DOMAIN APPROACH 1581
Jeung-tae Kim, Korea Standards Research Institute, Korea

THE EFFECT OF HEAVY FLUID LOADING ON EIGENVALUE LOCI VEERING AND MODE LOCALIZATION PHENOMENA 1587
Jerry H. Ginsberg, Georgia Institute of Technology, Georgia

MODAL ANALYSIS OF GYROSCOPICALLY COUPLED SOUND-STRUCTURE INTERACTION PROBLEMS 1595
Vijay B. Bokil and U.S. Shirahatti, Old Dominion University, Virginia

A SIMPLE METHOD OF STRUCTURAL PARAMETER MODIFICATION FOR A MDOF SYSTEM 1603
Q. Chen and C. Levy, Florida International University, Florida

APPLICATION OF LOCALIZED MODES IN VIBRATION CONTROL 1611
Daryoush Allaei, QRDC, Inc., Mississippi

MODAL ANALYSIS AND SYNTHESIS OF CHAMBER MUFFLERS 1619
Rudolf N. Starobinsky, Togliatti Polytechnical Institute, Russia

LATE PAPERS 1625

EVALUATION OF ADAPTIVE FILTERING TECHNIQUES FOR ACTIVE NOISE CONTROL 1627
J.C. Stevens and K.K. Ahuja, Georgia Institute of Technology, Georgia

EFFECT OF CYLINDER LENGTH ON VORTEX SHEDDING SOUND IN THE NEAR FIELD 1637
J.T. Martin and K.K. Ahuja, Georgia Institute of Technology, Georgia

SCATTERING FROM INHOMOGENEOUS PLANAR STRUCTURES 1647
William K. Blake and David Feit, Naval Surface Warfare Center, Maryland

AN INFERENTIAL TREATMENT OF RESONANCE SCATTERING FROM ELASTIC SHELLS 1653
M.F. Werby, Stennis Space Center, Mississippi
H. Überall, Catholic University of America, Washington, D.C.

SOUND POWER DETERMINATION OF A MULTINOISE SOURCE SYSTEM USING SOUND INTENSITY TECHNIQUE 1661
Mirko Čudina, University of Ljubljana, Slovenia

CALCULATION METHOD OF SOUND FIELDS IN INDUSTRIAL HALLS 1669
V.I. Ledenyov and A.I. Antonov, Tambov Institute of Chemical Machine Building, Russia

AN APPROXIMATE MODAL POWER FLOW FORMULATION FOR LINE-COUPLED STRUCTURES 1673
Paul G. Bremner, Paris Constantine and David C. Rennison,
Vibro-Acoustic Sciences Limited, Australia

NONDESTRUCTIVE EVALUATION OF CARBON-CARBON COMPOSITES 1681
U.K. Vaidya, P.K. Raju, M.J. Crocker and J.R. Patel, Auburn University, Alabama

ACOUSTIC WAVES EMISSION AND AMPLIFICATION IN FERROELECTRIC CERAMIC LAYER WITH NONSTATIONARY ANISOTROPY INDUCED BY THE ROTATING ELECTRIC FIELD 1687
I.V. Semchenko, A.N. Serdyukov and S.A. Khakhomov, Gomel State University,
The Republic of Byelarus

AUTHOR INDEX

KEYNOTE ADDRESSES

		PAGE
1.	Sir James Lighthill A GENERAL INTRODUCTION TO AEROACOUSTICS AND ATMOSPHERIC SOUND	5
2.	Lothar Gaul, Martin Schanz and Michael Plenge PROGRESS IN BOUNDARY ELEMENT CALCULATION AND OPTOELECTRONIC MEASUREMENT OF STRUCTUREBORNE SOUND	445
3.	Frank J. Fahy THE RECIPROCITY *PRINCIPLE AND APPLICATIONS IN VIBRO-* ACOUSTICS	611
4.	Robert E. Green, Jr. OVERVIEW OF ACOUSTICAL TECHNOLOGY FOR NONDESTRUCTIVE EVALUATION	879
5.	Louis R. Dragonette UNDERWATER ACOUSTIC SCATTERING	1075
6.	David Brown FUTURE DEVELOPMENTS IN EXPERIMENTAL MODAL ANALYSIS	1555

KEYNOTE ADDRESS

THE RECIPROCITY PRINCIPLE AND APPLICATIONS IN VIBRO-ACOUSTICS

Frank J. Fahy

SECOND INTERNATIONAL CONGRESS ON
RECENT DEVELOPMENTS IN AIR- AND
STRUCTURE-BORNE SOUND AND VIBRATION
MARCH 4-6, 1992 AUBURN UNIVERSITY, USA

THE RECIPROCITY PRINCIPLE AND APPLICATIONS IN VIBRO-ACOUSTICS

F J Fahy
Institute of Sound & Vibration Research
University of Southampton
England

ABSTRACT

Lord Rayleigh postulated the general theory of vibro-acoustic reciprocity in 1873, and in 1959 Lyamshev confirmed and elaborated it in application to vibrational interaction between elastic shells and compressible fluids. In many cases of sound radiation from vibrating structures, and of structural response to incident sound, reciprocal measurements of transfer functions are often cheaper, less labour intensive, more convenient and more accurate than the equivalent direct measurements. This paper summarizes the basic principles of vibro-acoustic reciprocity and illustrates its benefits by application to a wide range of practical problems.

1. INTRODUCTION

In its most general sense, the principle of reciprocity states that the vibrational response of a linear system to a time-harmonic disturbance which is applied at some point by an external agent, is invariant with respect to exchange of the points of input and observed response.

The Hon. J W Strutt (Lord Rayleigh) presented the most comprehensive proposition of the general principle of reciprocity for vibrating systems in a paper read before the Mathematical Society of London in 1873. However, it was the great German scientist Hermann von Helmholtz, who first asserted that acoustic fields exhibited reciprocity, in a paper of 1860 on the acoustic behaviour of open-ended pipes. He subsequently formalised his expression of the principle as applying to simple sources (point volumetric monopoles) and field point pressures, in the presence of an arbitrary number and form of rigid scatterers in the fluid.

In a development of crucial significance for the practical application of reciprocity, Rayleigh demonstrated that the principle can be extended to harmonic vibration of all *non-conservative* (dissipative) vibrating systems in which the dissipative forces are linearly dependent upon the velocities, or relative velocities, of the system elements. He concluded his 1873 paper by stating, in relation to acoustic reciprocity, that "*we are now in a position to assert that* (acoustic)*reciprocity will not be interfered with, whatever the number of strings, membranes, forks, etc. may be present, even though they are subject to damping*". Rayleigh was aware that his reciprocity theorem 'on account of its extreme generality, may appear vague'. In this he was indeed prescient. It was not until 1959 that the Russian scientist L M Lyamshev published a formal proof of the correctness of this supposition, and paved the way for many of the modern applications of the principle of reciprocity to vibro-acoustic problems, as described below.

2. RAYLEIGH AND RECIPROCITY

2.1 Vibrational Reciprocity

In the 'Acoustician's Bible', *The Theory of Sound*, Rayleigh presents explicit examples which clarify the implications of his theory. These are important, because they demonstrate applications in which forces and couples, and translational and rotational displacements are involved. The cases are illustrated in Fig 1, in which the tilde indicates complex amplitude of a harmonically varying quantity.

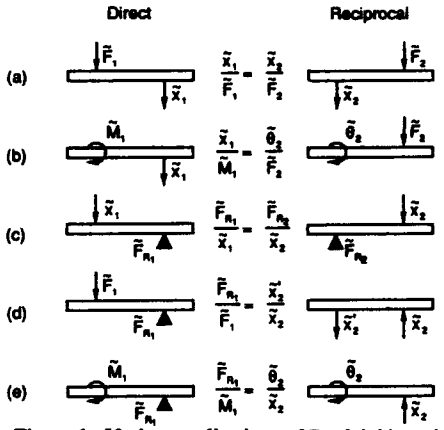

Figure 1. Various realisations of Rayleigh's reciprocity principle
[~ indicates complex amplitude of a time-harmonic quantity].

Reciprocity for transient, or non-periodic, events is not satisifed for mechanical systems with arbitrary distributions of non-velocity-dependent damping, such as the hysteretic loss model, often assumed to represent structural damping.

2.2 Acoustic Reciprocity

A homogeneous fluid at rest behaves like a linear elastic medium in response to small applied disturbances. In air, energy dissipation arises from visco-thermal, and molecular relaxation mechanisms, but, in cases of practical interest in the field of vibro-acoustics, dissipative effects are weak, and reciprocity is found to apply. The physical cases of primary practical interest are, however, rather different in the cases of fluids and solid structures. In a fluid, it is difficult to generate a known force in a known direction, and also difficult to measure particle velocity (at least it used to be). On the other hand, the fundamental acoustic source (the point monopole) displaces fluid at a rate described by its volume velocity Q, and the most common form of acoustic transducer, the pressure microphone, transduces the force F applied by the fluid to its diaphragm. Hence, provided that this force is not significantly altered by diaphragm motion, and that the microphone diaphragm is small compared with an acoustic wavelength (omni-directional), this system should exhibit reciprocal behaviour in the ratio F/Q, according to Rayleigh's principle. In fact, Rayleigh also extended the reciprocity relationship to acoustic dipoles and particle velocities in the resulting sound fields. Since a point dipole can also be represented by a point force applied to a fluid, this should not cause any surprise. This latter form of acoustic reciprocity does not seem to have found much practical application, but readers who can think of some might wish to communicate with the author. The basic cases of acoustic reciprocity in fluids are illustrated by Fig 2.

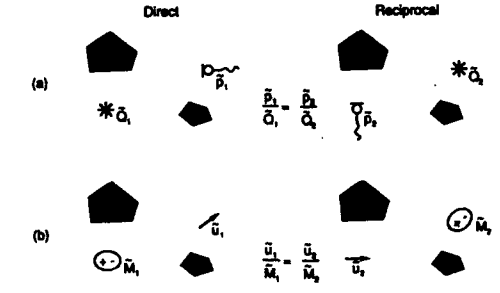

Figure 2. Acoustic reciprocity in fluids (a) monopole source (b) dipole source

3. FLUID BOUNDARIES

The question of the influence of the dynamic behaviour of the boundaries of a fluid on the validity of the acoustic reciprocity principle has exercised the minds of many scientists [See Ref.1]. Rayleigh and Helmholtz implied that the presence of *locally reacting boundaries*, or, in modern parlance, *impedance* boundaries, does not invalidate reciprocity. Later, Skudrzyk [11] confirmed the correctness of their conclusion. It would appear that the above-mentioned confined their analyses to locally reacting surfaces because the associated impedance boundary condition can readily be incorporated into the acoustic equations. However, the implication of Rayleigh's general reciprocity principle is that all components taking part in the dynamic behaviour can be incorporated into the total system, subject to the *proviso* that their kinetic, potential and dissipational energy functions are positive definite quadratic functions of velocity. The practical implications for the application of reciprocity to vibro-acoustic problems are profound. It is surprising that it was nearly a hundred years before Lyamshev formally demonstrated that elastic structures which are contiguous with a fluid may be incorporated into the total dynamic system to which reciprocity applies [5,6]. Vibro-acoustic reciprocity as applied to elastic systems such as plates and shells is illustrated by Fig 3.

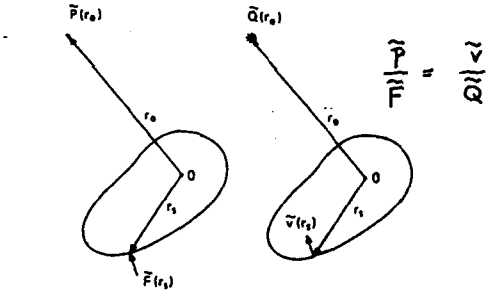

Figure 3. Lyamshev reciprocity relationship for elastic structures excited by a point force.

4. DISSIPATIVE BOUNDARIES AND SOUND ABSORBERS

The question of the validity of the vibro-acoustic reciprocity principle in the presence of dissipative mechanisms of the type exhibited by porous sound absorbers is a vexed one. Jannssen [15] concluded that the presence of gyrostatic terms in the governing equations of porous sound absorbers invalidates reciprocity: but ten Wolde [13] discounts this conclusion as an artefact of the model selected, which is phenomenological, and therefore inexact. In *The Theory of Sound*, Rayleigh argues that even dissipation due to thermal conduction or radiation is not expected to invalidate reciprocity under conditions of *harmonic* excitation, tentatively suggesting that "the theorem is perhaps sufficiently general to cover the whole field of dissipative forces." The theoretical arguements could continue indefinitely, but the rather limited amount of experimental evidence published to date suggests that reciprocity holds except where dissipation derives from the generation of turbulent flows (eg in IC engine exhaust silencers), and/or where non-linear fluid dynamic mechanisms operate (eg in aircraft engine intake absorbers operating at extremely high sound levels). Perhaps some readers might like to contribute new experimental evidence relevant to this problem.

5. MODERN APPLICATIONS IN VIBRO-ACOUSTICS

5.1 Sound Radiation from Vibrating Structures

Prediction of the sound field radiated by a vibrating body is a problem shared by many theoreticians and practitioners in the field of engineering acoustics, including the designers of active sonar transducers, submarine hulls, car engines and loudspeaker cabinets. Analytical estimates are largely limited to bodies of regular geometry which can be modelled as rigidly

baffled flat plates or cylindrical shells. In cases of bodies of irregular geometry, the theoretical requirement is to determine the *Green function* which relates surface normal vibrational acceleration to the sound pressure in the radiated field. Computational techniques such as finite element and boundary element analysis are now available for treating radiation from bodies or arbitrary geometry. They employ the *free-space* Green function, which means that the radiated field is expressed in the distributions of *both* normal acceleration and pressure over the surface of the vibrating body. Because the field pressure is the variable sought, iterative solutions are necessary; these can be costly and time consuming to apply if the bodies are large and highly irregular. The influence on the radiated field of geometrically and materially complex scatterers and absorbers, such as those present in the factory environment, cannot be represented within the limits of practical cost constraints.

An alternative empirical method of determining the appropriate Green function is offered by the reciprocity principle, as illustrated by Fig 4. An elemental area of a vibrating surface may be represented by a monopole source acting at the surface of the otherwise *motionless* body. The transfer function between source and receiver point is identical with that generated on the surface of the *rigid* body by a monopole at the original receiver point, irrespective of the acoustical environment (provided it is linear and has time-invariant physical properties). The total field generated by a continuous distribution of normal acceleration over the surface of the body may be represented by a discrete array of surface monopoles of appropriate amplitude and phase. Hence, the total field at a receiver point may be estimated by summing the product of measured (or calculated) surface accelerations, sampled at a set of discrete points on the surface, with the corresponding Green functions. The latter are measured by insonifying the rigid body with an omni-directional point source of known strength and measuring the sound pressures on the surface of the body with a small, omni-directional roving microphone placed close to the surface. Naturally, the acoustic environment should be the same for the reciprocal measurement as for the required estimation.

A fundamental problem in attempting to apply the reciprocity principle as described above is the experimental characterization of the surface vibration field. Adequate criteria for discretization of a surface have not yet been developed, particularly in cases where the structure is highly non-uniform in stiffness or mass distribution. It is clear that it is only necessary to acquire data which will produce a reasonably accurate estimate of the supersonic wavenumber components ($k_s < k$) of the surface vibration, because the subsonic components ($k_s > k$) don't radiate. Unfortunately, it is not simple to avoid spatial frequency aliassing, since a spatial equivalent of the anti-aliassing filter is not readily available. However, ISVR has developed one form of such a filter as desribed later in relation to sound transmission through aircraft fuselage models.

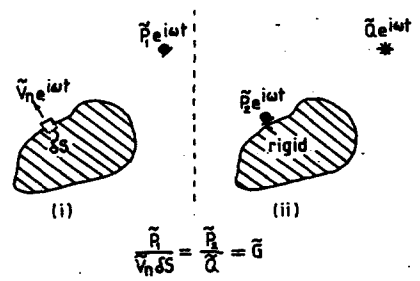

Figure 4. Reciprocal measurement of the Green Function.

Sound radiation from structures subject to localized input forces is of considerable practical interest: for example, vibrational sources mounted on resilient isolators are often modelled as force sources acting on the support structure. Lyamshev's form of the reciprocity principle can usefully be applied to such problems. An omni-directional source is placed at the receiver

position of interest and the vibrational velocity induced at the position of force application is determined (as in Fig.3). The validity of this principle has recently been demonstrated in an application to aircraft structures [14]. Earlier, many successful applications were made to sound radiation from ship structures by engineers at TPD/TNO in Delft [13]. Ten Wolde also determined transfer functions between machinery induced structural vibration velocities and sound field pressures by exciting the structures with a point-acoustic source, and measuring the blocked reaction forces/moments on the structure at the points of interest. Similar measurements could be made in land vehicles, with the source placed in the occupants' head positions. Such reciprocal tests are far simpler, less costly and less time-consuming than direct tests which require the replacement of vibrational sources by vibration generators, particularly since it is very difficult to restrict vibrational force input to a specified direction.

5.2 Acoustically-Induced Vibration

The response of structures to incident sound is of particular concern to us in the aero-space industry because of the combination of high noise levels and lightweight structures, which suffer fatigue damage. Acoustic fatigue has also been a problem in nuclear, gas and petrochemical industries [3, 9]. In the early 1960's, P W Smith demonstrated that the point reciprocity principle could be extended to derive a very useful reciprocal relationship between the radiation characteristics of an individual vibration mode of a structure, and the response of that mode to incident sound [12]. It is, in general, easier to solve a radiation problem than diffraction problem, and considerable modal radiation data exists. Modal reciprocity analysis has been applied to many practical engineering problems, including that of the response of gas-cooled nuclear reactor structures to excitation by the very high level sound (160-170dB) generated by the gas circulators in CO_2 at 30 bar [10] and the response of the Ariane V satellite fairing to launch noise.

A particularly valuable result of modal reciprocity analysis is that it clearly indicates the minimum amount of extra damping that it is necessary to apply to a structure to reduce its acoustically-induced response by a significant amount. To be effective, the mechanical damping must substantially exceed the radiation damping: this is particularly difficult to achieve in structures which radiate into water. Somewhat surprisingly, the acoustically-induced vibration of modern stiff, lightweight, sandwich panels used in aerospace structures is also controlled principally by acoustic radiation damping, and not by mechanical damping, because their radiation loss factors are so high.

5.3 Airborne Sound Transmission

The process of transmission of sound from one fluid volume to another via an intervening solid partition involves both the phenomena discussed above; namely, acoustically-induced response, and radiation from vibrating structures. The term airborne sound transmission will be used, although the principles described apply to any combinations of fluid media. The specific application described below is to aircraft fuselage structures subject to propeller noise, but the measurement principle and the practical implementation could be applied to any airborne sound transmission problem. A technique based upon exploitation of the Lyamshev reciprocity principle has been developed by ISVR and validated on 1/4 scale fuselage structures, both bare and insulated[7, 8].

The transfer function of concern is that between a point force acting on the external surface of a fuselage and the sound pressure generated at a point in the cabin space. Because a fuselage structure takes the form of a shell stiffened by frames and stringers, and it also contains windows and doors, the response of the structure, and hence the acoustic transfer function, will vary markedly with location of the force: no single point is 'typical' . This poses a dilemma in attempting experimentally to characterise dynamic behaviour in terms of transfer functions. However, because a forcing pressure field has a continuous distribution, it may be represented by an array of discrete, contiguous 'patches' of *uniform* pressure, provided that the dimensions of each patch are suitable small. On the basis that such a distribution may be represented by a dense distribution of uniform point forces acting on each patch, it is possible to extend Lyamshev's reciprocity principle, as illustrated in Fig 5.

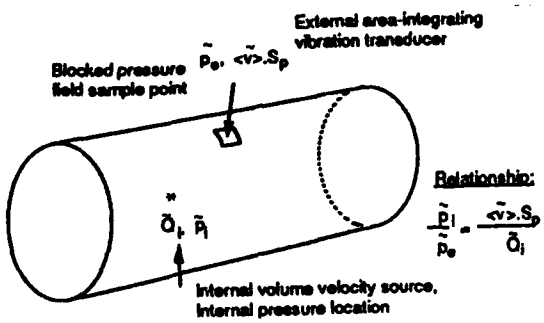

Figure 5. Extension of Lyamshev's relationship.

The vital innovation is that the surface vibration velocity created by the monopole source in the receiver space is spatially integrated over each patch by a capacitative transducer to generate a signal proportional to the surface *volume velocity*. A major advantages of such a transducer is that it acts as a spatial frequency (wavenumber) filter, thereby avoiding the aliassing problem encountered when making point measurements with the accelerometers.

A set of transfer functions between a source at a receiver point in the cabin and the surface volume velocities represents a unique, once-for-all calibration of the fuselage as a pressure transducer. The sound generated at that receiver point by any externally applied pressure field which satisfies the spatial discretisation criterion (1/8 wavelength) may be computed. Hence, the response to theoretically modelled propeller fields, plane waves, diffuse fields, concentrated pressure fields, etc. may be compared. Propeller and flight parameters may also be varied to study their influence on cabin noise. There appears to be no reason why the method should not be applied to full-scale static structures, with and without side-wall insulation, furnishings, etc., to provide rank-ordered performance data. Of course, the procedure may be repeated at a number of receiver points to obtain a 'spatial-average' estimate of mean square pressure. An example of the result of the validation exercise are shown in Fig. 6.

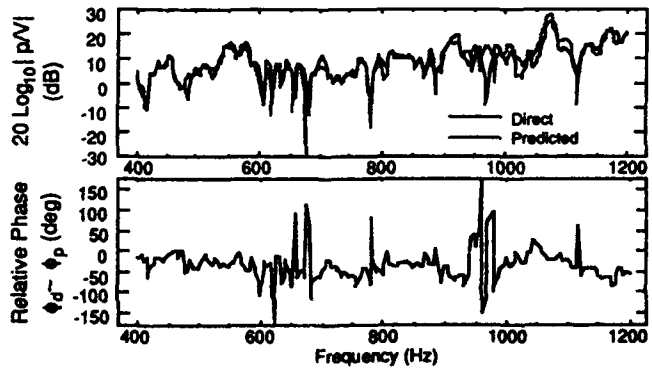

Figure 6. Validation of the extended Lyamshev reciprocity technique on a model fuselage.

5.4 Source Characterization

Experimental techniques based on reciprocity may be used to characterize sources of sound and vibration. Since reciprocity relates *to point* input and output quantities, the resulting characterization necessarily takes the form of an 'equivalent point source', even if its action is not physically concentrated in space. An examples is shown in Fig.7 based on the work at TPD-TNO in the Netherlands. A mechanical source of vibration mounted in a building on a number of 'feet' generates an *open-circuit* voltage in a loudspeaker (proportional to the induced coil velocity) in another part of the building. Lyamshev reciprocity,which incorporates the loudspeaker structure as part of the total dynamic system, shows that the transfer function between the vibration velocity generated at a (receiver) point on at the floor under the machine by the action of the loudspeaker, and the current through the coil, allows the equivalent point force acting at the receiver point to be evaluated. Unless the source is enclosed to minimise airborne sound radiation, the equivalent source will also account for this component of transmitted noise. Note that the loudspeaker does not have to approximate to a point monopole source: it must simply behave as a linear, anti-reciprocal, electroacoustic transducer.

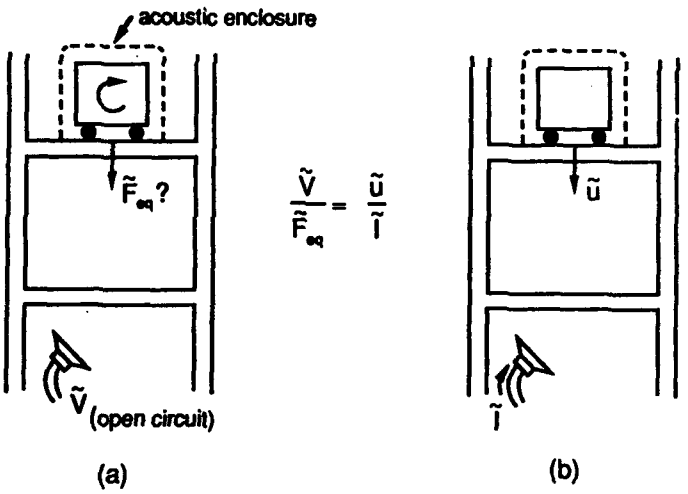

Figure 7. Evaluation of the equivalent vibrational force generated by a machine on a building of reciprocity (a) machine operating: loudspeaker open circuit; (b) loudspeaker driven; machine passive (after ten Wolde).

6. CONCLUSION

The vibro-acoustic reciprocity principle may be exploited in many cases of practical interest to provide information in a simpler, faster and cheaper manner than by direct tests methods. Further research is necessary to establish the accuracy and reliability of reciprocal test techniques, especially with regard to non-linear behaviour, sound absorptive elements and the discrete sampling of vibrational fields.

REFERENCES

1. Belousov, Yu. I. and Rimskii-Korsakov, A.V. The reciprocity principle in acoustics and its application to the calculation of the sound fields of bodies. Soviet Physics Acoustics 21(2), (1975) 103-109.
2. Cremer, L., Heckl, M. and Ungar, E. Springer-Verlag, Berlin. *Structure-borne Sound* (2nd Edition). (1987).
3. Fahy, F J . Noise and vibration in nuclear reactor systems. Journal of Sound and Vibration 28 (3), (1973) 505-512.
4. Fahy, F J. Sound and Structural Vibration - a Review. Proceedings of Internoise '86, (1986) 17-38.
5. Lyamshev, L M. A question in connection with the principle of reciprocity in acoustics. Soviet Physics Doklady 4, (1959a), 406.
6. Lyamshev L M. A method for solving the problem of sound radiation by thin elastic shells and plates. Soviet Physics Acoustics 5, (1959b), 122-124.
7. Fahy, F J and Mason J M. Measurements of the Sound Transmission Characteristics of Model Aircraft Fuselages Using a Reciprocity Technique. Noise Control Engineering Journal. 37(1), (1990), 19-29.
8. Mason, J M. A reciprocity technique for the characterisation of sound transmission into aircraft fuselages. University of Southampton PhD Thesis, (1990).
9. Norton, M P and Fahy, F J. Experiments on the correlation of dynamic stress and strain with pipe wall vibrations for statistical energy analysis applications. Noise Control Engineering Journal 30(3), (1988), 107-118.
10. Rivenaes, U. Design and acoustics tests of a dynamically scaled nuclear reactor structure. Ph.D. thesis, University of Southampton. (1972).
11. Skudrzyk, E. *Die Grundlagen der Akustik.*, Springer-Verlag, Vienna. (1954).
12. Smith, P W. Response and radiation of structures excited by sound. Journal of the Acoustical Society of America 34(5), (1962), 640-647.
13. Ten Wolde, T. On the validity and application of reciprocity in acoustical, mechano-acoustical and other dynamical systems. Acustica 28, (1973), 23-32.
14. Vér, I.L. Some uses of reciprocity in acoustic measurements and diagnosis. Internoise '85, Proc., 1311-1314.
15. Janssen, J M. A note on reciprocity in linear passive acoustical systems. Acustica 8(6), (1958).

GENERAL SOUND AND VIBRATION PROBLEMS

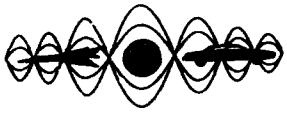

SECOND INTERNATIONAL CONGRESS ON
RECENT DEVELOPMENTS IN AIR- AND
STRUCTURE-BORNE SOUND AND VIBRATION
MARCH 4-6, 1992 AUBURN UNIVERSITY, USA

FLOW-INDUCED VIBRATION PROBLEMS IN THE OIL, GAS AND POWER GENERATION INDUSTRIES - IDENTIFICATION AND DIAGNOSIS

M.P. NORTON
Department of Mechanical Engineering
University of Western Australia
Nedlands 6009
Western Australia

ABSTRACT

Flow induced vibration and noise is of considerable interest to the process and power generation industries - it relates not only to occupational health and safety but also to condition monitoring, maintenance, structural fatigue and failure. There are many recorded instances of catastrophic failure associated with vibration and acoustic fatigue; in particular, high capacity gas and steam pressure reducing systems are sometimes prone to failure via acoustically induced fatigue. As such, flow induced vibration and noise in high capacity pressure reducing systems is a topical subject with designers of new offshore platforms and power stations and upgrades of existing installations. The subject is also of interest to liquid natural gas and petroleum refineries.

There are numerous flow-induced sources of vibration and noise in industrial installations. These sources are generally the least well defined in the literature and like the more well defined mechanical sources, they pertain not only to unacceptable vibration and noise levels but also to vibration induced and acoustic induced fatigue and failure. Typical flow-induced sources of vibration and noise include acoustic pulsations, acoustic resonances, cavity resonances, turbulence, propagating acoustic waves, valves, bends, orifice plates, vortex shedding, cavitation, rotating blades etc.

Typical practical situations where flow- and mechanically-induced vibration and noise problems have arisen include pressure relief valves in a wide variety of gas and steam flow systems, glycol pump lines on offshore platforms, high pressure/low pressure flare systems, turbine exhausts, large refrigerant (propane) circuits in LNG plants, compressor piping circuits, wellhead flow lines. The specific problem sources have included pressure pulsations, acoustic resonances, cavity resonances, turbulence, propagating acoustic waves, vortex shedding, cavitation, coincidence between acoustic and structural modes etc.

INTRODUCTION

This paper addresses a wide range of flow induced vibration and noise problems with particular emphasis being placed on the oil and gas and power generation industries. Both mechanically-induced vibration and noise, and flow-induced vibration and noise are considered from (i) an occupational health and safety, (ii) a condition monitoring and maintenance, and (iii) a structural fatigue and failure viewpoint.

Occupational health and safety aspects of flow induced vibration and noise include general vibration and noise criteria, whole body vibration, and speech interference particularly on platforms and in refineries. Condition monitoring and maintenance aspects include the management of rotating and reciprocating machinery, valves, and piping. Structural fatigue and failure aspects include vibration and noise source identification, buckling and stability analysis, prediction models for the estimation of dynamic stress and strain, and practical design considerations.

As a general background to flow induced vibration and noise in the oil and gas and power generation industries, and in particular high capacity pressure reducing systems, some typical problems that can occur are now summarised. They include:

- wave coincidence between structural flexural pipe modes and internal acoustic modes in piping, producing high noise and vibration levels;
- internal vortex shedding and cavity resonances;
- standing acoustic waves (acoustic resonances) inside various sections of pipework;
- turbulence excitation of the pipe wall at regions in proximity to bends, valves etc;
- cavitation;
- pipe instability (static instability (buckling), flutter and other dynamic instabilities) resulting from flow-induced vibrations and flow pulsations;

high dynamic stress levels, overstressing of vessel nozzles, and acoustic fatigue as a result of the phenomena listed above and/or as a result of excessive pressure drops at pressure reduction devices;
piping vibration and noise associated with reciprocating and rotating machinery;
aggravation of problems due to inadequate and/or inappropriate pipe support location;
fatigue failure at regions in proximity to small fittings, appendages, branch connections and other asymmetric flow discontinuities with regions of high stress concentration such as tees and poor quality welded connections (weld undercutting etc.);
fatigue failure at connections (branches, restriction orifices, valves etc.) where the flow is sonic (i.e. at a supercritical pressure drop).

Typical practical solutions to the preceding problems include:
usage of suitable prediction models for optimising for low vibration, noise and stress at the design stage;
reduce internal acoustic energy at pressure reduction devices and flow discontinuities;
eliminate piping weakness (add stiffness, mass or damping where appropriate);
control pressure drops via low noise valves and multi-stage restriction orifices;
usage of pulsation dampers, coincidence dampers, in-line silencers, diffusers etc;
eliminate/minimise all high stress concentration points at piping downstream of high capacity pressure reducing systems;
give careful consideration to the design of items such as branch connections, support saddles, restraint attachments - i.e. all these are possible fatigue failure points;
where possible, use axisymmetric discontinuities in preference to asymmetric discontinuities - axisymmetric discontinuities are generally not potential fatigue failure points;
ensure good quality full penetration welds with no undercut in flange, stiffener rings or welds;
if asymmetric disturbances/discontinuities are essential, minimise the abruptness of the discontinuity;
use adequate wall thickness at piping near discontinuities and immediately downstream of pressure reducing devices;
use welding tees or full wrap around reinforcements at all large branch connections.

From the discussion so far, it can be seen that the analysis and control of flow induced vibration and noise requires a working knowledge of (i) the identification of excitation sources such as turbulence, standing acoustic waves, vortex shedding, cavity resonances, wave coincidences, buckling and associated pipe instabilities, reciprocation pumps, rotating blades, slug flows, cavitation, acoustic pulsations, valves, orifices and bends, (ii) prediction models (such as normal mode models, statistical energy analysis models, finite element models etc.) for vibration, noise and dynamic stress levels, and (iii) practical design considerations for items such as pulsation dampers, coincidence dampers, low noise valves, multi-stage restriction orifices, in-line silencers, diffusers, Helmholtz resonators, and pipe supports. In addition, field experience and a clear understanding of the flow process is essential to identify *possible problem areas.*

SOURCES OF AND FUNDAMENTAL CONSIDERATIONS IN VIBRATION AND NOISE

It is useful to consider the two separately, even though there are numerous sources which contribute to both vibration and noise. Industrial vibration and noise can be either mechanically- or flow-induced, and this vibration and noise can result in (i) unacceptable vibration levels, (ii) unacceptable radiated noise levels, and (iii) vibration or acoustic induced fatigue and failure.

Vibration relates to oscillatory motion in solids whereas noise relates to oscillatory motion in fluids. Both vibration and noise can be generated by either mechanical- or flow-induced sources or a combination of both - a flow-induced acoustic excitation can cause a structure to vibrate and radiate noise just like a mechanically driven unit such as a motor can; alternatively, the vibrational energy from a machine can be converted into sound just like pressure fluctuations in a liquid or gas can. In general terms, vibration will cause *noise and noise will cause vibration! Therefore, it is desirable to consider the two in tandem in any analysis* although the relationship between vibration and noise is not necessarily linear.

Typical mechanical sources of vibration include unbalance associated with reciprocating and rotating machinery (turbines, compressors, pumps, fans, electric motors etc.), periodic variation of fluid pressures and acceleration of masses within reciprocating devices, branch connections, support saddles, restraint attachments and a variety of asymmetric discontinuities. With the exception of reciprocating and rotating machinery, most mechanical sources are simply associated with the amplified oscillations of asymmetric inertial masses - fluid forces at asymmetric discontinuities provide the excitation input to the piping systems which can be modelled as beam type elements with lumped inertial masses for the first few natural frequencies. Effects such as variable stiffness, variable mass, end constraints and the effects of axial bending, torsion and circumferential flexure have to be accounted for. Whilst the excitation sources are generally of the forced steady-state type, transient excitation sources can also be present.

Typical mechanical sources of noise include reciprocating and rotating machinery (turbines, compressors, pumps, fans, electric motors etc.), and the structure-borne transmission of vibrational energy from these sources to sections with large radiating areas. Any form of mechanically induced vibrational energy within the frequency range 25 Hz to 20000 Hz will manifest itself very efficiently as noise if it is transmitted to large radiating surface areas such as shells and plates. As a general rule, however, with the exception of regions in close proximity to reciprocating and rotating machinery, the dominant sources of piping noise are not mechanical but flow-induced.

There are numerous flow-induced sources of vibration and noise in industrial installations. These sources are generally the least well defined in the literature and like the more well defined mechanical sources, they pertain not only to unacceptable vibration and noise levels but also to vibration induced and acoustic induced fatigue and failure. Typical flow-induced sources of vibration and noise include acoustic pulsations, acoustic resonances, cavity resonances, turbulence, propagating acoustic waves, valves, bends, orifice plates, *vortex shedding, cavitation, rotating* blades etc.

Figure 1 is a flow chart which summarises the primary sources and the fundamental considerations in industrial vibration and noise. The main difference between fundamental considerations for vibration and noise is that vibration (mechanical- or flow-induced) is generally pertinent to condition monitoring and maintenance, dynamic stress and fatigue, and whole body vibration, whereas noise (mechanical- or flow-induced) is primarily pertinent to occupational health and safety and to environmental considerations. However,

because vibration causes noise and noise causes vibration (remember that the relationship is not necessarily linear) one can use vibration to quantify the effects of noise or visa versa. The primary emphasis in this paper is on diagnostics with a view to avoiding structural fatigue and failure. A thorough understanding of the physics of flow- and mechanically-induced vibration and noise and its role in structural fatigue and failure provides for more cost effective design and hence more cost effective occupational health and safety, and condition monitoring and maintenance. Figure 1 illustrates this important point.

Major sources of flow- and mechanically-induced vibration and noise, prediction models, experimental techniques for parameter measurement, practical design considerations and some specific practical examples are outlined in the flow chart in Figure 1. Prediction models are available for the prediction of vibration, noise and dynamic stress using normal mode analysis techniques, statistical energy analysis techniques, finite element analysis techniques, boundary element analysis techniques, and of course a wide range of empirical and semi-empirical techniques. Experimental techniques for parameter measurement include sound power, sound intensity and pressure fluctuation measurement procedures for source identification and ranking, vibration intensity and vibrational power flow for dynamic stress analysis, and modal density, damping and modal analysis for identifying structural dynamic characteristics. Practical design options for reducing both flow- and mechanically-induced vibration and noise include pulsation dampers, low noise valves, multi-stage restriction orifices, in-line silencers, diffusers, Helmholtz resonators, piping supports at appropriate locations, optimising flow conditions and optimising geometrical parameters.

Typical practical situations where flow- and mechanically-induced vibration and noise problems have arisen include pressure relief valves in a wide variety of gas and steam flow systems, glycol pump lines on offshore platforms, high pressure/low pressure flare systems, turbine exhausts, large refrigerant (propane) circuits in LNG plants, compressor piping circuits, wellhead flow lines. The specific problem sources have included pressure pulsations, acoustic resonances, cavity resonances, turbulence, propagating acoustic waves, vortex shedding, cavitation, coincidence between acoustic and structural modes etc.

The flowchart in Figure 2 serves as an example of how one should go about analysing a typical piping vibration and noise problem. The problem relates specifically to the effects of internal flow disturbances on the vibration response of and the acoustic radiation from high speed gas flows in piping systems, and the flowchart summarises the various technical aspects that one has to consider when dealing with the problem. Three primary issues need to be addressed. They are: (i) identification of the mechanisms of vibration and noise generation; (ii) the development of prediction models; and, (iii) practical design considerations for optimum reduction in response.

GAS AND LIQUID FLOWS

Fluid flow can be categorised into gas flows, liquid flows and two-phase flows, and as one would intuitively expect, the vibration and noise characteristics and the system dynamics are very different for each of these cases. The primary difference between gas flows and liquid/two-phase flows is that the latter two cases fluid load the structure. In addition, fluid loading can be categorised into two cases - small amplitude motions and large amplitude motions. The former does not affect the excitation forces whereas the latter leads to various forms of dynamic instabilities. These two cases have to be treated separately.

Fluid loading has two main effects on vibrating structures. Firstly, the fluid mass-loads the structure, and this alters the structural natural frequencies. Secondly, the fluid medium provides acoustic radiation damping, and this affects the sound radiation characteristics of the structure. When the fluid medium is a gas, the mass loading effects of the fluid are generally of a second order since fluid forces are proportional to density. Dense fluids (e.g. liquids/two-phase flows) have significant effects on the vibrational and sound radiation characteristics of structures. When the fluid volume is unbounded (e.g. a vibrating plate submerged in a large volume of fluid) it cannot sustain standing waves and it simply mass-loads the structure, and provides acoustic radiation damping; when the fluid volume is bounded (e.g. dense liquids contained within cylindrical shells), the problem is more complex because now both the structure and the fluid can sustain standing waves and natural frequencies, and there is feedback between the structure and the fluid. When this occurs the system is referred to as being strongly coupled. Whilst only dense fluids mass-load structures, all fluids (including air) possess acoustic radiation damping characteristics - energy is dissipated from the vibrating structure in the form of radiated sound.

In summary, fluid loading has the following general effects on vibrating structures.

(1) The natural frequencies of the structure are altered - this is associated with the fluid mass loading effects. The greatest effects occur at low wavenumbers.
(2) The acoustic radiation damping associated with sound waves radiating from the structure varies with the fluid density - radiation damping is also important in light fluid media.
(3) When the fluid volume is confined, the possibility of strong coupling between fluid and structural modes exists.
(4) The impedance of the structure is altered - numerous relationships are available for point and line forces and moments for plates and shells.
(5) The directivity and source characteristics of fluid-loaded radiators are modified.

The vibration and noise characteristics of fluid flows are summarised in Figure 3. The various sources (flow- and mechanically-induced) of vibration and noise (i.e. turbulence, standing acoustic waves, vortex shedding, cavity resonances, wave coincidences, acoustic pulsations, valves, orifices and bends etc.) are also found in liquid and two-phase systems. The latter have additional sources which include cavitation, static instabilities (buckling), dynamic instabilities (flutter, parametric resonance and combination resonance), pipe whip (i.e. the dynamic response of a pipeline to an instantaneous rupture), and of course mass loading.

Cavitation is peculiar to liquids and is associated with the generation of small, microscopic, unstable vacuum cavities which collapse (implode) very rapidly due to insufficient liquid entering a volume space. The continuing series of implosions is due to high frequency alternating pressures within the liquid - the bubbles grow to a particular size and then collapse causing very high instantaneous pressures and temperatures. This continuous implosion process can produce significant damage, and the associated noise and vibration is random and broadband.

Static instability is caused by fluid stiffness forces - buckling of an elastic pipe pinned at both ends and conveying a steady liquid flow is a classical example of static instability. The parameters that control the degree of static instability are structural stiffness, fluid stiffness and structural damping.

Flutter is a dynamic instability that arises because the fluid dynamic forces create negative damping - i.e. the structural velocity is in phase with the fluid dynamic forces. Single-mode flutter is a fluid-damping-controlled instability and coupled-mode flutter is a fluid-stiffness-controlled instability. Parametric resonance and combination resonance are dynamic instabilities associated with time-varying flow parameters - they usually predominate when the flow is pulsating (i.e. a periodic function of time) or when the fluid passing through the piping is in the two-phase flow regime (i.e. the density is time-varying). Parametric resonance is a dynamic instability which occurs when the flow period is a multiple of one of the natural frequencies of the cylinder. Combination resonance is a dynamic instability which occurs when the period of the flow is equal to the sum or difference and associated integer sub-harmonics of the natural frequencies of a cylinder. The parameters that control the degree of dynamic instability are structural stiffness, fluid stiffness, structural damping, fluid damping, structural mass and fluid mass.

QUANTIFYING FLOW-INDUCED VIBRATION

This paper is primarily concerned with reviewing various techniques for identifying and quantifying flow induced vibrations which are common in the oil, gas and power generation industries. The case is best presented by considering one of the most common target areas - piping systems.

Flow induced vibration and noise associated with high capacity pressure reducing piping systems can result in (i) unacceptable pipe vibration levels, (ii) unacceptable radiated noise levels, and (iii) acoustic fatigue (due to excessive vibration generated via internal flow disturbances).

Typical excitation sources and associated problems that can occur have been reviewed in the general introduction. They include wave coincidence, internal vortex shedding and cavity resonances, standing acoustic waves (acoustic resonances),turbulence excitation, cavitation, pipe instability (static instability (buckling), flutter and other dynamic instabilities) resulting from flow-induced vibrations and flow pulsations, high dynamic stress levels, overstressing of vessel nozzles, and acoustic fatigue as a result of the phenomena listed above and/or as a result of excessive pressure drops at pressure reduction devices, piping vibration and noise associated with reciprocating and rotating machinery, aggravation of problems due to inadequate and/or inappropriate pipe support location, fatigue failure at regions in proximity to small fittings, appendages, branch connections and other asymmetric flow discontinuities with regions of high stress concentration such as tees and poor quality welded connections (weld undercutting etc.), fatigue failure at connections (branches, restriction orifices, valves etc.) where the flow is sonic (i.e. at a supercritical pressure drop).

In general, possible problem areas of acoustic fatigue can be quantified via sound power emitted at regions of pressure reduction, pipe wall vibration levels, wall thickness, pipe diameter, flow quantity, Mach number, pipe support conditions, weld conditions at fittings, and flow discontinuities particularly asymmetric discontinuities. Problem areas relating to noise generally cover a much wider scope and include wave coincidence, cavity resonances, standing acoustic waves, vortex shedding, propagating acoustic waves, turbulence, etc.

The following analysis procedure is recommended for analysing high capacity pressure reducing systems such as that illustrated in Figure 4.

i. Study all drawings & data sheets and identify

   - pipe diameters
   - pipe wall thicknesses
   - pipe material
   - pipe lengths between supports
   - support conditions (clamped, fixed, simply supported etc.)
   - flow speed
   - gas density
   - gas molecular weight
   - gas temperature
   - gas specific heat ratio
   - internal pressures

ii. Evaluate speed of sound and Mach number at various locations in the flow process, taking temperature and density variations into account

iii. Analyse critical pressure reducing points and establish sound power and acoustic fatigue criteria

iv. Evaluate possible combinations of acoustic resonances (standing waves) inside critical sections of the piping

v. Evaluate possible wave coincidences between structural flexural pipe modes and internal acoustic modes at critical sections of pipe

vi. Identify sources of internal vortex shedding and cavity resonances

vii. Identify possible areas of possible pipe instability (buckling) resulting from flow-induced vibrations and flow pulsations

viii. Recommend solutions where and if possible to minimise the effects of the above

ix. Predict vibration levels for a variety of flow conditions by using either computer models or measured pipe vibration velocity levels on existing systems at numerous sections of the pipe so as to define the spatial variation of the vibration spectra along the pipe. This can be done at any flow speed provided that the flow speed and condition is identified - levels at other flow speeds can be scaled from the test results

x. Calculate dynamic stress levels from the vibrational velocity and/or displacement levels

xi. Use radiation ratios to estimate the noise effects for generating noise contours.

Primary pressure reduction sources are control valves, relief valves and orifice plates. In each case, the critical pressure reducing points need to be analysed and sound power and acoustic fatigue criteria established. This part of the study is usually the most important, as it establishes whether or not there is the possibility of a noise problem, an acoustic fatigue problem, a Mach number problem (i.e. Mach number too high), inadequate pipe wall thickness, and a piping support problem. The sound pressure level at a specific distance from the various pressure reduction devices can also be estimated.

The computational procedure for assessing the possibility of acoustic fatigue due to a pressure reduction device (e.g. the valves in Figure 4) is summarised.

i. Pressure drops across the various critical pressure reducing points are established.
ii. Sound pressure level associated with the pressure drop, Δp, is computed.
iii. A sound pressure level correction for valve style and pressure ratio is established.
iv. A sound pressure level correction for the gas sizing coefficient is established (function of flow rate).
v. The sound power for the pressure reduction device is computed from the adjusted sound pressure level. This provides a quantitative measure of the intensity of the acoustic energy inside the pipe.
vi. The sound power is scaled onto a design chart (Figure 5) for establishing the safe design limit of acoustically induced piping vibrations - this design chart is based on numerous test cases and provides a qualitative assessment of the likelihood of a problem.
vii. Based on the location of the particular pressure reducing point on the design chart, an assessment is made on the possibility of a noise problem, an acoustic fatigue problem, a Mach number problem (i.e. Mach number too high), an inadequate pipe wall thickness, and a piping support problem.

To assess the possibility of acoustic fatigue associated with pressure reducing devices, the following information is required:

- Item description + piping layout
- ΔP across the device
- Downstream pressure (dynamic and static)
- Upstream pressure (dynamic and static)
- Temperature (upstream and downstream)
- Flow rate
- % liquid weight
- Liquid density
- Vapour density
- Vapour molecular weight
- C_p/C_v
- Exit pipe dimensions
- Mach number

CASE STUDIES

Several case studies are summarised in this paper.

Flow-induced noise and vibration associated with industrial gas pipelines

Coincidence between higher order acoustic modes inside a cylindrical shell and pipe wall structural modes is a dominant mechanism for the generation of flow-induced noise and vibration in pipelines. Some field data relating to a gas pipeline installation where this is the case is presented here. Figure 6 illustrates typical piping layouts, Figure 7(a) schematically illustrates various sources of piping vibration and noise and Figure 7(b) illustrates typical vibration and noise measurement responses.

Excessive noise and vibration levels were experienced at the gas pipeline installations. It was observed that the noise and vibration originated from various tee-junction intersections, and that it propagated for large distances along straight runs of pipeline. A typical pipe wall acceleration spectra is presented in Figure 8, and the corresponding externally radiating sound pressure level spectra at some appropriate radial distance from the gas pipeline is presented in Figure 9. The internal diameter of the steel pipeline is 0.914 m, the speed of sound in the internal gas is ~ 385 m/s, and the mean flow Mach number is ~ 0.1. The precise details of the measurement locations are not directly relevant to this test case as one is only concerned with identifying the mechanism of noise and vibration generation.

From Figures 8 and 9, it is very evident that there are large increases in pipe wall vibration and externally radiated noise at certain discrete frequencies. Also, there is a one to one correlation between the vibration discrete frequencies and the radiated noise discrete frequencies. A close examination of Figures 8 and 9 reveals that the first three dominant peaks are at 275 Hz, 461 Hz and 676 Hz.

Coincidence is a possible source of the dominant peaks at 275 Hz, 461 Hz and 676 Hz. The cut-off frequencies of the various higher order acoustic modes can be evaluated from the equation below and Table 1. The cut-off frequencies are given by

$$(f_{co})_{pq} = \frac{\pi\alpha_{pq}c_i(1 - M^2)^{1/2}}{2\pi a_i}$$

where c_i is the speed of sound inside the pipe, M is the mean flow Mach number, a_i is the internal pipe radius, and the $\pi\alpha_{pq}$'s are obtained from Table 1. The coincidence frequency, f_c, is usually higher than the cut-off frequency, f_{co}, of the relevant higher order acoustic mode. Hence, if coincidence is the dominant mechanism for the vibration and noise spectra in Figures 4 and 5 respectively, then one would expect that the measured coincident peaks are in close proximity to, and generally higher than, the respective cut-off frequencies of the appropriate higher order acoustic modes. The calculated cut-off frequencies for the relevant higher order acoustic modes (as obtained from the above equation) and the experimentally observed dominant spectral peaks are presented in Table 2.

p	q	$\pi\alpha_{pq}$	p	q	$\pi\alpha_{pq}$
	0	1.8412	5	0	6.4156
	0	3.0542	2	1	6.7061
	1	3.8317	0	2	7.0156
	0	4.2012	6	0	7.5013
4	0	5.3175	3	1	8.0152
1	1	5.3314	1	2	8.5363

Table 1 Solutions to $J_p(\kappa_{pq}a_i) = 0$

Higher order mode	Measured spectral peaks	Calculated f_{co}
1,0	275	245
2,0	461	407
0,1	-	511
3,0	676	560
4,0	-	709

Table 2 Measured spectral peaks and calculated cut-off frequencies

It is clear from the table that the measured spectral peaks are both higher than and in close proximity to the calculated cut-off frequencies for certain higher order acoustic modes. It can thus be concluded that the spectral peaks at 275 Hz, 461 Hz and 676 Hz are associated with coincidence between the (1,0), (2,0), and (3,0) higher order acoustic modes and appropriate structural pipe modes. The fourth dominant measured peak at ~ 1022 Hz is due to a higher acoustic mode such as the (5,0) or the (2,1) modes - as one goes higher up in frequency it becomes harder to identify the specific higher order acoustic modes associated with coincidence.

Thus, the main conclusion to result from this test case is that the dominant source of pipeline vibration and externally radiated noise from the gas pipeline is coincidence between the higher order acoustic modes inside the pipeline and the pipe wall structural modes.

Identification of flow-induced vibration sources on pressure relief valve piping circuits

A pressure relief valve for a filter separator unit in an LNG plant vibrated very severely each time the valve lifted from its seat. A schematic arrangement of the valve and its associated piping is presented in Figure 10. The vibration levels were so severe that the piping and its support base experienced cracking.

A simple analysis indicated that the mass-spring natural frequency of the free-floating piston arrangement coincided with the fundamental acoustic standing wave in the riser piping. The solution was to vary the air-spring stiffness by introducing a gas volume with a pilot valve.

Identification of flow-induced vibration sources in boiler-feed pumps

Classical rotordynamic instabilities produce a whirl velocity equal to slightly less than half of rotor speed - hence rotordynamic instabilities generally produce a characteristic vibration at 42 - 48% of shaft speed.

It was established that a certain type of boiler feed pump sub-synchronous vibration which consistently occured at 80 -95% of shaft running speed was not due to classical rotordynamic instabilities but was due to excessive flow-induced vibration.
The boiler feed pump (Figure 11) has a double volute suction inlet - this causes additional flow disturbances and subsequently more fluid dynamic exciting forces than single entry suction inlets. In addition, wear ring grooves and spacings encourage localised flow irregularities and the associated unwanted flow patterns at the impeller shroud.

Hence, there are two primary sources of aerodynamically induced disturbed flow at the suction inlet - rotating, non-axisymmetric pressure fields at the impeller suction producing destabalising forces on the diffuser blades and pre-rotation of the fluid prior to entry into the clearances.

The combination of these fluid dynamic disturbances provides radial excitation of the shaft. A flexible shaft/stiffness analysis indicated that the shaft is not rigid at running speed because of its long length to diameter ratio. However, the shaft was only balanced dynamically as a rigid shaft and not as a flexible shaft by the owner. Hence, forced and/or resonant vibrations are readily induced - i.e. a flexible and unbalanced shaft excited by primary sources of aerodynamically induced disturbed flow induce a forced or a resonant vibration which ultimately leads to impeller rub and subsequent failure. The mechanisms leading to subsynchronous vibration and subsequent failure are summarised in Figure 12 and proposed means of reducing the vibration are summarised in Figure 13.

Flow-induced noise and vibration associated with a racing sloop

This test case illustrates how one can sometimes identify sources of noise and/or vibration armed only with a good fundamental knowledge of the subject and without the requirement for any sophisticated measurement instrumentation!
A situation arose where the manufacturers of a prototype 10 m aluminium hulled racing sloop (yacht) were faced with an excessive low frequency (~ 100-200 Hz) noise and vibration problem at certain speeds. Unfortunately, the noise and vibration levels peaked at a speed of ~ 10 knots which corresponded to the cruising speed of the yacht.

Because the problem was speed related, it was immediately recognised that the noise and vibration was probably flow-induced and in particular probably associated with vortex shedding - i.e. it was highly probable that the vortex shedding frequency coincided with a major structural resonance. Furthermore, since the yacht was constructed out of aluminium which is very lightly damped the problem was amplified.

Some simple field trials allowed for a rapid identification of the source of the problem. The possible primary sources of the vortex shedding were the mast and the keel. Towing the yacht forwards (at the 10 knot cruising speed) without the mast did not eliminate the noise and vibration. This suggested that the keel was the probable source. Towing the yacht backwards (!!) at 10 knots resulted in the complete elimination of the offending noise and vibration!! This proved beyond any doubt that the source of the problem was vortex shedding from the keel - the flow pattern around the keel altered when the yacht was towed backwards and this eliminated/reduced the vortex shedding. The source of the problem was confirmed yet again by temporarily attaching some diagonal boundary layer trip wires to the keel and sailing the yacht in its normal manner at its cruising speed. As expected, the boundary layer trip wires uncorrelated the vortex shedding pattern and this in turn eliminated the noise and vibration. Vortices only produce excessive structural vibrations when they are well correlated along the length of a structure - they oscillate in sympathy with each other and this sets up a tonal excitation. When they are uncorrelated they do not sustain the tonal excitation.

Thus, the source of the excessive noise and vibration on the yacht was identified without the need to obtain any quantitative measurements.

Additional case studies on (i) identification of flow-induced vibration sources on liquid reciprocating pump piping circuits, (ii) identification of flow-induced vibration sources in burners/furnaces, and (iii) identification of flow-induced vibration sources in large industrial air supply systems will be discussed during the presentation.

REFERENCES

1. Fundamentals of Noise and Vibration Analysis for Engineers, M.P. Norton, Cambridge University Press (1989)
2. Piping Vibration and Noise, M.P. Norton, Elsevier Applied Science Publishers (To be published in 1992)
3. Flow Induced Vibrations, R.D. Blevins,Van Nostrand Reinhold (1990)

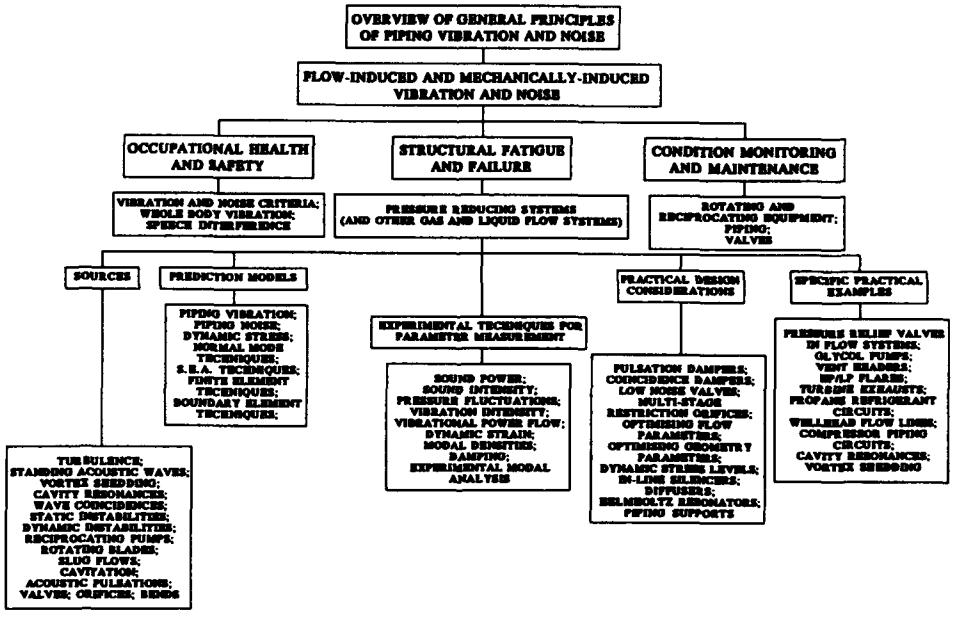

Figure 1 Primary sources and fundamental considerations in piping vibration and noise

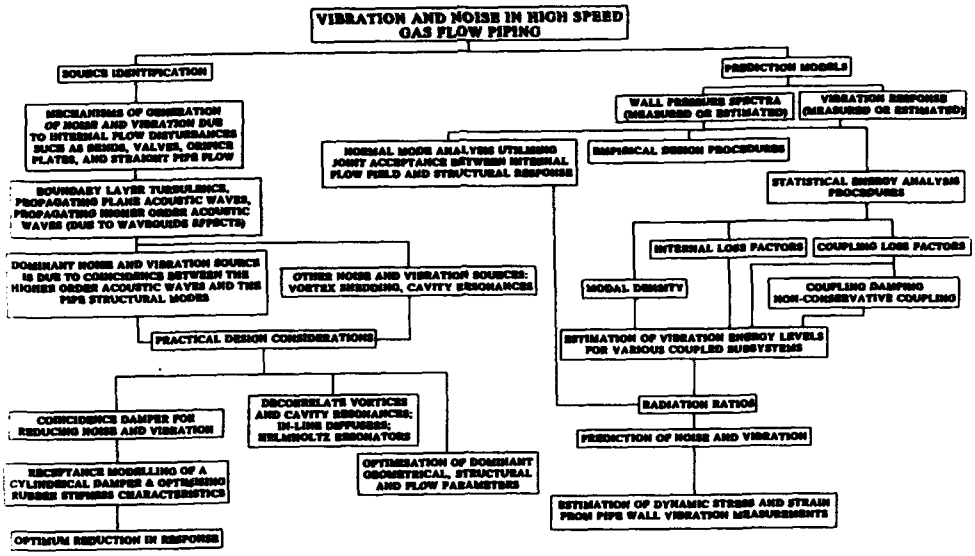

Figure 2 Source identification and prediction model flowchart for the effects of internal flow disturbances on the vibration response of and the acoustic radiation from high speed gas flows in piping systems

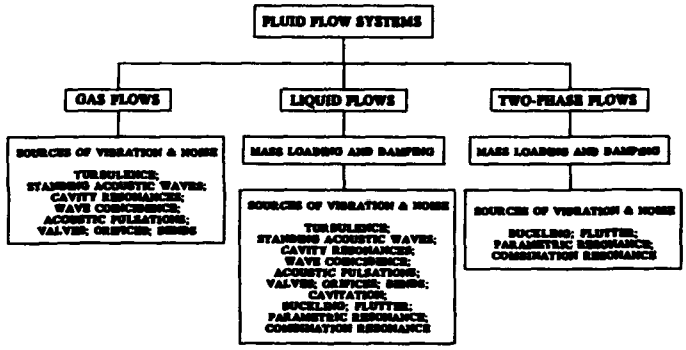

Figure 3 Vibration and noise characteristics of fluid flows

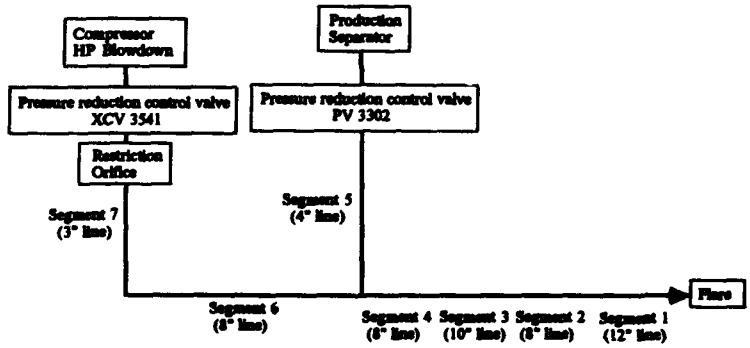

Figure 4 Schematic illustration of line segments for separator off gas (continuous flow) and compressor blowdown (transient)

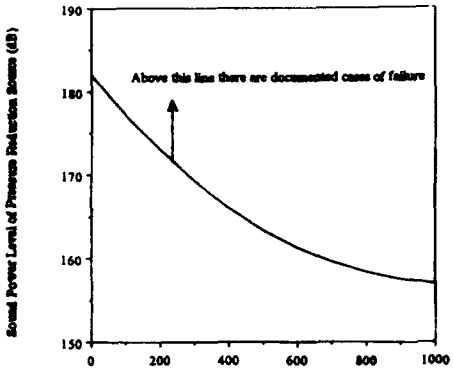

Figure 5 Recommended Design Limit for Acoustic Fatigue

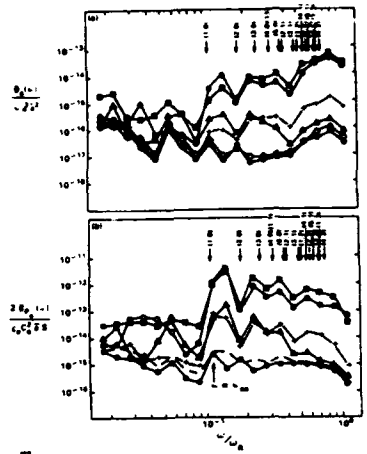

Figure 7b Nondimensional spectral density of (a) the pipe wall acceleration $M_t = 0.40$, and (b) the acoustic radiation. $M_t = 0.40$, butterfly valve. valve. $M_t = 0.41$, ■, 90° mitred bend. $M_t = 0.40$, ▲, 45° mitred bend. $M_t = 0.41$, ▲, gate valve. $M_t = 0.41$, ○, 90° radiused bend ($R/r = 6.2$). $M_t = 0.40$, ●, straight pipe. $M_t = 0.41$, —, 90° radiused bend ($R/r = 5.0$, $M_t = 0.40$. Cutoff frequencies of higher order acoustic modes are also shown. $S = \pi D_i L_i$ an[illegible] D_i/L. Flow disturbance located [illegible] diameters upstream. (From Norton [11])

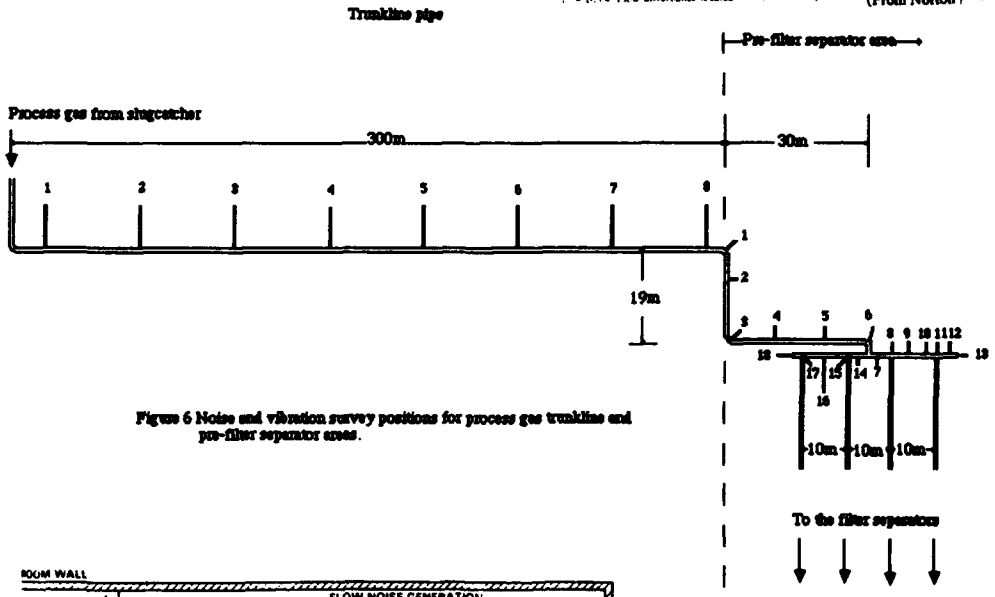

Figure 6 Noise and vibration survey positions for process gas trunkline and pre-filter separator areas.

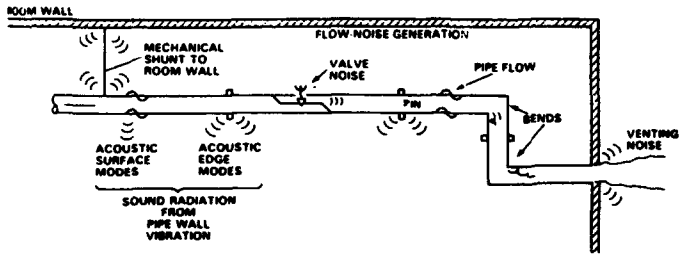

Figure 7a Schematic of various sources of vibration and noise generation and transmission mechanisms in pipes/ducts (from Blake, W.K., Mechanics of Flow-Induced Vibration, Academic Press)

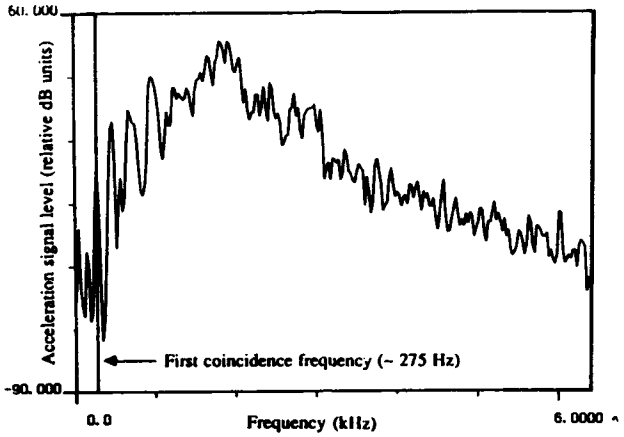

Figure 8 Typical pipe wall acceleration spectra for a gas pipeline (speed of sound ~ 385 m/s, mean flow Mach number ~ 0.1; internal diameter ~ 0.914 m)

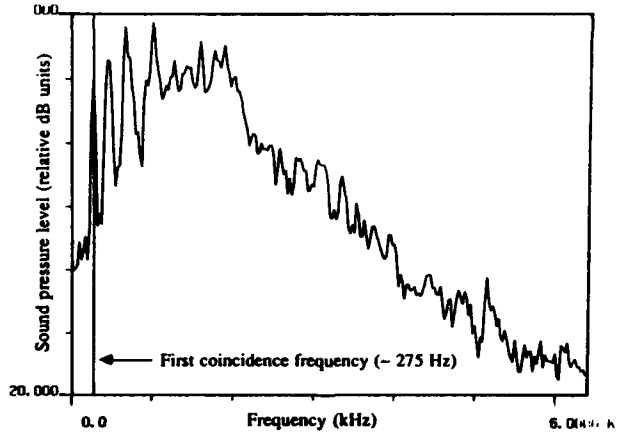

Figure 9 Typical externally radiated sound pressure levels for a gas pipeline (speed of sound ~ 385 m/s; mean flow Mach number ~ 0.1; internal diameter ~ 0.914 m)

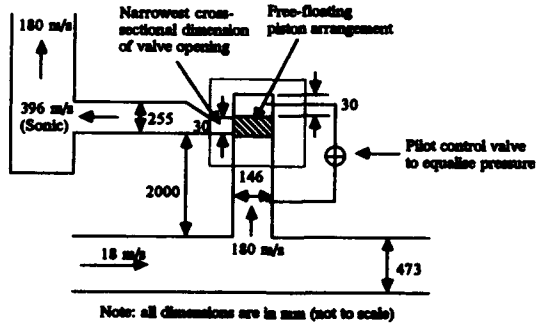

Figure 10 Pressure relief valve piping

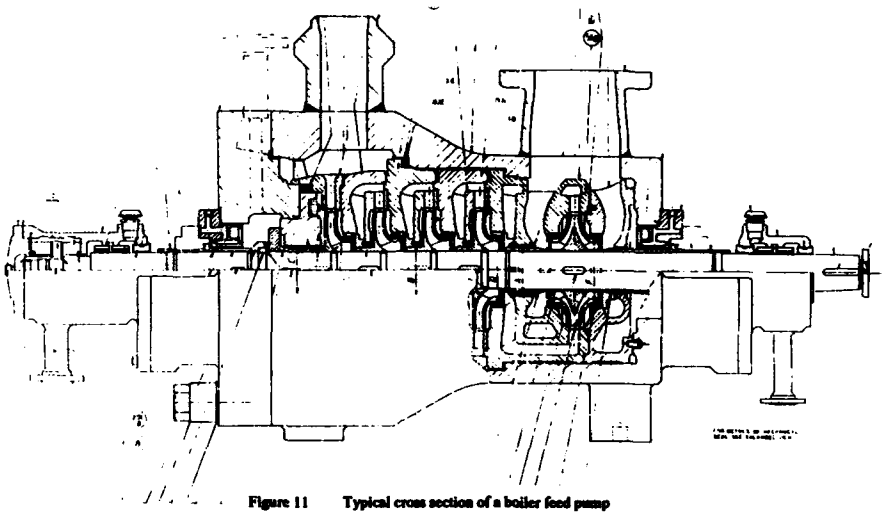

Figure 11 Typical cross section of a boiler feed pump

MECHANICMS LEADING TO SUBSYNCHRONOUS VIBRATION AND SUBSEQUENT FAILURE

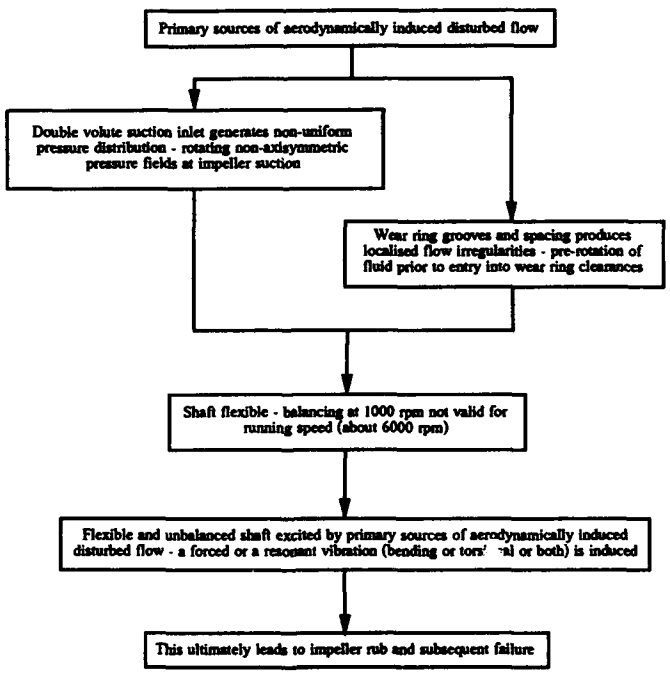

Figure 12

PROPOSED MEANS OF REDUCING SUBSYNCHRONOUS VIBRATION

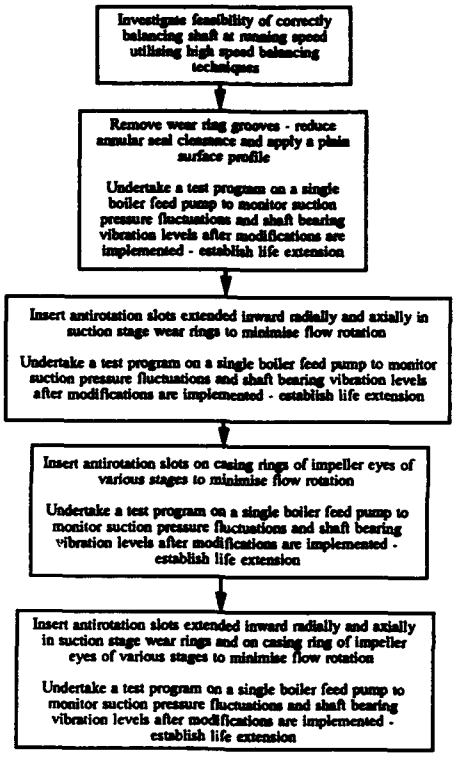

Figure 13

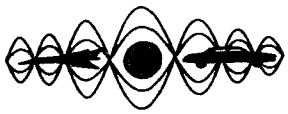

SECOND INTERNATIONAL CONGRESS ON
RECENT DEVELOPMENTS IN AIR- AND
STRUCTURE-BORNE SOUND AND VIBRATION
MARCH 4-6, 1992 AUBURN UNIVERSITY, USA

IMPEDANCE OF A VISCOUS FLUID LAYER BETWEEN TWO PLATES

Michael A. Latcha
Department of Mechanical Engineering
Oakland University
Rochester, Michigan 48309
U.S.A.

Adnan Akay
Department of Mechanical Engineering
Wayne State University
Detroit, Michigan 48202
U.S.A.

ABSTRACT

The impedance of a fluid layer separating two plates is obtained through a rigorous solution of the linearized Navier-Stokes equations for viscous fluids. The results are given for infinite and finite rigid and flexible plates and reduced to the well-known results for lossless fluids. It is also shown that in the case of thin layers of viscous fluids between rigid surfaces, the results reduce to those given in squeeze film studies.

INTRODUCTION

The ability of thin fluid layers to sustain pressure and to develop internal friction allows them to be used both as bearings to carry loads and to provide damping to vibrating structures [1]. Common applications of fluid layer damping are seen in rotating devices, such as journal bearings, spherical bearings, rotating disks, and in translating devices, such as bands and tapes.

Most squeeze film studies start from the Reynolds equation for thin films, which assumes that gravitational and inertial effects are negligible and the fluid is Newtonian and incompressible. Very few studies have considered the effect of compressibility on thin film dynamics and on the pressure and damping of squeeze film bearings [2-7].

In the present paper, we develop general expressions to describe the dynamics of a fluid layer between two surfaces. We start with the Navier-Stokes equations for acoustic perturbations and consider the linearized solutions for pressure and particle velocity in a medium with viscous losses. Expressions for the pressure and particle velocity in the fluid are derived for infinite and finite, flexible and rigid surfaces separated by the fluid layer and the results are given in terms of impedances. When the surfaces are rigid and in close proximity, the results reduce to those of squeeze films.

PROBLEM FORMULATION

Consider two thin plates located at $y = 0$ and $y = d$ and parallel to the $x - z$ plane. The plates are described by their normalized impedances, Z_{p1} and Z_{p2}

$$Z_p = -i2\beta(\omega/\omega_c)[1 - (\omega/\omega_c)^2(k_x c/\omega)^4] \tag{1}$$

where $\beta = \omega_c m/2\rho c$, m is the mass per unit area of the plate, $\omega_c = c^2\sqrt{12}/(v_p h)$, v_p is the longitudinal

wave speed in the plate material, and h is the thickness of the plate.

Considering bending wave motion of the plates only in the $x-$direction, the equations of motion can be written as

$$\begin{aligned} \rho c Z_{p1}\eta_1 &= F(x,\omega) + p(x,d,\omega) \\ \rho c Z_{p2}\eta_2 &= -p(x,0,\omega) \end{aligned} \tag{2}$$

where $p(x,y,\omega)$ is the pressure in the layer between the plates. In the case of two infinite plates, we represent the forcing function, $F(x,\omega)$, as a travelling wave, or a Fourier component of an arbitrary forcing function, as $F_0\exp(ik_x x)$. The x-dependence of the pressure in the layer is the same. As we shall see later, in the case of plates of finite length, the x-dependence of the pressure in the layer is influenced by the boundary conditions on either end of the layer.

The acoustic field in a fluid with viscous losses can be described to the first order by two coupled differential equations [7]

$$\begin{aligned} \nabla^2\Phi_p + k_p^2\Phi_p &= 0 \\ \nabla^2\vec{\Omega} + k_v^2\vec{\Omega} &= 0 \end{aligned} \tag{3}$$

where

$$k_p^2 = k^2(1+ikl_v') \qquad k_v^2 = ik/l_v \qquad l_v = \mu/\rho c \qquad l_v' = (4\mu/3\rho c)(1+3\alpha/4\mu)$$

where μ and α are the coefficients of shear and bulk viscosity in the fluid, respectively. Viscous effects are expressed in terms of characteristics lengths l_v and l_v'. The density of the fluid is ρ, c is the speed of sound, and $k = \omega/c$.

The velocity potential Φ_p represents the propagational or longitudinal mode of the wave, and the vector potential $\vec{\Omega}$ describes the transverse or rotational diffusive shear waves.

The particle velocity and the acoustic pressure are obtained from the potentials as

$$\vec{u} = \vec{\nabla}\Phi_p + \vec{\nabla}\times\vec{\Omega} \tag{4}$$

$$p = i\omega\rho(1+ikl_v')\Phi_p \tag{5}$$

The relationships between the wavenumbers in the x and y direction are given as follows:

$$k_{py}^2 = k_p^2 - k_{px}^2 \qquad k_{vy}^2 = k_v^2 - k_{vx}^2 \qquad k_{px} = k_{vx} = k_x$$

Using Eqs. (3-6), expressions for the pressure and particle velocity for the waves travelling across the layer can be used to obtain the total impedance of two infinite plates separated by a fluid layer as

$$\frac{Z}{\rho c} = \frac{(Z_{p1}+Z_{p2})(1+b) - (ik_p'/k_{py})\tan(k_{py}d) - iZ_{p1}Z_{p2}(k_{py}/k_p')\tan(k_{py}d)(1+a)}{(1+b) - i(k_{py}/k_p')\tan(k_{py}d)Z_{p2}(1+a)} \tag{7}$$

where

$$b = (\Gamma)\tan(k_{py}d)\cot(k_{vy}d)$$

$$a = (\Gamma^2) + (2\Gamma)\frac{1-\cos(k_{py}d)\cos(k_{vy}d)}{\sin(k_{py}d)\sin(k_{vy}d)}$$

with $k_p' = (\omega/c)(1+ikl_v')$ and $\Gamma = k_{px}^2/k_{py}k_{vy}$.

When viscous losses are negligible, $\Gamma = 0$, $a = b = 0$, and $k_p = k_p' = \omega/c$ and the impedance of the two plate system, Eq. (7), reduces to the well-known result

$$\frac{Z}{\rho c} = \frac{Z_{p1}+Z_{p2} - (i\omega/k_{py}c)\tan(k_{py}d) - iZ_{p1}Z_{p2}(k_{py}c/\omega)\tan(k_{py}d)}{1 - iZ_{p2}(k_{py}c/\omega)\tan(k_{py}d)} \tag{8}$$

When the impedance of the backing plate is much larger than the impedances of the layer and the forced plate, the system impedance, Eq. (7), can be written as

$$\frac{Z}{\rho c} = \frac{(1+b) - iZ_{p1}(k_{py}/k'_p)\tan(k_{py}d)(1+a)}{-i(k_{py}/k'_p)\tan(k_{py}d)(1+a)} \tag{9}$$

When the viscous losses are neglected for the case of rigid backing plate, Eq. (9) reduces to

$$\frac{Z}{\rho c} = \frac{i + Z_{p1}(k_{py}c/\omega)\tan(k_{py}d)}{(k_{py}c/\omega)\tan(k_{py}d)} \tag{10}$$

Rigid Plates

In the case of infinite, flat and rigid plates, there is no longer an x-dependent excitation. Consequently, the acoustic field in the layer is independent of x. Then, $k_{px} = 0$ and $k_{py} = k_p$. Now, since $\Gamma = k_x^2/k_{py}k_{vy}$, Γ, a, and b are all zero. In other words, when the infinite plates are rigid, viscous effects in the layer are confined only to the $y-$direction (through k_{py} and k'_p) and are small.

$$\frac{Z}{\rho c} = \frac{(Z'_{p1} + Z'_{p2}) - (ik'_p/k_{py})\tan(k_{py}d) - iZ'_{p1}Z'_{p2}(k_{py}/k'_p)\tan(k_{py}d)}{1 - iZ'_{p2}(k_{py}/k'_p)\tan(k_{py}d)} \tag{11}$$

where Z'_{p1} and Z'_{p2} are obtained by setting $k_x = 0$ in the plate impedance equation (1).

In the case of finite length plates, the spatial dependence of the acoustic field in the layer is determined not only by the force distribution on the plate(s) but also by the boundary conditions at the ends of the layer.

Finite Rigid Plates

Consider two parallel plates of length L separated by a distance d. Assume the coordinate system to be centered on the top surface of the lower plate. The pressure fluctuations in the layer must be symmetric with respect to its center and are assumed to vanish at its ends.

The pressure field in the layer can be expressed as

$$p_p(x,y) = \sum_n p_n \cos(k_{px})_n \{\sin[(k_{py})_n y] + \epsilon_n \cos[(k_{py})_n y]\} \tag{12}$$

with the boundary conditions

$$p(\pm L/2, y) = 0 \qquad \frac{\partial p(x,y}{\partial x}|_{x=0} = 0$$

where $(k_{px})_n = (2n+1)\pi/L$ and $(k_{py})_n^2 = k_p^2 - (k_{px})_n^2$.

The boundary conditions in the y direction of the particle velocities are the same as before, except that the x-dependence of the acoustic field is now determined through the flat rigid plate and the boundary conditions imposed on the acoustic pressure. Application of the boundary conditions gives

$$\epsilon_n = \frac{i\omega\rho}{(k_{px})_n}\frac{\delta_n V_n}{p_n}$$

$$V_n = -\frac{p_n}{i\omega\rho}\frac{(k_{py})_n(k_{vy})_n}{(k_{px})_n} = -\frac{p_n(k_{px})_n}{i\omega\rho\Gamma_n}$$

$$\delta_n = \frac{\sin[(k_{vy})_n d] + \Gamma_n \sin[(k_{py})_n d]}{\cos[(k_{py})_n d] - \cos[(k_{vy})_n d]}$$

where $\Gamma_n = (k_{px})_n^2/(k_{py})_n(k_{vy})_n$.

Modal pressure amplitude p_n is obtained by expanding the normal velocity U_0 of the top plate in Fourier cosine series as

$$U_0 = \sum_n U_n \cos[(k_{px})_n x], \qquad U_n = \frac{(-1)^n 4U_0}{(2n+1)\pi} \tag{13}$$

which gives

$$p_n = \left[\frac{(-1)^n 4U_0}{(2n+1)\pi}\right]\left[\frac{i\omega\rho}{(k_{py})_n}\right]\frac{1}{\{\cos[(k_{py})_n d] - \cos[(k_{vy})_n d]\}(1+\delta_n\delta_n')} \tag{14}$$

where

$$\delta_n' = \frac{\sin[(k_{py})_n d]/\Gamma_n + \sin[(k_{vy})_n d]}{\cos[(k_{py})_n d] - \cos[(k_{vy})_n d]}$$

The impedance that the top plate surface sees is obtained by integrating the pressure distribution in the x-direction, yielding

$$Z = \sum_n \left[\frac{-i\omega\rho}{(k_{py})_n}\frac{8L}{(2n+1)^2\pi^2}\right]\frac{\cos[(k_{py})_n d]\cos[(k_{vy})_n d]\{\tan[(k_{vy})_n d]/\Gamma_n + \tan[(k_{py})_n d]\}}{(1+\delta_n\delta_n')\{\cos[(k_{py})_n d] - \cos[(k_{vy})_n d]\}^2}$$

which can be rewritten to separate the viscous effects as

$$Z = \sum_n \left[\frac{-i\omega\rho}{(k_{py})_n}\frac{8L}{(2n+1)^2\pi^2}\right]\frac{1}{\tan[(k_{py})_n d]}\frac{1+b}{1+a}$$

Squeeze Films

In cases where the thickness of the fluid layer is much smaller than the viscous boundary layer d_v, such that $d_v/d \gg 1$, the problem reduces to that of a squeeze-film bearing. Applying appropriate approximations in Eq. (14), the pressure in the thin layer can be written as

$$p(x) = \rho c U_0 \frac{4(-1)^{n+1}(\omega l/c)}{(2n+1)\pi(d/L)\sigma}\cos\left(\sqrt{i\sigma}\frac{x}{L}\right) \tag{16}$$

where σ is called the squeeze number defined as

$$\sigma = \frac{12\mu L^2}{\rho c^2 d^2}$$

It is clear that in squeeze films pressure waves travel with a complex wavenumber which can be expressed in terms of the non dimen onal squeeze number.

DISCUSSION

The primary role of a fluid layer is to provide a coupling between the two plates. The strength of the coupling is determined primarily by the viscosity of the fluid and the thickness of the layer. Considering the fluid layer properties in terms of its impedance in the normal direction to the plates, it is clear that the layer impedance also depends on the impedances of the two plates bounding it. The impedances of the plates contribute to the overall resistance and reactance of the layer.

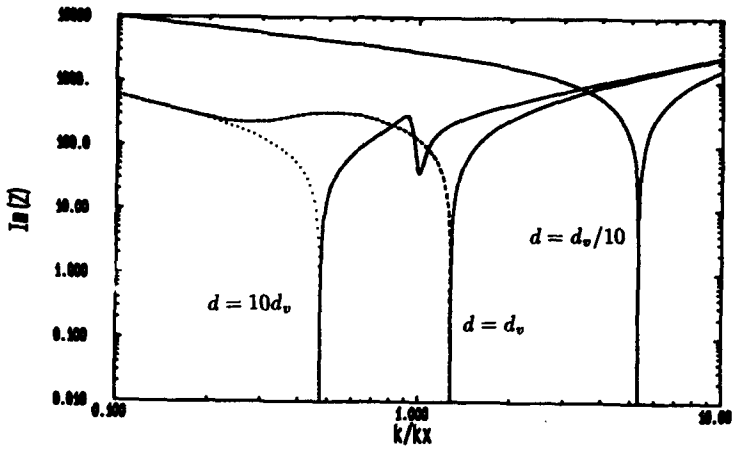

Figure 1. – Imaginary part of the impedance from Eq. (9) for an aluminum plate (h=1 mm) separated from a rigid backplate by air.

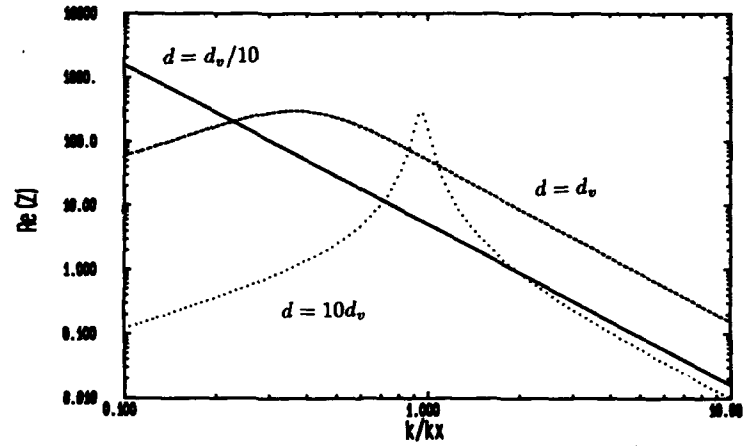

Figure 2. – Real part of the impedance from Eq. (9) for an aluminum plate (h=1 mm) separated from a rigid backplate by air.

In the absence of viscous losses in the fluid and neglecting radiation into the surrounding medium, radiation from the plate into the layer contributes to the resistive part of the overall impedance. At the coincidence frequency of the forced plate, the direction of radiation in the layer is (presumably) parallel to the plates, and we can expect it to provide a source of damping. Above the coincidence frequency, however, the radiation into the layer is no longer parallel to the plates. In the absence of the second plate, again, radiation damping would be expected, though to a lesser degree than at coincidence. However, the second plate reflects some or all of the radiated energy back. Thus, depending on the parameters of the layer and the plates, the effect of radiation into the fluid layer can have resistive and

reactive components, and that the reactance can be mass- or spring-like depending on the frequency regime.

The effects of the viscous properties of the layer are reflected through the wavenumbers k_p and k_v. The wavenumber, k_p, of the longitudinal waves has a relatively small imaginary component. Its effects are more significant at longer wavelengths. The wavenumber k_v of the shear waves has a large imaginary component and is dominant within the viscous boundary layers. In cases where the layer thickness is of the order of the boundary layer thickness, the damping due to shear waves dominates.

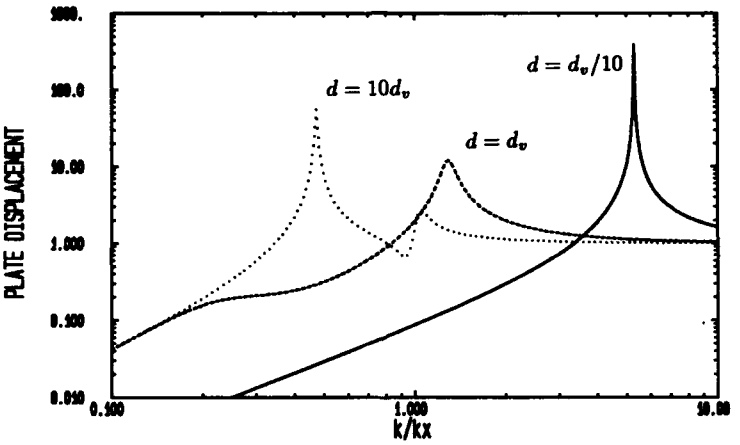

Figure 3. – Magnitude of the plate displacement.

The plates and the fluid layer form a coupled system of three elastic continua. In the case of infinite plates, we consider a "spatial" resonance of the plate *in vacuo* when the phase velocity of the excitation force equals the free bending wave speed of the plate. A similar resonance occurs between the plate and the fluid at the frequency where the bending wave speed and the speed of sound in the fluid are equal, i.e. the coincidence frequency. The properties of the fluid layer modify these resonant frequencies depending on the strength of the coupling it forms. The imaginary part of the impedance, given in Eq. (9), vanishes at the spatial resonances. As the layer thickness is decreased the frequency of the spatial resonance increases as a result of an increase in the stiffness of the system, as shown in Fig. 1. There are also resonances across the fluid layer thickness at relatively high frequencies.

The overall damping of the system depends on the layer thickness nonlinearly [7]. At very small layer thicknesses, although there is damping, stiffness dominates. Viscous damping attains a maximum as the layer thickness is of the order of boundary layer thickness [4]. At larger values of layer thickness, however, radiation from the plate into the layer becomes the dominant damping mechanism around the coincidence frequency, as shown in Fig. 2.

The resonant effects and the influence of the fluid layer are also seen in Fig. 3, where the magnitude of displacement of an infinite plate is plotted for different layer thicknesses. The damping effects of fluid layers are more prevalent at lower frequencies. However, the effect of layer thickness on damping has a dual role. Although small layer thicknesses provide higher damping, they also provide a higher stiffness thus shifting the resonant frequencies of the plate upward, away from the effective regime of layer damping, as shown in Fig. 2.

ACKNOWLEDGEMENT

This work was sponsored by a grant from the National Science Foundation.

REFERENCES

1. W. A. Gross, *Gas Film Lubrication*, Wiley, New York, N. Y., (1962).

2. W. E. Langlois, "Isothermal squeeze films," *Q. Appl. Math.*, **20** (1962), pp. 131-150.

3. W. S. Griffin, H. H. Richardson, and S. Yamanami, "A study of fluid squeeze-film damping," *ASME J. Basic Eng.*, **88** (1966), pp. 451-456.

4. M. J. H. Fox and P. N. Whitton, "The damping of structural vibration by thin gas films," *J. Sound and Vibration*, **73** (1980), pp. 279-295.

5. J. J. Blech, "On isothermal squeeze films," *J. Lubrication Technology*, **105** (1983), pp. 615-620.

6. L. C. Chow and R. J. Pinnington, "Practical industrial method of increasing structural damping in machinery, I: Squeeze-film damping with air," *J. Sound and Vibration*, **118** (1987), pp. 123-139.

7. P. M. Morse and K. U. Ingard, *Theoretical Acoustics*, Princeton University Press, Princeton, NJ (1986).

8. K. U. Ingard and A. Akay, "On the vibration damping of a plate by means of a viscous fluid layer," *J. Acoustics, Vibrations, Stress and Reliability in Design*, (1987), pp. 178-184.

SECOND INTERNATIONAL CONGRESS ON
RECENT DEVELOPMENTS IN AIR- AND
STRUCTURE-BORNE SOUND AND VIBRATION
MARCH 4-6, 1992 AUBURN UNIVERSITY, USA

VIBRATION SUPRESSION IN THE BUILDING FLOORS BY THE SYSTEMS WITH OXIDE-MAGNETES

Villen P. Khomenko
Laboratory for Investigation
of the Structures Service Features
Research Institute of Building
Structures (NIISK)
252037 Kiev, Ukraine

Leonid N. Tulchinsky
Laboratory for Magnetic Materials
Institute for Material Science
Problems of AS of the Ukraine
252142 Kiev, Ukraine

ABSTRACT

Systems using permanent magnets and magnetic liquids for supression of vibrations from various machines and mechanisms are well known in the world practice. Still they have some drawbacks that significantly limit their application area. Adoption of oxide magnetes having high specific power provides creation of reliable machines for vibration supression in the building floors. The repulsion force between the magnetic units made of strontium ferrite in a closed system can reach 3 MN that provides vibration damping from machines, large power-engines and other mechanisms and devices. The level of noise and vibrations from the above machines drops significantly as compared to the cases of traditional solutions. Corrosion resistance of oxide magnetes under conditions of high humidity contributes to reliability of the magnetic dampers.

INTRODUCTION

Vibration accompanies operation of almost any machine and technological equipment. It harmfully effects the very machines, the buildings they are located in, as well as the operator. It also limits a further improvement of these machines and mechanisms. Thus, effective vibro-protective means have become a must for further development of engineering and technology.

Traditional means (on rubber, with springs, etc.) have a number of limitations: low efficiency, inadequate durability and reliability, especially under conditions of aggressive medium (high humidity and a wide temperature range).

From practice, one of the effective techniques for vibration damping in buildings and structures is employment of special-purpose devices on magnetic and magnetic-active materials, e.g., devices utilizing permanent magnets for oscillations damping.

In the devices of [1-7], the amortization effect is reached due to the pull of two magnetes surrounded by magnetic liquid layers and divided by the movable non-magnetic partitions. Fig. 1 shows a peculiar engineering solution used in Japan [6]. Fig. 2 illustrates the one used in the USSR [7].

The bearing capacity of the above systems is not high, and their durability is determined by the velocity of liquid evaporation. The above devices employ not only permanent magnetes but liquid magnetes as well, and it considerably limits their area of application, especially in the temperature range, and it results in the cost rise since high-quality

magnetic liquids produced, e.g., by "Ferrofluidics Corporation" (U.S.A.), require expensive liquid bearers (fluoro-combinations of hydrocarbons or polycydoxans). Utilization of a natural phenomenon of like-pole magnets repulsion allows an intermediate liquid medium to be ignored.

TEXT

In the developed devices (one of which is shown in Fig. 3) the power of the magnetes demagnetization is used for damping, even poles of which get closer under loading effects.

The device consists of radially-magnetized hard magnet ring (1), the end of which contains a stable hard-magnet disk (2). The ring is connected with a non-magnetic cylinder (6), a movable hard-magnet disk (3) being replaced inside it. The ring (1) and disk (2) are located into a steel shell (4) which is a pole piece for the pole S. The inner disk (3) is reinforced with a steel pole piece (5) closed to a yoke (4) by means of magnetic wire.

Thus, poles N of the movable (3) and fixed (2) disks are placed inside the system. At their approaching, a partial demagnetization of the disks is occuring, while at moving off from one another, the magnetic flux running through the discs is increasing till the required magnitude is reached. This is due to the fact that the damping system employs high-ercetive magnetes with a liniar demagnetization characteristics (Fig.3). The magnetes being approached, the working point is shifted from starting position 1 on the demagnetization line to position 2; the magnetes being moved off from one another, the working point can enter position 3, ignoring position 1. Thanks to linearity of demagnetization characteristics, the working point moves freely over it, and it provides a durable system operation in the oscillation mode without the loss of the magnetic flux.

Large-size magnetic units made of strontium ferrite are utilized in the device. They have the following magnitudes: (i) residual induction: B_r = 0.41 T ; (ii) coercitive force on induction HcB = 300 kA/m; (iii) coercitive force on magnetization H_{cM} = 320 kA/m; (iv) power derivatives $(BH)_{max}$ = 32 kJ/m^3 .

The disc diameter may amount to 300 mm at its thickness of 100 mm.

The magnetic-hard ring prevents the magnetic flux scattering that is directed from one pole of the disc magnet to the other. In such a system, the induction value decreases down to 0.2 Tl at maximum approaching of the magnets, and it provides the repulsion force of both pairs of poles up to 3 MN that is estimated for each of them by the formula:

$$F = \frac{1}{2\mu_0} B^2 S \qquad (1)$$

where F - square of interacting poles; $\mu_0 = 4\pi \cdot 10^{-7}$ H/m - magnetic constant; B - induction in the interpole space; S pole square.

The magnetic system, shown in Fig. 3, is placed into the rubber shell that adds to the oscillation supression.

Opposite to traditional dampers, the described system has significantly non-linear characteristics (Fig. 5). Its advantage is also in employing fairly cheap ($ 10/kg) magnetes that are corrosion resistive by nature.

The frequency range makes up 0.1 to 30 Hrz depending on the mass of the damping system. In the latter case, small (50 mm diameter) magnetic modules, being placed between a vibration sauce and a floor, are used for damping. Application of magnetic damping systems is practically free of any service costs.

REFERENCES

1. USSR A.c. N° 804946. F16F9/06 Shock-absorber / Melnikov, E.N., Sinchenko, Zh.F., Popov, Yu.I. // Bul.I. N°7, 1981.

2. USSR A.c. 1060831. F16F6/00. Shock-absorber of the device / Zagoruyko, M.I. et all., Bul.I. N°46, 1983.

3. USSR A.c. 1062450F16F 6/00. Shock-absorber / Subbotina, B.I47,1983

4. USSR A.c. N° 1178982, F16F9/02. Air shock-absorber / Boguslavsky, V.A. // Bul.1. N°34, 1985.
5. USSR A.c. N° 1157293, F16F6/00. Shock-absorber / Rodionov, V.A., et all., Bul. N° 19, 1985.
6. Application N° 55-41370. Japan. Shock-absorber. Published 1980.
7. USSR A.c. N° 1213283, F16F6/00. A technique for magnetic-liquid shock-absorbing // Rodionov, V.A., et all // Bul.1. N° 7, 1986.

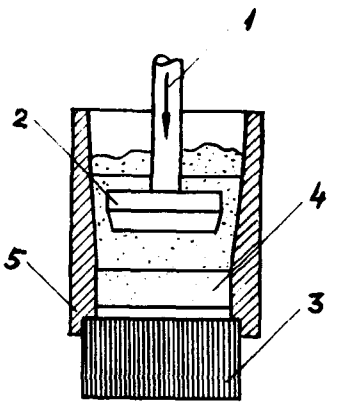

Figure 1-- Liquid-spring shock-absorber of levetizing type 6
1-rod; 2-piston; 3-permanent magnet; 4-magnetic liquid; 5-body.

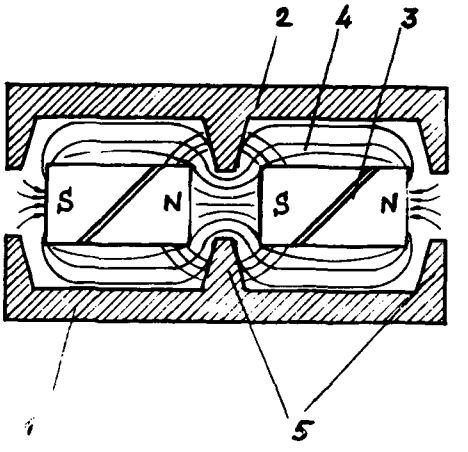

Figure 2--Damping system on permanent magnetes using magnetic liquid 7 . 1-base; 2-shifted elements; 3-permanent magnet; 4-magnetic liquid; 5-partitions.

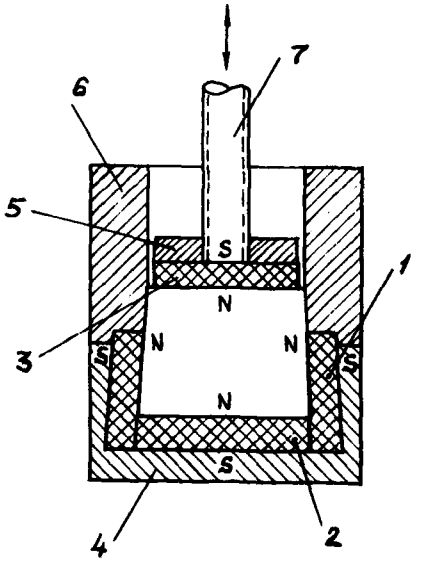

Figure 3--Damping module on oxide magnetes. 1-magnetic cylinder; 2-fixed magnetic disc; 3-shifted magnetic disc; 4-magnetic yoke; 5-pole piece of the movable system; 6-non-magnetic supressing cylinder; 7-anchor bolt for fixing the vibration source.

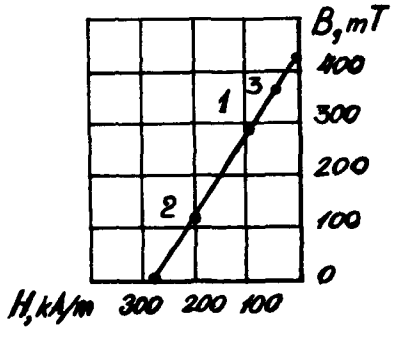

Figure 4--Demagnetization characteristics for the high energy oxide magnete.

A working point of the magnet system: 1 - at the starting state; 2 - at maximum loading; 3 - at complete disloading.

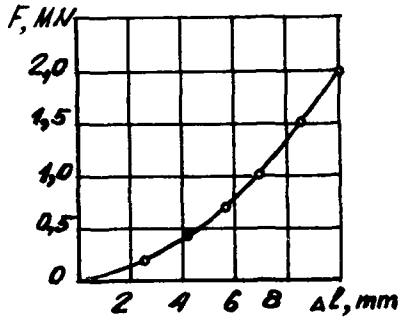

Figure 5--Loading characteristics of the damping module.

SECOND INTERNATIONAL CONGRESS ON
RECENT DEVELOPMENTS IN AIR- AND
STRUCTURE-BORNE SOUND AND VIBRATION
MARCH 4-6, 1992 AUBURN UNIVERSITY, USA

RECIPROCAL DETERMINATION OF VOLUME VELOCITY OF A SOURCE IN AN ENCLOSURE

Bong-Ki Kim , Jin-Yeon Kim , Jeong-Guon Ih
Department of Mechanical Engineering
Korea Advanced Institute of Science & Technology

Abstract

Volume velocity of an acoustic source can be widely used in determining the vibro-acoustic transfer functions , in measuring the acoustic transfer impedances and in finding the generated power of a source. Several techniques have been proposed for this purpose , such as the laser velocimetry, the internal pressure measurement and the face-to-face electro-acoustic measurement. However , for a source in an enclosure with flexible walls , acousto-structural coupling should be considered. Present method using an acousto-structural reciprocity principle results a good vibro-acoustic transfer impedance and can be used in determining the volume velocity of a source in-situ.

1. Introduction

The volume velocity of an acoustic source is useful in characterising the vibro-acoustic transfer functions , in measuring the acoustic transfer impedances and in determining the generated source power. For the study of these acoustic parameters , moving-coil type loudspeakers are popularly utilised as acoustic sources due to its ease of control and cheap price. Several methods have been proposed to estimate the acoustic volume velocity of a loudspeaker. Among them , the following three methods have been suggested for practical measurements : the laser velocimetry , the internal pressure method and the electro-acoustic reciprocity method. These methods require idealised environments or test rigs. In this paper , we propose a new technique for estimating the volume velocity of an acoustic source , in-situ. A reciprocity method using a structural-acoustic transfer function is adopted and the results are compared with other methods.

2. Determination of volume velocity using an acousto-structural reciprocity

Vibration and acoustic field in the flexible boundary, like shells or plates , which should be linear have the reciprocal relationship. When we consider two situations , shown in Fig.1 , the situation 1 is that the mechanical force at A is active and the acoustic pressure at B is measured , and , reciprocally , the situation

2 is that the acoustic source at B is active and the vibrational velocity at A is measured. Then , from the acoustic reciprocity principle we can find the following relationship[1]:

$$\frac{v^{(1)}(\vec{r}_A)}{Q^{(1)}(\vec{r}_B)} = \frac{P^{(2)}(\vec{r}_B)}{F^{(2)}(\vec{r}_A)} \qquad (1)$$

where $F(\vec{r})$ is the point excited force at $\vec{r} = \vec{r}_A$ and $Q(\vec{r})$ is the volume velocity of a monopole source at $\vec{r} = \vec{r}_B$. Here $v(\vec{r})$ is the vibrational velocity and $P(\vec{r})$ means the acoustic pressure. This principle states that if in an unchanged environment the locations of a small source and a small receiver are interchanged , the transfer function between point A and B will remain the same. Therefore, the acoustic volume velocity , Q , as a function of frequency can be given by

$$Q(f) = v(f)\left(\frac{P(f)}{F(f)}\right)^{-1} \qquad (2)$$

where the source should be considered as a monopole one. If the acoustic source can be assumed as a monopole , it is not necessary to consider the shape of source in this method. This fact is powerful in estimating the acoustic volume velocity of sources with irregular geometries[2].

3. Comparison with other measurement methods

3.1. Laser velocimetry

Using the laser velocimetry one can directly measure the velocity , u , of a point on the diaphgram of a loudspeaker. With this measured velocity the volume velocity of a source can be easily measured using $Q_L = \vec{u} \cdot \vec{n}\, S$ where $\vec{n}$ is the surface normal vector and S is the effective area of diaphgram. For this measurement the source is assumed to be a baffled rigid piston. In many cases at low frequencies a loudspeaker diaphragm is often considered "pistonlike" one. When using the monopole source assumption , the condition of $ka << 1$ should be satisfied where k is the wave number and a is the characteristic dimension of the loudspeaker. At higher frequencies , however , the motion of different parts of the loudspeaker diaphragm modes are excited. Under these conditions the loudspeaker will not behave as a monopole source. In this paper , we have a loudspeaker of 100 mm in diameter and interested in the low frequencies below 400 Hz where this problem can be considered as minimally affecting[3]. The laser displacement meter (KEYENCE , LC-2310) was used in this experiment . The output signal from the lasr displacement meter was differentiated to obtain the velocity.

3.2 Internal pressure method

Loudspeaker diaphgram housed in an acoustically sealed cylinder vibrates like a piston. The cylinder was made of PVC pipe of 650 mm in length , 100 mm in radius and 10 mm in thickness. As the piston vibrates, it causes changes in the total internal pressure P and volume V. For perfect gases the relationship between a small change in cavity pressure due to a small change in its volume can be given by[3]

$$P(\omega) = \frac{-\rho c^2}{V}\frac{Q}{j\omega} \qquad (3)$$

From this , one can determine the acoustic volume velocity by measuring only the acoustic pressure as follows :

$$Q_{IPM} = \frac{-j\omega V}{\rho c^2} P(\omega) \qquad (4)$$

where ρ is the air density , c is the speed of sound , V is the volume of enclosure , and $P(\omega)$ is the pressure fluctuation in the box. The wavelength should be larger than the characteristic dimensions of the enclosure. If the wavelength is small compare to any of the internal dimensions , the pressure will also be governed by a frequency-dependent spatial function[3]. In this case , the error in estimating the acoustic volume velocity would occur. However , we are interested in the low frequency range below 400 Hz , in which this problem need not to be considered .

The laser velocimetry method was used to be taken as a reference measurement of the acoustic volume velocity for other methods. The comparison is made in Fig.2 and 3 between the acoustic volume velocity using the internal pressure method and the laser velocimetry , $Q_{IPM}(f) / Q_L(f)$. Internal pressure measurement method underestimates the acoustic volume velocity by about 0.4 dB. Inaccuracies in the estimate of internal pressure measurement may be caused by the vibrations of box plate or due to some bias errors.

3.3 Acousto-structural reciprocity method

To implement and prove the method mentioned in section 2 , an irregularly shaped chamber as illustrated in Fig.4 is constructed using steel plates of 1mm in thickness. The dotted line in Fig.5 is the result of the acousto-structural reciprocity method between the points , say , A_1 and B. A large amount of deviations from Fig.2 can be observed. Large peaks and troughs in the figure is caused by the inverse of the structure-acoustic transfer function (P/F) and multiplicating it with the measured velocity. This fact means that the peaky curves are due to errors in handling the peaky velocity and the inverse of transfer function data. For these peaks , one needs a number of data points to average. If we choose several points on the boundary as shown in Fig.6 , the averaged acoustic volume velocity is given by

$$Q_{avg} = \frac{1}{n}\sum_{i=1}^{n} v_i(f)\left(\frac{P_i(f)}{F_i(f)}\right)^{-1} \qquad (5)$$

Fig.7 shows a comparison between the acoustic volume velocity derived from the reciprocal method and the laser velocimetry , $Q_R(f) / Q_L(f)$, where $Q_R(f)$ was determined by a reciprocal measurement when the number of averaging points is 5. This would become larger as the frequency goes up to higher frequencies due to the failure of the monopole source assumption. The acoustic volume velocity is influenced by the environment where acoustic source is placed and by the electrical source input as well. The interaction between the source and the flexible panels causes the change of radiation impedance of acoustic source. This means that the acoustic volume velocity will be changed due to the boundary effects. Another problem in these methods is irregular source shape. If the dimensions of a source are much smaller than the wavelength of the sound being radiated , as a monople source, then the details of the surface motion are not important and it will radiate exactly the same sound as any other simple source with the same acoustic volume velocity. In spite of this advantage , established methods cannot find the acoustic volume velocity if the shape of the source is complex. The acoustic reciprocity method which is introduced in this paper

overcomes this problem , because it is not necessary for this method to consider the motion of vibrating surfaces.

4. Prediction of interior sound field

If the system, illustrated in Fig.4 , is linear , P/F and V/Q represent the same transfer function between point A and B. When we consider two points or more on the flexible boundary , the pressure at point A will be given by

$$P_{total} = \sum_{i=1}^{n} \left(\frac{P}{F}\right)_i \hat{F}_i = \sum_{i=1}^{n} \left(\frac{V}{Q}\right)_i \hat{F}_i \qquad (6)$$

If the transfer functions of all points are found and the input forces are known , the interior acoustic pressure in the enclosure can be predicted. The two points on the panel , shown in Fig.4 , are selected as mechanical measuring points. The transfer functions , V/Q and P/F of A_1 to B and A_2 to B are measured. From Fig.7 , we can find that averaged volume velocity when n=5 , results more accurate transfer function than that from direct measurement. The interior sound pressure in an enclosure can be predicted by using the transfer functions , (P/F) and (v/Q). The measured pressures are shown in Fig.8-(a) and (b). If the system is linear and if we can estimate the acoustic volume velocity accurately , the vibration and acoustic fields will be in reciprocal relationship. Then , the two results from (P/F) and (v/Q) will coincide with each other in all frequency ranges. As depicted in the figure , the acousto-structural reciprocity method predicts the interior pressure very reasonably in all frequency ranges. Another complex situation considered is the chamber consisting of double panels and containing sound absorbing materials in the enclosed space. Fig.9 shows the comparison between the predicted and actually measured interior sound. Another good agreement can be observed.

6. Conclusion

A new method of measuring the volume velocity of an acoustic source is presented using the acousto-structural reciprocity. Acousto-structural reciprocity method overcome the problems of flexible boundary effects and indeterminable source shapes. This method was applied to the prediction of interior sound pressure due to the structural excitation and the result was in good agreement with the practically measured one.

REFERENCE

[1] L. M. Lyamshev , " A Question in Connection with the Principle of Reciprocity in Acoustics " , Sov. Phy. Acoust. ,vol.5 , pp. 406-409 (1960) .

[2] L. E. Kinsler et al. , " Fundamentals of Acoustics " , 3rd ed.Wiley , NewYork (1982) .

[3] D. K. Anthony and S. J. Elliott , " A Comparison of Three Methods of Measuring the Volume Velocity of an Acoustic Source " , J. Audio Eng. Soc. , vol.39 (1991) .

[4] J. M. Mason and F. J. Fahy , " Development of a Reciprocity Technique for the Prediction of Propeller Noise Transmission through Aircraft Fuselages " J. Noise Control Eng. , vol.34 , pp. 43-52 (1990) .

[5] T. Salava , " Sources of the Constant Volume Velocity and Their Use for Acoustic Measurements " J. Audio Eng. Soc. , vol.22, pp. 146-153 (1974).

[6] Lord Rayleigh , " The Theory of Sound " , 2nd ed. vol.II , Dover , NewYork (1945) .

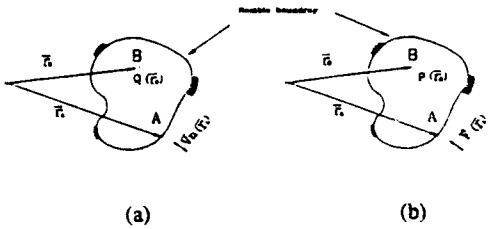

Fig.1. Reciprocal relationships between vibration and acoustic fields in flexible enclosures.

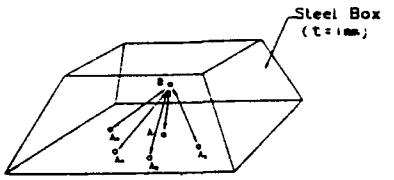

Fig.4. Transfer functions between boundary points , A_i and interior field point , B , in an enclosure.

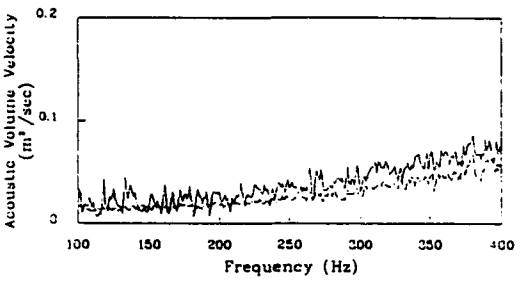

Fig.2. Acoustic volume velocity.
(— : Laser velocimetry , — · — : IPM)

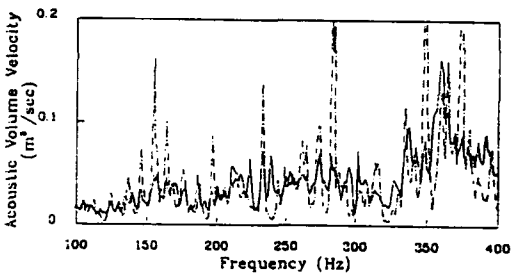

Fig.5. Acoustic volume velocity using reciprocal method. (— · — : n = 1 , — : n = 5)

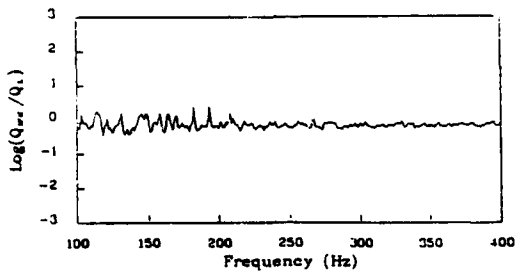

Fig.3. Comparison of measured volume velocity using IPM and laser velocimetry

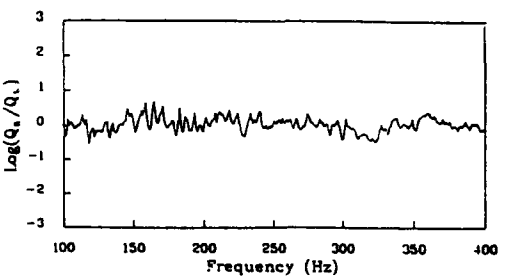

Fig.6. Comparison of measured volume velocity using reciprocity and laser velocimetry.

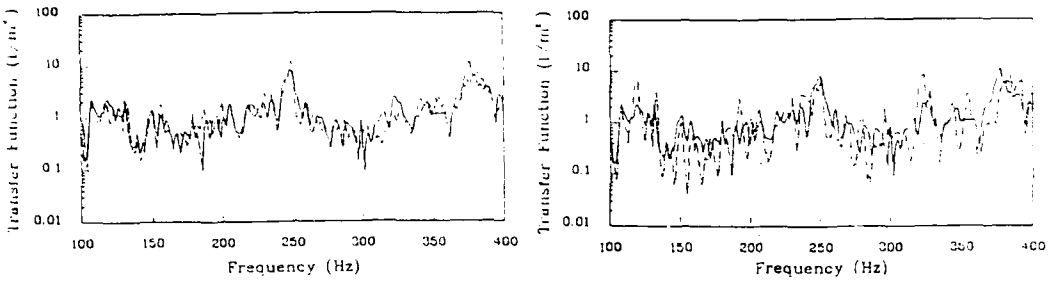

Fig.7. Transfer function at a point : volume velocity is obtained
(a) by averaging those of 5 points , (b) by measuring only one point.
(— : P/F , — · — : v/Q).

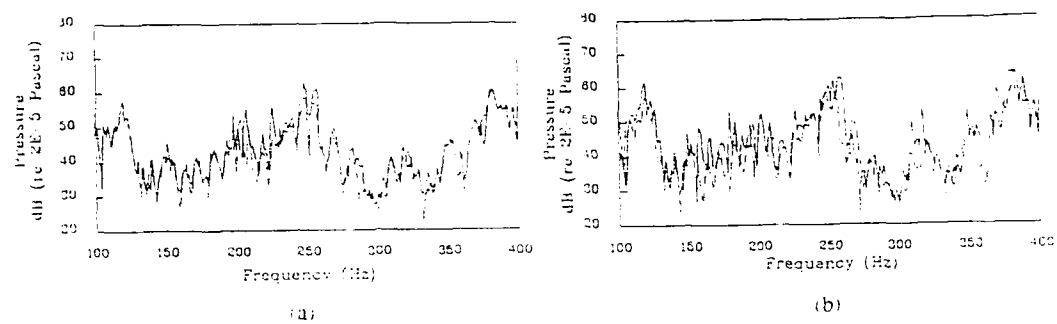

Fig.8. Prediction of interior sound pressure at a point in an enclosure with simple bare steel panels
(a) using the transfer function of P/F , (b) using the transfer function of v/Q.
(— : predicted , — - — : measured)

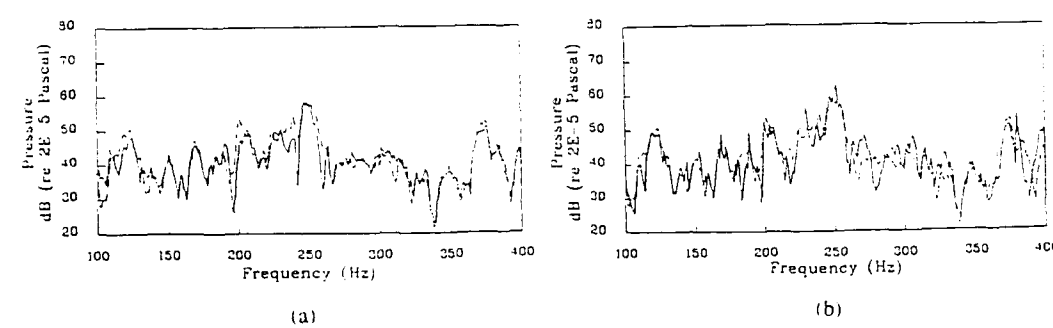

Fig.9. Prediction of interior sound pressure in case of complex system consisting of double panels and absorption materials in the enclosed space
(a) using the transfer function of P/F , (b) using the transfer function of v/Q.
(— : predicted , — - — : measured)

SECOND INTERNATIONAL CONGRESS ON
RECENT DEVELOPMENTS IN AIR- AND
STRUCTURE-BORNE SOUND AND VIBRATION
MARCH 4-6, 1992 AUBURN UNIVERSITY, USA

ANALYSIS OF FORCED ACOUSTIC FIELDS INSIDE STRUCTURALLY COUPLED CAVITIES

Arzu GÖNENÇ-SORGUÇ and Mehmet ÇALIŞKAN
Mechanical Engineering Department
Middle East Technical University
06531 Ankara, Turkey

ABSTRACT

Dynamic response characteristics of structurally coupled multicavity systems are studied. Acoustoelasticity method is used to model the structural-acoustical interaction under externally applied harmonic forcing.

It is demonstrated that effects of structural-acoustical interaction are more pronounced when excitation frequencies are close to in-vacuo acoustical and structural natural frequencies. When excitation frequency is near the cavity resonant frequency, the cavity acts like a vibration absorber for the structural wall and the natural frequency of the coupled system almost coincides with cavity resonant frequencies. When the coupled frequency is well separated from in-vacuo structural and acoustical frequencies, the interaction is found to dominate the response at this coupled natural frequency.

NOMENCLATURE

c_0	speed of sound	P_n	n'th acoustical modal pressure
E	Young's Modulus	q_m	m'th structural modal coordinate
h	wall thickness	$[Q]$	coupled system matrix
L_{nb}	acoustoelastic coupling coefficient	Q_m'	m'th external structural generalized force
m	structural mode index	V	volume
$M_{n,\lambda}$	n'th acoustical generalized mass	ν	Poisson's ratio for partitioning wall
M_m	m'th structural generalized mass	ρ_0	equilibrium density of fluid
n	acoustical mode index	ω_m	m'th structural natural frequency
N	total number of subcavities	$\omega_{n\lambda}$	n'th acoustical natural frequency

INTRODUCTION

A structure vibrating in contact with a fluid of comparable density experiences radiation loading comparable to its inertial and elastic forces. Radiation loading thus modifies the forces acting on the structure since the acoustic pressure depends on the velocity. Hence, a feedback coupling between the fluid and structure exists. Here, the structural and acoustical problems must be solved simultaneously [1].

Structural-acoustical coupling is pronounced in the dynamic analysis of totally enclosed spaces with flexible walls. Submarines, aircraft and passenger car cabins are typical examples of this type of coupling, commonly termed as gyroscopical coupling since the pressure in the vicinity of a flexible partition can be expressed in terms of the acceleration of the panel. Consequently, the dynamic behavior of the coupled system deviates from those of its in-vacuo constituents. The degree of deviation depends on the level of coupling.

In technical literature several methods of analysis have been described. Among these, the acoustoelasticity method is found to be a very popular and effective approach at low frequencies [2,3].

In the acoustoelasticity method, pressure is expanded in terms of the normal modes of rigid - walled cavity. The results are given in the form of linear ordinary differential equations for the response of each normal modes. The equations of motion of the flexible wall in terms of its structural modes are also expressed. Consequently, the coupled fluid - structural equations of motion are then obtained to [illegible] the acoustical natural frequencies and the corresponding modes [3].

In this study, acoustoelasticity method is employed to study the acoustoelastic field resulted from the interaction between isotropic structural wall and interior acoustic field under an external harmonic forcing in three dimensional spaces. Acoustical natural frequencies, structural natural frequencies and coupled natural frequencies are found. Sound pressure levels inside cavities in a specified frequency band are determined.

ACOUSTOELASTICITY METHOD

In order to apply the acoustoelasticity method, it is assumed that the first subcavity has the isotropic flexible walls on its right side while the other subcavities have flexible walls on both sides. Rectangular, three dimensional subcavities are chosen for convenience. A multi-cavity system and the related terminology are illustrated in Figure 1.

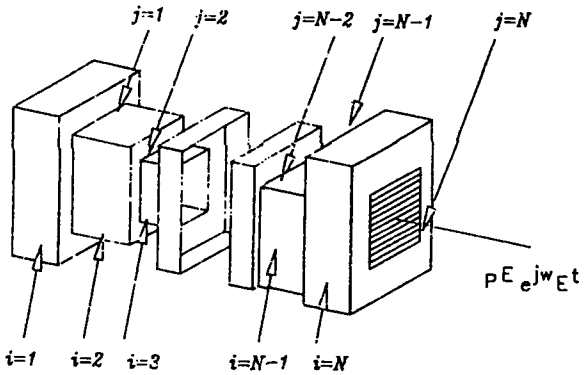

Figure 1 A Complex Shaped 3-D Cavity with an Outside Flexible Wall

Acoustical System

Acoustic fields in a general three dimensional cavity divided into N subcavities by isotropic flexible partitions is studied under external forcing. The wave equation is transformed into a set of ordinary differential equations by applying appropriate boundary conditions and Green's Theorem. Hence modal equations of motion for the acoustic pressure can be written as

$$\ddot{p}_n^{(i)} + \rho_0 c_0^2 \frac{A_A^{(i)} C_{nn}^{(i)}}{V^{(i)} M_{n,A}^{(i)}} \dot{p}_n^{(i)} \omega_{n,n}^{2(i)} p_n^{(i)} = -\left(\frac{A_F^{(i)}}{V^{(i)}}\right) \sum_m \ddot{q}_m^{(i)} L_{nm}^{ii} \qquad \text{for } i=1$$

$$\ddot{p}_n^{(i)} + \rho_0 c_0^2 \frac{A_A^{(i)} C_{nn}^{(i)}}{V^{(i)} M_{n,A}^{(i)}} \dot{p}_n^{(i)} + \omega_{n,A}^{2(i)} p_n^{(i)} = \frac{A_F^{(i-1)}}{V^{(i)}} \sum_m \ddot{q}_m^{(i-1)} L_{nm}^{i(i-1)} \qquad (1)$$

$$- \frac{A_F^{(i)}}{V^{(i)}} \sum_m \ddot{q}^{(i)} L_{nm}^{ii} \qquad \text{for } 1<i\leq N$$

where i represents the subcavity number, $\omega_{n,A}^{(i)}$ is the acoustical natural frequency of the i^{th} subcavity, $A_F^{(i)}$ is the area of the flexible wall, and $V^{(i)}$ is the volume of the i^{th} subcavity. L_{ns}^{ij} denotes the acoustoelastic coupling coefficient between the n^{th} acoustic mode of i^{th} subcavity and m^{th} structural mode of j^{th} flexible wall.

Structural System

Partitions formed by isotropic plates simply supported along four edges are considered in the analysis. Structural in - vacuo normal modes used in expressing the flexible wall deflection by modal expansion are specified by boundary conditions on the flexible wall area. Then the modal equations for the i^{th} structural wall can be expressed explicitly as

$$M_m^{(i)}\left(\ddot{q}_m^{(i)}+\omega_m^{2(i)}q_m^{(i)}\right)=\rho_0 c_0^2 A_F^{(i)}\sum_n \frac{P_n^{(i)}L_{nm}^{ii}}{M_{n,A}^{(i)}}-$$

$$\rho_0 c_0^2 A_F^{(i)}\sum_n \frac{P_n^{(i-1)}L_{nm}^{(i+1)i}}{M_{n,A}^{(i)}} \qquad \text{for } 1\le i<N \tag{2}$$

$$M_m^{(i)}\left(\ddot{q}_m^{(i)}+\omega_m^{2(i)}q_m^{(i)}\right)=$$

$$\rho_0 c_0^2 A_F^{(i)}\sum_n \frac{P_n^{(i)}L_{nm}^{ii}}{M_{n,A}^{(i)}}+Q_m^N \qquad \text{for } i=N$$

where $M_m^{(i)}$ is the m^{th} structural generalized mass of the i^{th} flexible wall. $\omega_m^{(i)}$ is the m^{th} structural in-vacuo natural frequency of the i^{th} wall.

Forced Acoustical - Structural System

In order to find the acoustical parameters of the acoustoelastically coupled system Equation 1 and the Equation 2 are combined and simplified by introducing a matrix Q_{sr}^{ij} which is defined as

$$Q_{sr}^{ij}=\begin{cases}\dfrac{A_F^{(i)}}{V^{(i)}}\displaystyle\sum_n \frac{\omega_E^2}{(-\omega_E^2+\omega_{n,A}^{2(i)})}\frac{L_{ns}^{ii}L_{nr}^{ii}}{M_{n,A}^{(i)}}+\frac{A_F^{(i)}}{V^{(i+1)}}\sum_n \frac{\omega_E^2}{(-\omega_E^2+\omega_{n,A}^{2(i+1)})} & \\ \quad\times\dfrac{L_{ns}^{(i-1)i}L_{nr}^{(i+1)i}}{M_{n,A}^{(i+1)}}+\left[-\dfrac{(\omega_E^2+\omega_r^{2(i)})}{\rho_0 c_0^2 A_F^{(i)}}M_r^{(i)}\right] & \text{for } 1\le i<N \quad \text{for } i=j\\ \dfrac{A_F^{(i)}}{V^{(i)}}\displaystyle\sum_n \frac{\omega_E^2}{-\omega_E^2+\omega_{n,A}^{2(i)}}\frac{L_{ns}^{ii}L_{nr}^{ij}}{M_{n,A}^{(i)}}+\left[-\dfrac{(-\omega_E^2+\omega_r^{2(i)})M_r^{(i)}}{\rho_0 c_0^2 A_F(i)}\right] & \text{for } i=N\\ -\dfrac{A_F^{(i-1)}}{V^{(i)}}\displaystyle\sum_n \frac{\omega_E^2}{-\omega_E^2+\omega_{n,A}^{2(i)}}\frac{L_{ns}^{i(i-1)}L_{nr}^{ij}}{M_{n,A}^{(i)}} & \text{for } i=j+1\\ -\dfrac{A_F^{(i+1)}}{V^{(i+1)}}\displaystyle\sum_n \frac{\omega_E^2}{-\omega_E^2+\omega_{n,A}^{2(i+1)}}\frac{L_{ns}^{(i+1)(i+1)}L_{nr}^{(i+1)j}}{M_{n,A}^{(i+1)}} & \text{for } i=j-1\end{cases} \tag{3}$$

In order to solve the acoustoelastically coupled system equations, {q} vector which represents the structural wall displacements is introduced and the coupled system equations are rewritten in matrix form as follows:

$$\begin{bmatrix} Q^{11} & Q^{12} & & \\ Q^{21} & Q^{22} & Q^{23} & \\ & & & \\ & Q^{(N-1)(N-2)} & Q^{(N-1)(N-1)} & \end{bmatrix}\begin{Bmatrix}\{q^1\}\\ \{q^2\}\\ \vdots\\ \{q^N\}\end{Bmatrix}=\begin{Bmatrix}\{0\}\\ \{0\}\\ \vdots\\ -\dfrac{1}{\rho_0 c_0^2 A_F}\{Q_m^N\}\end{Bmatrix} \tag{4}$$

Coupled natural frequencies of the acoustoelastic system are then found from Equation (4) by equating the determinant of the Q matrix to zero

$$Det\ [Q] = 0 \tag{5}$$

For the given excitation frequency band, solution of the equation (4) gives the resulting pressure amplitude and hence, the corresponding sound pressure level inside the subcavities can be calculated.

NUMERICAL SOLUTION TECHNIQUE

The information on eigenvalues of the coupled system is particularly helpful in identifying the peaks in the forced response characteristics. Therefore, the solution of Equation (5) is important to determine the dynamic behavior of the acoustoelastically coupled systems. Equation (5) is a non-standard eigenvalue problem due to the terms $(-\omega^2 I + \omega_{s,a}^2)$

appearing in the denominator of each term of the Q matrix. In order to solve this nonstandard eigenvalue problem, an iterative solution technique is adopted. The technique involves the determination of the sign of the determinant as a function of the frequency ω_ℓ. If the sign of the determinant of the Q matrix found from two successive trial values of ω_ℓ changes, then it is understood that there is a natural frequency lying between these two trial ω_ℓ's. Once the interval is determined, the well known Bisection Method is applied with a prespecified accuracy to find the coupled natural frequency.

Acoustic pressure distributions inside cavities are determined from the solution of Equation (4) by employing Gauss Elimination Method which gives the modal vectors {q} of the coupled systems. Acoustical modal pressure amplitudes, and finally total acoustic pressure amplitudes are also determined in the specified frequency band.

CASE STUDIES

Case study I

In this case study, the forced response of a three dimensional single cavity is examined in the frequency band of 0-200 Hz.

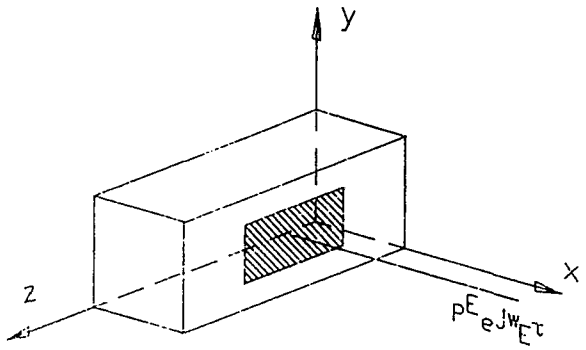

Figure 2 Case Study 1

The cavity given in Figure 2 is believed as a typical representation of cabins of twin-engine general aviation aircraft [4]. The cabin noise levels in such kinds of aircraft are reported to be very high. It is assumed that noise entered into the enclosed space by the airborne path only through the structural wall with no leakage. Noise generation inside the cabin was totally ruled out. The following baseline parameters were used in the foregoing analysis:

1. Rectangular cavity
   - working fluid : air
   - speed of sound : 340.46 m/s
   - density : 1.22 kg/m^3
   - dimensions : 1.22 m x 1.27 m x 3.61 m
2. Structural wall
   - boundary conditions : simply supported at all edges
   - location : center of y-z plane
   - dimensions : 0.27 m x 0.7 m
   - thickness (h) : 0.00356 m
   - modulus of elasticity (E) : (6.9) 10^{10} Pa
   - surface density (σ) : 9.6 kg/m^2
   - Poisson's ratio (ν) : 0.33
3. Receiver Position : P(0.304, 0.914,1.215) m
4. Excitation Force Amplitude : 0.1 Pa

Damping characteristics of the structural wall and sound absorbing properties of rigid walls were neglected in the present analysis.

For the in-vacuo acoustical natural modes, n_x, n_y, and n_z were taken from zero to 4. Structural in-vacuo natural modes, m_y, m_z were retained from 1 to 3. The present analysis was performed in the frequency band of 0-200 Hz. Tables 1 and 2 present the in-vacuo acoustical

and structural frequencies of uncoupled systems, respectively, calculated by the software. The coupled natural frequencies are tabulated in Table 3.

Table 1 In-vacuo Acoustical Natural Frequencies

n_x	n_y	n_z	f [Hz]
0	0	1	47.16
0	0	2	94.31
0	0	3	141.47
0	0	4	188.62
0	1	0	134.04
0	1	1	142.09
0	1	2	163.89
0	1	3	194.88
1	0	0	139.53
1	0	1	147.29
1	0	2	168.42
1	0	3	198.70
1	1	0	193.48
1	1	1	199.15

Table 2 In-vacuo Structural Natural Frequencies

m_y	1	1	1	2	2	2	3	3	3
m_z	1	2	3	1	2	3	1	2	3
f [Hz]	136.31	189.27	277.54	492.3	545.3	632.5	1085.6	1138.6	1226.8

Table 3 Coupled Natural Frequencies

$f_{coupled}$ [Hz]	59.43	94.72	167.79	186.23

In the case of weak coupling between the acoustic cavity and the structural wall, when the excitation frequency is near a structural or a cavity resonant frequency then the largest response will occur at these in-vacuo natural frequencies. On the other hand, when the coupling is strong, the contribution of the coupling into the response cannot be neglected.

Contributions by structural wall and cavity resonant frequencies into the response of the system are demonstrated in Figure 3 as well as the contributions of coupled frequencies. As depicted by the theory of acoustoelasticity, when the excitation frequency is well separated both from the structural and cavity in-vacuo natural frequencies, there may not be a single dominant structural and/or acoustical cavity natural frequency in the response [2]. For such a case, dominant peaks in the response are observed at the coupled frequencies. The peak at coupled frequency of 59.43 Hz seen in Figure 3 was associated with this phenomenon. The sound pressure level corresponding to this peak was found to be 135 dB [5].

According to the theory, when the excitation frequency is close to a cavity resonant frequency, the cavity acts like a vibration absorber for the structural wall. In such a case, coupled frequencies either coincide with the cavity natural frequencies or come very close to these frequencies. In the present analysis, the in-vacuo acoustical natural frequency at 94.31 Hz is shifted to 94.72 Hz while the acoustical natural frequency at 189.27 Hz shifted down to the coupled frequency of 167.79 Hz. Figure 3 illustrates peaks corresponding to the cavity resonant frequencies and the coupled frequencies of the structural-acoustical system [5].

When the structural and acoustical in-vacuo natural frequencies are close, the effect of the coupling is also pronounced in the system response [3]. The acoustic natural frequency

at 188.62 Hz and the structural wall natural frequency at 189.27 Hz for the given system is a typical example of such a case. The coupled frequency which was shifted down to 186.62 Hz due to such an interaction resulted in a peak in the response. As it is seen from Figure 3, together with the cavity and structural wall resonant frequencies, coupled frequencies must be taken into consideration to identify the peaks in the response if such special cases are encountered [5].

Case Study 2

The forced response of the multicavity system was considered in this case study. System was divided into two identical subcavities partitioned with identical flexible walls as shown in Figure 4.

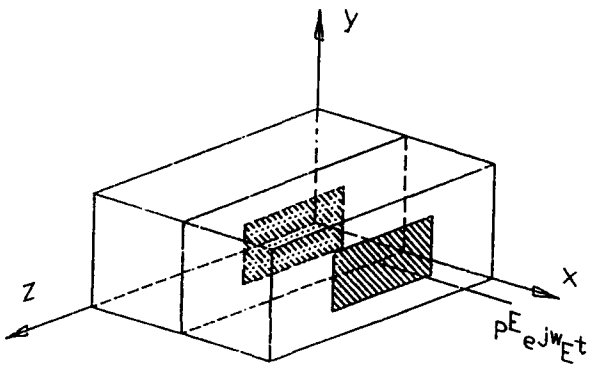

Figure 4 Case Study 2

The dimensions of the subcavities and the flexible walls are the same as the system given in Case Study 1. The external harmonic forcing is applied on to the second structural wall on the right end of the cavity. The amplitude of the forcing is taken to be 0.1 Pa as before.

The in-vacuo acoustical modes n_x, n_y and n_z were taken from 0 to 3. In-vacuo structural modes m_y and m_z were retained from 1 to 3 in modal expansion. The frequencies in 0 to 200-Hz frequency band were selected in the analysis. The in-vacuo acoustic and structural frequencies are identical for both subcavities and structural walls, respectively.

Coupled natural frequencies of the multicavity system were determined by the software and tabulated in Table 4.

Table 4 Coupled Natural Frequencies of the Multicavity System

$f_{coupled}$ [Hz]	41.31	78.64	94.37	94.93	140.51	141.33	184.20	188.11

In the case of the multicavity systems, acoustic pressure field in one of the subcavities is influenced by acoustic pressure fields inside the other subcavities. Degree of coupling between subcavities determines the level of interaction dependence of internal acoustic pressure fields.

Although dimensions of partitioning walls and cavities are the same, sound pressure levels in the first and the second subcavity are expected to be slightly different. The first subcavity has one flexible wall on its right side. The acoustic pressure inside this subcavity results from the acoustic pressure field inside the second cavity by acoustical energy interchange through the common wall. Second subcavity is bounded by two flexible walls on its left and right sides. Acoustic pressure field inside the second cavity depends on the acoustic pressure field inside the first subcavity and the external forcing applied through the flexible wall on its right side.

Responses of the first and second cavities for the specified points to the harmonic excitation described are illustrated in Figures 5 and 6, respectively. The in-vacuo acoustical natural frequency at 47.16 Hz is seen to shift down to 41.31 Hz due to the acoustoelastic coupling. This outcome is also consistent with the findings reported by E.M. Sözer [6]. At this frequency, acoustical natural mode (001) was dominant in the response of

the both cavities. The peak observed at the coupled frequency 78.64 Hz was also singled out as a distinct peak since the excitation frequency is well separated from the in-vacuo acoustical and structural natural frequencies as discussed in the previous case study. In such a case, the response peaks out at the coupled frequency in the vicinity of acoustical and/or structural natural frequencies while these frequencies do not appear in the response any more. On the other hand, the in-vacuo natural frequency at 94.31 Hz was seen to be coupled resulting in two closely coupled natural frequencies at 94.63 Hz and 94.93 Hz due to interactions between two subcavities. This type of coupling experienced between two subcavities can be termed as cavity coupling. The peak at this frequency in the second subcavity was observed to be higher than the one in the first subcavity. The same discussion also applies to the coupled natural frequencies of 140.51 Hz and 141.33 Hz resulting from the coupling of the in-vacuo acoustical natural frequency at 141.47 Hz. The in-vacuo structural natural frequency at 189.27 Hz was coupled by shifting down, giving two coupled natural frequencies at 184.20 Hz and at 188.11 Hz. The magnitude of the peak at 184.20 Hz in the second subcavity was higher than the one observed in the other subcavity. Conversely, the opposite was observed at 188.11 Hz [5].

When Figures 5 and 6 are compared to Figure 3, it can be concluded that when the acoustical system is partitioned by flexible walls to form multicavities one, the coupled natural frequencies rather than the in-vacuo acoustical or structural natural frequencies dominate the response. Special care should be exercised when identifying peaks in the response if the system to be analyzed is made up of multicavities [5].

CONCLUSIONS

The main conclusions reached after the case studies can be outlined as follows:

1. When the excitation frequency is well separated from in-vacuo acoustical and structural natural frequencies, there is no single dominant structural-cavity natural frequency, structural-acoustical interactions cannot be neglected, and the dominant peaks in the response are observed at coupled natural frequencies.

2. When the excitation frequency is near the cavity resonant frequency, cavity acts like a vibration absorber for the structural wall and the coupled frequency coincides with cavity resonant frequencies or come close to these frequencies.

3. If the in-vacuo acoustical and structural frequencies and the excitation frequency are close to each other, then structural-acoustical interaction is pronounced in the system response. The coupled frequency of the system happens to be close to these frequencies.

4. The accuracy of the present analysis depends on the number of acoustical and structural in-vacuo modes. The higher the number of acoustical and structural modes, the more accurate the results obtained would be.

5. The method is particularly applicable in the cases of low modal density. For this reason, it can be successfully employed to stucy structurally coupled interior acoustic fields with or without absorption.

6. Care should be exercised in specifying the frequency increment when the excitation frequency is near to in-vacuo acoustical-natural frequencies to avoid the trivial solutions.

7. For structural in-vacuo modes, simple trigonometric functions have employed in the analysis due to simply supported boundary conditions assumed for the partitions. One should be careful when interpreting the results in practical applications since partitioning walls are rarely simply supported. However, it is possible to adopt other orthogonal functions in modal expansion to account for real-life boundary conditions.

REFERENCES

1. Junger, C.J., Feit, D., 1986, "Sound Structure and Their Interaction", The MIT Press Cabridge, Massachusetts, London, England.
2. Sestieri, A., Del Vescove, D., Lucibello, P., 1984, "Structural-Acoustic Coupling in Complex Shaped Cavities", Journal of Sound and Vibration, vol. 96(2), pp. 219-233.
3. Dowell, E.H., Gorman, G.F., Smith, D.A., 1977, "Acoustoelasticity: General Theory, Acoustic Natural Modes and Forced Response to Sinusoidal Excitation, Including Comparisons With Experiment", Journal of Sound and Vibration, vol. 52(4), pp. 519-542.
4. Chao, C.F.B., 1981, "Modal Analysis of Interior Noise Fields", Finite Element Applications in Acoustics, pp. 39-56.
5. Gönenç-Sorguç, A., 1991, "Active Minimization of Acoustic Potential Energy Inside the Structurally Coupled Enclosed Spaces", M.Sc. Thesis, M.E.T.U., July 1991.
6. Sözer, M., 1989, "Analysis of Structurally Coupled Interior Acoustic Fields by Acoustoelasticity Method", M.Sc. Thesis, M.E.T.U., February 1989.

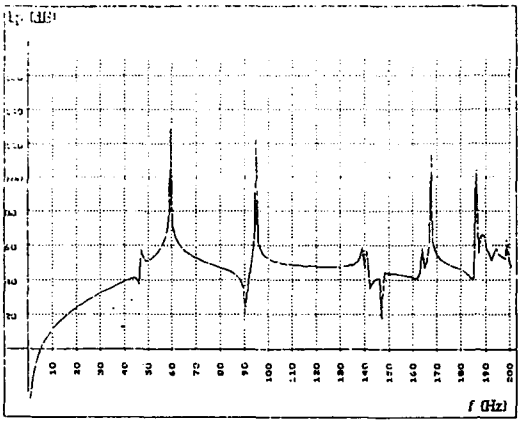

Figure 3 Lp vs External Exciting Frequency for Case Study 1

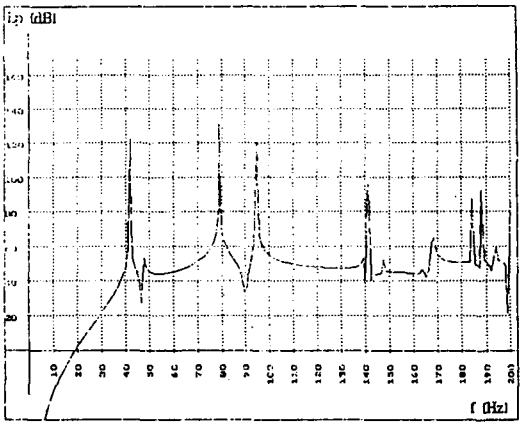

Figure 5 Lp vs External Exciting Frequency for the First Subcavity of Case Study 2

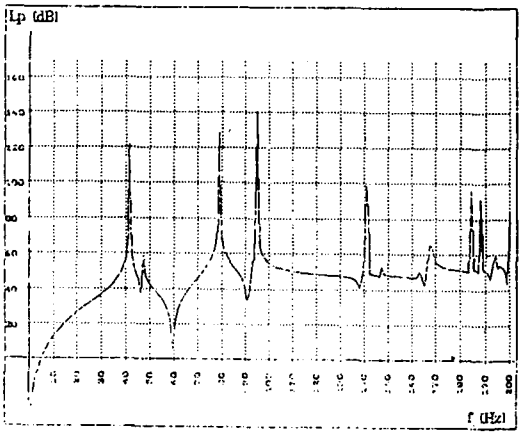

Figure 6 Lp vs External Exciting Frequency for the Second Subcavity of Case Study 2

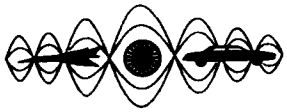

SECOND INTERNATIONAL CONGRESS ON RECENT DEVELOPMENTS IN AIR- AND STRUCTURE-BORNE SOUND AND VIBRATION

MARCH 4-6, 1992 AUBURN UNIVERSITY, USA

THEORETICAL AND EXPERIMENTAL ASPECTS OF ACOUSTIC MODELING OF ENGINE EXHAUST SYSTEMS WITH APPLICATIONS TO A VACUUM PUMP

B. S. Sridhara
Industrial Studies Department, Middle Tennessee State University
Murfreesboro, Tennessee 37132

and

Malcolm J. Crocker
Mechanical Engineering Department, Auburn University, Auburn, Alabama 36849

ABSTRACT

The engine exhaust system was modeled as a lumped source-muffler-terminations system. An expression for the predicted sound pressure was derived in terms of the source and termination impedances, and the muffler geometry. The developed prediction scheme is very efficient from computation point of view. Also, the predicted sound pressure can be calculated without computing the source pressure or the source velocity although these quantities can be calculated if necessary. The formulation was verified through a series of experiments. The source impedance was measured using the direct method. Sound pressure level measurements for the prediction scheme were made for several source-muffler and source-straight pipe combinations. In all cases, correlation of the experimental results and those predicted by the developed expressions was good.

INTRODUCTION

In an internal combustion engine, the engine is the noise source and the exhaust pipe is the main transmitter of noise from the source to the open end of the pipe. The open end of the exhaust pipe itself acts as a source and radiates the engine noise to the surroundings. The primary function of noise control devices used in the engine-exhaust pipe system should be to reduce the amount of sound energy radiated from the open end of the exhaust pipe to the surroundings. A series of experiments could be conducted on several mufflers installed in the exhaust pipe to achieve the desired reduction in the exhaust noise. But this is not a very efficient way of reducing the amount of sound energy radiated from the engine exhaust to the surroundings as the fabrication of mufflers and experimental work involve a great deal of time, effort and cost. Alternatively, if one can develop a method to predict the radiated sound pressure at a specified distance from the open end of the exhaust pipe so that the prediction scheme involves only a few measurements, then much of the laborious experimental work involved in muffler design can be avoided.

In order to reduce noise levels one should have a good knowledge of the sound source characteristics and the manner in which the sound is propagated. If the sound is propagated from the open end of a pipe, then the radiated sound pressure can be predicted at a particular location from the open end by

making one measurement at a convenient location near the pipe open end and knowing the source characteristics. Prasad and Crocker[1] developed a scheme to predict the sound pressure radiated from the open end of an unflanged pipe. The velocity source model was used and the source strength was expressed in terms of the source impedance, the radiation impedance, the four pole parameters and the measured sound pressure. The expression for the transfer impedance was derived in terms of the distance measured from the open end of the pipe, the source impedance, the radiation impedance and appropriate four pole parameters. The predicted sound pressure was obtained from the product of the transfer impedance and source velocity. The prediction of the radiated sound pressure from an open-ended pipe was studied by Boden[2,3,4]. The pressure and velocity source models were used in the prediction scheme. A total of 23 different pipe lengths (loads) ranging from 0.2 m to 3.2 m were used in the experiments. The source impedance values obtained from the two-load and three-load methods were used in the prediction scheme. The acoustic modeling of engine exhaust systems was applied to a reciprocating type vacuum pump by Sridhara[5]. A scheme to predict the sound pressure radiated from the exhaust pipe was developed using the pressure and velocity source models.

THEORY

Pressure Source Model

A schematic diagram of the pipe without and with a muffler in place is shown in figure 1. The sound pressure and velocity at sections 1-1 and 2-2 of the straight pipe without and with the muffler installed in the pipe are related by the four pole parameters. Block diagrams showing the sound pressure, velocity, and four pole parameters for the straight pipe without and with the muffler present are also shown in figure 1. The overall four pole parameters for the straight pipe without and with the muffler installed can be denoted by A', B', C', D' and A, B, C, D. The expression for the sound velocity at the source location for the straight pipe can be written (with reference to figure 1) in terms of the source pressure, source impedance, load impedance and sound pressure at section 1-1[6]. Thus

$$v = v_1' = \frac{p_s}{z_s + z_L'} = \frac{p_1'}{z_L'},$$

or

$$p_s = p_1' \frac{z_s + z_L'}{z_L'}. \qquad (1)$$

In the pressure source model, the source pressure is assumed to be a constant at a given frequency. Therefore, for the same source-pipe system with a muffler installed, it can be written that:

$$p_s = p_1 \frac{z_s + z_L}{z_L} . \tag{2}$$

It can be shown from equations (1) and (2) that

$$p_1' \frac{z_s + z_L'}{z_L'} = p_1 \frac{z_s + z_L}{z_L} . \tag{3}$$

Substituting for p_1' and p_1 in terms of the radiation impedance, four pole parameters and the sound pressure at section 2-2 (figure 1, cases i and ii) equation (3) can be written as

$$\frac{p_2'}{p_2} = \frac{A z_r + B}{A' z_r + B'} \frac{z_s + z_L}{z_s + z_L'} \frac{z_L'}{z_L} . \tag{4}$$

In equations (1) through (4), the impedances z_L' and z_L are the load impedances corresponding to the cases without and with the muffler installed.

Monopole Radiation Model

The open end of an unflanged pipe can be modeled as a monopole or point sound source for small values of the ratio of pipe diameter (at the open end) to the wavelength. In such a case, there will be plane and spherical wave propagation to the left and right of the exit plane of the pipe. The sound power transmitted through the open end of a pipe should be equal to the sound power radiated from the open end of the same pipe modeled as a monopole when there is no loss of energy.

The sound power transmitted through the exit plane of an open-ended pipe is given by the sound power incident on the exit plane minus the sound power reflected at the exit plane. It can be shown that at the exit plane of the pipe:

$$\frac{1}{2 \rho_o c_o} S' (|p_2'^{+}|^2 - |p_2'^{-}|^2) = \frac{1}{2 \rho_o c_o} |p_r'|^2 G' . \tag{5}$$

In equation (5), $|p_r|$ is the pressure amplitude of the spherical wave at a given radius, the cross sectional area of the pipe is denoted by S', the surface area of the imaginary sphere is represented by G' and other symbols have their usual meaning. Equation (5) can be written as

$$S' \; |p_2'^{+}|^2 \; (\; 1 - |R'|^2 \;) = |p_r'|^2 \; G' \; , \tag{6}$$

where $R' = (\; p_2'^{-} \; / \; p_2'^{+} \;)$ is the complex reflection coefficient at the open end of the pipe. The sound pressure can be written at the exit plane of the pipe in terms of its two components as

$$p_2' = p_2'^{+} + p_2'^{-} = |p_2'^{+}| \; |1 + R'| \; . \tag{7}$$

Solving for $|p_2'^{+}|$ in equation (7) and substituting into equation (6), it can be shown that

$$|p_2'| = [\; \frac{|1 + R'|^2}{(1 - |R'|^2)} \; \frac{G'}{S'} \;]^{1/2} \; |p_r'| \; . \tag{8}$$

In a similar way, a relation between the sound pressures p_2 and p_r can be established for the straight pipe in which a muffler is installed. Thus with reference to figure 1

$$|p_r| = [\; \frac{(\; 1 - |R|^2 \;)}{|1 + R|^2} \; \frac{S}{G} \;]^{1/2} \; |p_2| \; , \tag{9}$$

where the symbols have their usual meaning.

Prediction Scheme

Combining equations (4), (8) and (9) it can be shown that when there is no flow through the pipe and $R = R'$ (for $S = S'$), the predicted sound pressure level is given by

$$L_p = L_p' + 20 \log_{10} \; [\; \frac{|A' \; z_r + B'|}{|A \; z_r + B|} \; \frac{|z_s + z_L'|}{|z_s + z_L|} \; \frac{|z_L \; |}{|z_L'|} \;]$$

$$+ \; 20 \log_{10} (\; r' \; / \; r \;) \; . \tag{10}$$

The terms L_p and L_p' in equation (10) represent the predicted and measured values of the sound pressure level at distances r and r' from the open end of the pipes of lengths L and L'. L_p is given by the sum of the three quantities on the right hand side of equation (10). The first one is a measured quantity, the second term is derived from plane wave theory, and the third quantity is based on the monopole radiation model used at the open end of the pipe. Expressions for the predicted value of the sound pressure level

L_p can be derived from a suitable combination of equations (4), (8) and (9) for special cases such as

$(r' = 0, r > 0)$, $(r' > 0, r = 0)$, $(r' = 0, r = 0)$, when $L \neq L'$ and $L = L'$.

EXPERIMENT

Several experiments were conducted and the radiated sound pressure level was predicted for different source-straight pipe and source-muffler-straight pipe combinations. A reciprocating type vacuum pump was the source used during the experiment. The experimental set up is shown in figure 2. A simple expansion chamber was the muffler element installed in the pipe. The source impedance was measured using the direct method. The radiated sound pressure level was predicted using equation (10). Experiments were conducted in an open space with the ground below the open end of the pipe covered with an acoustic material to minimize the ground reflections. A frequency range from 0 to 3200 Hz was selected during the measurements to ensure only plane wave propagation in the pipe. A B&K type 2032 FFT analyzer and 0.006 m diameter microphones were used during the experiments.

Because of the size and weight of the vacuum pump and electric motor, measurements were made with the experimental set up mounted on a horizontal table. The sound pressure level measurements were made at a distance of 0.05 m from the open end of the pipe in order to maintain a 10 dB difference between the signal and electrical noise. Although several experiments were conducted only three plots are presented in this paper (figure 3).

RESULTS AND DISCUSSIONS

There are no theoretical methods to calculate the source impedance. The schemes used to predict the source impedance are complicated and are still to be proven. The accuracy of the measured values of the source impedance should be verified by experimental means. The reliability of the random excitation and transfer function methods of source impedance measurement can be tested against known theoretical cases such as open and rigid terminations of a pipe. The accuracy of the predicted values of the radiated sound pressure level can be determined by comparing the predicted quantities with the corresponding measured quantities. However, it should be remembered here that the predicted values of the radiated sound pressure level are functions of the measured values of the source impedance, theoretical source models and computed values of the radiation impedance. It should also be noted that the predicted values of the radiated sound pressure level depend on the monopole radiation model. Therefore, the results presented in this paper should be examined keeping all of these factors in mind.

The reliability of the computed value of the radiation impedance has been established in pipe acoustics[7]. The monopole radiation theory is valid for small values of the pipe end diameter to wavelength ratio. Thus the accuracy of the prediction scheme depends mainly on the accuracy of the measured values of the source impedance. Also, the prediction scheme can be used to verify the correctness of the source impedance values. Although the sound pressure level measurements were made at distances r' and r (figure 1) equal to 0.05 m it

has been established that the prediction scheme works well for small and large values of r' and r^5.

Referring to figure 3, the predicted values of the sound pressure level shown in case i were obtained using the source impedance measured when the pump was operating. In this se, it is seen that the predicted and measured values of the sound pressure level agree well below 1200 Hz and above 2400 Hz. The disagreement above 1200 Hz can be attributed to the increasing pipe diameter to wavelength ratio at the open end of the pipe, whereas the reason for the good agreement between the predicted and measured values from 2400 to 3200 Hz is not known. The sound pressure levels plotted in cases ii and iii (figure 3) correspond to the cases in which the source impedance was measured when the pump was operating and stationary. The agreement between the predicted and measured values is seen to be good below 1200 Hz except in the range from 100 to 250 Hz. A slight frequency shift between the predicted and measured values of the sound pressure level is seen in this case.

The acoustic model of an engine exhaust system is a powerful tool in predicting the behavior of a source- muffler-termination system. The model has been found to work well in the case of a system with a simple source such as a loudspeaker[5], and an actual source like the vacuum pump. It should be possible to extend the acoustic modeling to systems with more complicated sources than that covered in this article.

REFERENCES

1. M. G. Prasad and M. J. Crocker, "A Scheme to Predict the Sound Pressure Radiated from an Automotive Exhaust System," J. Acoust. Soc. Am., 70(5), 1345-1352 (1981).

2. H. Boden, "The Multiple Load Method for Measuring the Source Characteristics of Time Variant Sources," Summary of Paper 4, Ph. D. Thesis, Royal Institute of Technology, Sweden, 64 Pages (1989).

3. H. Boden, "Characterization of a Pneumatic Sliding Vane Motor as a Source of Fluid Borne Noise," Summary of Paper 5, Ph. D. Thesis, Royal Institute of Technology, Sweden, 34 Pages (1989).

4. H. Boden, "Characterization of a Multi-Cylinder Internal Combustion Engine Source of Fluid Borne Noise," Summary of Paper 6, Ph. D. Thesis, Royal Institute of Technology, Sweden, 40 Pages (1989).

5. B. S. Sridhara, "Theoretical and Experimental Aspects of Acoustic Modeling of Engine Exhaust Systems with Applications to a Vacuum Pump," Ph. D. Thesis, Auburn University, (1991).

6. M. J. Crocker, "Internal Engine Exhaust Muffling," Proceedings of NOISE-CON 77, 331-357 (1977).

7. A. F. Seybert and D. F. Ross, "Experimental Determination of Acoustic Properties Using a Two-Microphone Random-Noise Technique," J. Acoust Soc. Am., 65(1), 1362-1370 (1977).

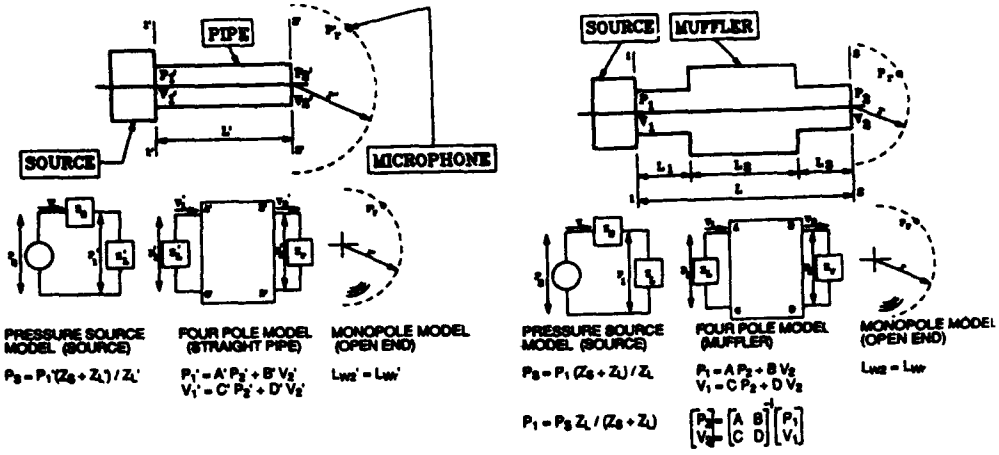

Case i Case ii

Figure 1--Schematic diagram and equivalent electrical circuits for the scheme to predict the sound pressure radiated from the open end of a pipe. Case i. Without the muffler installed. Case ii. With the muffler installed.

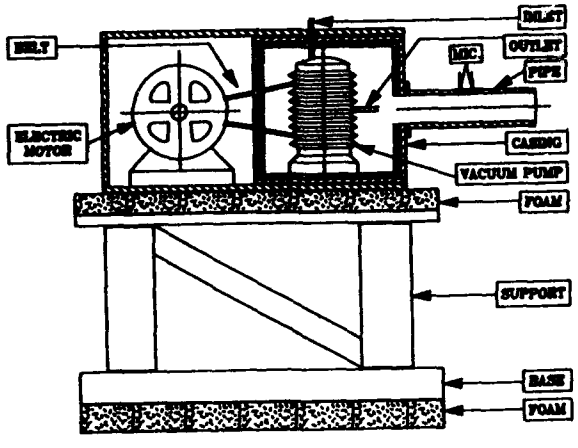

Figure 2--Experimental set up for the vacuum pump.

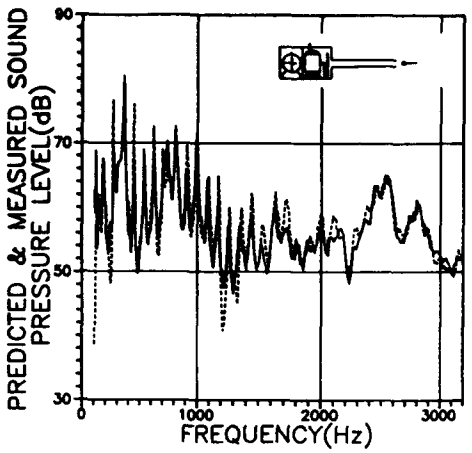

Case i

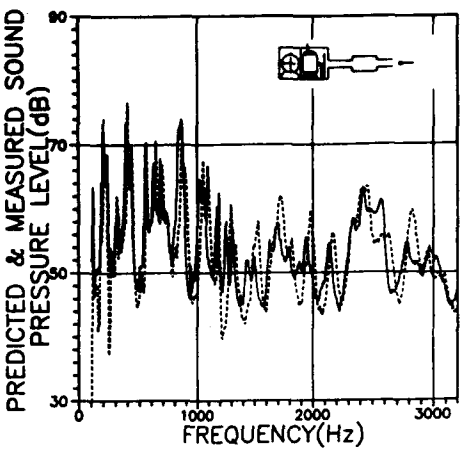

Case ii

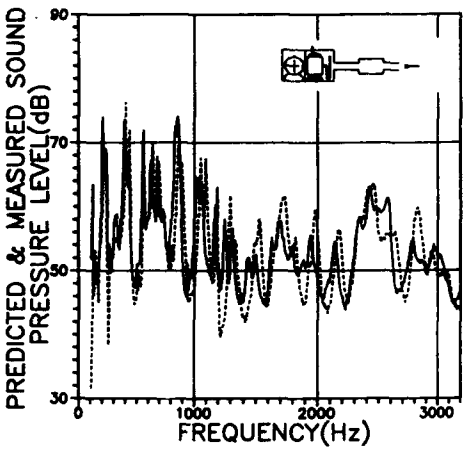

Case iii

Figure 3--Predicted and measured values of the radiated sound pressure level. Vacuum pump data. r' = r = 0.05 m, L' = 1.22 m, L = 1.83 m; _____ measured, ---------- predicted. The pump impedance was measured when the pump was operating in cases i and ii. A simle expansion chamber was installed in the pipe in cases ii and iii.

SECOND INTERNATIONAL CONGRESS ON
RECENT DEVELOPMENTS IN AIR- AND
STRUCTURE-BORNE SOUND AND VIBRATION
MARCH 4-6, 1992 AUBURN UNIVERSITY, USA

Russian church bell.

Boris N. Njunin, Alexander S. Larucow
Noise and Vibration laboratory
Moscow Automobile Plant (ZIL)
Moscow
USSR.

ABSTRACT.

The experimental studies of Russian church bell characteristics (eigenfrequencies, mode shapes, sound intensity vector mapping, etc.) were made using modal analysis and sound intensimetry methods. Experimental studies served as basis for the bell finite element model development and identification. The finite element model of a bell allows, by optimization of profile, weight, dimensions and material, on the stage of projection to obtain the design of a bell with required characteristics. As a result the church bells were manufactured using modern technology with "voice" similar to that of ancient Russian bells.

INTRODUCTION.

It's well known that as well as the most huge and the most remarkable in sound bells were only in Russia. Unfortunately, the secrets of art of casting of Russian church bells practically have been lost. The goal of our work is to tongue the sound of Russian church bell using modern research methods of sound sources acoustic parameters and modern casting technics. On the first stage of researches the experimental investigation of acoustic and vibration characteristics of ancient Russian church bell of Samgin company was done. The finite element model of this bell was developed and identified on the base of this experiments. This model was used for optimization of bell profile, dimensions, weight and material to obtain the bell design that closely approaches in sound to prototype (Samgin bell).

EXPERIMENTAL STUDIES.

Experimental studies of acoustic and vibration bell characteristics were made in unecho chamber. Samgin bell (dimensions : 550 mm high, 513 mm in max. diameter; weight ~ 83 kg) was suspended in the center of unecho chamber. In the course of experimental studies the following characteristics were determined :

- vibration acceleration and sound pressure spectrum;
- basic eigenfrequencies and eigenmodes, mode damping coefficients;
- sound active intensity map;
- bell surface zones that have most contribution to sound emission.

Measurement setup is shown on fig. 1. Excitation of bell vibration was done by the tongue of the bell. The mechanical arm was designed to insure the constant force of the stroke. Modal analysis of bell vibration were done using 126 measurement points (in each point acceleration spectra were measured in three directions) and reference point on the tongue was chosen. In excitation and measurement channels

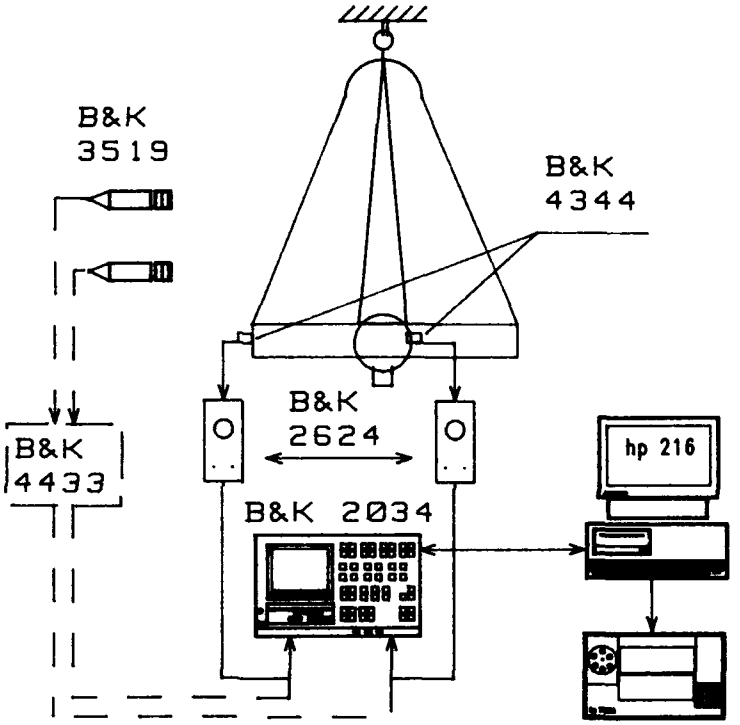

Fig.1. Measurement setup.

special type of windows were chosen to insure optimal Fourie analysis of transient vibration signal. Modal parameters extraction was made using modal analysis package of LMS company (Belgium). While study of most active emitting bell surface zones the spatial vector of active sound intensity was measured at 30 mm distance from bell surface relative the points of acceleration spectra measurements in modal analysis. Using intensity measurement package of LMS company measurement results were presented as intensity vector and amplitude maps. On fig. 2. the sound pressure spectrum of the bell is shown. Measurement was done on 1 m distance from the bell axe. Spectrum is composed of many discrete peaks. Time evolution of sound pressure spectrum shows that at the stroke moment sound spectrum is reach but in 1-1.5 seconds the spectrum is reduced to four basic discreet frequencies : 336 Hz, 652 Hz, 787 Hz, 1064 Hz, which form the bell "voice". Experimental modal analysis of the bell were done in frequency range 50-3000 Hz. In this frequency range was determined 14 modes. The first mode is the most active, it has frequency of 337 Hz (fig. 3). Information about bell mode shapes allowed to determine bell surface zones which were used for bell tuning on the finite element model on the design stage as well as tuning the bell after casting. Active sound intensity vector maps were studied for every bell mode shape. Analysis

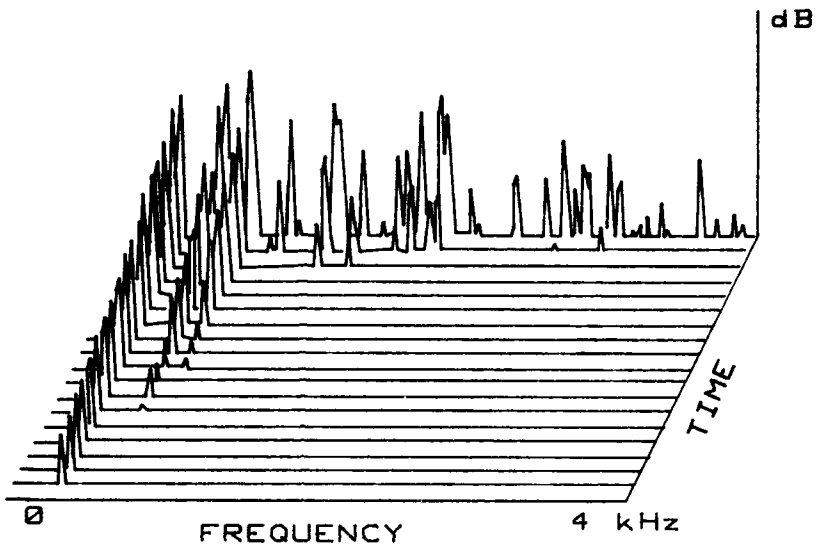

Fig. 2. Time evolution of sound pressure spectrum.

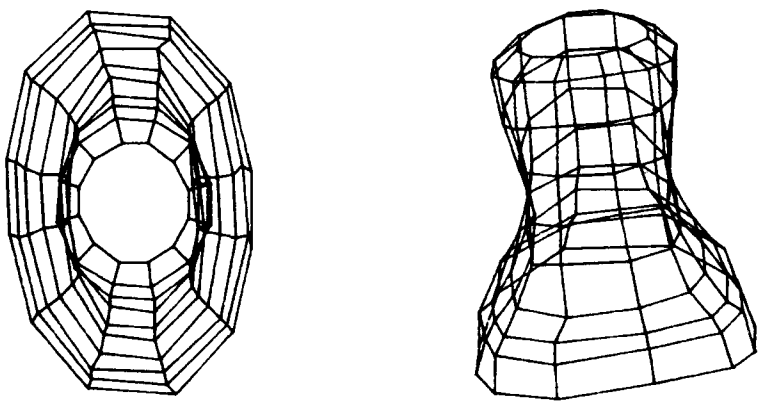

Fig. 3. First bell mode shape (336 Hz).

of active sound intensity amplitude and vector maps (fig. 4) allows to conclude that bell surface maximum deformation zones make maximum

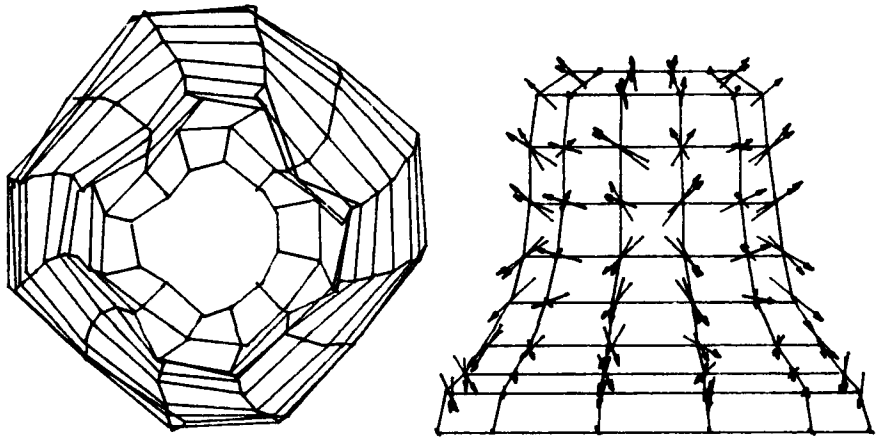

Fig. 4. Active intensity map (336 Hz).

contribution to sound emission. These zones could change their location on the bell in dependence on excitation point location (point of tongue stroke).

THEORETICAL STUDIES.

The goal of theoretical studies was to investigate dependence of bell eigenfrequencies and mode shapes on it's design (profile shape), alloy characteristics (elasticity module, specific density, Poison coefficient, etc.). Bell finite element model was developed composed of volume elements (8800 degrees of freedom, see fig. 5), which was used to compute eigenfrequencies and mode shapes. Computations were done on HP workstation model 350 . Optimal number of degrees of freedom was chosen which insured 1% of accuracy in eigenfrequencies calculation assuming frequency range of first four eigenfrequencies (up to 2000 Hz) which form the bell "voice".
This bell finite element model was identified using experimental modal analysis. Experimental and computed eigenfrequencies are shown in table 1. Correlation between experiment and computations is good enough. Finite element model identification also was done on the mode shapes and good correspondence was obtained. On fig. 5 first mode shape is shown, this mode shape corresponds to that from experimental modal analysis. This model was used for studies of influence of natural variation of Poison coefficient and elasticity coefficient on eigenfrequency

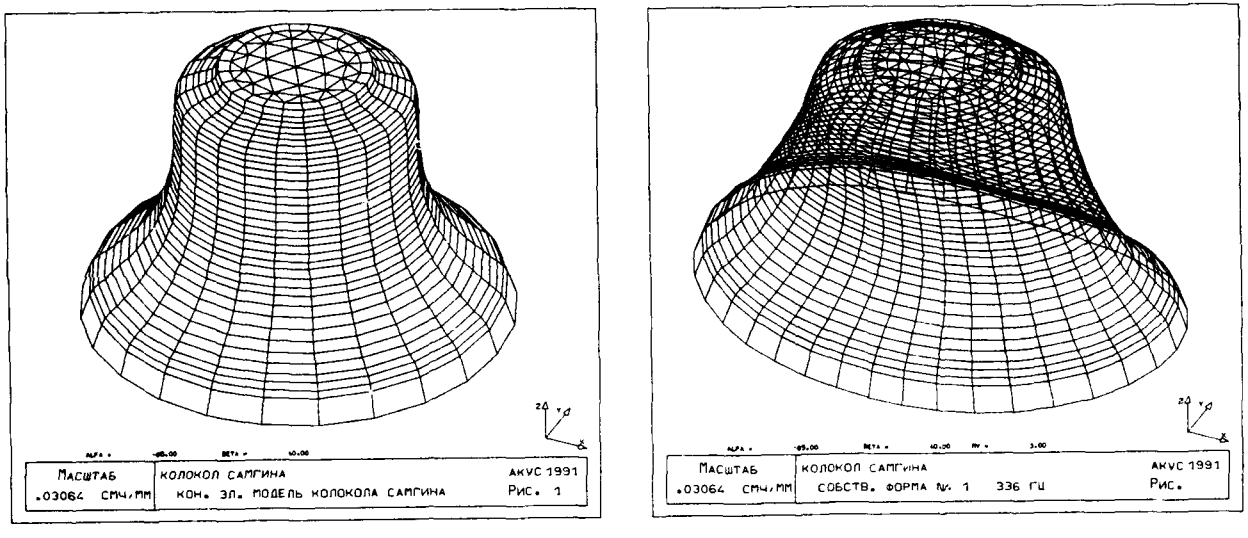

Fig. 5. Bell finite element model and computed mode shape (336 Hz).

variation. Variation of these coefficient in 2-3 percent range causes the variation of eigenfrequencies in 1-2 percent range. This finite element model was also used to develop methods of tuning the bell sound. Thus, developed bell finite element model allows on the stage of design to obtain bell design features (dimensions, weight, profile, alloy components) which provide the required sound characteristics of the bell. This design method allows to obtain drawings of bell ensembles to compose bellfries which conforms to ancient Russian sound harmonic raw. Now we have designs of bell ensembles with weight from 8 to 1600 kg, which produce sound within the range of 3 octaves.

Table 1. Experimental and computed bell eigenfrequencies.

Experiment	Computation
336 Hz	336 Hz
652 Hz	654 Hz
780 Hz	807 Hz
1064 Hz	1063 Hz

FIRST RESULTS.

Using developed drawings of 83 kg bells a number of bells were manufactured and their acoustic characteristics were studied. In table 2 eigenfrequencies and damping ratio one of these bells and the same parameters of Samgin bell are shown.

Table 2. Eigenfrequencies and damping ratio of new and Samgin bells.

New bell		Samgin bell	
Eigenfr.	Damping	Eigenfr.	Damping
327 Hz	0.0010	336 Hz	0.0021
664 Hz	0.0015	652 Hz	0.0017
725 Hz	0.0011	780 Hz	0.0018

The new bell surpasses Samgin bell in continuance of sound especially on the first tone. Eigenfrequencies of the new and Samgin bell are close enough. On the subjective estimation of specialists "voices" of mentioned above bells are very similar.

CONCLUSION.

The first stage in the bell sound research was implemented which consists of :

1. the acoustic characteristics of Russian ancient Samgin bell were studied;
2. the finite element model of a bell was developed and identified on the basis of experimental research;
3. using finite element model the methods of bell tuning were developed and the dependence of "voice" of the bell from alloy components, dimensions and profile geometry was studied;
4. the new bronze bell was manufactured which "voice" is similar to that of Samgin bell;
5. the drawings of bell ensemble weighting from 8 to 1600 kg which produce sound within the range of 3 octaves were obtained.

The following is assumed on the next stages of:

1. to simulate on the computer the real bell excitation (tongue stroke);
2. to study the stress distribution pattern of a bell to optimize the bell weight;
3. to study the bell sound emission process using the boundary element method;
4. to create a data base on "voices" of ancient Russian bells which could be find in Russia.

ACKNOWLEDGEMENTS.

The authors would like to express their gratitude to Mr. A.N. Shatow of editorial department of Moscow episcopate for support in this program.

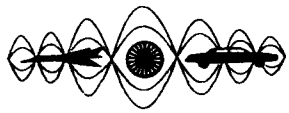

**SECOND INTERNATIONAL CONGRESS ON
RECENT DEVELOPMENTS IN AIR- AND
STRUCTURE-BORNE SOUND AND VIBRATION**
MARCH 4-6, 1992 AUBURN UNIVERSITY, USA

A COMPARISON OF MEMBRANE, VACUUM, AND FLUID LOADED SPHERICAL SHELL MODELS WITH EXACT RESULTS

Cleon E. Dean
Naval Oceanographic and Atmospheric Research Laboratory
Numerical Modeling Division, Building 1100
Stennis Space Center, MS 39529-5004
USA

ABSTRACT

A new set of spherical shell theories is presented with differing degrees of physicality, varying from a simple membrane model up to a fluid loaded shell theory that includes translational motion, rotary inertia, and transverse shearing-stress. Numerical results from these theories are compared with exact results from elastodynamic theory. The motivation of this study is to overcome the limitations of both modal analysis approaches and of the somewhat more general Extended Boundary Condition (EBC) method due to Waterman, sometimes called the T-matrix method. The spherical shell is studied with an eye towards generalizing the results obtained to spheroids. The aim of the present research is to yield a better understanding of the scattering event by employing more general and more physical shell theories.

INTRODUCTION

So-called "shell theories" simplify the calculations of the motion of thin elastic shells by making assumptions about the scatterer and its movements. We use the standard assumptions of shell theory as formulated by A. E. H. Love [1] and which are as follows: first the thickness of a shell is small compared with the smallest radius of curvature of the shell; second the displacement is small in comparison with the shell thickness; third the transverse normal stress acting on planes parallel to the shell middle surface is negligible; and finally the fibers of the shell normal to the middle surface remain so after deformation and are themselves not subject to elongation. These assumptions are used in the development of a shell theory for an elastic spherical shell in the spirit of Timoshenko-Mindlin[2,3] plate theory.

DERIVATION OF THE EQUATIONS OF MOTION

In spherical shells membrane stresses (proportional to β) predominate over flexural stresses (proportional to β^2) where

$$\beta = \frac{1}{\sqrt{12}}\frac{h}{a}. \tag{1}$$

We differ from the standard derivation for the sphere [4] by retaining all terms of order β^2 in both the kinetic and potential energy parts of the Lagrangian and by considering the resonance frequencies for the fluid loaded case to be complex. We note that this level of approximation will allow us to include the effects of rotary inertia and shear distortion in our shell theory, as well as damping by fluid loading. The parameter β itself is proportional to the radius of gyration of a differential element of the shell and arises from integration through the thickness of the shell in a radial direction. We will use an implicit harmonic time variation of the form $\exp(-i\omega t)$. We begin our derivation by considering a u,v,w axis system on the middle surface of a spherical shell of radius a (measured to mid-shell) with thickness h, as shown in Fig. 1.

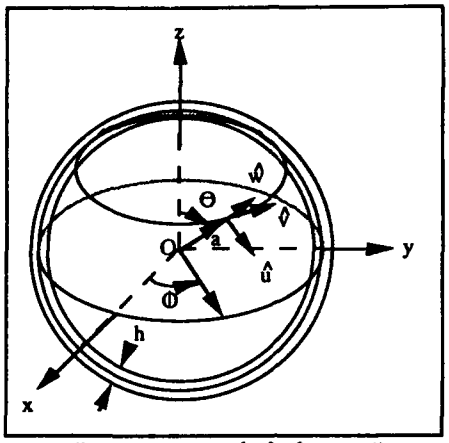

Fig. 1. --- Spherical shell showing coordinates used. The $\hat{u}$, $\hat{v}$, $\hat{w}$ - coordinate system is somewhere on the mid-surface.

Lagrangian variational analysis

The Lagrangian, L, is

$$L = T - V + W, \tag{2}$$

where T is the kinetic energy, V is the potential energy, and W is the work due to the pressure at the surface. The kinetic energy is given by

$$T = \frac{1}{2}\rho_s \int_0^{2\pi}\int_0^{\pi}\int_{-h/2}^{h/2} (\dot{u}_s^2 + \dot{w}_s^2)(a+x)^2 \sin\theta dx d\theta d\phi, \tag{3}$$

where the surface displacements are taken to be linear as in Timoshenko-Mindlin plate theory:

$$\dot{u}_s = (1+\frac{x}{a})\dot{u} - \frac{x}{a}\frac{\partial \dot{w}}{\partial \theta}, \tag{4}$$

and

$$\dot{w}_s = \dot{w}. \tag{5}$$

The motion of the spherical shell is axisymmetric since the sound field is torsionless. Thus there is no motion in the v-direction. Substitution of Eqs. (4) and (5) into Eq. (3) yields, after integration over x and θ,

$$T = \pi\rho_s \int_0^{\pi} \sin\theta [(\frac{h^5}{80a^2} + \frac{h^3}{2} + ha^2)\dot{u}^2 - 2(\frac{h^5}{80a^2} + \frac{h^3}{4})\dot{u}\frac{\partial \dot{w}}{\partial \theta} + (\frac{h^5}{80a^2} + \frac{h^3}{12})(\frac{\partial \dot{w}}{\partial \theta})^2 + (\frac{h^3}{12} + ha^2)\dot{w}^2]d\theta, \tag{6}$$

or, in terms of β,

$$T = \pi\rho_s ha^2 \int_0^{\pi} [(1.8\beta^4 + 6\beta^2 + 1)\dot{u}^2 - (3.6\beta^4 + 6\beta^2)\dot{u}\frac{\partial \dot{w}}{\partial \theta} + (1.8\beta^4 + \beta^2)(\frac{\partial \dot{w}}{\partial \theta})^2 + (\beta^2 + 1)\dot{w}^2]\sin\theta d\theta, \tag{7}$$

where the first and last terms in square brackets in Eq. (7) are associated with linear translational kinetic energies and the middle two terms are associated with rotational kinetic energies of an element of the shell.

The potential energy of the shell is

$$V = \frac{1}{2}\int_0^{\pi}\int_0^{2\pi}\int_{-h/2}^{h/2} (\sigma_{\theta\theta}\varepsilon_{\theta\theta} + \sigma_{\phi\phi}\varepsilon_{\phi\phi})(x+a)^2 \sin\theta dx d\theta d\phi, \tag{8}$$

where the nonvanishing components of the strain are

$$\varepsilon_{\theta\theta} = \frac{1}{a}\left(\frac{\partial u}{\partial \theta} + w\right) + \frac{x}{a^2}\left(\frac{\partial u}{\partial \theta} - \frac{\partial^2 w}{\partial \theta^2}\right), \tag{9}$$

and

$$\varepsilon_{\phi\phi} = \frac{1}{a}(\cot\theta u + w) + \frac{x}{a^2}\cot\theta\left(u - \frac{\partial w}{\partial \theta}\right), \tag{10}$$

and where the nonzero stress components are

$$\sigma_{\theta\theta} = \frac{E}{1-\nu^2}(\varepsilon_{\theta\theta} + \nu\varepsilon_{\phi\phi}), \tag{11}$$

and

$$\sigma_{\phi\phi} = \frac{E}{1-\nu^2}(\varepsilon_{\phi\phi} + \nu\varepsilon_{\theta\theta}), \tag{12}$$

where E is Young's modulus. By substitution the potential energy becomes

$$V = \frac{1}{2}\int_0^{\pi}\int_0^{2\pi}\int_{-h/2}^{h/2}\left[\frac{E}{1-\nu^2}\frac{1}{(x+a)^2}\left([(1+\frac{x}{a})\frac{\partial u}{\partial \theta} - \frac{x}{a}\frac{\partial^2 w}{\partial \theta^2} + w^2] + \{\cot\theta[(1+\frac{x}{a})u - \frac{x}{a}\frac{\partial w}{\partial \theta}] + w\}^2\right.\right.$$

$$\left.\left. +2\nu\{\cot\theta[(1+\frac{x}{a})u - \frac{x}{a}\frac{\partial w}{\partial \theta}] + w\}[(1+\frac{x}{a})\frac{\partial u}{\partial \theta} - \frac{x}{a}\frac{\partial^2 w}{\partial \theta^2} + w]\right)\right](x+a)^2\sin\theta dx d\theta\phi, \tag{13}$$

which after integration is

$$V = \frac{\pi E h}{1-\nu^2}\int_0^{\pi}[(w + \frac{\partial u}{\partial \theta})^2 + (w + u\cot\theta)^2 + 2\nu(w + \frac{\partial u}{\partial \theta})(w + u\cot\theta)$$

$$+\beta^2[(\frac{\partial u}{\partial \theta} - \frac{\partial^2 w}{\partial \theta^2})^2\cot^2\theta(u - \frac{\partial w}{\partial \theta})^2 + 2\nu\cot\theta(u - \frac{\partial w}{\partial \theta})(\frac{\partial u}{\partial \theta} - \frac{\partial^2 w}{\partial \theta^2})]]\sin\theta d\theta. \tag{14}$$

Terms in the potential energy proportional to β^2 are due to bending stresses.

And finally, the work done by the pressure of the surrounding fluid on the spherical shell is given by

$$W = 2\pi a^2\int_0^{\pi} p_a w\sin\theta d\theta, \tag{15}$$

where p_a is the pressure at the surface.

The Lagrangian density and its equations of motion

A Lagrangian density must be used instead of the Lagrangian since the integration along the polar angle is intrinsic to the problem. The Lagrangian density is

$$\mathcal{L} = \pi\rho_s h a^2[(1+6\beta^2+1.8\beta^4)\dot{u}^2 - (6\beta^2+3.6\beta^4)\dot{u}\frac{\partial\dot{w}}{\partial\theta} + (\beta^2+1.8\beta^4)(\frac{\partial\dot{w}}{\partial\theta})^2$$
$$+(1+\beta^2)\dot{w}^2]\sin\theta - \frac{\pi Eh}{1-\nu^2}[(w+\frac{\partial u}{\partial\theta})^2 + (w+u\cot\theta)^2 + 2\nu(w+\frac{\partial u}{\partial\theta})(w+u\cot\theta)$$
$$+2\pi a^2 p_a w\sin\theta, \tag{16}$$

with corresponding differential equations of motion

$$0 = \frac{\partial\mathcal{L}}{\partial u} - \frac{d}{d\theta}\frac{\partial\mathcal{L}}{\partial u_\theta} - \frac{d}{dt}\frac{\partial\mathcal{L}}{\partial u_t}, \tag{17}$$

and

$$0 = \frac{\partial\mathcal{L}}{\partial w} - \frac{d}{d\theta}\frac{\partial\mathcal{L}}{\partial w_\theta} - \frac{d}{dt}\frac{\partial\mathcal{L}}{\partial w_t} + \frac{d^2}{d\theta dt}\frac{\partial\mathcal{L}}{\partial w_{\theta t}} + \frac{d^2}{d\theta^2}\frac{\partial\mathcal{L}}{\partial w_{\theta\theta}}, \tag{18}$$

where subscripts denote differentiation of the variable with respect to the subscript.

By substitution of Eqs. (17) and (18) into (16) we obtain

$$0 = (1+\beta^2)\left[\frac{\partial^2 u}{\partial\theta^2} + \cot\theta\frac{\partial u}{\partial\theta} - (\nu+\cot^2\theta)u\right] - \beta^2\frac{\partial^3 w}{\partial\theta^3} - \beta^2\cot\theta\frac{\partial^2 w}{\partial\theta^2}$$
$$+[(1+\nu)+\beta^2(\nu+\cot^2\theta)]\frac{\partial w}{\partial\theta} - \frac{a^2}{c_p^2}[(1.8\beta^4+6\beta^2+1)\frac{\partial^2 u}{\partial t^2} - (1.8\beta^4+3\beta^2)\frac{\partial^3 w}{\partial\theta\partial t^2}], \tag{19}$$

and

$$-p_a\frac{(1-\nu^2)a^2}{Eh} = \beta^2\frac{\partial^3 u}{\partial\theta^3} + 2\beta^2\cot\theta\frac{\partial^2 u}{\partial\theta^2} - [(1+\nu)(1+\beta^2)+\beta^2\cot^2\theta)]\frac{\partial u}{\partial\theta}$$
$$+\cot\theta[(2-\nu+\cot^2\theta)\beta^2 - (1+\nu)]u - \beta^2\frac{\partial^4 w}{\partial\theta^4} - 2\beta^2\cot\theta\frac{\partial^3 w}{\partial\theta^3}$$
$$+\beta^2(1+\nu+\cot^2\theta)\frac{\partial^2 w}{\partial\theta^2} - \beta^2\cot\theta(2-\nu+\cot^2\theta)\frac{\partial w}{\partial\theta} - 2(1+\nu)w$$
$$+\frac{a^2}{c_p^2}[-(1.8\beta^4+3\beta^2)\frac{\partial^3 u}{\partial\theta\partial t^2} - (1.8\beta^4+3\beta^2)\cot\theta\frac{\partial^2 u}{\partial t^2}$$
$$+(1.8\beta^4+\beta^2)\frac{\partial^4 w}{\partial\theta^2\partial t^2} + (1.8\beta^4+\beta^2)\frac{\partial^3 w}{\partial\theta\partial t^2}\cot\theta - (\beta^2+1)\frac{\partial^2 w}{\partial t^2}. \tag{20}$$

These differential equations of motion (19) and (20) have solutions of the form

$$u(\eta) = \sum_{n=0}^{\infty} U_n(1-\eta^2)^{1/2}\frac{dP_n}{d\eta}, \tag{21}$$

and

$$w(\eta) = \sum_{n=0}^{\infty} W_n P_n(\eta), \tag{22}$$

where $\eta = \cos\theta$ and $P_n(\eta)$ are the Legendre polynomials of the first kind of order n. When the differential equations of motion (19) and (20) are expanded in terms of Eqs. (21) and (22), we obtain a set of linear equations in terms of U_n and W_n, whose determinant must vanish. We shall consider two cases: with and without fluid loading.

The vacuum case

The vacuum case is the simpler problem that occurs when the spherical shell is surrounded by a vacuum such that there is no damping. Thus, the pressure at the surface vanishes: $p_a = 0$. The set of linear equations the expansion coefficients must satisfy are

$$0 = [\Omega^2(1+6\beta^2+1.8\beta^4)-(1+\beta^2)\kappa]U_n+[\Omega^2(3\beta^2+1.8\beta^4)-\beta^2\kappa-(1+\nu)]W_n, \tag{23}$$

and

$$0 = -\lambda_n[(\kappa-3)\beta^2-1.8\beta^4+1+\nu]U_n+[\Omega^2(1+2\beta^2+1.8\beta^4)-2(1+\nu)-\beta^2\kappa\lambda_n]W_n, \tag{24}$$

where $\Omega = \omega a / c_p$, $\kappa = \nu + \lambda_n - 1$, and $\lambda_n = n(n+1)$. In order for Eqs. (23) and (24) to be satisfied simultaneously with a non-trivial solution the determinant of the system must vanish:

$$\begin{aligned} 0 = {} & \Omega^4(1+6\beta^2+1.8\beta^4)(1+2\beta^2+1.8\beta^4)+\Omega^2[(3\beta^2+1.8\beta^4)\lambda_n[(\kappa-3)\beta^2-1.8\beta^4+1+\nu] \\ & -[2(1+\nu)+\beta^2\kappa\lambda_n](1+6\beta^2+1.8\beta^4)-(1+\beta^2)\kappa(1+2\beta^2+1.8\beta^4)] \\ & +(1+\beta^2)\kappa[2(1+\nu)+\beta^2\kappa\lambda_n]-\lambda_n[(\kappa-3)\beta^2-1.8\beta^4+1+\nu](\beta^2+1+\nu). \end{aligned} \tag{25}$$

Since there are no damping terms, the shell vibrates theoretically forever. Thus, the normalized frequency Ω can be taken to be real. Equation (25) is quadratic in Ω^2, thus we expect two real roots to (25) and thus two modes for the motion of the shell. They are the symmetric and antisymmetric Lamb modes.

The fluid loaded case

The fluid loaded case requires that we consider a modal expansion of the surface pressure in terms of the specific acoustic impedance z_n. In its most general form this is

$$p(a,\theta,\phi) = \sum_{n=0}^{\infty}\sum_{m=0}^{\infty} z_n \dot{W}_{mn} P_n^m(\cos\theta)\cos m\phi, \tag{26}$$

where

$$z_n = i\rho c\frac{h_n(ka)}{h_n'(ka)}. \tag{27}$$

The specific acoustic impedance z_n can be split into real and imaginary parts:

$$z_n = r_n - i\omega m_n, \tag{28}$$

where

$$r_n = \rho c\,\mathrm{Re}\left\{\frac{ih_n(ka)}{h_n'(ka)}\right\}, \tag{29}$$

and

$$m_n = -\frac{\rho c}{\omega}\mathrm{Im}\left\{\frac{ih_n(ka)}{h_n'(ka)}\right\}. \tag{30}$$

For the case of axisymmetric motion we are considering, the surface pressure is

$$p_s(\theta) = -\sum_{n=0}^{\infty} z_n \dot{W}_n P_n(\cos\theta), \tag{31}$$

or by substitution,

$$p_s(\theta) = -\sum_{n=0}^{\infty} (-i\omega W_n r_n - \omega^2 W_n m_n) P_n(\cos\theta). \tag{32}$$

Use of Eq. (32) in our set of differential equations of motion (19) and (20) yields the following set of linear equations for the expansion coefficients in the case of a fluid loaded spherical shell:

$$0 = [\Omega^2(1+6\beta^2+1.8\beta^4) - (1+\beta^2)\kappa]U_n + [\Omega^2(3\beta^2+1.8\beta^4) - \beta^2\kappa - (1+\nu)]W_n, \tag{33}$$

and

$$0 = -\lambda_n[(\kappa-3)\beta^2 - 1.8\beta^4 + 1 + \nu]U_n + [\Omega^2(1+\alpha+2\beta^2+1.8\beta^4) - 2(1+\nu) + \Omega i\gamma - \beta^2\kappa\lambda_n]W_n, \tag{34}$$

where

$$\alpha = \frac{m_n}{\rho_s h}, \tag{35}$$

and

$$\gamma = \frac{a}{h}\frac{r_n}{\rho_s c_p}. \tag{36}$$

Again the determinant of Eqs. (33) and (34) must vanish. However, in this instance the value of Ω must be taken to be complex; the resonances have a width that depends on the damping. The result of setting this determinant to zero is

$$\begin{aligned} 0 = {} & \Omega^4(1+6\beta^2+1.8\beta^4)(1+\alpha+2\beta^2+1.8\beta^4) \\ & +\Omega^3 i\gamma(1+6\beta^2+1.8\beta^4) + \Omega^2\{(3\beta^2+1.8\beta^4)\lambda_n[(\kappa-3)\beta^2 - 1.8\beta^4 + 1 + \nu] \\ & -[2(1+\nu)+\beta^2\kappa\lambda_n](1+6\beta^2+1.8\beta^4) - (1+\beta^2)\kappa(1+\alpha+2\beta^2+1.8\beta^4)\} + \Omega[-i\gamma(1+\beta^2)\kappa] \\ & +(1+\beta^2)\kappa[2(1+\nu)+\beta^2\kappa\lambda_n] - \lambda_n[(\kappa-3)\beta^2 - 1.8\beta^4 + 1 + \nu](\beta^2+1+\nu). \end{aligned} \tag{37}$$

Equation (37) has at least four complex roots. From work with an exact modal solution to the problem, we expect two roots to be associated with the symmetric and antisymmetric modes of the shell. We expect the other two roots to be associated with a water-borne pseudo-Stoneley wave.

CONCLUSIONS

The next step is to plot the roots of Eqs. (25) and (37) to compare the resonances predicted by these models with those given by exact modal expansion solutions. By suppressing α and γ, the model associated with Eq. (37) reverts to the vacuum case model associated with Eq. (25). Similarly suppression of factors of β in Eq. (25) will result in a reversion to a previously derived solution (Junger and Feit, 1986). We may then rank the three different models according to their degree of physicality and compare their results for various relative shell thicknesses against each other and against the exact results of the modal expansion model. We may also consider the limitations of each of the models including the exact solution, as well as those of shell models in general.

By setting the values of α and γ in Eq. (37) to zero, we revert the shell theory model to one without fluid loading. Similarly, by setting β to zero as well, the model reverts to a membrane model. These models, fluid loaded, vacuo case, and membrane, are successively less physically sophisticated and give successively less good comparison with exact (modal expansion) results. Starting with the least sophisticated model, we see in Fig. 2 thick spherical steel shell dilatational (symmetric) and flexural (antisymmetric) mode resonances calculated by the membrane model. Here and in the succeeding figures thick means h/a =0.1; thin means h/a=0.01. The shell material is a generic steel with density ρ_s = 7.7 times that of water, shear velocity v_s = 3.24 km/s, and longitudinal velocity v_l = 5.95 km/s. The surrounding fluid is taken to be water with density ρ = 1000 kg/m^3 and sound velocity c_w = 1.4825 km/s. The symmetric mode shows a good comparison between exact and shell theory predictions, but the antisymmetric shell theory results for this approximation compare poorly with the exact flexural results. Note that some symmetric mode resonances were not found by our exact theory algorithm. In Fig. 3 we see thin spherical steel shell dilatational (symmetric) and flexural (antisymmetric) mode resonances calculated by the membrane model. Again there is good comparison between dilatational (symmetric) mode resonances calculated by the two methods, except for the first couple of resonances. Only a few exact flexural resonances were picked up by our algorithm. And again the shell theory flexural (antisymmetric) mode resonances show the do not asymptote properly with increasing order. In Fig. 4 we have thick spherical steel shell dilatational (symmetric) and flexural (antisymmetric) mode resonances calculated by shell theory without fluid loading (vacuum). As in the membrane model the shell theory and exact calculations compare well for the dilatational (symmetric) mode resonances. In contrast with the membrane model, however, the exact and shell theory calculations for this model show much better agreement for the flexural (antisymmetric) mode resonances. This model does not include fluid loading, but does include the effects of shear distortion and rotary inertia. The vacuum shell theory flexural mode resonances do not asymptote for large size parameter ka to the exact results, however. In Fig. 5 we see thin spherical steel shell dilatational (symmetric) and flexural (antisymmetric) mode resonances calculated by shell theory without fluid loading (vacuum). As in the membrane model [illegible] ry and exact calculations compare well for the dilatational (symmetric) mode resonances except for the [illegible] of resonances. This vacuum model does not have fluid loading, and has insufficient damping for [illegible] o dilatational (symmetric) mode resonances. Again, the flexural (symmetric) mode resonances show [illegible] the correct behavior, but it is not possible to tell what the asymptotic value of the phase velocity would be for large size parameter on this scale. Next in Fig. 6 we have a plot of thick spherical steel shell dilatational (symmetric) and flexural (antisymmetric) mode resonances calculated by shell theory with fluid loading. As in the vacuum case as well as for the membrane model, the dilatational (symmetric) mode resonances compare well for exact and shell theory methods. The flexural (antisymmetric) mode resonances, as calculated by shell theory with fluid loading, do not appear to have the correct asymptotic limit for large size parameter, although they do exhibit roughly the correct behavior for lower values of ka. Finally, in Fig. 7 we see thin spherical steel shell dilatational (symmetric) and flexural (antisymmetric) mode resonances calculated by shell theory with fluid loading. The exact and shell theory calculations agree well for the dilatational (symmetric) resonances and exhibit a marked improvement for the first several shell theory symmetric mode resonances. This is due to the inclusion of fluid loading in the model. The flexural (antisymmetric) mode resonances show the appropriate behavior on this rather limited size parameter scale.

ACKNOWLEDGMENTS

We wish to thank the Office of Naval Research, the Office of Naval Technology, and NOARL management including Drs. Chin-Bing, Franchi, and Moseley. Dr. Dean is at NOARL on an ONT Fellowship. This work was funded by NOARL Program Element 61153N, G. Car, Program Manager.

REFERENCES

1. Love, A. E. H., *A Treatise on the Mathematical Theory of Elasticity*. 4th ed., Dover, New York, 1944, pp. 515-537.
2. Timoshenko, S., On the correction for shear of the differential equation for transverse vibrations of prismatic bars, *Phil. Mag.* **41**, 744-746, 1921.
3. Mindlin, R. D., Influence of rotary inertia and shear on flexural motions of isotropic elastic plates, *J. Appl. Mech.*, **18**, 31-38, 1951.
4. Junger, M. C. and D. Feit, *Sound, Structures, and Their Interaction*, 2nd ed., MIT Press, Cambridge, Mass., 1986, pp. 245-251.

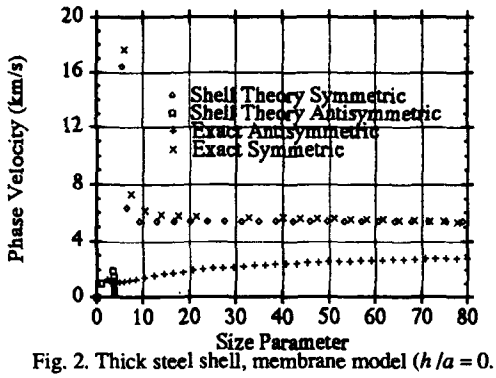

Fig. 2. Thick steel shell, membrane model ($h/a = 0.1$).

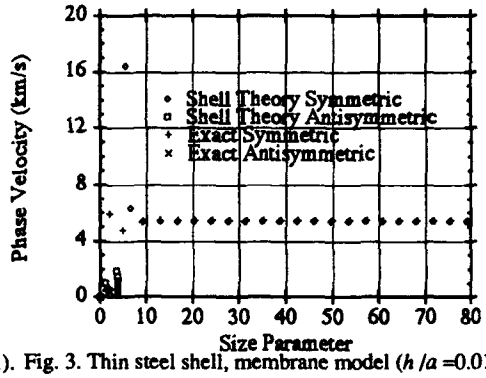

Fig. 3. Thin steel shell, membrane model (h/a =0.01).

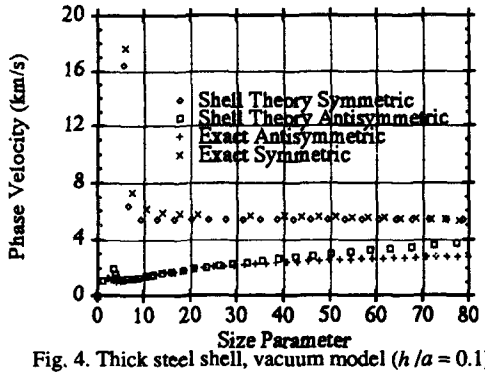

Fig. 4. Thick steel shell, vacuum model ($h/a = 0.1$).

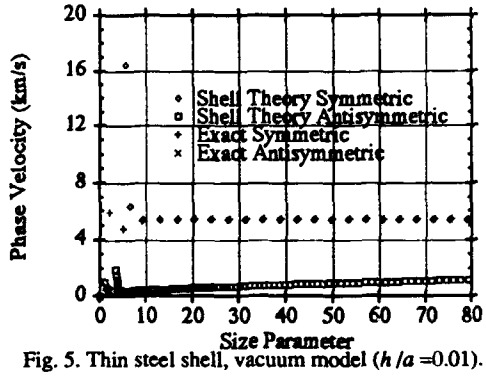

Fig. 5. Thin steel shell, vacuum model (h/a =0.01).

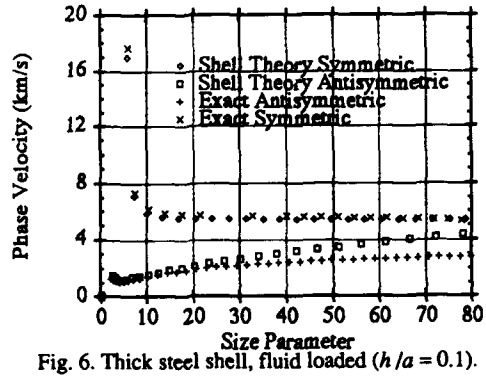

Fig. 6. Thick steel shell, fluid loaded ($h/a = 0.1$).

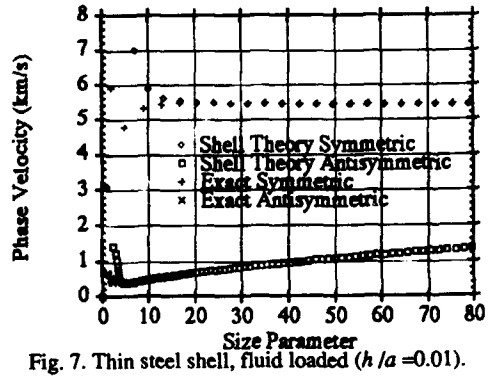

Fig. 7. Thin steel shell, fluid loaded (h/a =0.01).

SECOND INTERNATIONAL CONGRESS ON
RECENT DEVELOPMENTS IN AIR- AND
STRUCTURE-BORNE SOUND AND VIBRATION
MARCH 4-6, 1992 AUBURN UNIVERSITY, USA

EXPERIMENTAL STUDIES OF WAVE PROPAGATION IN A SUBMERGED, CAPPED CYLINDRICAL SHELL

Earl G. Williams
Naval Research Laboratory, CODE 5137, Washington D.C. 20375
USA

ABSTRACT

Experimental measurements on point-driven, fluid-loaded cylindrical shells in the frequency region $0 < ka < 10$ are processed using nearfield acoustical holography and wave vector filtering in order to expose the details of wave motion on the structure. Gabor transform tools along with the creation of various filters in the k-ω space domain are used to study impulsive wave packets as a function of space and time excited by a point drive inside the shell. This technique provides a very powerful tool for the study of experimental data. In particular, we are able to visualize the difference between phase and group velocities for helical waves traveling on the shell. Of particular note is the ability to display wave conversion at discontinuities, such as the ends of the shell. This wave conversion consists of flexural to longitudinal, longitudinal to flexural, and conversion into radiated pressure. Similar conversions occur with shear waves, which are shown to be excited by a normal point force in the frequency region $ka > 2$.

INTRODUCTION

It is the objective of this work to uncover basic mechanisms of wave propagation on, and radiation from simple shell structures through the use of signal processing techniques. One of the simplest shell structures is a cylindrical shell with spherical-like endcaps, driven into vibration by a point force inside. Although simple in structure, this vibrator is rich is basic physics. To study this simple structure, the Naval Research Laboratory has several advanced research, large pool facilities. Robotic scanners under computer control track predefined contours and measure the pressure fields generated from the vibrator very close to the shell. These contours are either cylindrical or conformal. Using nearfield acoustical holography (NAH)[1] this information is processed to yield the normal velocity on the surface of the shell as well as the surface pressure. At this point wave vector filtering (WVF) techniques are applied to provide an experimental dispersion analysis (free waves of propagation) of the shell. We will discuss in this paper the processing steps which are taken in WVF leading to the final result: the impulse response of the structure in the time domain.

DESCRIPTION OF PROCESSING

Figure 1 shows a typical measurement grid for the nearfield pressure created by the vibrations of a point-driven shell. The point driver located inside the shell is excited with a chirp signal so that a broad range of frequencies can be covered with a single experiment.[1] The radial surface velocity is reconstructed using NAH on a grid concentric to the measurement grid at a radius equal to that of the shell. Where this grid coincides with the surface of the shell, the radial *surface* velocity is reconstructed.

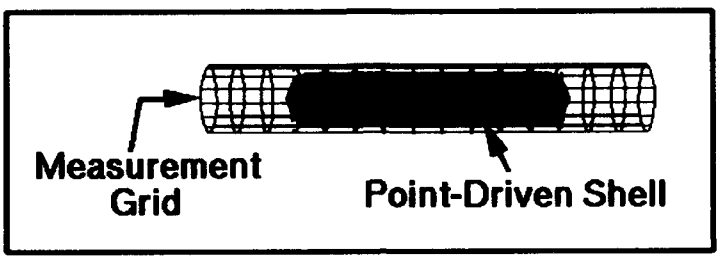

Figure 1– A computer controlled, robotic scanner measures the pressure over the grid shown (128x64) axial x circumferential points. The point-driven shell is excited by a chip time signal.

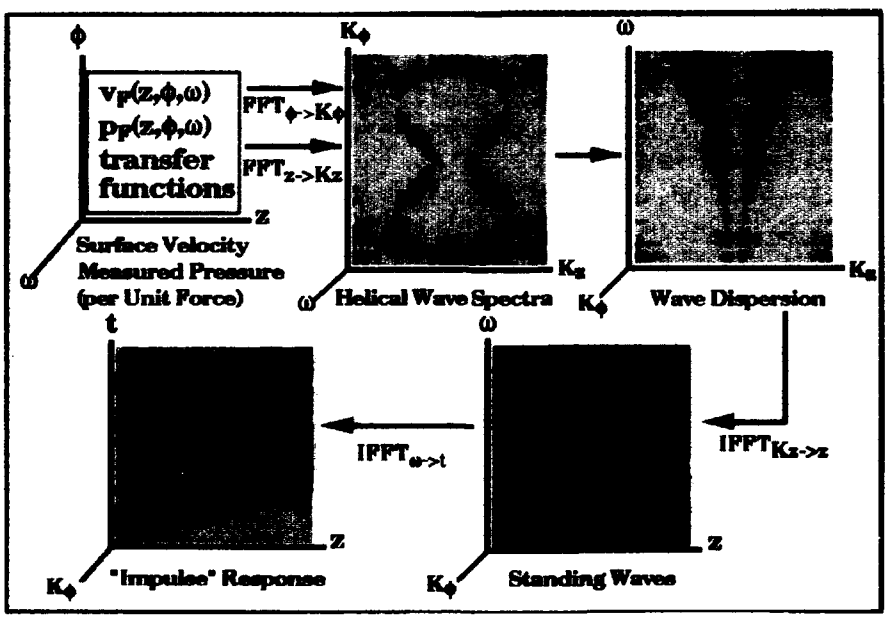

Figure 2– Flowchart of the wave vector filtering process. The various Fourier transforms are indicated which take us through the flow chart in the clockwise direction.

The processing steps of WVF are shown in fig. 2. Note that the reconstructed surface velocity is normalized by the driving force generated by the point driver. The same normalization is applied to the measured pressure, creating transfer functions which provide the input to WVF. These transfer functions are Fourier transformed to the frequency domain to provide the first box in the flow chart in fig. 2. The three-dimensional coordinate system indicates that a cube of data exists, with two-dimensional slices displayed in the figure. A typical data set consists of 128x64x512 points corresponding to the triplet (z, ϕ, ω).

The first processing step takes spatial Fourier transforms in the circumferential and axial directions. Thus $v_F(z, \phi, \omega) \rightarrow V_F(k_z, k_\phi, \omega)$. The second box in figure 2 demonstrates this process and displays the magnitude of V_F for a particular frequency. The magnitude of V_F forms a "figure 8" locus (the DC wavenumber is at the center of the "8"). This locus is produced by the quasi-bending free waves which are excited on the shell and are discussed at length in a recent paper.[2]

The third panel in figure 2 represents an important processing step in which the ω and k_ϕ axes have been interchanged. This plot shows the magnitude of V_F for a particular circumferential harmonic, $k_\phi = n$. This plot is called an experimental dispersion curve, and provides the dispersion character of the n'th harmonic. The origin is at the center of the k_z axis (not as shown) so that the right branch indicates free waves traveling to the right on the shell, and the left branch waves to the left. As usual the slope of the curve at any point provides the axial group velocity of this wave. Note that the axial phase velocity is given by $c_z = \omega / k_z$.

The fourth panel in fig. 2 is derived from an inverse FFT on k_z. Thus we have $V_F(z, n, \omega)$. This plot is called a standing wave plot as it shows the distribution of nodes and antinodes as a function of frequency for a given value of n. (The gray scale representation has been reversed in this plot so that the light areas represent the largest magnitude.) One can see the number of antinodes increasing with frequency (the slow quasi-bending wave) until the rapid oscillation gives way to a much longer wavelength wave (the fast shear wave) about midway up the frequency axis.

The final step in the WVF flowchart is an inverse FFT in ω to yield $v_F(z, n, t)$. This is called the radial velocity, impulse response. Since all quantities are normalized to the driving force (in the frequency domain), this inverse transform simulates the response of the system to a impulsive force in time. This is a band-limited impulse since generally a limited band of frequencies is selected from the standing wave data before the inverse FFT is applied. The actual location of the driver is just to the right of the displayed origin in fig. 2. The dark areas represent the tracks of the impulse as the wave travels down the shell, reflecting off of the endcaps to travel in the opposite direction. The slope of these tracks provides the group velocity of the wave. Further processing can be applied to this type of display to uncover the reflection coefficients of these waves at the ends of the shell, presented in another paper in these proceedings.[3]

Figure 3 illustrates some other processing schemes of the WVF approach used in the study of wave propagation in shells. The wave dispersion data (panel 3 in fig. 2) can be used as a starting point of three different filtering schemes. We will discuss the second scheme in this paper. In this case the wave dispersion data is filtered by zeroing out the negative part of the k_z spectrum (illustrated by the stop band in the figure). A Tukey window is used in the transition region to smooth the data. Proceeding with the processing as shown in the last two panels of figure 2 one then arrives at the impulse response with waves traveling only to the right in the shell, as shown in the center plot of figure 4. If one zeros out the right half of the k_z spectrum, then waves traveling only to the left are obtained as shown in fig. 4. In this way the tracks of the waves can be analyzed better, and reflections more clearly studied. For example, the left-going waves in fig. 4 indicate waves emanating from the center of the shell, corresponding to an internal ring discontinuity in the shell. This discontinuity was extremely small, and was not detectable in the surface velocity plots ($v_F(z, \phi)$ at a given frequency). Unfortunately the gray scale rendition of the wave tracks obscures a lot of the details, which are much clearer shown in the color viewgraphs presented in the talk corresponding to this paper.

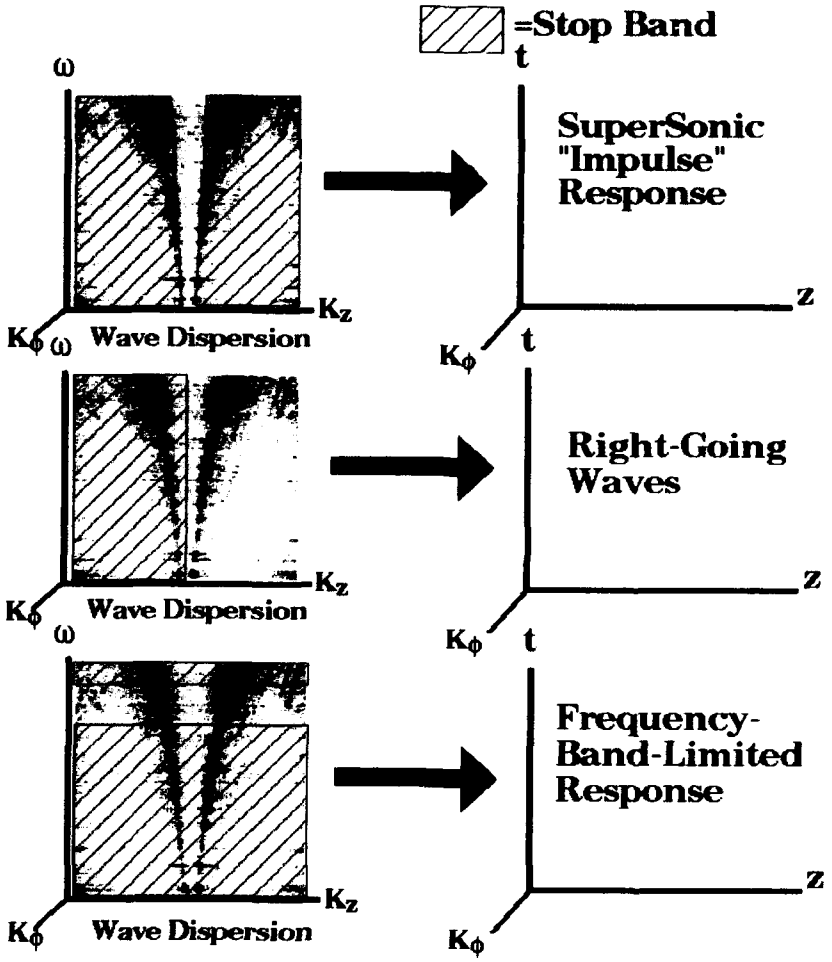

Figure 3– A example of the three kinds of filters which are applied to the data in the "wave dispersion domain". The center filter provides waves traveling only to the right, as shown in the center plot of fig. 4.

Another observation from fig. 4 is the left-going wave which appears at the very bottom right of the 3rd panel. There does not appear to be any right-going wave which causes it. Further processing uncovered a fast longitudinal wave launched at $t = 0$ from the point driver and traveling to the right with a nearly horizontal slope (about 5000 m/s). When this wave struck the right end of the shell, it apparently was converted into the slow quasi-flexural wave shown in fig. 4. The details of the fast waves are easily studied from the impulse response of the pressure recorded on the measurement contour (fig. 1), as will be shown in the lecture. This phenomenon of wave conversion at the ends of the shell is a significant one, especially in light of the fact that the slow wave is subsonic, as thus is a poor radiator, whereas the fast wave is supersonic and an efficient radiator.

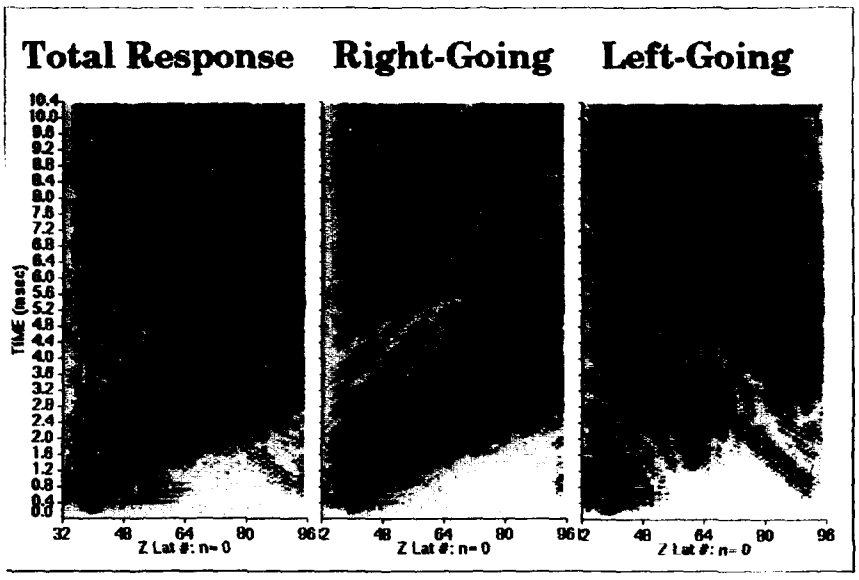

Figure 4– Normal surface velocity as a function of (z, t) for the $n = 0$ circumferential harmonic. The drive point is at $t = 0$, Z Lat $= 40$. The filter shown in the middle of fig. 3 is applied to expose waves traveling to the right (center panel) and a similar filter to provide waves traveling to the left (right panel). The dark lines indicate wave tracks of the quasi-flexural wave. Slight widening of the tracks is the result of dispersion.

ACKNOWLEDGMENTS

This work is supported under a contract with the Office of Naval Research.

REFERENCES

1. E.G. Williams, B. Houston, and J. Bucaro, "Broadband nearfield acoustical holography for vibrating cylinders", J. Acoust. Soc. Am. **86**, 674-679 (1989).
2. E.G. Williams, B. Houston, and J. Bucaro, "Experimental investigation of the wave propagation on a point-driven, submerged capped cylinder using K-space analysis", J. Acoust. Soc. Am. **87**, 513-522 (1990).
3. J.A. Mann III and E.G. Williams, "Determining the amplitude of propagating waves as a function of phase speed and arrival time", 2nd International Congress on Recent Developments in Air- & Structure-borne Sound and Vibration, Auburn University, (1992).

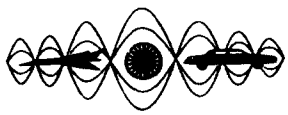

SECOND INTERNATIONAL CONGRESS ON RECENT DEVELOPMENTS IN AIR- AND STRUCTURE-BORNE SOUND AND VIBRATION
MARCH 4-6, 1992 AUBURN UNIVERSITY, USA

SOUND ABSORBING DUCTS

Alan Cummings
Department of Engineering Design and Manufacture
University of Hull
Hull, N. Humberside HU6 7RX
U.K.

ABSTRACT

Some examples of approximate variational solutions to problems involving sound absorbing ducts are given. More or less simple Rayleigh-Ritz type formulations are applied to sound transmission in ducts - of various cross-sections - having porous bulk-reacting liners, and to sound propagation in capillary tubes. Comparisons are made between these approximate solutions, exact solutions and experimental data (where these are available).

INTRODUCTION

Exact solutions to physical problems may, in some cases, not exist or (in others) may involve higher functions that are difficult to compute. In such circumstances, purely numerical solutions to the governing equations of the problem may be sought, finite element (FE), boundary element (BE) and finite difference (FD) techniques being examples of methods that are fairly widely used. In most cases, the implementation of these solutions would involve computer software packages or else computer codes that were specially written for the purpose. In either case, considerable effort is likely to be expended on the solution, and in some cases the use of numerical methods can result in a certain loss of "feel" for the physics of the problem. Examples of numerical studies in duct acoustics are the work of Astley and Eversman [1], who have applied a FE technique to sound propagation in flow ducts with locally-reacting liners, and that of Chang and Cummings [2], who utilized a 2D method in perforated tube flow duct silencers with hydrodynamic nonlinearities. There is a large body of published work describing the application of various types of numerical technique in both acoustics and vibration.

An alternative to FE methods is the use of simpler variational formulations such as the Rayleigh-Ritz technique, which is closely related in its basic principles to FE methods, but is generally much less demanding in terms of computational effort. Indeed, the least complicated Rayleigh-Ritz approaches can yield approximate solutions in explicit form (see, for example, the paper by Astley [3]), which can permit fairly easy physical interpretations of the results. There are many problems which lend themselves readily to this type of treatment, and we discuss some of them in this paper.

GENERAL FORMULATION

One of the attractive features of a variational formulation is that the governing differential equations and most (or all) of the boundary conditions

(b.c.s) in the problem are implicit in a single equation. If the field variable (which may be the acoustic pressure, the temperature perturbation or a particle velocity component) is denoted ψ, and the problem is two-dimensional in the (y,z) plane, with ψ being defined in the region R, then a functional $F(\psi)$ may be defined,

$$F(\psi) = \iint_R f(\psi, \psi_{yy}, \psi_{zz}) dR, \tag{1}$$

where $f(\ )$ is a function of ψ, $\partial^2\psi/\partial y^2$, $\partial^2\psi/\partial z^2$, that could (in principle) also include derivatives such as $\partial\psi/\partial y$ *et cetera*. If F is minimized w.r.t. ψ, then

$$\delta F = 0. \tag{2}$$

This equation gives rise to Euler equations, which embody the governing differential equations and the natural b.c.s (which may or may not be the same as the physical b.c.s). The function $f(\ )$ may be chosen to yield the desired Euler equations and natural b.c.s. In the Rayleigh-Ritz (R-R) method, a trial function ψ is employed,

$$\bar{\psi} = \sum_{n=1}^{N} a_n \phi_n(y,z), \tag{3}$$

where a_n are arbitrary coefficients and the functions ϕ_n are chosen so that they satisfy the physical b.c.s on C, the boundary of R; we note that ψ and $\bar{\psi}$ are different functions, unless ψ *happens* to be an exact solution to the governing differential equations, subject to the prevailing b.c.s. Equation (2) requires $F(\bar{\psi})$ to be minimized w.r.t. the a_n, that is

$$\partial F/\partial a_n = 0 \qquad (n = 1,2,.....N). \tag{4}$$

Equation (4) yields a series of N simultaneous, homogeneous or inhomogeneous, linear equations in the cases (respectively) of homogeneous and inhomogeneous governing differential equations. In the first case, an eigenproblem results, from which the *relative* values of the a_n may be found, and in the second instance, the absolute values of the a_n are determined. In either case, the approximate solution $\bar{\psi}$ is found and the accuracy of the approximation usually improves as N is increased.

A RECTANGULAR FLOW DUCT WITH AN ANISOTROPIC BULK LINER

Our first example of the use of Rayleigh-Ritz methods in sound absorbing ducts is a two-dimensional planar sound field in a rectangular duct with an anisotropic, porous, bulk liner placed against one wall. A uniform airflow

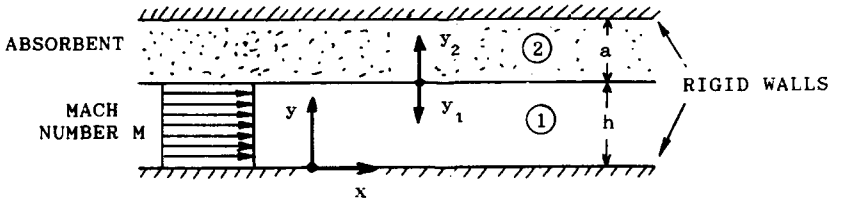

Figure 1. A rectangular flow duct

passes along the duct as shown in Figure 1. A fairly simple exact solution exists in this case (see the more general analysis of Sormaz and Cummings [4]), and we may compare our approximate solutions to the exact result. We seek modal solutions of the form

$$p(x,y;t) = \exp(i\omega t) \sum_{i=1}^{\infty} A_i\ Y_i(y)\ \exp(-i\alpha_i kx), \tag{5}$$

ω being the radian frequency, k the acoustic wavenumber and α_i a dimensionless

axial wavenumber. If we choose

$$F(Y) = [1/2(1-\alpha M)^2]b\int_0^h [(Y_1')^2 - k^2[(1-\alpha M)^2-\alpha^2]Y_1^2]dy$$
$$+ (\rho/2\rho_y)b\int_h^{h+a} [(Y_2')^2 - k^2(1-\alpha^2/\gamma_x^2)\gamma_y^2\, Y_2^2]dy, \qquad (6)$$

where b is the depth of the duct and ρ_y, γ_x, γ_y are the complex effective density of the fluid in the absorbent in the y direction, and the propagation coefficients (in units of ik) in the x and y directions respectively, the Euler equations of this functional are: (i) the convected wave equation in region 1, (ii) the wave equation in the absorbent, (iii), (iv) the hard-wall b.c.s at the duct wall, (v) the b.c. of continuity of normal particle displacement at the interface between absorbent and airflow passage. Boundary conditions (iii)-(v) are the natural b.c.s, and constitute all but one of the physical b.c.s. The remaining b.c. is that of continuity of pressure at the interface, and we satisfy this by choosing a trial function that is continuous at y = h. The choice of the trial function is to some extent determined by the prior knowledge that Y(y) (for a particular mode) is a sinuous function (this is apparent from the exact solution, which involves sine and cosine functions). Even without this information, we would have guessed as much, and therefore trigonometric functions are appropriate for the ϕ_n. While it is perfectly possible to choose $\phi_n = \cos[n\pi y/(h+a)]$, we note from b.c. (v) that there is a discontinuity in Y' at y = h which cannot be accommodated by a finite number of terms in the summation, so it is more satisfactory to select separate trial functions for regions 1 and 2, *viz.*

$$\tilde{Y}_1 = A + \sum_{n=1,3,..}^{N} B_n \sin(n\pi y_1/2h), \quad \tilde{Y}_2 = A + \sum_{n=1,3,..}^{N} C_n \sin(n\pi y_2/2a), \qquad (7a,b)$$

where A, B_n, C_n are complex coefficients. Equations (4), (6) and (7) give rise to an eigenproblem from which α_i may be found. The modal attenuation rate is then $\Delta = -8.6858\ \mathrm{Im}(k\alpha_i)$ dB/m (if SI units are used); the axial phase speed is given by $c_p = \omega/\mathrm{Re}(k\alpha_i)$ m/s.

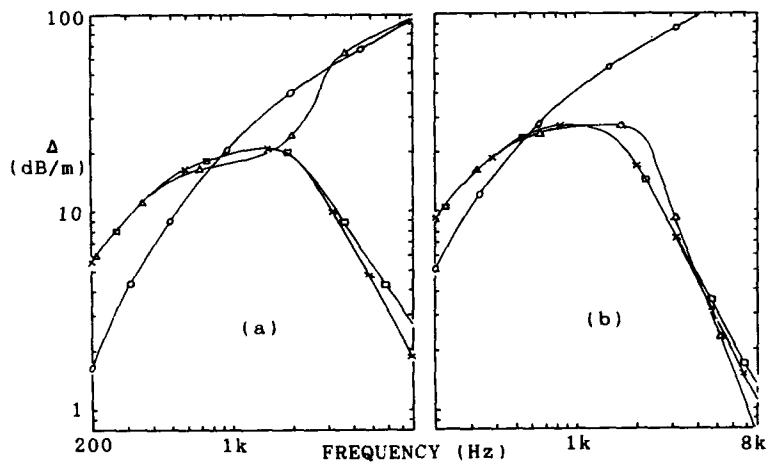

Figure 2. Comparison between Δ for the exact solution, ×——×, and single, o——o, three, Δ——Δ, and seven, □——□, d.o.f. R-R solutions for the fundamental (i=1) mode in a duct with a fibrous absorbent having steady flow resistivities of 10^4 and 2×10^4 SI rayl/m parallel and normal (respectively) to the laminae of fibres; a = h = 100 mm; (a), M = 0.1, (b), M = -0.1.

The simplest solution involves a single degree of freedom (d.o.f.), with a uniform pressure trial function, and is found by putting B_n, $C_n = 0$. A quartic equation must be solved to find α if there is mean flow, but this equation becomes quadratic if $M = 0$, and an explicit expression may therefore be obtained for α. Solutions with more degrees of freedom may be found and in such cases, we may cast the problem either in the form of a determinantal eigenproblem (which may be solved by an iterative procedure such as Newton's or Muller's method) or a generalized matrix eigenvalue problem (which may be solved by a standard routine). Each method has its advantages and drawbacks, but in the computations presented here, Newton's method was utilized.

In Figure 2, comparison is made between the exact solution and three R-R solutions for the attenuation rate of the fundamental mode in a rectangular duct. In the case of downstream propagation ($M = 0.1$), the uniform-pressure R-R model gives poor predictions even at low frequencies, while the three d.o.f. model yields acceptable predictions up to 1.8 kHz, beyond which the predictions become increasingly inaccurate as the frequency rises. The seven d.o.f. model gives quite good results up to about 3-4 kHz. For upstream propagation, the R-R predictions are generally better (because the transverse pressure distribution is more uniform), although the one d.o.f. curve is still not adequate. The three d.o.f. model gives sensible predictions, even up to 8 kHz, and the seven d.o.f. solution yields good accuracy up to 8 kHz. Other data (not shown here) indicate that the simplest, single d.o.f., R-R model gives its best predictions for ducts with either large or small a/h ratios, for absorbents of low flow resistivity and at low frequencies, that is, where the *actual* transverse acoustic pressure profile is at its most uniform. The general trend is for more d.o.f. to produce more accurate results. In practical terms, there is no reason for one to use a R-R type solution for a rectangular duct, since the exact solution may readily be calculated, but in the case of (for example) a circular duct, there may be some advantage, since Bessel and Neumann functions are more time-consuming to compute than circular functions. We next discuss the case of a circular geometry.

A CIRCULAR FLOW DUCT WITH AN ISOTROPIC BULK LINER

To avoid excessive complication in turning to a circular geometry, we examine a duct with an isotropic bulk liner, placed against the wall; the analysis follows that of the rectangular duct very closely. The trial function is essentially similar and so is the expression for the functional, though $\partial/\partial y$ is replaced by $\partial/\partial r$ and the integrals over the areas of regions 1 and 2 take on a somewhat different form. Figure 3 shows a comparison between axial attenuation rates of the fundamental mode in a duct with a liner consisting of an open-celled polyether foam with a steady flow resistivity of 5 430 SI

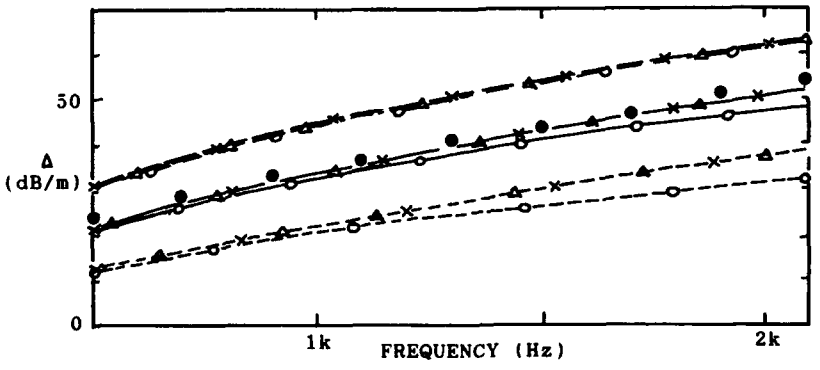

Figure 3. Comparison between the exact solution (×—×, M = -0.197, ×———×, M = 0, ×- - -×, M = 0.197), single d.o.f. (○—○, M = -0.197, ○———○, M = 0, ○- - -○, M = 0.197) and three d.o.f. (△—△, M = -0.197, △———△, M = 0, △- - -△, M = 0.197) R-R solutions for Δ in the fundamental (i=1) mode in a circular duct with a polyether foam liner; inner radius = 19.8 mm, outer radius = 38 mm; ●, experimental data for M = 0.

rayl/m, predicted from the exact theory (which involves Bessel functions of the first and second kinds) and from one and three d.o.f. R-R formulations. Numerical data are shown for three mean flow Mach numbers: 0, -0.197 and 0.197; experimental data are also shown, for zero flow.

It is clear from Figure 3 that even the single d.o.f. R-R solution gives generally quite fair predictions of Δ, though for M = 0.197 the accuracy deteriorates above about 1.5 kHz. The three d.o.f. R-R solution yields results that are indistinguishable from the exact solution at all frequencies and for all three Mach numbers; predicted and experimental data for M = 0 agree well. The more favourable performance of the simpler R-R solutions in this case results partly from the lower flow resistivity of the foam as compared to the fibrous material and partly from the lower frequency range, smaller percent flow area and smaller duct width in this example.

AN APPROXIMATELY ELLIPTICAL FLOW DUCT WITH A CIRCULAR GAS FLOW PASSAGE AND AN INHOMOGENEOUS ABSORBENT

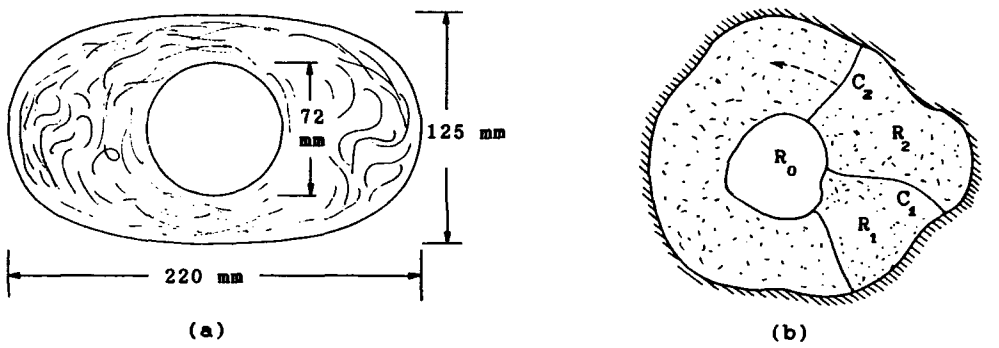

Figure 4. The SAAB silencer: (a) cross-sectional geometry, (b) subdivision of absorbent in the R-R formulation.

This is the practical case of a SAAB automobile silencer, and is the most demanding of those discussed so far, in view of its awkward geometry and the inhomogeneity of the absorbent. Whereas in the previous two cases, exact solutions have been available, this is not the case here; partly because of the geometry, and partly because of the inhomogeneous nature of the porous medium, we cannot find analytical solutions to the present problem. The cross-sectional geometry of the silencer is shown in Figure 4(a); the flow passage occupies 18% of the total cross-sectional area. The casing is approximately elliptical in cross-section and the flow passage is circular. Though there is a layer of very coarse stainless steel wool and a perforated tube immediately within the periphery of the flow passage, the presence of these is ignored since they would be expected to present little impediment to the passage of sound waves. The absorbent (a basalt wool) was found to have a relatively high steady flow resistivity (about 24 000 SI rayl/m) where it was thinnest, but a low flow resistivity (about 8 000 SI rayl/m) at the thickest points. The flow resistivity was relatively insensitive to the coordinate direction, and so the acoustic properties were taken to be isotropic. Because of the inhomogeneity, however, the absorbent was subdivided into regions of constant properties. Figure 4(b) illustrates how this was done. Provided we take a sufficient number of these regions, the effects of inhomogeneity will be adequately taken into account.

For the purposes of a R-R formulation, the sound field in region R_0 (which is circular), may be assumed to be axisymmetric if only the fundamental mode is of interest, but in regions R_1, R_2,... it should be allowed to vary both radially and perimetrally. These regions were chosen to be radial segments, and a radial variation in the trial function for sound pressure was permitted, though the perimetral variation was suppressed. The trial function was axisymmetric - with two d.o.f. and a form similar to that in equation (7a) - in R_0, and continuous at the interface between flow passage and absorbent.

Separate two d.o.f. trial functions (like those in equation (7b)) were allowed in the sub-regions of absorbent; the coefficient A was common to all regions (including the flow passage), ensuring continuity of sound pressure at the interface, but the coefficients of the quarter-sine function differed between segments. Because a perimetral pressure discontinuity existed between segments in the trial functions, natural b.c.s of continuity of pressure and normal particle displacement between segments were required, in addition to the natural b.c.s of the rectangular duct problem. A more complicated functional is required here, and has the form

$$F(p) = 1/[2(1-\alpha M)^2]\iint_{R_0}\{\nabla_t p_0\cdot\nabla_t p_0 - k^2[(1-\alpha M)^2-\alpha^2]p_0^2\}dR_0$$

$$+\sum_{i=1}^{N}(\rho/2\rho_a)\iint_{R_i}[\nabla_t p_i\cdot\nabla_t p_i - k^2(\gamma^2-\alpha^2)p_i^2]dR_i + \rho\omega^2\sum_{i=1}^{N}\int_{C_i}\xi_i(p_{i+1}-p_i)dC_i, \qquad (8)$$

where γ is, *a priori*, the dimensionless propagation coefficient (the same in all coordinate directions in this problem), ∇_t is the two-dimensional Laplacian operator on the duct's cross-section, ρ_a is the effective density, p is the transverse spatial factor in the sound pressure field and ξ is the acoustic particle displacement normal to the boundaries between segments. This functional has all the required natural b.c.s. Because ξ appears in the functional together with p, it too has to be allotted a trial function in each segment, and a single quarter-sine curve (zero at the interface and maximum at the wall) was chosen; the arbitrary coefficients appearing in these trial functions differed between segments. It should be noted that the pressure trial function does not satisfy the hard-wall boundary condition, but this is unimportant, since this requirement is catered for by one of the natural b.c.s. For the fundamental mode, symmetry permits the solution of only one-quarter of the sound field in the duct, the natural b.c. of zero normal pressure gradient along the dividing lines between this region and the other three being physically correct. There are N segments of absorbent, and the total number of d.o.f. in the problem is 2N+1. The actual formulation was carried out for an anisotropic, inhomogeneous liner, though the former feature has so far proved to be unnecessary in this particular problem. For higher order modes to be resolved accurately by the above formulation, subdivision of the flow area into segments (as with the absorbent in this case), together with more degrees of freedom per segment, would prove necessary.

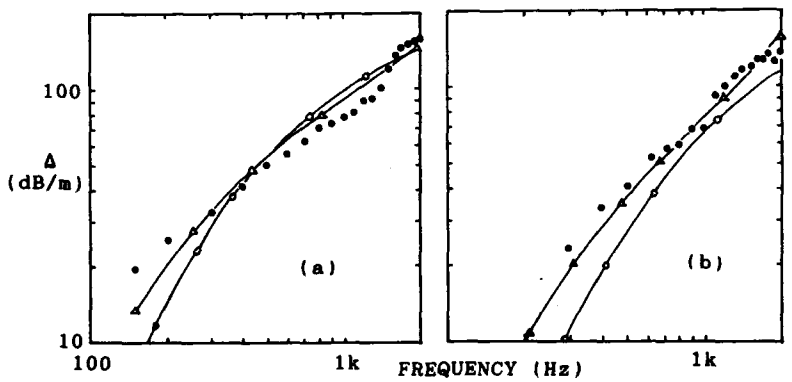

Figure 5. The SAAB silencer: predicted and measured Δ; (a), M=0, (b), M=0.13; o——o, Δ——Δ, 1, 13, d.o.f. R-R formulations; ●, measured data.

Single d.o.f. (with a uniform trial function for p only) and 13 d.o.f. R-R predictions for Δ of the fundamental mode in the SAAB silencer are shown in Figure 5, for two flow Mach numbers. No exact solution can be plotted, but experimental data are shown instead. Agreement between the 13 d.o.f. curves

and measurements is good. The 1 d.o.f prediction for zero flow is fair because of the small open area fraction, but rather poor for M=0.13 because of the less uniform sound pressure profile in this case.

SOUND PROPAGATION IN A CAPILLARY TUBE OF ARBITRARY CROSS-SECTION

Here we consider a uniform narrow tube of arbitrary cross-section, containing a viscous, heat-conducting fluid. In the simplified, uncoupled, problem, the linearized Navier-Stokes (N-S) equation for parallel flow and the linearized energy equations turn out to be isomorphic (see Stinson [5]), with the form

$$(\nabla_t^2 - i\omega/\eta)\psi = -i\omega/\eta, \qquad (9)$$

where $\psi = (\omega\rho/\lambda p)u$, $\eta = \nu$ in the N-S equation, $\psi = (\rho C_p/p)T$, $\eta = \nu/Pr$ in the energy equation, p is the sound pressure (assumed uniform), λ the axial wavenumber, u the velocity perturbation, C_p the specific heat ratio, ν the kinematic viscosity, Pr the Prandtl number and T the temperature perturbation. The b.c. in both the thermal and viscous problems is $\psi = 0$ on C (the boundary of R, the cross-section). A variational functional,

$$F(\psi) = (1/2)\iint_R [\nabla_t\psi\cdot\nabla_t\psi + (i\omega/\eta)\psi^2 - (i2\omega/\eta)\psi]dR, \qquad (10)$$

may be defined, and has equation (9) as one of the Euler equations, though the other is the natural b.c. $\partial\psi/\partial n = 0$ on C (n being the normal to C), which is not the physical b.c. A forced b.c. is imposed by ensuring that the trial function has $\psi = 0$ on C, in which case $\delta\psi = 0$ on C. The cross-section may be split up into triangular elements, all with one vertex at a central point in the tube, C thereby being approximated by a series of line segments. In each element, a coordinate is specified, running from the centre normally to the opposite side and ψ is assumed to vary (within the element) only in this direction. Clearly, ψ must have the same value in all elements at the centre, and be zero at the wall. At low frequencies, a single d.o.f. parabolic trial function may be employed, $\tilde{\psi} = A(1-\zeta^2)$ (ζ being the dimensionless coordinate); at high frequencies, $\tilde{\psi}$ is put equal to the constant A for $0 \le \zeta \le 1-\delta/L$, δ being the viscous or thermal boundary-layer thickness (as appropriate) and L the distance from the central point to the base of the triangular element, and is given a linear fall-off to zero for $1-\delta/L \le \zeta \le 1$.

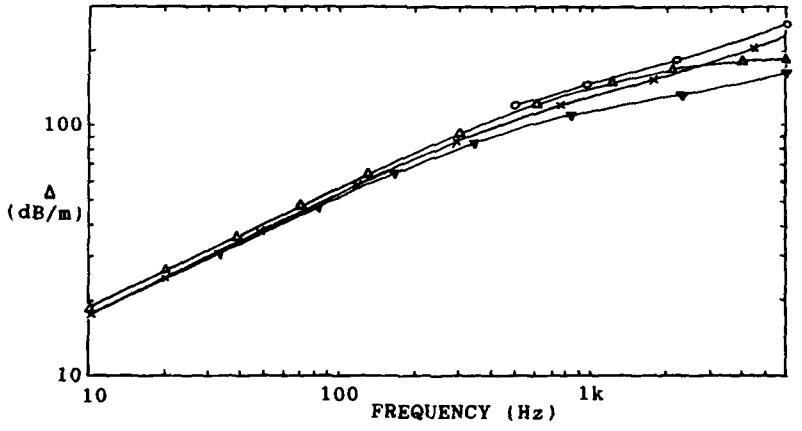

Figure 6. Δ in a square section tube of side 0.2 mm: ×——×, exact solution; △——△, ○——○, low, high frequency 1 d.o.f. R-R solutions; ▽——▽, Craggs' and Hildebrandt's isothermal FE solution [6].

In Figure 6, the low and high frequency R-R predictions for a square section tube are compared to the exact solution (see reference [5]) and to an FE solution to the viscous problem by Craggs and Hildebrandt [6] (in which the assumption of an isothermal process was made). The R-R data compare

favourably to the exact result; the FE predictions agree well with the exact solution at low frequencies (where the isothermal solution would be valid), but - as expected - are in error at higher frequencies. The 1 d.o.f. R-R method produces simple explicit expressions for Δ both at low and high frequencies, even for cross-sectional geometries that do not permit analytical solutions.

DISCUSSION

It has been shown that even quite simple R-R solutions to sound fields in dissipative ducts can yield results that are sufficiently accurate for practical purposes. The method is attractive because of its considerable versatility; it can be used on awkward geometries where analytical solutions are impossible, and is used to best advantage with relatively few d.o.f., since excessive complication would render a full FE solution more appropriate in many cases.

ACKNOWLEDGEMENTS

Research on the SAAB silencer forms a part of a project, based in the Department of Technical Acoustics at the Royal Institute of Technology, Stockholm, Sweden, and supported by the Swedish National Board for Technological Development. Investigations on rectangular and circular ducts are being carried out with support from the Science and Engineering Research Council, under Research Grant GR/F/59407, and from Sound Attenuators Ltd., of Colchester.

REFERENCES

1. Astley, R.J. and Eversman, W., A finite element formulation of the eigenvalue problem in lined ducts with flow. Journal of Sound and Vibration **65** [1979], 61-74.

2. Chang, I.-J. and Cummings, A., A time domain solution for the attenuation, at high amplitudes, of perforated tube silencers and comparison with experiment. Journal of Sound and Vibration **122** [1988], 243-259.

3. Astley, R.J., Acoustical modes in lined ducts with flexible walls: a variational approach. Proceedings, Inter-Noise 90 Conference [1990], 575-578.

4. Sormaz, N. and Cummings, A., Acoustic attenuation in dissipative splitter silencers containing mean fluid flow. Proceedings, Institute of Acoustics **13** [1991], 443-452.

5. Stinson, M.R., The propagation of plane sound waves in narrow and wide circular tubes, and generalisation to uniform tubes of arbitrary cross-sectional shape. Journal of the Acoustical Society of America **89** [1991], 550-558.

6. Craggs, A. and Hildebrandt. J.G., Effective densities and resistivities for acoustic propagation in narrow tubes. Journal of Sound and Vibration **92** [1984], 321-331.

SECOND INTERNATIONAL CONGRESS ON
RECENT DEVELOPMENTS IN AIR- AND
STRUCTURE-BORNE SOUND AND VIBRATION
MARCH 4-6, 1992 AUBURN UNIVERSITY, USA

Duct acoustics: junctions and lattices, application to perforated tube mufflers

Jean Kergomard
Laboratoire d'acoustique de l'Université du Maine
Av. Olivier Messiaen B.P. 535
72017 Le Mans Cedex
FRANCE

ABSTRACT

Complete solutions for junctions between several guides can be found by using modal expansion and matricial formalism. Thus exact analysis of modes of an acoustic lattice can be made. In the case of a perforate tube muffler, this approach leads in two steps (calculation of junction and lattice analysis) to physical interpretation of practical interest.

INTRODUCTION

Propagation of acoustic waves in ducts of simple shape is well known, even when dissipation or mean flow occurs. Nevertheless, propagation in a lattice, or network, of ducts is a relatively new topics for research. The analysis of this problem can be divided into two parts: the calculation of the effect of junctions of tubes, and the study of the properties of the lattice. The problem of a general lattice can be considered and solved , using for example methods of condensed matter physics (see e.g. ref [1]). Here the discussion is restricted to a problem of great practical interest, i.e. the perforated tube muffler. Our interest lies both in a precise description of perforations and in a physical interpretation of the propagation in such a muffler.

Several approaches have been used for solving the problem: in general the effect of the perforation is assumed to be described by a shunt inductance (at low levels), but this inductance is not calculated. We show that a complete solution of the Helmholtz equation by using modal expansion allows to calculate this inductance, to show that there is another (series) inductance and to obtain the result in a form leading to a simple interpretation of the lattice modes.

MODELLING A JUNCTION USING MODAL THEORY: GENERAL APPROACH

Classically a perforation or a diaphragm or zero thickness can be regarded as a guide of zero length. Thus modal decomposition can be made both in the perforations and in the guides (the internal and the external ones): problems occur with the truncation of matrices (see e.g. Mittra and Lee [2] or Vassallo [3]), but the method can be very useful.

Consider a junction between several guides (see fig.1)

Fig. 1: junction between several guides

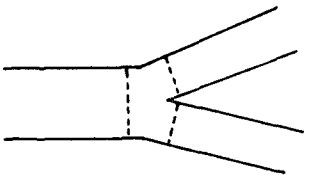

The junction can be firstly described as an n.m(i) port network, where m(i) is the number of modes considered in guide i (see e.g. Jones [4] or Kergomard [5]). If the junction is sufficiently far from discontinuities , or sources, in each guide, the termination of the ports corresponding to evanescent modes is closed on their characteristic impedance. The distance condition is that the ratio ℓ/d is sufficiently large, where ℓ and d are the length and the transverse dimension of the guide, respectively. Thus it is possible to reduce the order of the network to n.p(i), where p is the number of propagating modes in guide i at the considered frequency.

The junction being passive, the most simple method in order to obtain the impedance matrix (see e.g. Cotte [6]) of the n.m port-network is to use the wave equation in its integral form, thus:

$$\mathbf{P} = \mathbf{Z}\ \mathbf{U} \qquad (1)$$

where **P** and **U** are pressure and velocity (multiplied by the area S) vectors, respectively, (of dimension n.m), considered the output surface of the guides and **Z** the impedance block-matrix given by:

$$Z_{ij} = \frac{j\omega\rho}{S_i S_j} \int_{S_i} \int_{S_j} \psi_i(r_i)\ G(r_i, r'_j)\ {}^t\psi_j(r'_j)\ dS_i\ dS'_j$$

where Z_{ij} is a matrix of order (m(i), m(j)), G is the Green function of the closed cavity, limited by the output surfaces of the guides , and ψ the dimensionless eigenmodes vector defined as follows:

$$\int_S \psi\ {}^t\psi\ dS = S\ \mathbf{1}.$$

Here **1** is the unit matrix . ω is the angular frequency, and ρ the gas density. At low frequencies, only the plane mode propagates in each guide, the characteristic impedance of the evanescent modes is inductive, and the problem is solved by the determination of the square matrix of the junction, of order n. By decomposing the Green function on the eigenmodes of the cavity, one can show that this matrix involves a capacitance, corresponding to the compressibility of the gas contained in the cavity, i.e. to the uniform mode of the cavity, and inductances, corresponding to the coupling between the higher modes of the cavity and both the plane modes and the evanescent modes of the guides (by neglecting the evanescent modes one obtains the classical plane piston approximation: see e.g. for the case of an expansion chamber Ih and Lee [7]).

MODELLING THE JUNCTION: THE CASE OF THE PERFORATION IN A MUFFLER

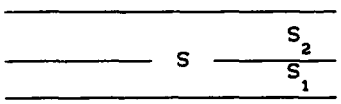

Fig.2: shema of a perforation between two guides

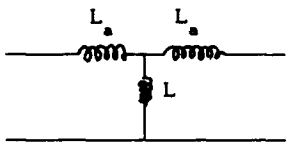

Fig.3: equivalent circuit for the (ABCD) matrix

In figure 2 is shown a simplified schema for perforation in a perforated tube muffler. The first step of the calculation is concerned with the junction between one guide (left and right sides) and the hole. This junction is a particular case of a junction between three guides. This problem is classical and was solved by some authors. The above described method is not well adapted, it is more simple to use the Green function of the infinite tube. Of course the integral formulation is modified: Lapin [8] or Keefe [9] used the integral equation by considering the plane mode existing without branch as a volume source. Leppington [10] prefered to consider the plane modes on the two sides of the hole as boundary sources. With the same idea, we solved the problem of the junction between three guides and obtained the general shape of the equivalent circuit at low frequencies [11]. The circuit involves five lumped elements and a transformer.

It is possible to apply the same method for a perforation between two guides. If one notes p_{1L}, p_{2L}, p_{1R}, p_{2R} the plane mode pressures on the left and right sides of the hole, respectively, and v_{1L}, v_{2L}, v_{1R}, v_{2R} the the plane mode velocities, one obtains the two following equations:

$$\begin{pmatrix} \dfrac{S_1 p_{1L} + S_2 p_{2L}}{S_1 + S_2} \\ \dfrac{S_1 v_{1L} + S_2 v_{2L}}{S_1 + S_2} \end{pmatrix} = \begin{pmatrix} 1 & 0 \\ 0 & 1 \end{pmatrix} \begin{pmatrix} \dfrac{S_1 p_{1R} + S_2 p_{2R}}{S_1 + S_2} \\ \dfrac{S_1 v_{1R} + S_2 v_{2R}}{S_1 + S_2} \end{pmatrix} \qquad (2)$$

$$\begin{pmatrix} p_{1L} - p_{2L} \\ v_{1L} - v_{2L} \end{pmatrix} = \begin{pmatrix} A & B \\ C & D \end{pmatrix} \begin{pmatrix} p_{1R} - p_{2R} \\ v_{1R} - v_{2R} \end{pmatrix}$$

In these equations, the plane mode quantities are considered in the abcissa corresponding to the center of the hole. The elements A, B, C, D, correspond to the equivalent T-circuit shown in figure 3, where the inductances L_a and L are given by the following expressions:

$$j\omega L_a = \frac{1}{2} \frac{S_1 + S_2}{S_1 S_2} \rho^2 c^2 {}^t\beta \, (Z_1 + Z_2)^{-1} \beta$$

$$j\omega L = -\frac{1}{2} j\omega L_a + j\omega L_s \qquad (3)$$

$$1/j\omega L_s = \frac{S_1 + S_2}{S_1 S_2} {}^t\alpha \, (Z_1 + Z_2)^{-1} \alpha$$

The vectors α and β and the matrices Z_1 and Z_2 are given by the follwing formulae:

$$\alpha = \frac{1}{S} \int_S \cos kz \; \psi \, dS \quad ; \quad \beta = \frac{1}{S} \int_S \sin kz \; \psi \, dS \qquad (4)$$

$$Z_i = \frac{j\omega\rho}{S^2} \int_S \int_S \psi(r) \; \mathrm{Re}(G_i(r,r')) \; {}^t\psi(r') \, dS \, dS'.$$

S is the area of the perforation, ψ the eigenmodes vector of the perforation, i = 1 or 2, Re(G) the real part of the Green function of the infinite guides, and z the longitudinal coordinate. The Green function can be easily calculated by using a decomposition on the eigenmodes of the infinite guides. In these expressions, we assume for simplicity that the hole is symmetrical with respect to a plane perpendicular to the z-axes of the guides. Thus the two indices a and s correspond to the two kinds of modes in the hole: the antisymmetrical modes, and the symmetrical modes (including the plane one), respectively.

We notice that the classical modelling of perforate tube muffler [12] omits the antisymmetrical term. Keefe [9] remarked that the inductance L_a is negative. Concerning the calculation of the inverse matrix of (Z_1 and Z_2), a variational calculation is often sufficient (see Schwinger and Saxon [13] or Keefe [9]). Nevertheless, by considering the hole as a limit of a guide of finite length, it is possible to calculate this matrix by using a double perturbation, the zeroth order term being the plane piston appoximation, the first perturbation is the result for a guide of infinite length, and the second the result for a guide of zero length. This method was used for the calculation of the inductance of a diaphragm of zero thickness in a guide (see ref. 5).

Of course, the modal decomposition is possible only for particular geometries. As an example, using the two kinds of Bessel functions, the exact calculation for a concentric perforated tube muffler is possible. Nevertheless, the power of the present method is to obtain an exact form of the equivalent circuit for any geometry, even when frequency increases. The elements of the circuit can be determined by numerical computation (e.g. F.E.M.) or by experiment.

LATTICE ANALYSIS: THE CASE OF A PERFORATED TUBE MUFFLER

With the above results, it is now possible to analyse the wave propagation in a given lattice. Some authors (see e.g. Peat [14], Munjal [15]) tried to obtain a decoupled approach of the perforate tube mufflers, by using the simple model ignoring the antisymmetrical modes, by calculating the diagonal matrix of fourth order . We see here that the modal calculation leads directly to this decoupled approach, even for irregular perforations. As a matter of fact, the two above matricial

equations (2), are the two submatrices of the required fourth order matrix . The diagonal matrix is unnecessary, the form (2) defines directly the two lattice modes, and are easily extended to a portion of muffler with several perforations. Between two successive perforations, the plane mode transfer matrices are *identical* for the two lattice modes, they are:

$$\begin{pmatrix} \cos k\ell & \rho c j \sin k\ell \\ (\rho c)^{-1} j \sin k\ell & \cos k\ell \end{pmatrix}$$

Here ℓ is the distance between two perforations .The condition of validity of this matrix for both modes is that the propagation constant is the same in the two guides, i.e. the temperature is the same. Thus the interpretation of the lattice modes is very clear: the first one is the plane mode which exists without perforation, and can be called the "expansion chamber mode" . The second one is a mode in a cylindrical tube with perforations, like a musical wind instrument with open side holes. This mode can be called the "flute" mode. In the case of regular perforations, Benade [16] showed that this mode is evanescent at low frequencies, and propagating and high frequencies, above a certain cutoff frequency.

CONCLUSION: TRANSMISSION THROUGH A PERFORATED TUBE MUFFLER

It remains to analyse the transmission through a perforate tube expansion chamber. Below the cutoff of the flute mode, the effect of this mode is only a kind of length correction to the input and output of the expansion chamber, i.e. a small shift in the resonance frequencies. The cutoff increasing when the perforations become nearer, one understands why the effect of the perforated tube in the muffler is very small at low frequencies, as it is well kwown by engineers. Above cutoff, the effect of the flute mode is very important, and ignoring the perforate tube is impossible. We notive that for a small number of perforations, the effect of the flute mode can be important even below cutoff: this effect is the well known tunneling effect.

As a conclusion, modal theory with matricial formalism allows to obtain both the most simple exact description of a perforation between two guides and the interpretation of the properties of a perforated tube silencer in terms of lattice modes. This practical result can be extended in order to take into account the effect of losses. Concerning the effect of mean flow, the modal analysis of the junction is valid, but the propagation constant can be different in the two guides, then the interpretation of the lattice modes is less simple. Nevertheless, for small Mach numbers, a perturbation calculation allows to use the above results as zeroth order results, and the interpretation remains valid at least in a qualitative sense. Concerning the interaction of close spaced perforations through evanescent guide modes, a further investigation is needed.

Finally, at our mind, this analytical approach is very useful for physical interpretation. An alternative method leading to relatively simple numerical computation is the method of Stredulinsky et al [17] or Eversman [18], mixing FEM for junctions and transfer matrices for simple pipes. Moreover, our analysis is limited to linear cases, we notice that nonlinear methods exist, e.g. the method of Chang and Cummings [19], or the method of Morel et al [20] .

REFERENCES

[1] Depollier C., Kergomard J., Lesueur J.C., J. Sound Vib.142, 1990, 153-170.
[2] Mittra R. and Lee S.W., Analytical techniques in the theory of guided waves (Macmillan, New York) 1971.
[3] Vassallo C., Théorie des guides d'ondes électromagnétiques, Tome 2 (Eyrolles, Paris) 1985.
[4] Jones D.S., Acoustic and electromagnetic waves (Clarendon Press, Oxford) 1986.
[5] Kergomard J., J.Acoustique 4, 1991, 111-138.
[6] Cotte-Dunajewski T. Contribution à l'étude des résonateurs. Thèse de spécialité en acoustique, Aix-Marseille 1, 1977.
[7] Ih J.G. and Lee B.H., J.Acoust.Soc.Am. 77, 1985,1377-1388.
[8] Lapin, A.D., Soviet Phys. Acoust. 7, 1961, 77-79.
[9] Keefe, D.H., J.Acoust.Soc.Am. 72, 1982, 676-687.
[10] Leppington F.G., J. Sound Vib.83, 1982, 526-532.
[11] Kergomard J., Khettabi A., 2e Congrès Français d'Acoustique, Arcachon (France), 1992.
[12] Sullivan J.W., J.Acoust.Soc.Am. 66, 1979, 772-778.
[13] Schwinger J. and Saxon D.S., Discontinuities in waveguides (Gordon and Breach, New York) 1968.
[14] Peat K.S., J.Sound Vib. 123, 1988, 199.
[15] Munjal M.L., Acoustics of ducts and mufflers (Wiley, New York) 1987.
[16] Benade A.H., J.Acoust.Soc.Am.32,1960, 1591-1608.
[17] Stredulinsky D.C., Craggs A., Faulkner M.G., Canadian Acoustics 15, 1987, 3-14.
[18] Eversman W., Transactions of the ASME, J. of Vibration, Acoustics, Stress and Reliability in Design, 109, 1987, 168-177.
[19] Chang I.J. and Cummings A., J.Sound Vib. 122 1988, 243.
[20] Morel T., Morel J., Blaser D.A., SAE technical paper series n° 910072, February-March 1991.

SECOND INTERNATIONAL CONGRESS ON
RECENT DEVELOPMENTS IN AIR- AND
STRUCTURE-BORNE SOUND AND VIBRATION
MARCH 4-6, 1992 AUBURN UNIVERSITY, USA

EFFECTIVENESS OF IMPROVED METHOD AND TECHNIQUES FOR HVAC DUCT SOUND ANALYSIS AND PREDICTION

Michihito Terao
Department of Architecture,
Kanagawa University,
Kanagawa-ku, Yokohama-shi, 221,
Japan

ABSTRACT

To include reflected wave contributions in the sound pressure level prediction of air ducts at lower frequencies, the acoustic driving wave pressure amplitude of each port and the coherence between them as the acoustic active properties besides the complex pressure reflection and transmission factors for each port as the passive properties of a component are employed. Experimental and numerical determination methods and their application results to a duct network are presented. Especially a two-step determination method and undesired microphone signal suppression techniques under airflow has been developed.

INTRODUCTION

In HVAC sound prediction for frequencies below few hundreds Hz is most important in the building space design stage, because of its large space requirement of roughly a half wave length dimensions for sound treatment whose installation cannot be allowed after this design stage. The calculation method which is most widely used in the area is of ASHRAE [1] by means of the energy transmission loss summation of the components in series from the source towards the

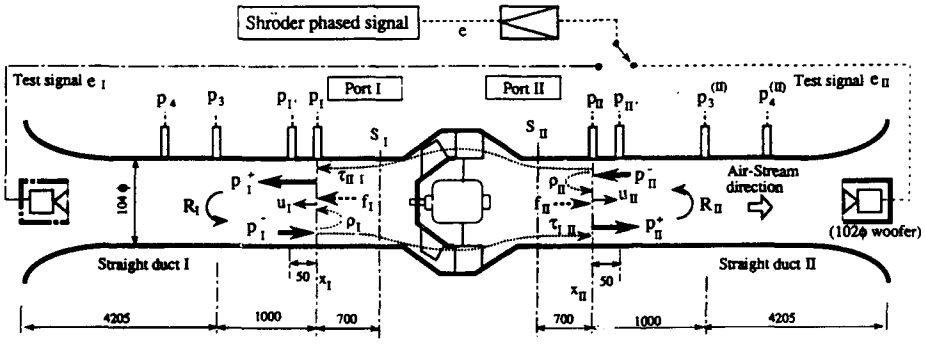

Fig.1. Test arrangement and definitions for two-step acoustic property determination of a duct component.

location of interest. This method disregards the reflected wave contributions of every components and frequently gives under-estimation by about 10 dB in octave band SPL. Recent developments of computers and signal processing techniques have ability to realize to implement the complex sound pressure calculation instead of the sound energy calculation to regain the reliability of the prediction. In this line, a semi-complex sound pressure expression of a sound source component, improved determination methods and a synthesis method of the component properties, and some realistic applications of them are presented.

ACOUSTIC EXPRESSIONS OF A DUCT COMPONENT

Interface Acoustic Expressions for a Component

Taking a interface in a plane wave region of every straight duct as shown in Fig.1 for a two-port (K=I, II) coherent source, the relationships between the complex pressure amplitudes of outgoing and incoming waves , p_K^+ and p_K^-, the characteristic reflection and transmission factor, ρ_K and τ_{KJ}, and transmission factor, the driving wave pressure. f_K^+ are given [2,3] as;

$$\begin{bmatrix} p_I^+ \\ p_{II}^+ \end{bmatrix} = \begin{bmatrix} \rho_I & \tau_{II} \\ \tau_{II} & \rho_{II} \end{bmatrix} \begin{bmatrix} p_I^- \\ p_{II}^- \end{bmatrix} + \begin{bmatrix} f_I^+ \\ f_{II}^+ \end{bmatrix} \tag{1}$$

Load-side Reflection Factor

The the outgoing and incoming waves of the wave number of k can be detected through the load-side reflection factor, R_K , by measuring the transfer function, $H_{KK'}$, of two locations, x_K and $x_{K'}$, as shown in Fig.1., by using following relationships [4];

$$p_K^+ = p_K / (1+R_K), \quad \text{and} \quad p_K^- = R_K p_K^+ \tag{2}$$

$$R_K = [\exp\{-jk(x_{K'} - x_K)\} - H_{KK'}] / [H_{KK'} - \exp\{jk(x_{K'} - x_K)\}] \tag{3}$$

Ensemble Average Expression of a Source Component

Taking the ensemble average of Eq.(1) to include partial coherent sources, we have a pair of semi-complex sound pressure expressions as;

$$\begin{bmatrix} |f_I^+|^2 \\ |f_{II}^+|^2 \\ \mu_{II}^{(f+)} |f_I^+| |f_{II}^+| \end{bmatrix} = \begin{bmatrix} |\eta_{II}|^2 & |\eta_{II}|^2 \\ |\eta_{II}|^2 & |\eta_{II}|^2 \\ \eta_{II}^* \eta_{II} & \eta_{II}^* \eta_{II} \end{bmatrix} \begin{bmatrix} |p_I^+|^2 \\ |p_{II}^+|^2 \end{bmatrix} + |p_I^+| |p_{II}^+| \begin{bmatrix} \eta_{II}^* \eta_{II} & \eta_{II} \eta_{II}^* \\ \eta_{II}^* \eta_{II} & \eta_{II} \eta_{II}^* \\ \eta_{II}^* \eta_{II} & \eta_{II}^* \eta_{II} \end{bmatrix} \begin{bmatrix} \mu_{II}^{(p+)} \\ (\mu_{II}^{(p+)})^* \end{bmatrix} \tag{4}$$

$$\begin{bmatrix} |p_I^+|^2 \\ |p_{II}^+|^2 \\ \mu_{II}^{(p+)} |p_I^+| |p_{II}^+| \end{bmatrix} = \frac{1}{|\eta_D|^2} \begin{bmatrix} |\eta_{II}|^2 & |\eta_{II}|^2 \\ |\eta_{II}|^2 & |\eta_{II}|^2 \\ -\eta_{II}^* \eta_{II} & -\eta_{II}^* \eta_{II} \end{bmatrix} \begin{bmatrix} |f_I^+|^2 \\ |f_{II}^+|^2 \end{bmatrix} + \frac{|f_I^+| |f_{II}^+|}{|\eta_D|^2} \begin{bmatrix} -\eta_{II}^* \eta_{II} & -\eta_{II}^* \eta_{II} \\ -\eta_{II}^* \eta_{II} & -\eta_{II}^* \eta_{II} \\ \eta_{II}^* \eta_{II} & \eta_{II}^* \eta_{II} \end{bmatrix} \begin{bmatrix} \mu_{II}^{(f+)} \\ (\mu_{II}^{(f+)})^* \end{bmatrix} \tag{5}$$

where the following property expression and complex coherence factors are introduced;

$$\eta_{II} = 1 - \rho_I R_I, \quad \eta_{II} = 1 - \rho_{II} R_{II}, \quad \eta_{II} = -\tau_{II} R_{II}, \quad \eta_{II} = -\tau_{II} R_I \quad \text{and} \quad \eta_D = \eta_{II} \eta_{II} - \eta_{II} \eta_{II}$$

$$\mu_{I\,II}^{(f+)} = \langle (f_I^+)^* f_{II}^+ \rangle / (|f_I^+||f_{II}^+|) \quad \text{and} \quad \mu_{I\,II}^{(p+)} = \langle (p_I^+)^* p_{II}^+ \rangle / (|p_I^+||p_{II}^+|) \tag{6}$$

The absolute symbol(| |) and angle bracket(<>) attached values are of ensemble averaged. By using Eq.(2), we have

$$|p_K^+| = |p_K| / |1 + R_K| \tag{8}$$

$$\mu_{I\,II}^{(p+)} = \{ |1 + R_I| / (1 + R_I)^* \} \{ |1 + R_{II}| / (1 + R_{II}) \} \, \mu_{I\,II}^{(p)} \tag{9}$$

$$\mu_{I\,II}^{(p)} = \langle (p_I)^* p_{II} \rangle / (|p_I||p_{II}|) = 2\, S_{I\,II}^{(p)} / (|p_I||p_{II}|) \tag{10}$$

EXPERIMENTAL DETERMINATION OF ACOUSTIC PROPERTIES OF A COMPONENT

A two-step determination method [2,3] of the characteristic passive and active acoustic properties of a sound source component under air stream have been introduced instead of the anechoic termination method [5] and the multiple-load methods [6,7].

Passive Acoustic Property Determination

The passive property is determined first. Superposing an external test signal e_J (from J-th port side, for J= I and II in turn) incoherent with the primary sound source, the outgoing and incoming plane wave pressures, $p_K^{(e_J)+}$ and $p_K^{(e_J)-}$, coherent with the signal e_J, can be observed. The unknown passive properties can be determined by solving Eq.(11), which can be derived from Eq.(1) disregarding the driving pressure terms incoherent with the test signal e_J;

$$\begin{bmatrix} p_I^{(e_J)+} \\ p_{II}^{(e_J)+} \end{bmatrix} = \begin{bmatrix} \rho_I & \tau_{I\,II} \\ \tau_{II\,I} & \rho_{II} \end{bmatrix} \begin{bmatrix} p_I^{(e_J)-} \\ p_{II}^{(e_J)-} \end{bmatrix}, \quad J = I, II \tag{11}$$

To extract the acoustic pressures, $p_K^{(e_J)}$ and $p_{K'}^{(e_J)}$, from the microphone pressures, $p_K^{c(e_J)}$ and $p_{K'}^{c(e_J)}$, contaminated by the the primary source and flow induced noise, Eq.(12) was employed;

$$p_K^{(e_J)} = 2\, S_{eK}^{(e_J)} / |e_J| \,, \text{ and } H_{KK'}^{(e_J)} = S_{eK'}^{(e_J)} / S_{eK}^{(e_J)} \,, \quad J = I, II \tag{12}$$

where $S_{eK}^{(e_J)} = \langle e^*_J \, p_K^{c(e_J)} \rangle / 2$ is the cross-spectrum between e_J and contaminated pressure $p_K^{c(e_J)}$ By replacing R_K and $H_{KK'}$ by $p_K^{(e_J)}$ and $H_{KK'}^{(e_J)}$ in Eqs.(2) and (3), R_K, p_K^+, and p_K^- can be observed.

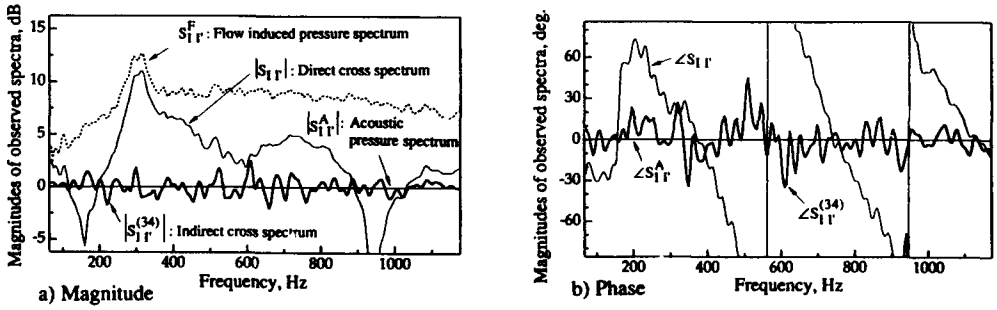

Fig. 2. Flow induced microphone noise suppression by an indirect cross-spectrum measurement

Active Acoustic Property Determination

In this stage, removing the externally superposed test sound in the Fig.1., the magnitude and cross-spectrum, $|p_K|$ and $S_{I\,II}^{(p)}$, of both port pressures originated from the primary source is observed. Applying the previously determined passive properties and the reflection factors, R_K, the active properties $|f_K^+|$ and $\mu_{I\,II}^{(f+)}$ can be determined explicitly by using Eqs.(4),(8), (9) and (10).

To suppress the flow induced microphone noise in measuring the pressure magnitude, an indirect power spectral measurement by means of Eq.(13) have been introduced;

$$|p_K| = \{ 2 S_{3K}^{(f)} S_{K4}^{(f)} / S_{34}^{(f)} \}^{1/2} \quad , \quad K = I, II \quad , \tag{13}$$

In which the two additional microphones, numbered 3 and 4 are employed as shown in Fig.1.These additional microphones are positioned far from each other in comparison with the correlation length of the turbulence. As seen in.Fig.2, the difference between the indirectly extracted pressure and the acoustic pressure is within a few dB when the acoustic pressure is less than the flow induced fluctuation pressure by 10 dB [2].

Acoustic Properties by Two-Step Experiment

Fig .3 and 4. shows the acoustic properties of fans under operation determined by the two-step method by using the experimental setup illustrated in Fig.1. The properties are evaluated at the source side discontinuity, $x_{[K]}$, of the straight duct, extending the data from that at the measured stations, by using the loss free plane wave model.

For the mixed flow fan (Fig.3), the transmission factors under operation (Mach number of 0.01) are still reciprocal in magnitude. For the centrifugal blower (Fig.4), the reciprocity of the transmission factor under operation (Mach number of 0.05) does not hold. For both fans tested, the driving wave pressure magnitudes towards both sides are roughly similar., $|f_I^+| \approx |f_{II}^+|$.

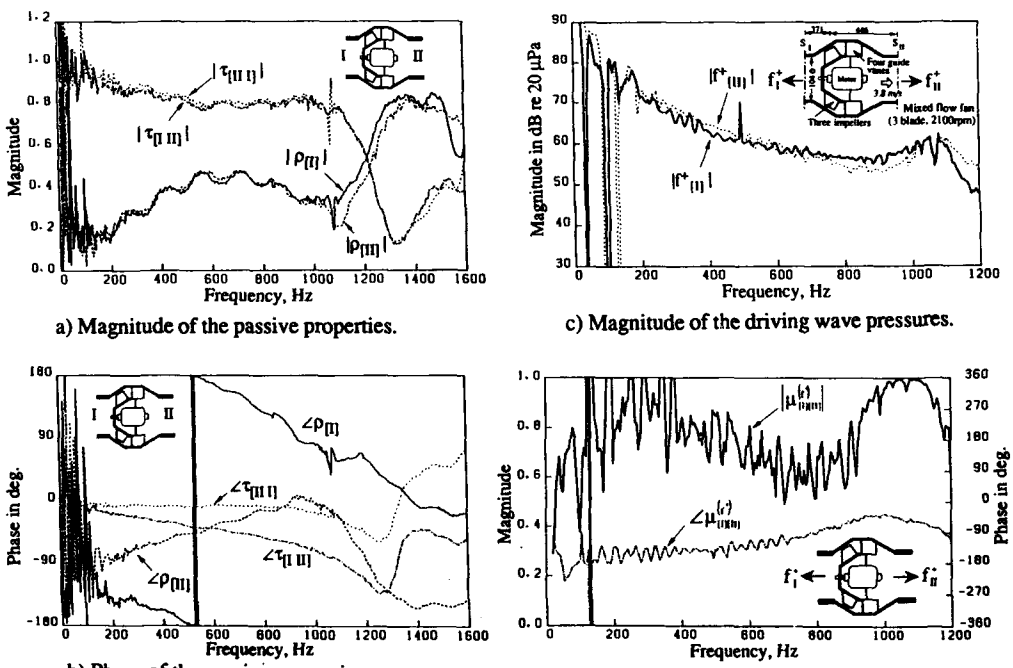

a) Magnitude of the passive properties.

c) Magnitude of the driving wave pressures.

b) Phase of the passive properties.

d) Coherence between the driving wave pressures.

Fig.3. Acoustic properties of a semi-axial fan in operation, at mean airflow velocity of 3.8 m/s.

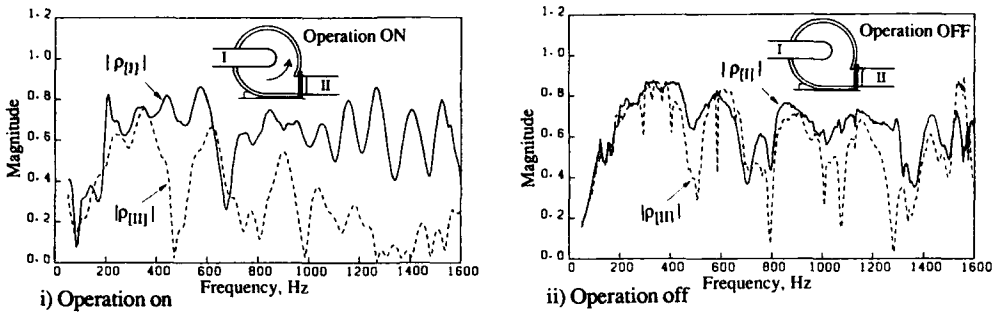

a) Magnitude of the reflection factors.

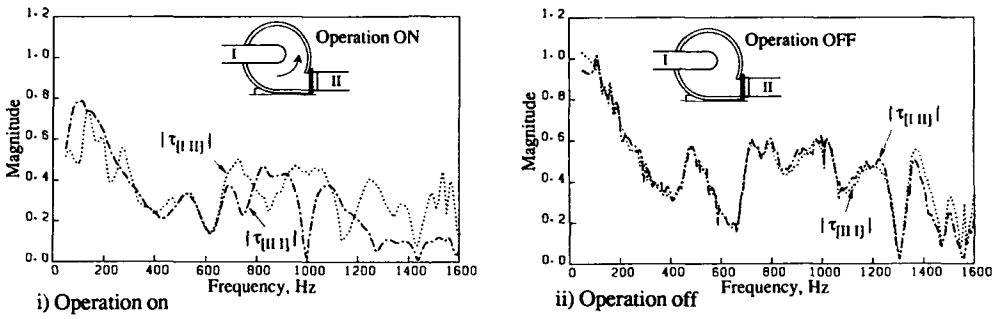

b) Magnitude of the transmission factors.

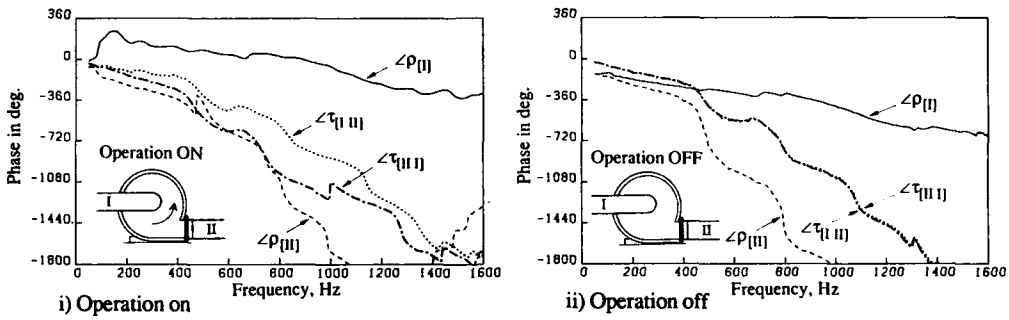

c) Phase of of the reflection and transmission factors.

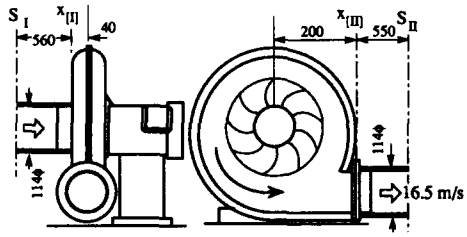

d) Centrifugal blower tested.

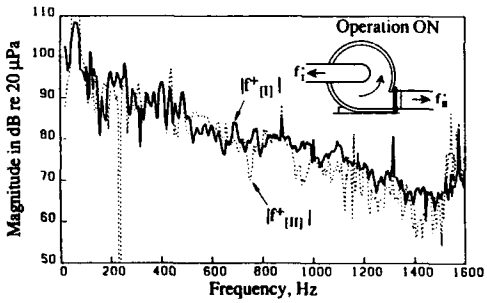

e) Magnitude of the driving wave pressures.

Fig.4. Acoustic properties of a centrifugal blower at operation on (at mean airflow velocity of 16.5 m/s).and at operation off (no flow).

NUMERICAL DETERMINATION OF PASSIVE ACOUSTIC PROPERTIES

For few HVAC duct components, their characteristic reflection and transmission factors are available for both acoustically passive and active components. Fortunately most passive property of HVAC duct components will be determined by using the numerical approaches such as FEM and BEM, as far as the stream effects can be negligible.

Straight Section Length for Plane Wave Interface

The transmission losses of the double elbows are shown in Fig.5. CPM stands for the the semi-complex sound pressure method in which the active property terms are omitted in Eq.(4), instead EGM stands for the energy transmission loss method in which both the active property and interference terms are omitted in Eq.(4). There is some upper limit in the Helmholtz number , kW/π, to be able to obtain a combined section property from its sub-divided component properties. To apply plane wave approximation, there must be some region of section with uniform pressure. To achieve this up to the Helmholtz number of 0.95 beneath the first cross-mode cut on of the the straight section between two sub-divided components, the straight duct length is required longer than roughly four times its cross sectional dimension[8,9].

Branch Takeoffs

For branch takeoffs, the transmission coefficient is dealt equal to the ratio of the sectional area of the particular branch to that of all the branches and the reflection factors are zero in ASHRAE. As seen from Fig.6. [9], this may leads to a large error since grate many branch takeoffs are usually installed in a HVAC duct network.

A Component Including Sound Absorbent Materials

Fig.7 shows the transmission loss of an expansion chamber which include absorbent materials. BEM combined with the sub-structure procedure and the characteristic properties in

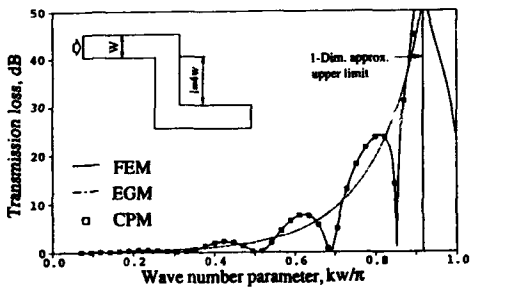

a) Transmission loss

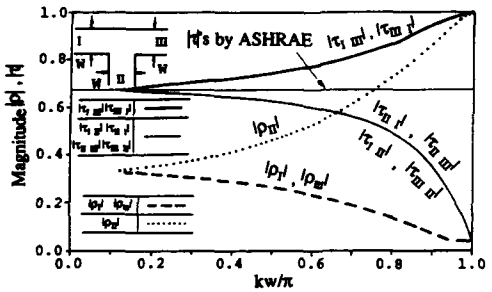

a) Magnitude

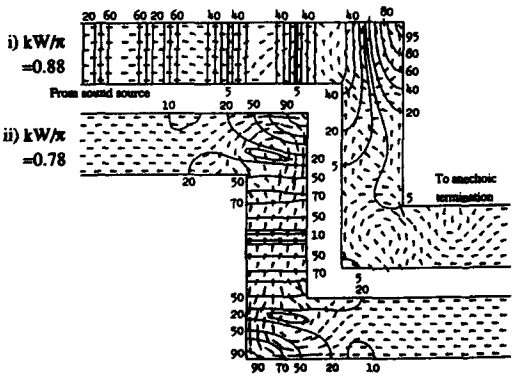

Fig.5. Acoustic properties of a double elbow.

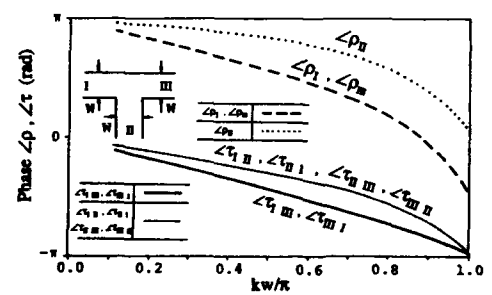

b) Phase

Fig.6. Reflection and transmission factors of a rectangular T-shaped takeoff, by FEM.

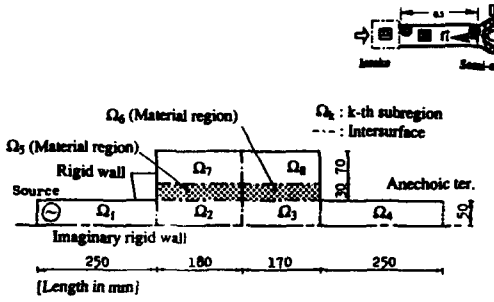

a) A substructure model.

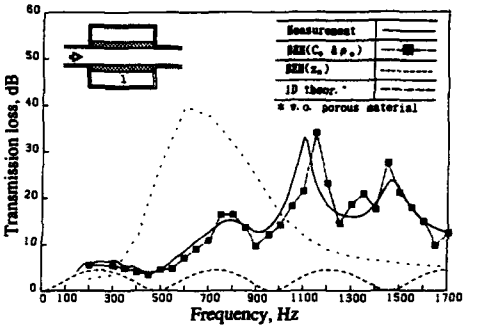

b) Transmission factor.

Fig. 7. A BEM substructure model of an expansion chamber with urethane-foam.

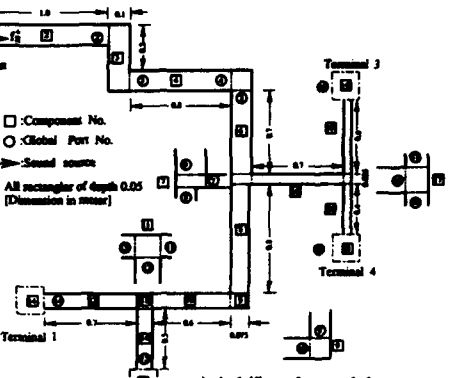

a) A 1/5 scale model of a HVAC duct network.

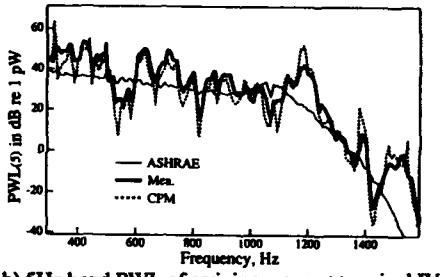

b) 5Hz band PWL of arriving wave at terminal IV.

Fig. 8. Sound predictions of a duct network.

terms of the effective sound velocity and the effective density of the acoustic material, ρ_e and c_e [10 ,11], gives good results in contrast to the analysis by the normal impedance., z_n.

ACOUSTIC PREDICTION OF A HVAC DUCT NETWORK

Load-Side Reflection Factor Calculation

To calculate the sound pressure level at a desired position using the acoustic properties of the sub-divided components, a classic but simple synthesis procedure [9] is presented here.

For the j-th acoustically passive component in the load-side duct network of an active component port, an expression (14) and its explicit solutions (15), (16) and (17) introducing the source-side reflection factor $R_I^{<i>}$ and load-coupled transmission factors, $T_{II}^{<j>}$ and $T_{III}^{<j>}$, defined as Eq. (18), is given for a three-port component instead of Eq.(1) for general explanation, as;

$$\begin{bmatrix} p_I^{<j>+} \\ p_{II}^{<j>+} \\ p_{III}^{<j>+} \end{bmatrix} = \begin{bmatrix} \rho_I^{<j>} & \tau_{I\,II}^{<j>} & \tau_{I\,III}^{<j>} \\ \tau_{II\,I}^{<j>} & \rho_{II}^{<j>} & \tau_{II\,III}^{<j>} \\ \tau_{III\,I}^{<j>} & \tau_{III\,II}^{<j>} & \rho_{III}^{<j>} \end{bmatrix} \begin{bmatrix} p_I^{<j>-} \\ p_{II}^{<j>-} \\ p_{III}^{<j>-} \end{bmatrix} \tag{14}$$

$$R_I^{<i>} = \rho_I^{<j>} + \tau_{I\,II}^{<j>} R_{II}^{<j>} T_{II}^{<j>} + \tau_{I\,III}^{<j>} R_{III}^{<j>} T_{III}^{<j>} \tag{15}$$

$$T_{II}^{<j>} = \{ (1 - \rho_{III}^{<j>} R_{III}^{<j>}) \tau_{II\,I}^{<j>} - \tau_{II\,III}^{<j>} R_{III}^{<j>} \tau_{III\,I}^{<j>} \} / T_D^{<j>} \tag{16}$$

$$T_{III}^{<j>} = \{ (1 - \rho_{II}^{<j>} R_{II}^{<j>}) \tau_{III\,I}^{<j>} - \tau_{III\,II}^{<j>} R_{II}^{<j>} \tau_{II\,I}^{<j>} \} / T_D^{<j>} \tag{17}$$

$$T_D^{<j>} = (1 - \rho_{II}^{<j>} R_{II}^{<j>}) (1 - \rho_{III}^{<j>} R_{III}^{<j>}) + \tau_{II\,III}^{<j>} R_{III}^{<j>} \tau_{III\,II}^{<j>} R_{II}^{<j>}$$

$$R_I^{<i>} = p_I^{<i>-} / p_I^{<i>+} = p_I^{<j>+} / p_I^{<j>-}, \quad T_{II}^{<j>} = p_{II}^{<j>+} / p_I^{<j>-} \text{ and } T_{III}^{<j>} = p_{III}^{<j>+} / p_I^{<j>-} \tag{18}$$

Giving the terminal side reflection factors, $R_{\blacksquare}^{<j>}$ and $R_{\blacksquare}^{<j>}$, from the terminal towards the source component in turn, $R_{I}^{<i>}$, $T_{\blacksquare}^{<j>}$ and $T_{\blacksquare}^{<j>}$ of every component can be determined by using Eqs.(15), (16) and (17).

Acoustic Connection of A Source Component to Its Loads

Using the load-side reflection factor, R_K, determined above and the active and passive acoustic properties of the source component, the traveling wave pressure magnitude $|p_K^+|$ of every port of the source component can be obtained by applying Eq.(5). Then the sound pressure magnitude of a given location can be calculated applying $T_{\blacksquare}^{<j>}$ and $T_{\blacksquare}^{<j>}$ of Eq.(18) from the source towards the terminal in turn.

Predicted and Experimental results

Fig.8 shows the 5 Hz band power level, $PWL_{(5)}$, of the arriving wave at the terminal IV of an 1/5 scale model of a middle scale duct network as shown in the figure. The semi-axial fan shown in the previous section was used as the source component. The active property of this fan under operation was measured again directly in this duct network. For the passive properties, the numerically determined properties were used in the semi-complex pressure coupling method (CPM), instead the data of ASHRAE were used [1] in the sound energy transmission method (EGM-ASHRAE). The agreement of the present method (CPM) with measurement is good.

SUMMARY

For acoustic predictions of HVAC duct networks, fundamental effectiveness of a two-step method for the passive and active acoustic property determination, FEM and BEM approaches for the passive property determination of an air-duct component and a semi-complex sound pressure synthesis method for a duct network acoustic prediction has been presented.By applying these methods and properties to an about 1/5 scale model of a middle scale duct network, the sound pressure prediction agrees fairly well with measurement.

REFERENCES

[1]ASHRAE HANDBOOK,Systems,Chapter32,Sound and vibration control,(1984).
[2] M.Terao and H.Sekine:In-duct Pressure measurements to determine sound generation, characteristic reflection and transmission factors of an air moving device in air-flow,Inter-noise 89,(1989),143-146.
[3] M.Terao,R.J.Bernhard,N.L.Denton and H.Sekine:Sound source strength sensitivity to load impedances in an air-duct system,Inter-noise 90,(1990),591-594.
[4] ASTM,E1050,Standard test method for impedance and absorption of acoustical materials using a tube, two microphones, and a digital frequency analysis system,1985.
[5]W.Neise,F.Holste and G.Hoppe,Experimental comparison of standard sound power measurement procedures for fans,Inter-noise 88,Vol.2,(1988),1097-1100.
[6] M.G.Prasad and M.J.Crocker:On the measurement of the internal source impedance of a multi-cylinder engine exhaust system,J. Sound and Vibration 90,(1983),479-490.
[7] M.L.Munjal and A.G.Doige:On uniqueness,transfer and combination of acoustic sources in one-dimensional systems,J.Sound and Vibration 121(1),(1988),25-35.
[8] M.Terao and H.Sekine:A method to detect separately sound of traveling wave in each direction at a point in air-moving system,Inter-noise 88,89-92(1988).
[9] M.Terao:A method to estimate sound transmission losses in air-duct network including the contribution of reflected-waves from discontinuities,Inter-noise 86,Vol.1,(1986),571-576.
[10] M.Terao and H.Sekine:On substructure boundary element techniques to analyze acoustic properties of air-duct components,Inter-noise 87,(1987),1523-1526.
[11]H.Utuno T.Tanaka, T.Fujikawa and A.F.Sybert:Transfer function method for measuring characteristic impedance and propagation constant of porous materials, J.Acoust.Soc.Am.86(2),(1989),637-643.

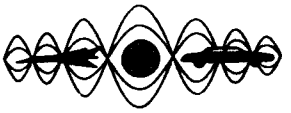

SECOND INTERNATIONAL CONGRESS ON
RECENT DEVELOPMENTS IN AIR- AND
STRUCTURE-BORNE SOUND AND VIBRATION
MARCH 4-6, 1992 AUBURN UNIVERSITY, USA

FLOW DUCT SILENCER PERFORMANCE

J. L. Bento Coelho
CAPS- Instituto Superior Técnico
1096 Lisboa Codex
PORTUGAL

Flow ducts are widely used in industrial plants and internal combustion engine exhausts. High levels of acoustic energy may propagate inside the duct system, owing to existing noise sources and to internally generated noise, which might be undesirable to the environment and to the duct structure. Silencers are employed, of which the straight-through resonator chamber is a typical configuration where the interference of geometry with the flow is kept to a minimum. Modelling techniques are available to a great degree of accuracy. Testing procedures are straightforward and can be easily implemented on site. Although most design work is based on linear conditions, these may not actually apply in many real situations. The silencer performance may then significantly deviate from predictions, depending strongly on acoustic and flow conditions.

INTRODUCTION

Industrial fluid distribution systems as well as internal combustion engine exhausts make use of flow ducts which in some cases carry high levels of sound energy generated at noise sources like engines, pumps or other. Duct geometry changes, which may occur frequently in industrial arrangements and can be rather complex owing to needs for fluid distribution and control, may also be responsible for internally generated noise. Various duct elements that disturb the flow and the acoustic field may be considered, like side branches, orifices, valves, sudden constrictions or enlargements on any cross section area changes. These may act as secondary noise sources with the energy generated locally being radiated both up and downstream. The noise carried by the flow inside the duct is radiated to the outside from apertures or exhausts or by the duct structure itself, causing a negative impact on the environment. Noise enhanced fluid-structure interaction may also have destructive effects on the supporting structure causing material fatigue and degrading reliability and performance of the system.

Design of a complete piping system is, usually, a very complex task. Each element is selected by considering its particular performance, cost and also the interaction with the whole system and the corresponding effects on the overall system performance or reliability. Noise is a factor which plays a major role, in some cases. A particular duct component may interfere with either the acoustic field and its propagation or, most especially, with the flow which, eventually, increases the noise levels inside the duct, becoming a secondary noise source. Insertion of silencing elements may then be essential. Good performance of duct silencers can be achieved with high levels of attenuation resulting for selected frequency bands. The silencer itself may, however, represent a further disturbance on the flow, thereby requiring a careful design where the relevant physical mechanisms are dully accounted for. Translation of all the complex physics

involved in sound propagation inside a flow duct can be difficult, but in the current state of the art represents a good understanding of the process is achieved. That is not exactly the case for the phenomena of interaction of the sound field with the flow, and, especially, the secondary sound generation at duct discontinuities owing to interchanges between acoustic and mechanical energies where rather complex physical mechanisms, strongly dependent on geometry and on acoustic and flow conditions, are present.

These subjects have been studied in the last decades in many countries since they combine needs for understanding of the physical phenomena and for technological advance towards reduction in costs and noise pollution. An European project [1] which involves Portugal, France, Gt. Britain and Denmark is currently developing and assembling a great deal of work on piping systems where a further insight on sound propagation and generation inside a duct system is being investigated.

SILENCER DESIGN

A good silencer design procedure should use reliable prediction methods and efficient testing techniques for effective cost and performance minded quality control. Computer implemented mathematical modelling has been presented in the literature [2-6, for example] based on analytical or parametric descriptions of the silencer chamber. The complexity of the models vary from the very simple to rather complicated ones. Mathematical complexity is usually linked to complexity in geometry and to flow effects. Some of these may be overlooked for simplicity sake in well controlled situations where linear plane wave conditions apply and second order mechanisms play minor roles.

Consider a straight-through resonator chamber, as sketched in Fig. 1, a common configuration in many applications bearing the advantage of causing minimum disturbance to the fluid flow in the duct. A perforated bridge is most frequently used between the side branches in order to minimise vortex formation at discontinuities and its interaction with the acoustic waves, by eliminating the free shear layer that would exist in the otherwise open chamber, and to take advantage of the further attenuation provided by the perforated wall, owing to dissipative and to reactive effects that alter the acoustic coupling between the main duct and the resonating cavity.

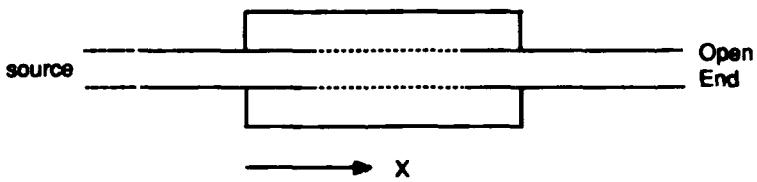

Figure 1 - Straight-through silencer chamber.

In this simple geometry, the wave equations may be separately applied to all the elementary regions which the chamber can be assumed to be composed of. Equations of continuity of pressure and velocity are then applied as boundary conditions at the interfaces between those regions. By assuming plane wave propagation and a uniform mean flow inside the main pipe, the acoustic pressure in the perforated region results from

$$[(1-M^2)\frac{\partial^2}{\partial x^2} - \frac{2M}{c}\frac{\partial^2}{\partial x \partial t} - \frac{1}{c^2}\frac{\partial^2}{\partial t^2}]\,p = \frac{2}{R}\frac{Du}{Dt} \qquad (1)$$

where M (M=V/c, with V the mean flow velocity and c the speed of sound in the fluid) is the Mach number, R is the main pipe radius, p is the acoustic pressure inside the duct and u is the radial velocity. Continuity of the particle velocity is assumed at the perforated wall. This has been shown [7] to provide a more realistic model for the actual behaviour of the perforated wall than a particle displacement continuity condition, both from physical considerations (the perforate does not act as an impervious membrane and in most applications where M>0.1 spatial disturbances at the different locations of the boundary are expected to be uncorrelated) and from fits to experimental data. This velocity is given by

$$u = \frac{1}{Z}(p - p_c) \qquad (2)$$

where p_c is the pressure in the resonator region and Z is the perforate wall impedance. By applying the wave equation to this region and combining with Eqs. (1) and (2), the pressure p may be obtained from:

$$p = \sum_{n=1}^{4} \varepsilon_n P_n e^{i\gamma_n x}$$

where

$$\varepsilon_n = \frac{i}{bsk}(k^2 - \gamma_n^2 - ibsk)$$

where $s = \rho c/Z$, ρ is the fluid density and γ_n are the roots of the complex polynomial equation

$$c_0 D^4 + c_1 D^3 + c_2 D^2 + c_3 D + c_4 = 0$$

with b, c_0, c_1, c_2, c_3 and c_4 being complex numbers depending on chamber radial geometry, convection effects (Mach number), fluid conditions (density, temperature), acoustic frequency and liner wall impedance, $k = 2\pi/\lambda$ is the wave number, $i = \sqrt{-1}$ and the coefficients P_n are determined by application of the pressure and velocity continuity conditions at the boundaries of the sections of the chamber.

Computation of this model is fairly straightforward and fast. Although the major physical mechanisms were included in the mathematics, three-dimensional effects at discontinuities or non-linear behaviour can not be accounted for. The latter can, however, be included, up to a point, in the model of the perforated wall.

The perforate wall impedance, Z= R+iX, should be considered for different regimes of operation and the appropriate description be adopted in each one. These regimes are essentially determined by the amplitudes of the mean flow velocity and of the acoustic pressure inside the duct. For low pressure amplitudes, with the fluid at rest, the liner impedance is given by

$$Z = \frac{\rho}{\sigma}\{(\frac{d}{\phi} + 1)\sqrt{8\nu\omega} + \frac{1}{8c}(\omega\phi)^2 + i\omega[d + (\frac{d}{\phi} + 1)\sqrt{8\nu/\omega} + \frac{8}{3\pi}\phi(1 - 0.7\sqrt{\sigma})]\}$$

where σ is the open to total area ratio of the perforate, d is the length of the orifice, ϕ is its diameter, ν is the gas kinematic viscosity and $\omega = 2\pi f$.

For values of M larger than 0.05, Z becomes

$$Z = 0.3\rho c\frac{(1-\sigma^2)}{\sigma}M + i\omega\frac{\rho}{\sigma}[\sqrt{8\nu/\omega}(1+d/\phi) + d + \frac{8}{3\pi}\phi(1-0.7\sqrt{\sigma})(1+305M^3)^{-1}]$$

An intermediate grazing flow regime, for $0.025 \le M \le 0.05$, can be considered where the resistance is given by $0.6\rho c(M-0.025)(1-\sigma^2)/\sigma - 40R_0(M-0.05)$, with R_0 being the resistance for M=0.0, and the reactance is given by the same expression for $M > 0.05$. The above expressions quantify viscosity, inertial and grazing flow effects as well as those of orifice interaction. All these effects contribute to the overall silencing performance.

Another more powerful and comprehensive approach [4,5] considers the discontinuities of the boundary wall (any finite impedance wall) of the main pipe to be a disturbance of the otherwise rigid wall. They are, then, replaced by equivalent virtual sources understood to be responsible for the generation of superimposed pressure fields.The acoustic pressure field inside the duct may then be assumed to be composed of a pressure field generated upstream and propagating in a straight pipe plus a perturbation field generated by a distribution of virtual sources located at the discontinuities. In the presently considered straight-through configuration, these would replace the perforated bridge. This would be considered as a set of elementary ring sources, for which simple mathematical solutions are known and can be applied.

All the major phenomena can be included in the mathematical formulation. By making use of appropriate Green's functions, a complete description of the 3-D pressure distribution inside the duct can be obtained and computed.

The pressure field inside the main duct can thereby be derived from

$$p = \frac{i}{2k}\rho c^2 S\,(e^{-ikx/(1+M)} + e^{i2\psi}e^{ikx/(1-M)}) - \rho k^2 c^2 \sum_{j=1}^{N}\int_{\Delta_j} G_j\,(1 - i\frac{M}{k}\frac{\partial}{\partial x})\,z\,dx$$

The first term represents the acoustic pressure inside the duct in the absence of the silencer, where S is a non-dimensional amplitude, ψ accounts for an end reflection (open end at an exhaust), x is the longitudinal coordinate and the other quantities have already been defined. The second term represents the contributions of the various perturbations of the boundary wall, in terms of elementary sources of length Δ_j, where G_j describes the pressure field generated by an impulsive ring source and z is a displacement function normal to the wall (the operator of z represents the interaction between the acoustic wave field and the moving fluid).

Although this might appear to be much more complex than the previously mentioned technique, that is not so. Various effects, like those of higher order modes or high pressure amplitudes, can be accounted for where required, which is not possible in a 1-D model.

This model allows a segmentation of the silencer chamber along its axis with each segment being assigned a different wall impedance, thereby accounting for its pressure dependence. It also accounts for the presence of evanescent higher order modes. This was seen to be of a relative influence in certain cases, especially on the location of the resonant frequencies and on the values of the larger attenuations. It is a highly power and flexible model, although it may require some computation time depending on the number of the elementary virtual sources which is related to the length of the discontinuity (perforate bridge).

SILENCER ATTENUATION

Figure 2 depicts typical attenuation curves of a silencer chamber of 0.392 m length, main pipe radius of 0.019 m and outer/inner diameter ratio of 2.6, with a perforated liner of 15.7% open area ratio, for two conditions of mean flow. The curves represent Insertion Loss, which can be

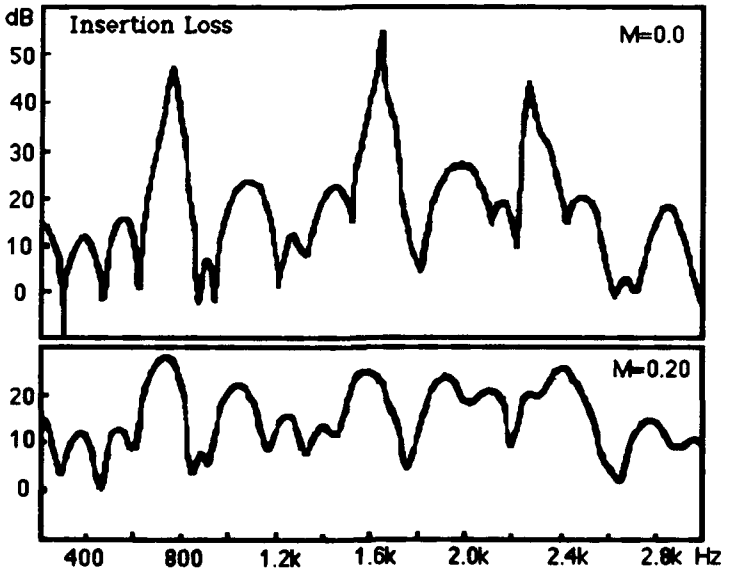

Figure 2. Insertion Loss of a straight-through resonator.

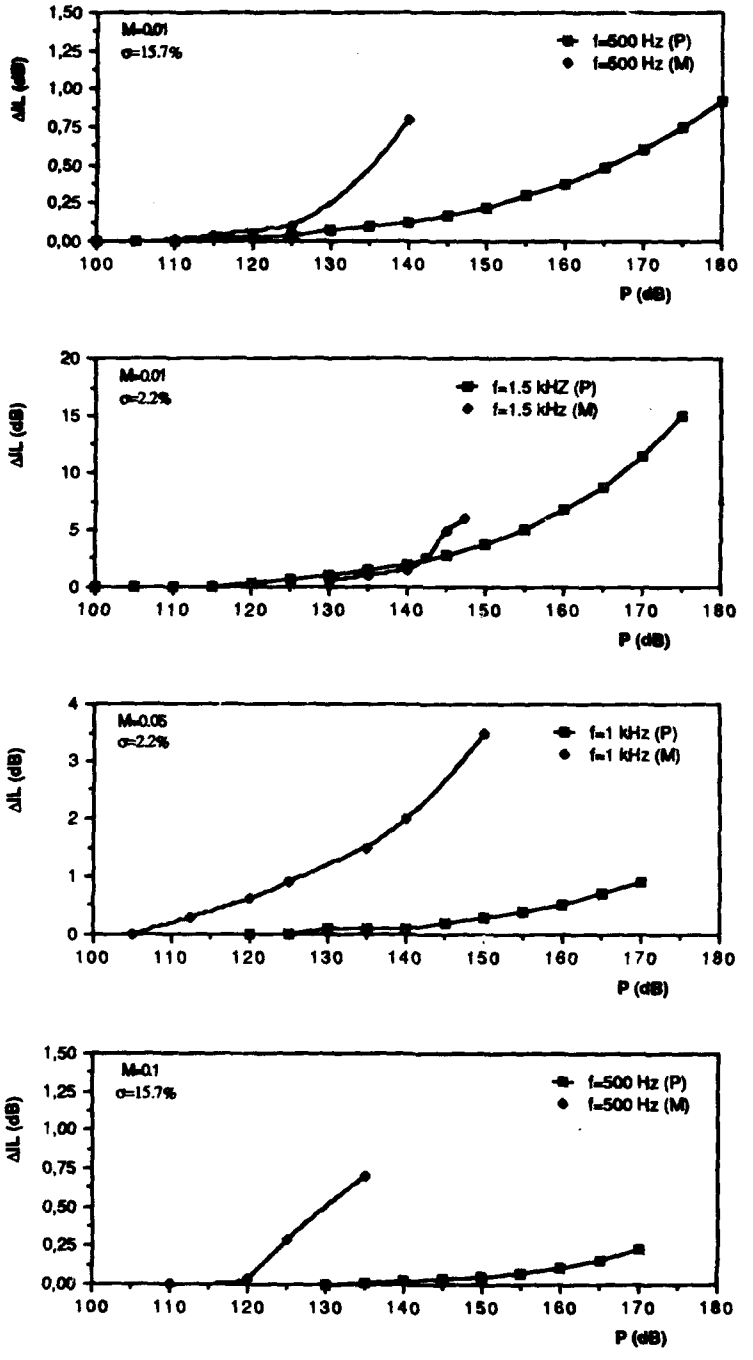

Figure 3. Measured (M) and predicted (P) changes in Insertion Loss for various conditions.

assessed from $IL = 20 \log_{10} p_+^u / p_+^d$, where p_+^u and p_+^d are the positive going waves upstream and downstream of the silencer, respectively, under the assumption of a non-reflecting source, which seems good enough.

Although the above models assume linear operating conditions, as do most theoretical developments, that might not be the case in many applications where high pressure amplitudes are present and non-linear effects are expected to play a significant role.

Figure 3 shows comparisons of changes in Insertion Loss, relative to the linear value (values of P below 100 dB), as function of duct pressure amplitude, from experimental tests and from attempts to model the silencer chamber by using a pressure amplitude dependent model for the perforate wall impedance. Different frequencies, liner open area ratio and mean flow velocities are considered.

In this model, the resistance is given by $\frac{1}{\sigma}\sqrt{2\rho(1-s^2)}\,10^{(-2.25+0.0185P)}$, where P is the pressure amplitude, and the reactance is given by the previous expression with the last factor multiplied by $(1 + 5.10^3 M_0^2)/(1 + 10^4 M_0^2)$ where $M_0 = [0.5\rho c^2(1-\sigma^2)]^{-1/2}\,10^{(-2.5+0.025P)}$.

This model is applied for values of pressure $P > 193 + 40 \log_{10} M$ dB (this limit is different when no mean flow is present or its velocity is very low). When the operating regime is not pressure amplitude or mean flow controlled, that is, the value of P is lower than the above limit but $P > 175 + 40 \log_{10} M$ dB, an intermediate regime may be defined where the reactance is determined by the mean flow and the resistance is the geometric mean value of the pressure amplitude and the grazing flow resistances.

Although this model was observed to yield good fits to a large number of experimental measurements of perforate impedances reported in the literature, the mathematical description of the silencer performance does not lead to good fits to measured silencer attenuation, as the figures illustrate. Similar trends in the variation of Insertion Loss with pressure amplitudes above 100 dB are observed, however, in the comparisons. Results seem to suggest that the linear wave propagation laws, which were assumed in the prediction, do not correctly apply.

The results of the experimental tests have shown a generally increase of the silencer attenuation with pressure amplitude, although some decreases were occasionally observed. These variations may be explained by jetting and vortex formation and disintegration above orifices, vortex-acoustic wave interaction and to alteration of the acoustic coupling between the chamber regions. The efficiency of these mechanisms is reduced by the convection of the acoustic wave by the mean flow, thereby resulting a balance of those major physical mechanisms.

This field seems yet to be quite open for research in order to fully understand and mathematically describe all the physical phenomena taking place inside a flow duct, so that the performance of duct silencers can be well predicted for the different conditions found in practical situations.

REFERENCES

[1] "Decision Support Environment for the Design of Piping and Flow Systems", CEC Brite Project BREU-0109-C.

[2] Sullivan, J. W. and Crocker, M. J., Analysis of Concentric-Tube Resonator Having Unpartitioned Cavities, JASA, 64 (1), 1978, 207-215.

[3] Sullivan, J. W., A Method for Modelling Perforated Tube Muffler Components. I. Theory, JASA, 66 (3), 1979, 772-778.

[4] Bento Coelho, J. L., and Davies, P. O. A. L., Prediction of the Acoustical Performance of Cavity Backed Perforate Liners in Flow Ducts, Proc. 11th ICA, Vol. 5, 1983, 317-320.

[5] Bento Coelho, J. L., Modelling of Cavity Backed Perforate Liners in Flow Ducts, Proc. Nelson Acoustics Conf., 1984.

[6] Munjal, M. L., Rao, K. N. and Sahasrabudhe, A. D., Aeroacoustic Analysis of Perforated Muffler Components, J. Sound and Vib. 114(2), 1987, 173-188.

[7] Bento Coelho, J. L., Acoustic Characteristics of Perforate Liners in Expansion Chambers, ISVR PhD Thesis, 1983.

SECOND INTERNATIONAL CONGRESS ON
RECENT DEVELOPMENTS IN AIR- AND
STRUCTURE-BORNE SOUND AND VIBRATION
MARCH 4-6, 1992 AUBURN UNIVERSITY, USA

TRANSFER MATRICES FOR PIPING ELEMENTS WITH FLOW

K.K. Botros
NOVA HUSKY Research Corporation
2928 - 16th Street N.E.
Calgary, Alberta, Canada
T2E 7K7

ABSTRACT

The influence of local flow phenomena such as velocity gradients, flow separation, and shear layers on the pulsation propagation through piping elements is accounted for by the developing of a pressure loss transfer matrix. This matrix is derived for compressible, adiabatic flow through the element, and is coupled with the pure acoustic transfer matrix describing the inertial effects without flow, to delineate the overall transfer matrix (TM) for the element. For geometrically simple elements such as orifice plates and ball valves, the overall TM is obtained by direct multiplication of the two matrices. For more complicated elements (e.g. globe valve) such separation of effects is not possible and the overall TM was found to contain mixed terms resembling both effects. Semi-empirical models to describe the transmission characteristics of acoustic waves through the above elements were developed, based on measurements of the overall TM and fitting the data to a prescribed model.

NOMENCLATURE

- A - area
- Ba - inertial parameter matrix
- Bp - mean flow parameter matrix
- co - speed of sound
- Cp - specific heat at constant pressure
- D - diameter
- fi - defined factors
- i - square root of (-1)
- ℓ, L - acoustic equivalent lengths
- Mo - Mach number
- P - pressure
- R - wave number = ω/c
- T - temperature
- t - time
- Ta - acoustic transfer matrix
- Tp - pressure loss transfer matrix
- U - mean flow velocity
- x - space dimension
- Y - state vector
- Z_c - characteristic impedence = $\rho c/A$

GREEK LETTERS

- α - valve opening, or dimensionless coefficient
- β - dimensionless coefficients
- γ - isentropic exponent

λ_o - pressure loss coefficient
ρ - density
ω - frequency
ξ - pressure loss coefficient

INTRODUCTION

The influence of local flow phenomena such as flow velocity gradients, flow separation and shear layers on the pulsation transmission is often overlooked and not accounted for. In many instances, discrepancies are encountered between pulsation thus predicted and that measured in the presence of fluid flowing through the installation. The main reason for this problem is the fact that the plane wave theory, though useful when applied to pulsation propagation in long pipes, failes to describe the refraction/deflection of acoustic waves at the shear layers caused by flow separation. In the literature there are several basic studies dealing with pulsation transmission in internal flow systems or particular piping elements [1,2,3]. A time domain solution for the transmission of intense sound waves through the orifice plate was derived from fairly simple flow model [1], accounting for the effect of irreversible pressure drop on the wave transmission. Propagation of pressure wave through a sudden pipe enlargement has been solved by the multiplication of a pure acoustic transfer matrix, a matrix related to pressure loss [2] and an adjusted coupling matrix [3].

More recently, some efforts have been made to develop more precise and consistent models of pressure pulsation transmission through various piping elements [4,5,6,7]. the motivation was to be able to describe the overall transmission characteristics of an element, despite that it is 3-dimensional in nature, by a simple but accurate enough one-dimensional model. This can conveniently be incorporated into a general tool utilizing the plane wave theory for the entire network of piping. This concept was driven from the fact that whatever complex phenomenon takes place within the element, the net effect is a plane wave transmitting both upstream and downstream of it in a one-dimensional mode (if the frequency of propagation is below the cut-off frequency of the pipe). These models are based on the transfer matrix (TM) approach and a concept of accounting for mean flow effects. Some sort of coupling between the pure acoustic transfer matrix (T_a) without flow, and another transfer matrix (T_p), describing the effects of flow recounted only by the unrecovered pressure drop across the element, is the main feature of these new developments.

The manner by which these two matrices are coupled is governed by the type of element under examination. The developed overall TM takes into account interactions between the acoustic field and the highly non-uniform flow downstream of an element where a shear layer, recirculation, flow reattachment and pressure recovery exist.

In this paper, the concept of the dependence of the overall TM on the two effects is laid out followed by a derivation of the pressure loss transfer matrix T_p for a compressible, adiabatic flow through an element. Based on this concept, semi-empirical models of an orifice plate, ball valves and globe valves were developed containing characteristic parameters which were obtained by flow-acoustic measurements. Experiments were carried out on two facilities with air (90 kPa) and natural gas (600 kPa) [4]. Basically, the method used in determining experimentally the four components of TM of a piping element was either the two-load (2L) method [8,9] or the two-source (2S) method [10]. it is shown that for relatively geometrically simple elements (such as the orifice plates and the ball valves) separation of the two matrices T_a and T_p was possible, and the overall TM results from simple multiplication of T_a and T_p in a proper order [4].

For more geometrically complicated elements, such as the globe valves, the inherent complication of the interaction between local flow phenomena, internal flow passages, wall reflection and acoustic waves make this separation of the two matrices impossible. The paper presents results of the transmission characteristics of the above three elements as examples of both separable and inseparable transfer matrices, for the range of flow Mach number permitted by the experimental facilities.

CONCEPT OF TRANSFER MATRIX WITH FLOW

The complicated flow through an element of complex geometry can be modelled by a stream tube of varying cross-sectional area following the development of Miles [11]. The pertinent conservation equations describing the flow-acoustic phenomena are as follows:

$$\frac{\partial(\rho A)}{\partial t} + \frac{\partial(\rho U A)}{\partial x} = 0 \qquad (1)$$

$$\frac{\partial(\rho UA)}{\partial t}+\frac{\partial(\rho U^2A)}{\partial x}=-A\frac{\partial P}{\partial x}+\frac{\lambda_o}{D}\frac{\rho_o U_o^2}{2} \tag{2}$$

$$\rho T\frac{ds}{dt}=\frac{\lambda_o}{D}\rho_o U_o^3/2 \tag{3}$$

and $$P=P_o(x)+P'(x,t)\ ,\ U=U_o(x)+U'(x,t)\ ,\ \rho=\rho_o(x)+\rho'(x,t) \tag{4}$$

where losses are accounted for by the pressure loss parameter $\lambda_0(x)$. When the above equations are linearized, the set of equations for the perturbations transformed to the frequency domain [1] can be written in the following matrix form:

$$\frac{dY}{dx}=(B_a+B_p)Y \tag{5}$$

where $$Y(x,\omega)=\begin{bmatrix}P'(\omega)\\U'(\omega)\end{bmatrix} \tag{6}$$

$$B_a=ik_M\begin{bmatrix}-M_o & \rho_o c_o\\ 1/(\rho_o c_o) & -M_o\end{bmatrix}\ ;\ B_p=G_M\begin{bmatrix}-M_o^2 & 2M_o\rho_o c_o\\ o & 1+M_o^2\end{bmatrix} \tag{7}$$

$$G_M=\left(\frac{d\ell nM_o}{dx}\right)\left[(1-M_o^2)\left(1+\frac{\gamma-1}{2}M_o^2\right)\right]\ ;\ k_M=k/(1-M_o^2) \tag{8}$$

The matrix B_a above contains the inertial effects while matrix B_p contains the effects of mean flow parameters and their gradients through the element. In general, it is not possible to retain such a clear separation of these two effects in the integration of Eq. (5) since the two matrices B_a and B_p do not commute, i.e., $B_p \cdot B_a \neq B_a \cdot B_p$. Additionally, integration of Eq. (5) requires solution of the mean flow parameters $M_0(x)$, $P_0(x)$, $\rho_0(x)$, $c_0(x)$ which are affected by the complicated geometry of the transmission element (e.g. a globe valve). Flow separation, circulation and non-uniformities clearly add to the complication. Therefore, a closed form (analytical) solution of Eq. (5) is only posible for simple geometry elements such as pipes [2,3] where the two matrices B_a and B_p are constant along x, and also for area discontinuities [4,5,6].

For geometrically complicated element, a rather heuristic approach is adopted to overcome this problem. The approach stipulates that a general solution of Eq. (5) should take the form:

$$Y_2=T(B_a',B_p')Y_1 \tag{9}$$

where $T(B_a',B_p')$ is the transfer matrix, subscripts 1 and 2 are stations at the element boundaries: inlet and outlet, and B_a',B_p' are average representations of the inertial and mean flow effects, respectively. Generally $T(B_a',B_p') \neq T(B_a')\cdot T(B_p')$, however, two limiting cases are obvious:

1. *No mean flow, $G_M = 0$ (i.e. pure acoustic)*
2. With mean flow effects much higher than inertial effects.

In the first case $T \rightarrow T_a = T(B_a)$, while in the second case $T \rightarrow T_p \neq T(B_p)$. The two matrices T_a and T_p are called the acoustic and pressure loss transfer matrices [7], respectively. The first (acoustic) transfer matrix can be obtained by direct measurements utilizing the concept of the two-load [8,9] or two-source methods [10], when there is no flow through the element. Semiempirical parameters are commonly introduced to fit the data obtained by either method above. The second (pressure loss) matrix is derived from simple considerations based on the compressible flow through the element with known pressure loss coefficient ξ and takes the following form:

$$T_p=\begin{bmatrix}T_p^{11} & T_p^{12}\\ T_p^{21} & T_p^{22}\end{bmatrix} \tag{10}$$

which will be derived in the following section.

The overall transfer matrix for the element with flow is obtained by utilization of the above two matrices, T_a and T_p to fit the data obtained from direct measurements of transmission characteristics with flow by either the two-load of the two-source method. In less complicated elements, such as orifice paltes and ball valves, direct

multiplicationof these two matrices fit the data quite well, while in more complex geometry such as a globe valve, the two matrices' parameters are imbedded in the overall matrix suggesting that the two effects (inertial and mean flow) are inseparable, as will be seen later.

PRESSURE LOSS TRANSFER MATRIX

The pressure loss transfer matrix for incompressible flow was derived in [5] which is applicable to liquid piping networks or low Mach number flows. The same concept can be extended to compressible flow through piping elements.

Consider the general element shown in Fig. 1 where compressible fluid is flowing from station 1 to station 2 of different areas, and a source of pulsation is placed upstream. The following pertinent gas dynamics equations for adiabatic flow with losses can be written:

continuity: $$\rho_1 A_1 U_1 = \rho_2 A_2 U_2 \tag{11}$$

energy: $$C_p T_1 + \frac{1}{2}U_1^2 = C_p T_2 + \frac{1}{2}U_2 \tag{12}$$

pressure loss: difference in stagnation pressures $= \frac{1}{2}\xi\rho_1 U_1^2$, i.e.

$$P_1\left[1+\frac{U_1^2}{2C_pT_1}\right]^{\frac{\gamma}{\gamma-1}} = P_2\left[1+\frac{U_2^2}{2C_pT_2}\right]^{\frac{\gamma}{\gamma-1}} + \frac{1}{2}\xi\rho_1 U_1^2 \tag{13}$$

Perturbing the above equations (11, 12 and 13), utilizing the following isentropic perturbation relation at the source (Station 1):

$$\frac{\delta\rho_1}{\rho_1} = \frac{1}{\gamma}\frac{\delta P_1}{P_1} \text{ and } \frac{\delta T_1}{T_1} = \frac{\gamma-1}{\gamma}\frac{\delta P_1}{P_1} \tag{14}$$

while on the other side, the following general relation between perturbed parameters:

$$\frac{\delta P_2}{P_2} = \frac{\delta\rho_2}{\rho_2} + \frac{\delta T_2}{T_2}\ , \tag{15}$$

the following relationship between upstream and downstream perturbations of pressures and velocities is obtained:

$$\begin{bmatrix}\delta P_1\\ \delta U_1\end{bmatrix} = \begin{bmatrix}T_p^{11} & T_p^{12}\\ T_p^{21} & T_p^{22}\end{bmatrix}\begin{bmatrix}\delta P_2\\ \delta U_2\end{bmatrix} \tag{16}$$

where:

$$T_p^{11} = \frac{f_3 f_6 - f_2 f_7}{f_1 f_6 - f_2 f_5}\ ,\quad T_p^{12} = \frac{f_4 f_6 - f_2 f_8}{f_1 f_6 - f_2 f_5}$$

$$T_p^{21} = \frac{f_3 - f_1 T_p^{11}}{f_2}\ ,\quad T_p^{22} = \frac{f_4 - f_1 T_p^{12}}{f_2}$$

and:

$$f_1 = \frac{1}{\gamma P_1} + \frac{\gamma-1}{\gamma P_2}\left(\frac{T_1}{T_2}\right)$$

$$f_2 = \frac{U_1}{C_pT_2} + \frac{1}{U_1}$$

$$f_3 = \frac{1}{P_2}$$

$$f_4 = \frac{U_2}{C_pT_2} + \frac{1}{U_2}$$

$$f_5 = \alpha^\gamma - \frac{\alpha U_1^2}{2C_pT_1} + \frac{\beta T_1 P_2 U_2^2}{2P_1 C_p T_2^2} - \xi\frac{U_1^2\rho_1}{\gamma P_1}$$

$$f_6 = \frac{\alpha\gamma P_1 U_1}{(\gamma-1)C_pT_1} + \frac{\beta\gamma P_2 U_1 U_2^2}{2(\gamma-1)C_p^2T_2^2} - \xi\rho_1 U_1$$

$$f_7 = \beta^\gamma$$

$$f_8 = \frac{\beta\gamma P_2 U_2}{(\gamma-1)C_pT_2} + \frac{\beta\gamma P_2 U_2^3}{2(\gamma-1)C_p^2T_2^2}$$

$$\alpha = \left[1 + \frac{U_1^2}{2C_p T_1}\right]^{\frac{1}{\gamma-1}} \quad ; \quad \beta = \left[1 + \frac{U_2^2}{2C_p T_2}\right]^{\frac{1}{\gamma-1}}$$

The above factors (f_1 through f_8) are calculated based on mean flow parameters at inlet and outlet of the element (Stations 1 and 2) using Eq. (11, 12 and 13). It can be shown that for an element with zero losses ($\xi = 0$) and same areas at inlet and outlet (i.e. $A_1 = A_2$), the pressure loss matrix will be reduced to a unit matrix.

EXAMPLES OF SEPARABLE TRANSFER MATRIX

The propagation of pressure waves through an orifice plate of diameter d_0 placed in a circular pipe of internal diameter D has been investigated and the influence of the inertial effects has been described by the so-called equivalent acoustic length (ℓ_e) [6]. This equivalent length was first obtained by the 2L method for cases without flow and is shown in Fig. 2 (plot marked M = 0), as a function of the β-ratio (where $\beta = d_0/D$). In the case of wave transmission with flow, separation of the two effects; pure acoustic and influence of flow, was possible and the overal transmission chracteristics can be described by direct multiplication of two TM's: the acoustic T_a and the pressure loss T_p. The former was assumed independent of the Mach number as a first approximation, while the latter was derived from the perturbation formulation described in the previous section as the pressure loss coefficient ξ is known for orifice plates. With the recent evolvement of the 2S method, refinement of this semi-empirical model was possible as better quality data were obtained from measurements [6,10]. The equivalent acoustic length (ℓ_e) was found to be dependent on the mean flow Mach number in the main pipe in a manner shown in Fig. 2. This dependence most likely delineates the interaction that is taking place between the acoustic field and the highly non-uniform flow downstream of the orifice.

The second examle of a separable TM is that for a ball valve. Likewise, the pure acoustic TM was obtained by the 2L method for various valve openings (α). A semi-empirical model was then devised consisting of two orifices of equivalent β-ratio equal to the square root of valve opening area ratio, and a separation of constant area pipe of diameter D and length L determined from fitting the experimental data. The model is depicted in Fig. 3 while results of the equivalent length L is shown in Fig. 4 (two equivalent lengths are shown, L_A is used for calculating T_a^{11}, T_a^{22}, while L_B for T_a^{12}, T_a^{21}). The overall TM for the ball valve with flow was also obtained experimentally using the 2L method and was then compared to the postulated multiplication scheme of the two TM's: T_a and T_p. Good agreement was obtained and is discussed in more detail in [4].

EXAMPLE OF INSEPARABLE TRANSFER MATRIX

The multiplication scheme of T_a and T_p that worked successfully with the above two elements did not apply to globe valve. Even in the case of pure acoustic without flow, it was also not possible to construct a basic model with say orifices and straight pipes like in the case of a ball valve. Separation of the two effects thus constitutes a rather difficult task and mathematically impossible since the two corresponding matrices B_a and B_p do <u>not</u> commute for such complicated element. An earlier attempt to describe the transmission characteristics of such valves by means of parallel TM's; one for the valve resistance, and another for its capacitance [15] did not include the inertial component which is rather important at high frequencies

It was then found that each component of the overall TM is a combination of mixed terms associated with pure acoustic and pressure loss parameters. These two parameters are mixed in a manner that did not permit distinct separation to the two matrices T_a and T_p as before.

From the data measured for a globe valve (100 mm diameter - trim number 2.62 - stroke 50 mm - seat area 3490 mm^2) with varied opening and Mach number, and using the 2L method, it was possible to construct a semi-empirical matrix describing the two effects. For example the overall TM for pulsation propagation from downstream to upstream is as follows:

$$\begin{bmatrix} T_p^{11}\cos(k\ell_e) + ikL_A & ; & T_p^{12} + ikL_B Z_C \\ \dfrac{iT_p^{22}}{Z_C}\sin(k\ell_e) & ; & T_p^{22}\cos(k\ell_e) + ikL_A \end{bmatrix} \qquad (17)$$

where Z_C is the characteristic impedence of the attached pipe. Some similarity between the above matrix and the one that would result from direct multiplication of two matrices T_p and T_a for a pipe of length ℓ_e exists and is given in [7]. Figures 5, 6 and 7 present results of the characteristic parameters ℓ_e, L_A and L_B as functions of the flow Mach number and valve opening.

CONCLUSION

Transm of pressure pulsation through piping elements is controlled by the inertial effects caused by the intern netry of the element, and also by local flow phenomena such as flow velocity gradients, flow separa nd shear layers. Generally, the interaction between the two effects is so complex to permit separation of their respective contribution to the transmission characteristics of the element. However, for some elements, some sort of coupling between the pure acoustic transfer matrix without flow, and another transfer matrix describing the effects of flow recounted only by the unrecovered pressure drop across the element, exists. Full description of the overall TM for an element contains these two matrices coupled in a manner depending on the complexity of the element. For example, simple multiplication of the two matrices matched the measured data for an orifice plate and a ball valve, quite well. Such multiplication was not possible, however, in the case of a globe valve. Semi-empirical modesl were developed for the above elements which are practical and useful for incorporation into prediction models for the propagation of pressure pulsation through piping networks.

It is important to emphasize that the above approach though works for certain elements, it has some limitations in that identification of parameters containing either effects is not always possible without extensive flow-acoustic measurements. Also, even in case of separable TM, the pure acoustic transfer matrix may contain parameters that are dependent on mean flow (e.g., the acoustic length t_o in the case of orifice plate). The challenge for future work in this area is to develop models based on a one-dimensional approach to quantify and resemble the three effects: inertial, resistive and capacitive, in a more distinct, separable and consistent manner.

ACKNOWLEDGEMENT

The work presented here is part of a research program sponsored by NOVA CORPORATION OF ALBERTA. The author wishes to acknowledge the contribution of two of his colleagues towards this program: Dr. W.M. Jungowski and Dr. W. Studzinski, whose work are cited in the reference section.

REFERENCES

1. Cummings, A. and Chang, I.J., "The Transmission of Intense Transient and Multiple Frequency Sound Waves Through Orifice Plates with Mean Flows", Rev. Phys. Appl., 21, 1986, 151-161.

2. Parrott, T., "Improved Method for Design of Expansion Chamber Mufflers with Application to an Operational Helicopter", NASA-TND7309, 1973.

3. Lambert, R.F., and Steinbrueck, E.A., "Acoustic Synthesis of a Flowduct Area Discontinuity", J. Acoust. Soc. Am., 67 (1), 1980, 59-64.

4. Jungowski, W.M., Botros, K.K., Studzinski, W. and Szabo, J.L., "Measuring the Transmission Characteristics of Pulsating Flows Through Orifice Plates and a Ball Valve", Measuring and Metering of Unsteady Flows, FED-Vol 40, ASME, New York, 1986, 21-32.

5. Jungowski, W.M., Botros, K.K. and Studzinski, W., "Generation of Pressure Pulsations at the Ball Valve", NOISE_CON 87, The Pennsylvania State University, State College, Pennsylvania, June 8-10, 1989, 65-69.

6. Botros, K.K., Jungowski, W.M., and Studzinski, W., "On the Transfer Matrix of Orifice Plate with Flow", NOISE-CON 88, Purdue University, West Lafayette, Indiana, June 20-22, 1988, 475-480.

7. Botros, K.K., Jungowski, W.M., Studzinski, W., and MacLeod, J., "Influence of Flow in Pulsating Simulation of Gas Pipeline Installations", Proceedings of Gas and Liquid Pulsations in Piping Systems - Prediction and Control, Institute of Mechanical Engineers, London, UK, December 1-2, 1988, 89-96.

8. To, C.W.S., and Doige, A.G., "A Transient Testing Technique for the Determination of Matrix Parameters of Acoustic Systems", J. Sound & Vib., 62, 1979, 207-233.

9. Lung, T.Y., and Doige, A.G., "A Time-Averaging Transient Testing Method for Acoustic Properties of Piping Systems and Mufflers with Flow", J. Acoust. Soc. Am. 73 (3), 1983, 867-876.

10. Doige, A.G., Munjal, M.L., and Alves, H.S., "An Improved Experimental Method for Determining Transfer Matrices of Pipeline Elements with Flow", NOISE-CON 88, Purdue University, West Lafayette, Indiana, June 20-22, 1988, 481-486.

11. Miles, J.H., "Acoustic Transmission Matrix of a Variable Area Duct or Nozzle Carrying a Compressible Subsonic Flow", J. Acoust. Soc. Am. 69 (6), June 1981, 1577-1586.

12. Munjal, M.L., "Acoustics of Ducts and Mufflers", Wiley, New York, 1987.

13. Ingard, U. and Singhal, U.K., "Sound Attenuation in Turbulent Pipe Flow", J. Acoust. Soc. Am., 55 (3), 1974, 535-538.

14. Cummings, A., and Eversman, W., "High Amplitude Acoustic Transmission Through Duct Termination: Theory", J. Sound. Vibr., 91 (3), 1983, 503-518.

15. Johnston, D.N. and Edge, K.A., "Simulation of the Pressure Ripple Characteristics of Hydraulic Circuits", Proceedings of Gas and Liquid Pulsations in Piping Systems - Prediction and Control, Institute of Mechanical Engineers, London, UK, December 1-2, 1988, 13-22.

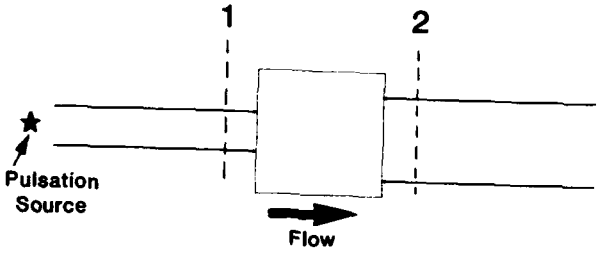

Fig. 1 Schematic of a Piping Element With Flow

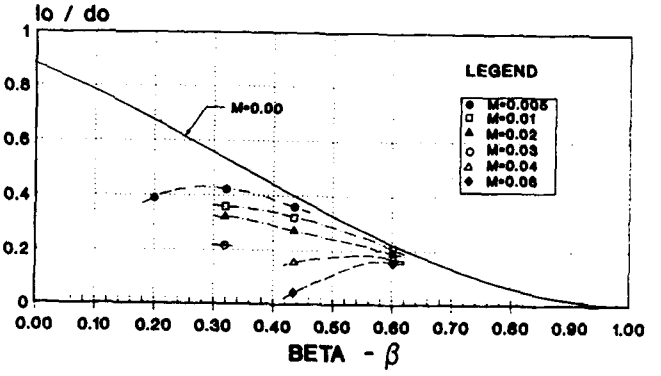

Fig. 2 Dimensionless Acoustic Equivalent Length for Orifice Plate With Flow

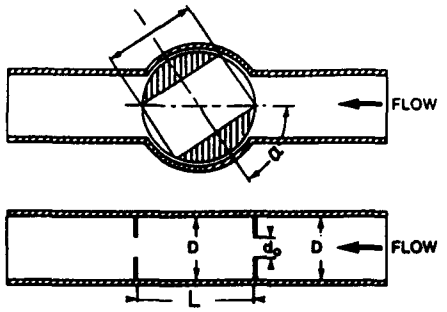

Fig. 3 Acoustic Model for a Full-bore Ball Valve

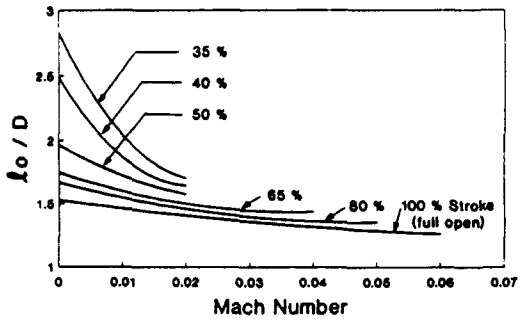

Fig. 5 Dimensionless Acoustic Equivalent Length for Globe Valve With Flow

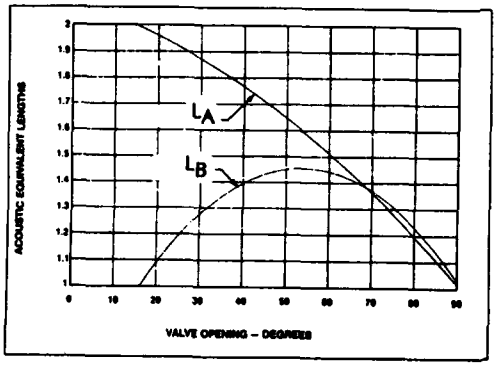

Fig. 4 Dimensionless Acoustic Equivalent Lengths For a Ball Valve

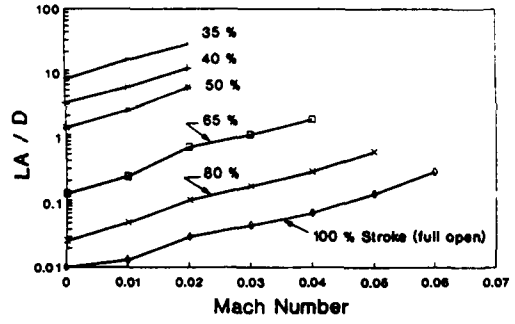

Fig. 6 Dimensionless Acoustic Parameter L_A for Globe Valve

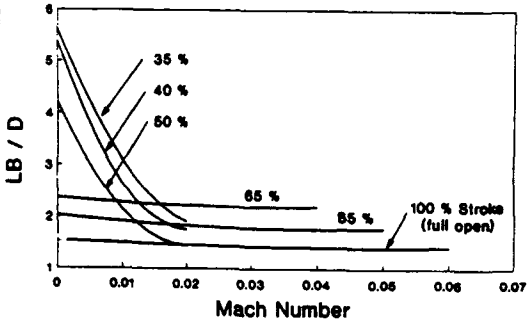

Fig. 7 Dimensionless Acoustic Parameter L_B for Globe Valve

SECOND INTERNATIONAL CONGRESS ON
RECENT DEVELOPMENTS IN AIR- AND
STRUCTURE-BORNE SOUND AND VIBRATION
MARCH 4-6, 1992 AUBURN UNIVERSITY, USA

RESONANT FREQUENCIES OF THE LONG PIPES

L.N.Kljachkin, I.I.Novikov, L.I.Ustelencev
Noise and Vibration Control Laboratory
VNIITBchermet
Chelyabinsk, USSR

ABSTRACT

Vibration and resonant frequencies of the long pipes are considered. The resonant frequency formula is sugested, which is in good correlation with experimental data. On the basis of this consideration, a construction for the long pipes noise reduction was designed. Sound pressure level was reduced by 14 dB.

The sound radiation from long pipes is a common situation for the noise control problems. In most cases this rediation is caused by resonant vibration of pipes. For example, at a weld pipes production shop the pipe, under heat treatmeht of the seam, radiated sound with 100 - 110 dBA pressure levels at 1 m distance. After investigation it turned out, that there were coincidence between the first resonant frequency of the pipe and the working frequency of heating indictors, both were about 950 Hz. The resonant peak was rather narrow, its width approximately 20 Hz. It is obvious, that to prevent such a coincidence, one has to calculate the pipe resonant frequencies very accurately.

Formulae, usually recommended for this calculations, are derived in two ways. Firstly, the pipe oscillations are supposed to be of the beam-type, with undeformable cross-section. But in this case the resonant frequencies tend to zero when pipe length tends to infinity. Hence, this way is unsuitable. Secondly, the pipe is considered as a thin cylindrical shell. The well-known result is [1]

$$\omega_{mn} = \frac{ch}{\sqrt{12}} \sqrt{\left(k_m^2 + k_n^2\right)^2 + \frac{k_m^4 \cdot k_o^4}{\left(k_m^2 + k_o^2\right)^2}} \qquad (1)$$

where ω_{mn} - resonant frequency of the (m,n) - mode, c - velocity of longitudinal wave in material of the shell, h - shell wall thickness, $k_m = \pi m/\ell$, $k_n = n/R$, ℓ - shell length, R - shell radius, $k_o = \sqrt[4]{12(1-\nu^2)/hR^2}$, ν - Poisson's ratio, m - axial mode number, n - circumferential mode number, $n \geq 2$ in Eq.(1). For infinitely long shell, $\ell \longrightarrow \infty$ and Eq.(1) becomes

$$\omega_n = \frac{ch}{R^2} \frac{n^2}{\sqrt{12}} . \qquad (2)$$

But the value of the first ($n = 2$) resonant frequency calculated from Eq.(2) was 1,5 times as much as mesured value. The reason for such difference is neglect of the tangential inertia forces when obtaining Eq.(1).

To get more accurate results consider shell equations of free motion

$$\sum_{i=1}^{3} L_{ij} U_i = \frac{1}{c^2} \frac{\partial^2 U_j}{\partial t^2}, \qquad j = 1,2,3, \tag{3}$$

where U_1, U_2 and U_3 are the axial, circumferential and radial displacements of cylindrical shell; they are functions of axial coordinate $x (0 \le x \le \ell)$, circumferential coordinate $y (0 \le y \le 2\pi R)$ and time t. The L_{ij}'s are differential operators in x and y, their forms are dependent on the shell theory assumptions.

The solution of Eq.(3) may be written as

$$\begin{aligned} U_1 &= A_1 e^{i\omega t} \varphi_1(k_m x) \cos k_n y, \\ U_2 &= A_2 e^{i\omega t} \varphi_2(k_m x) \sin k_n y, \\ U_3 &= A_3 e^{i\omega t} \varphi_3(k_m x) \cos k_n y, \end{aligned} \tag{4}$$

A_1, A_2 and A_3 are displacement's amplitudes, ω - frequency, φ_1, φ_2 and φ_3 - trigonometric functions, determianed from boundary conditions at $x = 0$ and $x = \ell$.

After substituting Eqs.(4) in Eqs.(3), one obtains a sistem of 3 algebraic equations with determinant $\Delta(\omega)$. For each (m,n) there is a set of roots of equation $\Delta(\omega) = 0$, the lowest of the roots is the main resonant frequency ω_{mn} of the (m,n) - mode.

In particular case when ω_{mn}'s are determined by Eq.(1), they have following property. For each integer n exists such integer p, that $\omega_{pn} = \min_m \{\omega_{mn}\}$. This p is a function of ℓ and $\lim_{\ell \to \infty} (p/\ell) = 0$.

Assume, that this property is conserved in general case. Tables for frequencies of free vibration of cylindrical shells in paper by Baron and Bleich [2] confirm validity of this assumption. Then to obtain the resonant frequencies of infinitely long pipes ($\ell \to \infty$), it is correct bo put $k_m = 0$ in Eqs.(4) from the beginning. This operation, after omitting terms, negligable in comparision with $h^2/12R^2$, results in

$$\omega_n = \frac{ch}{R^2} \cdot \frac{n(n^2-1)}{\sqrt{12}\sqrt{n^2+1}}. \tag{5}$$

It should be noted, that the same result is oftained for some another forms of the operators L_{ij}. For $n = 2$, Eq.(5) gives the first resonant frequency $f_r = \frac{1}{2\pi} \omega_2 = 0{,}12 \frac{ch}{R^2}$ Hz, that equals 2/3 of the f_r from Eq(2).

For comparision, a shell with $h/R = 1/30$, $k_m R = 10/\pi$ in paper [2] has the exact resonant frequency (after slight arithmetical transform) $\omega_{ex} = 0{,}0334 \frac{c}{R}$, here, from Eq.(5), $\omega_2 = 0{,}0258 \frac{c}{R}$.

This analysis turned out to be necessary to reduce noise at the above-mentioned shop. The pipe moved continuously, so it was impossible to compress it by the dampers on the finite area, only point-touching dampers were applicable. Besides, to avoid any skewness in pipe, dampers should be located symmetrically around the pipe. The number of the dampers was determined in following way.

For steel pipe, $c = 5300$ m/s, pipe wall thickness $h = 0{,}008$ m, ra-

dius R = 0,074 m, then f_2 = 955 Hz, while mesured value was 930 Hz. This meant, that the sound was generated by the mode with n = 2, that is by the wave with 4 nodes along circumference. For example, when in experimental set-up 4 dampers were applied, the resonant mode turned around the pipe's axis (from the theoretical point of view it meant, that k_m in Eqs.(4) became very small, but not zero) and the nodes matched with the dampers. Sound remained at the same level. To elaborate an effective damper construction, an analogous pipe was investigated in laboratory. The length of the pipe was 5 m and it was enough bo consider it as infinite. Two different damper construction were worked out. Mechanical one consisted of 8 dampers, symmetrically located at an angle 45° from each other. Each damper was a bearing, which rotated with pipe's movement and transmitted vibration energy to the elastic base, were energy was absorbed. Electromagnetic damper was mounted with 5 mm space from the pipe, wich worked ar a core for it. In both cases noise level reduction equaled 14-15 dB at the 1000 Hz octave band.

REFERENCES

1. Vibration in Engineering. Handbook. Moskow: "Mashinostroenie", v.1, 1978, p.221 (in Russian).

2. M.L.Baron, H.H.Bleich Tables for Frequencies and Modes of Free Vibration of Infinitely Long Thin Cylindrical shells. Journal of Applied Mechanics. 1954, v.21, N 2, p.178-184.

SECOND INTERNATIONAL CONGRESS ON
RECENT DEVELOPMENTS IN AIR- AND
STRUCTURE-BORNE SOUND AND VIBRATION
MARCH 4-6, 1992 AUBURN UNIVERSITY, USA

GENERIC BUCKLING ANALYSIS OF ORTHOTROPIC PLATES WITH CLAMPED AND SIMPLY SUPPORTED EDGES

S.D. Yu and W.L. Cleghorn

Department of Mechanical Engineering
University of Toronto
Toronto, Ontario
Canada M5S 1A4

ABSTRACT

Buckling problem of orthotropic rectangular plates with clamped and simply supported boundary conditions is investigated by the method of superposition. Bidirectional compression loads are considered in the analysis. Accurate buckling coefficients with four digits of accuracy are tabulated for various load and material parameters along with a number of plate geometries. This work may be extended to plates with other boundary conditions by simply changing the generating functions utilized in this paper.

NOMENCLATURE

a, b	plate dimension in x and y directions, respectively
$D_{11}, D_{12}, D_{22}, D_{66}$	orthotropic plate flexural rigidity parameters
D^*	generalized rigidity parameter = $(D_{12} + 2D_{66}) / [(D_{11}D_{22})^{1/2}]$
K	number of terms used in analytical solution
k_o	buckling coefficient = $Pb^2 / [\pi^2(D_{11}D_{22})^{1/2}]$
N_x	compression load in x direction = $-P$
N_y	compression load in y direction = $-\alpha P$
W	plate lateral displacement divided by side length a
x, y	real space plate co-ordinates
x_o, y_o	plate affine coordinates
α	load ratio = N_y / N_x
α_o	affine load ratio = N_{y_o} / N_{x_o}
ε	generalized Poisson's ratio = $D_{12}/(D_{12} + 2D_{66})$
η	nondimensional distance = y_o/b_o
λ^2	eigenvalue = $\omega a^2\sqrt{\rho/D_{11}}$
ξ	nondimensional distance = x_o/a_o
ρ	mass per unit area
ϕ	plate aspect ratio = b/a
ϕ_o	plate affine aspect ratio = b_o/a_o

INTRODUCTION

Since plates of anisotropic materials are extensively used in enginering structures, the accurate knowledge of critical buckling loads and associated buckling modes is essential for reliable and lightweight structural design. However, accurate results for orthotropic rectangular plates are few in the literature. As is indicated by Leissa [1], buckling of isotropic, homogeneous plates is already complicated, not to mention the orthotropic plates. Because of this, energy methods, such as Rayleigh-Ritz method, and finite element method, are commonly used in obtaining approximate solutions for free vibration and buckling of plates.

Accurate buckling results are typically available for two types of plates, i.e., simply supported plates and plates with one pair of edges simply supported. Fourier series may be used to find accurate solutions for simply supported plates. Analytical solutions for plates with one pair of edges simply supported may be obtained by using the Levy method.

In order to extend analytical type solutions for free vibration to plates with arbitrary classical boundary conditions, Gorman [2] introduced the superposition method. Now with this method one may obtain accurate results of free vibration for all classically-supported isotropic and orthotropic thin rectangular plates. A number of complicated supports, such as point supports, line supports, concentrated masses, distributed elasticity may also be handled by this method. In addition to rectangular plates, the superposition method is applicable to triangular and parallelogram plates. Recently, Yu and Cleghorn [3,4] investigated the buckling and vibration of in-plane stressed rectangular plates. A sum of publications using the method of superposition is estimated on the order of one hundred in the technical literature. Interested readers are invited to refer to these publications by Gorman, Saliba, and the authors.

Generic buckling was proposed by Brunelle and Oyibo [5] in investigating buckling of orthotropic plates. By introducing a simple affine transformation, the rigidity parameters are replaced by a generalized rigidity parameter D^*, and a generalized Poisson ratio ε. The advantage of this transformation is that it reduces the two independent rigidity parameters into one single generalized rigidity parameter because the generalized Poisson ratio has no effect on free flexural vibration of plates with clamped and simply supported edges. This will result in a dramatic storage save in tabulating the computed buckling coefficients. For plates with free edges, the storage requirement may also reduced considering that limits of D^* and ε for all composite materials fall in the following range [6,7]: $0 \le D^* \le 1.0$ and $0.12 \le \varepsilon \le 0.65$.

In this paper, the generic buckling of orthotropic rectangular plates with clamped and simply supported edges is investigated using the method of superposition. The results presented are accurate because our solutions satisfy both the governing differential equation and the boundary conditions.

GOVERNING DIFFERENTIAL EQUATIONS

The governing equation for plate buckling may be obtained by considering the equilibrium of an infinitesimal plate element, or by simply letting the eigenvalue be zero in the equation for free vibration of in-plane stressed plates. Since critical buckling and zero frequency problems for a statically stable plate are mathematically equivalent, a buckling mode must coincide with a certain vibration mode in which the corresponding eigenvalue vanishes due to the in-plane loads. The governing equation for buckling of specially orthotropic plates is written as:

$$D_{11}\frac{\partial^4 w}{\partial x^4} + 2(D_{12}+2D_{66})\frac{\partial^4 w}{\partial x^2 \partial y^2} + D_{22}\frac{\partial^4 w}{\partial y^4} - N_x\frac{\partial^2 w}{\partial x^2} - N_y\frac{\partial^2 w}{\partial y^2} = 0 \tag{1}$$

To reduce the number of rigidity parameters used for orthotropic plates, the transformation is introduced:

$$\begin{array}{llll} x = (D_{11})^{1/4}x_o & a = (D_{11})^{1/4}a_o & \alpha = (D_{22}/D_{11})^{1/2}\alpha_o & N_x = (D_{11})^{1/2}N_{x_o} \quad M_x = (D_{11})^{1/2}M_{x_o} \\ y = (D_{22})^{1/4}y_o & b = (D_{22})^{1/4}b_o & \phi = (D_{11}/D_{22})^{1/4}\phi_o & N_y = (D_{22})^{1/2}N_{y_o} \quad M_y = (D_{22})^{1/2}M_{y_o} \end{array} \tag{2}$$

Substituting the above relations into Eqn.(1), we obtain

$$\frac{\partial^4 w}{\partial x_o^4} + 2D^*\frac{\partial^4 w}{\partial x_o^2 \partial y_o^2} + \frac{\partial^4 w}{\partial y_o^4} + k_o\left(\frac{\pi}{b_o}\right)^2\left[\frac{\partial^2 w}{\partial x_o^2} + \alpha_o\frac{\partial^2 w}{\partial y_o^2}\right] = 0 \tag{3}$$

where parameters that appear in above equations are defined in the Nomenclature. For buckling analysis of plates with clamped and simply supported edges, one needs to find the expressions for the bending moments transformed into the affine plane. Considering the transformation in Eqn.(2), these expressions may be written as

$$\begin{Bmatrix} M_{x_o} \\ M_{y_o} \end{Bmatrix} = \begin{bmatrix} 1 & \varepsilon D^* \\ \varepsilon D^* & 1 \end{bmatrix} \begin{Bmatrix} \dfrac{\partial^2 w}{\partial x_o^2} \\ \dfrac{\partial^2 w}{\partial y_o^2} \end{Bmatrix} \tag{4}$$

In order for the results to be valid for all orthotropic plates, it is advantageous to introduce the nondimensional transformation:

$$x_o = a_o\xi\,, \quad y_o = b_o\eta\,, \quad w = aW = (D_{11})^{1/4}a_oW \tag{5}$$

One further rewrites the governing equation as:

$$\frac{\partial^4 W}{\partial \eta^4} + 2D^*\phi_o^2\frac{\partial^4 W}{\partial \xi^2 \partial \eta^2} + \phi_o^4\frac{\partial^4 W}{\partial \xi^4} + \pi^2 k_o\phi_o^2\left[\frac{\partial^2 W}{\partial \xi^2} + \alpha_o\phi_o^2\frac{\partial^2 W}{\partial \eta^2}\right] = 0 \tag{6a}$$

$$\frac{\partial^4 W}{\partial \xi^4} + \frac{2D^*}{\phi_o^2}\frac{\partial^4 W}{\partial \xi^2 \partial \eta^2} + \frac{1}{\phi_o^4}\frac{\partial^4 W}{\partial \eta^4} + \frac{\pi^2 k_o}{\phi_o^2}\left[\frac{\partial^2 W}{\partial \xi^2} + \alpha_o\phi_o^2\frac{\partial^2 W}{\partial \eta^2}\right] = 0 \tag{6b}$$

The nondimensional bending moments consequently become

$$M_\xi = \frac{M_x a_o}{(D_{11})^{1/4}} = -\left[\frac{\partial^2 W}{\partial \xi^2} + \varepsilon D^* \phi_o^2 \frac{\partial^2 W}{\partial \eta^2}\right], \quad M_\eta = \frac{M_y b_o^2}{(D_{11})^{1/4} a_o} = -\left[\frac{\partial^2 W}{\partial \eta^2} + \frac{\varepsilon D^*}{\phi_o^2} \frac{\partial^2 W}{\partial \xi^2}\right] \tag{7}$$

SOLUTION TECHNIQUE

The superposition method is based on the linearity of the governing differential equations. The mathematical treatment draws the inference from the Levy method. Since rotations of plate normals about x, or y axis are due to the bending moments, M_x and M_y may be chosen to fulfill the superposition procedure. For a rectangular plate without simply supported edges, one needs to construct four building blocks. Along each edge of the four building blocks, one of the two boundary conditions, i.e., zero lateral displacement, is satisfied. The second boundary condition is associated with the driving bending moments.

For clarity, four edges of a rectangular plate are denoted by i, and building blocks corresponding to the rectangular plate are denoted by j. For plates without simply supported edges, $i,j = 1,2,3,4$; for plates involving simply supported edges, $j = 4 - N_s$, where N_s is the number of simply supported edges. For consistence, the edge number i is counted counterclockwise from the bottom edge; and the j-th building block is the one whose j-th edge is driven by a distributed bending moment. A clamped edge i of a plate is treated as the simply supported edge in the j-th building block ($i \neq j$). For $i = j$, the edge is subjected to a bending moment M_j.

Levy type solutions for each of the so-constructed building blocks may be readily obtained because there are a pair of opposite edges simply supported in all four building blocks. For reference, a summary of Levy type solutions and the boundary conditions along the other two edges for the employed building blocks is shown in Table 1. A solution to the original plate may then be found by superimposing four sets of solutions and requiring the released boundary conditions to be satisfied. This will result in a number of algebraic equations relating the bending moment expansion coefficients. Buckling loads may be obtained by searching those k_o which cause the determinant of the coefficient matrix of the algebraic equations to vanish.

Table 1 Levy type solutions for all four building block

Building Blocks	Lateral Displacement	Bending Moment	Boundary Conditions
First	$W_1=\sum_1^K Y_m(\eta)\sin m\pi\xi$	$\frac{M_1\phi b}{D_y}=\sum_1^K E_m \sin m\pi\xi$	$W_1(\xi,0)=W_1(\xi,1)=M_\eta(\xi,0)=0,\ M_{\eta 1}(\xi,1)=M_1(\xi)$
Second	$W_2=\sum_1^K Y_n(\xi)\sin n\pi\eta$	$\frac{M_2 a}{D_x}=\sum_1^K E_n \sin n\pi\eta$	$W_2(0,\eta)=W_2(1,\eta)=M_\xi(0,\eta)=0,\ M_{\xi 2}(1,\xi)=M_2(\eta)$
Third	$W_3=\sum_1^K Y_p(\eta)\sin p\pi\xi$	$\frac{M_3\phi b}{D_y}=\sum_1^K E_p \sin p\pi\xi$	$W_3(\xi,0)=W_3(\xi,1)=M_\eta(\xi,1)=0,\ M_{\eta 3}(\xi,0)=M_3(\xi)$
Fourth	$W_4=\sum_1^K Y_q(\xi)\sin q\pi\eta$	$\frac{M_4 a}{D_x}=\sum_1^K E_q \sin q\pi\eta$	$W_4(0,\eta)=W_4(1,\eta)=M_\xi(1,\eta)=0,\ M_{\xi 4}(0,\xi)=M_4(\eta)$

Solutions for the First Building Block

Substituting the Levy type solutions given in Table 1 into Eqn.(6a), one obtains the following ordinary differential equations:

$$Y_m^{IV} - 2\delta_m Y_m^{II} + \Delta_m Y_m = 0 \quad (m = 1,2,\ \infty) \tag{8}$$

where Roman superscripts indicate the order of differentiation with respect to η, and the coefficients δ_m and Δ_m are given by

$$\delta_m = D^*(m\pi/\phi_o)^2 - 0.5\pi^2 k_o \alpha_o, \quad \Delta_m = (m\pi/\phi_o)^4 - \pi^2 k_o (m\pi/\phi_o)^2$$

Three families of solutions to Eqn.(8) may be written as:

$$Y_m = A_m \sinh\beta_m\eta \sin\gamma_m\eta + B_m \sinh\beta_m\eta \cos\gamma_m\eta + C_m \cosh\beta_m\eta \sin\gamma_m\eta + D_m \cosh\beta_m\eta \cos\gamma_m\eta \tag{9}$$

$$Y_m = A_m \sinh\beta_m\eta + B_m \cosh\beta_m\eta + C_m \sin\gamma_m\eta + D_m \cos\gamma_m\eta \tag{10}$$

$$Y_m = A_m \sinh\beta_m\eta + B_m \cosh\beta_m\eta + C_m \sin\gamma_m\eta + D_m \cos\gamma_m\eta \tag{11}$$

where β_m and β_m are the known constants in terms of δ_m and Δ_m. Constants A_m, B_m, C_m and D_m may be found by considering the boundary conditions shown in Table 1. After determining the four sets of constants, the lateral displacement for the first building block is written as

$$W_1 = \sum_{m\in\Omega_1} E_m\theta_{1m}\left\{\frac{\sinh\beta_m\eta}{\sinh\beta_m}\frac{\cos\gamma_m\eta}{\cos\gamma_m} - \frac{\cosh\beta_m\eta}{\cosh\beta_m}\frac{\sin\gamma_m\eta}{\sin\gamma_m}\right\}\sin m\pi\xi$$
$$+ \sum_{m\in\Omega_2} E_m\theta_{2m}\left\{\frac{\sinh\beta_m\eta}{\sinh\beta_m} - \frac{\sinh\gamma_m\eta}{\sinh\gamma_m}\right\}\sin m\pi\xi + \sum_{m\in\Omega_3} E_m\theta_{3m}\left\{\frac{\sinh\beta_m\eta}{\sinh\beta_m} - \frac{\sin\gamma_m\eta}{\sin\gamma_m}\right\}\sin m\pi\xi \tag{12}$$

where

$$\theta_m = \frac{\cosh\beta_m \sin\gamma_m}{\sinh\beta_m\cos\gamma_m}, \quad \theta_{1m} = \frac{\theta_m}{2\beta_m\gamma_m(1+\theta_m^2)}, \quad \theta_{2m} = \frac{-1}{\beta_m^2-\gamma_m^2}, \quad \theta_{3m} = \frac{-1}{\beta_m^2+\gamma_m^2}$$

Solution for the Second Building Block

Substitution of the Levy type solutions for the second building block into Eqn.(6b) gives

$$Y_n^{IV} - 2\delta_n Y_n^{II} + \Delta_n Y_n = 0 \tag{13}$$

where

$$\delta_n = \left\{D^*(n\pi)^2 - 0.5k_o\pi^2\right\}\phi_o^2, \quad \Delta_n = \left\{(n\pi)^4 - \alpha_o k_o[i^2(n\pi)^2\right\}\phi_o^4$$

Similarly, one may obtain the lateral displacement for the second building building block. It is written as

$$W_2 = \sum_{n\in\Omega_1} E_n\theta_{1n}\left\{\frac{\sinh\beta_n\xi}{\sinh\beta_n}\frac{\cos\gamma_n\xi}{\cos\gamma_n} - \frac{\cosh\beta_n\xi}{\cosh\beta_n}\frac{\sin\gamma_n\xi}{\sin\gamma_n}\right\}\sin n\pi\eta$$
$$+ \sum_{n\in\Omega_2} E_n\theta_{2n}\left\{\frac{\sinh\beta_n\xi}{\sinh\beta_n} - \frac{\sinh\gamma_n\xi}{\sinh\gamma_n}\right\}\sin n\pi\eta + \sum_{n\in\Omega_2} E_n\theta_{3n}\left\{\frac{\sinh\beta_n\xi}{\sinh\beta_n} - \frac{\sin\gamma_n\xi}{\sin\gamma_n}\right\}\sin n\pi\eta \tag{14}$$

Solutions for the Third and Fourth Building Blocks

Derivation of solutions for the third and fourth building blocks is not necessary. Solutions for the third and fourth building blocks may be inferred from solutions for the first and second building blocks, respectively. Solution for the third building block is obtained by replacing η with $1-\eta$, and m with p in Eqn.(12). Similarly, solution for the fourth building block is obtained by replacing ξ with $1-\xi$, and n with q in Eqn. (14).

Formulation of Algebraic Equations

Solutions for the four building blocks, which satisfy the imposed boundary conditions, are now available. A solution to the clamped plate may be obtained by simply superimposing the four solutions. However, the so-superimposed solution does not satisfy boundary conditions for the clamped edges. In order for the solution to satify the boundary conditions, it is required the released boundary condition along each of the four rectilinear edges be exactly satisfied. Fortunately, one notices that there are four sets of unknown constants appearing in expressions for the displacements. By forcing the zero slope conditions to be satisfied, we obtain a system of $4K$ linear algebraic equations relating the constants E_m, E_n, E_p and E_q. Buckling loads are sought for values of k_o which cause the determinant of the coefficient matrix of the algebraic equations. Buckling modes may be found by simply solving the linear algebraic equations. To quantitatively determine lateral defelection of a plate which is in post-buckling mode, one needs to consider nonlinear factors.

Algebraic Equations for Plates with Simply Supported Edges

It is noticed that in all building blocks three of the four edges are simply supported. The remaining edge is considered as simply supported when the driving moment vanishes. Therefore, solutions for the plates with simply supported edges may be obtained by eliminating contributions of appropriate building blocks. This indicates that analysis for plates involving simply supported edges is simpler.

PRESENTATION OF COMPUTED RESULTS

A Fortran code is developed to handle the numerical calculation of buckling coefficient for various geometries,

loading cases and rigidities. In running the program, it is found that convergence of buckling coefficient for all interested cases is very rapid. Four digits of accuracy may be obtained by using only ten terms in the truncated series expressions.

Before presenting the results, we wish to make comparison with those by Wong and Bettess. They studied buckling of isotropic rectangular plates clamped on all four edges using the Taylor's theory. Since the generalized Poisson ratio does not affect vibrational characteristics of orthotropic plates with clamped and simply supported edges, buckling coefficients for an orthotropic plate with $D^* = 1$ should be the same as those for the isotropic plate, provided that the loading and geometry for the two types of plates are the same. Results of present paper and Wong and Bettess are tabulated in Table 2. Excellent agreement is encountered.

Table 2 Comparison of buckling coefficients for isotropic CCCC plates

D^*	α_o	ϕ_o	Wong & Bettess	Present paper
1.0	0.0	1.0	10.0738	10.07
		1.6	8.2050	8.201
		2.0	7.8674	7.867
		2.4	7.5812	7.581
		3.0	7.3608	7.359
1.0	0.2	1.0	8.6382	8.638
		1.6	7.3486	7.342
		2.0	7.0692	7.063
		2.4	6.7650	6.765
		3.0	6.6102	6.606
1.0	1.0	1.0	5.3035	5.304
		1.6	4.0507	4.051
		2.0	3.9234	3.923
		2.4	3.8950	3.895
		3.0	3.8604	3.861

To decide how the tabulation of computed buckling coefficients for plates with different supports, a relationship between the buckling coefficient and the generalized rigidity parameter for the given load ratio and aspect ratio is shown in Fig. 1. By examining the figure, one may quickly conclude that the buckling coefficient changes linearly with the generalized rigidity parameter in the interval [0,1]. This indicates that only two values of D^* need to be considered in tabulation. As a result, the storage space is dramatically reduced. Buckling coefficients for any other values of D^* may be obtained with great accuracy by interpolation. This result may be significant in optimal design of composite plates.

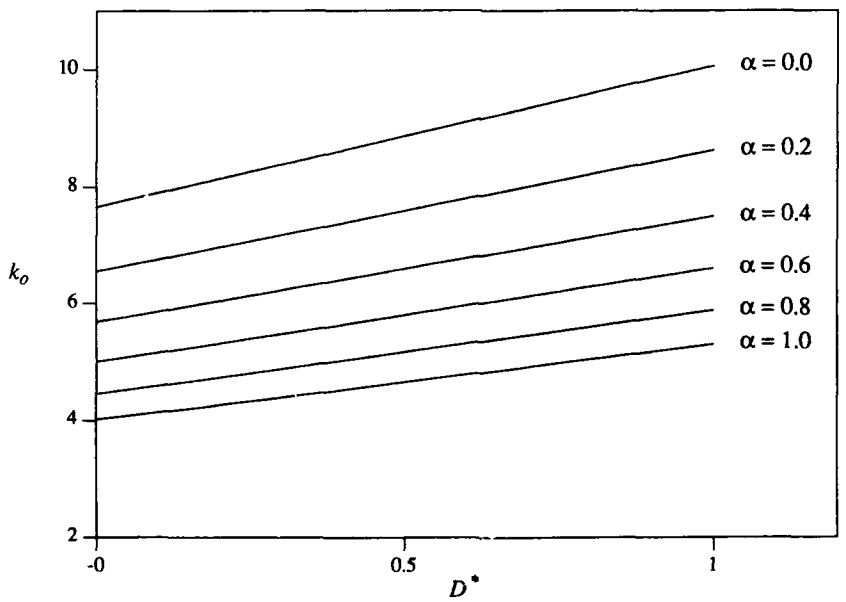

Fig. 1 Buckling coefficient k_o of CCCC plates versus D^*.

Table 3 shows buckling coefficients for the the camped orthotropic plates with D^*=1.0 and 0.5, respectively. Buckling coefficients for plates with one simply supported edge and two adjacent edges simply supported are presented in Table 4 and 5. All computed data given in this paper possess four digits of accuracy.

Table 3a Buckling coefficients of CCCC plates ($D^* = 1.0$)

aspect ratio ϕ_o	load ratio α_o										
	0.0	0.2	0.4	0.6	0.8	1.0	1.2	1.4	1.6	1.8	2.0
0.4	27.81	26.86	26.49	25.78	25.07	24.33	23.04	21.47	20.07	18.80	17.66
0.6	14.89	14.00	13.19	12.45	11.78	11.15	10.58	10.04	9.528	9.051	8.549
0.8	11.09	9.970	9.028	8.231	7.550	6.964	6.455	6.011	5.619	5.273	4.964
1.0	10.07	8.638	7.505	6.608	5.889	5.304	4.819	4.413	4.068	3.772	3.515
1.2	9.581	8.316	6.973	5.954	5.175	4.569	4.085	3.692	3.366	3.093	2.770
1.4	8.605	7.878	6.841	5.704	4.859	4.221	3.727	3.334	3.015	2.751	2.530
1.6	8.201	7.342	6.619	5.627	4.721	4.051	3.542	3.144	2.826	2.565	2.348
1.8	8.102	7.119	6.295	5.615	4.666	3.966	3.441	3.037	2.716	2.457	2.241
2.0	7.867	7.063	6.149	5.402	4.649	3.923	3.385	2.973	2.650	2.389	2.177
2.2	7.657	6.914	6.103	5.292	4.644	3.903	3.352	2.934	2.608	2.346	2.132
2.4	7.581	6.765	6.059	5.244	4.555	3.895	3.333	2.909	2.580	2.317	2.102
2.6	7.541	6.703	5.942	5.231	4.505	3.892	3.322	2.893	2.560	2.296	2.081
2.8	7.416	6.690	5.883	5.196	4.482	3.890	3.316	2.882	2.547	2.281	2.066
3.0	7.359	6.606	5.861	5.138	4.472	3.861	3.312	2.874	2.537	2.270	2.054

Table 3b Buckling coefficients of CCCC plates ($D^* = 0.5$)

aspect ratio ϕ_o	load ratio α_o										
	0.0	0.2	0.4	0.6	0.8	1.0	1.2	1.4	1.6	1.8	2.0
0.4	26.36	26.07	25.34	24.59	23.54	21.71	20.10	18.67	17.38	16.22	15.18
0.6	13.70	12.85	12.07	11.33	10.61	10.16	9.604	9.079	8.533	7.850	7.267
0.8	9.896	8.879	8.028	7.310	6.698	6.172	5.716	5.318	4.969	4.660	4.384
1.0	8.872	7.595	6.594	5.804	5.172	4.658	4.233	3.876	3.574	3.314	3.088
1.2	8.395	7.314	6.142	5.251	4.570	4.037	3.612	3.266	2.980	2.738	2.533
1.4	7.410	6.773	6.063	5.081	4.341	3.779	3.341	2.991	2.707	2.471	2.273
1.6	7.000	6.256	5.635	5.054	4.269	3.676	3.202	2.850	2.566	2.332	2.137
1.8	6.899	6.053	5.351	4.776	4.257	3.640	3.169	2.802	2.458	2.237	2.050
2.0	6.670	6.011	5.241	4.611	4.101	3.634	3.150	2.774	2.476	2.235	2.036
2.2	6.456	5.821	5.219	4.545	3.999	3.560	3.145	2.762	2.459	2.215	2.014
2.4	6.377	5.682	5.091	4.529	3.954	3.493	3.122	2.758	2.451	2.204	2.002
2.6	6.342	5.631	4.994	4.460	3.941	3.461	3.075	2.757	2.448	2.198	1.994
2.8	6.215	5.614	4.955	4.389	3.919	3.448	3.051	2.730	2.447	2.195	1.990
3.0	6.155	5.518	4.947	4.356	3.940	3.446	3.039	2.711	2.444	2.194	1.987

Table 4a Buckling coefficients of CCCS plates ($D^* = 1.0$)

aspect ratio ϕ_o	load ratio α_o										
	0.0	0.2	0.4	0.6	0.8	1.0	1.2	1.4	1.6	1.8	2.0
0.4	15.81	15.35	14.91	14.49	14.09	13.70	13.33	12.96	12.60	12.25	11.89
0.6	9.581	8.968	8.419	7.925	7.480	7.076	6.710	6.375	6.069	5.787	5.528
0.8	8.201	7.342	6.619	6.011	5.497	5.058	4.681	4.353	4.066	3.813	3.589
1.0	8.087	7.063	6.149	5.402	4.800	4.311	3.908	3.572	3.288	3.045	2.834
1.2	7.737	6.988	6.097	5.244	4.555	4.011	3.579	3.228	3.938	2.704	2.490
1.4	7.416	6.707	6.017	5.229	4.482	3.890	3.428	3.061	2.764	2.519	2.313
1.6	7.347	6.551	5.849	5.189	4.470	3.843	3.356	2.974	2.669	2.421	2.214
1.8	7.313	6.528	5.764	5.098	4.464	3.828	3.321	2.927	2.615	2.362	2.154
2.0	7.208	6.497	5.751	5.042	4.431	3.826	3.303	2.899	2.581	2.325	2.115
2.2	7.161	6.427	5.736	5.027	4.393	3.825	3.296	2.882	2.559	2.300	2.089
2.4	7.155	6.394	5.693	5.025	4.373	3.816	3.292	2.872	2.545	2.284	2.071
2.6	7.119	6.391	5.664	5.008	4.368	3.802	3.292	2.866	2.535	2.272	2.058
2.8	7.088	6.371	5.659	4.985	4.367	3.791	3.291	2.862	2.527	2.263	2.048
3.0	7.083	6.345	5.654	4.972	4.361	3.785	3.291	2.859	2.522	2.256	2.040

Table 4b Buckling coefficients of CCCS plates ($D^* = 0.5$)

aspect ratio ϕ_o	load ratio α_o										
	0.0	0.2	0.4	0.6	0.8	1.0	1.2	1.4	1.6	1.8	2.0
0.4	14.63	14.17	13.73	13.27	13.00	12.61	12.22	11.83	11.27	10.57	9.960
0.6	8.395	7.846	7.356	6.915	6.517	6.157	5.830	5.532	5.261	5.010	4.780
0.8	7.000	6.256	5.635	5.113	4.673	4.299	3.976	3.697	3.453	3.238	3.047
1.0	6.887	6.011	5.241	4.611	4.101	3.689	3.345	3.053	2.809	2.602	2.423
1.2	6.541	5.912	5.213	4.529	3.954	3.493	3.122	2.819	2.486	2.298	2.133
1.4	6.215	5.614	5.063	4.505	3.940	3.448	3.051	2.730	2.469	2.252	2.070
1.6	6.142	5.470	4.888	4.383	3.911	3.445	3.036	2.701	2.429	2.205	2.019
1.8	6.111	5.454	4.828	4.289	3.831	3.423	3.034	2.694	2.413	2.183	1.993
2.0	6.005	5.411	4.823	4.262	3.780	3.375	3.021	2.694	2.411	2.177	1.983
2.2	5.956	5.339	4.786	4.259	3.765	3.345	2.993	2.688	2.411	2.174	1.978
2.4	5.951	5.312	4.739	4.234	3.764	3.335	2.975	2.664	2.408	2.174	1.975
2.6	5.916	5.309	4.722	4.202	3.750	3.334	2.967	2.661	2.403	2.174	1.975
2.8	5.883	5.283	4.720	4.189	3.729	3.329	2.966	2.654	2.395	2.172	1.975
3.0	5.878	5.259	4.704	4.188	3.717	3.316	2.965	2.652	2.389	2.168	1.975

Table 5a Buckling coefficients of CCSS plates ($D^* = 1.0$)

aspect ratio ϕ_o	load ratio α_o										
	0.0	0.2	0.4	0.6	0.8	1.0	1.2	1.4	1.6	1.8	2.0
0.4	15.19	14.89	14.49	14.11	13.74	13.39	13.04	12.70	12.34	11.90	11.34
0.6	8.638	8.119	7.650	7.226	6.841	6.491	6.170	5.875	5.602	5.349	5.111
0.8	6.719	6.030	5.457	4.974	4.565	4.214	3.910	3.645	3.412	3.205	3.021
1.0	6.223	5.315	4.605	4.049	3.607	3.248	2.951	2.703	2.493	2.312	2.155
1.2	6.180	5.123	4.266	3.628	3.147	2.775	2.480	2.241	2.043	1.877	1.735
1.4	5.996	5.106	4.146	3.426	2.907	2.520	2.223	1.987	1.797	1.639	1.507
1.6	5.773	5.030	4.119	3.329	2.773	2.372	2.071	1.837	1.650	1.500	1.371
1.8	5.679	4.902	4.115	3.283	2.695	2.281	1.975	1.741	1.557	1.408	1.284
2.0	5.668	4.827	4.085	3.264	2.647	2.221	1.912	1.678	1.494	1.347	1.226
2.2	5.636	4.806	4.035	3.257	2.618	2.181	1.868	1.633	1.451	1.305	1.185
2.4	5.575	4.803	4.000	3.256	2.598	2.153	1.837	1.601	1.419	1.274	1.156
2.6	5.543	4.780	3.984	3.255	2.585	2.132	1.813	1.577	1.395	1.251	1.133
2.8	5.539	4.748	3.982	3.250	2.577	2.117	1.796	1.559	1.377	1.233	1.117
3.0	5.528	4.730	3.980	3.241	2.571	2.105	1.782	1.544	1.363	1.219	1.103

Table 5b Buckling coefficients of CCSS plates ($D^* = 0.5$)

aspect ratio ϕ_o	load ratio α_o										
	0.0	0.2	0.4	0.6	0.8	1.0	1.2	1.4	1.6	1.8	2.0
0.4	14.22	13.82	13.44	13.06	12.71	12.32	11.83	11.16	10.49	9.869	9.308
0.6	7.506	7.025	6.582	6.273	5.929	5.613	5.322	5.051	4.798	5.558	4.330
0.8	5.595	5.011	4.528	4.125	3.783	3.488	3.237	3.011	2.816	2.644	2.490
1.0	5.094	4.343	3.762	3.307	2.946	2.652	2.410	2.208	2.036	1.888	1.760
1.2	5.051	4.192	3.500	2.983	2.591	2.287	2.045	1.849	1.686	1.550	1.433
1.4	4.871	4.176	3.443	2.864	2.438	2.117	1.862	1.667	1.508	1.377	1.267
1.6	4.645	4.058	3.437	2.832	2.374	2.037	1.781	1.582	1.402	1.276	1.170
1.8	4.548	3.925	3.384	2.829	2.352	1.998	1.734	1.531	1.370	1.239	1.131
2.0	4.536	3.863	3.307	2.818	2.346	1.981	1.709	1.502	1.339	1.208	1.100
2.2	4.507	3.854	3.261	2.783	2.346	1.974	1.695	1.484	1.319	1.187	1.079
2.4	4.445	3.844	3.248	2.750	2.340	1.972	1.688	1.473	1.306	1.174	1.065
2.6	4.412	3.808	3.247	2.733	2.327	1.971	1.684	1.467	1.299	1.163	1.055
2.8	4.407	3.778	3.236	2.728	2.312	1.971	1.683	1.463	1.294	1.159	1.050
3.0	4.397	3.768	3.215	2.728	2.303	1.968	1.682	1.460	1.290	1.154	1.045

CONCLUSION

This paper investigated generic buckling of orthotropic rectangular plates with combination of clamped and simply supported edges by studying a clamped plate. Results obtained by the superposition method are accurate, and the procedure itself is analytical. The method may be employed to solve buckling of plates involving free edges by modifying generating functions used for the clamped plates.

REFERENCES

[1] A.W. Leissa, Buckling of composite materials, *Composite Structures, Vol.1 (1983), 51-66.*

[2] D.J. Gorman, *Free Vibration Analysis of Rectangular Plates,* New York: Elsevier North Holland, 1982.

[3] Yu,S.D., Cleghorn, W.L., Free Vibration Analysis of Clamped Orthotropic Rectangular Plates Subjected to Constant In-Plane Loads", presented at *1991 ASME Presure Vessels and Piping Conference,* San Diego, California, published in *Piping Components Analysis: Piping and Structural Dynamics,* PVP-Vol. 218 (1991), 113-119.

[4] W.L. Cleghorn and S.D. Yu, Analysis of buckling of rectangular plates using the method of superposition, to appear in *Transactions of Canadian Society for Mechanical Engineering, Vol.15, No.4, 1991.*

[5] E.J. Brunelle and G.A. Oyibo, Generic buckling curves for specially orthotropic rectangular plates. *AIAA Journal, Vol.21 (1983), 1150-1156.*

[6] E.J. Brunelle, The fundamental constants of orthotropic affine plate/slab equations, *AIAA J., Vol.23 (1985), 1957-*

[7] I.H. Yang and W.S. Kuo, The global constants of in orthotropic affine space, *J. CSME, Vol.7 (1986), 355-*

[8] P.M. Wong and P. Bettess, Elastic buckling of rectangular clamped plates, *Int. J. Solids Structure, Vol.15 (1979), 457-466.*

SOUND AND VIBRATION MEASUREMENTS

SECOND INTERNATIONAL CONGRESS ON
RECENT DEVELOPMENTS IN AIR- AND
STRUCTURE-BORNE SOUND AND VIBRATION
MARCH 4-6, 1992 AUBURN UNIVERSITY, USA

A FREQUENCY DOMAIN IDENTIFICATION SCHEME FOR DAMPED DISTRIBUTED PARAMETER SYSTEMS

R. Chander
Aerostructures, Inc., Arlington, Virginia, USA
M. Meyyappa
McDonnell Douglas Helicopter Co., Mesa, Arizona, USA
S. Hanagud
Georgia Institute of Technology, Atlanta, Georgia, USA

ABSTRACT

A parameter identification technique in the frequency domain is discussed. For this purpose, a distributed parameter model of a dynamic system within the framework of Euler-Bernoulli beam theory is assumed to be known. Internal material damping and external viscous damping are included in the model. The parameters are approximated using cubic cardinal splines, and their derivatives are evaluated from such approximations. For a given input, the response is assumed to be measured at discrete locations in the system. Quintic B-splines are used to obtain approximate spatial representations of the response and its derivatives from these measurements. A Galerkin-type approach in conjunction with an equation error technique is used to estimate the unknown parameters. Numerically simulated responses obtained from an independent finite element model of an Euler-Bernoulli beam is used to validate the identification technique. Estimated values of the mass, stiffness and damping distributions are discussed.

INTRODUCTION

For structures that can be modelled as continuous systems, discretization reduces modeling accuracy. In such cases, if the form of the governing differential equation is known along with the initial and boundary conditions, the actual distributed system itself can be considered for parameter identification without resorting to approximate models. A distributed representation of the system thus identified is likely to yield more accurate prediction of the system behavior. Also, the identified values can be used to reconstruct the response, which can be compared with the measured response to check the validity of the physical representation of the system itself. In the recent past, several identification techniques suitable for distributed structural dynamic systems have been reported [1-4].

At present, there are few techniques available to identify the unknown parameters of distributed structural dynamic systems in the presence of damping. Among these, the finite element and spline-based techniques have received considerable attention. The finite element techniques are primarily concerned with the identification of systems that include proportional or general viscous damping. The spline-based techniques involve using time domain data for systems with constant or spatially varying parameters, and include different types of damping models.

Damping is present in virtually all types of structures and materials encountered in practice. Characterization and understanding of the damping behavior becomes even more critical if, in addition to vibration, noise control problems are also addressed. In such cases, the material (internal or structural) damping should also be included along with the external damping of the system. In this vein, an identification scheme

suitable for one-dimensional systems, including both types of system dampings, is discussed in this paper.

The identification scheme uses data in the frequency domain, and a model of a distributed dynamic system within the framework of the Euler-Bernoulli beam theory. The parameters of the system, such as mass, damping and stiffness, are assumed to be uniformly varying along the length of the beam. The external and internal dampings are included by using the linear viscous and viscoelastic models respectively. The spatially varying parameters are approximated using cubic cardinal splines, and their derivatives are obtained from such approximations. For a given input, the response chosen to be acceleration, is assumed to be known at discrete locations along the beam. Quintic B-splines are then used to obtain approximate spatial representations of the response and its derivatives from these discrete measurements.

A Galerkin-type approach in conjunction with an equation error technique is then used to estimate the unknown parameters, which are values of the parameter splines at the knot locations. Numerically simulated responses obtained from an independent finite element model of an Euler-Bernoulli beam are used to validate the identification technique. Estimated values of the mass, stiffness and damping distributions are presented.

PHYSICAL SYSTEM MODEL

The physical system is assumed to be modeled within the framework of the Euler-Bernoulli beam theory. The effects of internal and external dampings are included using the linear viscoelastic and viscous damping models, respectively. A model governing the behavior of such beams is assumed to be known *a priori* in the frequency domain, and is taken to be as follows.

$$d^2/dx^2\,[\{EI(x)+jC_sI(x)\}d^2a^*(x,\omega)/dx^2]+$$

$$[j\omega C_v(x)-\omega^2\ \rho A(x)]a^*(x,\omega)\ =\ -\omega^2\ F(x,\omega) \qquad (1)$$

where $a^*(x,\omega)$ is the acceleration response caused by the known forcing function $F(x,\omega)$, x is the distance along the beam, and ω is the frequency in radians/second. The beam is assumed to be fixed at $x=0$, and free at $x=L$, where L is the length of beam. EI and ρA are stiffness and mass distributions respectively. C_s and C_v correspond to the internal and external damping coefficients respectively. The above parameters are assumed to be continuous functions of x, and are the unknown parameters to be identified. In eq. (1), the initial conditions were assumed to be equal to zero.

For identification purposes, it is assumed that the acceleration is known at as many frequencies as required, at a number of discrete locations. From this data an approximation to the continuous response is constructed using quintic B-splines. Each of the parameters appearing in eq. (1) is approximated in the identification process by cardinal cubic splines. The task of identifying the unknown parameters then reduces to estimating the values at the knot locations of these parameter splines. To accomplish this, a Galerkin type weighted residual procedure in conjunction with an equation error approach is used.

SPLINE APPROXIMATIONS

Cubic cardinal splines and quintic B-splines were chosen as the approximating functions for the parameters and response respectively.

Response Representation: The acceleration response is represented as follows.

$$a^*(x,\omega)\ =\ \sum_{i=0}^{N} a_i(\omega)\ \phi_i(x) \qquad (2)$$

where $\phi_i(x)$ are the basis functions that satisfy appropriate boundary conditions, and $a_i(\omega)$ are constants to be determined at each frequency. The functions $\phi_i(x)$ are constructed using the quintic B-spline basis functions [5], so as to satisfy the given boundary conditions.

Though many such combinations are possible, the following is used in this paper.

$$\phi_1(x) = B_1^{(5)}(x) - (9/4)B_{-1}^{(5)}(x) + (65/2)B_{-2}^{(5)}(x)$$

$$\phi_2(x) = B_2^{(5)}(x) - (1/8)B_{-1}^{(5)}(x) + (9/4)B_{-2}^{(5)}(x)$$

$$\phi_N(x) = B_N^{(5)}(x) + (3/2)B_{N+1}^{(5)}(x) + 3B_{N+2}^{(5)}(x)$$

$$\phi_{N-1}(x) = B_{N-1}^{(5)}(x) - 2B_{N+2}^{(5)}(x)$$

$$\phi_{N-2}(x) = B_{N-2}^{(5)}(x) - 0.5\, B_{N+1}^{(5)}(x)$$

$$\phi_i(x) = B_i^{(5)}(x), \qquad i=3,4,\ldots,N-3 \tag{3}$$

where

$$B_i^{(5)}(x) = 1/h^5[(x-x_{i-3})_+^5 - 6(x-x_{i-2})_+^5 + 15(x-x_{i-1})_+^5$$

$$-20(x-x_i)_+^5 + 15(x-x_{i+1})_+^5 - 6(x-x_{i+2})_+^5 + (x-x_{i+3})_+^5]$$

$$x_{-3} < x_{-2} < x_{-1} < x_0 \text{ and } x_{N+3} > x_{N+2} > x_{N+1} > x_N$$

and

$$(x-x_i)_+^5 = (x-x_i)^5, \quad \text{if } x \geq x_i$$
$$= 0 \qquad\quad \text{if } x < x_i$$

For a given set of measured response at the knot locations i=0,1,2,....N, at a given frequency, the coefficients $a_i(\omega)$ in eq. (2) can be uniquely obtained. The response derivatives required in eq. (1) can be calculated by differentiating eq. (2) as many times as necessary.

Parameter Splines: The unknown structural parameters are expressed in terms of basis functions as follows.

$$\theta^p(x) = \sum_{i=0}^{M} \theta_i^p\, C_i(x), \qquad p = 1,2\ 3 \text{ and } 4 \tag{4}$$

where $\theta^{(1)}$, $\theta^{(2)}$, $\theta^{(3)}$ and $\theta^{(4)}$ represent EI, $C_s I$, C_v and ρA, and $\theta_i^{(1)}$, $\theta_i^{(2)}$ $\theta_i^{(3)}$ and $\theta_i^{(4)}$ represent the coefficients corresponding to these parameters respectively. The values of M depend on the number of locations at which the parameters are to be identified. The basis functions $C_i(x)$ are taken as cubic cardinal splines [6] having the following characteristics.

$$C_j(x_i) = \delta_{ij}, \quad C'_j(x_0) = C'_j(x_N) = 0 \qquad i,j = 0,1,\ldots,N$$

$$C_{N+1}(x_i) = C_{N+2}(x_i) = 0, \quad C'_{N+1}(x_0) = C'_{N+2}(x_N) = 1$$

$$C'_{N+1}(x_N) = C'_{N+2}(x_0) = 0 \tag{5}$$

where ()' represents differentiation with respect to x. Also, it has been assumed that the parameter knots coincide with the knots used for the response. In this case M=N+2.

$$\theta^p(x) = \sum_{i=0}^{N+2} \theta_i^p\, C_i(x) \tag{6}$$

Due to the manner the cardinal splines are defined, θ_i^p, i=0,1,..,N are the values of the parameters θ^p at the knots x_i, and θ^p_{N+1} and θ^p_{N+2} are the derivatives of θ^p at x=0 and x=L respectively. The identification procedure now involves computing the coefficients θ_i^p for p=1,2, 3 and 4.

IDENTIFICATION SCHEME

Substituting eqs. (2) and (6) into eq. (1) and regrouping, the following set of equations is obtained.

$$\left[\sum_{k=0}^{N+2}[\theta_k^{(1)}+j\theta_k^{(1)}]C_k(x)\right]\left[\sum_{k=0}^{N}a_k(\omega)\phi_k''''(x)\right]$$

$$+\,2\left[\sum_{k=0}^{N+2}[\theta_k^{(1)}+j\theta_k^{(1)}]C_k'(x)\right]\left[\sum_{k=0}^{N}a_k(\omega)\phi_k'''(x)\right]$$

$$+\left[\sum_{k=0}^{N+2}[\theta_k^{(1)}+j\theta_k^{(1)}]C_k''(x)\right]\left[\sum_{k=0}^{N}a_k(\omega)\phi_k''(x)\right]$$

$$+\left[\sum_{k=0}^{N+2}\{j\omega\theta_k^{(2)}-\omega^2\theta_k^{(3)}\}C_k(x)\right]\left[\sum_{k=0}^{N}a_k(\omega)\phi_k(x)\right]\quad+\omega^2\,F(x,\omega)=0 \qquad (7)$$

At this stage, the coefficients a_k and the excitation F are known complex quantities at any given frequency and can be written as

$$a_k(\omega) = a_k^R(\omega) + ja_k^I(\omega)$$

$$F(x,\omega) = F^R(x,\omega) + jF^I(x,\omega) \qquad (8)$$

The number of unknowns θ_k in eq. (7) equals 4(N+3), corresponding to the values of (N+1) knot locations and also the derivatives at end points of each of the parameters. If an arbitrary number of equations is used in solving these unknowns in eq. (7), the resulting equation will not be equal to zero, but will result in some error. The identification procedure involves orthogonalizing this error with respect to each of the basis functions used in the parameter splines and computing the unknowns from the resulting equations. Thus, a set of equations is obtained for each frequency used in identification. By combining these sets of equations for many frequencies, an overdetermined system can be generated, a least squares solution of which yields estimates for the unknowns. The equations involved in this procedure are summarized below. The following matrices are defined for convenience.

$$R_{1,2} = \int_0^L \left[\{C\}\{\phi''''\}^T\{a^{R,I}\}\{C\}^T + 2\{C\}\{\phi'''\}^T\{a^{R,I}\}\{C'\}^T + \{C\}\{\phi''\}^T\{a^{R,I}\}\{C''\}^T\right]dx$$

$$R_{3,4} = \int_0^L \{C\}\{\phi\}^T\{a^{R,I}\}\{C\}^T dx \quad ; \qquad F_\theta^{R,I} = \int_0^L F^{R,I}\{C\}\,dx \qquad (9)$$

Incorporating eqs. (8) and (9) into the weighted residual procedure, the following equations involving coefficients of the unknown parameters is obtained.

$$\begin{bmatrix} R_1 & -R_2 & -\omega R_4 & -\omega^2 R_3 \\ R_2 & -R_1 & \omega R_3 & -\omega^2 R_4 \end{bmatrix} \begin{Bmatrix} \theta^{(1)} \\ \theta^{(2)} \\ \theta^{(3)} \\ \theta^{(4)} \end{Bmatrix} = \begin{Bmatrix} \{F_\theta^R\} \\ \{F_\theta^I\} \end{Bmatrix} \qquad (10)$$

Eq. (10) is obtained for a single frequency. Similar sets of equations can be written at other frequencies. Combining the different sets at various frequencies leads to an equation of the form

$$[C_\theta]\ \{\theta\} = \{F_\theta\} \tag{11}$$

in which $[C_\theta]$ is a coefficient matrix of the order $2(N+3)n$ times $4(N+3)$, where n is the number of frequencies used in the estimation. Elements of this matrix are made up of the elements of matrices defined in eq. (9) evaluated at different frequencies. $\{\theta\}$ and $\{F_\theta\}$ are the parameters and force vectors of length $4(N+3)$. Using the ordinary least squares technique, a solution $\{\theta^*\}$ to eq. (11) can be written as,

$$\{\theta^*\} = C_\theta^T\ C_\theta^{-1}\ C_\theta^T\ F_\theta \tag{12}$$

NUMERICAL RESULTS

The identification scheme discussed in the previous sections is demonstrated in this section using simulated data for a cantilever beam with the following properties.

$$\begin{aligned} L &= 0.61\text{m}; \\ EI(x) &= 18.01*10^2\ [1-(x/2L)]^4\ \text{N-m}^2; \quad C_s I(x) = 5.51\ [1-(x/2L)]^4\ \text{N-m}^2 \\ \rho A(x) &= 4.22\ [1-(x/2L)]^2\ \text{N/m}; \quad C_v(x) = 17.3\ [1-(x/2L)]^2\ \text{N-sec/m}^2 \end{aligned}$$

The beam was subdivided into 6 regions (N=6), and an independent finite element program was used to calculate the response at the resulting 7 knots. In the identification, the frequency response data in the following frequency bandwidths at 1Hz intervals was used: 25-34Hz and 39-48Hz (around first mode), 144-153Hz and 158-167Hz (around second mode), and 376-385Hz and 390-399Hz (around third mode).

The regions in the immediate vicinity of the modal peaks were omitted. This is because, less accurate estimates were obtained, if these areas were included especially for viscous damping. The elements in the coefficient matrix $[C_\theta]$ are integral terms involving products of polynomials. A sixth order Gauss-Legendre numerical procedure [7] was used to compute the elements in the matrix. A total of 36 parameters were estimated, viz., the values at the 7 knot locations and the derivatives at the ends for stiffness, damping and mass distributions. Computed values for these unknowns at the assumed knot locations are presented in Figures 1-4. It can be seen from these figures that the estimated values are in good agreement with the actual values used in generating the frequency response functions at all the interior knots.

SUMMARY AND CONCLUSIONS

A spline based identification technique in the frequency domain that is suitable for damped distributed structural dynamic systems was developed. A uniformly tapered beam whose behavior can be modeled within the framework of the Euler-Bernoulli beam theory was considered for the identification scheme. The infinite-dimensional response and parameter spaces were approximated by quintic B-splines and cubic cardinal splines respectively. A Galerkin type weighted residual procedure was used to estimate the unknown parameters. Simulated acceleration frequency response data around the first three modes, for an applied impulse, was used to validate the technique. None of the parameters was assumed to be known *a priori*. The estimated results showed good agreement with the actual values at all the interior locations of the beam.

REFERENCES

1. Banks, H.T. and Crawley, J.H., "Parameter Identification in Continuum Models," Proceedings of the 1983 American Control Conference, San Francisco, California, 1983.
2. Banks, H.T., Fabiano, R.H., Wang, Y., Inman, D.J., and Cudney, H., "Spatial Versus Time Hysteresis in Damping Mechanisms," Proceedings of the 27th IEEE Conference on Decision and Control, 1988, pp 1674-1677.
3. Baruch, H. and Meirovitch, L., "Parameter Identification of Distributed Systems," Journal of Sound and Vibration, 1985, pp 551-564.
4. Meirovitch, L. and Norris, P., "Parameter Identification in Distributed Spacecraft Structures," Journal of the Astronautical Sciences, 1986, pp 341-352.
5. Prenter, R.M., "Splines and Variational Methods," Wiley Interscience, 1975.
6. Shultz, M.H. "Spline Analysis," Prentice Hall, 1973.

7. Zienkiewicz, D.C., "The Finite Element Method," McGraw Hill Book Company, 1977.

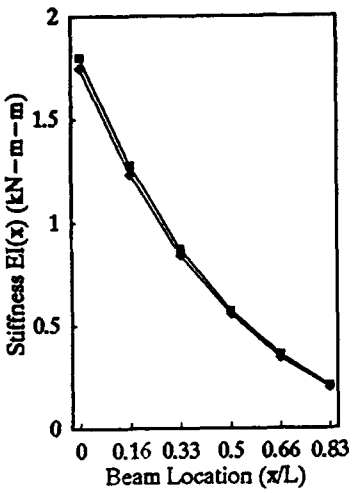

Figure 1 Stiffness Estimates

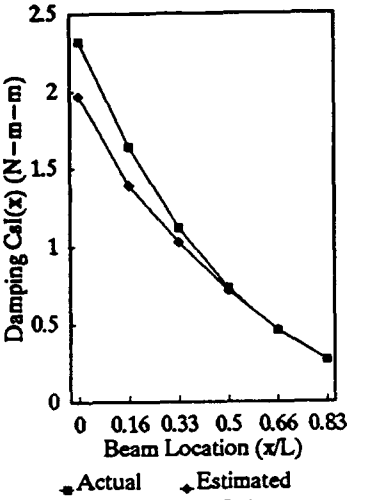

Figure 2 Damping Estimates (Internal)

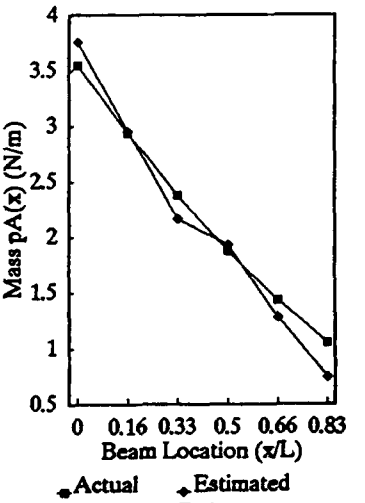

Figure 3 Mass Estimates

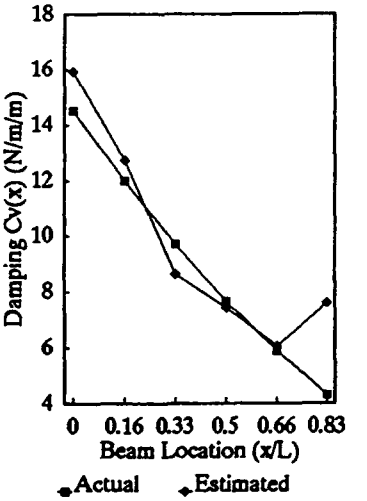

Figure 4 Damping Estimates (External)

SECOND INTERNATIONAL CONGRESS ON
RECENT DEVELOPMENTS IN AIR- AND
STRUCTURE-BORNE SOUND AND VIBRATION
MARCH 4-6, 1992 AUBURN UNIVERSITY, USA

ELASTIC BEHAVIOUR OF MIXED Li-Zn AND Li-Cd FERRITES

D.Ravinder
Department of Physics
Post Graduate College of Science
Saifabad
Osmania University, Hyderabad-500 004
INDIA.

ABSTRACT

Polycrystalline samples of mixed ferrite systems having the chemical formula $Li_{0.5-x/2}M_xFe_{2.5-x/2}O_4$ (M = Zn or Cd) where x = 0.2, 0.4, 0.6, 0.8 and 1.0 were prepared by conventional double sintering method. The final sintering temperature was done at 1250°C. The ultrasonic compressional (V_l) and shear (V_s) velocities at room temperature of all the mixed Li-Zn and Li-Cd ferrites were determined by the ultrasonic pulse transmission technique. The elastic moduli of the specimens have been computed and corrected to zero porosity. The corrected values of the elastic moduli and the Debye temperatures are presented. Lithium-Zinc ferrite with x = 0.6 is found to have minimum Young's and rigidity moduli. But in the case of mixed Li-Cd ferrite with x = 0.4 is found to have maximum Young's and rigidity moduli .

The values of E, n, E_o, n_o and K_o of the mixed Li-Zn ferrites are found to decrease with increasing zinc content (x = 0.6 mole). Beyond x=0.6 mole, these paramenters, show an increase for further addition of zinc. They, however, decrease once again for zinc ferrites with 100% Zn. But in the case of Lithium-Cadmium ferrites the values of E, n, E_o, n_o and K_o are found to increase with increasing cadmium content (x=0.4 mole). Bevond x=0.4 mole these parameters show an decrease for further addition of cadmium. In both cases Poisson's ratio remains constant. The variation of elastic moduli with composition may be interpreted in terms of binding forces between the atoms.

INTRODUCTION

A study of the elastic behaviour of solids is of great significance in understanding the nature of interatomic and interionic forces in solids. The elastic properties of ferrites possessing the spinel structure have not been studied so systematically as their magnetic and electrical properties. Moreover, there is a need for a thorough study of the elastic behaviour of these ferrites with new compositions possessing certain desired elastic properties in view of their extensive applications in computers as memory cores and in several microwave devices like isolators, circulators, gyrators, phase shifters, etc. It is with this view that

a systematic study of the elastic behaviour of polycrystalline Li-Zn and Li-Cd ferrites has been undertaken at room temperature.

EXPERIMENTAL DETAILS

Mixed Li-Zn and Li-Cd ferrites having the chemical formula $Li_{0.5-x/2}M_xFe_{2.5-x/2}O_4$ where x = 0.2, 0.4, 0.6, 0.8 and 1.0 were prepared by conventional double sintering process with a final sintering temperature 1250°C. The details of the method of preparation have been given in an earlier publications [1,2]. X-ray diffractometer studies of the samples using CuK_α radiation confirmed the spinel formation. From the diffraction data, lattice parameter values and hence the values of X-ray densities have also been calculated and are given in Table-I.

TABLE-I Ambient elastic data (uncorrected) on Lithium-Zinc and Lithium-Cadmium ferrites

Ferrite Composition	Bulk density $10^3 Kgm^{-3}$	X-ray density $10^3 Kgm^{-3}$	Percentage Porosity (%)	V_l $(m.S^{-1})$	V_s $(m.S^{-1})$	E $(x10^{10} Nm^{-2})$	n $(x10^{10} Nm^{-2})$
$Li_{0.4}Zn_{0.2}Fe_{2.4}O_4$	4.66	4.86	4.1	6243	3806	16.25	6.75
$Li_{0.3}Zn_{0.4}Fe_{2.3}O_4$	4.81	4.98	3.3	6131	3967	15.26	5.57
$Li_{0.2}Zn_{0.6}Fe_{2.2}O_4$	4.97	5.09	2.4	5200	2737	9.74	3.72
$Li_{0.1}Zn_{0.8}Fe_{2.1}O_4$	5.14	5.22	1.6	6281	4023	19.16	8.31
$ZnFe_2O_4$	5.30	5.32	0.5	4934	3028	11.64	4.86
$Li_{0.4}Cd_{0.2}Fe_{2.4}O_4$	4.58	4.64	1.3	5751	3502	13.54	5.62
$Li_{0.3}Cd_{0.4}Fe_{2.3}O_4$	4.87	4.94	1.4	8962	5333	33.96	13.85
$Li_{0.2}Cd_{0.6}Fe_{2.2}O_4$	5.16	5.24	1.4	5580	3988	21.81	8.68
$Li_{0.1}Cd_{0.8}Fe_{2.1}O_4$	5.46	5.53	1.3	5560	3271	13.67	5.52
$CdFe_2O_4$	5.75	5.82	1.1	4267	2300	7.88	3.04

The compressional (V_l) and shear (V_s) velocities at room temperature of all the mixed ferrites were determined by the ultrasonic pulse transmission technique [3], but modified and improved by using a digital Textronic 2230 oscilloscope and utilising curser movement for travel time measurements [4]. The error in the measurement of velocities is less than ± 0.5% .

RESULTS AND DISCUSSIONS

The measured values of the compressional (V_l) and shear (V_s) velocities, along with the computed values of the Young's modulus (E), and rigidity modulus (n), are in Table-I. Since the ferrites under investigation are porous (porosity ranging from 4.1 to 0.5%), the elastic moduli have been corrected to zero porosity using McKenzie's formula [5]. The corrected values of E_o, n_o, K_o and σ_o are in Table-II.

TABLE-II Elastic data of Li-Zn and Li-Cd ferrites corrected to zero porosity

Ferrite Composition	(x 10^{10} Nm^{-2})			σ_o
	E_o	n_o	K_o	
$Li_{0.4}Zn_{0.2}Fe_{2.4}O_4$	17.69	7.37	9.83	0.20
$Li_{0.3}Zn_{0.4}Fe_{2.3}O_4$	15.76	5.73	8.89	0.21
$Li_{0.2}Zn_{0.6}Fe_{2.2}O_4$	10.19	4.35	5.16	0.17
$Li_{0.1}Zn_{0.8}Fe_{2.1}O_4$	19.98	8.26	11.46	0.21
$ZnFe_2O_4$	11.75	4.90	6.53	0.20
$Li_{0.4}Cd_{0.2}Fe_{2.4}O_4$	13.53	5.79	6.80	0.17
$Li_{0.3}Cd_{0.4}Fe_{2.3}O_4$	33.84	14.57	16.75	0.16
$Li_{0.2}Cd_{0.6}Fe_{2.2}O_4$	22.26	9.37	11.87	0.16
$Li_{0.1}Cd_{0.8}Fe_{2.1}O_4$	13.60	5.87	6.64	0.19
$CdFe_2O_4$	8.02	3.41	4.15	0.18

It can be seen from Tables-I and II that the values of E, n, E_o, n_o and K_o of the mixed Li-Zn ferrites are found to decrease with increasing zinc content (x=0.6 mole). Beyond x=0.6 mole, these parameters, show an increase for further addition of zinc. They, however, decrease once again for zinc ferrite with 100% Zn. From Table II, it can further be seen that the Poisson's ratio remains constant. Following Wooster's work [6], the variation of elastic moduli with composition may be interpreted in terms of binding forces between the atoms. As such, it can be understood from the experimental values of E_o and n_o (Table-II) that the atomic binding between the ions of Li-Zn mixed ferrites, decreases with increasing zinc content upto x=0.6 mole. Beyond x=0.6 mole, the binding forces show an increase for further addition of zinc. They, however, once again decrease for zinc ferrite. But in the case of Li-Cd ferrites the values of E, n, E_o, n_o, and K_o of the mixed Li-Cd ferrites are found to increase with increasing cadmium content (x=0.4 mole). Beyond x=0.4 mole,

these parameters show decrease for further addition of cadmium. From Table-II, it can further be seen that the Poission's ratio remains constant. Following Wooster's work [6], the variation of elastic moduli with composition may be interpreted in terms of binding forces between the atoms. As such, it can be understood from the experimental values of E_o and n_o (Table-II) that the atomic binding between ions of mixed Li-Cd ferrites, increases with increasing cadmium content upto x=0.4 beyond x=0.4 mole the binding forces show decrease for further addition of cadmium. This composition variation of elastic moduli in the case of Li-Zn and Li-Cd ferrites is similar to what has been observed in several other ferrites like Co-Zn [7] and Li-Ni [8] studied earlier.

Debye temperature (θ_D) for the mixed Li-Cd ferrites have been calculated using the simple method given by Anderson [9]

$$\theta_D = \frac{h}{K}\left(\frac{3Nq\rho}{4\pi m}\right)^{\frac{1}{3}} \times V_m$$

where

h	=	plank's constant
K	=	Boltzmann's constant
N	=	Avogadro's Number
M	=	Molecular weight of the specimen
q	=	Number of atoms in a molecule
ρ	=	density of the specimen, and
V_m	=	Average sound velocity

given by

$$V_m = \left[\frac{1}{3}\left(\frac{2}{V_s^3} + \frac{1}{V_l^3}\right)\right]^{-\frac{1}{3}}$$

From the values of compressional (V_l) and shear (V_s) velocities and X-ray density, V_l/ρ and V_s/ρ are calculated and are shown in Table-III. The mean atomic weight m/q of the ferrite under investigation, calculated from the molecular weight m and the number of atoms q in the chemical fromula are also included in Tble-III. The values of θ_D and V_m thus obtained are also given in Table-III.

TABLE-III Reltionship between atomic weights and velocities

Ferrite Composition	m/q	V_l/ρ	V_s/ρ	V_m ($m.S^{-1}$)	θ_D (K)
$Li_{0.4}Zn_{0.2}Fe_{2.4}O_4$	30.55	1274	783	4204	564
$Li_{0.3}Zn_{0.4}Fe_{2.3}O_4$	31.53	1231	797	4353	584
$Li_{0.2}Zn_{0.6}Fe_{2.2}O_4$	32.50	1022	538	3060	411
$Li_{0.1}Zn_{0.8}Fe_{2.1}O_4$	33.54	1203	771	4420	594
$ZnFe_2O_4$	34.44	927	569	3342	450
$Li_{0.4}Cd_{0.2}Fe_{2.4}O_4$	31.90	1239	755	3868	509
$Li_{0.3}Cd_{0.4}Fe_{2.3}O_4$	34.21	1814	1080	5904	780
$Li_{0.2}Cd_{0.6}Fe_{2.2}O_4$	36.53	1065	761	4316	564
$Li_{0.1}Cd_{0.8}Fe_{2.1}O_4$	38.64	1005	592	3626	475
$CdFe_2O_4$	41.16	733	395	2568	335

It cn be seen from the tble that there is a continuous increase in the vlue of mean atomic weight with increasing zinc and cadmium contents.

In the case of Li-Cd ferrites, the values of V_l/ρ , V_s/ρ , V_m and θ_D are also increases continuously with increasing cadmium content upto x=0.4 mole. Beyond x=0.4 mole the above values show a decrease for further addition of cadmium. Plot of θ_D against V_m is shown in Fig.I. It is interesting to note from the figure θ_D varies linearly with V_m. A similar variation of θ_D with V_m was reported by Narayana and Swamy [10,11] in the case of rare eaarth and noble metals, and Reddy et al., in the case of Li-Ti [12] mixed ferrites.

ACKNOWLEDGEMENTS

The author is grateful to Prof.Anwar Kamal, Head of the Department of Physics, Osmania University, Hyderabd, for his interest in this work. The author also thank the Prof.T.Seshagiri Rao, Prof.K.Shankariah, Principal, Principal and Prof.U.V.Subbaa Rao, Head of the Department of Physics, Post Graduate College of Science (O.U.), Saifabad, Hyderabd for their cooperation.

Fig.1 Plot of Debye temperature (θ_D) against the average sound velocity (V_m) for the Li-Zn and Li-Cd mixed ferrites.

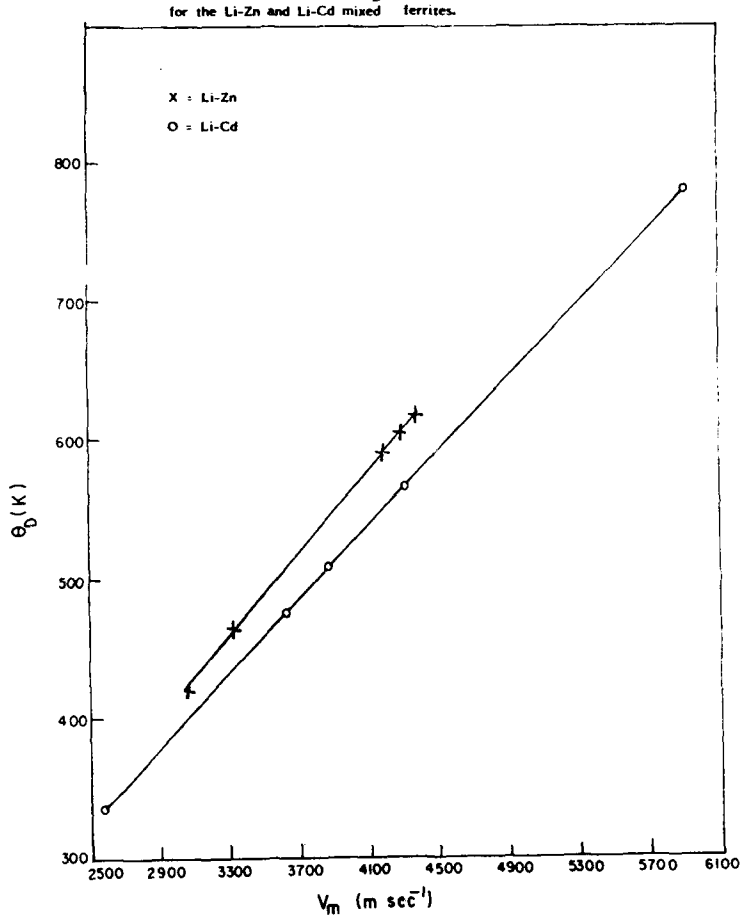

REFERENCES

1. RAVINDER,D. and SESHAGIRI RAO,T.
   Cryst.Res.Technol. **25** (1990) 1079.

2. RAVINDER,D. and SESHAGIRI RAO,T.
   Cryst.Res.Technol. **25** (1990) 963.

3. RAMANA, Y.V.
   Int.J.Roc.Mech.Min.Sci. **6** (1969) 191.

4. RAMANA,Y.V. and REDDY,P.V.
   Acoustics Letters Vol.**13**, No.5 (1989) 83.

5. McKENZIE,J.K.
   Proc.Phys.Soc.(Lond) **B63** (1950) 2.

6. WOOSTER,W.A.
   Rep.Prog.Phy. **16** (1953) 62.

7. REVATHI,B. and SESHAGIRI RAO,T.
   J.Less Comm.Met. **34** (1974) 91.

8. VENUGOPAL REDDY,P., SESHAGIRI RAO,T. and RAMANA,Y.V.
   Solid St.Commun. **56** (1985) 985.

9. ANDERSON,O.L.
   Physical Acoustics-III p.43,
   (Edited by W.P.Mason) Academic Press, New York, 1965.

10. NARAYANA,K.L. and SWAMY,K.M.
    Material Sci.Eng., **18** (1975) 157.

11. NARAYANA,K.L. and SWAMY,K.M.
    Acoustica **39** (1978) 336.

12. REDDY,P.V., REDDY,M.B., MULEY,V.N., REDDY,K.B. and RAMANA,Y.V.
    J.Mater.Sci.Lett. **7** (1988) 1243.

**SECOND INTERNATIONAL CONGRESS ON
RECENT DEVELOPMENTS IN AIR- AND
STRUCTURE-BORNE SOUND AND VIBRATION**
MARCH 4-6, 1992 AUBURN UNIVERSITY, USA

OBSERVATION OF ELASTIC WAVE LOCALIZATION

Ling Ye, George Cody, Minyao Zhou, Ping Sheng
Exxon Research & Engineering Co.
Annandale, NJ 08801

Andrew Norris
Department of Mechanical & Aerospace Engineering
Rutgers University
Piscataway, NJ 08855
U. S. A.

ABSTRACT

Spatial localization of bending waves was observed on a steel plate (72"X72"X1") decorated with lucite blocks (3.5"X3.5"X3") arranged in either a periodic or a random array. The exponential decay length of the localized modes was found to be as short as 12 cm at 2.8 kHz, and increased with frequency as $(f_0 - f)^{-1}$, where $f_0 \approx 3.5$ kHz is a quasi-mobility edge. The experimental data and finite-element calculations suggest that the observed localization of bending waves is due to the strong resonant scattering of bending waves by the shear modes of the lucite/steel system. The generic nature of this localization phenomenon suggests its potential use as an attenuation mechanism for bending waves.

The bending wave[1,2] is a special type of wave which propagates only in plates, but which includes both longitudinal and transverse displacements and is dispersive. The bending wave is generated by acoustic waves obeying the full compressional and shear wave equations,[3] but its properties can also be derived by simple mechanical models when the plate thickness is considerably smaller than the bending wavelength. Although the propagation of bending waves in smooth plates has been extensively studied,[4] scientific questions remain about the propagation of bending waves in non-uniform composite plates. Recent experimental data[5] on inhomogeneous steel-refractory, composite walls do not agree with theoretical calculation[6] in either the shape of the transfer function or its spatial dependence. The resolution of this discrepancy was one motivation for this study, another was to explore the possibility of Anderson localization[7] of elastic waves in a two-dimensional system.

The concept of wave localization was first proposed by Anderson[7] in 1958 in the context of electronic transport in disordered materials, and since then the importance of the localization concept in the physics of electronic transport and the metal-insulator transition has been extensively documented[8]. However, Anderson localization has eluded direct observation in electronic systems due to inherent difficulties in mapping electronic wave functions as well as distinguishing Anderson localization from electron-electron interactions and many-body phenomena. The fact that these complexities are absent in classical wave systems is one reason for the current interest in both elastic wave and light localization.[9-11]

The spatial dimensionality of the system is a critical parameter in the study of wave localization. In the Anderson theory, waves in one- or two-dimensional systems exhibit localization for any degree of disorder.[12] In three dimensions, waves can be localized in some frequency regimes but delocalized in others, and the frequency separating the regimes is denoted as the "mobility edge".

The subject of this paper is the first examination of the propagation of bending waves in randomly or periodically inhomogeneous (rough) composite plates. We have discovered a strong resonant scattering of the bending waves which leads to spatial localization of the bending wave over a broad frequency range and where the localization phenomenon exhibits a "quasi-mobility edge" in frequency, characteristic of 3D-localization. This experimental observation confirms both the resonance frequencies and the resonance eigenstates calculated by a finite-element calculation. A 1D modal calculation[13] of reflection coefficient for bending waves reflected by a single block mass with internal resonances also gives a pronounce reflection peak at the block resonance frequency, which supports the measurement results.

The experimental system consists of a 1.83mx1.83mx2.54cm steel plate set on four vibration-isolation supports. Edge reflections have been reduced, but not eliminated, by gluing a glass bar around four sides of the plate and sealing with a flexible viscoelastic damping material[14]. This treatment reduces the edge reflection coefficient for f > 2 kHz to ~0.5, estimated from the quality factor of the plate modes, as displayed in Fig. 1. Two hundred 8.89cm x 8.89cm x 7.62cm lucite blocks are bonded to the steel plate in either a periodic, checkerboard or a random pattern. The contact material is "salol", which has a melting point of 45 C. Due to the poor wetting of salol on steel, even the periodic arrangement of blocks has significant randomness introduced from the steel-lucite contacts. The excitation source used is a force transducer, (B&K 8203) which produces a pulse 0.025-0.04 ms in duration in an area less than 1 mm^2. The frequency content of the pulse is flat within 10% from 0 to 6 kHz. The detector is an accelerometer (B&K 4384), which is magnetically attached to the plate and measures the local vertical acceleration. The highly polished contact surfaces of the accelerometer magnet and the plate shifts any mounting resonance above 25 kHz. The signals from both the force transducer and the accelerometer are analyzed with a Dual Channel Signal Processor (B&K 2032), whose output is the transfer, or Green's, function $H(f) = \langle a(f)^*F(f)\rangle / \langle F(f)^*F(f)\rangle$, where a(f) denotes the Fourier transform of measured acceleration, F(f) is the Fourier transform of the excitation force, * denotes complex conjugation, and the angular brackets denote averaging over repeated excitation-detection measurements under identical conditions. In general, the averaging process reduces both electronic noise and transient signals from edge reflections.

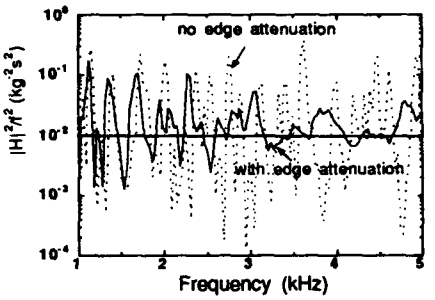

Figure 1.

A comparison of the square of the magnitude of velocity transfer function for the infinite and finite steel plate (d = 2.54cm) with/without edge attenuation. The flat solid line is theoretical calculation for infinite plate using bending wave approximation.

Excitations of an elastic plate[4], of thickness, d, can generally be divided into two frequency regimes — a low frequency range where the propagating modes are two dimensional, and a high frequency range with a three dimensional character. The critical frequency separating these regimes is $C_S/2d$, where C_S is the shear velocity. For the steel plate of d = 2.54cm, f ~ 65 kHz. In the frequency range of interest, 0-6 kHz, while three propagating modes are possible along the plate (longitudinal, transverse and the bending mode) only the bending mode is excited and detected. The wavelength of the dispersive bending wave in meters, λ_B, is given by $\lambda_B = 15.7/\sqrt{f}$ and hence in this frequency range $d << \lambda_B$ as well. Comparison of the experimental spatial intensity distribution of the plate excitation at 1.5 kHz is in excellent agreement with calculation[15] (a changed boundary condition is used) including the separation between intensity maxima of 39 cm.

Figure 2 displays the frequency spectrum of the square magnitude of the velocity transfer function for the composite system with the lucite blocks arranged in a checkerboard pattern. Excitation and detection are along lines parallel to the edge of the plate and separated by a distance of 160cm. There are three frequency regimes in Fig. 2: (1), for $f < 2$ kHz, the response is characterized by numerous sharp resonance peaks of the modes of the plate; (2), for $f > 3.5$ kHz, there is a broad frequency response with broadened modal peaks due to damping of edge reflections; (3), for 2 kHz $< f < 3.5$ kHz, the square of the magnitude of the velocity transfer function is roughly three orders of magnitude smaller (basically indistinguishable from noise) from the response in the other two regimes. In this gap regime λ_B is of the order of two to four lucite blocks. The same frequency gap is found when the source-detector lines are rotated 45°, which indicates the gap is isotropic, and is not due to the Brillouin zone effects.

Figure 2.

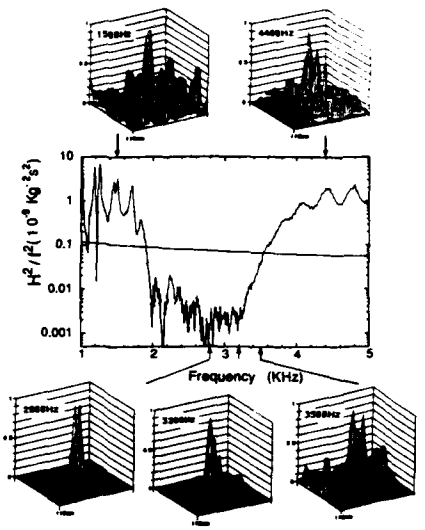

The square of the displacement velocity transfer function, expressed as $|H|^2(f)/f^2$, for the line source-line detector configuration at a separation of 160 cm. Two hundred lucite blocks are glued on the steel plate in a checkerboard pattern. The spatial dependence of $|H|^2(f)/f^2$ at five different frequencies are mapped at a fine mesh of detector locations by using a fixed point source. Localization is clearly seen in the frequency gap extending from 2 kHz to 3.5 kH.

The spatial intensity distributions of the velocity transfer function at five different frequencies are also shown in Figure 2. The spatial distributions were mapped with a fine mesh of detector locations for excitation at a fixed point on the plate. For $f = 1.5$ kHz and $f = 4.4$ kHz, the spatial modes are essentially identical to those of the bare steel plate. In contrast, for the gap regime the responses are localized, and characterized by high peaks for each frequency with a rapid decay. The position of the peak is independent of the source position as long as the source remains inside the spatial domain where the mode has significant amplitude, with an exponential decay of the envelope. At 2.8 kHz, the decay length is as small as 12 cm, of the order of the lucite block diagonal. This surprisingly small localization length, 40% of λ_B at 2.8 kHz, can only be understood on the basis of a strong interaction between lucite blocks and the steel plate which has completely altered the character of the bending wave. Indeed, the excitation of the plate outside the localized domain exhibits a "quiescent state" which is characterized by both vertical and horizontal displacements (as measured by detectors placed on the sides of the lucite blocks) falling below background and system noise.

Figure 3.

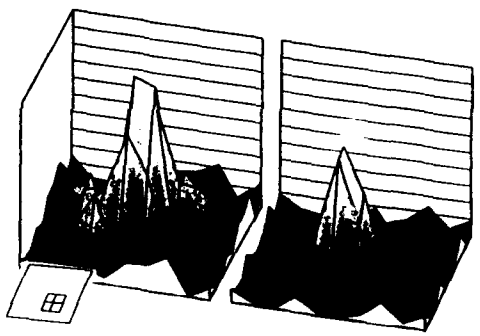

The spatial dependence of $|H|^2(f)/f^2$ at the frequency of 2.8 kHz measured from the center area (80cm x 80cm) of the steel plate, which shows the spatial orthogonality property of the localized mode. The left was measured with the point source located in the center of the plate which has four lucite blocks bonded to it, as indicated by the caption at left corner. The spatial dependence of $|H|^2(f)/f^2$ at the right was measured as the point source located in the center of sixteen blocks bonded on the plate.

Localized modes should be insensitive to the conditions outside the localization length. This hypothesis was verified in a separate experiment by removing successive layers from a square array of two hundred lucite blocks centered at the intensity peak of the spatially localized mode. It is found that the mode at f = 2.8 kHz does not alter its configuration up to the removal of the third layer of 6x6 blocks from the center. Placing the source on the steel plate outside the third layer does not excite the localized mode, as expected from the spatial orthogonality property of a localized mode. Spatial orthogonality of this mode is also strikingly illustrated by the fact that the excitation spreads around the domain of the localized state, leaving it an island of quietitude, as shown in the left of Fig. 3. However, with the removal of the third layer the intensity peak drops abruptly (by 40%), together with the appearance of plate response everywhere on the plate, which is indicated on the right part in Fig. 3. This last observation confirms that the localization is not due to local dissipation (within the blocks or at the contact area) because dissipation is local in nature, and thus can not be the cause of the observed large non-local effect.

Figure 4.

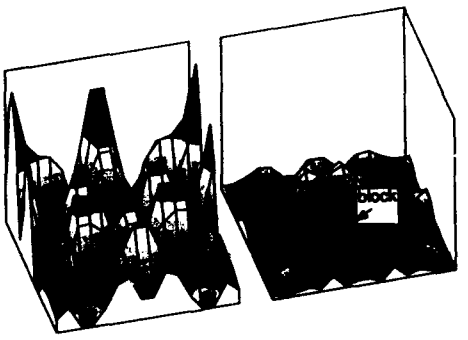

The left: the bare plate mode at 2.8 kHz. The right: the square of the difference of the spatial velocity transfer function with/without a single lucite block bonded on the center of the steel plate for f = 2.8 kHz, which shows the effect of a bonded lucite block to the bending wave at the block resonant frequency range. The plate was excited by a point source located near the edge of the plate, and the spatial dependence of the velocity transfer function was mapped with a fine mesh of detector locations.

Indeed, no localization can be found for a single block where multiple scattering is absent. Figure 4 displays the effect of bending wave scattered by a single lucite block bonded on the steel plate. The spatial difference of the intensity distribution of the velocity transfer function at 2.8 kHz with/without the lucite block is plotted on the right of Fig. 4, and a comparison is made by the bare plate mode at 2.8 kHz shown at the left.

Figure 5.

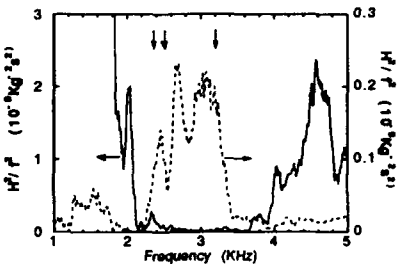

The solid line denotes the square of the displacement velocity transfer function, $|H|^2(f)/f^2$, for point source point detector configuration with a separation of 160 cm. The dashed line denotes the square of the displacement velocity transfer function when the source is present on the steel plate and the detector is attached to the side of a lucite block with a separation between the source and the detector 80 cm. The three peaks delineated by the dashed line represent resonance modes of the lucite block. The vertical arrows indicate the frequency positions of finite element calculation of block shear resonances.

Measurements were repeated for a random arrangement of lucite blocks in a square array. A point source/point detector configuration was used. As shown in Fig. 5, the velocity transfer function exhibits a frequency gap between 2 kHz and 3.5 kHz. Figure 5 also shows the frequency response of a lucite block bonded on the steel plate with an accelerometer attached on the side of the block.

We draw several conclusions from both Fig. 2 and Fig. 5. First, coherent scattering due to periodic mass-loading is not the source of the observed frequency gap between 2 kHz and 3.5 kHz. Finite element calculations for an infinite steel plate of uniform d = 2.54 cm thickness, where the mass of the lucite blocks is modeled as a periodic modulation of density, show that the induced gap in the

velocity transfer function is smaller than 100 Hz, and also strongly dependent on direction, with its center frequency varying from ~2 kHZ in {10} direction to ~4 kHz in {11} direction. The superimposed power spectrum of the shear response of the lucite block coincides precisely with the gap and indicates that strong resonant coupling of bending waves to a lucite/plate shear mode is responsible for the observed frequency gap of Fig. 2 (and Fig.5.) The role of resonant scattering in enhancing localization has been predicted by numerous theoretical calculations[12,16] and Fig. 5 strongly supports this view.

Figure 6.

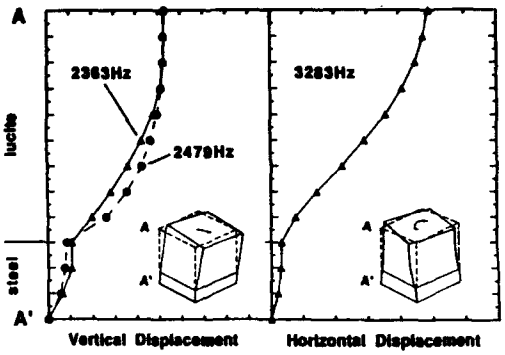

The configurations of three shear resonance modes calculated by the finite element method. For f = 2.36 and 2.48 kHz, the dominant motion is represented by the relative shear of the upper lucite block surface relative to the steel plate along the diagonal direction, accompanied by a slight relative vertical shift of the two corners. One of these two degenerate, purely shear, modes has motion along the {10} direction, and the other along the {01} direction. The vertical displacement is plotted, in arbitrary units, along the line AA'. The configuration of the higher frequency mode at 3.28 kHz clearly indicates it as a torsional mode.

To explore the effect of resonance scattering in enhancing localization, a finite element calculation was carried out by dividing a single lucite block into 8x8x9 elements, with traction-free boundary conditions on five sides and the sixth, 8.89cm x 8.89cm, side joined on to a 8.89cm x 8.89xm x 2.54cm steel plate, with the bottom of the steel plate fixed at four corners. The steel plate is divided into 8x8x3 elements. The three lowest vibrational eigenstates obtained have the character of shear and torsional resonances with the frequencies of 2.36, 2.48 and 3.28 kHz, as indicated by the arrows in Fig. 5. These modes are separated by more than 1 kHz from the next higher resonance mode and span the observed frequency gap between 2 and 3.5 kHz. The configuration of the three shear resonance modes are plotted in Fig. 6. It is seen that whereas the two lower-frequency modes involve the relative shear of the upper block surface with respect to the bottom in the diagonal directions, the higher-frequency mode is torsional in character. Since for a given displacement the relative shear in these modes should increase as the block height is decreased, it is expected that the restoring force, and hence the resonance frequency, should vary inversely with the block height. A check with both the measurement of shear resonances for a single block bonded on the steel plate and the finite-element calculation show this is indeed the case.

Figure 7.

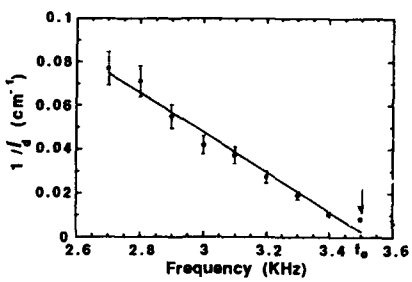

The inverse exponential decay length, $1/l_d$, for the amplitude plotted as a function of frequency. The decay length is measured by the line-source-line detector configuration through the variation of the source-detector separation. The solid line is linear fit by $l_d^{-1} = 0.09(f-f_0)$, where $f_0 = 3.5$ kHz, f is in units of kHz, and l_d is in units of cm.

The transition between the localized and the more extended states of the lucite block and steel plate system is also of theoretical interest.[17-19] In two dimensions, waves of every frequency are localized in the presence of any disorder, and there can not be a true mobility edge. Nevertheless, it has been conjectured that there could be "quasi mobility edge(s)" in a two-dimensional disordered system[17,18,20] which separate strongly localized states from those whose localization lengths may be transcendentally large or

even power-law localized instead of exponentially localized.

We have measured the exponential decay length of the intensity as a function of frequency in both source-detector configurations, and found it to increase rapidly as the edge of the frequency gap is approached. In Fig. 7, the inverse of the measured amplitude decay length, $1/l_d$, is plotted as a function of frequency. A linear relationship is seen up to $l_d \approx 100$ cm, which is about half the size of the total system. A linear fit to the data yield $l_d \approx 11(f_0-f)^{-1}$ cm, where f and f_0 are expressed in kHz, and $f_0 \approx 3.5$ kHz. This behavior is suggestive of a "quasi mobility edge" at $f = f_0$. Due to the finite size of the system, the true nature of the states for $f > f_0$, and whether they are power-law or exponentially localized, is impossible to determine in this experiment.

In conclusion, we have observed the first spatial localization of bending waves in a composite system over the relatively broad frequency range from 2 - 3.5 kHz. The physical mechanism for the localization is resonant scattering of bending waves by three shear resonances of the coupled lucite block/plate system. The minimum attenuation length is 12 cm, which is in the order of a block diagonal and about 40% of the wavelength of the bending wave. The significant attenuation of bending waves by the relatively light mass suggests that the mechanism may have practical applications for broad band attenuation of solid borne sound in structures.

The authors are grateful to G. V. Storch and D. J. Goldfarb for their technical support, and to P. K. Dixon for the helpful suggestion of using "salol" as bonding material.

REFERENCES

[1]. L. Rayleigh, Proc. Lond. Math. Soc. **17,** 4 (1887).
[2]. H. Lamb, Phil. Trans. R. Soc. **A203**, 1 (1904).
[3]. L. Cremer and M. Heckl, Structure-Borne Sound (Spring-Verlag, Berlin, 1988).
[4]. R. L. Weaver and Y. H. Pao, J. Appl. Mech. **49**, 821 (1982).
[5]. George Cody, to be published.
[6]. Andrew Norris, to be published.
[7]. P. W. Anderson, Phys. Rev. 109, 1492 (1958).
[8]. P. A. Lee and T. V. Ramakrishnan, Rev. Mod. Phys. **51**, 287 (1985).
[9]. S. He and J. D. Maynard, Phys. Rev. Lett. **37**, 3171 (1986).
[10]. R. L. Weaver, Wave Motion, **12**, 129 (1990).
[11]. For light localization, see B. Levi in Search & Discovery, Physics Today, 17, June 1991, and references therein.
[12]. P. Sheng, Ed., Scattering and Localization of Classical Waves in Random Media (World Scientific Publishing Co., Singapore, 1990).
[13]. Andrew Norris, ASA fall meeting, Houston (1991).
[14]. They are manufactured by SoundCoat as product GP-3.
[15]. L. D. Landau and E. M. Lifshitz, Theory of Elasticity, 3rd Edition (Pergamon Press, 1986), p.103. Also, see G. B. Warburton, The Dynamical Behaviour of Structures, 2rd Edition (Pergamon Press, 1976).
[16]. P. Sheng and Z. Q. Zhang, Phys. Rev. Lett. **57**, 1879 (1986).
[17]. Y. Meir, A. Aharony and A. B. Harris, Europhys. Lett. **10**, 275 (1989).
[18]. M. Kaveh, Phil. Mag. **B52,** 521 (1985).
[19]. C. M. Soukoulis and G. S. Grest, Phys. Rev. B**44,** 4685 (1991).
[20].The Koslowski and W. von Niessen, Phys. Rev. B**42,** 10342 (1990).

SECOND INTERNATIONAL CONGRESS ON
RECENT DEVELOPMENTS IN AIR- AND
STRUCTURE-BORNE SOUND AND VIBRATION
MARCH 4-6, 1992 AUBURN UNIVERSITY USA

FREE FIELD MEASUREMENT AT HIGH FREQUENCIES OF THE IMPEDANCE OF POROUS LAYER

Jean F. Allard, Denis Lafarge
Laboratoire d'Acoustique - URA 1101 CNRS
Université du Maine - Avenue Olivier Messiaen
BP 535 - 72017 Le Mans Cedex
France

ABSTRACT

A method of measuring the surface impedance in a free field is presented. New measurements at frequencies up to 10 kHz are compared with predictions obtained by the use of the characteristic dimensions.

INTRODUCTION

The Kundt tube method cannot be used at oblique incidence and offers some drawbacks. The high frequency range can be reached only if the tube has a small diameter, and the preparation of homogeneous samples can be difficult for these geometries. A method previously described in Ref. [1] is set out, and the accuracy of the method is verified at high frequencies, in a frequency range where the acoustical properties of the studied material can be predicted with no adjustable parameters.

THE METHOD

A sketch of the measurement set up is represented in Figure 1.

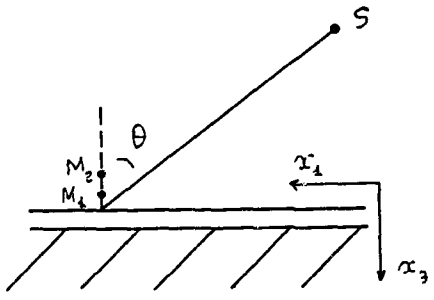

Figure 1 - Free field measurement of the surface impedance

Two small electret microphones are set at M_1 and M_2 above a sample of porous material of several m^2. Typically, M_1 is located 0.5 cm and M_2 1.5 cm from the material. The source S is located several meters from the microphones. If the distance from the source to the microphones, and the area of the material is large enough, the acoustic field around the microphones is not noticeably different from the acoustic field induced by a plane incident wave above a porous layer of infinite lateral dimensions. The angle of incidence is θ. Let p, v_3 and p', v_3' be the pressure and the x_3 component of velocity for the incident and the reflected wave respectively :

$$p(x_1, x_2) = a \exp\left(j(- kx_1 \sin\vartheta - kx_3 \cos\vartheta)\right) \quad , \qquad (1)$$

$$v_3(x_1, x_3) = \frac{a\cos\vartheta}{Z_c} \exp\left(j\ (- kx_1\sin\vartheta - kx_3\cos\vartheta)\right), \qquad (2)$$

$$p'(x_1, x_3) = R(\vartheta)\ a \exp\left(j\left((- kx_1\sin\vartheta - kx_3\cos\vartheta)\right)\right), \qquad (3)$$

$$v'(x_1, x_3) = -R(\vartheta)\ a \frac{\cos\vartheta}{Z_c} \exp\left(j\left((- kx_1\sin\vartheta + kx_3\cos\vartheta)\right)\right), \qquad (4)$$

where k and Z_c are the wave-number and the characteristic impedance in air.

The quantity $R(\vartheta)$ is the reflection coefficient, which can be rewritten :

$$R(\vartheta) = \frac{\exp(j\ kd_1\ \cos\vartheta) - \exp(j\ kd_2\cos\vartheta)\ p(M_1)\ /\ p(M_2)}{\exp(j\ kd_2\ \cos\vartheta)\ p(M_1)/p(M_2) - \exp(-jkd_1\ \cos\vartheta)} \qquad (5)$$

and the surface impedance is given by :

$$Z(\vartheta) = j\ \frac{Z_c}{\cos\vartheta}\ \frac{\sin(kd_1\ \cos\vartheta) - \sin(kd_2\cos\vartheta)\ p(M_1)\ /\ p(M_2)}{\cos(kd_2\ \cos\vartheta)\ p(M_1)/p(M_2) - \cos(kd_1\cos\vartheta)} \ . \qquad (6)$$

As in the case of the Kundt tube, phase and amplitude mismatches between the two signal channels have to be taken into account and a precise relative calibration must be performed.

VALIDATION OF THE METHOD AT HIGH FREQUENCIES

For a porous material having a rigid frame, the propagation constant k_m and the characteristic impedance Z_m of the waves propagating in the material are given by :

$$k_m = \omega \sqrt{\frac{\rho}{K}} \quad , \qquad (7)$$

$$Z_c = \sqrt{\rho K} \qquad (8)$$

where ρ and K are an effective mass which takes into account the viscous forces and the tortuosity, and K is the dynamic bulk modulus of the air in the material. Johnson, Koplik, and Dashen [2] have shown that ρ at high frequencies can be written :

$$\rho = k_s \left[1 + (1-j) \frac{\delta}{\Lambda} \right] , \qquad (9)$$

where δ is the viscous skin depth, k_s the tortuosity, and Λ a characteristic dimension for the viscous forces. In the same way, Champoux and Allard [3] have shown that the bulk modulus K at high frequencies is given by :

$$K = \gamma P_o / \left[\gamma - (\gamma-1) \left[1 - (1-j) \frac{\delta}{B\Lambda'} \right] \right] , \qquad (10)$$

where Λ' is a characteristic dimension for the thermal exchanges between the frame and the air in the porous material, B the square root of the Prandtl number, P_o the atmospheric pressure, and γ the ratio of the specific heats of air, Slightly more complicated expressions of K and ρ are given in Refs. [2] and [3] for the medium frequency range, which present the adequate asymptotic behavior.

$$\rho = k_s \rho_o \left(1 + \frac{\sigma\phi}{j\omega\rho_o k_s} \left(1 + \frac{4jk_s^2 \eta\rho_o\omega}{\sigma^2\Lambda^2\phi^2} \right)^{1/2} \right) , \qquad (11)$$

$$K = \gamma P_o / \left[\gamma - (\gamma-1) \left[1 + \frac{8\eta}{j\Lambda'^2 B^2 \omega\rho_o} \left(1 + j\rho_o \frac{\omega B^2 \Lambda'^2}{16\eta} \right)^{1/2} \right]^{-1} \right] , \qquad (12)$$

where ρ_o and η are the density and the viscosity of air, and σ and ϕ the flow resistivity and the porosity of the material. It was shown by Allard and Champoux [4] that at normal incidence for the case of materials like glass-wools made cup of cylindrical fibers of radius R lying in planar planes, Λ and Λ' were given by

$$\Lambda = 1/(2\pi RL) , \qquad (13)$$

$$\Lambda' = 2\Lambda , \qquad (14)$$

where L is the total length of fibers per unit volume of material. The surface impedance Z was calculated for a glass wool having a tortuosity and a porosity close to one, and σ, Λ, and Λ' equal to :

$$\Lambda = 1.9.10^{-4} m , \qquad \Lambda' = 3,84.10^{-4} m , \qquad \sigma = 9,10^{3} Nm^{-4}s .$$

The surface impedance is given by :

$$Z = -j\, Z_m \operatorname{cotg} k_m e \quad , \qquad (15)$$

where e is the thickness of the material, equal to 10cm , and Z_m, and k_m, are given by Eqs. (9) and (10).

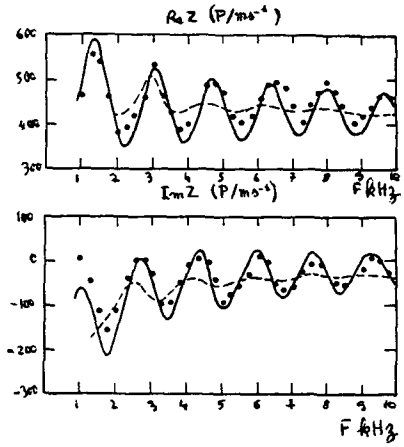

Figure 2 - The surface impedance at normal incidence of a layer of glass wool at high frequencies.
Measurement ●●●
Prediction by Eqs. (11)-(12) ———
Prediction by the empirical laws of Delany and Bazley — — —

The predicted and the measured surface impedances are represented in Figure 2. There is a good agreement between prediction and measurement. It may be noticed that at frequencies higher than 1000 Hz, the measurement can be performed with samll samples of material of area 0.4 x 0.4 m^2.

CONCLUSION

The method presented is very simple, and does not offer the drawbacks of the Kundt tube. It is not destructive, and can be used in situ on small samples of material at high frequencies.

REFERENCES

[1] J.F. Allard, Y. Champoux, "In situ free field measurements of the surface acoustic impedance of materials", Noise Control Engineering Journal 32, 1989,

[2] D.L. Johnson, J. Koplik, R. Dashen, "Theory of dynamic permeability and tortuosity in fluid-saturated porous media", J. Fluid Mech. 176, 379-402.

[3] Y. Champoux, J.F. Allard, "Dynamic tortuosity and bulk modulus in air-saturated porous media", Journal of Applied Physics 70, 1991, 1975-1979.

[4] J.F. Allard, Y. Champoux, "Empirical equations for sound propagation in rigid frame fibrous materials", to be published in J.A.S.A.

SECOND INTERNATIONAL CONGRESS ON
RECENT DEVELOPMENTS IN AIR- AND
STRUCTURE-BORNE SOUND AND VIBRATION
MARCH 4-6, 1992 AUBURN UNIVERSITY, USA

EVALUATION OF A DYNAMIC MECHANICAL APPARATUS

Gilbert F. Lee
Naval Surface Warfare Center
10901 New Hampshire Avenue
Silver Spring, MD 20903-5000
U.S.A.

ABSTRACT

A dynamic mechanical apparatus (Seiko Instruments Model DMS 110) was used to determine complex Young's modulus on a soft elastomeric material (a polyurethane), a rigid plastic (polymethylmethacrylate), and steel. The modulus is determined by bending a beam. The ends of the beam are clamped, while the center of the beam is driven at fixed frequencies between 0.01 and 100 Hz. It was found that the modulus measured on the soft material varied by 50 percent when the clamping pressure was varied by a factor of two. It was also found that the measured modulus varied up to 17 percent over a two hour period even though no changes were made to the instrument. The modulus of the rigid materials did not show as much variation as the soft material. It is concluded that instruments of this type are very sensitive to clamping pressure.

INTRODUCTION

Dynamic mechanical techniques are used to characterize polymeric materials for sound and vibration damping applications. There are many commercial instruments [1] as well as apparatus that were developed in laboratories [2] but are not sold commercially. Round robin testing [3] comparing many of these instruments has shown that data from these instruments can differ from each other and that extreme care must be taken in obtaining accurate results. In many applications, accurate measurements are needed in order to predict the damping performance of a polymeric material in a designed structure. In order to determine the accuracy and precision of a new instrument, it is necessary to make measurements under carefully controlled conditions.

A dynamic mechanical apparatus (Seiko Instruments Model DMS 110) was evaluated. This paper will briefly describe the apparatus, present the results on three different materials, discuss the effect of clamping pressure on the measurements, and determine the accuracy and precision of the apparatus.

EXPERIMENTAL

The dynamic mechanical apparatus (Seiko Instruments Model DMS 110)

uses a forced vibration nonresonant method. The complex modulus is determined from the amplitude and phase difference between the applied sinusoidal force and the strain induced in the sample. The apparatus can be operated in a temperature range from -150 to 500°C and at 13 discrete frequencies between 0.01 to 100 Hz. A computer is used to automate the measurements and analysis. A special function key is provided on the computer keyboard, which allows a quick determination of the modulus at one frequency as opposed to using a programmed measurement. This function key was used in most of the measurements reported here. A flexural test fixture is provided to determine the complex Young's modulus, while a shear test fixture is provided to obtain complex shear modulus. The complex Young's modulus is defined as $Y^* = Y' + iY''$, where Y' is the real part or storage modulus, Y'' is the imaginary part or loss modulus, and $i^2 = -1$. The loss factor is defined as Y''/Y'. The shear modulus can be also defined in a similar manner as the Young's modulus. In this paper, the storage modulus will be referred to as Young's modulus.

Measurements were made using only the flexural test fixture, while the shear test fixture was not used. Using the flexural test fixture, the ends and the center of the sample are clamped as shown in Figure 1. The center of the sample is mechanically driven. The clamping pressure is adjusted by tightening the screws on the clamps. The instruction manual did not give any recommendation on this pressure. It was found, as will be discussed later in more detail, that the measured modulus is dependent on the applied clamping pressure. For the measurements made here, a torque screwdriver was used to apply a known clamping pressure. The same torque value was used on each clamp.

For this test fixture, the manufacturer's specifications state that materials with modulus between 10^{-1} and 10^{6} MPa can be tested. Three materials were selected to cover this range of modulus values. A soft elastomeric material (polyurethane) was chosen for the low end of the recommended range, a rigid plastic (polymethylmethacrylate PMMA) was chosen for the middle of the range, and steel was chosen for the high end of the range.

Three types of measurements were made. In the first measurement, Young's modulus was measured as a function of time at 23°C and 1 Hz using torque values ranging from 0.014 to 0.71 N-m for the three materials. For the polyurethane, torque values in the low end of this range were used because at values greater than 0.14 N-m the sample was noticeably deformed by the clamps. For PMMA, higher torque values (0.07 to 0.56 N-m) were used. For steel, the highest values were used (0.14 to 0.71 N-m). A procedure was devised such that only one sample of each material was used. This procedure was the following: 1) a sample was clamped in the fixture starting with the lowest torque value to be tested, 2) Young's modulus was measured as a function of time, using the function key, for at least one hour, 3) on the same sample, the clamping pressure was increased to the next higher torque value and step 2 was repeated, 4) step 3 was repeated up to the highest torque value.

In the second measurement, Young's modulus and loss factor were determined as a function of temperature from 23 to 180°C at a programmed heating rate of 1°C/min on two PMMA samples using two different torque values. These measurements were made at a frequency of 1 Hz. These measurements were in the program mode, not using the function key.

In the third measurement, Young's modulus was determined as a function of sample thickness (0.20, 0.25, 0.38, and 0.52 mm) at 23°C, 1 Hz, and a torque value of 0.35 N-m for steel. The function key was also used in this measurement.

The length and width of the polyurethane and PMMA test samples were nominally 50 mm long and 10 mm wide. The length of the steel samples was 76 mm with a width of 10 mm. The distance between either end clamp and the center clamp is 10 mm. Thus, the total length between the clamps was 20 mm, which was used in the determination of modulus and loss factor. The thickness for the polyurethane samples was about 2 mm and for PMMA was

about 1.5 mm. The steel thickness was already mentioned above.

RESULTS AND DISCUSSION

Young's modulus versus time for the polyurethane is shown Figure 2 for two different torque values at 1 Hz and 23°C. The modulus near time zero (about 30 seconds of elapsed time) is about seven percent lower than the modulus after two hours at a torque value of 0.07 N-m. Increasing the torque by a factor of two, the modulus curve at 0.14 N-m is about 50 percent lower than the curve at 0.07 N-m. Also the initial modulus is about 17 percent less than the modulus after two hours at 0.14 N-m. The change in modulus as a function of time is unexpected, since no adjustments were made to the instrument at any time during the measurement. It is believed that the sample is creeping in the clamps. The clamping pressure is decreasing with time, which, as shown below, leads to an increase in the modulus.

To illustrate this point, Young's modulus for the polyurethane is plotted as a function of torque at 1 Hz, 23°C, and for a given time of 5 minutes in Figure 3. A smooth curve is drawn through the data points. Interpolating between the data points, the modulus increases with decreasing torque for the two torque values of 0.07 and 0.14 N-m. A broad maximum occurs at a torque value of about 0.028 N-m with a modulus value of 52 MPa. The lowest modulus value is about 32 MPa at 0.14 N-m. The difference between the highest and lowest value of the modulus is about 62 percent.

An independent measurement of the modulus was made using the well established resonance apparatus [2,4]. The operating principle of the resonance apparatus is based on producing resonances in a bar test sample. Measurements are made over 1.5 decades of frequency in the kHz region. For the polyurethane, measurements were made over a temperature range of 15 to 70°C. Time-temperature superposition [5] was used to extend the data to frequencies lower than actually measured. The resulting modulus from the resonance apparatus is 33 MPa at 30 Hz and room temperature. As shown in Figure 2, this modulus is in the middle of the range of values found in the Seiko instrument at 1 Hz as a function of time for a torque of 0.14 N-m. For a torque of 0.07 N-m, the Seiko value is higher than the resonance value by 50 percent. It was found by measuring two different polyurethane samples that the precision of the Seiko measurements is about ±5 percent for a given torque value.

Young's modulus versus time curves at 1 Hz, 23°C, and four different torque values (0.07, 0.14, 0.35, and 0.56 N-m) for PMMA are shown in Figure 4. The modulus increases with increasing time, similar to the polyurethane. However the difference between the initial modulus (30 seconds of elapsed time) and the modulus after 1 hour is on average 5 percent, which is a smaller increase than for the polyurethane. It is possible to measure a modulus as low as 3 GPa (0.07 N-m) and as high as 4.9 GPa (0.56 N-m), which is 60 percent difference. Nielsen [6] has reported a shear modulus determined by torsional pendulum on PMMA to be 1.1 GPa at room temperature. To convert shear modulus to Young's modulus, the Poisson's ratio must be known. Using estimates of Poisson's ratio between 0.35 and 0.5, the estimated Young's modulus values are between 2.9 and 3.3 GPa. From these estimated modulus values, the torque value one would use with PMMA is 0.07 N-m. It was found by measuring two different PMMA samples that the modulus is reproducible to within ±1 percent for a given torque value. The agreement may be fortuitous, since the comparison was done only at room temperature. It is possible that the clamping pressure may change with temperature due to the difference between the thermal expansion of the sample and clamps. Then it may be difficult to separate the effects of clamping pressure and temperature on the modulus.

To illustrate the effects of temperature and clamping pressure on modulus and loss factor, two PMMA samples were measured as a function of temperature at two different torque values. Data for the first sample was

obtained using a torque value of 0.35 N-m. The results are shown in Figure 5. Data for the second sample was obtained by a different operator with an unspecified torque. A comparison of the two measurements will demonstrate the variability of results between two users. The percent difference in Young's modulus and loss factor between the two measurements is shown in Table 1 at six different temperatures. The first three temperatures (22.8, 46.5, and 74.7°C) are in the glassy region of PMMA, the next two higher temperatures (102 and 126°C) are in the region of the glass transition, and the final temperature (158°C) is in the melt region. The differences are large in the glassy region, the smallest in the glass transition, and becoming large again in the melt region.

Table 1: Percent Difference in Young's Modulus and Loss Factor Between Two Measurements on PMMA as a Function of Temperature

TEMPERATURE (°C)	PERCENT DIFFERENCE IN YOUNG'S MODULUS	PERCENT DIFFERENCE IN LOSS FACTOR
22.8	27	-14
46.5	27	-23
74.6	18	-18
102	4	6
126	5	2
158	-8	-3

Young's modulus for steel at 1 Hz and 23°C increases with increasing time for a given torque value, but the increase is only about 2 percent (Figure 6). A range of modulus values (216 to 246 GPa) can be obtained depending on the torque values (0.14 to 0.71 N-m) used. From the literature [7], a value of Young's modulus was found to be 207 GPa, which is within 4 percent of the lowest value measured here. It was found that the modulus can be reproduced to within ±1 percent for a given torque value.

Young's modulus at 0.35 N-m deceases with increasing steel thickness as shown in Figure 6. The lowest modulus value for a thickness of 0.52 mm is 139 GPa and the highest modulus value for a thickness of 0.20 mm is 232 GPa.

CONCLUSIONS

A dynamic mechanical apparatus (Seiko Instruments DMS 110) was evaluated to determine the effects of clamping pressure, temperature, and sample thickness on Young's modulus and loss factor. Measurements were made on three materials: a soft polyurethane, rigid PMMA, and steel. Based on these measurements, the following conclusions were reached:

- Young's modulus increases with time when the samples are clamped in the flexural test fixture. Young's modulus increases by as much as 17 percent for the polyurethane, 5 percent for PMMA, and 2 percent for the steel.

- Young's modulus is dependent on the torque used in clamping the sample. For polyurethane, the modulus is 32 MPa at a high torque value of 0.14 N-m. However, at a low torque value of 0.028 N-m, the modulus is 52 MPa. For PMMA, the modulus varies from 3.0 to 4.9 GPa using torque values ranging from 0.07 to 0.56 N-m. For steel, the modulus varies 216 to 246 GPa for torque values ranging from 0.14 to 0.71 N-m.

● The effect of clamping pressure and temperature on the modulus and loss factor was determined by comparing measurements made on two PMMA samples. Differences of 27 percent in modulus and 18 percent in loss factor were found at temperatures in the glassy region. Differences of 5 percent in modulus and 4 percent in loss factor were found in glass transition region. In the melt region, differences of 8 percent in modulus and 3 percent in loss factor were found.

● Young's modulus deceases with increasing steel thickness at a torque of 0.35 N-m. For a thickness of 0.20 mm, the modulus is 232 GPa and for a thickness of 0.52 mm, the modulus is 139 GPa.

● The precision is about ±5 percent for polyurethane and ±1 percent for PMMA and steel. The accuracy depends on the clamping pressure used.

REFERENCES

1. Read, B. E., G. D. Dean, and J. C. Duncan, Physical Methods of Chemistry, vol. VII, Rossiter, B. W. and R. C. Baetzold, eds., John Wiley & Sons, Inc.: New York, 2nd ed., ch. 1, 1991.
2. Dlubac, J. J., G. F. Lee, J. V. Duffy, R. J. Deigan, and J. D. Lee, Sound and Vibration Damping with Polymers, Corsaro, R. D. and L. H. Sperling, eds., American Chemical Society Symposium Series 424, ch. 3, 1990.
3. Jones, D. I. G., Proceedings of Damping '91, WL-TR-91-3078, vol. II, 1991.
4. Madigosky, W. M. and G. F. Lee, J. Acoust. Soc. Am., 1983, 73, 1374-1377.
5. Ferry, J. D., Viscoelastic Properties of Polymers, 3rd ed.; John Wiley and Sons, Inc.: New York, 1980.

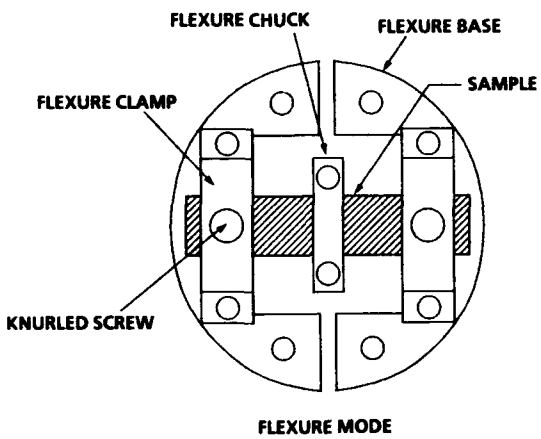

Fig. 1: Flexural Test Fixture

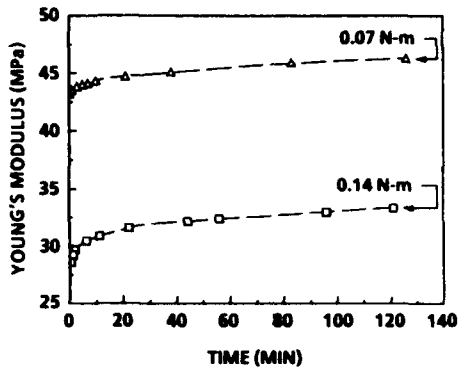

Fig. 2: Young's Modulus vs Time at 1 Hz and 23°C for Two Torque Values for Polyurethane

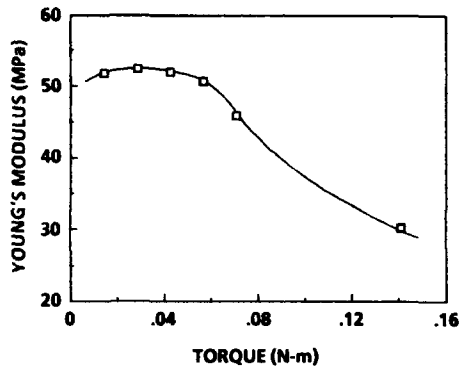

Fig. 3: Young's Modulus vs Torque at 1 Hz and 23°C for Polyurethane (5 Minute Values)

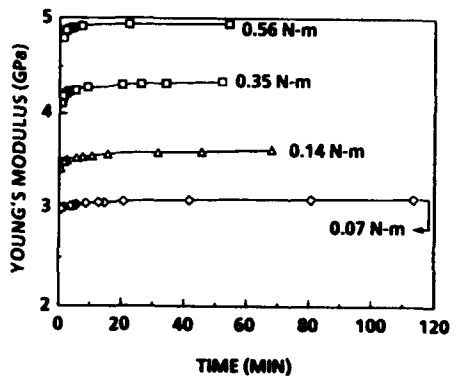

Fig. 4: Young's Modulus vs Time at 1 Hz and 23°C for Four Torque Values for PMMA

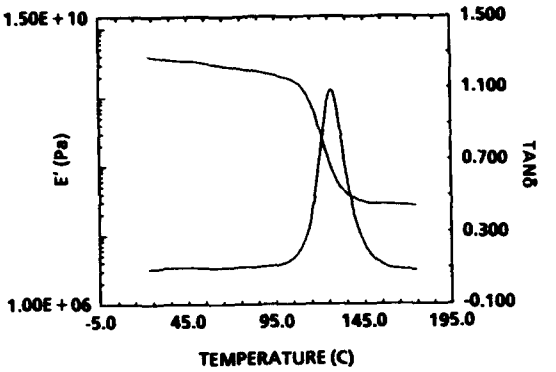

Fig. 5: Young's Modulus and Loss Factor vs Temperature For PMMA at 1 Hz

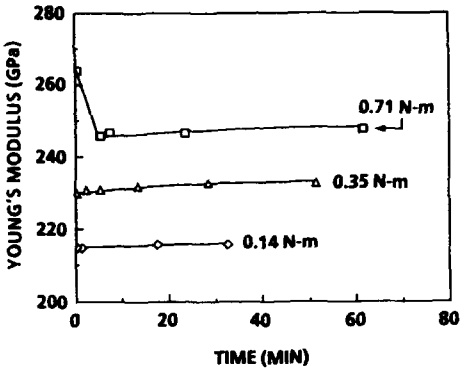

Fig. 7: Young's Modulus vs Thickness at 1 Hz, 23°C, and a Torque of 0.35 N-m for Steel

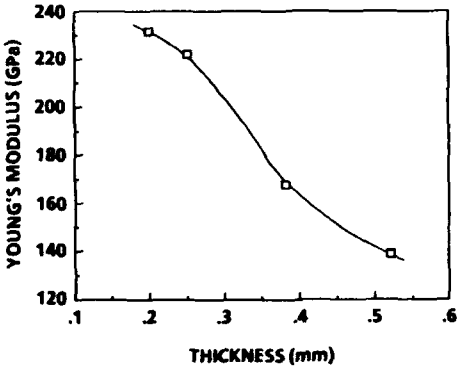

Fig. 6: Young's Modulus vs Time at 1 Hz and 23°C for Three Torque Values for Steel

SECOND INTERNATIONAL CONGRESS ON
RECENT DEVELOPMENTS IN AIR- AND
STRUCTURE-BORNE SOUND AND VIBRATION
MARCH 4-6, 1992 AUBURN UNIVERSITY, USA

Determining the Amplitude of Propagating Waves as a Function of Phase Speed and Arrival Time

J. Adin Mann III
Dept. of Aerospace Eng. & Eng. Mechanics
Iowa State University
Ames, Iowa 50011

Earl G. Williams
Code 5137
Naval Research Laboratory
Washington, D.C. 20375-5000

ABSTRACT

A method will be presented which calculates the amplitude of waves propagating through a region of a structure as a function of phase speed and time. The processing is carried out on synthetic data which models a one-dimensional wave incident on a boundary with subsequent reflected and transmitted waves. Both dispersive, non-dispersive, and frequency band limited waves are investigated. Results show successful determination of reflections coefficients. The process is also applied to measured data from a fluid-loaded, point-driven, finite cylindrical shell. There are many waves propagating in the shell that the filtering techniques help to distinguish and quantify. The results allow experimental estimations of the reflection coefficients of waves incident on the shell ends.

INTRODUCTION

The filtering technique outlined here determines the amplitude of a wave propagating with a specified phase speed and frequency. Similar work is abundant in the seismology literature [1-6] and in the tomography literature [7]. The emphasis in the seismology literature is to determine the group speed of waves propagating in the earth crust. The analysis used in such studies is equally valuable for applications of studying wave propagation in vibrating structures. This is especially true for waves with a finite time duration.

The application that this paper addresses is waves propagating in cylindrical shells. The broad goal of such work is to study the characteristics of waves propagating in a structure so that the modeling of the phenomena can be simplified. The specific end result we are working for in this paper is a technique to experimentally estimate the reflection coefficient at discontinuities in the shell. The results from the filtering techniques described here are for one-dimensional propagation.

FILTERING THEORY

Consider a wave of frequency ω_1 propagating at the speed c_{p1}. This wave will have the form

$$u(t,x) = \cos[\omega_1(t-(x/c_{p1})) + \phi_1] \tag{1}$$

where ϕ_1 is the phase of the wave. The filter we use is

$$W(t,x,\omega_2,c_{p2}) = \begin{cases} \cos[\omega_2(t-(x/c_{p2})) + \phi_2] & t_1<t<t_2 \quad x_1<x<x_2 \\ 0 & \text{else} \end{cases} \tag{2}$$

where ω_2 is the frequency, c_{p2} is the phase speed and ϕ_2 is the phase of the wave the filter is searching for. The filtering procedure involves multiplying the field (Eq. 1) by the filter (Eq. 2) and integrating over space and time.

$$A(\omega_2,c_{p2},t',x') = \int_{-\infty}^{\infty}\int_{-\infty}^{\infty} u(t,x)W(t,x,\omega_2,c_{p2})\ dXdT \tag{3}$$

where $t' = (t_2+t_1)/2$ and $x' = (x_2+x_1)/2$. This integral will give the largest value when $\omega_1 = \omega_2$, $c_{p1} = c_{p2}$, and $\phi_1 = \phi_2$. If there are several waves propagating at several frequencies and phase speeds this filter can be used to distinguish between the different waves.

The filter is centered at a time t' and position x'. We can then view the result of the filtering to give the wave amplitude propagating through a region centered at the point x' at time t'. If the filter is small ($X = x_2-x_1$ and $T = t_2-t_1$ are small) the results begin to give the amplitude of waves propagating through the point. This is important if we are going to use the filtering results to track waves as they propagate and interact with boundaries or other material discontinuities.

The results presented here come from centering the filter at one spatial position and varying the time t' (the filter center) and the phase speed c_{p2} of the filter. The result is the amplitude of waves propagating through a small area as a function of time and phase speed. We refer to plots of this data as phase speed vs. time plots or cp-t plots. The time at which waves arrive or leave a point and the phase speed at which they are propagating can be determined from the resulting data. At boundaries or discontinuities this information can be used to determine reflection coefficients.

K-SPACE VIEW

The effect of the filter size and the way in which the filter works can best be seen in wavenumber-frequency space (k-ω space) The filtering process (Eq. 3) in k-ω space is

$$A(\omega_2,c_{p2}\omega',k') = \int_{-\infty}^{\infty}\int_{-\infty}^{\infty} U(\omega,k)W(\omega,k,\omega_2,c_{p2})\ dk\ dw \tag{4}$$

where U(ω,k) is the two-dimensional Fourier transform of the surface velocity u(t,x). The filter in k-ω space is

$$W(\omega,k,\omega_2,c_{p2}) = 8XT\left[\frac{\sin[T(\omega_2-\omega)]}{T(\omega_2+\omega)}\ \frac{\sin[X(\omega_2/c_{p2}-k)]}{X(\omega_2/c_{p2}-k)} + \frac{\sin[T(\omega_2+\omega)]}{T(\omega_2+\omega)}\ \frac{\sin[X(\omega_2/c_{p2}+k)]}{X(\omega_2/c_{p2}+k)}\right] \tag{5}$$

where $X = x_2 - x_1$ and $T = t_2 - t_1$ are the spatial and time width of the filter. The filter is a sinc function centered at the frequency and wavenumber of the filter (ω_2 and ω_2/c_{p2}).

A wave of frequency ω' propagating with the phase speed cp' will be a point in the k-ω space centered at $\omega=\omega'$ and $k=\omega'/cp'$. Thus all the waves propagating in the structure represent a point in the k-ω space spectrum. If the filter is going to distinguish between the various waves then the filter must not have too large of a bandwidth in k-ω space. Equation (5) shows that the larger the filter is in real space and time, the more focused the filter is in k-ω space (the k-ω bandwidth is small). Thus a large filter in real space and in time distinguishes between different wave types more accurately. However, if the filter is too large in real space and time, then we lose the effect of knowing the wave amplitude at a specific point x' and time t'. The following simulations will show how the filter can distinguish between wave types.

SIMULATIONS

All the simulations are of one or two waves incident on a boundary. The boundary has a reflection coefficient of 0.5 and a transmission coefficient of 0.1. In all the simulations a dispersion curve for the waves is used to create the real space and time data (called x-t plots). In one case the full impulse response is used and in the other cases the frequencies will be limited. The frequency limitation is accomplished by filtering the data with a Kaiser-Bessel filter. The Kaiser-Bessel filter has a bandwidth from 7000Hz to 11000Hz and a filter parameter alpha of 7.865. In all the results shown, the phase speed filter is spatially centered at the boundary and the frequency is 9000Hz. The filter size is X = 0.31m and T = 1.24msec.

The first results are for a single wave with a linear dispersion relation. The wave has a phase speed of 400m/s at all frequencies. The x-t plot is shown in Fig. 1a, and Fig. 1b shows the cp-t plot of the right going (incident) waves. We see in Fig. 1a that the phase speed and group speed are the same in this case. Fig. 1b shows that the filter successfully indicates a peak at the correct phase speed and time. With this data we should only have a peak in Fig. 1b at the phase speed and arrival time of our wave. This figure shows how the finite filter size distorts the data.

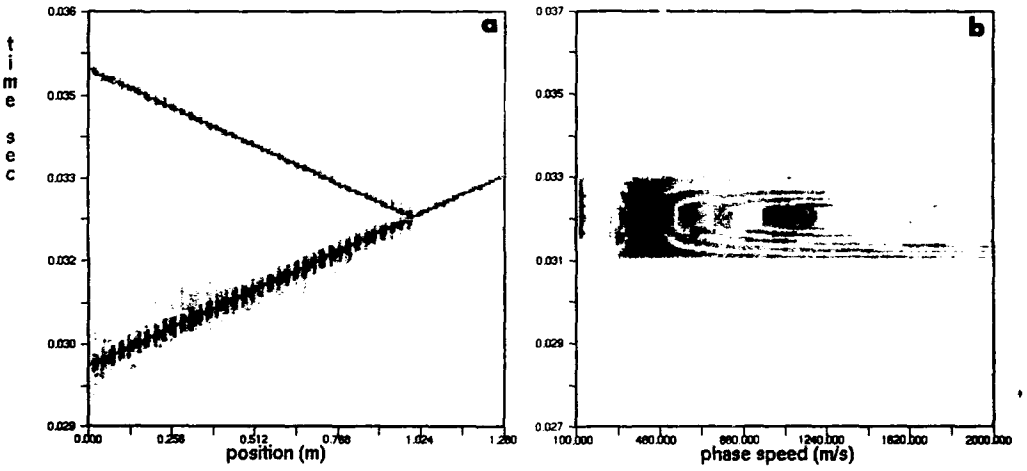

Figure 1. Single non-dispersive wave propagating at 400m/s.
a) real space and time plot
b) phase speed vs. time plot

The next example is a single wave with a dispersion relation that is not a linear function of frequency. The dispersion curve is for a cylindrical bending wave propagating down the axis of a fluid-loaded cylindrical shell. These results have been bandlimited with the Kaiser-Bessel filter. Fig. 2a contains the x-t plot. Note that the wave changes shape as it propagates. Fig. 2b contains the cp-t plot for the right going wave incident on the boundary. These results show more spreading of the peak in the cp-t plot. The peak occurs at the correct phase speed (401.6m/s) and arrival time is 0.029sec.

The final simulation uses two waves. The first is a wave with the same dispersion relation as in the previous example. The second wave is a wave with a linear dispersion relation propagating at 5000m/s at all frequencies. This example is a simulation of a bending wave and a longitudinal wave propagating down a fluid-loaded cylinder. The x-t results are shown in Fig. 3a and the cp-t results are shown in Fig. 3b. Both waves can be seen propagating down the cylinder in Fig. 3a. Figure 3b when compared to Fig. 2b shows that the presence of the fast second wave did not distort the results except for a faint shadow at early times in the cp-t plot (Fig. 3b).

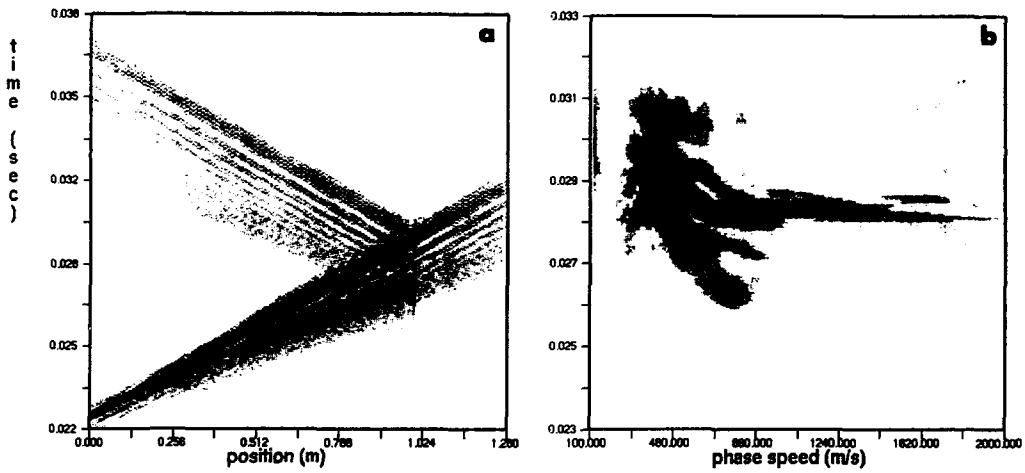

Figure 2. Single dispersive wave. The dispersion curve models a bending wave propagating down a fluid-loaded cylinder.
a) real space and time plot
b) phase speed vs. time plot

We now look at this third simulation in k-ω space to see how the filter can distinguish between the different waves. Figure 4 is the k-ω space plot of the filter and the dispersion curves of the two waves. The filter is represented by the grey scale plot and the dispersion curves are represented by solid lines. The straight line represents the fast (5000m/s) longitudinal wave and the other represents the bending wave. The filter is set for a phase speed of 401.6m/s and a frequency of 9000Hz. We can see that the peak of the filter is centered on the bending wave dispersion curve. But we can also see how the filter has nonzero values at the shear wave dispersion curve and at other frequencies and wavenumbers of the bending wave.

Now use Fig. 4 to consider the case of a filter centered in the frequency range of 2000Hz to 5000Hz. We can see that in this frequency range the filter centered on the bending wave will be greatly influenced by the shear wave dispersion curve, making it more difficult to separate the different wave types. Thus there are some limitations to the filtering technique for separating different wave types if their dispersion curves are close in k-ω space.

Although cp-t plots for the reflected wave (the left going waves) were not shown for any of the examples here they were comparable to the incident wave results.

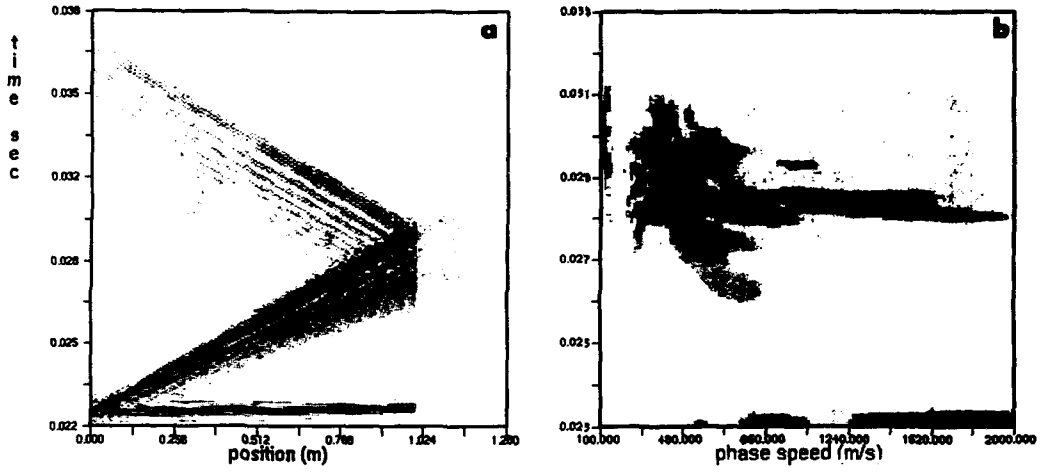

Figure 3. Two waves. The slower wave is the bending wave modeled in Fig. 2 and the *faster wave* is a non-dispersive wave propagating at 5000m/s.
a) real space and time plot
b) phase speed vs. time plot

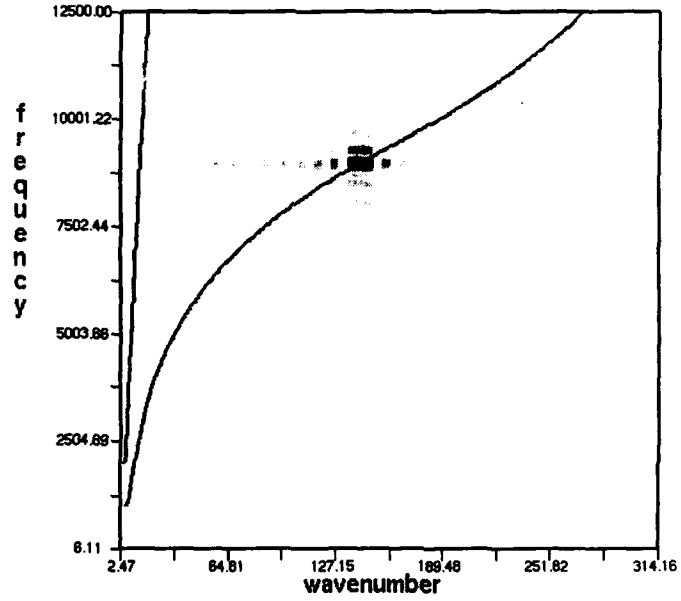

Figure 4. Wavenumber-frequency plot of the two waves from Fig. 3 (the solid lines) superimposed with the filter centered at 9000Hz and 401.6m/s.

ESTIMATING REFLECTION COEFFICIENTS

To calculate the reflection coefficient at a discontinuity we need to know the amplitude and phase of the wave incident on the discontinuity and the resulting reflected wave. The filtering technique demonstrated can be used to separate wave types and directions. Thus we must search for waves of the same phase speed amplitude but opposite in sign. The waves with the positive phase speed propagate to the right and waves with negative phase speed propagate to the left. These correspond to the incident and reflected waves.

In the simulations there is one boundary with a reflection coefficient of 0.5. The results from the third simulation (Fig. 3b) will be used as an example. We begin by looking at the peak in both the incident wave cp-t plot (Fig. 3b) and the reflected wave cp-t plot. For the incident wave the peak occurs at 401.59m/s and a time of 0.029sec and for the reflected wave the peak is at -401.59m/s and a time of 0.03sec. The ratio of the amplitude of the peak values is 0.503. We are, however, interested in the effect of integrating about each peak in the cp-t plots. The cp-t data is integrated over a rectangle centered at the peak. The reflection coefficient is calculated from the ratio of the two integrals. Table 1 gives the value for the calculated reflection coefficient as the integration area is increased.

Table 1. Comparison of the integration area for the estimation of reflection coefficients.

Integration time	Integration Phase Speed	Reflection Coefficient Estimation
0.00	0.0	0.503
0.00008	60.3	0.498
0.00016	120.6	0.493
0.00024	181.0	0.503
0.00030	241.3	0.508
0.00038	301.6	0.510
0.00044	361.0	0.509
0.00052	422.2	0.512
0.00060	482.5	0.518
0.00068	542.9	0.533
0.00074	603.2	0.537
0.00082	663.5	0.538

These results suggest that the most accurate estimate of the reflection coefficient is obtained by integrating over a small area around the peak value. An integration time of 0.00030sec and integration phase speed of 241.3 in this case represents a 9x9 point grid.

EXPERIMENTAL RESULTS

Results from experimental data are shown in Figure 5. These are results from a point-driven fluid-loaded finite shell. The velocity data is obtained from NAH [8], then the wave of zero order in the circumferential direction is used. Thus the data that the filter is applied to are symmetric bending and longitudinal cylindrical waves propagating down the cylinder. The filter is centered at one end of the cylinder. The filter width is 32 out of 128 points along the shell and T = 0.128msec. Figure 5 shows the incident waves. From the simulations we can interpret 4 peaks indicating separate waves incident on the end. From this plot we can determine the time they arrive and their phase speed.

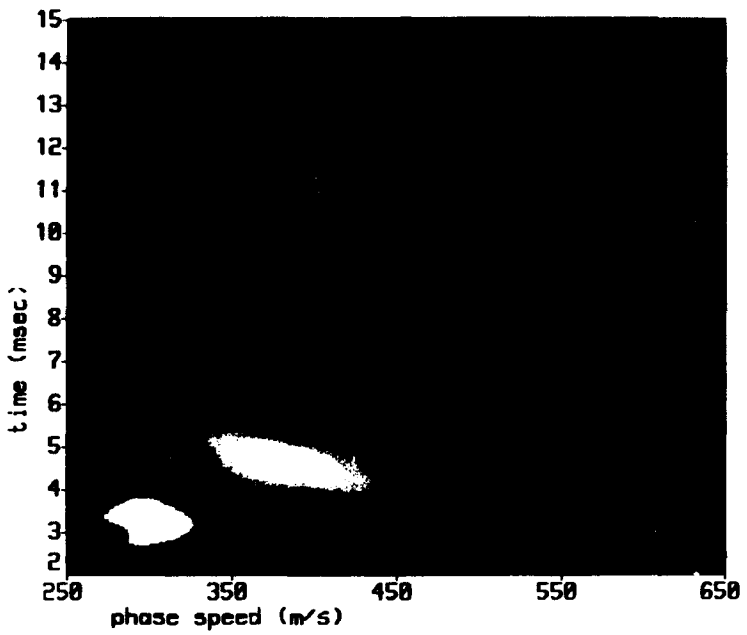

Figure 5. Phase speed vs. time results from experimental data. The filter is centered at one end of a finite fluid-loaded cylinder.

CONCLUSIONS

The simulation results indicate the accuracy that should be expected from the filtering technique. As long as the dispersion curves of different waves are far apart in k-ω space then the different wave types can be distinguished. We have also shown that accurate estimations of reflection coefficients can be obtained from the processing.

ACKNOWLEDGMENTS

This work is supported by a contract with the Office of Naval Research. The first author acknowledges contract support by Dr. Earl Williams and the Naval Research Laboratory.

REFERENCES

1. S. Bloch and A. L. Hales, "New Techniques for the Determination of Surface Wave Phase Velocities," *Bulletin of the Seismological Society of America*, Vol. 58, No. 3, pp. 1021-1034, June 1968.

2. M. Landisman, A. Dziewonski, and Y. Sato, "Recent Improvements in the Analysis of Surface Wave Observations," *Geophys. J. R. Astr. Soc.*, 17, 369-403, 1969.

3. A. Dziewonski, S. Bloch, and M. Landisman, "A Technique for the Analysis of Transient Seismic Signals," *Bulletin of the Seismological Society of America*, Vol. 59, No. 1, pp. 427-444, February, 1969.

4. A. Dziewonski, J. Mills, and S. Bloch, "Residual Dispersion Measurement - A New Method of Surface-Wave Analysis," *Bulletin of the Seismological Society of America*, Vol. 62, No. 1, pp. 129-139, February 1972.

5. H. J. Hwang and B. J. Hitchell, "Interstation Surface Wave Analysis by Frequency Domain Wiener Deconvolution and Modal Isolation," *Bulletin of the Seismological Society of America*, Vol. 76, No. 3, pp. 847-864, June 1986.

6. D. J. Buchanan and P. J. Jackson, "Dispersion Relation Extraction by Multi-Trace Analysis," *Bulletin of the Seismological Society of America*, Vol. 73, No. 2, pp. 391-404, April 1983.

7. Avinash C. Kar and Malcolm Slaney, Principles of Computerized Tomographic Imaging IEEE Press, New York, NY, 1988.

8. E. G. Williams, H. D. Dardy, and K. B. Washburn, "Generalized nearfield acoustical holography for cylindrical geometry: Theory and experiment," *J. Acoust. Soc. Am.*, 81, 389-407, 1987.

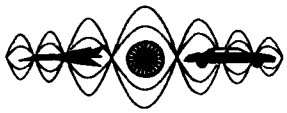

SECOND INTERNATIONAL CONGRESS ON
RECENT DEVELOPMENTS IN AIR- AND
STRUCTURE-BORNE SOUND AND VIBRATION
MARCH 4-6, 1992 AUBURN UNIVERSITY, USA

ISOLATING BUILDINGS FROM VIBRATION

David E Newland
Department of Engineering
University of Cambridge
Trumpington Street
Cambridge CB2 1PZ
England

ABSTRACT

This paper discusses recent calculations and measurements of vibration transmission in buildings as a result of excitation from the ground. The objective is to find a reliable design method for estimating a building's total vibration environment when there is vibration transmission from roads, railways or machinery.

INTRODUCTION

Anyone who lives near a railway is likely to be aware of the low-frequency vibration that is transmitted when a train passes. If this occurs only occasionally, it may not be troublesome; but regular excitation from frequent trains on an underground railway, or from heavy road vehicles, or from nearby machinery, can be most intrusive. To reduce transmitted vibration, buildings are isolated from their foundations by springs. Albany Court, a six-storey apartment block built over a railway in London in the late 1960s, was the first building in the UK to be mounted on rubber springs. Its vibration isolating performance was good [1]. Now there are many isolated buildings in the UK and elsewhere, particularly where underground railways exist, and more such buildings are under construction or planned.

The simplest dynamical model, which is sometimes still used for design calculations, represents the building as a rigid mass on springs. In order to be effective, the natural frequencies of the mass/spring system have to be low compared with the frequency range of the excitation. This model is only reliable when the building is sufficiently stiff; otherwise local structural resonances interact with the rigid body modes. Then the vibration response is more complicated than a rigid-body model suggests. A resiliently-mounted building is now recognised to be a complex dynamical system in which the properties of the foundation, the method of isolation and the flexibility and damping of the building all contribute to its dynamic response. More realistic models represent flexible columns and floors by finite elements and use a lumped-parameter or other approximate representation of the foundation. This paper describes research in progress at Cambridge to (i) develop more accurate vibration models of buildings and their foundations and (ii) validate these models against measured data from a major building development in London.

METHOD OF CONSTRUCTION

There are at present two main types of rubber springs. One has solid blocks of rubber bonded to steel plates; the other has laminated rubber pads. For the laminated pads, the inter-layers may be metal sheets or they may be woven textile materials into which the rubber has been forced under pressure during processing. In both cases the isolators are mounted at base level, usually on top of foundation piles.

The building is constructed on a base framework or raft that is supported on the rubber bearings; these provide its only means of communication with the ground. Typically these bearings may be of plan area 1/2 m x 1/2 m and thickness 1/4 m and they carry a static pressure when the building is complete of about 10 MN/m^2 [2]. As construction proceeds, the load on the pads increases and therefore their deflection increases. The design must allow for this and must also ensure that the isolated structure is not "bridged" by connecting pipework or substructures or by debris from building operations.

The Albany Court building was small. It was mounted on laminated rubber springs that were designed to give a vertical natural frequency of 7 Hz. The vibrations generated in a previous (unsprung) building on the same site were said to be "fairly perceptible", and had vibration levels up to 1 mm/s rms. According to measurements taken after completion, the sprung building had vibration levels in the range 0.16 to 0.25 mm/s rms in a bandwidth of 3 to 30 Hz [3].

At the time it was concluded that the building was performing "substantially as a rigid body" and that predictions based on the theory of a rigid mass on springs agreed satisfactorily with theory. But as larger buildings were mounted on springs, it became apparent that such a simplified theory was inadequate. This was due to a number of factors. The Albany Court building was a small one; later buildings were progressively larger. The Albany Court frequency of 7 Hz led to constructional problems for larger buildings; their mounted frequency was increased up to 14 Hz. No narrow band vibration analyses were made at Albany Court; much more sophisticated measurements are now possible. The upshot is that it is now understood that the dynamic response of a building must be included in response predictions.

This is illustrated in fig. 1 which shows the calculated transmissibility for a mass on a spring in vertical vibration [4]. The solid curve shows the response of a rigid mass when the spring is such that the vertical natural frequency is 10 Hz and the damping ratio is 0.1. The other two dashed curves show the response for the same spring when the mass is flexible and has the properties of an elastic column of height 30 m with the density and Young's modulus of concrete. The two dashed curves differ because different damping assumptions are made; these will be described below. Because of the interaction between the properties of the mounted mass and its suspension system, the attenuation achievable is very much reduced. Instead of obtaining an attenuation of 30 dB at about 70 Hz, this may be only about 5 dB.

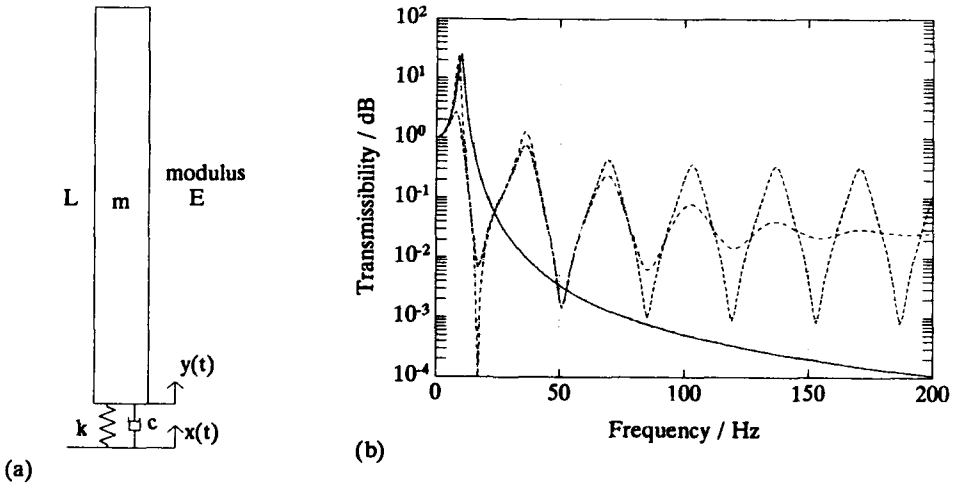

Fig. 1 Theoretical transmissibility curves for a 30 m concrete column on a rubber bearing

PROPERTIES OF RUBBER ISOLATORS

The performance of rubber isolators depends on their dynamic stiffness for very small amplitude deflections (1 mm/s at 10 Hz corresponds to an amplitude of 16 microns) while subjected to high static pressures (7-10 MN/m^2). Both natural and synthetic rubber are used for building applications and there is considerable skill in the selection and processing of the rubber to give low dynamic stiffness at the same time as high static stiffness (to prevent large deflections occurring during building construction).

Dynamically testing sample bearings is difficult because of the high static loads that have to be applied and the very small dynamic amplitudes that are needed. This means that a very stiff dynamic testing machine is required with very small amplitude load cycling possible. An alternative method involves simulating the actual loading conditions by a concrete or steel loading block and then measuring the natural frequencies and damping of the mounted assembly. To prevent movement of the underside of the test bearing, this is mounted on a large concrete inertia block, as shown in fig. 2. Damping is measured from the width of the recorded resonant peak. In order to make measurements at fixed strain amplitude, the usual method of testing is to apply a variable-amplitude dynamic force to the loading block in order to give constant dynamic strain amplitude. The measured force amplitude gives an "upside down" resonance diagram from which the natural frequency (and therefore dynamic stiffness) and the damping can be extracted.

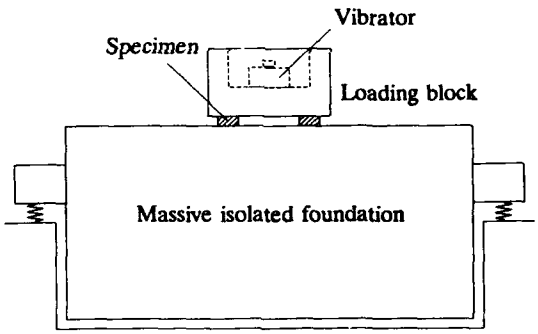

Fig. 2 Apparatus for the direct measurement of the dynamic properties of rubber bearings

MODEL EXPERIMENTS AT CAMBRIDGE

A realistic dynamic model of a building requires accurate data on damping. In order to obtain fundamental data on the damping properties of reinforced concrete columns, which are one of the principal components of many large buildings, model experiments are being carried out in Cambridge. So far, three different columns have been tested: (i) prestressed by a central rod, (ii) reinforced but not prestressed, (iii) reinforced and prestressed. Each column weighs about 700 kg and is 4 m long and 0.3 m diameter. Impulse-response tests have been carried out with the columns suspended in different ways [5,6].

Typical frequency-response curves for axial and bending vibration are shown in figs. 3a and b. These have been derived from measured impulse responses taken with the beams suspended horizontally on axially-thin supports located as close as possible to the nodes of the fundamental bending mode. Fig. 3a shows the axial modes, excited by lightly tapping the end of the columns; natural frequencies are spaced uniformly at intervals of about 500 Hz. Fig. 3b shows the bending modes, excited by tapping sideways at mid-span. The bending natural frequencies should follow the sequence 3^2, 5^2, 7^2, ..., but it can be seen that even modes are absent because the point of excitation at the middle of the columns is a nodal point for these modes. The interaction of the supports is responsible for the subsidiary peaks in fig. 3b and for the natural frequencies deviating from their theoretical values.

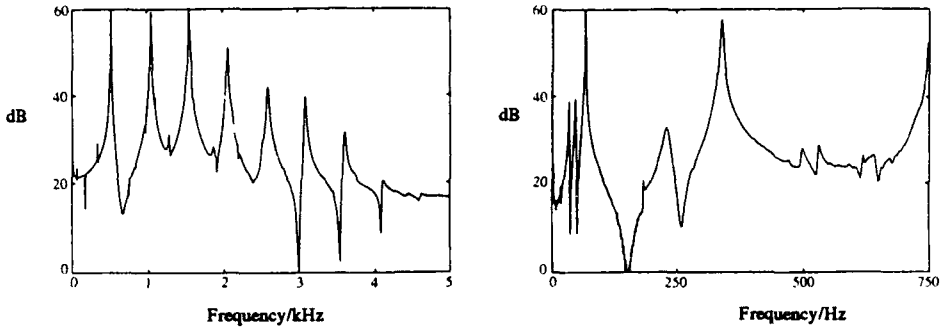

(a) Axial response (b) Bending response

Fig. 3 Calculated frequency-response functions for a reinforced concrete column derived from laboratory measurements of its impulse response

Damping factors have been calculated for the columns by a method due to McIntyre and Woodhouse [7]. This involves calculating the spectra of adjacent short lengths of the decaying transient. For a given mode, the decaying height of its spectral peak is monitored with time in order to estimate the rate of decay of the modal damping coefficient. This method has been found to work well except when there are two modes very close together.

The conclusions are that the damping Q factors for the fundamental axial (500 Hz) and bending (65 Hz) modes lie in the range 100 to 150 (damping ratios ·005 to ·0033). These do not appear to correlate with the different constructions of the columns; also the damping coefficients appear to be similar in magnitude for higher modes.

The sources and magnitude of damping found in full-scale buildings, and the best method of modelling damping for calculations, are subjects of continuing study.

FULL-SCALE MEASUREMENTS AT GLOUCESTER ROAD

A major redevelopment project has been carried out at the Gloucester Road underground station site in London in the last few years and is now approaching completion. The old buildings have been demolished and in their place a combined shopping and residential complex has been built. The shopping arcade is built on columns immediately above the three surface tracks of the District and Circle Line and close to the two tracks of the Piccadilly Line which pass underground and use the same station. The residential block is to the side of the surface tracks; it is a ten-storey structure, supported on piles that pass within a few metres of one of the Piccadilly Line's tunnels. The shopping arcade is mounted on a concrete raft that is partially isolated by resilient bearings on top of its supporting columns. The residential block is fully isolated by rubber bearings above each pile; its rigid-body design natural frequency is 10 Hz.

By arrangement with the site developers and their consulting engineers, access to the site for vibration measurements has been possible at all stages of the construction; measurements have been taken when the site was cleared and at stages during the progressive construction of the buildings.

These measurements have been of two types: (i) ambient vibration records taken under various conditions but mostly at weekends when construction had stopped and the principal source of ground vibration comes from passing trains, and (ii) impulse vibration response records obtained using a calibrated impulse hammer and also taken mostly at weekends.

Typical spectra from acceleration recorded on the ground and first floors of the residential block are shown in fig. 4. Below the spectra, the computed transmissibility between these two records is plotted. If

$x(t)$ denotes ground-floor acceleration and $y(t)$ first-floor acceleration, and $S_{xx}(\omega)$, $S_{xy}(\omega) = S_{yx}{}^*(\omega)$, $S_{yy}(\omega)$ are their direct and cross-spectra, the total transmissibility (solid line curve) is given by the formula [8]

$$T_{\text{total}}(\omega) = \left(S_{yy}(\omega) / S_{xx}(\omega)\right)^{1/2} \tag{1}$$

and the direct transmissibility (dashed curve) by the formula

$$T_{\text{direct}}(\omega) = |S_{xy}(\omega)| / S_{xx}(\omega) \ . \tag{2}$$

The first formula is based on the total response at the first floor measuring point, regardless of its correlation with vibration at the ground floor measuring point. In contrast, the second formula is based only on that part of the response at the first floor measuring point which is correlated with vibration at the ground floor measuring point.

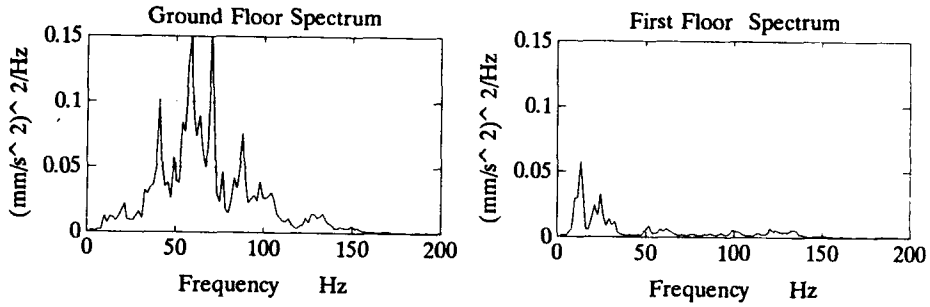

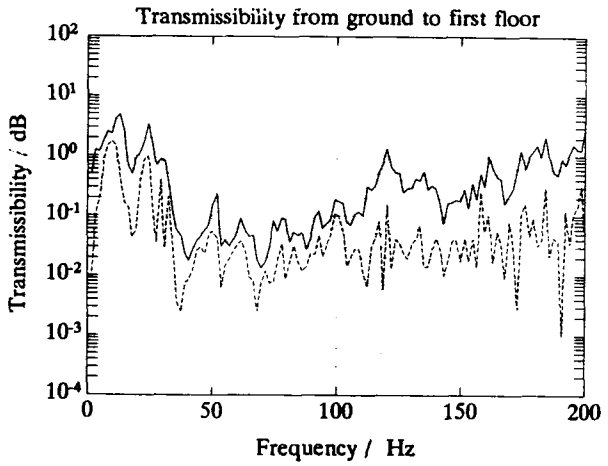

Fig. 4 Vibration records taken on the ground and first floors at Gloucester Road and the corresponding calculated transmissibility

It is evident from the two transmissibility curves in fig. 4 that there is a large proportion of vibration reaching the first-floor measuring point that is not correlated with vibration at the ground floor measuring point. This is not surprising given the complex construction of the building and its multiple points of support and therefore excitation.

In order to examine pile response, impulse tests were carried out on some of the piles before the structure had been built on them. This was done by applying a calibrated vertical impulse to the pile head and measuring the pile's response [9,10]. Five consecutive pile impulses (force versus time) and the resulting accelerations of the pile head are superimposed in figs. 5a and b. By averaging these records (to reduce the effect of ambient noise), and then taking their Fourier transforms, the magnitude and phase of the pile cap's frequency-response function have been computed. The results are shown in figs. 5c and d as the solid curves. They are compared with corresponding theoretical results (the dashed curves) calculated using a pile model in which the pile/soil interaction is obtained by treating the soil as a series of infinitesimally-thin horizontal layers and using soil properties derived from site measurements.

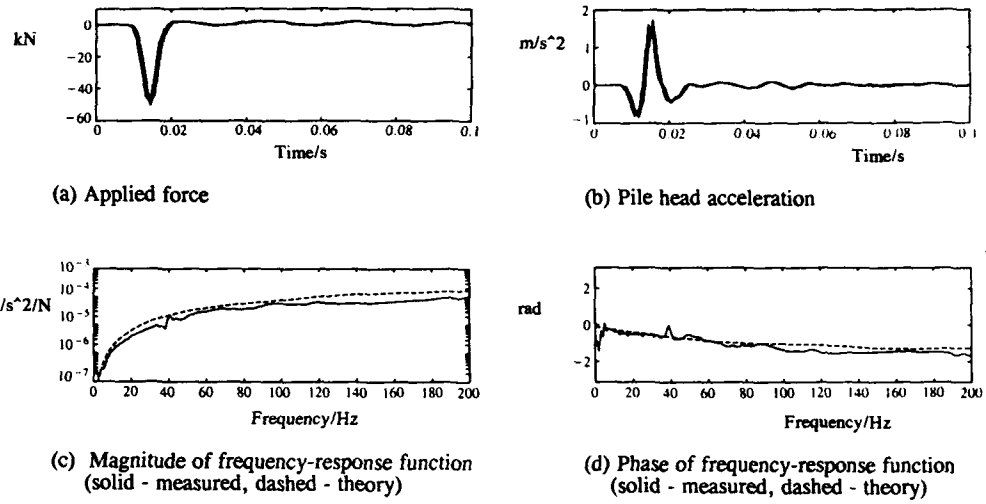

(a) Applied force

(b) Pile head acceleration

(c) Magnitude of frequency-response function (solid - measured, dashed - theory)

(d) Phase of frequency-response function (solid - measured, dashed - theory)

Fig. 5 Pile response properties measured at Gloucester Road

Vibration data has now been measured throughout the completed buildings at Gloucester Road and further measurements will be made when the buildings are furnished and in use. This extensive data bank will be used to validate the theoretical models of vibration transmission which are the subject of extensive further research [10].

DEVELOPMENT OF ANALYTICAL MODELS

Preliminary results on finite-element models have been reported already [11]. The conclusion from this work is that, in order to accurately model the higher frequencies (above 20 Hz) of realistic three-dimensional structures, it is necessary to include a very large number of elements. Our research in Cambridge includes the development of a more computationally-efficient numerical model. Instead of being composed of very many small finite-elements, it has relatively fewer macro-elements. For example, a building has its main structural framework, each length of which can be modelled as a beam. Each beam length is a macro-element and its theoretically exact frequency response can be calculated analytically. A set of frequency-response functions then represents the behaviour of that macro-element. Each floor slab and wall panel is a plate macro-element. A similar approach can be followed to develop a describing set of frequency-response functions, although these must now be stored numerically. All these macro-elements are joined together by appropriate equilibrium and compatibility conditions which allow the complete collection of macro-elements to be assembled into a numerical model for frequency-domain calculations. Preliminary results from this work will

be published shortly [10] and it appears that there is a good prospect that the vibrational behaviour of large buildings can be approximated satisfactorily by this approach.

Work on pile response is currently based on idealisations of soil interaction either (i) as a layered two-dimensional medium or (ii) as a continuous three-dimensional elastic half-space. Calculations based on the first have successfully predicted the transient response of unloaded piles to vertical impulses, fig. 5. Research is aimed at showing how the design of a building's foundation affects the transmission of vibration into the building. This has three stages: (i) determination of the ground excitation at source, either by calculation or by measurement; (ii) calculation of the transmission of vibration through the ground from source to a building; and (iii) calculation of the combined response of the building/resilient interface/foundation assembly to its ground excitation. Research at Cambridge has made progress on problems (i) and (ii) [12,13] and interest at present centers on (iii). The objective is to be able to convert ground vibration conditions in the vicinity of a building into calculated pile head movements under the resilient seatings. In particular it is important to know how the excitation under adjacent seatings is correlated and how the response of the building modifies the calculated excitation amplitudes.

Probably the most important design parameter is the damping. This includes soil damping, damping of the pile movements, damping of the resilient seatings, damping of the building's skeleton, damping of floor and wall panels, and damping arising from fittings and furnishings. Damping affects not only the overall level of vibration but also the spatial and frequency distribution of the total vibration environment. For example, from fig. 1 it can be seen that two different models of damping produce markedly different variations of transmissibility with frequency. Both are viscous damping models. In damping model A, each (incremental) mass is assumed to be subjected to a damping force proportional to the velocity of the mass. In damping model B, each (incremental) mass is assumed to be subjected to a damping force proportional to the relative velocity of adjacent masses [4].

FUTURE RESEARCH

These are complicated computational problems. Work on modelling a complete building using macro-elements is well advanced and appears to offer good results. Calculations and measurements of ground vibration transmission as a result of excitation from continuous road traffic have been successful. Primitive modelling of piles is complete but the inclusion of piles in a moving ground model is under continuing development. The most challenging and, so far, least understood subject, is damping. Although reliable laboratory tests have been completed on concrete columns and on model concrete frames, the damping values extracted from these measurements do not apparently tally with those occurring in the field with typical buildings. The aim is to extend the modelling process so that a complete building, including its resilient seatings, foundations and ground conditions can be taken account of when estimating the building's vibration environment. Although the completion of such an all-embracing model is still in the future, progress in showing vibration transmission within buildings is good and it is already possible to demonstrate a model building's dynamic behaviour by animating its response to ground vibration. This is likely to become a valuable design tool in optimising the structural features of buildings during their design.

FUTURE BUILDING DEVELOPMENTS

The construction of isolated buildings continues to run ahead of detailed knowledge of their dynamic performance. The small Albany Court building had a calculated 7 Hz vertical natural frequency; larger buildings that followed it had considerably higher frequency suspensions (up to 14 Hz) and performed satisfactorily according to the standards set at the time. But the increasing awareness of the environment combined with the pressure to build close to or on top of railways and roads, and still include high-performance lecture rooms, studios and residential accommodation, has meant that frequencies demanded for very large buildings are now as low as 5 Hz or less. This makes the design of the resilient elements more taxing, and their long-term stability, freedom from creep, resistance to ageing, fire-resistance, low dynamic but high static stiffness, all become increasingly difficult to achieve.

The demand for higher performance at an economical cost has led to design solutions in which different parts of a building are isolated in different ways. For example, part only of a building may be isolated; or the whole building may be isolated to a moderate specification while quiet spaces within the

building are additionally isolated by separate bearings to achieve a higher specification. The "box within a box" construction, traditionally used for studio design, is now reproduced on a larger scale for complete suites of rooms or concert halls.

The lowest natural frequencies for elastomeric bearings have so far been achieved by using solid rubber block constructions, with rubber blocks bonded to steel spacers and end plates. Recently lower-frequency steel spring assemblies, usually incorporating mechanical dampers, have been receiving attention and have been used in a number of applications. There is considerable interest in these and other methods of isolating complete buildings, particularly when earthquake protection is also necessary. The task of achieving good isolation of low-frequency ground vibration at the same time as reducing higher-frequency noise transmission and, if necessary, protecting against large sudden ground movements remains a difficult engineering design problem.

ACKNOWLEDGEMENTS

I am grateful to my colleague Dr Hugh Hunt and to our doctoral students Atul Bhaskar and David Cryer, who have contributed to or supplied data for this paper. More details of various aspects of the work described here are given in reference [14]. We are indebted to Bickerdike Allen Partners, consulting acoustical engineers, and to Tiflex Ltd, resilient bearing manufacturers, for providing information about the Gloucester Road development.

REFERENCES

1. Waller, R. A. Buildings on springs. *Nature*, **211** (5051), 1966, 794-796.
2. Grootenhuis, P. Structural elastomeric bearings and resilient seatings, chapter 9 of *Polymers and polymer composites in construction*. Thomas Telford, London, 1989.
3. Waller, R. A. *Building on springs*, International Series of Monographs in Civil Engineering, Vol. 2, Pergamon Press, Oxford, 1969.
4. Newland, D. E. *Mechanical vibration analysis and computation*, Longman, Harlow and John Wiley, New York, 1989.
5. Bhaskar, A. *Damping in mechanical vibrations: new methods of analysis and estimation*, PhD thesis, University of Cambridge, 1992.
6. Bhaskar, A. Damped vibration of concrete bars and beams. Proc. Int. Conf. on *Traffic effects on structures and the environment*, Slovak Academy of Sciences, The Low Tatras, Czechoslovakia, 1991.
7. McIntyre, M. E. and Woodhouse, J. *Acta Metall.*, **36**, 6, 1988, 1397-1416.
8. Newland, D. E. *Random vibrations and spectral analysis*, 2nd edition, Longman, Harlow and John Wiley, New York, 1984.
9. Hunt, H. E. M. and Cryer, D. P. Site and laboratory experiments on vibration transmission. *Proc. Inst. Acoustics Conf. Vibr. in Buildings*, **12** (7), 1990, 39.
10. Cryer, D. P. *Vibration of Buildings* (provisional title), PhD thesis, University of Cambridge, 1992/93.
11. Newland, D. E. and Bhaskar, A. Calculation of vibration in structures. *Proc. Inst. Acoustics Conf. Vibr. in Buildings*, **12**, 7, 1990, 11.
12. Hunt, H. E. M. Modelling of road vehicles for calculation of traffic-induced ground vibration as a random process. *J. Sound Vibr.*, **144** (1), 1991, 41-51.
13. Hunt, H. E. M. Stochastic modelling of traffic-induced ground vibration. *J. Sound Vibr.*, **144**(1) 1991, 53-70.
14. Newland, D. E. and Hunt, H. E. M. Isolation of buildings from ground vibration: a review of recent progress. *J. Mech. Engng Sci.*, Proc. Instn Mech. Engrs, **205**, 1991, 39-52.

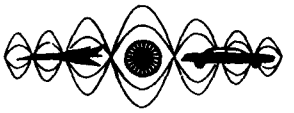

**SECOND INTERNATIONAL CONGRESS ON
RECENT DEVELOPMENTS IN AIR- AND
STRUCTURE-BORNE SOUND AND VIBRATION**

MARCH 4-6, 1992 AUBURN UNIVERSITY, USA

LINEAR DYNAMIC BEHAVIOR OF VISCOUS COMPRESSIBLE FLUID LAYERS: APPLICATION OF A COMPLEX SQUEEZE NUMBER

T. Önsay
Michigan State University
Department of Mechanical Engineering
East Lansing, MI 48824
U.S.A.

ABSTRACT

Linear dynamic behavior of viscous compressible fluid layers is studied by considering the squeezing oscillations of the enclosing surfaces. A nondimensional complex squeeze number is introduced to characterize different dynamic regimes of a fluid layer. Free and forced vibrations of a rectangular geometry fluid layer are determined by using modal analysis methods. The asymtotic forms of system response are discussed by comparing the thickness of the fluid layer with the viscous boundary layer thickness. The surface impedance and the time-averaged power absorbed by the fluid layer are determined. Application of the complex squeeze number is demonstrated on a rectangular fluid layer with constant surface velocity distribution.

INTRODUCTION

A thin layer of fluid trapped between two vibrating surfaces has a well-known damping capacity. The squeezing vibrations of the enclosing surfaces pump the fluid back and forth in the layer, while the viscous shear forces resist the flow and dissipate the energy. This dissipative property of fluid layers has been utilized in varity of applications, such as damping of vibrations in rotor-bearing systems and attenuation of flexural vibrations of panels in enclosures of machineries.

The literature on dynamic behavior of fluid layers involves two groups of studies; squeeze films in bearings and fluid layers in structures, where some of the selected work are listed in references [1-9] and [10-14], respectively. The major difference between the two groups of applications is the thickness of the fluid layer, which in part defines the dynamic regime. Other important parameters are the geometry, equilibrium properties of the fluid and the frequency and amplitude of vibrations of the enclosing surfaces. In squeeze film studies, the combined effects of parameters are represented by nondimensional ratios, such as the squeeze number and the bearing number [1-4]. The concept of squeeze number can be utilized in the study of coupled plate-fluid layer systems, if its definition is based on a wider range of frequencies and layer thicknesses.

In this study, the linear dynamic behavior of finite fluid layers is studied by introducing a complex squeeze number. The new form of the squeeze number provides a more general description of the linear dynamic regimes of a fluid layer. In the following analysis, the equations governing the motion of the fluid layer are given in a nondimensional form by using the complex squeeze number. Then, the study is focused on rectangular geometries, where the time-averaged vibrational power absorbed by the the fluid layer is determined by defining a surface impedance.

GOVERNING EQUATIONS

Consider a viscous compressible fluid layer enclosed between two surfaces, as sketched in Figure 1. The enclosing surfaces are vibrating with time harmonic oscillations of the form $V(x,z,\omega)e^{-i\omega t}$. The

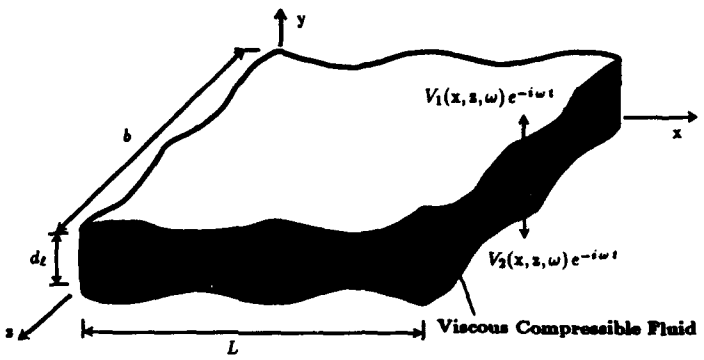

Figure 1. A rectangular geometry fluid layer.

squeezing motion of the boundaries generates pressure gradients in the fluid layer. The fluid is forced back and forth in the layer parallel to the surfaces. Viscous shear forces resist the motion of the fluid and dissipate the vibrational energy. The dissipative effects of viscous shear forces are influenced by the equilibrium pressure, the frequency of oscillations and the thickness of the fluid layer.

In this study, narrow fluid layers are focused. The thickness of the fluid layer is considered much smaller than the wave length of pressure fluctuations. In addition, the vibration amplitudes of the enclosing surfaces are considered much smaller than the average thickness of the layer. Under such conditions, the acoustic motion in the fluid layer is represented by a set of linearized fist-order differential equations which govern the continuity of the fluid mass flow and the fluid momentum density [15,16]. As a result of the narrow fluid layer assumption, the fluid pressure gradients and the viscous shear forces are limited to the plane of the layer [1,12,14]. The resulting governing relation for the pressure distribution is a Helmholtz equation with a source term on the right-hand side:

$$\nabla^2 \mathrm{p} + k_f^2 \mathrm{p} = K_c V_\ell \tag{1}$$

where ∇^2 is a two-dimensional Laplacian operator defined in the plane of the layer. In equation (1), the rate of variation of the layer thickness is represented by $V_\ell = V_1 - V_2$, where V_1 and V_2 correspond to the velocity distributions of the upper and lower surfaces, respectively. In addition, the propagation and the coupling constants are given as

$$k_f^2 = k_\ell^2 \frac{1}{1 - F(\mathrm{x}_\ell)} \qquad \text{and} \qquad K_c = \frac{-i\omega\rho_\ell}{[1 - F(\mathrm{x}_\ell)]d_\ell} = \frac{-i\,\mathrm{P}_\ell\, k_f^2}{\omega\, d_\ell} \tag{2}$$

where $k_\ell = \omega/c$ is the acoustic wave number with c representing the speed of sound in the fluid. The complex function $F(\mathrm{x}_\ell)$ appearing in equation (2) is defined as [15]

$$F(\mathrm{x}_\ell) = (1+i)\,\mathrm{x}_\ell \tanh[(1-i)/(2\mathrm{x}_\ell)] = \begin{cases} (1+i)\mathrm{x}_\ell\,, & \mathrm{x}_\ell \ll 1 \\ 1 + \frac{i}{6\mathrm{x}_\ell^2}\,, & \mathrm{x}_\ell \gg 1 \end{cases} \tag{3}$$

where the ratio $\mathrm{x}_\ell = d_v/d_\ell$ represents a relative measure of the viscous boundary layer thickness, $d_v = \sqrt{2\mu/\omega\rho_\ell}$, with respect to the average thickness of the layer, d_ℓ.

COMPLEX SQUEEZE NUMBER

Equation (1) is restated in a non-dimensional form

$$\nabla^2 P + \sigma P = -\sigma\epsilon \tag{4}$$

The non-dimensional parameters appearing in Eq. (4) are defined as

$$P = \frac{\mathrm{p}}{P_\ell}, \qquad \sigma = (\xi\, k_f)^2, \qquad \epsilon = \frac{Y_\ell}{d_\ell} \tag{5}$$

where $Y_\ell = V_\ell/(-i\omega)$ is the spatial distribution of the layer thickness, P_ℓ is the equilibrium pressure in the fluid layer and ξ is a characteristic length of the layer geometry. The two-dimensional Laplacian operator ∇^2 appearing in Eq. (4) contains spatial coordinates which are normalized with respect to ξ.

A unique feature of Eq. (4) is that it contains a complex squeeze number, σ. This new complex form of the squeeze number generalizes the classical real form, which is defined for an isothermal process as $\sigma' = 12\mu\xi^2\omega/(P_\ell d_\ell^2)$ [1-4]. As explained in the following analysis, under additional dynamic constraints the complex squeeze number can be simplified to the classical real form.

The real and imaginary parts of the normalized complex squeeze number are plotted in Figure 2 with respect to the ratio x_ℓ. The real part of the complex squeeze number represents the reactive and the imaginary part the resistive effects of forces in the fluid layer. In Figure 2, the magnitudes of the real and the imaginary parts of the complex squeeze number σ have an opposite relative significance at small and large values of x_ℓ, and they become equal to each other only at a unique value of $x_\ell = 0.444$. This particular value of x_ℓ defines a borderline between the resistive and reactive dynamic behaviors of the fluid layer.

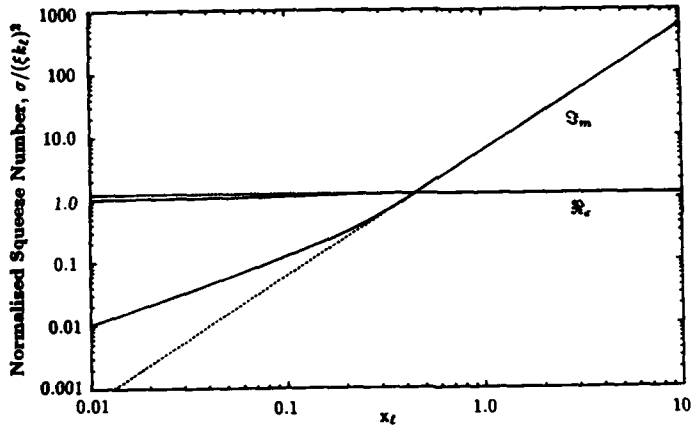

Figure 2. Complex squeeze number. (—— Exact, – – – Approximation).

The borderline value of $x_\ell = 0.444$ is utilized to define the asymtotic forms of the complex squeeze number:

$$\sigma \simeq \begin{cases} (\xi k_\ell)^2 (1 + i x_\ell), & x_\ell \ll 0.444 \\ 1.19 (\xi k_\ell)^2 (1 + i), & x_\ell = 0.444 \\ (\xi k_\ell)^2 (1.2 + i 6 x_\ell^2), & x_\ell \gg 0.444 \end{cases} \tag{6}$$

where again $k_\ell = \omega/c$ with $c = \sqrt{P_\ell/\rho_\ell}$ for isothermal conditions.

The second limiting case in Eq. (6) can be approximated from the third case by using $x_\ell = 0.444$. In fact, for values of $x_\ell \geq 0.444$, the asymptotic form of the squeeze number corresponding to $x_\ell \gg 0.444$ in Eq. (6) gives results which are almost equivalent to the exact values obtained directly from Eq. (5). Therefore, the following definition is suggested as an approximate form:

$$\sigma \simeq 1.2 (\xi k_\ell)^2 + i\sigma' \qquad \text{for} \qquad x_\ell \geq 0.444 \tag{7}$$

where again σ' is the classical squeeze number. A plot of this approximate form of the squeeze number is given by the dashed curves in Figure 2. Note that, this approximation starts to deviate from the exact values when the ratio x_ℓ is decreased below 0.444.

Further simplification of Eq. (7) is possible for $6x_\ell^2 \gg 1.2$ or equivalently for $12\mu/d_\ell^2 \gg 1.2\omega\rho_\ell$. Under such conditions, the inertial effects which are represented by the real part of the squeeze number become negligibly small. Then, the complex squeeze number reduces to $\sigma \simeq i\sigma'$. In squeeze-film bearing studies [1-4], generally very small layer thicknesses are considered, and thus the use of the classical form of the squeeze number is justified. However, in the application of fluid layers to attenuation of bending vibrations in plates [10-14], a wide range of layer thicknesses and frequencies may need to be considered. For such applications, Eq. (4) provides a more comprehensive governing relation for the linear dynamic

behavior of viscous compressible fluid layers.

RECTANGULAR GEOMETRY FLUID LAYERS

In the following, the governing relation given in Eq. (4) is applied to a rectangular geometry fluid layer which has boundaries open to ambient conditions, as sketched in Figure 1. The dynamic behavior of the rectangular geometry fluid layer is studied independent of the dynamic charateristics of the enclosing surfaces. An arbitrary velocity distribution is assigned to the enclosing surfaces and the corresponding pressure response of the fluid layer is determined. In the solution process, first the eigenvalues and the eigenfunctions of the corresponding homogenous problem are determined. Then, the forced response of the system is obtained by utilizing the orthonormal eigenfunctions in a Fourier series representation of the system variables.

UNFORCED RESPONSE

In order to determine the eigenvalues and eigenfunctions of the rectangular fluid layer, the following boundary value problem is considered:

$$\frac{\partial^2\Phi}{\partial x^2} + \frac{\partial^2\Phi}{\partial z^2} + \sigma\,\Phi = 0\,, \qquad BCs: \quad \Phi(0,z) = \Phi(1,z) = \Phi(x,0) = \Phi(x,\psi) = 0 \tag{8}$$

where $\Phi(x,z)$ represents the unforced pressure distribution in the layer, $x = \mathrm{x}/L$ and $z = \mathrm{z}/L$ are the normalized coordinates and $\psi = b/L$ is the aspect ratio. For the rectangular geometry, the characteristic length is chosen as $\xi = L$.

The eigenvalues and the eigenfunctions of the homogenous problem are obtained as

$$\sigma_{mn} = (m\pi/\psi)^2 + (n\pi)^2 \qquad \text{and} \qquad \Phi_{mn}(x,z) = \frac{2}{\sqrt{\psi}}\sin(n\pi\,x)\sin(m\pi\,z/\psi)\,, \qquad m,n = 1,2,\ldots \tag{9}$$

Then, the characteristic equation for the modal frequencies of the fluid layer is given by

$$\left(\frac{\omega_{mn}}{c}\right)^2 - \frac{1 - F(\mathrm{x}_{\ell_{mn}})}{L^2}\left[(n\pi)^2 + (m\pi/\psi)^2\right] = 0\,, \qquad m,n = 1,2,\ldots \tag{10}$$

where $\mathrm{x}_{\ell_{mn}} = \mathrm{x}_\ell(\omega_{mn})$. Note that, due to dissipative viscous effects induced in the fluid layer, the natural frequencies ω_{mn} are complex valued. Therefore, the time dependence $e^{-i\omega_{mn}t}$, considered earlier in this study, implies standing waves with time-decaying amplitudes for each independent solution.

Since Eq. (10) is a complex transcendental equation, it is unlikely that it will allow a closed form solution. The modal frequencies ω_{mn} can be determined by numerical methods. As an alternate solution, the asymptotic forms of Eq. (10) are considered to find approximate relations for the modal frequencies of the fluid layer. In the following, limiting cases corresponding to $\mathrm{x}_\ell \ll 0.444$ and $\mathrm{x}_\ell \geq 0.444$ are discussed.

Case $\mathrm{x}_\ell \ll 0.444$. The characteristic frequencies are approximated by

$$(\omega_{mn})_{1,2} \simeq \pm\frac{c}{L}\left[(n\pi)^2 + (m\pi/\psi)^2\right]^{1/2}\,, \qquad m,n = 1,2,\ldots \tag{11}$$

For this particular case, viscous shear waves which are induced near the enclosing surfaces are not able to penetrate towards the center of the fluid layer. Therefore, the dissipative viscous shear forces have no effect on the main motion of the fluid. Since during the derivation of the governing equations the narrow channel assumption was made, the viscous shear components other than the one parallel to the enclosing surfaces were neglected. Consequently, the characteristic frequencies given by Eq. (11) implies non-dissipative fluid motion.

Case $\mathrm{x}_\ell \geq 0.444$. In this regime, use of a mass-stiffness-damping (*M-S-R*) representation facilitates the analysis. For this case, the characteristic equation is given by

$$M_{mn}\,\omega_{mn}^2 + i\,R_{mn}\,\omega_{mn} - S_{mn} = 0, \qquad m,n = 1,2,\ldots \tag{12}$$

where

$$M_{mn} = 1.2\,\rho_\ell = M_0\,, \qquad R_{mn} = \frac{12\,\mu}{d_\ell^2} = R_0\,, \qquad S_{mn} = \frac{P_\ell}{L^2}\left[(n\pi)^2 + (m\pi/\psi)^2\right] \tag{13}$$

These modal parameters M_{mn}, R_{mn} and S_{mn} represent the mass, damping and the stiffness of a rectangular geometry fluid layer, where each is defined per unit volume of the fluid. Equation (13) implies same constant values M_0 and R_0 for each mode, while S_{mn} depends on the order (m,n) of a mode. Further anology with a lumped-parameter multi-degree of freedom system yields the undamped modal frequencies $\omega_{mn_0} = \sqrt{S_{mn}/M_0}$ and the modal damping ratios $\zeta_{mn} = R_0/(2\sqrt{M_0 S_{mn}})$. Then, the characteristic equation takes a more familiar form

$$\omega_{mn}^2 + i\,2\zeta_{mn}\,\omega_{mn_0}\,\omega_{mn} - \omega_{mn_0}^2 = 0 \tag{14}$$

which yields

$$(\omega_{mn})_{1,2} = \omega_{mn_0}\left[-i\zeta_{mn} \pm \sqrt{1-\zeta_{mn}^2}\right], \qquad m,n = 1,2,\ldots \tag{15}$$

The free vibration response of the fluid layer is determined by considering the separable form of the fluid pressure $p(x,z,t) = \Phi(x,z,\omega)\,q(t)$. Since the time dependent part was represented by $q(t) = e^{-i\omega t}$, the complex modal frequencies, ω_{mn_1} and ω_{mn_2} give two independent solutions $q_{mn_1}(t) = e^{-i\omega_{mn_1}t}$ and $q_{mn_2}(t) = e^{-i\omega_{mn_2}t}$. Then, the general unforced response of the fluid layer is obtained by forming a linear combination of these independent solutions

$$p(x,z,t) = \frac{2}{\sqrt{\psi}} \sum_{m,n}^{\infty} e^{-\zeta_{mn}\omega_{mn_0}t}\left\{A_{mn}\,e^{-i\omega_{mn_d}t} + B_{mn}\,e^{i\omega_{mn_d}t}\right\}\sin(n\pi x)\,\sin(m\pi z/\psi) \tag{16}$$

where $\omega_{mn_d} = \omega_{mn_0}\sqrt{1-\zeta_{mn}^2}$ is the damped modal frequency. The constants A_{mn} and B_{mn} are determined from initial conditions. Equation (16) implies that each mode may contribute to the pressure response of the fluid layer in one of two possible ways.

i) When $\zeta_{mn} < 1$ or equivalently $R_0^2 < 4\,M_0\,S_{mn}$, then the mnth mode performs harmonic oscillations with an amplitude that decays in time. Since the rate of decay is governed by $\zeta_{mn}\,\omega_{mn_0} = 6\mu/(1.2\,\rho_\ell\,d_\ell^2)$, the response of the corresponding mode decays faster in time if the layer is made narrower.

ii) When $\zeta_{mn} \geq 1$ or equivalently $R_0^2 \geq 4\,M_0\,S_{mn}$, then no oscillations are possible, and the fluid motion can be given as a superposition of two exponential time-decaying functions.

Since the damping ratio, ζ_{mn}, is inversely proportional to the order of a mode (m,n), the case $\zeta_{mn} \geq 1$ is more likely to happen for low-ordered modes. For a general set of initial conditions, the pressure response of the fluid layer will be composed of modal contributions with different types of time-dependence; the low-frequency modes will contribute with pure exponential time-decay, while the high-frequency modes perform sinusoidal oscillations with time-decaying amplitudes.

FORCED RESPONSE

In the forced response analysis, the squeezing vibrations of the enclosing surfaces are considered. The pressure induced in the fluid layer is determined by assigning an arbitrary space distribution, $V_\ell(x,z,\omega)$, to the rate of layer thickness variation. The orthonormal eigenfunctions $\Phi_{mn}(x,z)$ are utilized in Fourier series representation of variables $V_\ell(x,z,\omega)$ and $P(x,z,\omega)$:

$$V_\ell(x,z,\omega) = \sum_{m,n}^{\infty} V_{\ell_{mn}}(\omega)\,\Phi_{mn}(x,z) \qquad \text{and} \qquad P(x,z,\omega) = \sum_{m,n}^{\infty} P_{mn}(\omega)\,\Phi_{mn}(x,z) \tag{17}$$

where the coefficients $V_{\ell_{mn}}(\omega)$ are given by

$$V_{\ell_{mn}}(\omega) = \frac{2}{\sqrt{\psi}} \int_0^1 \int_0^{\psi} V_\ell(x,z,\omega)\,\sin(n\pi x)\,\sin(m\pi z/\psi)\,dx\,dz, \qquad m,n = 0,1,2,\ldots \tag{18}$$

The pressure response of the fluid layer is obtained from Eq. (4) as

$$P(x,z,\omega) = \frac{2}{\pi^2\sqrt{\psi}} \sum_{m,n}^{\infty} \frac{\sigma\,\epsilon_{mn}}{\left[(m/\psi)^2 + n^2 - \sigma/\pi^2\right]}\sin(n\pi x)\,\sin(m\pi z/\psi) \tag{19}$$

where $\epsilon_{mn} = Y_{\ell_{mn}}/d_\ell$. The pressure response of the fluid layer depends strongly on ϵ_{mn} and σ which describe the spatial distribution of the layer thickness and the dynamic regime of the fluid layer.

In order to represent the dynamic behavior of the fluid layer, a surface impedance is defined,

$Z_\ell(x,z,\omega) = -p(x,z,\omega)/V_\ell(x,z,\omega)$. Equations (17) and (19) are utilized in finding an explicit form for the surface impedance:

$$Z_\ell(x,z,\omega) = \frac{-i\,16\,P_\ell}{\pi^4\,\omega\,d_\ell} \sum_{\substack{m,n \\ odd}}^{\infty} \frac{\sigma}{(m\,n)\left[(m/\psi)^2 + n^2 - \sigma/\pi^2\right]} \sin(n\,\pi\,x)\,\sin(m\,\pi\,z/\psi) \tag{20}$$

The denominator of Eq. (20) implies that the resonances will occur when $\Re_e\{\sigma\} \equiv R_\sigma = (m\pi/\psi)^2 + (n\pi)^2$. At a resonance, the impedance of the fluid layer becomes infinitely large. Thus, the layer becomes very stiff as felt by the enclosing surfaces. This resonance behavior is just the opposite of what is observed commonly in other mechanical systems, where at a resonance the impedance would go to zero.

The real part of this surface impedance can be utilized to determine the dissipative behavior of the fluid layer. The time-averaged vibrational power flowing into the fluid layer through the oscillating surfaces is defined as:

$$\mathcal{I}_\ell(x,z,\omega) = < p(x,z,t)\,v_\ell(x,z,t) > = \frac{1}{2}\left|V_\ell(x,z,\omega)\right|^2 \Re_e\{\,Z_\ell(x,z,\omega)\,\} \tag{21}$$

Substituting $Z_\ell(x,z,\omega)$ from Eq. (20) and integrating Eq. (21) over the spatial domain gives the total time-averaged vibrational power absorbed by the fluid layer:

$$\mathcal{I}_T(\omega) = \frac{32\,\psi\,P_\ell\left|V_\ell(x,z,\omega)\right|^2}{\pi^6\,\omega\,d_\ell} \sum_{\substack{m,n \\ odd}}^{\infty} \frac{\left[(m/\psi)^2 + n^2\right] I_\sigma}{(m\,n)^2\left\{\left[(m/\psi)^2 + n^2 - R_\sigma/\pi^2\right]^2 + I_\sigma^2/\pi^4\right\}} \tag{22}$$

where $\sigma = R_\sigma + i\,I_\sigma$. The denominator of Eq. (22) implies possible peaks in dissipated energy as the frequency approaches the resonances of the fluid layer.

ASYMPTOTIC FORMS

The limiting forms of the complex squeeze number are utilized in the discusion of the following asymptotic forms.

Case $x_\ell \ll 0.444$. Since the transverse shear waves that are induced by the oscillations of the enclosing surfaces decay rapidly within distances in the order of d_v, this case corresponds to negligible dissipative effects in the fluid layer. The coupling constant K_c becomes strongly inertia-controlled, since its part representing the viscous effects is inversely proportional to the third power of the layer thickness. Thus, the main motion of the fluid layer becomes inertially coupled to the motion of the surfaces. This coupling behavior should not be confused with the actual motion of the fluid, where in addition to the inertia, the compressibility of the fluid also plays an important role. For this special case, $\sigma = L^2\omega^2\rho_\ell(1 + i x_\ell)/P_\ell$ and the fundamental resonance occurs at $f_{11} = (1/2\,L)[(1/\psi^2 + 1)\,P_\ell/\rho_\ell]^{1/2}$ (Hz). For example, a $10 \times 10\ cm$ air layer at atmospheric equilibrium pressure gives $f_{11} = 2850 Hz$.

Case $x_\ell \gtrsim 0.444$. The complex squeeze number is given by $\sigma = (\omega\,M_0 + i\,R_0)\,L^2\omega/P_\ell$. Then, the surface impedance of the fluid layer becomes

$$Z_\ell(x,z,\omega) = \frac{16\,P_\ell}{\pi^2\,d_\ell} \sum_{\substack{m,n \\ odd}}^{\infty} \frac{(-R_0 + i\,\omega\,M_0)}{(m\,n)\,(\omega^2\,M_0 - S_{mn} + i\,\omega\,R_0)} \sin(n\pi\,x)\,\sin(m\pi\,z/\psi) \tag{23}$$

Since $R_0 = 12\mu/d_\ell^2$, the bandwidth of resonances increases as the layer is made narrower.

APPLICATION

The application of the above results are demonstrated on a rectangular fluid layer which has constant distribution of surface velocities, $V_\ell(x,z,\omega) = V(\omega)$. In literature, special cases of this problem has been considered for gas bearings [2,3,6].

For this example, integration of the fluid pressure over the surface area yields a total reaction force:

$$F_T(\omega) = \frac{64\,\epsilon_\ell\,\psi\,P_\ell}{\pi^6} \sum_{\substack{m,n \\ odd}}^{\infty} \frac{\sigma}{(m\,n)^2\left[(m/\psi)^2 + n^2 - \sigma/\pi^2\right]} \tag{24}$$

where $\epsilon = V(\omega)/(-i\omega d_\ell)$. Under special limiting conditions, when the complex squeeze number is approximated by $\sigma \simeq i\sigma'$, Eq. (24) gives the same the results as given by Blech [3].

In this case, the dynamic behavior of the fluid layer can be described in terms of an effective

impedance $\mathcal{Z}_T(\omega) = -F_T(\omega)/V(\omega)$, which is given as:

$$\mathcal{Z}_T(\omega) = = \frac{-i\,64\,\psi\,P_\ell}{\pi^6 \omega d_\ell} \sum_{\substack{m,n \\ odd}}^{\infty} \frac{\sigma}{(m\,n)^2 \left[(m/\psi)^2 + n^2 - \sigma/\pi^2\right]} \tag{25}$$

The normalized magnitude of the layer impedance is plotted in Figure 3 with respect to the real and the imaginary parts of the complex squeeze number for an arbitrary value of the aspect ratio $\psi = 0.7$. According to Figure 3, when both R_σ and I_σ have small values, the fluid layer has a low impedance. This case corresponds to relatively large layer thicknesses and low frequencies. Then, starting from this low-end-corner in Figure 3 and increasing the frequency of vibrations or decreasing the thickness of the layer increases the contribution of the inertial and the viscous effects in the response of the fluid layer. The net result is an increase in the impedance of the fluid layer. Again starting from the low-end-corner, if the frequency is kept constant and the layer thickness is decreased, then the resistance due to viscous

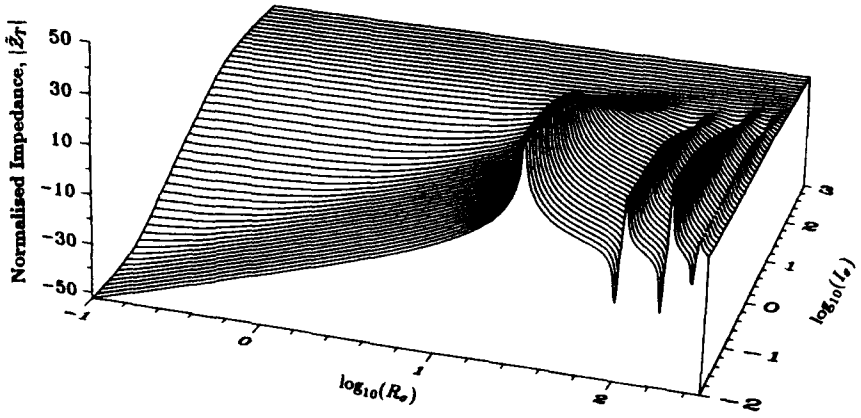

Figure 3. The normalised impedance of a rectangular geometry fluid layer which has a constant spatial distribution of the surface velocities. ($\sigma = R_\sigma + i I_\sigma$).

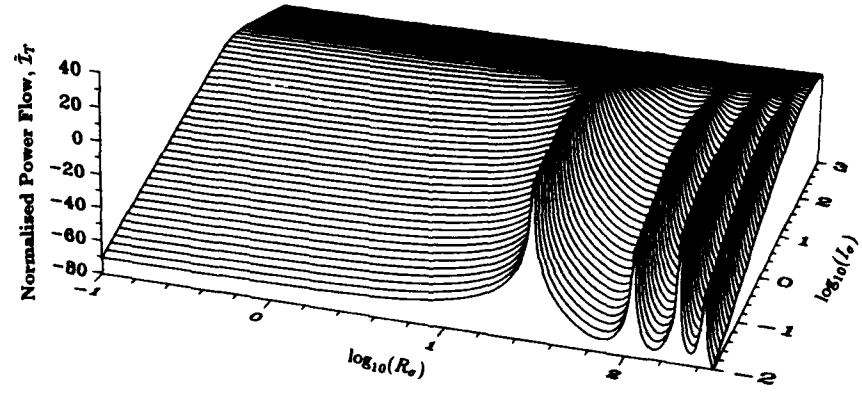

Figure 4. The normalised time-averaged power flowing into a rectangular geometry fluid layer which has a constant spatial distribution of the surface velocities. ($\sigma = R_\sigma + i\,I_\sigma$).

forces, $R_0 = 12\mu/d_f^2$, increases, which raises the impedance of the fluid layer until it reaches a maximum. Then, any further decrease of the layer thickness causes a decrease in the impedance since the flow becomes blocked due to increased stiffness of the layer [4].

In the other direction, if the viscous shear effects are kept relatively small and the inertial fluid forces are increased by increasing the frequency, then the layer impedance starts to show some peaks and valleys, which correspond to the resonances of the rectangular geometry fluid layer. In this example, the fundamental resonance occurs at $R_\sigma = 30.0$, which corresponds to $\log_{10}(R_\sigma) = 1.477$. As observed from Figure 3, this fundamental resonance has a sharp peak for small I_σ, which corresponds relatively large layer thicknesses. But, as the layer thickness is made smaller, then the peaks are smoothed out due to the increased viscous dissipation in the fluid layer. A similar behavior is observed for the higher modes of the fluid layer.

In addition to the layer impedance, the dissipative behavior of the fluid layer is analyzed. The normalized time-averaged power absorbed by the fluid layer is plotted in Figure 4 with respect to real and imaginary parts of the squeeze number. In Figure 4, as a resonance of the fluid layer is approached, the total power absorbed by the fluid layer shows a sharp increase. Under such conditions, the contribution of the resonated mode to the total power becomes inversely proportional to R_0. Therefore, as observed from Figure 4, lowering the thickness of the layer has an inverse effect of decreasing the total power flowing into the fluid layer. Away from resonances and at lower R_σ values, the total time-averaged power flowing into the layer increases with decreasing layer thickness.

CONCLUSIONS

Consideration of a complex squeeze number resulted in an efficient representation of linear dynamic behavior of viscous compressible fluid layers. Since the formulation of the problem was based on a general surface velocity distribution, the results presented in this study can be applied to any special case. The surface impedance of the fluid layer, given in this study, can be utilized in the analyis of coupled dynamic behavior of finite plate-fluid layer systems.

ACKNOWLEDGEMENTS

This research was conducted in the Department of Mechanical Engineering at Wayne State University (WSU), Detroit. Financial support of the Institute of Manufacturing Research at WSU is gratefully acknowledged.

REFERENCES

1. W.E.Langlois, "Isothermal Squeeze Films," *Quarterly of Applied Mathematics*, Vol. **20**(2), 1962, 131–150.
2. W.S.Griffin, H.H.Richardson and S.Yamanami, "A Study of Fluid Squeeze-Film Damping," *Journal of Basic Engineering, Transactions of the ASME*, Vol. **88**, 1966, 451–456.
3. J.J.Blech, "On Isothermal Squeeze Films," *Journal of Lubrication Technology*, Vol. **105**, 1983, 615–620.
4. E.O.J.Salbu, "Compressible Squeeze Films and Squeeze Bearings," *Journal of Basic Engineering*, June 1964, 355–366.
5. S.Ishizawa, "The Unsteady Laminar Flow Between Two Parallel Discs with Arbitrarily Varying Gap Width," *Bulletin of JSME*, Vol. **9**(35), 1966, 533–550.
6. D.F.Hays "Squeeze Films for Rectangular Plates," *Journal of Basic Engineering*, 1963, 243–246.
7. R.M.Terrill, "Flow Between Two Parallel Circular Disks, One of Which is Subject to a Normal Sinusoidal Oscillation," *Journal of Lubrication Technology*, 1969, 126–131.
8. W.A.Gross, "Gas Bearings: A Survey," *Wear*, Vol. **6**, 1963, 423–443.
9. D.F.Moore, "A Review of Squeeze Films," *Wear*, Vol. **8**, 1965, 245–263.
10. G.Maidanik "Energy Dissipation Associated with Gas-Pumping in Structural Joints," *Journal of the Acoustical Society of America*, Vol. **40**, 1966, 1064–1072.
11. E.E.Ungar and G.Maidanik, "High-Frequency Plate Damping Due to Gas Pumping in Riveted Joints," *Journal of the Acoustical Society of America*, Vol. **44**, 1966, 292–295.
12. M.J.H.Fox and P.N.Whitton, "The Damping of Structural Vibrations by Thin Gas Films," *Journal of Sound and Vibration*, Vol. **73**(2), 1980, 279–295.
13. L.C.Chow and R.J.Pinnington, "Practical Industrial Method of Increasing Structural Damping in Machinery, I : Squeeze-Film Damping with Air," *Journal of Sound and Vibration*, Vol. **118**(1), 1987, 123–139.
14. K.U.Ingard and A.Akay, "On the Vibration Damping of a Plate by Means of a Viscous Fluid Layer," *Journal of Vibration, Acoustics, Stress, and Reliability in Design*, Vol. **109**, 1987, 178–184.
15. P.M.Morse and K.U.Ingard, *Theoretical Acoustics*, Princeton University Press, Princeton, New Jersey, 1968.
16. S.Temkin, *Elements of Acoustics*, John Wiley and Sons, Inc., New York, 1981.

SECOND INTERNATIONAL CONGRESS ON
RECENT DEVELOPMENTS IN AIR- AND
STRUCTURE-BORNE SOUND AND VIBRATION
MARCH 4-6, 1992 AUBURN UNIVERSITY USA

FUZZY COMPREHENSIVE EVALUATION OF SHOCK INTENSITY OF WARSHIP PROPULSIVE SYSTEM

Pang Jian* Shen Rongying**

* Dept. of Acoustic & Vibration, Wuhan Ship Dev. & Design Inst. Wuhan, 430064, Box 64291, China

** Institute of Vib., Shock & Noise Research, Jiao Tong University, Shanghai, 200030, China

ABSTRACT

This paper deals with shock intensity of warship propulsive system (WPS) and its fuzzy comprehensive evaluation. The level of shock intensity and the factor reference set which consists of all the intensity evaluating factors are presented. The method of single and two stage multifactorial evaluation is used to evaluate the shock intensity. This method is applied to analysing a damage problem of WPS of a mine countermeasures vessel under explosion circumstances. The theoretical analysis result is compared with experimental one and the agreement is encouraging.

INTRODUCTION

Warship Propulsive System (WPS) is the heart of a warship. Whether a warship can operate normally or not, it mainly depends on the reliability of WPS. With the development of new vibration isolation system on warship, more and more study has been done on its resisting shock function, especially when WPS is exposed to shock circumstance caused by underwater non-contact explosion.

It is well known that shock evaluation is a very important subject in investigation of shock response. How to determine an evaluation criterion is the key problem in analysis of a damage caused by shock. So far the shock response magnitude has almost been adopted to be a criterion in most standards and references. Generally, acceleration is used to be an evaluation criterion in shock measurement and analysis, because it is easy to measure and has directly relation with force. Therefore shock damage level of structure is supposed to be determined by acceleration. Acceleration spectrum and its time history have also been widely used. Another criterion of shock evaluation is velocity response. H.A.Gaberson analyzed transverse wave in rod and longitudinal wave in beam and concluded that

modal stress has only relation with velocity function and independence of frequency[11]. He also pointed out that acceleration magnitude has not direct relation with shock damage level and modal velocity should be chosen as shock evaluation criterion. In engineering design and measurement, shock velocity spectrum, especially pseudo velocity spectrum is widely used. However, shock is very complicated, so shock criterion should reflect such a complexity. Unfortunately, above evaluation criterion only considered one aspect of shock, that has not included all the intensity evaluating factors. In this paper shock intensity of WPS and its fuzzy comprehensive evaluation are presented. The level of shock intensity and the factor reference set are established. The method of single and two stage multifactorial evaluation is applied to analysing a damage problem of WPS of a mine countermeasures vessel under explosion circumstances. The theoretical analysis result is compared with experimental one and the agreement is good.

SHOCK INTENSITY

Shock damage is not only related to response magnitude, but also to shock resource, shock pulse time, structure material, equipment arrangement, human reaction and etc. Therefore, in order to entirely assess the damage level of structure or equipment caused by shock, all above factors must be considered. Shock intensity presented in this paper includes all these factors. Shock intensity is defined as follows: when structure or equipment is subjected to shock excitation, multi-factors, such as response magnitude, shock resource and single element damage index, must be included to evaluate structure or equipment damage level caused by shock.

SHOCK INTENSITY SET AND FACTOR SET

Under shock circumstance caused by non-contact underwater explosion, WPS may be subjected to different damage: no damage basically, damage to some extent, complete damage and etc. Shock intensity of WPS exposed to underwater explosion is classified into five levels as follows

$$U = \left(I_1,\ I_2,\ I_3,\ I_4,\ I_5 \right) \tag{1}$$

in which

I_1 — normal operation.

I_2 — slight damage, but the system still maintain operating normally.

I_3 — damage to some extent that means structure or equipment of the system is damaged and its function decreases greatly, but the system can still operate.

I_4 — damage heavily, serious malfunction happens in the system and its matching function decreases greatly, but through emergency measures it can be operated for short time.

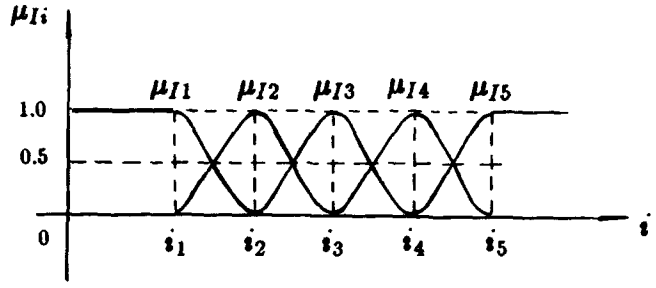

Figure 1: Graphic membership function

I_k — loss of survivability.

U — the shock intensity reference set, which is a discrete set.

Instead of a jump discrete point set, the shock intensity varies from one level to its adjacent level gradually, which shows the fuzzy characteristics of definition of shock intensity.

Usually, it is easy to determine two situations of the system: normal operation I_1 and loss of survivability I_k. Therefore, after determining boundary i_1 of I_1 and boundary i_k of I_k, the shock intensity set becomes a closed interval on real-axis, i.e.

$$W = \left\{ i \mid i \in [0,5] \right\} = \left[0, \ 5 \right] \tag{2}$$

whereas each intensity level $I_i (i = 1, \ldots, 5)$ in the discrete set U is a fuzzy subset in a continuous set, i.e. a fuzzy interval in a closed interval [0, 5], its membership function μ_{I_i} is given in figure 1.

Shock intensity level I is also a fuzzy interval and has to satisfy two characteristics:

(1) The membership level at midpoint of interval reaches a maximum and equals to 1;

(2) At a joining point of two intensities, both of two membership levels are the same and equal to 0.5.

There are two types of membership function: sinusoidal and normal. Sinusoidal membership function is only extended to adjacent intensity level, whereas normal membership function can be extended to every intensity level. Therefore normal membership function is more widely used than sinusoidal one. In this paper normal membership function is adopted.

The factor reference set which consists of all the intensity evaluating factors, can be defined as

$$V = \left(V_1, \ V_2, \ V_3, \ V_4 \right) \tag{3}$$

where, each $V_j (j = 1, \ldots, 4)$ represents a factor subset which means individually as follows

Subset 1 (V_1): damage index S for different kind of structure or equipment;

Subset 2 (V_2): base motion magnitude, such as vertical acceleration a_v, horizontal a_h, vertical shock velocity v_s;

Subset 3 (V_3): factors influencing on intensity that may be got partly, such as the deformation of warship under explosion, relation between shock resource and warship;

Subset 4 (V_4): intensity magnitude, which is very difficult to give out , such as human reaction.

For V_3 and V_4 factor subset, it is difficult to get the real value of shock intensity. So fuzzy statistical data or expert evaluation is inevitable to determine these factor levels, whereas for V_1 and V_2 factor subset, membership function can be set up, and single factor evaluation can be obtained based on these function. Unfortunately, so far the shock test data is very limited, it is very difficult to establish corresponding membership function which needs much more data and information on shock. Therefore, membership function of V_1 and V_2 established in this paper and evaluation matrix derived from these functions are subjective to a certain extent. A large number of test is needed to check these functions.

Damage level of each equipment or structure is expressed by its shock damage value. 0 means normal operation; 1 represents complete damage. Other damage level between these two extreme level are divided into several levels listed in table 1.

Table 1

shock intensity		I_1	I_2	I_3	I_4	I_5
damage index S	*average*	0	0.15	0.45	0.8	1.0
of equipment	*range*	0	0-0.3	0.3-0.6	0.6-1.0	1.0

Due to complication of warship structure and different arrangement of equipment, the shock damage level of structure or equipment is different. In this paper we consider shock intensity on the foundation structure or equipment, and assume that structure or equipment are rigidly jointed with the foundation. Therefore, both damage levels of structure or equipment and foundation may be considered as the same. The acceleration and shock velocity of five shock intensity level are shown in table 2.

Table 2

shock intensity		I_1	I_2	I_3	I_4	I_5
vertical acceleration	average	60	140	180	220	∞
a_v (g)	range	0-120	120-160	160-200	200-240	240-∞
vertical shock velocity	average	1.25	2.75	3.5	4.5	∞
v_s (m/s)	range	0-2.5	2.5-3.0	3.0-4.0	4.0-5.0	5.0-∞

FUZZY COMPREHENSIVE EVALUATION OF SHOCK INTENSITY

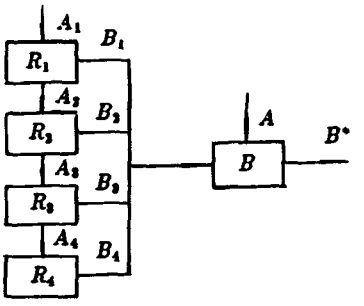

Figure 2: Block diagram of evaluation process

There are many factors that may be considered in evaluating shock intensity. Here we use the method of two-stage evaluation, whose steps are as follows.

Because each factor subset includes some sub-factors, first we have to evaluate every V_j by using single-stage evaluation. Second, based on the results of single-stage evaluation two-stage evaluation is treated. Thus the two-stage fuzzy evaluation model is established[3].

Single-stage comprehensive evaluation: each factor subset includes r_i factors. In order to derive the evaluation matrix R_j, weighting function A_j should be determined. Weighting function A_j represents the contribution of each factor in factor subset V_j. Assuming the evaluation matrix of V_j to be as R_j, the corresponding fuzzy level vector B_j is obtained as follows

$$B_j = A_j \times R_j \tag{4}$$

Two-stage comprehensive evaluation: B_j is the result of single-stage comprehensive evaluation about V_j. Based on this result, we decide the total weighting function, which represents the contributions of each factor subset in factor set V. The total evaluation matrix B consists of b_j. The final fuzzy vector is obtained as follows

$$B^* = A \times B \tag{5}$$

Above process is shown in figure 2.

Before using the fuzzy comprehensive evaluation, it is necessary to determine membership function. Here normal membership function is adopted, that is

$$\mu(x) = exp\,(-(\frac{x-c}{m})^2) \tag{6}$$

in which m and c are constants. The constant c may be obtained from the condition of

$$exp\,(-(\frac{x_{j+1}-x_j}{2c})^2) = 0.5 \tag{7}$$

Then we can get

$$c = 0.6\,(x_{j+1}-x_j) \tag{8}$$

where x_j, x_{j+1} $(j = 1,...,4)$ are the boundary values of intervals. The calculation results are given in table 3.

According to Equation (6), each element of fuzzy relation R_j is obtained, i.e. $r_{ij} = \mu_{ij}$ $(i = 1,\ldots,5,\ j = 1,\ldots,4)$

$$r_{ij}(V_j) = exp\,(-(\frac{V_j - m_{ij}}{c_{ij}})^2) \tag{9}$$

Table 3

factor / intensity	$S(V_1)$		$a_v(V_2)$		$a_h(V_3)$		$v_s(V_4)$	
	m_{ij}	c_{ij}	m_{ij}	c_{ij}	m_{ij}	c_{ij}	m_{ij}	c_{ij}
I_1	0	0	60	72	36	36	1.25	1.5
I_2	0.15	0.18	140	24	84	12	2.75	0.3
I_3	0.45	0.18	180	24	108	12	3.5	0.6
I_4	0.8	0.24	220	24	132	12	4.5	0.6
I_5	1.0	0	∞	∞	∞	∞	∞	∞

Based on r_{ij}, each fuzzy evaluation can be treated to each single factor of a practical problem, and the evaluation results R_i $(i = 1,\ldots,4)$ can be obtained.

The fuzzy comprehensive evaluation is applied to checking a practical shock evaluation problem in reference [3]. Explosion test results give out factor values at foundation of a diesel engine : $S(V_1) = 0.7$, $a_v(V_2) = 179$, $a_h(V_3) = 107.4$ and $v_s(V_4) = 3.5$. Fuzzy vector of its shock intensity is required to be determined. Substituting V_j values and data listed in table 3 into equation (9), we can obtain

$$R_1 = \left[\ 0.00,\ \ 0.00,\ \ 0.15,\ \ 0.84,\ \ 0.00\ \right]$$

$$R_2 = \left[\ 0.03,\ \ 0.07,\ \ 1.00,\ \ 0.05,\ \ 0.37\ \right]$$

$$R_3 = \left[\ 0.02,\ \ 0.02,\ \ 1.00,\ \ 0.01,\ \ 0.37\ \right]$$

$$R_4 = \left[\ 0.11,\ \ 0.00,\ \ 1.00,\ \ 0.06,\ \ 0.37\ \right]$$

After single factor evaluation, vector R_j $(j = 1, ..., 4)$ is obtained, single-stage comprehensive evaluation can be calculated according to equation (4).

Only one factor is included in subset V_1, i.e. damage value of equipment $S(V_1) = 0.7$. Weighting vector, $A_1 = [1.0]$ is chosen because of only one factor. Therefore, we have

$$B_1 = A_1 R_1 = \left[\ 1.0\ \right]\left[\ 0.00,\ \ 0.00,\ \ 0.15,\ \ 0.84,\ \ 0.00\ \right] = \left[\ 0.00,\ \ 0.00,\ \ 0.15,\ \ 0.84,\ \ 0.00\ \right]$$

Three factors, a_v, a_h and v_s are included in subset V_2. Weighting vector A_2 is given according to experience data, i.e. $A_2 = [0.4, 0.2, 0.4]$. We obtain

$$B_2 = \left[\ 0.4,\ \ 0.2,\ \ 0.4\ \right]\begin{bmatrix} 0.03 & 0.07 & 1.00 & 0.05 & 0.37 \\ 0.02 & 0.02 & 1.00 & 0.01 & 0.37 \\ 0.11 & 0.00 & 1.00 & 0.06 & 0.37 \end{bmatrix} = \left[\ 0.06,\ \ 0.03,\ \ 1.00,\ \ 0.05,\ \ 0.37\ \right]$$

So far the research on underwater explosion, the deformation of warship and human reaction are very limited. Therefore it is hard to determine the evaluation factors of V_3 and V_4. Here, comparing the research result of earthquake with one of underwater explosion, single stage evaluation results of fuzzy vector are obtained:

$$B_3 = \left[\ 0.00,\ \ 0.36,\ \ 0.48,\ \ 0.32,\ \ 0.00\ \right]$$

$$B_4 = \left[\ 0.00,\ \ 0.48,\ \ 0.50,\ \ 0.12,\ \ 0.00\ \right]$$

Determining total weighting vector, $A = [0.3, 0.4, 0.15, 0.15]$, the two-stage comprehensive evaluation is obtained

$$B^* = \left[\ 0.3,\ \ 0.4,\ \ 0.15,\ \ 0.15\ \right]$$

It is the final evaluation result. Analysing the membership level in intensity fuzzy vector B^*, we can conclude that main intensities are located in I_3 and I_4, and this analysis is basically in agreement with the explosion test result.

CONCLUSIONS

From above investigation, some conclusions may be drawn:

1. Shock intensity is a comprehensive index in analysing the damage of WPS equipment or structure subjected to underwater explosion shock excitation, and includes shock response, structure or equipment, explosion resource and etc. The method of single and two stage comprehensive evaluation may be a suitable way for solving evaluation problem of shock intensity of WPS.

2. Basically, shock intensity set and factor set include almost all information of shock intensity analysis. It is reasonable to evaluate shock intensity using two stage fuzzy comprehensive evaluation. The theoretical analysis is basically in agreement with the experimental result.

3. It is an exploration to apply the method of fuzzy comprehensive evaluation into investigating shock intensity of WPS. The concept and analysis methods presented in this paper should be further improved.

REFERENCES

1. H.A.Gaberson, *Modal velocity as a criterion of shock severity* The Shock and Vibration Bulletin, Dec. 1969.

2. Guang-Yuan Wang, *Two-stage comprehensive evaluation of earthquake intensity and application* Earthquake engineering and structural dynamics, Vol.13,No.1,1985.

3. *The proceeding of underwater explosion tests on 082G mine countermeasures vessel* Technical Report of Marine Design & Research Institute of China, Apr. 1982.

SECOND INTERNATIONAL CONGRESS ON
RECENT DEVELOPMENTS IN AIR- AND
STRUCTURE-BORNE SOUND AND VIBRATION
MARCH 4-6, 1992 AUBURN UNIVERSITY, USA

ON THE EVALUATION OF NOISE OF THE CAM TYPE MECHANISMS

A.J.Chistiakov and N.L. Suhanov
S.M.Kirov Institute of Textile and Light Industry
St.Petersburg,
USSR

This paper presents the results of evaluation of sound radiation of com mechanisms.The terms for Energy Accounting Equation have been obtained for this kind of mechanisms. The equation of the radiation efficiency of a shaft with a finite lenght and flexural mode of vibration has been obtained.

The prediction of the level of noise of the cam mechanisms based on the results of the investigations has been validated experimentally.

INTRODUCTION

In a first approximation a number of cam mechanisms could be modeled as a system with an elastic body impacting a metal cylindrical shaft. The solution of the problem of sound radiation from this system has been based on the statistical energy method.

The level of the sound energy (A-weighted) radiated by an element of this system per one shock can be presented in the form of the Energy Accounting Equation [1]:

$$L_{eq}(A,f_0,\Delta f)=10\lg|F'(f_0)|^2+10\lg Re[H_c(f_0)/j]+10\lg(\sigma_{rad}A/f_0)+$$
$$+10\lg(\Delta f/f_0)-10\lg\eta+10\lg(S/M)+10\lg(\rho_0 c_0/2\pi\ 10^{-12}) \qquad (1)$$

where $F'(f_0)$- is the force derivative spectrum;
$H_c(f_0)$- is the structural response of the element;
σ_{rad} - is the radiation efficiency of the element;
η,S,M -are the loss factor,surface area and the mass of the element;
$f_0,\Delta f$ - is the band centre frequency and frequency band;
ρ_0,c_0 - are the density and speed of sound in air.

This method has been used succesfully for prediction of machine noise in many cases [1]. Thus,in this paper, Energy Accounting Equation has been obtained for evaluation of noise of the cam type mechanisms.

For the mechanisms under study the load is usually standard and is given by $F=F_0\sin^2(\pi t/\tau)$. Then the value $|F'(f)|^2$ will be:

$$|F(f)|=F_0^2\sin^2(\pi\tau f)/(1-(f\tau)^2)^2 \qquad (2)$$

where F_o, τ - are the amplitude and duration of the shook;
f - is the frequency.

The amplitude of the force could be determined from the properties of the mechanism:

$$F_o = \pi MV/\tau$$

where M - is the mass of the impacting body;
V - is the impact velocity.

The value $Re(H_c/j)$ of the shaft in the region of frequencies above the first resonance could be obtained using its characteristic impedance[2]:

$$Re(H_c/j)=1/[f^{3/2}r^{5/2}(2\pi^2\rho_1(\pi c_1)^{1/2})] \quad (3)$$

where c_1, r, ρ_1 -are longitudinal wave velocity, radius and dencity of the shaft.

The value $Re(H_c/j)$ for the impacting body is equal to:

$$Re(H_c/j)=k\eta/[(k-\omega^2M)^2+(k\eta)^2] \quad (4)$$

where k, M, η -are the assisting stiffness, mass and loss factor of the body.

The radiation efficiency σ_b of the impacting body can be assessed from the formula[3]:

$$\sigma_b=(k_oR)^4/(4+(k_oR)^4) \quad (5)$$

where R-is the equivalen radius of the impacting body(radius of the sphere with equivalent to impacting body surface area);
$k_o=2\pi f/c_o$-is wave number in air.

It has been determined experimentally that the assessment of the radiation efficiency of the shaft by presenting it as an infinite oscilating cylinder leads to a great number of errors. That is why the task of assessment of the radiation efficiency of a shaft with a finite length and flexural mode of vibration has been put forward.

The radiation efficiency of an infinite shaft is equal to[3]:

$$\sigma_\infty=2/[\pi k_o r|H_1^{(2)'}(k_o r)|]^2\approx[1+(2/\pi k_o{}^3r^3)^2]^{-0.5} \quad (6)$$

It is known that the radiation efficiency of a linear group of n correct phase sources with their own efficiency σ_o can be determined from the expression[4]:

$$\sigma_{gr}=\sigma_o[1+(2/n)\sum_{i=1}^{n-1}((n-i)\sin(ik_od)/(ik_od))] \quad (7)$$

where d - is the distance between the sources.

When $n \to \infty$ and $nd = l = const$, after a number of transrormations the expression (7) can be rewritten in the form of:

$$\sigma=\sigma_\infty[(\pi/2)Si(k_ol)-(\pi/k_ol)\sin^2(k_ol/2)]\approx\sigma_\infty(1+(\pi/k_ol)^2)^{-0.5} \quad (8)$$

In the Eq.(8) the expression between the parentheses characterizes the influence of the cylinder on its efficiency.

Taking into account Eq.(6), the expression (8) can be rewritten in the form of:

$$\sigma=[1+(1+2/\pi k_o{}^3r^3)^2]^{-0.5}[1+(\pi/k_ol)^2]^{-0.5} \quad (9)$$

The expression (9) determines the radiation efficiency of the oscilating cylinder of a finite length. When $k_o l >> \pi$ the expression corresponds to an infinite oscilating cylinder, but when $k_o l, k_o r << \pi$, i.e. on low frequencies, it corresponds to the dipole.

When the oscilations of the shaft take place on its own frequencies, its portions with a length of $\lambda_f/2 = l/n$ are moving with the alternating phase (λ_f is the length of the flexural wave in the shaft).

That is why let us consider a linear group of sources with the alternating phase.

The radiation efficiency of the group has been obtained in the form of:

$$\sigma_{gr} = \sigma_o [1 + (2/n) \sum_{i=1}^{n-1} ((-1)^i (n-i) \sin(i\, k_o d)/i k_o d)] \qquad (10)$$

Finally, taking account of Eq.(9) and Eq.(10), radiation efficiency of a finite cylinder oscilating in one of its own forms can be rewritten in the form of:

$$\sigma_n = [1 + (2/n) \sum_{i=1}^{n-1} (-1)^i 2 \sin(i k_o \lambda_f/2)/i k_o \lambda_f] / [(1 + (2/\pi k_o^3 r^3)^2)(1 + (2\pi/k_o \lambda_f)^2)]^{0.5} \qquad (11)$$

where n - is the number of the oscilation mode.

The expression of the denominator of the formula (12) reflects the interaction of the sections of the cylinder moving in the antiphase and substantially diminishes the total radiation efficiency and more so when n-is even.

In the frequency band Δf the average radiation efficiency is equal to:

$$\sigma_{\Delta f} = [\sum_{n=n_l}^{n=n_u} \sigma_n / f_n] / [\sum_{n=n}^{n=n} 1/f_n] \qquad (12)$$

where n_l, n_u - are the lower and upper number of the mode of the oscilations in the frequency band Δf;

f_n -is the n-resonance frequency of cylinder.

The analysis of the solution has shown that in a general case, the sound radiating system can be dominated both by the radiation of the shaft and by the radiation of the impacting body.

The Table 1 presents, as an example, the results of the calculations of the sound energy radiated by a system for the following parameters of the system:

$r = 2 \times 10^{-2}$m $R = 3 \times 10^{-2}$m $\rho_1 = 8 \times 10^3$kg/m^3 $M = 2 \times 10^{-2}$kg

$k = 10^7$N/m $\eta_1 = 10^{-3}$ $\eta = 10^{-1}$ $\tau = 10^{-3}$s

Table 1- The level of the sound energy of the system (dB re 10^{-12}J)

Source Type	Octave band centre frequency,(KHz)					Total(A)
	0.5	1	2	4	8	
The shaft	68	62	61	39	27	66
The impacting body	56	63	64	56	46	69

Chistiakov p.4

The calculation has shown that the noise of the mechanisms under study is determined by the radiation of sound of the elastic body. The solution has made it possible to obtain the dependencies of the radiation of sound from mechanisms on the characteristics of the system and, consequently, to predict the efficiency of the constructional means of reduction of noise.

REFERENCES

1. E.I.Richards: On the prediction of impact noise, 3: Accountancy in industrial machines. Journal of Sound and Vibration, 1981, v 76, p.187-232.
2. V.S.Nikiforov, S.V.Budrin: Propagation and Absorbtion of Vibration on Ships, Sudostroyenie, Leningrad, 1968, 216p. (in Russian).
3. E.Skudzyk: Simple and complex systems, The Pennsylvania State University Press, University Park and London, 1968, 558p..
4. V.N.Tjulin: Introduction to the Theory of Radiation and Dispersion of Sound, Nauka, Moscow, 1976, 256p. (in Russian).

SECOND INTERNATIONAL CONGRESS ON
RECENT DEVELOPMENTS IN AIR- AND
STRUCTURE-BORNE SOUND AND VIBRATION
MARCH 4-6, 1992 AUBURN UNIVERSITY, USA

MULTIFUNCTIONAL CEILINGS

T,I. GALAKTIONOVA

Central Research and design Institute
of school Buildings
Tretykovskiy p. 2 TsNIIEP
103012 Moscov, USSR

ABSTRACT

The possibity to advance the parameters of the internal surroundings of the premises by the pendulous ceilings was appeared. The construction of the pendulous ceilings recommended by us are intended for the complex improvement of the aeroionic and acoustic rates in the different purpose premises.

INTRODUCTION

At present in the rooms for various purpose the hanging ceiling made of the sound absorbing materials are commonly used. The drawback of such hanging ceilings is that facilitating the improvment of the sound absorption in the room and to a considerable extent of the optimal noise conditions achievement, they do not effect on the improvement of such parameters of the microclimate as aero-ionic conditions. The task of the work was an optimization of the internal medium parameters for rooms by multipurpose devices, having the sound absorbing and aero-ionizing properties.

MAIN BODY

The numerous observations of the aero-ionic conditions in the rooms show that with time in the air medium the reduction of the concentration of light aeroions and the increase of the concentration of heavy aeroions occur. The bringing of the aeroionic conditions to the optimal ones by ventilation of the rooms is not always possible and gives good results. Therefore, in order to achieve the set task, alongside with the revealing of the optimum architectural-construction parameters and the room physical parameters, influencing on the internal medium formation the artificial air ionization was studied.

The aero-ionizing devices can be mounted into the constructions of the hanging ceiling. Such construction must combine the following important qualities:bioresistance, fire resistance, decorativity, easy mounting and the possibility to cover the technical communications with an easy access.

The recommended by us construction of "the Hanging ceiling", designed for the complex optimization of aero-ionic and acoustic conditions in the rooms of various purpose, includes the hanging ceiling and control unit by which the electric potential to the hanging ceiling is supplied. The hanging ceiling is designed as a construction, including the frame and the perforated dielectric plates. In the holes of the plates with a

certain pitch the tapered metal elements-needles, connected with each other, are located. Such plates, as it is known, absorb sound in various frequency bands depending on the applied material and in our case they create the concentration of light aeroions at the breathing level /1.0-1.5 m/ of order 3-5 $.10^3$ of aerions per 1 cm^3 /Fig.1 /.

The voltage of 30-40 KV from the control unit is supplied to the metal interconnected needles. In this the autoelectron emission takes place, which leads to the formation of light aeroions.

Simultaneously with the concentration of light aeroions the decrease of the heavy aeroion concentration occurs due to their deposition under the action of the electric field on thee floor surface.

In order to create the necessary micriclimate in the room we have also, developed "A sound absorbing device" for the hanging ceiling, including a metal frame in the form of a grate with a face thickness of 3-5mm, installed with the clearance on the enclosing construction, provided with a film, located between the frame and the enclosing construction. The faces of the grate, turned inside the room, are tapered to naught. During the voltage of 30-40 kV supply from the control unit to the grate the autoelectron emission occurs, leading to the formation of light aeroions depends on the supplied voltage value and the sharpening extent of the elements. In order to create the necessary potential gradient the ratio of the sharpened part to the non-sharpened one must be within 1:2 -1:4 range at the ratio of the edge thickness to its height 1:10 - 1:5. The sound absorption coefficient of the construction under study is determined from the boundary conditions on the grate for the total field of the incident and reflected waves, as well as for the field, excited in the intervals between the edges, where the film, which works as a membrane; is located.

We have measured the sound absorption coefficients of various versions of proposed constructions in a small-size reverberation chamber on the samples, the area of which did not exceed 1.5 m^2 and in a large reverberation chamber. The results of the measurement are presented in the table.

Another version of similar constructions can be an acoustical multicavity panel with a slit perforation. The acoustical factors of such panel, also, have been determined in the reverberation chambers.

The geometric parameters of the panel with the slit perforation, in which the needles for the air aeroionozation can be located, are given in Fig.2 . Considering the geometry of the panel one can see that it can attributed to a physical model of the related resonance systems of Helmholtz resonator type.

REFERENCES

The results of the measurements have shown that the absorbing properties of the panel with the links are 30-80% improved in comparison with the smooth reinforced concrete plate and 20-60% improved in comparison with the perforated plate.

The studies, performed in the small-size reverberation chamber, have shown:

- the complex sound absorbing ceiling from "Akmigran" plates, perforated for the aeroion radiators, has a broader sound absorption spectrum in comparison with the non-perforated "Akmigran" plate /α=0.9 - at 250Hz/
- the complex construction from the sheets of gypsum plaster board, perforated for the aeroion radiators, is a pronounced resonance construction with maximum sound absorption coefficient at 250 Hz frequency;
- the optimum height from the breathing area of a man to the aeroion radiation source must not exceed - 2.5 m, and the total height of the room from the floor to the hanging ceiling must not exceed 4 m.

Taking into account good sound absorbing properties and multifunctionality of the ceilings with aeroionization of air, these constructions can be recommended for noise reduction in public buildings.

Table

Frequency characteristics of sound absorption coefficients of proposed constructions for multifunctional purpose

No	Material or construction	Measurement conditions		Sound absorption coefficients at frequencies, Hz					
		Aggregate layer, mm	Air gap, mm	125	250	500	1 t	2t	4t
1	Plates "Akmigran" per. 10/80		50	0.51	0.9	0.88	0.77	0.74	0.68
2	The same, without perfor.		50	0.19	0.73	0.76	0.76	0.77	0.77
3	Metal grate, filled by felt	25		0.04	0.16	0.4	0.71	0.43	0.38
4	Grate without filler		25	0.02	0.06	0.12	0.2	0.24	0.29
5	Basalt mats with a glass mesh shell			0.8	0.26	0.2	0.24	0.27	0.21
6	GPB(Gypsum plaster board)10/60-perforation parameters	50		0.23	0.83	0.18	0.1	0.06	-
7	Panel with slit perforation(without slit filling by SAM)			0.09	0.25	0.2	0.12	0.19	0.1
8	The same, with slit filling by SAM(mineral cotton γ = 50 kg/m^3)			0.28	0.13	0.32	0.29	0.55	0.48
9	The same, with the application of sound absorbing links from FG plates in the shell 500x500mm with 50mm thickness			0.3	0.3	0.55	0.52	0.7	0.65

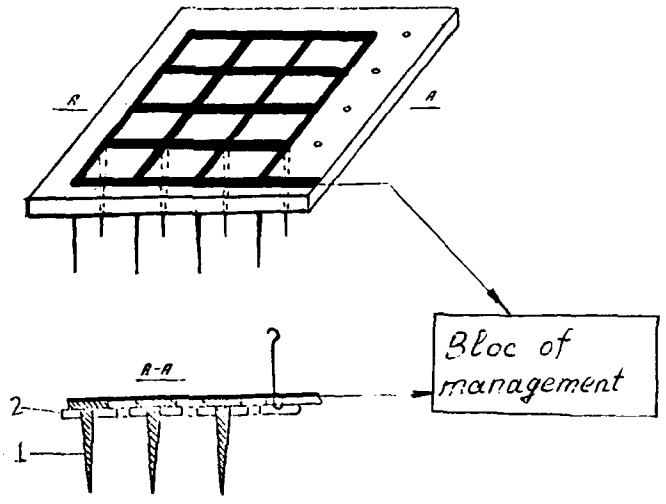

1-needle ; 2-plate

Fig.1.

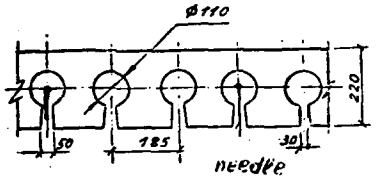

Mass of area unit, kg/m2 400
Thickness of slab, mm 220
Diameter of openings, mm 110
Distance between openings, mm 185
Width of slit, mm 4,30-50

Fig.2

SECOND INTERNATIONAL CONGRESS ON RECENT DEVELOPMENTS IN AIR- AND STRUCTURE-BORNE SOUND AND VIBRATION

MARCH 4-6, 1992 AUBURN UNIVERSITY USA

PHASE FEATURES OF MAN AND ANIMALS REACTION TO INFRASOUND EFFECT

B.J.Fraiman[1], A.S.Faustov[2], A.N.Ivannikov[3], V.I.Pavlov[3],

[1] Medical Laboratory of Voronezh Electronics Plant, Druzhinnikov 1, 394068 Voronezh

[2] Voronezh Medical Institute, 394068 Voronezh

[3] Department of Acoustics,Faculty of Physics, Moscow State University, 119899 Moscow Russia

ABSTRACT

Infrasound effect on biological systems is investigated by us within three main positions.

INTRODUCTION

First, we have studied the development of the interaction process between infrasound and human body within the time. Parameters of the functionality of the nervous and cardiovascular human and animal systems are studied according to ordinary techniques. The investigation covered hemodynamics, hemocoagulation, oxygen transportation, histology and histochemistry of myocardium, vessels, adipose cells changes, managerial function of the vegetative centers of the nervous system, and psychophysiological functions of the man-operator. Traditional techniques are used. In this paper all techniques are used not to investigate human and animals functions, but only to mark the direction of explored systems reaction to infrasound effect.

Secondly, the investigation was carried out within positions of physical acoustics.We came from the following assumptions. Majority of all interactions between infrasound and man takes place in official and domestic apartments. However, the dimensions of these apartments are comparable with a wavelength (at least, up to 100 Hz). A man who is either by force of official duties, or domestic habits in one or another part of the room, will interact with different energetic components of the acoustic field. In this connection various biological response at infrasound effect can be expected [1].

Thirdly, we have come from the physiology of sensorysystems with rich actual material, which allows to make a conclusion that ear added mechanism of interaction between man and infrasound should exist.

EXPERIMENTAL RESULTS

It is stated by an experiment that man and animals reaction on infrasound within the first seconds begins from activization ob the vegetative nervous system, starting up the humoral channel of the human body function regulation within several minutes from beginning of interaction. At the same time changes of the functional activity of the subcortical structures and human efficiency level arise.

By the end of 4-6 hours from the beginning of the effect the reversible changes of hemocoagulation and activity of respiratory myocardial ferments are being developed. The next phase is the phase of latent modifications which changes by 18-20 day of the effect with preventive force consumption of the human body and arising of the morphological modifications in the cardiovascular system.

The whole chain of the response reactions develops when the object is in that part of the laboratory where the vectors of active and reactive intensity are collinear (zone D). It is found that starting-up point of the development of the response reaction chain is the direct effect of acoustic wave and vascular system in D-zone which is cleared out by us [2].

All reactions investigated by us begin and go out in the determined time intervals called by us the phases of the human body reaction on the infrasound [3].

The person and animal reaction on the infrasound action begins from the reaction of the nervous system. In the first minute the regulating activity of the sympathetic section of the vegetative nervous system is strengthened and the tension index of other structures of the central nervous system is increased.

Then to the twentieth minute of influence the activity of the subcortical structures of the brain becomes worse and the level of the person capacity for work is reduced. At that time the indications of switching on of more plastic and longer functioning humoral channel of the person function regulation are appeared.

On the first day at the end of the fourth - sixth hour of everyday six hour influence of infrasound of the level 100 dB on frequency of 10 Hz the expressed reaction of increasing the coagulation activity of blood is developed. At that time the decrease of oxygen consumption from blood is registered, oxygen content is increased in venous blood without changing its percent level in arterial blood.

On the third day of influence the increased activity of some ferments of heart muscle respiratory cycle and activity oppression of other are clearly registered.

To the sixth day of influence the coagulation activity of blood is reduced to the development of hypocoagulation.

To the twelfth day of influence the oxygen content in arterial and venous blood is normalized.The state of coagulation activity of blood, the activity of respiratory ferments of the myocardial don't differ from the initial data. The histological changes of the muscular cells of the heart in the first day have a reversible character.

To the twenty fourth day of influence the hypercoagulation of blood is appearing again, the activity of respiratory ferments of the myocardial is diminished almost on 50 %. The destructive changes of the myocardial are appeared.

Particularly must be said about the reaction of the cells containing substance - protector geparin. At first labrozit content is changed, then their content per unit of area is gradually decreased maximal reducing to the twenty fourth day of influence.

DISCUSSION

All changes have a phase character. Under the phase of development we understand limited spaces of development of human body - reaction on infrasound. So the primary reaction of the nervous system is going out, the nervous centers get over a new level of functionality directing the humoral reaction to the infrasound action. At first this reaction has a time - serving character, the trustworthy changes from the 12th to the 18th day of influence are not found, at least, by out methods. And only after the 18th day of influence the reserve possibilities of human body are grown weak and visible changes in organs and systems can be seen. The second important moment, in our opinion, is the revealing of the ear added mechanism of the infrasound interaction and it is appeared that the infrasound can act directly on the wall of the blood vessel model. The analogous changes are registered from the vascular basin of persons and animals. The reaction is developed instantly with the appearance of forced acoustic interaction and disappears with the turning of the acoustic generator without decrement. The revealed direct action of the infrasound on the vessels explains the instant development of the reciprocal reaction of the nervous system when the infrasound is actinggand the development of all above stated functional and morphological changes in it.

In addition, the revealing of direct mechanism of the interaction of the blood vessel system and infrasound explains the fact that practically in all publications describing the morphological changes those or other changes in the vessels of the investigated organ or ischaemic changes in it are pointed out.

All above stated biological changes are developed not in all places of laboratory room but only in places where vectors of active and reactive intensity are collinear. Where the active sound intensity vector vortex is not equal to zero, the changes do not appear at all or has a character of the reactions developing in the conditions of comfort. And this is in spite of the same level of sound pressure.

The results clearly point out on the phase character of person and animals reaction, on the interaction with the infrasound. The basic phase of this interaction are:

1.The functional phase

a) a primary reaction of the nervous system on interaction between infrasound and vascular system,

b) a neurohumoral reaction,

c) a functional organs and tissue reaction on infrasound effect.

2.The phase of the functional systems tension followed by the organs and systems transfer on a new level of functioning in order to support a homoeothase.

3.Functional systee consumption phase.

4.Phase of the expressed morphofunctional modifications development.

CONCLUSION

The possibility of the development of this phase of man and animal reaction on interaction with infrasound depends on the place of their position in the space of the official apartment. More exactly, it depends on their interaction with one or another component of the acoustic field energetic structure (zone V and zone D according to our terminology). An important conclusion follows from this. Under the equal sound pressure level experiments carried out in V zone caused development of reactions similar with those ones as at the rest. It can lead into error the investigators and cause erroneous conclusions.

Besides, the application of non-adequate, not sensitive techniques either at "short-term test", or "hits" of the time of material collection to the latent phase can cause erroneous conclusions even at position of the object in the zone D. And, a level of sound pressure which influences upon reaction development rate may be so low that a duration of each phase can be estimated as an absence of process development or adaptation to it. In reality, the reaction develops since afferent vascular system receptors have very low limit of the sensibility.

To transfer to a higher limit of excitation these receptors need very powerful irritant. With sound pressure level of 130 dB the receptors consumption appears very quickly and the reaction may be weakly expressed as these is no signal of neurohumoral reaction starting-up. Whereas self-damaging of vessel walls quite protracted process causing protracted hypocoagulation which does not cause any guarded reaction of investigator.

So, phase development of man and animals reaction on infrasound in zone D must be taken into account in elaboration of the hygienic standards on infrasound.

We will present the above-described results in graphical forms. So, fig.1 a) ,b),c), d) show:

1.Nervous system reaction.

2.Humoral reaction.

3.Reaction of hemocoagulation.

4.Oxygen content in venous blood.

5.Level of person capacity for work.

6.Activity of respiratory cycle ferments.

7.Morphological changes of myocardial and cells-protectors.

REFERENCES

1.Fraiman B.J., Ivannikov A.N., Zhukov A.N. *On the Influence of Infranoise Fields on* Humans. 6-th International Meeting on Low frequency Noise and Vibration.Leiden 1991, p.49-56.

2.Zhukov A.N., Ivannikov A.N., Pavlov V.I., Fraiman B.J. Infranoise in closed Volumes, Fortschritte der Akustik, DAGA-91 Bochum, Teil A, s.385-388.

3.Zhukov A.N., Ivannikov A.N., Kravchenko D.I., Pavlov V.I. Distinctive features of energy fine structure of a sound field. Sov. Phys. Acoust. 1989, vol.35, no4, p.367-369.

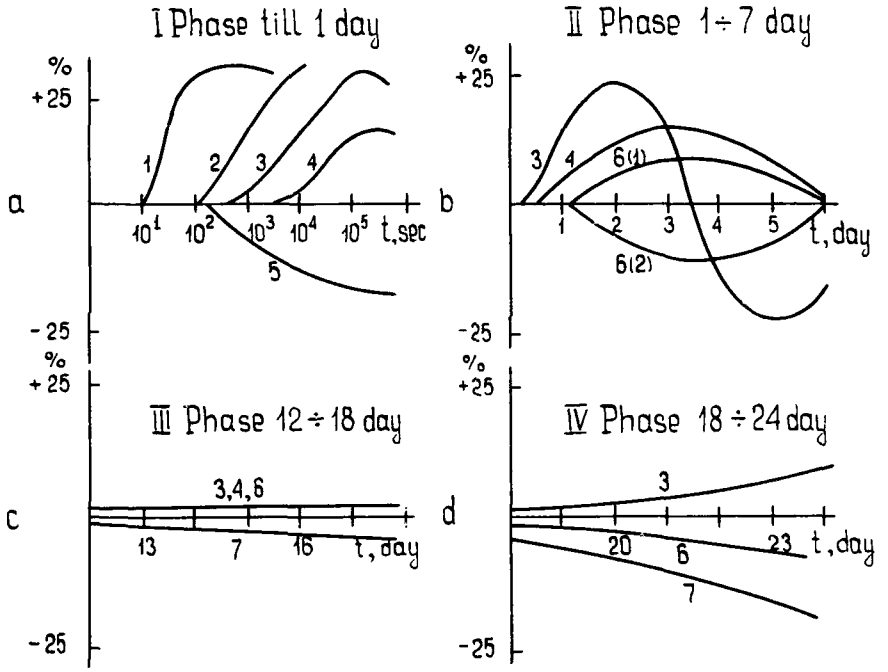
I Phase till 1 day
II Phase 1÷7 day
III Phase 12÷18 day
IV Phase 18÷24 day
%
+25
-25
a
b
c
d
1
2
3
4
5
6(1)
6(2)
6
7
10^1
10^2
10^3
10^4
10^5
t,sec
t,day
3,4,6
13
7
16
20
23

SECOND INTERNATIONAL CONGRESS ON
RECENT DEVELOPMENTS IN AIR- AND
STRUCTURE-BORNE SOUND AND VIBRATION
MARCH 4-6, 1992 AUBURN UNIVERSITY, USA

MEASURING OF THE TURBULENCE AND SOUND ABOVE THE OCEAN

A.N.Ivannikov, S.V.Makeev, V.I.Pavlov
Department of Acoustics
Faculty of Physics
Moscou State University
Moscou, 119899
USSR.

ABSTRACT

In this paper the original results of the observation of low-frequency atmospheric pressure fluctuations are presented. The results have been obtained straight over the Pacific Ocean surface during the 17-th expedition of the "Academician Nesmejanov" ship. The theoretical expressions for the degree law of the amplitude spectrum decrease and its connection with the wind velocity were found. It was carried out the experimental results analysis and its comparison with the proposed theoretical model of turbulence. The spikes on the background of fluctuation spectra have been discovered.

INTRODUCTION

There are a lot of publications concerning the atmospheric low frequency (less then 20 hz) noise and most of them deal with a pressure fluctuation above a ground but not upon water, because of experimental difficulties in the latter case. The measurements of a pressure fluctuation above a ocean surface especially at far distances from a coast are very interest. The data of such experiment are analyzed in this work. The atmosphere pressure fluctuations have been obtained above ocean surface during of the "Academician Nesmejanov" scientific ship's expedition (October 1989 - February 1990). The ship's route lay in the west area of the Pacific Ocean from Vladivostok to New Zealand.

EXPERIMENTAL PROCEDURE

The atmosphere pressure fluctuations were registered by high sensitive microphone carrier system type 2631 "B&K". During the measurements the microphone of carrier system has been removed at 2 m from ship board and 3 m from ocean surface by special bracket. The frequency of acoustic signal above 100 Hz was cut by low-pass-filter 01013 "Robotron". Then the signal was amplified by intrinsic amplifier of the indication block 02022 "Robotron" and one was recorded to the FM channel of gauging tape recorder MAS-34 "Telefunken".

Simultaneously with registration of acoustic signal the vibration of ship frame has been recorded to other tape recorder channel. It was made to except the "psevdoinfrasound" caused by the ship's vibrations. At the same time the coordinates of the ship, its velocity and course, the direction and velocity of wind, atmospheric pressure have been fixed too. Frequency analysis of recorded analog signals was carried out with the help of FFT-analyzer CF-300 ONO SOKKI in the range 0-20 Hz by means of linear average of 512 instant amplitude spectra. The duration of signal analysis was about seven minutes.

The typical averaged frequency spectrum in log-log scale is presented in Fig.1. Corresponding record was made 9 February 1990 in the Pacific Ocean's region removed more then 1500 km from New Guinea coast to North-West. The analysis of obtained spectrum

shows that in the investigated frequency band 0,5-20 Hz there is monotone decrease of amplitude spectra of pressure fluctuations with respect to frequency. Linear dependence in range 0,8-20 Hz is good observed too. It testifies of the degree law of decrease of amplitude spectrum with respect to frequency. The fall of spectrum at frequency 0,5 Hz and below is caused by the low frequency rolloff of gauging channel. It is necessary to note that about 10-15% spectra differ considerably from one shown in Fig.1. The connection of this phenomenon is not revealed yet.

THEORETICAL MODEL

Let assume the atmosphere pressure field $p(\mathbf{X},t)$ to be described by the expression

$$p(\mathbf{X},t) \simeq \rho_0 \mathbf{V}\cdot\mathbf{u}(\mathbf{X},t) \qquad (1)$$

where ρ_0 is the air density, $\mathbf{V}$ is the velocity of the air flow, $\mathbf{u}(\mathbf{X},t)$ is the field of the velocity fluctuations. Then the correlation function is

$$\langle p(\mathbf{X}_1 t_1)p(\mathbf{X}_2 t_2)\rangle = B(\mathbf{X}_1-\mathbf{X}_2, t_1-t_2) = \rho_0^2 V^2 n_i \langle u_i(\mathbf{X}_1, t_1)u_j(\mathbf{X}_2, t_2)\rangle n_j \qquad (2)$$

The brackets mean the average procedure. $n_i = V_i / |V|$. Following the hypothesis of "frozen" turbulence [1] we can write:

$$\langle u_i(\mathbf{X}_1, t_1)u_j(\mathbf{X}_2, t_2)\rangle = \int d\omega d\mathbf{k}\, D_{ij}\frac{E(k)}{4\pi k^2}\delta(\omega - \mathbf{kV})\cdot exp\left[-i\omega(t_1-t_2) + i\mathbf{k}(\mathbf{X}_1-\mathbf{X}_2)\right] \qquad (3)$$

Here $\omega = 2\pi f$ is circular frequency, $\mathbf{k}$ is wave vector, tensor $D_{ij} = \delta_{ij} - \frac{k_i k_j}{k^2}$ accounts the medium's incompressibility, i.e. the condition $div\ \mathbf{u} = 0$ is satisfied. The quantity $E(k)$ is spectral density of the turbulence fluctuations energy normed by condition:

$$\langle u^2(x,t)\rangle = 2\int_0^\infty dk\, E(k) \qquad (4)$$

For the calculations it is convenient to use spherical frame with Z-axis along of the vector $\mathbf{V} = V\mathbf{n}$. Taking account of the properties of the δ-function we have:

$$\langle p(\mathbf{X}, t_1)p(\mathbf{X}, t_2)\rangle = \int d\omega e^{-i\omega(t_1-t_2)}\frac{\rho_0^2 V}{2}\int_{\omega/V}^\infty dk\left[1 - \frac{\omega^2}{V^2k^2}\right]\frac{E(k)}{k} \qquad (5)$$

In the inertial interval of turbulence there is the condition $M^{-1} \ll \frac{\omega}{V} \ll m^{-1}$, where M and m are external and internal scale of turbulence correspondingly, the quantity $E(k) = K^2\cdot k^{-\mu}$. Here $K^2 = K\cdot\varepsilon^{2/3}$, K and μ are constants, ε defines the average dissipation of energy per time unit and per mass unit of the medium.

Then we obtain:

$$\langle p^2(x,t)\rangle = \int_0^\infty d\omega\left[C_\mu\,\rho_0^2\,K^2\,V^{\mu+1}\omega^{-\mu}\right] \qquad (6)$$

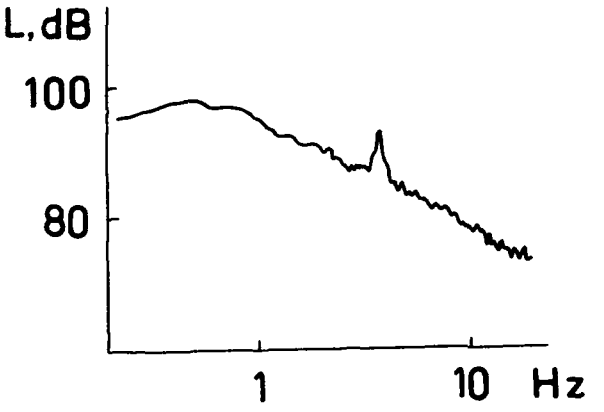

Figure 1--The typical *averaged spectrum.*

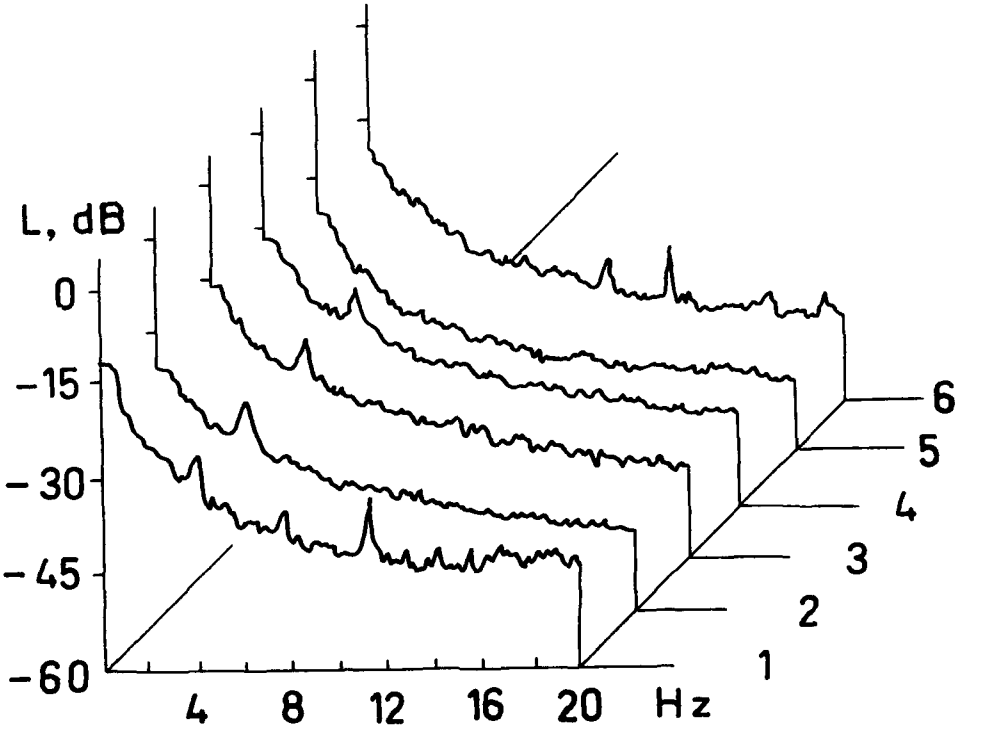

Figure 2--The spectra in different days:1 - Feb.2, 2 - Feb.5, 3 - Feb.8, 4 - Feb.11, 5 - Feb.14, 6 - Feb.17, 1990.

Here the coefficient is $C_\mu = \frac{2}{(\mu+1)(\mu+3)}$. The expression in square brackets is $|p(\omega)|^2$, where $|p($ is the amplitude spectrum of pressure fluctuations. It yields

$$|p(\omega)| = C_\mu^{1/2} \rho_0 \cdot R \cdot V^{\frac{\mu+1}{2}} \cdot \omega^{-\frac{\mu}{2}} \qquad (7)$$

It was these fluctuations that were measured in the experiments and their amplitude spectrum was determined as the result of analysis of data tape records. For comparison of the experimental results and theoretical model we represent Eq.(7) in log-log scale:

$$L(f) = A + B\ lgV - C\ lgf \qquad (8)$$

Here $A = 20lg\, C_\mu^{1/2} \cdot \frac{\rho_0 R}{(2\pi)^\mu \rho_0}$; $B = 20\frac{\mu+1}{2}$; $C = 20\frac{\mu}{2} \equiv 20n$; $p_0 = 2 \cdot 10^{-5}$ Pa is base level of sound pressure, $L(f)$ is the level of amplitude spectrum component in dB. For Kolmogorov's isotropic turbulence $\mu = 5/3$ [1]. Therefore, the dependencies $L \sim 26.6$ lgV at the fixed frequency and $L \sim 16.7$ lgf at the constant wind velocity will to confirm the Kolmogorov-Obuchov theory.

EXPERIMENTAL RESULTS

To our opinion the part of the way from the New Hebrides to Japan is of the most interest (02 February to 17 February 1990), where the ship sailed to North-West with the approximately constant velocity of 12-13 knots. Total path of the way in the west area of the Pacific ocean was more than 9000 km and it took 16 days. The most distance from coasts was 1500 km. On the whole the way the fluctuations spectra were similar to the one shown in Fig.1. In Fig.2. one shown the dynamics of the spectra in this time period in linear frequency scale. In different days the averaged spectra were processed by the least squares method on PC.

It is interesting to consider the connection of atmospheric pressure fluctuations and the infrasound with the oceanic and atmospheric parameters to examine the suggested theoretical model. The dependence of the typical parameters of the fluctuations spectra from the wind velocity is of the most important. In Fig.3. the dependence $n(V_{eff})$ is where V_{eff} is the module of the vector sum of the wind and the ship's velocities. The line in Fig.3. is described by formula:

$$n = 1.01 - 7.94 \cdot 10^{-3} \cdot V_{eff} \qquad (9)$$

i.e. there is a weak trend to decrease n with respect to the effective wind velocity. In this period the average value of $n = 0.92 \mp 0.08$ that correlate good with the theoretical value of $n = 5/6 = 0.83$. The similar situation exists for dependence of n from a roughness of the ocean's surface. Though in this case one has to account the connection between the wind velocity and the ocean's roughness.

It results from Eq.(8) that an amplitude of spectral components is a linear function of lgV. The integral sound level L_{int} in a fixed frequency range is proportional to lgV. The dependence L_{int} in range 0-20 Hz of lgV is shown in Fig.4.(points on the chart). There is an increasing of the pressure fluctuations level though the experimental value of the coefficient B turns out smaller than the theoretical one.

DISCUSSION OF THE SPIKES OF SPECTRUM

The obtained results contain often spikes on the background of almost monotonous decreasing of the fluctuation spectrum. Perhaps it is infrasound. For example analysis of the fluctuation record on the way from the New Hebrides to Japan reveals spikes in range 3.5-4.0 Hz. The exceeding of these spectral components over background is 4-10 dB. The notable spike at frequency 3.9 Hz and the exceeding above the background of 7 dB is

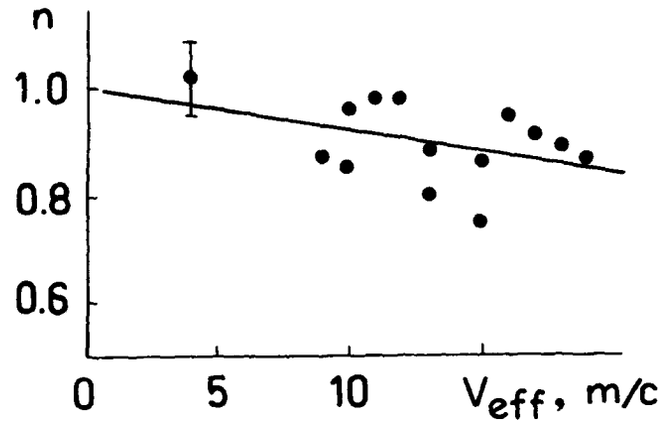

Figure 3--Experimental value of the coefficient n.

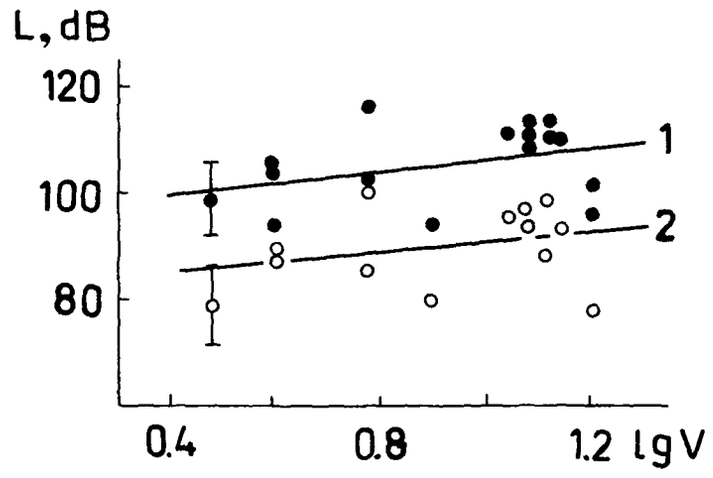

Figure 4--Integral sound level (points) and infrasound level (circles).

shown in Fig.1.

The level of infrasound in this time period was fluctuated from 80 to 100 dB, i.e. the value of the sound pressure of infrasound wave was approximately p = 1Pa. Infrasound levels reach maxima in the period of February 7-11. It is necessary to note that the observed invariability of the spikes frequency and the relative narrowness of their spectra are similar to peculiarity of "marine voice" [2]. This allows to make a supposition about their similar origin. Naturally it appears the question about origin of this infrasound. Unfortunately our data do not allow to give correct answer.

The dependence of an infrasound level on wind velocity at frequency 3.5-4.0 Hz is shown in Fig.4. (circles on the chart). One can to see the weak trend to its increasing at great wind velocities. In spite of the considered data do not allow to make correct conclusion about the oceanic infrasound's origin, we may suppose the one described in [2].

CONCLUSION

During the three months of the expedition the ship sailed more than 30,000 km in the Pacific Ocean. It gave exceptional observations of the atmospheric turbulence and the infrasound at large distances in the wide band of infrasonic frequencies (more than five octaves). The experimental investigations were carried out in the frequency band of 0.5-20 Hz.

The spectra of the atmospheric pressure fluctuations were shown to decrease proportionally to ω^{-n}. The index n was determined. Its dependence on the wind velocity was established. Also the spikes on the background of the fluctuations spectra were discovered. They are expected to be connected with the infrasonic waves. It was offered a theoretical model of a description of pressure fluctuations and its comparison with the experimental results.

REFERENCES

1. G.K.Batchelor. The theory of homogeneous turbulence. Cambridge, 1953.
2. Pavlov V.I., Sukhorukov A.I. Infrasound radiation into atmosphere by an eddy inhomogeneity located near the ocean surface. Acad. Sci. USSR, Atmos & Oceanic Phys.(USA), vol.20, no.8, 1984, p.674-681.

SECOND INTERNATIONAL CONGRESS ON
RECENT DEVELOPMENTS IN AIR- AND
STRUCTURE-BORNE SOUND AND VIBRATION
MARCH 4-6, 1992 AUBURN UNIVERSITY, USA

COMPARISON TESTS BETWEEN ACOUSTIC EMISSION TRANSDUCERS FOR INDUSTRIAL APPLICATIONS

S.C. KERKYRAS*, W.K.D. BORTHWICK°, R.L. REUBEN+,
P.A. DRAKATOS* and K.L. TZANETOS*

* DEPARTMENT OF MECHANICAL ENGINEERING, UNIVERSITY OF PATRAS, GREECE.

+ DEPARTMENT OF MECHANICAL ENGINEERING,
HERIOT-WATT UNIVERSITY, EDINBURGH, U.K.

° Present Address: CEC BRITE DIRECTORATE.

1. ABSTRACT

In this work the response of some commercial PZT Acoustic Emission (AE) transducers is examined under a set of controlled conditions in order to isolate the resulting effects of surface excitation (controlled by wave propagation conditions) and characteristics of the sensor itself (i.e. resonances). The behaviour of the two commercial transducers is compared with an experimental transducer based on PVdF film.

2. INTRODUCTION

The increasing interest in improving the productivity of manufacturing processes has naturally emphasised the role of automation of these processes. The successful automation of manufacturing operations requires continuous knowledge of the state of the operation. The control of manufacturing processes also requires on-line information on the behaviour of the manufacturing systems. In this light, Acoustic Emission (i.e. stress wave emissions from materials undergoing deformation, fracture, or other internal mechanisms releasing energy) has great potential as a technique to monitor such processes. It has therefore become very important to investigate the factors that influence the responses of commercial AE sensors and to compare these responses with those obtained by some non-commercial, high fidelity AE transducers.

3. REVIEW ON SOME TYPES OF AE TRANSDUCERS

In this work, two different types of AE sensor are compared. AE can be measured using piezoactive, capacitive, electromagnetic methods. The following brief review describes the two types relevant to this work and also an optical sensor against which the PVdF sensor has already been compared [1].

i) Commercial Piezoelectric AE sensors

The majority of the commercial AE sensors belong in this category. The piezoelectric active element is lead-zirconate-titanate (PZT) and these sensors may be "broadband" or "resonant" devices. The large aperture (phase interference effects due to large contact surface) of the commercially available devices (shoe sizes are typically of the order 10 to 20 mm) restrict

the response to the different wave modes. The directionality depends on crystal geometry and polarization. Normally commercial sensors are omni-directional.

ii) **The PVdF displacement transducer**

The semi-crystalline polymer polyvinylidene fluoride (PVdF) processes piezoelectric properties. It is flexible and compliant and has excellent bandwidth and sensitivity. PVdF has been successfully used in a strain-gauge-like application as an AE transducer for monitoring composites [2]. Scott and Carlyle [3] indicate that PVdF transducers suffer much less from ringing than commercial broadband devices and are capable of a flat frequency response over a wide range. Chang and Sun [4] have developed a PVdF transducer which, depending on the backing geometry, may be used either as a displacement or a velocity transducer. For displacement measurements a brass backing with a conical extension is pressed against the PVdF film and onto the surface being monitored. The use of a long acrylic rod as backing significantly changes the response to being more like that of a velocity transducer.

A PVdF displacement transducer with brass backing has been used to monitor a turning operation on a lathe (Kerkyras et al [5]), and its frequency response appeared to be very promising for power spectrum diagnosis of AE signals, something which has proven very difficult using commercial AE devices. The basic conclusion from this work was that this AE sensor showed high fidelity, mode separation and had a broadband response free from resonances. These characteristics, together with its low cost make it a potentially very useful device.

iii) **The Fibre Optic Interferometer**

Optical trandsucers for AE monitoring are attractive because of the possibility of using both contacting and non-contacting probes and because of their flat frequency response over a very large bandwidth.

It has been shown that fibre optic techniques can be used to realise robust interferometers with a wide range of applications in physical sensing. In particular, fibres have been used effectively as displacement and velocity transducers [6].

4. EXPERIMENTAL SET-UP

The transducers studied in this work were tested using a range of propagation media and their response was analysed by using standard signal processing methods. The sensors used were the Dunegan S9204 and D9201A and the experimental PVdF displacement transducer. A standard AE source, the Nielsen pencil lead break, was used as excitation. Fig.1 shows a block diagram of the instrumentation used in the experiments.

The three propagation media that were evaluated were:

a) A large cylindrical steel block of height 19 cm and diameter 18 cm, well lapped on both flat surfaces.

   This structure was used as a propagation medium in an attempt to eliminate reflections as far as possible. In order to achieve this the highest available sampling rate (40 or 20 MHz) was used to acquire AE data.

b) A steel plate of dimensions 54 x 28.2 x 0.65 cm.

   The reason this structure was chosen as a propagation medium was the availability of analytical solutions which can provide a comparison between measured and calculated responses (e.g. Ceranoglu and Pao [7]).

c) A long steel bar of rectangular cross-section having dimensions 177 x 7.5 x 1.3 cm.

This structure was proposed by Kerkyras et al [8] as a simple propagation medium in order to increase the number of reflections of bulk waves at the free surfaces and in this way to minimise their influence on the received signal by placing the sensor at a long distance from the source. In this way it was expected that the dominant wave mode captured by the sensors would be surface waves. Fig.2 shows these three difference propagation media schematically.

5. RESULTS AND DISCUSSION

In all experiments a 40dB gain pre-amplifier was used. The first 4096 data points were stored in the computer memory. These data were then averaged over at least 8 pencil lead breaks in each case. The data were normalized and an FFT was performed. It should be noted that amplitudes in the obtained plots are affected by gain and trigger level settings which were chosen to give the best reliability of data capture. Furthermore the data were ranged to ensure maximum resolution within the window. This means that amplitudes in the frequency domain are relative only but the visual content of the graphs is maximised.

Figures 3 to 7 and 9 to 13 show frequency domain responses for the various propagation media for the D9201A and S9204 sensors respectively. Also, Figures 8 and 14 show time domain responses for these two sensors obtained on the steel plate propagation medium. Finally, figures 15 and 16 show, respectively, time- and frequency-domain responses for the PVdF based transducer to excitation on the cylindrical steel block.

By comparing Figures 9-13 with Figures 3-7 it can be seen that the D9201A sensor is sensitive to surface waves with broad frequency responses in the range of 0.1 to 1MHz whereas the S9204 sensor is sensitive in the frequency range of 50 to 450 kHz. Also, both sensors showed similar sensitivity both in surface and compression waves. The influence of the three different propagation media on the transducers' response is quite obvious in the frequency domain. Furthermore, epicentral excitations changed the frequency responses significantly.. The steel block gave the clearest results, the data from the steel plate and the rectangular bar being influenced by multiple reflections as indicated by the decaying higher frequencies.

According to the manufacturer, both transducers should respond to the surface velocity. However, as can be seen from Figures 8 and 14 the time-responses of these commercial AE transducers are dominated by the basic resonances of the sensor (ringing). This means that the output of such sensors is not the averaged velocity of the area on which they have been placed but is dominated by the characteristics of the sensor. Furthermore, it has been shown elsewhere [9] that integrated time domain responses (considering the sensors as velocity transducers) did not give the type of trend predicted by the Ray Theory of Ceranoglu et al [7].

Concerning the selection of the appropriate propagation medium for sensor calibration, it is obvious that this will depend on the specific requirements for each test. The massive steel block gives results which correspond closely to the calibration data for Rayleigh waves although reflections were not totally avoided because of its limited size. More massive structures and higher sampling rates give a good solution to the problem but the expense of such structures for propagation media is quite high. The steel plate was chosen as a possible propagation medium because of the availability of an analytical solution and because steel plate of the required dimensions is readily obtained.

Finally the long rectangular bar showed frequency responses which could be due to Rayleigh excitation merely because of the rapid decay of bulk waves with distance from the source, a factor that does not affect Rayleigh waves as much.

The time- and frequency-domain responses of the PVdF transducer on the cylindrical block are shown in Figures 15 and 16. The time domain response is

typical of that expected of a normal surface response for an infinite half-space [7] and back-to-back tests with an interferometric sensor have shown a striking agreement in response [1]. A comparison of the frequency domain response (Figure 16) with those obtained under similar conditions for the two commercial transducers (Figures 3 and 9) illustrates how the information from these latter two sensors is dominated by their own resonance. This is especially important if one means to analyse the frequency content of acoustic emission signals and suggests that either a careful calibration against a flat response transducer or the direct use of such a transducer is required for such applications.

6. CONCLUSIONS

The comparison of two commercial transducers with one experimental transducer based on brass-backed PVdF film has highlighted the effect of crystal resonances on the response of the former type.

The use of a variety of propagation media has further illustrated that wave propagation effects can also influence the frequency contact of the response to a white noise source.

REFERENCES

1. KERKYRAS, S.C., BORTHWICK, W.K.D., REUBEN, R.L., McBRIDE, R., BARTON, J.S. and JONES, J.D.C.: work to be published.

2. STIFFLER, R. and HENNEKE, E.G., J. Evaluation, vol.42, pp 956-960, Jul. 1983.

3. SCOTT, W.R. and CARLYLE, J.M., Naval Air Development Centre Report IR, Task No. ZR011088, 1976, Warminster, Pa.

4. CHANG, C. and SUN, C.T., J. Acoustic Emission, vol.7, pp 21-29, 1988.

5. KERKYRAS, S.C., WILCOX, S.J., BORTHWICK, W.K.D. and REUBEN, R.L., Proceedings of 4th World Meeting on Acoustic Emission, Boston, Sept. 15-18, 1991.

6. McBRIDE, R., BARTON, J.S., JONES, J.D.C. and BORTHWICL, W.K.D., Electro-Optics and Laser International Conference, Birmingham, March 20-22, 1990.

7. CERANOGLU, A.N. and PAO, Y.H., J. of Applied Mechanics, vol.48, Mar. 1981.

8. KERKYRAS, S.C., REUBEN, R.L. and BORTHWICK, W.K.D., Non-Destructive Testing and Evaluation. To be published.

9. KERKYRAS, S.C., M.Phil. Thesis, Heriot-Watt University, Edinburgh, 1991.

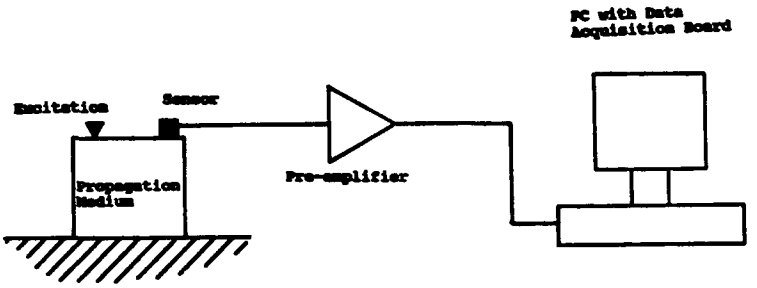

Figure 1: Block diagram of experimental setup

4

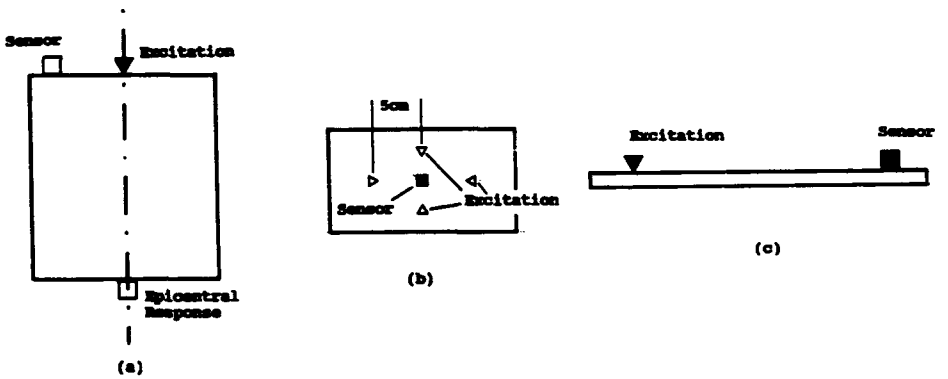

Figure 2: The three propagation media used
(a) Cylindrical steel block
(b) Steel plate
(c) Long steel bar

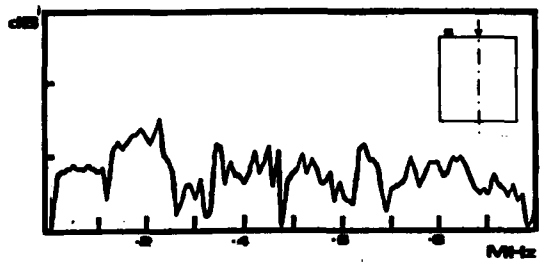

Figure 3: Frequency domain response for transducer D9201A on surface of cylindrical block (sampled at 40MHz).

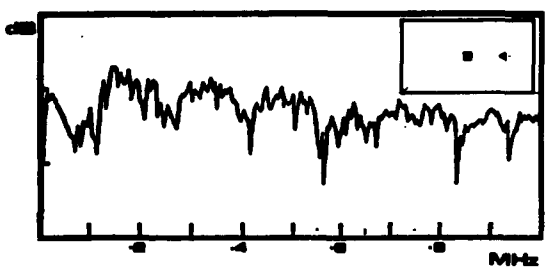

Figure 4: Frequency domain response for transducer D9201A on surface of plate (sampled at 20MHz).

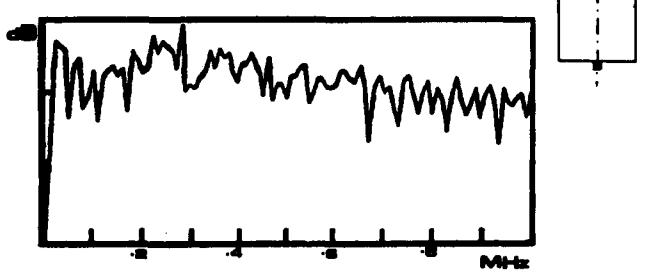

Figure 5: Epicentral frequency domain response for transducer D9201A on cylinrical block (sampled at 40MHz).

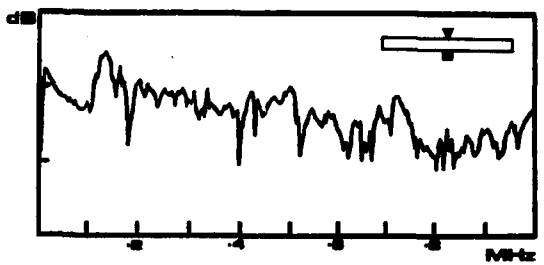

Figure 6: Epicentral frequency domain response for transducer D9201A on plate (sampled at 20MHz).

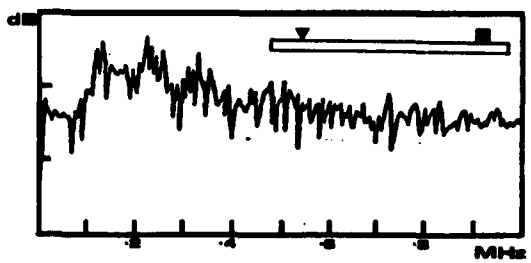

Figure 7: Frequency domain response for transducer D9201A on long rectangular bar (sampled at 20MHz).

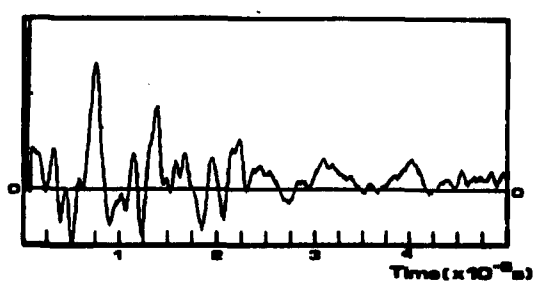

Figure 8: Time domain response of transducer D9201A to surface waves on steel plate.

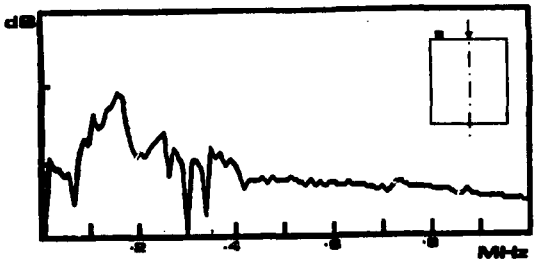

Figure 9: Frequency domain response for transducer S9204 on surface of cylindrical block (sampled at 40MHz).

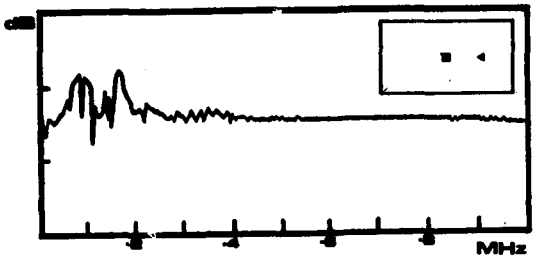

Figure 10: Frequency domain response for transducer S9204 on surface of plate (sampled at 20MHz).

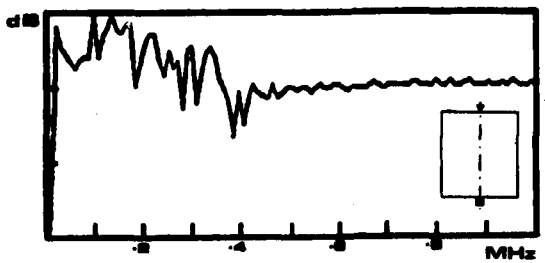

Figure 11: Epicentral frequency domain response for transducer S9204 on cylinrical block (sampled at 40MHz).

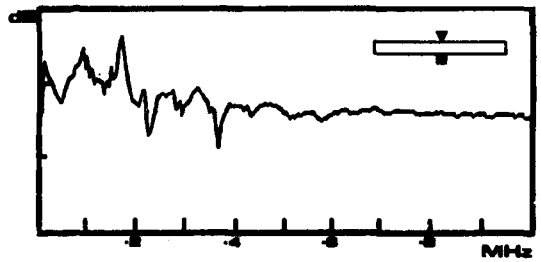

Figure 12: Epicentral frequency domain response for transducer S9204 on plate (sampled at 20MHz).

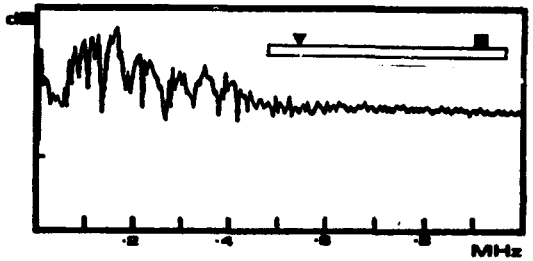

Figure 13: Frequency domain response for transducer S92014 on long rectangular bar (sampled at 20MHz).

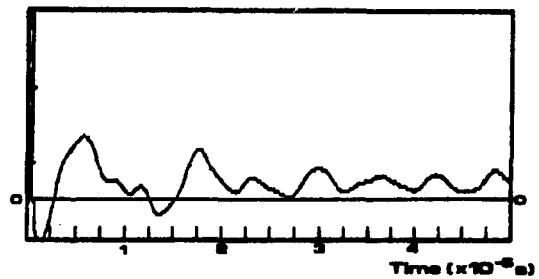

Figure 14: Time domain response of transducer S9204 to surface waves on steel plate.

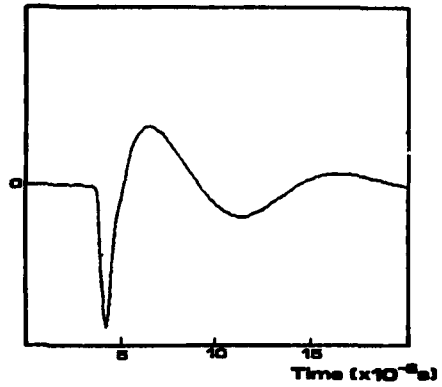

Figure 15: Time domain response of PVdF transducer to surface waves on cylindrical block.

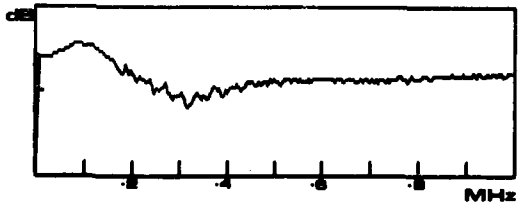

Figure 16: Frequency domain response of PVdF transducer to surface waves on cylindrical block.

SECOND INTERNATIONAL CONGRESS ON
RECENT DEVELOPMENTS IN AIR- AND
STRUCTURE-BORNE SOUND AND VIBRATION
MARCH 4-6, 1992 AUBURN UNIVERSITY, USA

USING A CIRCUMFERENTIAL TRANSDUCER TO MEASURE INTERNAL PRESSURES WITHIN A PIPE

R.J. Pinnington and A.. Briscoe
Institute of Sound and Vibration Research
University of Southampton
Southampton, SO9 5NH
England

ABSTRACT

A circumferential transducer has been devised which measured the dynamic pressure of gas or fluid within a pipe. The transducer consists of a piezoelectric wire wrapped circumferentially around the pipe wall. Such an arrangement ensures only sensitivity to axi-symmetric waves as waves with more than one circumferential half wave length will not be detected. The transducer is therefore only sensitive to the predominantly fluid-borne wave and the predominantly compressional wave in the pipe wall. The sensitivity to these two wave types is calculated and approximate expressions given. The applicability of the method is assessed for soft and hard pipes containing water. Some measurements are presented for a perspex pipe filled with water.

1.0 INTRODUCTION

Fluid-filled pipes can represent a significant vibration path, in both the fluid and pipe wall, from a machine to the supporting structure. To assess this problem a non-intrusive pressure sensor has been devised which involves an integral number of turns of a piezoelectric sensor around the pipe wall. The device is therefore only sensitive to n = 0 axisymmetric waves as others have equal positive and negative radial motions and cancel.

There are two n = 0 waves; a predominantly fluid based wave termed s = 1, and the s = 2 wave which is predominantly longitudinal motion in the pipe wall [1]. The s = 1 wave is the main contributor to the pressure and radial wall motion, and their relationship gives the sensitivity of the transducer. Unfortunately the s = 2 wave also has small pressure and radial motion contributions which disturb the accuracy of measurement of pressure. The sensitivity of the radial wall motion to both wave types is calculated here and comparisons made on a perspex pipe, with and without water.

The calculations involved approximate values for the wavenumbers for the n = 0; s = 1 and s = 2 waves.

2.0 THEORY

2.1 The equations of motion

With reference to Figure 1 the shell displacements are u and w in the axial and radial directions. σ_x, σ_θ refer to axial and circumferential stress. The fluid pressure is p and axial displacement u_f. The following equations are simplified forms of Kennard's equations [2].

Equilibrium of forces in the axial direction gives

$$\rho \ddot{u} = - \frac{\partial \sigma_x}{\partial x} \tag{1}$$

Equilibrium of forces in the radial direction leads to

$$P \frac{a}{h} = \sigma_\theta + \rho a \ddot{w} \tag{2}$$

The Hooke's Law relationships for the shell are

$$\sigma_\theta = \frac{E}{1 - \nu^2} \left(\frac{w}{a} + \nu \frac{\partial u}{\partial x} \right) \tag{3}$$

$$\sigma_x = \frac{E}{1 - \nu^2} \left(\frac{\partial u}{\partial x} + \nu \frac{w}{a} \right) \tag{4}$$

E, ν are the shell material Young's modulus and Poisson's ratio; w/a, $\partial u/\partial x$ represent the circumferential and axial strain. Equations (1) and (4) may be combined to give

$$\rho \ddot{u} + \frac{E}{1 - \nu^2} \left(\frac{\partial^2 u}{\partial x^2} + \frac{\nu}{a} \frac{\partial w}{\partial x} \right) = 0 \ , \tag{5}$$

and Eqs. (2) and (3) yield

$$\frac{E}{1 - \nu^2} \left(\frac{w}{a} + \nu \frac{\partial u}{\partial x} \right) + \rho a \ddot{w} = \frac{Pa}{h} \tag{6}$$

These are the two coupled shell equations for the n = 0 motion.

If travelling wave solutions of the form

$$u = U_s e^{i(\omega t - k_s x)} \ , \ w = W_s e^{i(\omega t - k_s x)}$$

are used, Eqs. (5) and (6) become

$$\left(\Omega^2 - \alpha_s^2 \right) U_s = i \nu \alpha_s W_s \tag{7}$$

$$W_s \left(1 - \Omega^2 \right) - i \nu k_s a \, U_s = \frac{Pa^2}{hE} \left(1 - \nu^2 \right) \tag{8}$$

where $\alpha_s = k_s a$, $\Omega = k_L a$, k_L is the wave number of a compressional wave in a plate $k_L^2 = \omega^2 \left(\frac{\rho (1 - \nu^2)}{E} \right)$

The pressure within the fluid p can be described by a Bessel Function of order zero. For each wavenumber s = 1, 2 there is a travelling wave solution

$$p = P_s J_o \left(k_s^r \, r \right) e^{i(\omega t - k_s x)} \tag{9}$$

where the radial wavenumber k_s^r is related to the fluid wave number k_f by

$$\left(k_s^r \right)^2 = k_f^2 - k_s^2 \tag{10}$$

The pressure wave must have a radial displacement w_r at the boundary r = a which is equal to the shell displacement W_s.

$$W_s = \frac{1}{\rho_f \omega^2} \frac{\partial P_s}{\partial r} \ , \ \frac{J_o (\alpha_s^r)}{\alpha_s^r J_o' (\alpha_s^r)} \approx \frac{- 2}{(\alpha_s r)^2} \tag{11}$$

where ρ_f is the fluid density.

Using the small argument identity the pressure becomes

$$P_s = \frac{-2B}{1 - \left(\frac{\alpha_s}{\alpha_f}\right)^2} \cdot \frac{W_s}{a} \qquad s = 1, 2 \qquad (12)$$

where $\alpha_f = k_f a$, B is the Bulk Modulus of the fluid.

Equations (7), (8) and (12) may now be used to find the wave numbers s = 1, 2 and then all the sensitivities or cross-sensitivities.

2.2 The wave numbers s = 1, s = 2

Substitution of Eq. (12) into (6) gives a relationship in k_s,

$$1 - \Omega^2 = -\beta\left(\frac{k_f^2}{k_f^2 - k_s^2}\right) - \nu^2\left(\frac{k_s^2}{k_L^2 - k_s^2}\right) \qquad (13)$$

It is known that one value of k_s, s = 1 is always less than k_L and k_f. Thus assuming $k_s^2 \gg k_L^2$, Eq. (13) becomes

$$1 - \Omega^2 - \nu^2 = -\beta\left(\frac{k_f^2}{k_f^2 - k_,^2}\right) \qquad (14)$$

The solution for the wave number k_s, s = 1 is

$$k_1^2 = k_f^2\left(\frac{1 + \beta - \nu^2 - \Omega^2}{1 - \nu^2 - \Omega^2}\right) \qquad (15)$$

where the fluid loading term β is

$$\beta = \frac{2Ba}{E\,h}(1 - \nu^2) \qquad (16)$$

The fluid wave in the pipe k_1 is therefore always slower than the wave in an infinite medium k_f. The wave s = 1 decreases in speed with decreasing wall stiffness (increasing β).

The approximate solution to the second wave number k_s, s = 2 is obtained with the knowledge that it is always smaller than the fluid wave number k_f. This means that the wave length in the pipe shell is greater than in the fluid. The fluid is experienced as a stiffness (controlled by the fluid bulk modulus) by the shell wall. Equation (12), on setting $k_s \ll k_f$ is

$$1 - \Omega^2 + \beta = -\nu^2 \frac{k_s^2}{k_L^2 - k_s^2} \qquad (17)$$

which on rearranging becomes

$$k_2^2 = k_L^2\left(\frac{1 - \Omega^2 + \beta}{1 + \beta - \Omega^2 - \nu^2}\right) \qquad (18)$$

If there is no contained fluid $\beta = 0$

$$k_2^2 = k_L^2\left(\frac{1 - \Omega^2}{1 - \Omega^2 - \nu^2}\right) \qquad (19)$$

At low frequencies $\Omega \ll 1$ and $k_2 = \omega\sqrt{\frac{\rho}{E}}$, i.e. the cylinder behaves as a rod. Setting $\sigma_\theta = 0$ in Eq. (3) (on account of the empty pipe) indicates that the radial motion is just controlled by the Poisson's ratio, as for a rod.

$$\frac{W}{a} = -\nu\frac{\partial u}{\partial x} \tag{20}$$

As the frequency increases such that $\Omega^2 \gg \nu^2$ the radial wall motion is constrained by inertia effects and the wave number k_2 becomes slightly lower, i.e. that of a plate k_L.

$$k_2 = k_L = \omega\sqrt{\frac{\rho(1-\nu^2)}{E}} \tag{21}$$

The effect of the contained fluid, as described by β, is to restrict radial wall motion, causing axial wave number k_2 to tend to that of the plate. This implies that these waves should not have large radial motions, making them relatively insensitive to a radial motion transducer.

2.3 The relationship between internal pressure and radial wall motion for the two wave types

The relationship between fluid pressure and radial wall motion for both wave types s = 1, 2 is available by substitution in turn of Eqs. (15) and (18) into (12).

$$W_1 = \frac{P_1 a^2}{hE}\left(\frac{1}{1 - \frac{\Omega^2}{1-\nu^2}}\right) \qquad s = 1 \tag{22}$$

$$W_2 = -\frac{P_2 a}{2B} \qquad s = 2 \tag{23}$$

The negative sign for W_2 indicates that for this wave most energy is within the shell. The shell motion drives the fluid, hence an increasing shell radius w causes a rarefaction in the fluid. Note that the fluid pressure is only controlled by the Bulk Modulus, i.e. the fluid acts as a spring for s = 2. Equations (22) and (23) lead to the general relationship

$$\frac{W_2}{W_1} = -\frac{P_2}{P_1}\left[\frac{1-\nu^2-\Omega^2}{\beta}\right] = -\frac{1}{\gamma}\left(\frac{P_2}{P_1}\right) \tag{24}$$

The radial and axial displacements are related by Eq. (7), substitution of the two wave numbers k_1 and k_2 yields

$$U_1 = -\frac{i\nu W_1}{k_1 a} \qquad s = 1 \tag{25}$$

because $k_L^2 \ll k_1^2$.

$$U_2 = \frac{-iW_2(1+\beta-\Omega^2)}{\nu k_L a} \qquad s = 2 \tag{26}$$

Division of these two expressions leads to the general relationship

$$\frac{U_2}{U_1} = \frac{W_2}{W_1}\left(\frac{1+\beta-\Omega^2}{\nu^2}\right)\frac{k_1}{k_2} = \frac{1}{\chi}\frac{W_2}{W_1} \tag{27}$$

The axial stress given from Eqs. (4) and (7) can be written

$$\sigma_{sx} = \frac{W_s}{a}\left[\frac{k_L^2}{k_L^2 - k_s^2}\right]\cdot\frac{E\nu}{1-\nu^2} \qquad s = 1,2 \tag{28}$$

2.4 The radial wall motion for shell axial excitation

If at a boundary x = 0 there is a free surface, but an imposed axial wall stress, the two pressures $P_1 + P_2 = 0$.

Therefore the ratio of the two wall motions becomes from Eq. (24)

$$W_2/W_1 = 1/\gamma \quad . \tag{29}$$

For a steel pipe a/h = 10, with water inside $\gamma \approx 0.2$ and the radial motion is dominated by the shell wave giving $W_2/W_1 = 5$. The radial sensor would be inaccurate using Eq. (22); in fact Eq. (23) would be appropriate if there was no fluid excitation.

For a rubber pipe of the same a/h ratio $\gamma \approx 20$ and $W_2/W_1 = 0.05$. The radial wall sensor would give accurate pressure measurements from Eq. (22).

2.5 The radial wall motion for fluid excitation

If at a boundary x = 0 the axial stress was zero, but a pressure was imposed on the fluid, the sum of the axial stresses $\sigma_{1x} + \sigma_{2x} = 0$, there from Eq. (28)

$$W_2/W_1 = -\frac{k_2}{k_1}\,\chi \tag{30}$$

For this case for hard or soft shells the radial stress W_2 associated with the shell wave is negligible and so Eq. (22) can be used to measure the pressure.

3.0 EXPERIMENTAL WORK

Some experimental work was carried out on a vertical perspex pipe shown in Figure 2. The pipe was 1.9 m tall, with a 69 mm internal radius and 6 mm wall thickness. The fluid inside the pipe was excited using a honeycomb piston at the base. Longitudinal structural excitation was applied at the top of the pipe using a B&K mini-shaker upon a honeycomb disc. The shaker was centred to excite predominantly n = 0 shell waves (s = 2).

A B&K hydrophone was hung vertically to monitor internal pressure at any point. A PVDF wire with three turns was located towards the pipe mid height position. This sensor detects only pipe radial motion in the n = 0 mode. Four piezo-resistive strain gauges, of gauge factor 50 were located at 90° intervals around the circumference. These were also employed to detect the longitudinal strain, largely associated with the s = 2 wave.

3.1 Measurements of longitudinal and radial motion on the empty pipe

The pipe was excited axially on the empty shell using the top vertical shaker. The input accelerance at the top honeycomb cap is given in Figure 3. This displays a series of resonances superimposed upon a stiffness characteristic below 1 kHz, and a mass characteristic above 1 kHz. It is likely that these characteristic lines correspond to the properties of the honeycomb cap, the separating resonance occurring at about 1 kHz. The resonances below 1 kHz are associated with the tube longitudinal motion and the support plate at the tube base.

Figure 4 displays the radial displacement W divided by the axial strain at the monitoring position. Below about 400 Hz the result is quite close to the theoretical expectation of Eq. (26). $\beta = 0$ for an empty pipe, $\nu = 0.4$ for perspex.

The measurement is close enough at low frequencies to suggest that the PVDF is useful for measurement of the pipe longitudinal motion for the n = 0 structural wave, as well as the n = 0 fluid wave for which it was originally intended.

3.2 Measurements of longitudinal and radial motion on a water filled pipe

The pipe was filled with water. An air gap of one centimetre was left between the fluid surface and the top honeycomb cap.

The fluid column was excited with the honeycomb piston at the base. A hydrophone suspended just above the piston monitored the generated fluid pressure. The piston acceleration was monitored by a centrally mounted accelerometer.

Figure 5 gives the modulus of the acceleration per unit pressure at the base of the fluid column. The main features of interest are the resonance frequencies of the fluid column which occurred at intervals of 110 Hz, as integral numbers of half wave lengths within the fluid.

The fluid filled pipe was then excited axially on the shell from the top as had been done with the empty shell. The input accelerance at the shell cap is compared in Figure 3 with that of the empty pipe. Most resonances increase by about 10% with the water present. The reason for this is seen in Eq. (18). β is zero for the empty pipe, and about 12.4 for the full pipe. The presence of the water suppresses the Poisson's ratio motion of the pipe wall causing the axial shell wave speed c_2 to increase.

The hydrophone was located adjacent to the piezoelectric ring and the pressure was measured using the constant form from Eq. (22). The two pressure estimates are plotted as a ratio in Figure 6. Below 1 kHz the value is close to unity suggesting an accurate result. As the ring frequency is approached (4 kHz) the piezoelectric ring tends to over estimate because of the frequency dependence of the denominator in Eq. (22).

4.0 CONCLUSIONS

(1) The s = 1 and s = 2 shell and fluid wave numbers and wave speeds have been derived and confirmed by measurement.

(2) The radial wall motion for the s = 1 fluid wave has been calculated. This is the basic sensitivity of the PVDF sensor.

(3) The radial wall motion for the s = 2 shell based wave has been calculated for any material.

(4) This wall motion (3) is negligible for perspex or rubber pipes, which means that the radial sensor will accurately measure the fluid pressure in the presence of wall vibration.

(5) The radial wall motion for the s = 2 shell wave is similar for a steel water filled pipe as for a pipe in vacuo. The radial motion is controlled by the Poisson's ratio. A radial motion sensor will therefore pick up contributions from both s = 1 and s = 2 waves, and would be inaccurate.

(6) For fluid based excitation, from a pump on a steel pipe, the main wall motion is attributed to the s = 1 fluid wave. A radial sensor will be accurate in magnitude and phase.

5.0 REFERENCES

[1] C.R. Fuller and F.J. Fahy. (1981) Characteristics of wave propagation and energy distributions in cylindrical elastic shells filled with fluid. Journal of Sound and Vibration, **81**(4), 501-508.

[2] A.W. Leissa. (1973) Vibrations of shells. NASA SP-288, Scientific and Technical Information Office, NASA, Washington D.C.

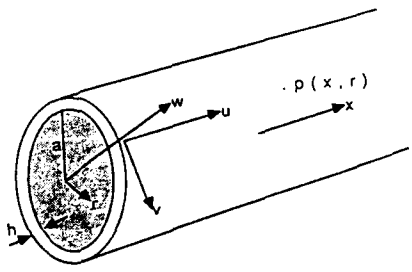

Figure 1 Coordinate system, displacements and geometry.

Figure 2 Experimental Setup

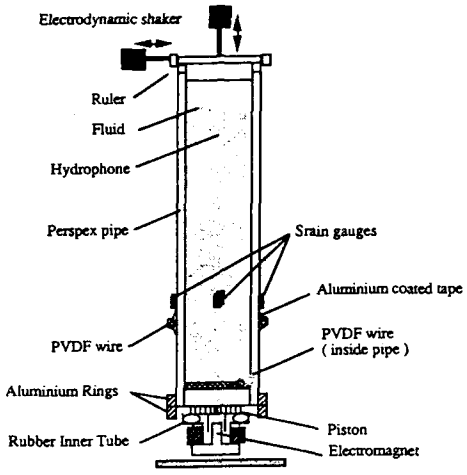

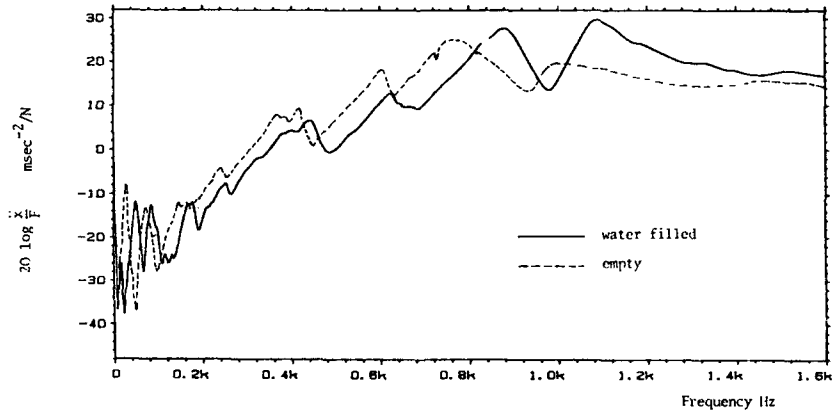

Figure 3 Input accelerance on the tube cap.

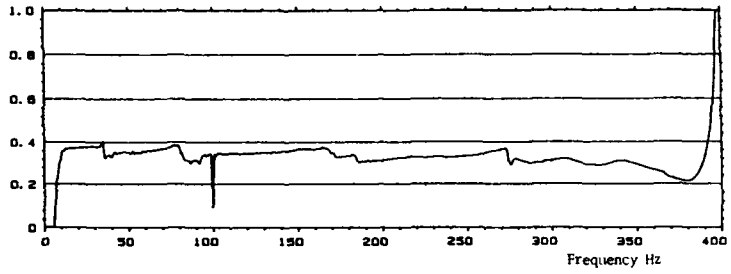

Figure 4 Poisson's ratio measured on an empty pipe.

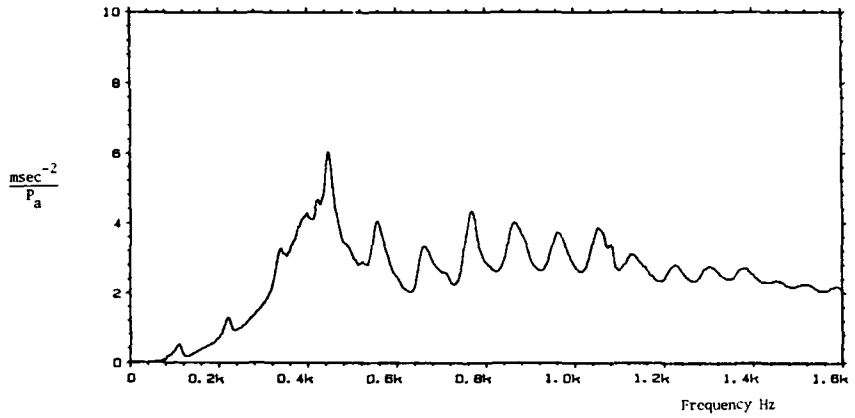

Figure 5 Base acceleration/fluid input pressure of fluid filled pipe, fluid excitation.

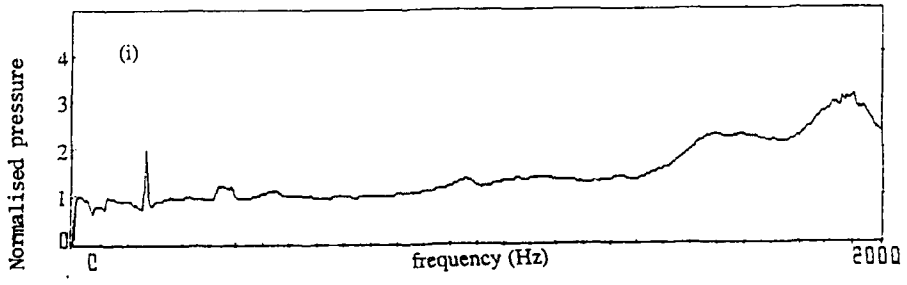

Figure 6 Normalised PVDF pressure measurement.

**SECOND INTERNATIONAL CONGRESS ON
RECENT DEVELOPMENTS IN AIR- AND
STRUCTURE-BORNE SOUND AND VIBRATION**
MARCH 4-6, 1992 AUBURN UNIVERSITY, USA

CONDITION OF OLD MACHINES IN THE LIGHT OF VARIOUS VIBRATION STANDARDS

R.L.Murty
Head of Production Engineering
Regional Engineering College
Warangal - 506 004
INDIA

ABSTRACT:

Vibrations are accepted as an indicator of the health of a machine. In the earliest times, the subjective method of human feel was adopted to judge the severity of vibration. This led to disputes of all kinds and over the last 100 years, many attempts have been made to set "acceptance standards". The important ones are as follows: 1) Goldman's chart 2) Rathbone's tolerance chart, 3) Federna's chart, 4) General machinery vibration severity chart, 5) Polacek's recommendations 6) Recommendations of Central Machine Tool Institute (CMTI), Bangalore, India. In the present work, the existing standards have been reviewed and the vibrations of a large number of used machine tools were measured. The quality of these machine tools was assessed in the light of various standards.

INTRODUCTION:

Vibration has been a guage of performance of a machine since the beginning of the industrial age. When measurement of vibration was difficult, people adopted the subjective method of human feel. This led to disputes and some kind of measurement was invented in the middle of 19th century. It is now felt that vibration like temperature and noise can be an acceptable indicator or parameter for gauging machinery. In this paper important literature on the subject has been reviewed. At the end, some examples based upon a number of case studies conducted under the guidance of the author are presented.

The scope of vibration in the present study is concerned only with severity of the mechanical vibration of individual machines and not individual parts of a machine. The idea is to evaluate vibrations with respect to reliability, safety and human perception and to use vibration as a criterion for acceptance, maintenance, quality control, inspection and installation of machinery.

EVALUATION OF VIBRATION INTENSITY:

Vibration may be defined by two important factors or parameters:1) amplitude, 2) the peak or R.M.S value of velocity, these factors are to be evaluated over a band of frequencies. Most existing standards on vibration adopt these two parameters.

Double Amplitude:

Double amplitude of vibration is the peak to peak value of particle displacement and is a very useful vibration parameter as it can cover sinusoidal as well as non-sinusoidal vibrations. When one is concerned with the degree of imbalance and relative deflections, amplitude is the relevant factor.

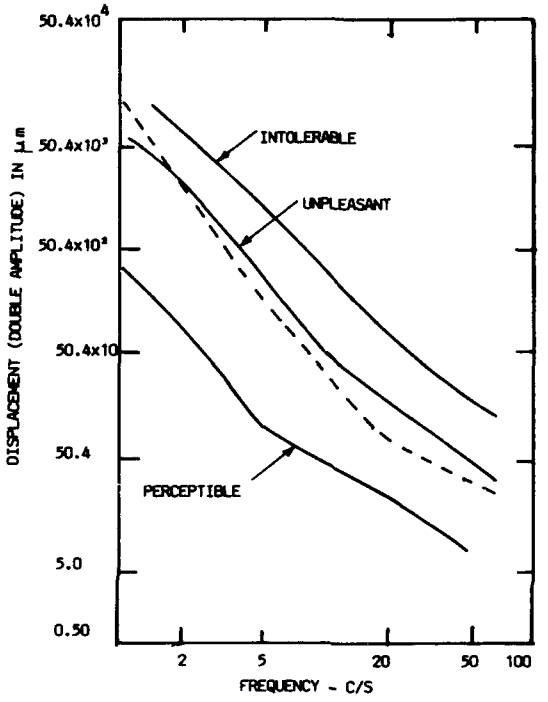

Fig. 1 : Human Response to Vibration (Goldman)
(---- : Vertical vibrations limits for passenger comfort - Janeway)

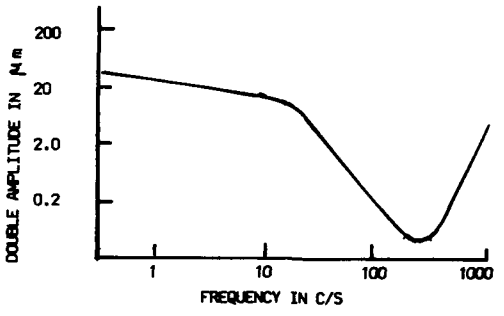

Fig.2 : Threshold of perception of Tangential vibration applied to fingertip
(after Bekesy)

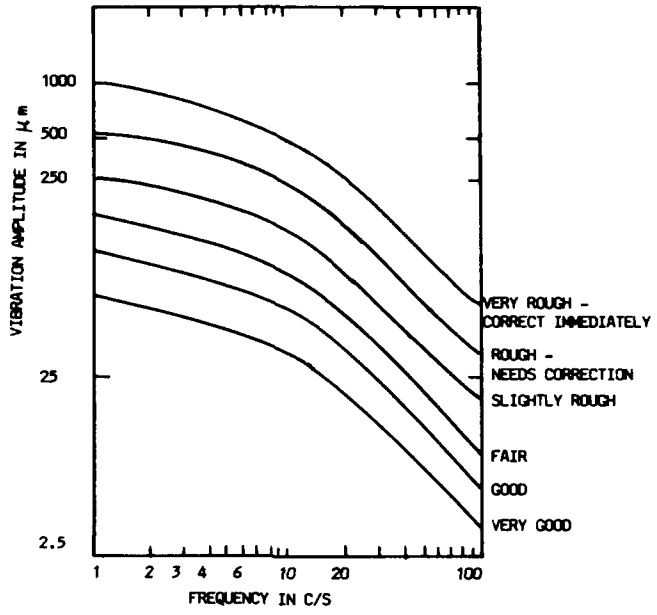

Fig. 3: Rathbone chart of Vibration Severity.

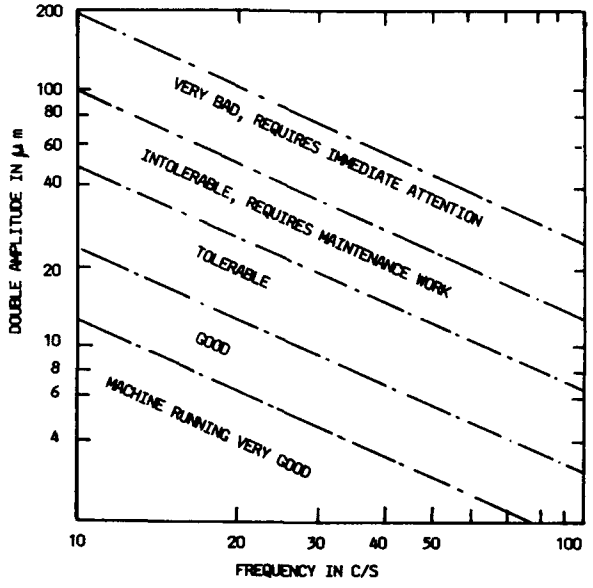

Fig. 4: Federna's recommendations on vibration.

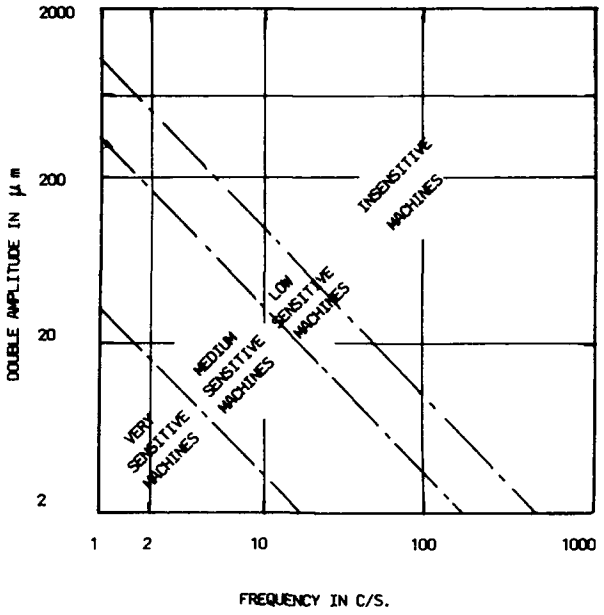

Fig. 5: Russian standard on vibration (I - 200 - 54)

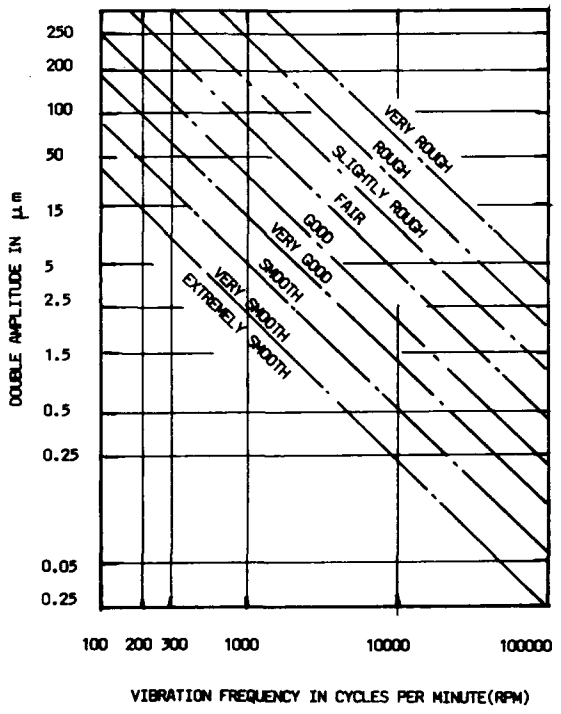

Fig. 6: General machinery vibration severity chart.

Velocity:

When one is concerned with internal wear and machine failure, velocity measurement is important. The energy of vibration is proportional to the square of the mean velocity. As the velocity directly affects wear, it is a valuable parameter when vibration is used for maintenance purposes. Vibrations with the same RMS velocity in the frequency band 10 to 1000 are generally considered to be of equal severity. Succeeding ranges of the evaluation classifications have a ratio of 1.6 giving a step of 4 dB between severity levels.

IMPORTANT STANDARDS:

The first human response curves for vibration were obtained during 1920-1950 by U.S. Navy Scientists.

Goldman's Chart of Human Response:

Goldmann's human response curves are shown in Fig.1. These are very important for travelling in automobiles, ships etc. The response values were obtained by statistical methods and are valid for the majority of people.

The threshold perception of tangential vibration applied to the finger tip is given in Fig.2.

Rathbone's tolerance chart:

This was given in 1939 and was prepared for the sake of safety and insurance rather than maintenance. Fig.3.

Federna's tolerance chart: (DIN 4150) (Fig.4)

These are based upon constant velocity curves following preferred series R.5. Federna's recommendations seen to cover only low speed machines.

Russian Standards:

The Russian standard on vibration covers a speed range of 600 to 6000 RPM. The curves in the Russian standards are steeper than Federna's curves.

General Machinery Vibration Severity Chart:

This chart is given in Fig.6. The curves in this chart provide a guide to establish vibration tolerances for machinery running at speeds upto 100,000 RPM.

German Standard:

This is given in Fig.7. This is similar to the chart shown in Fig.6.

There are other less known or rather similar standards and recommendations which are skipped in this paper.

RECOMMENDATIONS FOR MACHINE TOOLS:

Machine tools are mother machines and their accuracy and performance affect the manufacturing quality of all other machines. Comprehensive recommendations regarding vibrational tolerance limits for machine tools were first proposed by Polacek. In the more recent times recommendations have also been made by the Central Machine Tool Institute, India. These recommendations for 4 types of commonly used machine tools are summarised in Table 1. It may be seen that vibrational amplitudes are required to be measured upto speeds of 600 RPM, whereas velocities are to be measured at speeds of 600 RPM and above.

It may be seen that the recommendations made by CMTI allow higher amplitudes and lower velocities for the same vibrational severity description in comparison with the recommendations of Polacek. From this it may be said that Polacek's recommendations are more suitable for acceptance purposes, whereas CMTI recommendations are more relevant for maintenance purposes.

EXAMPLES OF CASE STUDIES CONDUCTED:

Extensive data on vibrational amplitudes and velocities was obtained on a large number of machine tools using the Bruel & Kjaer Piezo-electric vibration meter (type 2511). Two examples only are presented here.

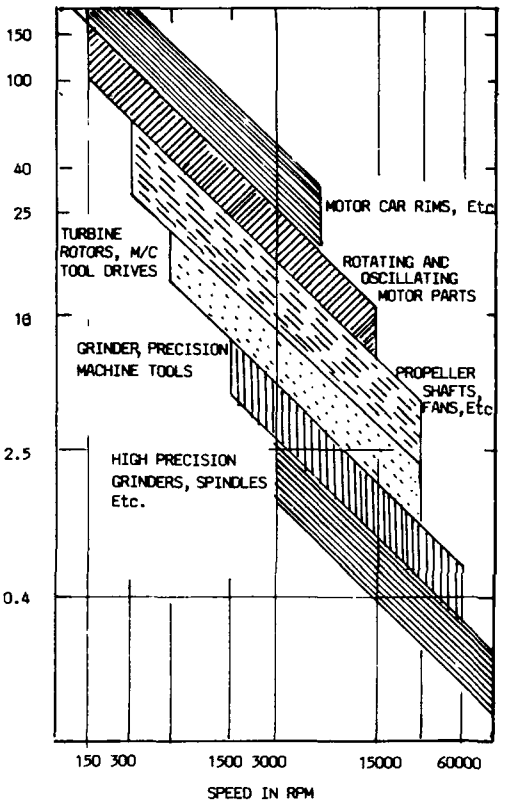

Fig.7 : Limit zone of vibrations: (VDI -205-210)

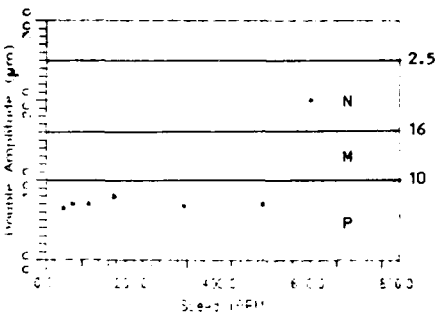

(8.1 A)

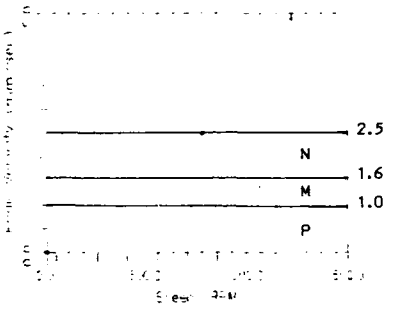

(8.1 B)

Fig.8.1. Vibrational behaviour of a specific lathe judged by Polacek's recommendations.

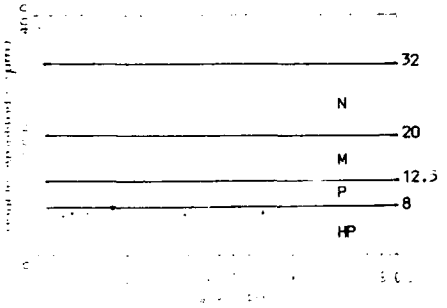

(8.2 A)

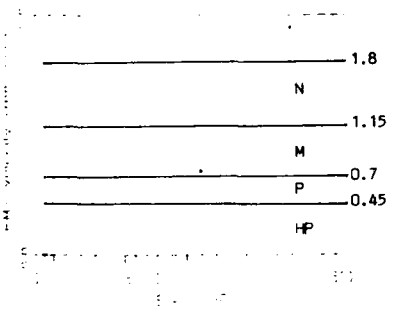

(8.2 B)

Fig.8.2. Vibrational behaviour of the same lathe as in Fig.8.1 judged by CMTI recommendations

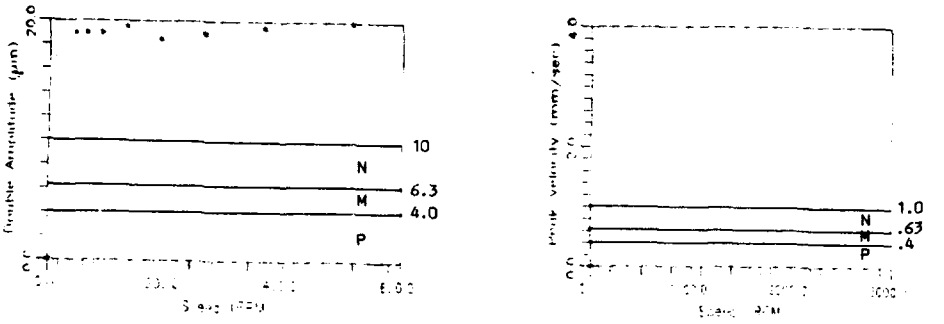

(9.1 A) (9.1 B)

Fig. 9.1. Vibrational behaviour of a specific Milling Machine judged by Polacek's recommendations.

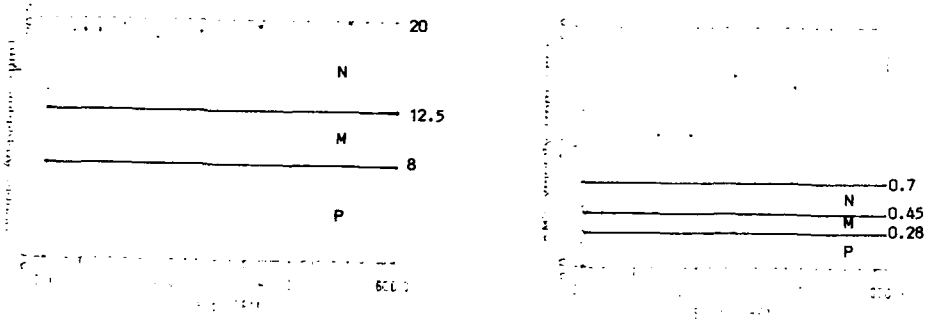

(9.2 A) (9.2 B)

Fig. 9.2. Vibrational behaviour of the same milling machine as in Fig. 9.1 judged by CMTI recommendations.

Table 1

Machine	Polacek: Double amplitude (μ m) (frequency ≤ 10 Hz)	Polacek: Peak velocity (mm/sec) (frequency > 10 Hz)	Double amplitude (μ m) (frequency ≤ 10 Hz)	RMS velocity (mm/sec) (frequency 10-1000 Hz)	Description of vibration severity
Lathe	25	2.5	32	1.8	Normal(N)
	16	1.6	20	1.15	Medium (M)
	10	1.0	12.5	0.7	Precision(P)
	-	-	8	0.45	High Precision (HP)
Milling	10	1.0	20	0.7	N
Machine	6.3	0.63	12.5	0.45	M
	4.0	0.4	8	0.28	P

Table 1: Recommendations on limits of vibrational severity of M/c tools.

Figures 8 and 9 are typical charts showing double amplitude/peak velocity/RMS velocity at various speeds for a lathe and milling machine respectively. Figures 8.1 A, 8.1B, 9.1A and 9.1B correspond to Polacek's recommendations. Figures 8.2A, 8.2B, 9.2A and 9.2B correspond to CMTI recommendations. It may be seen that in general, amplitudes of vibration are within limits of P,M, or N up to speeds of 600 RPM. At speeds higher than 600 RPM the amplitude may exceed the P-M-N range. The milling machine under question has its vibrational amplitudes as well as velocities exceeding the P-M-N range. It is interesting to note that these three machines are roughly of the same age. However, the higher amplitudes for the milling machine seems to be not due to its original design or quality but its higher rate of bear. It is common knowledge that milling machines are continuously subjected to oscillating loads and so wear more rapidly than other machine tools.

CONCLUSION:

The various recommendations on vibrational limits are very useful for accurately assessing the condition of old machine tools which are expensive.

It is necessary to establish proper vibrational standards for precision and high precision machines and vital drive components going into them. The auther has initiated work in this direction.

REFERENCES:

1) "Specifications and Tests of Metal Cutting Machine Tools," Vol.1 & 2, Proceedings of the conference 19th and 20 Feb. 1970. The U.M.I.S.T.

2) "Machine Tool Design", Vol.1,2, & 3, by N.Acherkan, et al, MIR Publishers, 1969.

3) "Machine Tool Design" hand book, published by Central Machine Tool Institute, Bangalore, India, 1978.

4) Francis S.Tse, Ivan E.Morse, Rolland T.Hinkle, "Mechanical Vibrations", CBS Publishers and Distributors, New Delhi, 1983.

5) ISO Standard 2372 on Mechanical Vibrations of Machines.

SECOND INTERNATIONAL CONGRESS ON
RECENT DEVELOPMENTS IN AIR- AND
STRUCTURE-BORNE SOUND AND VIBRATION
MARCH 4-6, 1992 AUBURN UNIVERSITY, USA

PHOTOACOUSTIC METHOD OF THE DETERMINATION OF AMPLITUDE NON-RECIPROCALNESS IN GYROTROPIC MEDIA

Mityurich G.S., Zelyony V.P., Sviridova V.V., Serdyukov A.N.
Department of Physics
Gomel State University
Soviet. st.,104, 246699, Gomel
The Republic of Byelorus

There is investigated a possibility of measuring the amount of amplitude (dichroic) non-reciprocalness in gyrotropic media put in external field using the method of photoacoustic (PA)spectroscopy. We get the expressions for the amplitude and phase characteristics of PA - signal corresponding to the orthogonally polarized isonormal waves in opposite directions. We suggest a way of determination of amplitude non-reciprocalness of ring laser resonators, containing elements with natural and magnetic dichroism measuring the difference of amplitudes and phases of PA signals due to the different absorption of waves propagating in direct and reverse directions.

It follows from some studies [1-3] that the effects of optical non-reciprocalness take place in gyrotropic crystals under the action of external magnetic field. Irreversibility of light propagation is due to the difference in phase velocities of isonormal waves propagation in the opposite directions. There is also a polar non-reciprocalness of forward and reverse wave [3] due to different ellipticity of intrinsic waves. As a gyrotropic crystal, put in external magnetic field, is characterized by absorption that it is obvious that one more similar effect can take place, i.e. dichroic non-reciprocalness of direct and reverse waves due to different absorption of orthogonally polarized isonormal waves.

The given effect has important practical implementation, for example, for the realization of one directed generation of optical radiation of ring laser in which the resonator is used with amplitude non-reciprocalness containing the elements with magnetic and(or) natural circular dichoism [4].

In this study we investigate a possibility of using the method of photoacoustic (PA) spectroscopy for measuring the amount of amplitude (dichroic) non-reciprocalness in gyrotropic media.

We shall discuss the subject on the basis [1] of

$$\underline{D} = \left[\varepsilon + i(\gamma\, h)^{\times} \right] \underline{E} + i\alpha\, \underline{H} ,$$

$$\underline{B} = \underline{H} - i\alpha\, \underline{E} , \quad (\mu = 1) \qquad (1)$$

that describe naturally activity media with applied external magnetic field. In (1) γ -antisymmetric tensor of the 2-nd range, dual to the

magnetic gyration vector γ , the imaginary part of which, γ'' , relates to the magnetic circular dichroism, $\alpha = \alpha' + i\,\alpha''$, with α'' -the natural circular dichroism, $\underline{H}$ - the external magnetic field.

Solving the equation for normals, on the basis of (1) and Maxwell equations $[\underline{n}\ \underline{E}] = \underline{B}$, $[\underline{n}\ \underline{H}] = -\underline{D}$, we get the refractive indexes for circulary polarized waves [1], imaginary part of which, calculated up to the 1-st order of magnitude of gyration parameters, is of the form:

$$n''_{\pm} = \frac{\varepsilon''_0}{2\sqrt{\varepsilon'_0}} \pm \left[\alpha''_0 + \frac{\gamma''_0 \sqrt{\varepsilon'_0}}{2(\varepsilon'_0 + (\varepsilon''^2_0/4\varepsilon'_0))}\ \underline{n}\ \underline{h} \right] \qquad (2)$$

where $\underline{n}$ is the unit vector of a wave normal and parameters ε_0 ,α_0; γ_0, correspond to the isotropic media without the inversion center, $\underline{n}\ \underline{h} = = nh\cos(\theta)$, θ - angle between vector $\underline{n}$ and direction of the external magnetic field.

In our case the sample under consideration is located in gas-microphone rotating cell for measuring in transmittance mode [5]: to the cell being in the external magnetic field . Selecting the optimal condition of thermally thick optically thin sample, we can write the bellow expressions for the PA signal amplitude:

$$q_{\pm} = A\,\frac{1}{\Omega\,\alpha_{\pm}}\,, \qquad \alpha_{\pm} = 4\pi\, n''_{\pm}/\lambda, \qquad (3)$$

where Ω - the modulation frequency of incident light beam, A - value, determined by parameters of the media and PA cell. Taking into account (2) and (3), and determining the difference of PA signal amplitudes for the direct and reverse waves we can derive $\delta q_{1,2} = |q_+ - q_-|_{1,2}$

$$\delta q_{1,2} \sim 2\alpha''_0 \pm \gamma''_0\ \underline{n}\ \underline{h}$$

from which we conclude that the resulting signal, measured in forward (δq_1) and reverse (δq_2) directions differs by the magnitude that is proportional to the doubled value of magnetic circular dichroism parameter γ''_0 . It is obvious that the difference of the PA phases for left/right-polarized waves $\Delta\Phi = |\Phi - \Phi| = \mathrm{arctg}((x-y))/(1+xy))$, where $x = 1 - 2\varkappa_+^2 + (1 - 2\varkappa_+)$, $y = 1 - 2\varkappa_-^2\ (1 - 2\varkappa_-)$, $\varkappa_{\pm} = \alpha_s/\alpha_{\pm}$, measured in opposite directions, differ by $2\gamma''_0$ multiplied $f(\varkappa_{\pm})$, (where f - is function of optical and thermal parameters of a medium).

Therefore, measuring the amplitude and phase characteristics of PA signal, corresponding to circulary-polarizes of incident light, let us determination the magnitude of the dichroic non-reciprocalness of gyrotropic media or amplitude non-reciprocalness of resonators ring lasers.

References

1. Belyi V.N., Serdyukov A.N.//Crystallography, 1974, V.19, N6, p.1279.
2. Markelov V.A., Novikov M.A., Turkin A.A. //Letters ZETF, 1977, V.25, N9, p.404.
3. Mityurich G.S., Filipov V.V.//Crystallography, 1984, V.29, N.5, p.837.
4. Voitovich A.P., Severinov V.A. Lasers in anisotropic resonators. Minsk "Science and Technique", 1988, p.270.
5. Cahen D. //Rev.Sci.Instrum., 1981, V.52, N.9, p.1306.

SECOND INTERNATIONAL CONGRESS ON
RECENT DEVELOPMENTS IN AIR- AND
STRUCTURE-BORNE SOUND AND VIBRATION
MARCH 4-6, 1992 AUBURN UNIVERSITY, USA

A SOLUTION TO THE NOISE PREDICTION PROBLEM AT LOW FREQUENCIES.

Yurii I .Bobrovnitskii

Machinery acoustics laboratory
Blagonravov Institute of Engineering Research,
Griboedov st., 4, Moscow 101830, USSR.

ABSTRACT

An approach to the noise prediction problem for a complicated source (e.g., a machine) in a complicated room is presented for the frequency range where sound wavelength is greater or comparable to the source and room dimensions. Solution obtained to the problem is expressed through a finite number of parameters of rigorously defined models of the sound source and room which can be measured experimentally.

A sound source is modeled by an ensemble of secondary point sources (monopoles and dipoles located at an enveloping surface) which correspond to radiation in the free space. Sound scattering by the source body is taken into account as a matrix of scattering coefficients. A method of experimental identification of these model parameters in arbitrary closed room is proposed. The method is based on the properties of Helmholtz integral operator and on the two-microphone measurement techniques.

Acoustic model of a room is defined, in the approach, by a matrix of integral coefficients of sound reflection from the room walls. The coefficients may also be measured experimentally.

A number of laboratory experiments has been carried out which prove practical validity of the source model as well as the experimental method of identification of its parameters.

1 INTRODUCTION

Of great interest in noise control engineering is the problem of predicting sound field radiated from a source in an enclosed space. In fact, the prediction problem is the central problem in general field theory, and there is a large body of literature on the subject, especially in electrodynamics and underwater acoustics. In machinary acoustics, the problem is distinguished by the extreme geometric and physical complexity of sound sources (machines and other operating equipment) and rooms (such as manufacturing halls or vehicle compartments). Here the problem has solutions in limiting cases of very low and high frequencies. In wide frequency range where the sound wave length is comparable to the source and room dimentions the problem cannot be considered as solved. There are a number of attempts to treat it (see, e.g. [1–4]), but a solution practically acceptable in this frequency range seems possible only on the experimental basis [5].

It is the purpose of this paper to present a new approach to the problem which provide such solution to a large class of complicated sources and rooms. The key point of the approach is the theory in which the sound field is expressed via a finite number of parameters of the sources and room. Starting from the theory, formal acoustic models of a sound source and a room are rigorously defined, and experimental procedures are proposed for identifying their parameters. The model parameters of given room and source may be measured separately in rather arbitrary acoustic conditions. Knowledge of these parameters allows

one to predict the sound pressure levels in the room when the source is installed and operating in this room.

2 SOLUTION TO THE PREDICTION PROBLEM

Consider a sound source of finite dimension (a machine) operating in an enclosed space (in a room). Suppose that other noise sources are absent and the sound field is harmonic in time. The starting point of the theory is the representation of the total pressure field $p(x)$ in the form:

$$p(x) = \sum_{m=0}^{\infty} p_m(x), \tag{1}$$

where x is coordinates of any point of the room, the time dependence $\exp(-i\omega t)$ is supressed. Here the function $p_0(x)$ is the pressure field of the machine in the free space. The field $p_1(x)$ corresponds to the "first" reflection of the field $p_0(x)$ from the bounding surfaces of the room (walls). More exactly, the function $p_1(x)$ describes the field in the room without the machine if the walls of the room are excited by the field $p_0(x)$. The pressure function $p_2(x)$ corresponds to scattered field when the field $p_1(x)$ impinges on the body of nonoperating machine. Each term with odd index, $p_{2j+1}(x)$, is the field produced by a single reflection from the walls when incident is the field $p_{2j}(x)$ which, in turn, is produced by scattering of the field $p2j-1(x)$ by the machine body.

After combining the terms with odd and even indices Eq.(1) can be rewriten as

$$p(x) = p^d(x) + p^s(x), \tag{2}$$

where $p^d(x) = \sum_{j=0}^{\infty} p_{2j}(x)$ is the direct field consisting of outgoing fields radiated and scattered by the machine, $p^s(x) = \sum_{j=0}^{\infty} p_{2j+1}(x)$ denotes the field of standing waves in the room without the machine.

The next step in the theory is to relate the partial fields $p_m(x), m = 0, 1...$ to each other. The best way to do it is to expand them in appropriate set of functions. In this report we use the spherical functions. Let $\vec{a}^d$, $\vec{a}^s_m$ and $\vec{a}_m$ be vectors of coefficients of expansions of the fields $p^d(x), p^s(x)$ and $p_m(x)$ in these functions. The direct fields, $p^d(x), p_{2j}(x)$, are expanded in the outgoing spherical function (the radial functions are the spherical Hunkel functions of the first kind $h_n^{(1)}(kr)$). The standing waves fields, $p^s(x) and p_{2j+1}(x)$, are expanded in regular functions (the radial components are the spherical Bessel functions $j_n(kr)$). Now we introduce two matrices, R and T, relating the coefficient vectors:

$$\vec{a}_{2j+1} = R\vec{a}_{2j}, \qquad \vec{a}_{2j} = T\vec{a}_{2j-1} \tag{3}$$

The matrix T is the matrix of coefficients of sound scattering by the nonoperating machine (similar to the T-matrix introduced by Waterman [6]), and R is the matrix of spherical coefficients of sound reflection from the room walls. These matrices are fully defined by the machine (T) and the room (R) properties and do not depend on interconnected fields (on the index j).

Substitution of Eq.(3) into the representation (2) gives

$$\vec{a}^d = (E - TR)^{-1}\vec{a}_0, \qquad \vec{a}^s = R\vec{a}^d, \tag{4}$$

E is the identity matrix. In general situation, which is the case in practice, when there are auxiliary sound sources in the room, the following equations can be derived which generalise the Eq.(4)

$$\vec{a}^d = (E - TR)^{-1}\vec{a}_0 + T(E - RT)^{-1}\vec{b}_1, \ \vec{a}^s = R(E - TR)^{-1}\vec{a}_0 + (E - RT)^{-1}\vec{b}_1 . \tag{5}$$

where $\vec{b}_1$ is the vector of coefficients of the field generated by the auxiliary sources in the room without the machine.

Equations (5) give a full formal salution to the noise prediction problem. The total sound field in a room is expressed as a function of sound fields of the sources in standard conditions (for the machine - in the free space, $\vec{a}_0$, and for auxiliary sources - in the room without the machine, $\vec{b}_1$), the matrix R describing acoustic properties of the room and the matrix T characterising the machine as a scatterer of sound. The solution (5) is obtaind in terms of spherical coefficients, all the phisycal field quantities (pressure, particle velocity, etc.) can be easily rebuilt as the series in spherical functions.

The exact formal solution (5) implys that the vectors $\vec{a}_0$, $\vec{b}$ and matrices R, T have an infinite number of components. In practice, their order is finite, and Eqs.(3)–(5) are approximate. The difference between the exact and approximate solutions depends on the properties of the acoustic field under study(its smoothness on S) and is one of components of the total error which can be estimated experimentally.

3 DEFINITION OF THE MODELS

It is seen from the solution (5) that the sound source under study (the machine) is modeled by its sound field in the free space, $\vec{a}_0$ and by the scattering matrix T, The reflecting matrix R is in this case the acoustic model of the room.

It should be noted that the vector parameters of the source model, $\vec{a}_0$, may be replaced by more physical parameters, namely, by two vectors, $\vec{p}_0 = p_0(s_1), ..., p_0(s_N)$ and $\vec{v}_0 = v_0(s_1), ..., v_0(s_N)$, which describe the pressure and particle velocity distributions on the hemisphere S enveloping the machine, in the free space conditions ($s_j, j = 1, .., N$, are the grid points on S). The machine in this case is modeled by an ensembly of the secondary point sources - N monopoles and N dipoles located on the enveloping surface S. It is apparent that model parameters $\vec{a}_0$ and parameters $\vec{p}_0$, $\vec{v}_0$ are equivalent, they are linearly interconnected via spherical harmonics.

4 FIELD FACTORIZATION

One of the main points of the approach presented here is the field factorisation, i.e. presentation of the field as a sum of outgoing and standing waves (see Eq.(2)). We use for the purpose the Helmholts integral operator

$$H(p, v) = \int\int_S [p(s)\partial g(x, s)/\partial n - \imath\rho\omega v(s)g(x, s)dS, \tag{6}$$

where S is a closed surface, $g(x, s) = \exp(\imath kr)/4\pi r$ is the Green function of the free space, $p(s)$ and $v(s)$ are values of the sound pressure and particle velocity on S, $s \in S$, $\vec{n}$ is the outward normal vector, x is a space point, $r = |x - s|$. According to the basic property of the operator[7] we have $H(p, v) = p^d(x)$ for x outside S, and $H(p, v) = -p^e(x)$ for x inside S. In other words, when the H-operator acts on arbitrary sound field, measured at the surface S, it gives: in the exterior region of S - the field component p^d generated by sources placed inside S; and in the interior region of S - the field component p^e generated by sources operating outside S. Contrary to the commonly used method [8], this method of factorisation is valid at all frequencies and is applicable to any closed surface S.

In practical application of the method, we calculated the integral operator (6) replaced by its discrete analogue. Measurements of the total presure and particle velocity, p and v, on the surface S were performed, in this work, using the two-microphone technique.

5 IDENTIFICATION OF THE MODEL PARAMETERS

Here it will be shown how the parameters of the source model, $\vec{a}_0$ and T, and the parameters of the room model, R, can be obtained experimentally in rather arbitrary acoustic conditions, using convensional measuring techniques.

The vector parameters of the source model, $\vec{a}_0$ or $\vec{p}_0$,$\vec{v}_0$, can be obtained by direct measurements in an anechoic room. However, many sources cannot be installed in anechoic rooms. Besides, the frequency range considered here includes low freguences at which it is not simple to simulate free-space conditions. Therefore experiment procedure is proposed for parameter identification in arbitrary closed room. The idea of the procedure follows directly from Eqs.(5): multiplying the second Eq.(5) by the matrix T and substracting it from the first Eq.(5) yield

$$\vec{a}_0 = \vec{a}^d - T\vec{a}^e \,. \tag{7}$$

This equation shows that the parameters of the source model ($\vec{a}_0$) can be extracted from experimentally measured total field in a room, if the scattering matrix T is known and if the total field is factorised according to Eq (2).

The matrix T of the scattering coefficients can be determined in the following experiment. Let the nonoperating machine be installed in any room and subjected to sound radiation from a small probe source located outside a hemisphere S enveloping the machine. Measuring the sound fields on S, factorising it and expanding into the spherical functions one can obtain vectors $\vec{a}^d$ and $\vec{a}^e$, which are intereconnected by the equation $\vec{a}^d = T\vec{a}^e$, which strictly follows from Eq.(5) for $\vec{a}_0 = 0$. Having done the procedure for several sites of the probe source outside S, one can obtain the matrix T. (*Fig.*)

The reflecting matrix R, i.e. the parameters of the room model, can be determined experimentally by similar procedure. In this case, the room under study without a machine is insinified by the small probe source placed at several points inside the measurement sphere S.

6 EXPERIMENTAL VERIFICATION

A number of numerical method and laboratory experiments have been carried out aimed at investigating the discretisation error of the operations involved, the experimental errors, and at verifying the source model and the parameter identification procedures. The laboratory experiments were performed with a complicated sound source in the frequency range 90–250 Hz. The scattering matrix T was determined according to the scheme described above. The parameters of the source model were obtained by the direct measurements in the free space as well as in several enclosed rooms. The pressure and particle velocity were measured by intensimetric probes at 22 grid points of enveloping hemisphere, then were factorised and expanded in spherical harmonics. The model parameters were computed according to Eq.(7). It was found that the difference between the values of parameters obtained in various rooms and in the free space did not exceed the experimental error 10%.

The experiments showed that the method of source model parameter identification works good even in hard acoustic environ- ments. We have managed to extract the model parameters (which correspond to the free space conditions) from the total field measured in a small undamped empty room, the total pressure ampli- tude exceeding 18 dB the amplitude of the extracted component. It became possible due to high efficiency of the field factorisation procedure based on use of the Helmholts operator.

The experiments performed have proved practical validity of our approach. Besides, they have demonstrated that the H-operator is a very useful tool for experimental study of complicated acoustic fields.

REFERENCES

1. G.H.KOOPMAN and H.BENNER. Method for computing the sound power of machines based on Helmholts integral. Journal of the Acoustical Society of America, 71(1), 1982, p.78–89.

2. E.LUZZATO and C.LECOINTRE. Some simple and effective methods for sound source identification with geometrical acoustic models. Journal of Sound and Vibration, 105(3), 1986, p.473–490.

3. P.J.T.FILIPPI, D.HABAULT and J.PIRAUX. Noise sources modeling and intensimetry using antenna measurement and identification procedures. Journal of Sound and Vibration, 124(2),1985,p.285–296.

4. T.M.TOMILINA and Yu.I.BOBROVNITSKII. Modelling by point sources and sound field analysis of machines and vibrating structures. Proceedings of the Inter-Noise Conference, Gothenburg, Sweden. V.2, 1990, p.895–898.

5. Summaries of Reports to the International Conference on Prediction of the noise emitted by Vibrating Structures, March 1991. CETIM, Senlis, France, 1991.

6. P.C.WATERMAN. New formulation of acoustic scattering. Journal of the Acoustical Society of America, 45(6), 1969, p.1417–1429.

7. F.T.BAKER and B.B.COPSON. The Mathematical Theory of Huygens principle. Oxford: The Clarendon Press, 1950.

8. G.WEINREICH and E.B.ARNOLD. Method for measuring acoustic radiation fields. Journal of the Acoustical Society of America, 68(2), 1980, p.404–411.

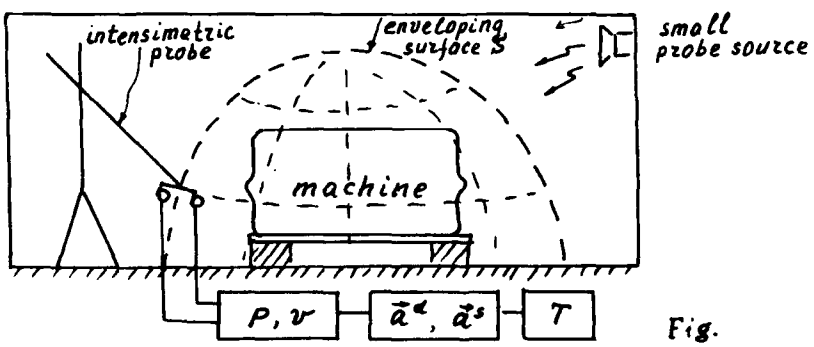

Fig.

SECOND INTERNATIONAL CONGRESS ON
RECENT DEVELOPMENTS IN AIR- AND
STRUCTURE-BORNE SOUND AND VIBRATION
MARCH 4-6, 1992 AUBURN UNIVERSITY, USA

A PARALLEL PATH DIFFERENCE ON-LINE MODELLING ALGORITHM FOR ACTIVE NOISE CANCELLATION

Yong Yan and Sen M. Kuo
Department of Electrical Engineering
Northern Illinois University
DeKalb, IL 60115
815-753-9967

ABSTRACT

In the commonly used active noise cancellation configuration, on-line system identification of the auxiliary path and error path has been a difficult problem. The algorithms already proposed are not satisfactory. A new algorithm, using a "parallel path difference" scheme, is developed theoretically. Simulation results successfully proved the validity of the theory and the feasibility of the new algorithm. Steady state and dynamic performance is analyzed.

I. INTRODUCTION:

In the commonly used active noise cancellation configuration (Fig.1), a copy of the transfer function products Hs(z)He(z) is needed for the filtered-X [1] or filtered-U [2] algorithms. On-line system identification of Hs(z)He(z) is preferred to accommodate the changing environment, thus the changing parameters of Hs(z) and/or He(z). This is a difficult task since the signal picked up by the error microphone, e''(n), is always a mixture of signals from P(z) and Hs(z) and we have no way of distinguishing the two. From another point of view, if we use an adaptive filter T(z) to identify Hs(z)He(z) (Fig. 2) [1], the disturbance in the modelling scheme is closely correlated with the input signal to T(z), resulting in a biased optimal solution of T(z), as described by the following mathematical deduction.

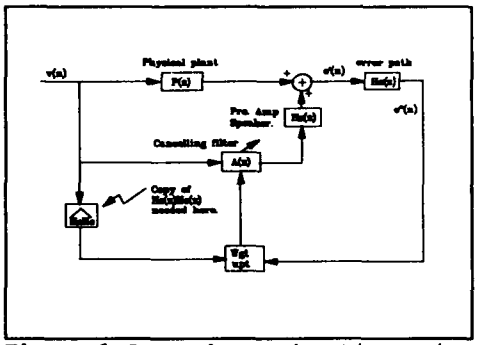

Figure 1 Commonly used active noise control configuration

From Fig. 2, when adaptive filter T(z) converges, the Z-transform of the error sequence e(n), according to Mason's law, is:

$$E(z) = (P(z)He(z) + A(z)Hs(z)He(z) - A(z)T(z)) * V(z) \qquad (1)$$

if e(n)=0, then E(z)=0, we have :

$$T(z) = Hs(z)He(z) + \frac{P(z)He(z)}{A(z)} \qquad (2)$$

therefore T(z) is not the desired Hs(z)He(z), instead, it is biased by an unknown part $\frac{P(z)He(z)}{A(z)}$.

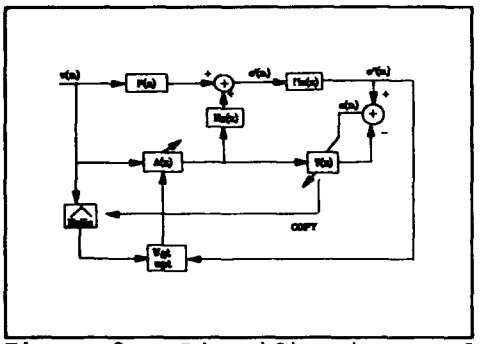

Figure 2 Identification of Hs(z)He(z) with T(z)

II. NEW PARALLEL PATH DIFFERENCE ALGORITHM:

The algorithms already proposed to solve the above problem are analyzed and found unsatisfactory [2][3][4][5]. To meet the need for better algorithms to identify Hs(z)He(z), a parallel path difference algorithm is proposed in this research (Fig.3). There are three key points:

a) We separate the process of identifying Hs(z)He(z) and that of reducing noise, because unless we get the right copy of Hs(z)He(z), the effort of trying to reduce the noise will be in vain. Therefore we use software to detect the change of Hs(z)He(z) by detecting the trend of e1''(n) and e2''(n). Once change detected, the software will go to a routine in which it fixes the noise canceling filters and tracks the new Hs(z)He(z), then it adapts the filters to cancel the noise.

b) In the process of modelling Hs(z)He(z), we do not model Hs(z)He(z) directly. Instead, we use two parallel paths and split the input sequence into odd-numbered and even-numbered sequences to drive the two adaptive paths alternately. After the two adaptive filters both converge, we use the optimal coefficients of the two filters to CALCULATE Hs(z)He(z), i.e. the information about Hs(z)He(z) is extracted from the difference of the two paths. The switching between the two paths is accomplished by software.

c) Software detectors to detect the convergence conditions are crucial in this algorithm.

There are two detectors involved here. One is the detector to detect the change of Hs(z)He(z). This can be easily done by detecting the changing trend of $e''^2(n)$. In normal mode, the main path is used. (Fig. 2) If Hs(z)He(z) has not changed, we have the right copy in the filtered-X path, $e''^2(n)$ should be going down. If Hs(z)He(z) has changed so much that the copy we had can no longer be used as an approximation of the real Hs(z)He(z), $e''^2(n)$ will be going up(tending to diverge). Thus by detecting the trend of $e''^2(n)$, we can detect the change of Hs(z)He(z), then the software will go to a routine in which it switches the input between the two paths to determine the new Hs(z)He(z). The second detector is the one to detect the convergence of the two switching paths. This one is even more crucial and may be more difficult to implement. Only when the two switching paths have converged(i.e. T1(z) & T2(z) have converged), can we calculate the new Hs(z)He(z) by the following method. More of this point will be discussed near the end of this paper.

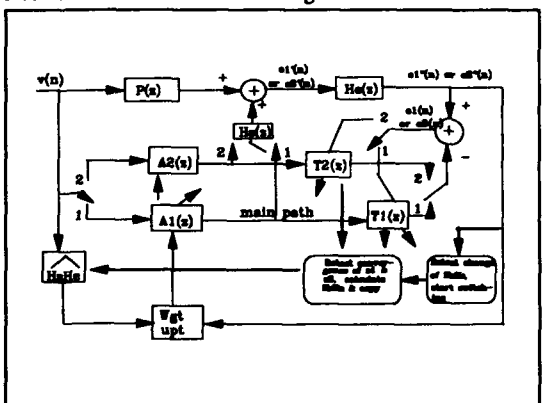

Figure 3 Parallel Path Difference algorithm, no feedback case

After convergence of the two switching paths, Hs(z)He(z) can be calculated as follows:

1. The case without feedback:

In the system diagram shown in Fig. 3, when the filters T1(z) and T2(z) converge, we have:

$$E1(z) = (P(z)He(z) + A1(z)Hs(z)He(z) - A1(z)T1(z)) * V_{odd}(z) \quad (3)$$

$$E2(z) = (P(z)He(z) + A2(z)Hs(z)He(z) - A2(z)T2(z)) * V_{even}(z) \quad (4)$$

When T1(z) and T2(z) have enough coefficients:

$$E1(z) = E2(z) = 0 \quad (5)$$

we can assume:

$$V_{odd}(z) = V_{even}(z) \quad (6)$$

subtract the two equations and solve for Hs(z)He(z), we have:

$$Hs(z)He(z) = \frac{A1(z)T1(z) - A2(z)T2(z)}{A1(z) - A2(z)} \quad (7)$$

This is a significant result compared with [Equ.2] since the unknown term P(z)He(z) is canceled, thus the error path Hs(z)He(z) can be estimated correctly.

During the modelling process, we can let A2(z) and A1(z) have a fixed relation such as: A2(z)=m*A1(z) where m is an adjustable constant, then the above equation becomes:

$$Hs(z)He(z) = \frac{T1(z) - m * T2(z)}{1 - m} \quad (8)$$

so we calculate Hs(z)He(z) from the final coefficients of T1(z) and T2(z).

2. The case with feedback:

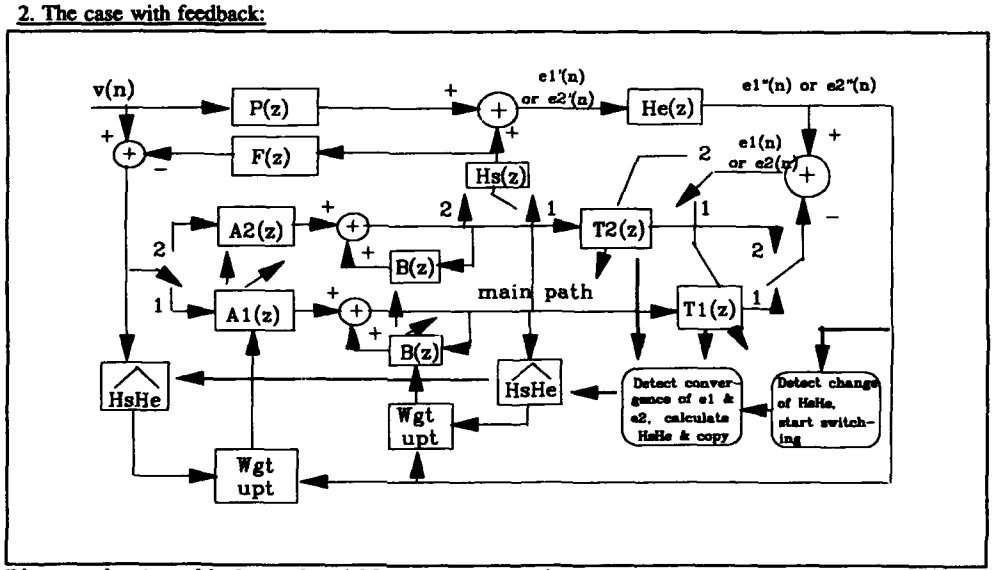

Figure 4 Parallel Path Difference algorithm, with feedback

The system diagram is shown in Fig.4. When the filters T1(z) and T2(z) converge, we have:

$$\frac{E1(z)}{V_{odd}(z)} = P(z)He(z) + \frac{A1(z)Hs(z)He(z) - A1(z)T1(z)}{1 - B(z) + A1(z)Hs(z)F(z)} \quad (9)$$

$$\frac{E2(z)}{V_{even}(z)} = P(z)He(z) + \frac{A2(z)Hs(z)He(z) - A2(z)T2(z)}{1 - B(z) + A2(z)Hs(z)F(z)} \quad (10)$$

Since F(z) is the feedback, we can use a directional speaker at the canceling point and a directional microphone at the input point to make sure that feedback is weak, in other words, the coefficients of F(z) are much smaller than those of He(z). Then if we let : A2(z)=m*A1(z) and choose m close to 1, e.g. m=0.99, it is reasonable to assume that the two denominators are equal while A1(z)Hs(z)He(z) and A2(z)Hs(z)He(z) are not (we need the difference between the two).

Solve for Hs(z)He(z), we have the same result:

$$Hs(z)He(z) = \frac{T1(z) - m * T2(z)}{1 - m} \quad (11)$$

III. STEADY STATE ANALYSIS IN TIME DOMAIN:

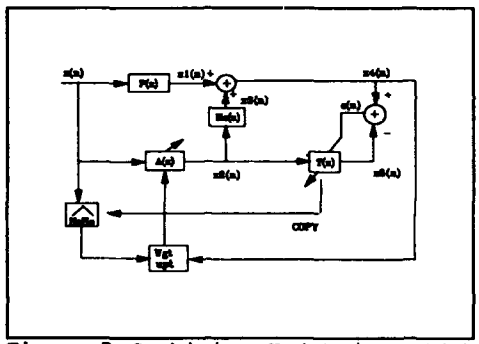

Figure 5 Combining He(z) into P(z) and Hs(z)

To demonstrate the inner workings of the system in more detail, we now use the more classical approach to derive the mean square error function in time domain, to get the Wiener solution and to compare it with the above results obtained using Mason's law. To simplify the expressions, we can combine He(z) into P(z) and Hs(z) [2], obtaining the equivalent system block diagram in Fig 5. If the impulse responses of the plant and the error path are $P = [p_0, p_1, \ldots, p_{N-1}]^T$ and $Hs = [hs_0, hs_1, \ldots hs_{N-1}]^T$, respectively, and the coefficients of the adaptive filters A and T at the same instant are $A_n = [a_0(n), a_1(n), \ldots, a_{N-1}(n)]^T$ and $T_n = [t_0(n), t_1(n), \ldots, t_{N-1}(n)]^T$ respectively, then we have: (capital letters denote vectors and matrices while lower case letters denote scalars, for vectors, we use subscripts to denote time index while for scalars we use function convention,i.e. f(n))

$$x_1(n) = X_n^T P \quad and \quad x_2(n) = X_n^T A_n \quad (12)$$

where $X_n = [x(n), x(n-1), \ldots, x(n-N+1)]^T$

Define:

$$X_{2_n} = \begin{bmatrix} x_2(n) \\ x_2(n-1) \\ \cdot \\ \cdot \\ \cdot \\ x_2(n-N+1) \end{bmatrix} = \begin{bmatrix} x(n) & x(n-1) & \ldots & x(n-N+1) \\ x(n-1) & x(n-2) & \ldots & x(n-N) \\ \cdot & & & \\ \cdot & & & \\ \cdot & & & \\ x(n-N+1) & \ldots & \ldots & x(n-2N+2) \end{bmatrix} A_n = S_n A_n \quad (13)$$

where S_n is used to designate the matrix and is obviously symmetric. Then:

$$x_3(n) = X_{2_n}{}^T H_s = A_n^T S_n H_s \tag{14}$$

$$x_4(n) = x_1(n) + x_3(n) = X_n^T P + A_n^T S_n H_s \tag{15}$$

$$x_5(n) = X_{2_n}{}^T T_n = A_n^T S_n T_n \tag{16}$$

$$\begin{aligned} e(n) &= x_4(n) - x_5(n) \\ &= A_n^T S_n (H_s - T_n) + X_n^T P \end{aligned} \tag{17}$$

therefore:

$$\begin{aligned} E[e^2(n)] &= E[e^T(n)\, e(n)] = E\{[(H_s^T - T_n^T)\ S_n A_n + P^T X_n]\ [A_n^T S_n\ (H_s - T_n) + X_n^T P]\} \\ &= E[(T_n^T - H_s^T)\ S_n A_n A_n^T S_n\ (T_n - H_s)] - 2E[(T_n^T - H_s^T) S_n A_n X_n^T P] + E[P^T X_n X_n^T P] \end{aligned} \tag{18}$$

a) For the modelling process, in which A is fixed and T adapts, let $\nabla_T = 0$, we have:

$$\nabla_T = 2\ E(S_n A A^T S_n)(T_n - H_s) - 2E(S_n A X_n^T)\ P = 0 \tag{19}$$

if $[E(S_n A A^T S_n)]^{-1}$ exists, then we have:

$$T^* = Hs + [E(S_n A A^T S_n)]^{-1}\ E[S_n A X_n^T]\ P \tag{20}$$

This result is comparable with the previous one obtained using Mason's law [Equ.2], that is, the Wiener solution of T is biased from Hs by an unknown part related with P. The corresponding minimum MSE is:

$$E[e^2(n)]_{min} = E[(P^T X_n)^2] - E[P^T X_n A^T S_n]\ [E(S_n A A^T S_n)]^{-1} E[S_n A X_n^T P] \tag{21}$$

the coefficient updating equation is :

$$\begin{aligned} T_{n+1} &= T_n - \mu \nabla_T = T_n - \mu \frac{\partial e^2(n)}{\partial T} = T_n - \mu 2 e(n) \frac{\partial e(n)}{\partial T} \\ &= T_n + \mu 2 e(n) S_n A \end{aligned} \tag{22}$$

which is the normal LMS algorithm, with input signal sequence to T as *SA*

b) For the noise control process, in which A adapts, the error signal is:

$$e'(n) = x_4(n) = A_n^T S_n Hs + X_n^T P \tag{23}$$

therefore, the mean square error is:

$$\begin{aligned} E[e^2(n)] &= E[e(n)\, e^T(n)] = E[(A_n^T S_n H_s + X_n^T P)\ (H_s^T S_n A_n + P^T X_n)] \\ &= E[A_n^T S_n H_s H_s^T S_n A_n] + 2E[X_n^T P H_s^T S_n A_n] + E[X_n^T P P^T X_n] \end{aligned} \tag{24}$$

This is a quadratic function about A, the global minimum is determined by:

$$\nabla_A = 2E[S_n H_s H_s^T S_n] A + 2E[S_n H_s P^T X_n] = 0 \tag{25}$$

so the Wiener solution for A is:

$$A^* = [E(S_n H_s H_s^T S_n)]^{-1} E[S_n H_s P^T X_n] \tag{26}$$

the coefficient updating equation is :

$$\begin{aligned} A_{n+1} &= A_n - \mu \nabla_A = A_n - \mu \frac{\partial e^2(n)}{\partial A} \\ &= A_n - \mu 2 e(n) S_n H_s \end{aligned} \tag{27}$$

which is the filtered-X LMS algorithm. We see here the need for the identification of Hs(z).

IV. DYNAMIC PERFORMANCE ANALYSIS IN FREQUENCY DOMAIN:

To analyze the dynamic performance of the system, we use the approach developed by Clarkson [6], which describes the LMS adaptive filter by a transfer function. In general case, this is only an approximation, since an adaptive system is time varying thus can not be described by a transfer function. For some special cases, including the periodic input case, however, the Z-transforms of the input and output signal become independent of time, therefore the adaptive system can be described by an equivalent transfer function. From this function, we can study the stability and convergence properties of the adaptive process. In this paper, we will give the salient points of this approach used in our case for periodic input signals.

Referring to Fig.5, for the identification process, in which A is fixed and T adapts, the updating equation for $T_n = [t_0(n), t_1(n), \ldots, t_{N-1}(n)]^T$ is:

$$T_n = T_{n-1} + \mu e(n-1) X_{2_{n-1}} \tag{28}$$

using the above equation iteratively and assuming T(0)=0, we have:

$$T_n = \mu \sum_{i=0}^{n-1} e(i) X_{2_i} \tag{29}$$

so we have:

$$\begin{aligned} x_5(n) &= T_n^T X_{2_n} = \mu \sum_{i=0}^{n-1} e(i) X_{2_i}^T X_{2_n} = \mu \sum_{i=0}^{n-1} \left[e(i) \sum_{j=0}^{N-1} x(i-j) x(n-j) \right] \\ &= \mu \sum_{i=0}^{n-1} [e(i) N r_{ni}] \end{aligned} \tag{30}$$

where r_{ni} is an autocorrelation estimate, N is the order of filter. As $N \to \infty$, , r_{ni} will be the actual autocorrelation, for which $r_{ni} = r_{n-i}$ for periodic signals. So if the filter length is long enough, we have:

$$x_5(n) = \mu N \sum_{i=0}^{n-1} e(i) r_{n-i} \tag{31}$$

and:

$$\begin{aligned} e(n) &= x_4(n) - x_5(n) = x_1(n) - x_3(n) - x_5(n) \\ &= x(n) * P - x(n) * A * H_s - \mu N \sum_{i=0}^{n-1} e(i) r_{n-i} \\ &= x(n) * P - x(n) * A * H_s - \mu N \sum_{i=0}^{n} e(i) r_{n-i} + \mu N r_0 e(n) \end{aligned} \tag{32}$$

where "*" denotes convolution. Rearranging terms and taking Z-transform of the equation, we get:

$$\frac{E(z)}{X(z)} = \frac{P(z) - A(z)Hs(z)}{1 - \mu N r_0 + \mu N R(z)} \tag{33}$$

where $R(z)$ is the Z-transform of the autocorrelation sequence $R = [r_0, r_1, \ldots, r_{n-1}]$.

This is a very important result, since it describes the whole adaptation process, the dynamic state as well as the steady state. At first sight, it appears contradictory to the result we got previously [Equ.1]. The reason for the difference is that the former one is the Z-transform of the error sequence at the steady state, while the current one is the Z-transform of the whole error sequence starting from the beginning of the adaptation process.

Using this result, we can study the stability property of the system by studying the root loci as μ changes, given input signal (thus given R(z)). We can also study the convergence property of the system by approximating the denominator to a second order polynomial of Z^{-1} and relating the damping property of MSE to the pole locations.

Using the final value theorem of Z-transform, it is easy to see that $e(\infty) = 0$. So for periodic input signal, there is no excess mean square error for both paths. This is ideal for the parallel path difference algorithm.

To analyze the effects of error in estimating Hs(z), we use the results from Elliott[7]. To further simplify the problem, Elliott et al. used a sinusoidal signal for the input, so that the effects of the estimated Hs(z) can be specified by $Ae^{j\phi}$. After some involved derivation, the following result is obtained:

$$\frac{E(z)}{X(z)} = \frac{P(z)\,[\,1 - 2z\cos\omega_0 + z^2\,]}{1 - 2z\cos\omega_0 + z^2 + \frac{\mu AN}{2} H_s(z)\,(z\cos(\omega_0 - \phi) - \cos\phi)} \tag{34}$$

From this equation, we can determine the effects of the estimation error of Hs(z) on the total system performance.

V. SIMULATIONS AND DISCUSSIONS:

Simulations of this algorithm for nonfeedback and feedback-present cases are performed with some simple transfer functions. We let the initial state of the system be at optimal state so that the noise is perfectly canceled. Then we changed Hs(z) to a totally different one and observed the performance of the system. When we do not track Hs(z)He(z) at all, the MSE of error signal e'(n) diverges as in Fig.6. When we use PPD algorithm, tracking of Hs(z)He(z) has been observed in all but large feedback cases. Fig. 7 shows a result with no feedback in which Hs(z) changed to another function such that we knew our 5th-order adaptive filters T1(z) and T2(z) could still identify with zero MSE. The cases with feedback are shown in Fig.8 and Fig.9. When tracking of Hs(z)He(z) is not ideal, i.e. when T1(z) and T2(z) are not flexible enough to adapt themselves to make MSE's of e1(n) and e2(n) zero, the error signal e'(n) will perform as in Fig.10.

Simulations of the algorithm using measured real world transfer functions have also been done. The results are similar to those with simple transfer functions except that the excess MSE's are not zero.

From the simulation results, we can see that the algorithm works very well for nonfeedback case and works fine for weak feedback (less than 5%). When the

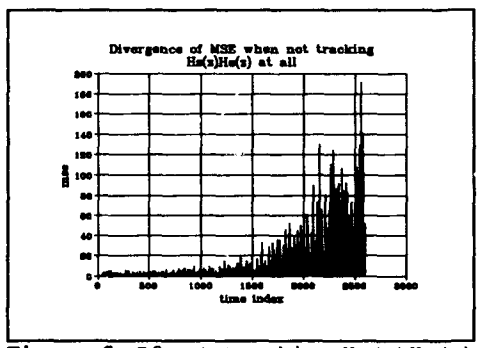

Figure 6 If not tracking Hs(z)He(z)

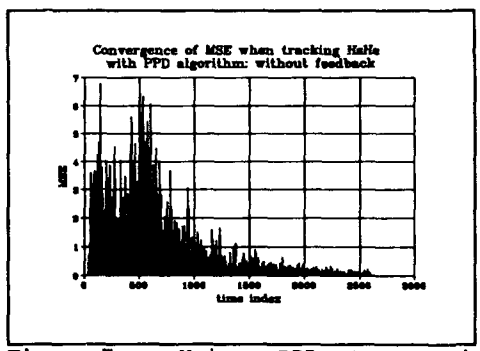

Figure 7 Using PPD to track Hs(z)He(z), with no feedback

feedback is larger than 5%, however, it does not work very well. This is because when we derived the equation to calculate Hs(z)He(z), we assumed that F(z) was very small by using a directional speaker at the canceling point and a directional microphone at the input point.(otherwise it is difficult to separate the unknown A(z)Hs(z)F(z) term.) If F(z) is large, we need to derive some other equation to calculate Hs(z)He(z), which is not easy.

VI. CONCLUSION:

This paper proposed a new algorithm to identify the error path for filtered-X algorithm in active noise cancellation. This parallel path difference algorithm can be used in a more general system identification context when the plant noise is closely correlated with the input signal to the adaptive filter.

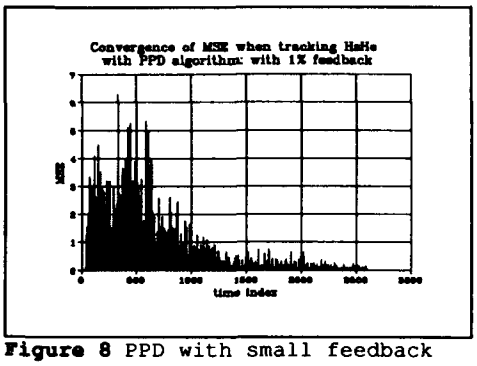

Figure 8 PPD with small feedback

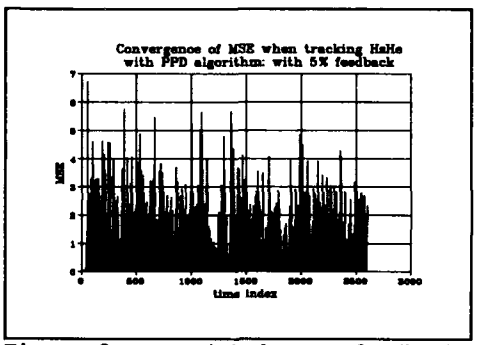

Figure 9 PPD with larger feedback

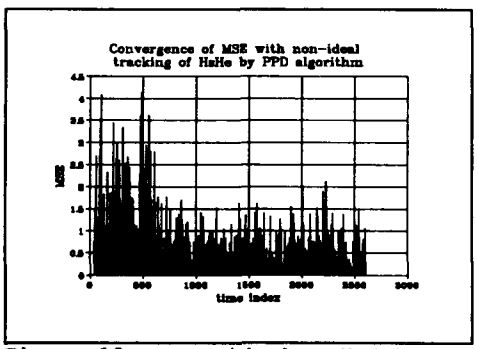

Figure 10 Non-ideal Hs(z)He(z) tracking due to finite T(z) length

REFERENCES:

1. B. Widrow and S.D. Stearns, Adaptive Signal Processing, Prentice-Hall, Englewood Cliffs, NJ, 1985;
2. L.J. Eriksson, "Active Sound Attenuation Using Adaptive Digital Signal Processing Techniques", Ph.D. Thesis, University of Wisconsin-Madison, August, 1985;
3. L.J. Eriksson, M.C. Allie and R.A. Greiner, "A New Approach to Active Attenuation in Ducts", Paper C5-2 in Proceedings of 12th International Congress on Acoustics, Toronto, Ontario, Canada, 24-31 July, 1986 (Canadian Acoustical Association, Toronto,1986);
4. L.J. Eriksson and M.C. Allie, "Use of random noise for on-line transducer modeling in an adaptive attenuation system", J.Acoust. Soc. Am., 85.797-802(1989);
5. L.J. Eriksson, "Development of the filtered-U algorithm for active noise control", J.Acoust. Soc. Am., 89(1) 257-265, (Jan. 1991).
6. P.M. Clarkson and P.R. White, "Simplified Analysis of the LMS Adaptive Filter Using a Transfer Function Approximation", IEEE Transactions on Acoustics, Speech, and Signal Processing, Vol. ASSP-35, No.7, July 1987;
7. S.J. Elliott, I.M. Stothers and P.A. Nelson, "A Multiple Error LMS Algorithm and Its Application to the Active Control of Sound and Vibration", IEEE Transactions on Acoustics, Speech, and Signal Processing, Vol. ASSP-35, No.10, October 1987.

**SECOND INTERNATIONAL CONGRESS ON
RECENT DEVELOPMENTS IN AIR- AND
STRUCTURE-BORNE SOUND AND VIBRATION**
MARCH 4-6, 1992 AUBURN UNIVERSITY, USA

STUDIES OF THE BUILDING CONSTRUCTIONS BY MEANS OF NONLINEAR DIAGNOSTICS

Ekimov A.E., Kolodieva I.I., Korotin P.I.
Institute of Applied Physics Academy of Sciences of the USSR,
603600, N. Novgorod, USSR.

ABSTRACT

In diagnostics of constructions with broken integrity (cracks, adhesion failures, etc.) the methods using nonlinear phenomena find an increasingly frequent practical application. The second harmonic generation mechanisms are best investigated but the real processes are more diversified. In this communication we report on the experimental investigation of the turbo-set bearer where subharmonics were observed along with the fundamental frequency harmonics. This allowed the turbo-set having a polyharmonic vibration spectrum to be used for crack diagnostics of the bearer.

INTRODUCTION

The crack-type defects in building constructions such as machine bearers can appear both at the building stage and when operated because of the large vibration load. Such defects can strongly modify the strength characteristics of the bearers and increase their damage in some cases. Therefore, the timely diagnostics is the first element in the system of preventive measures for longer service of building and other constructions. As a rule, with any arbitrary method of control, the defects are revealed by indirect signs (for example, by time delay in the pulsed procedure). The task of the researcher is to choose the set of indirect signs with high noise protection, which are best suited to a particular object subject to control.

In this communication we report on the vibration test of the turbo-set bearer used in the N.Novgorod heat-and-power station. In the long-term service (over 30 years), when the vibration load was large, extended cracks formed in the bearer interier, which were stopped by sealing with a synthetic binder. Meanwhile, after a decade since the cracks were sealed the increased vibrations at some sites of the bearer made it necessary to control the sealing quality and the possible crack development. To answer these questions we carried out a series of vibrational tests of the bearer. It was found that the cracks in the bearer have produced the nonlinear phenomena which can be used as cracks attributes for the diagnostic purposes.

EXPERIMENTAL PROCEDURE

The vibrations of a bearer (20 m in length, 6 m in width and 8 m in height) were investigated both when the turbo-set (25 MW) was operated and run-out and when the bearer vibrations were excited (with the turbo-set switched off), successively at several points, by a linearly tunable harmonic forse (50 newtons) produced by an electrodynamic vibrator.

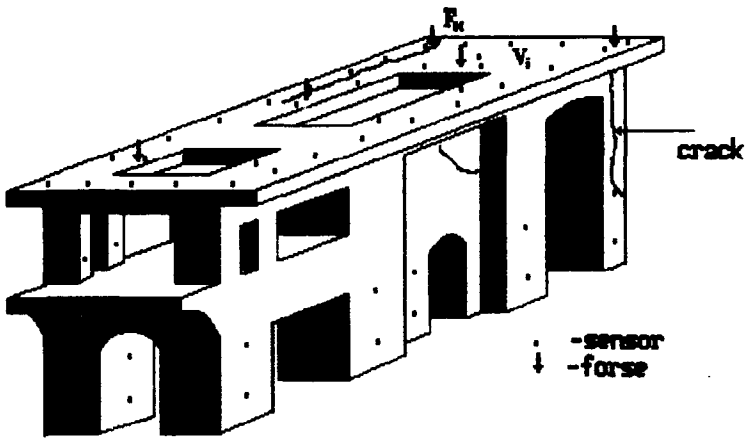

Figure 1.

Figure 1 shows the scheme of a bearer with vibration receivers (accelerometers) mounted at fixed points; the signals from the vibration receivers were processed cogerently. In the case of artifical excitation we determined the induced vibration V_{ki}, where V_{ki} is the vibrational velocity at point 1 from an external forse F applied to point k (V and F are complex quantities). The matrix of transfer functions Y_{nm} was calculated in the frequency range 20-150 Hz (n is the number of the receiver and m is the number of the excitation point). The components of the Y_{nm} matrix are given by

$$Y_{ki} = V_{ki}/F_k , \quad (1)$$

where Y_{ki} is the transfer admittance. The external force frequency (ω) was varied linearly

$$\omega = \omega_1 + q \cdot t \quad (2)$$

Here q is the proportionality coefficient that describes the rate of frequency variation, ω_1 is the initial frequency of the operating range and t is time.

When the monolithic part of the bearer (the domain far from the cracks), the vibrovelocity spectrum V_{kk} coincided with the spectrum of the driving force F_k (Figs. 2a,b). At other points of the construction, at a given F_k, the vibrosignals were insufficient to be detected against the noise background.

When the point at which the external force was applied was transferred from the monolithic part of the bearer to a domain containing cracks, the admittance Y_{ii} increased and the spectrum composition of the vibrations was enriched at point 1 and other points of the construction, where the signal was distinguished against the noise background. As a result, harmonics appeared in the vibrosignal spectrum; the harmonic generation effect is used in the nonlinear diagnostics, for crack

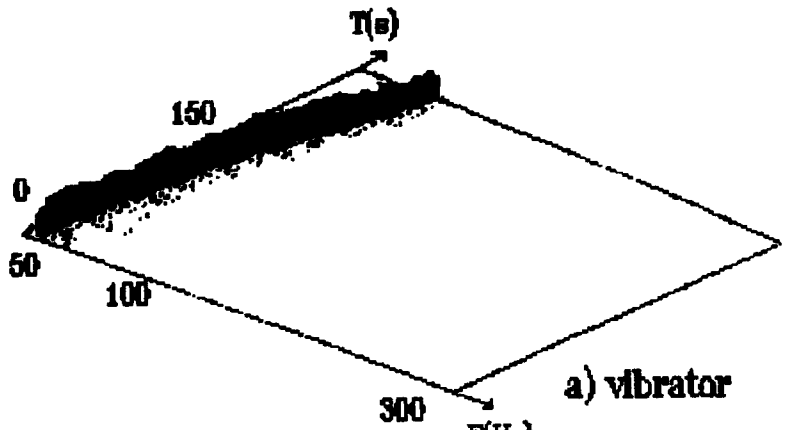

a) vibrator

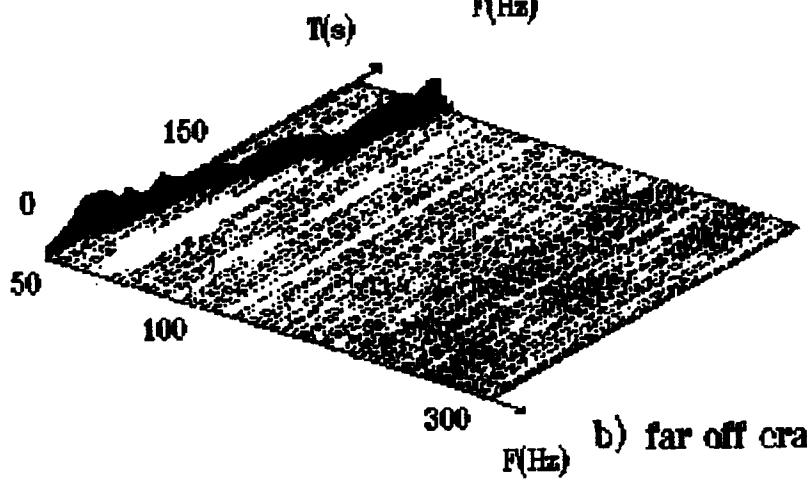

b) far off crack

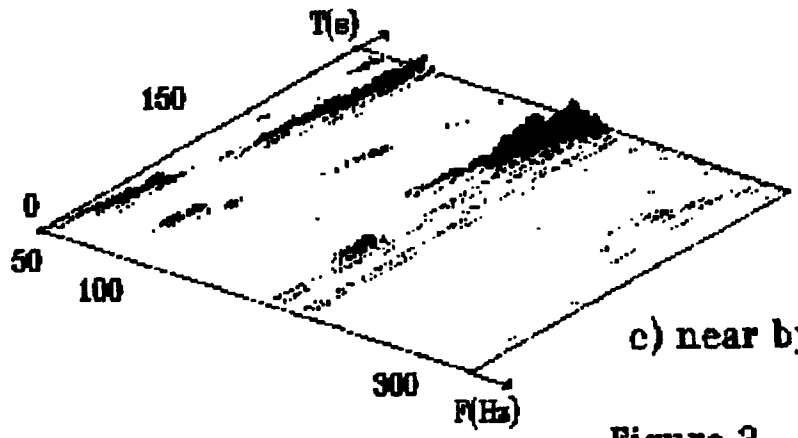

c) near by crack

Figure 2

detection for example. Moreover, in the vibrosignal spectra of the sensors located near the cracks we observed the appearance of subharmonics as the excitation frequency approached the resonance frequencies of the construction (Fig. 2c). The localization of subharmonics near the cracks indicated that the excitation of subharmonics is stimulated and the resonances of the construction enhance the effect.

From Fig. 2c it follows that the subharmonic level is sufficient to use this effect as a diagnostic sign of presence and localization of cracks.

The use of the appearance of subharmonics in the vibroresponse spectrum as a diagnostic sign makes it possible to use polyharmonic sources for the excitation, for example, the turbo-set itself in the run-out regime. Besides, the dynamic force from the turbo-set is mostly sufficient for this effect to be manifested in the bearer irrespective of the crack location. As an illustration, Fig.3 shows the spectrum of the bearer vibrations in the crack region, which was obtained during the run-out of the turbo-set. Figure 3 clearly shows the vibrations in the frequency range $\omega=3/2\cdot\omega_g$, where ω_g is the lower frequency of the vibration source.

The assumption of the parametric nature of the vibration spectrum enrichment has made it possible to define the characteristic thickness of the cracks from the time the nonlinear phenomena appear in the vibration response when the exciting force level is changed.

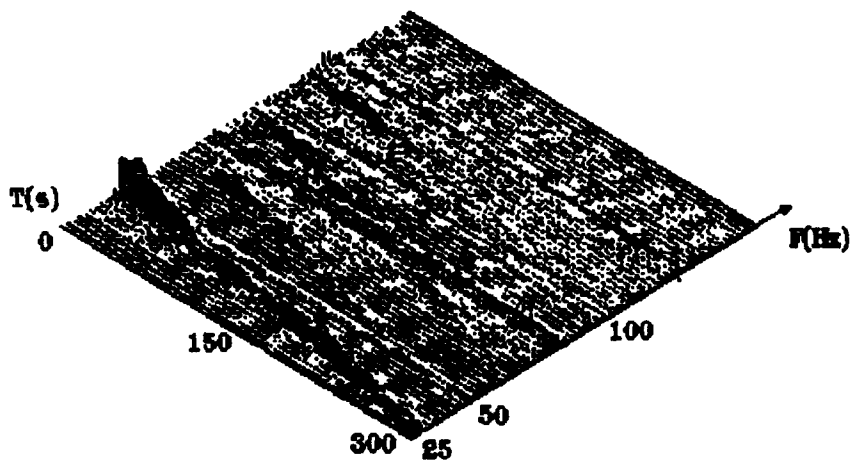

Figure 3.

SUMMARY

1. Analysis of the transfer matrix on the basis of the subharmonic generation effect permitted to reveal the crack and localization in the bearer interior, and the excitation levels at which the nonlinear distortion appeared in the response permitted the defects to be measured.

2. The possibility of using the vibroactivity of the mechanisms, when operated, for monitoring the state of the building construction (bearers, clikes, bridges,etc.) on the basis of the subharmonic generation effect is demonstrated in practice.

SECOND INTERNATIONAL CONGRESS ON
RECENT DEVELOPMENTS IN AIR- AND
STRUCTURE-BORNE SOUND AND VIBRATION
MARCH 4-6, 1992 AUBURN UNIVERSITY, USA

MEASUREMENT OF ACOUSTIC POWER OF FANS UNDER CONDITIONS OF REVERBERANT NOISE OF AERODYNAMIC TEST RIG

V.M. Kazarov, Dr. V.G.Karadgi, Dr. A.S.Mirskov
Central Aerohydrodynamics Institute (TSAGI),
Moscow Branch, Acoustic Division, USSR

ABSTRACT

Acoustic characteristics of fans along with their aerodynamic characteristics are essential factors that determine their high-quality performance. Acoustic and aerodynamic tests conducted jointly usually call for use of specialized sound-level measuring chambers.

Achievements in sound intensity measurement make it possible to measure acoustic power directly on the aerodynamic test rig under conditions of reverberant noise.

In this investigation the technique of measurements of acoustic power of fans in the plenum chamber and its hardware implementation are reported.

The results of acoustic power measurements made on reference source of sound and model fan are given in the work. The technique is available for measurement of an useful signal on the background of significant reverberant noise in the range of low frequencies.

NOMENCLATURE

I - Sound intensity, W/M^2 ;
$I_0 = 10^{-12}$ W/M^2 - Reference quantity of sound intensity;
f - Frequency, Hz;
$L_I = 10\lg(I/I_0)$ - Sound intensity level, dB;
$L_p = 20\lg(\bar{P}/P_0)$ - Sound pressure level, dB;
$L_W = 10\lg(W/W_0)$ - Sound power level, dB;
$L_{\bar{p}} = 1/N \sum_{i=1}^{N} L_{p_i}$ - Mean sound pressure level, dB;
N - Number of measuring points;
P - Sound pressure, N/M^2 ;
$P_0 = 2*10^{-5}$ N/M^2 - Reference quantity of sound pressure;
$\bar{P} = \sqrt{\bar{P}^2}$ - Root-mean-square of sound pressure, N/M^2 ;
$\bar{Y} = \sqrt{1/T \int_0^T Y(t)dt}$;
S - Measurement surface, m^2
t - Time, s;
V - Particle velocity, m/s;
W - Sound power, W;
$W_0 = 10^{-12}$ w - Reference quantity of sound power;
$\sigma_L = \sqrt{1/N \sum_{i=1}^{N} (L_{p_i} - \bar{L}_p)}$ - Root-mean-square dispersion of sound pressure level, dB;

i - Current number of measurement;
n - Component normal to the measurement surface;
* - Conjugate value.

INTRODUCTION

Acoustic characteristics of fans are very important and determine their quality along with reliability and economy. The demand of low noise is one of the most important in the competition ability of new technique products. As a criterion of low noise the sound power, radiated by the fan during its work is used.

The traditional methods and rigs for experimental defining of sound power are well worked out and realised in standards now [1,2]. But in spite of the fact that traditional methods of defining sound power are based on simple apparatus for acoustic measurements, the great expenditures of time and money are needed for the building of sound measuring chambers.

Moreover it is useful and important to check acoustic characteristics of fans and to provide their aeroacoustic parametric analysis during the working out of new advanced aerodynamic schemes.

The modern achievements in the field of experimental sound intensimetry open the wide posibilities for solutions of a series of research and industrial acoustic problems [3,4,5].

Therefore it seems perspective the working out of techniques for measuring the sound power of fans in parallel with their aerodynamic tests on the aerodynamics test rigs, that is the combination of aerodynamic and acoustic tests.

This work offers the possibility to carry out acoustic tests of fans in the plenum chamber of the aerodynamic test rig.

AERODYNAMIC TEST RIG AND ITS ACOUSTIC CHARACTERISTICS

The measurements of fan aerodynamic characteristics are made in the cylindrical plenum chamber of thick steel (Fig.1), having diameter and length about 2m, according to standards. The chamber is provided with a smooth input channel and with a choke valve in it, honeycomb and grids for turbulence surpression. The fan is connected with the output opening of the chamber. The whole plenum chamber is axisymmetrical.

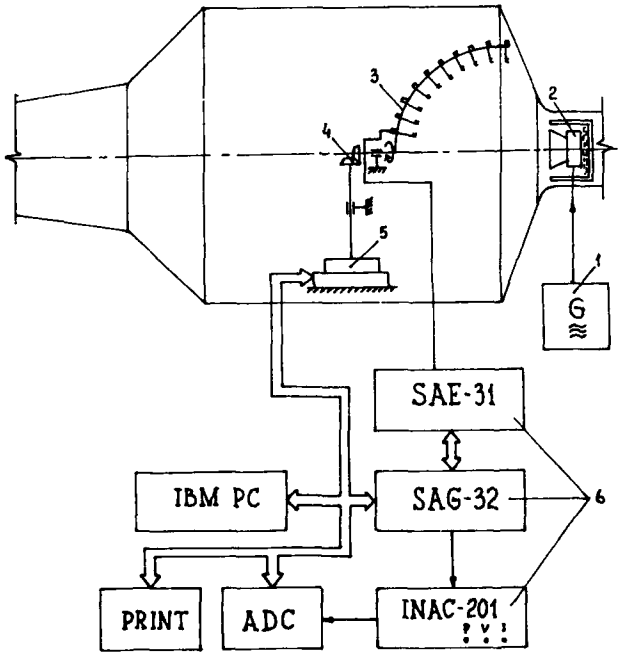

Fig.1.The system for measurement of sound field in plenum chamber:
1-generator; 2-loudspeaker;
3-array of intensity probes;
4-reductor; 5-coordinate system;
6-intensimeter with multiplexer;

The chamber is not adapted to the sound measurements and it could be acoustically improved for the measurements at frequencies above 1 kHz with well enough accuracy. But it is necessary to conduct sound measurements at least from the frequencies of about 100 Hz during the aerodynamic tests of fans, when the noise is low frequency

one in the main.

The standard sound power measurement techniques suppose the placing of checked sound source tested into the anechoic chamber (free field) or reverberant chamber (diffused field). The choice of measurement technique is determined by the field characteristics.

The investigations were carried out for clearing up the correspondence of plenum chamber sound field to reverberant or free field conditions where conducted.

A wide band noise source was installed at the chamber in place of the fan (Fig.1), and sound pressure measurements were conducted in the octave frequency bands at the points on the halfsphere surface with the radius R=0.75 m,centered by a loudspeaker. The number of measurement points was N=200 for every frequency band.

The statictical analyses of measurement results gave mean $\overline{L_p}$ and root-mean-square pressure levels in octave frequency bands, and also gave the bargraphs of pressure distribution onto the measurement surface of halfsphere (Fig.2). The bargraphs are made with the method of rectangular "contributions."

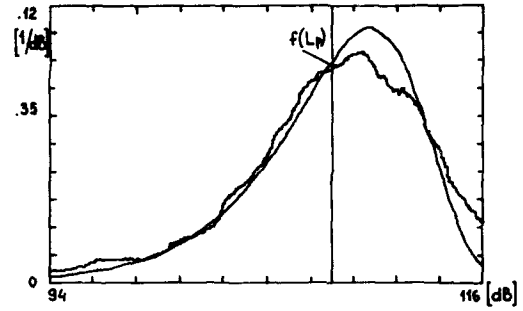

Fig.2. Statistical and theoretical distribution density for sound pressure on the surface of measuring sphere in the plenum chamber.Central octave frequency 500 Hz

The theoretical and statictical distribution from the point of view of their smoothing was performed according to Romanovsky rule [6] showed a good agreement with the type 1 distribution for minimum values [7]:

$$f(L_p) = 1/\sigma_1 \cdot \exp\{[(L_p - M_1)/\sigma_1] - \exp[(L_p - M_1)/\sigma_1]\} \ , \qquad (1)$$

where $\sigma_1 = \sigma_L/1.283$; $M_1 = \overline{L_p} + 0.577 \cdot \sigma_1$ - the distribution parameters.

The character of distributions confirms a significant pressure level dispersion on the surface of measurement sphere in the plenum chamber for all octave frequency bands. Thus, the root-mean-square dispersion of pressure level is within the limits of 3 - 5.6 dB for different octave bands. The root-mean-square dispersion should not exceed 1.5 dB for the reflected field. At the same time the character of chamber space pressure distribution shows the presence of reflected waves and cannot be explained from the point of view of a free field sound source.

Hence, the measurements of plenum chamber sound field and the consequent result analysis show, that the chamber field is neither free nor reverberant. The application of standard methods of fan sound power measurements in the plenum chamber is impossible without its special modernization.

EXPERIMENTAL TECHNIQUE AND MEASUREMENT SYSTEM

The vector of sound intensity characterizes the rate of sound energy flow at a point of space. Therefore it is necessary to know the distribution of the normal component of acoustic intensity vector active part on the surface, enclosing the source, in order to determine its sound power [5]. Then the sound power of the source inside the measurement surface is

$$W = \oint_S \mathrm{Re}(I_n)\, dS \ , \qquad (2)$$

where $I_n = \overline{p V_n^*}$.

The intensity method of sound power measurement has some advantages the main of which are the possibilities of making measurements at the place of utilization of the studied sound source (in situ) and in the presence of significant background noise, exceeding

the useful source level. The important advantage of this method consists in its simplicity.

The posibility of using intencity method for measurements power of sound source in the presence of high levels of background noise is due to the energy flux throw the surface. The integral of the normal component of sound intensity throw the surface S without any sound sources inside is equal to

$$\oint_S Re(I_n)\,dS = 0 . \qquad (3)$$

The expression is true if there is no power absorption inside the measurement surface.

Expressions (2) and (3) are also true if the sound source is on an ideally reflecting surface and is surrounded by the measurement surface closing on it.

To define practical application possibilities of this method it was necessary to clear out its abilities under plenum chamber conditions on a specific measurement system and to evaluate the measurement accuracy.

The measurement system was based on a two microphones intensimetry probe and a finite difference scheme for practical velocity definition.

$$I_n = \overline{\frac{(P_1+P_2)}{2} \cdot \frac{1}{\rho}\int_T \frac{(P_1-P_2)}{\Delta}\,dt} . \qquad (4)$$

It consisted (Fig.1) of 8 - 10 intensity probes array in the form of 1/4 part of circle with the radius of .75 m connected through a multiplexer with an analogue intensimeter, type INAC-201 Metravib company (France). A traverse device provided antenna rotation around the system symmetry axis for obtaining the measurement half shere. A personal computer provided the traverse device control, cyclic probe switching at the continuous traverse device movement, information aqusition from the intensimeter, its secondary processing and measurement results display.

The measurements were performed in octave bands of 125,250,500,1000,2000,4000 Hz central frequency.

In the course of measurements every intensity probe moved along its own circle. If the movement trajectories are central lines of sphere segments the surface areas of wihich are equal and the intensity measurements by each probe are carried out discreately, then:

$$W = \oint_S I_n\,dS = \sum_{i=1}^{N} I_{n_i}\,\Delta S = \Delta S \sum_{i=1}^{N} I_{n_i} , \qquad (5)$$

$\Delta S = 2\pi r^2 / N$ - surface area of the measurement sphere with radius - r for one discrete intensity measurement.

MEASUREMENT RESULTS

The measurements were performed in two stages. First the accuracy was evaluated using model sound sources. Fig.3 presents the results characterizing sensitivity of the intensimetry method of acoustic source power measurements to the background noise effects. The measurements were carried out in an anechoic chamber with the help of intensity measurement system (Fig.1).

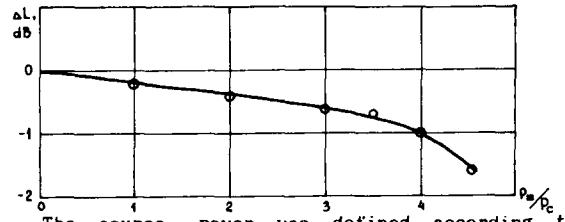

Fig.3. The error of sound power measurements using intensity method

The source power was defined according to the expression (5) . Abscissa expresses relations of the noise pressure $\tilde{P}_ш$ and the useful signal $\tilde{P}_c$ in the measurement point (Fig.4), ordinate axis shows the difference ΔL_w between the power level Li_w measured under background noise conditions and the power level Lo_w - without noise, i.e.

$$\Delta L_w = Li_w - Lo_w \qquad (6)$$

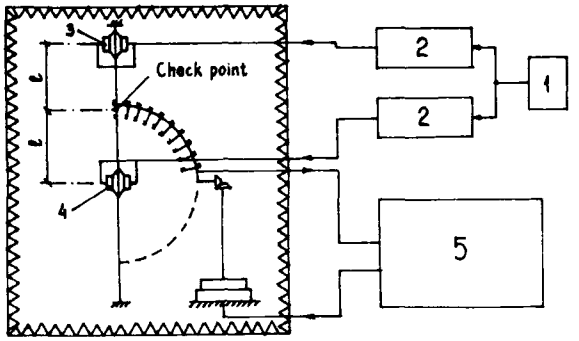

Fig.4.The system for study the background noise influence on the intensimetry method of sound power measurement: 1-generator; 2-power amplyfier ; 3,4-loudspeakers; 5-measurement system (Fig.1)

According to data in Fig.3 the intensimetry method gives the possibility to define the acoustic source power in presence of background noise exceeding the useful signal by 10 - 15 dB with sufficient accuracy.

Fig.5 gives the results of acoustic power measurements of a model noise source in an anechoic chamber and in a plenum chamber of aerodynamic rig using the intensimetry method. The electrical power supplied to the sound source during these measurements was controlled and kept fixed. Acoustic conditions in the anechoic chamber and plenum chamber were essentially different. Thus in Fig.6 there are given mean $\overline{L_p}$ and root-mean-square values of the sound pressure during the measurements in the anechoic chamber and plenum chamber for octave bands of the analysis. These data indicate an essential exceedence of the sound pressure in the plenum chamber over the sound pressure in the anechoic chamber. Root-mean-square dispersion of pressure distributions in the plenum chamber is less. It proves the pressure equalization in the plenum chamber volume at the expense of reflection from the hard walls.

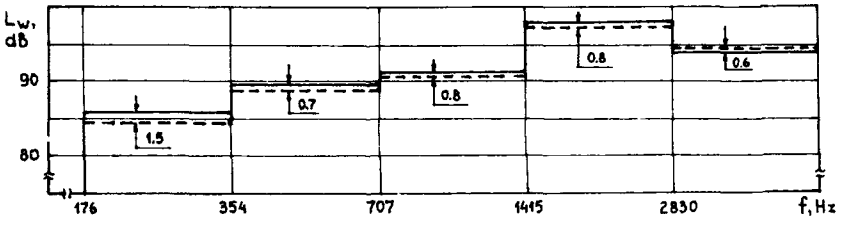

Fig.5. The acoustic power of model sound source:
——— - anechoic chamber;
– – – – - aerodynamic test rig

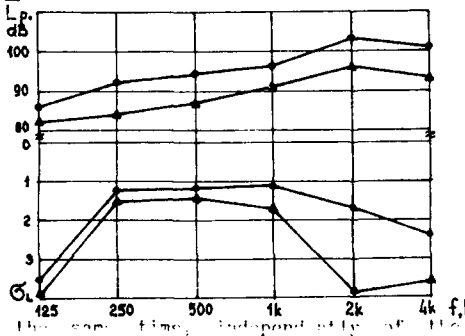

Fig.6.The statistical parameters of pressure distribution in the anechoic chamber (1) and plenum chamber (2) in the octave bands for model source

At the same time, independently of the acoustic utilities, acoustic power

measurement results differs not more than by 1.5 dB (Fig.5) and this proves high accuracy of intensity measurements.

The measurements in the plenum chamber showed that the sound field pressure - intensity index $L_p - L_I$ on the measurement surface for all the octave bands does not exceed 10 -13 dB. This fact confirms the possibility of the intensimetry method application in this case.

Fig.7 gives the acoustic power measurement results for a centrifugal fan Ц14-46 in the plenum chamber at the revolution number n1=600 rev/min and n2=700 rev/min. The character of the variation of the acoustic power level radiated by the fan with the variation of the revolution number of the fan impeller corresponds well enough to the data of [8] where criterial equations of the acoustic power of fans are presented.For comparison, Fig.7 gives the experimental results of fan Ц14-46 noise investigations for the revolution number 700 rev/min from the work [9]. The agreement seems satisfactory.

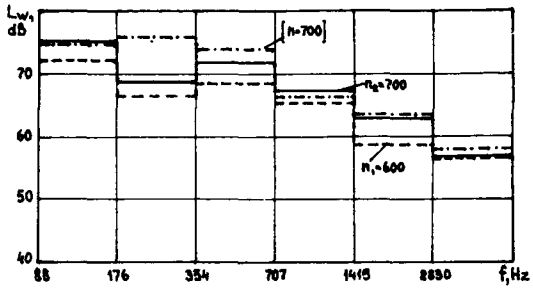

Fig.7. Octave bands acoustic power of centrifugal fan Ц14-46.
Intensimetry method
— · — · — - work [9]

The investigations described in this work permitted to draw the following conclusions:

1. The statistical analysis of pressure level distibutions in the plenum chamber of the aerodynamic rig at the radiation of broad-band noise into it showed that the acoustic field of the chamber is not free and reverberant therefore the standardized methods of fans acoustic power measurements in the plenum chamber of the aerodynamic rig proves to be impossible.
2. The intensimetry method provides acoustic power measurements of the source under conditions of the aerodynamic rig in the low frequency range beginning from the octave band 125 Hz in the presence of background noises exceeding the useful signal by 10 - 15 dB. The measurement accuracy is within 1.5 dB.
3. The developed method and automatized measurement system provide the combination of aerodynamic and acoustic measurements in the course of tests in the aerodynamic rig.

REFERENCES

1.ГОСТ 12.1.024-81. ШУМ. Определение шумовых характеристик источников шума в заглушенной камере.
2.ГОСТ 12.1.027-80. ШУМ. Определение шумовых характеристик источников шума в реверберационном помещении.
3.Intensity Measurements. The analysis technique of the ninties. "Bruel & Kjer", December 1988.
4.Методика и техника интенсиметрических измерений в авиационной акустике. Сборник работ Советско-Французского симпозиума.Москва,17-18 марта 1987г.
5.Писаревский Н.Н.,Каурова Н.Ф.,Макарчик Н.А. Методика и техника измерений звуковой мощности источника шума. Обзор ОНТИ ЦАГИ, N 696,1989г.
6.Митропольский А.К. Техника статистических вычислений. М.,"Наука",1971г.
7.Хан Г.,Шапиро С. Статистические модели в инженерных задачах. М, "Мир",1969г.
8.Соломахова Т.С.Центробежные вентиляторы.М.,"Машиностроение",1975г.
9.Юдин Е.Я.Борьба с шумом на производстве.Справочник.М.,"Машиностроение",1985г.

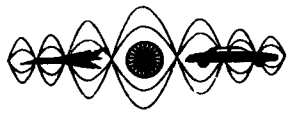

SECOND INTERNATIONAL CONGRESS ON
RECENT DEVELOPMENTS IN AIR- AND
STRUCTURE-BORNE SOUND AND VIBRATION
MARCH 4-6, 1992 AUBURN UNIVERSITY, USA

STATISTICS ON REVERBERANT TRANSFER FUNCTIONS

Mikio Tohyama[1], Richard H. Lyon[2], and Tsunehiko Koike[3]

[1]NTT Human Interface Laboratories, #3-9-11, Midoricho, Musashino-shi, Tokyo, 180 Japan
[2]Department of Mechanical Engineering, Massachusetts Institute of Technology, U.S.A.
[3]NTT Advanced Technology, Tokyo, 167 Japan

ABSTRACT

The transfer function (TF) can be thought of as a stochastic process on the frequency axis due to random occurrences of poles and zeros in the complex frequency plane. This paper describes the pole-spacing statistics of the TFs based on the random matrix theory, and shows that the zeros distribute following a Cauchy distribution in the complex frequency plane. The trend and fluctuations of the accumulated phase is also analyzed using the group delay which is the first derivative of the phase. Inverse filtering for waveform recovery in a reverberant space is mentioned as an important example on machinery diagnostics based on the TF statistics.

1. INTRODUCTION

The control of acoustical systems require signal processing methods that take the complexity and variability of their transfer functions(TFs) into account. We look for certain stable characteristics in the statistical properties of the TFs, which may be represented by thousands of poles and zeros[1].

The TF can be thought of as a stochastic process due to random occurrences of both the poles and zeros of a TF[1][2][3]. Schroeder[4][5] measured the normal-frequency spacing distribution of a rectangular electromagnetic cavity. For large normal-frequency separations, the exponential Poisson distribution appears to be adequate; however for smaller separations his results did not give an exponential decrease, but rather a distribution with a maximum at a frequency spacing that was different from zero.

Work since the early 1950's on the distribution of energy levels in complex nuclei has a bearing on discussions of normal-frequency spacing statistics in acoustics[3]. In 1957, Wigner[6] showed theoretically that 2 * 2 matrices had eigenvalue separation following Rayleigh distribution rather than Poisson distribution. And, recently, Davy [7] and Weaver [8] experimentally confirmed that the resonance-frequency spacing follows the Rayleigh distribution in a large reverberation room and in elastic vibrations, respectively. The authors illustrate the transition from the Poisson- to Rayleigh distribution of the spacings based on the Wigner's random matrix theory [9].

The poles are distributed along the pole-line following a Poisson-like distribution; however, the "cloud" of zeros is distributed two-dimensionally throughout the complex frequency plane. In this paper, the authors introduce a Cauchy distribution function into the cloud of zeros, and we analyze the statistical properties of the accumulated phase[10,11]. Inverse filtering in a reverberant space is also mentioned, since source waveform recovery is an important issue on machinery diagnostics based on the TF statistics[1].

2. POLE-SPACING STATISTICS

Perhaps Wente's paper[12] is the earliest scientific report in which the transmission irregularity in a room was considered as a statistical process[3]. Bolt[2] expressed the transmission irregularity introducing a Poisson model which is an exponential distribution into the normal-frequency spacing statistics. The eigen frequencies(poles) of a rectangular room (Lx, Ly, Lz) with rigid boundaries is given by

$$\omega_{lmn} = (c\pi./L)\sqrt{(l/a)^2+(m/b)^2+(n/c)^2} \qquad \text{(rad/s)} \qquad (1)$$

where c denotes the sound speed (m/s), l, m, n are integer numbers, the length of the sides (m) are $Lx = a\,L$, $Ly = b\,L$, $Lz = c\,L$, and a, b, c shows the ratio of the lengths. The pole occurring process is not stationary, since the density of the poles in a unit frequency interval $n_p(\omega)$ ($\simeq 1/D$, D : average pole-separation) increases in proportion to the square of the frequency. Thus, we normalize the pole distribution by the pole density in every frequency interval of interest. The frequency interval becomes short, as the frequency increases, so that all the intervals of interest have an equal number of poles.

Figure 1 illustrates the histogram for the pole-spacing distributions. We can clearly see the exponential distribution. The upper part of the graph shows an ensemble average over 16 frequency intervals all of which contain 200 poles. The lower data are samples for the distributions obtained in several frequency intervals.

Schroeder's experimental data[4] in an electromagnetic cavity, however, illustrated that the Poisson distribution is not adequate for small frequency separations. The tendency for the small frequency separations to be less probable can perhaps be explained by considering effects of perturbations[3]. Groups of modes that may have degenerate eigen frequencies will suffer a splitting of the eigen frequencies in the presence of perturbations in practical acoustical spaces and structures[13].

The effects of the perturbations on the modal spacings can be approximately estimated by coupled mechanical oscillators[3]. With reference to Fig.2, the masses and spring constants of the two oscillators are M_1, M_2, and K_1, K_2, respectively, and the coupling spring constant is K_{12}. The "eigen matrix E" for the eigen frequencies is written as

$$(E) = (E_o) + (E_p) = \begin{pmatrix} \omega_1^2 & 0 \\ 0 & \omega_2^2 \end{pmatrix} + \begin{pmatrix} b^2 & -b^2 \\ -c^2 & c^2 \end{pmatrix} \qquad (2)$$

where $\omega_1 = \sqrt{K_1/M_1}$, $\omega_2 = \sqrt{K_2/M_2}$, $b = K_{12}/M_1$, and $c = K_{12}/M_2$. In Eq.(2) above, matrix E_o has the eigen frequencies of two "independent" oscillators and matrix E_p represents the coupling effects.

The eigen frequencies of the coupled oscillators are given by positive square roots of the eigen values λ_1 and λ_2 of the matrix E. We are now interested in the statistics of the spacings. This is because the perturbation caused in a practical acoustic space like an irregularly shaped room results in the random coupling between adjacent modes[14]. We can assume that the modal coupling randomly varies as the frequency changes. Following Wigner's random matrix theory[6,9], suppose that the elements b and c of matrix E_p are mutually independent Gaussian variables which have standard deviation of σ. The spacing of the two eigen frequencies, $S = \Delta\omega = \sqrt{\lambda_1} - \sqrt{\lambda_2}$, can be written by

$$S^2 = (\Delta\omega)^2 = \omega_1^2 + \omega_2^2 + b^2 + c^2 - 2\sqrt{(\omega_1^2+b^2)(\omega_2^2+c^2) - b^2c^2} \simeq b^2 + c^2 \qquad (3)$$

as σ becomes much larger than ω_1 and ω_2. The random variable of $\Delta\omega$ is a positive square root of the squared sum of the two independent Gaussian variables. Consequently, the spacing between two eigen frequencies is distributed following a Rayleigh distribution as the perturbation becomes large.

Figure 2 illustrates the transition of the spacing histograms from a Poisson distribution to a Rayleigh distribution. We produced randomly 5000 pairs of two eigen frequencies whose spacings follow the Poisson distribution, when the coupling effect is nothing. The random coupling parameters b and c both of which have zero mean value are controlled by changing the standard deviation σ. We assumed that σ becomes large, as the effects of the coupling is strong. We can see that the modal spacing distributes following the Rayleigh distribution, as the modal coupling becomes large.

3. THE DENSITY FUNCTION FOR THE CLOUD OF ZEROS AND PHASE TREND

3.1 Modal Expansion of a TF

The modal expansion of a transfer function with source at X_s and observer X_o is given by

$$H(\omega) = \text{const} \sum_m \frac{\Psi_m(x_s)\ \Psi_m(x_o)}{(\omega - \omega_m - j\,\delta_m)(\omega + \omega_m - j\,\delta_m)} \qquad (4)$$

where Ψ_m are mode shapes, $\omega = 2\pi f$, f is the frequency in Hz, ω_m are the undamped resonance (radian) frequencies. The poles of this function are at $\omega = \pm\omega_m + j\,\delta_m$. If we assume that the reverberation time $T_R = 6.9/\delta_m$ is the same for all modes ($\delta_m = \delta_0$), then the poles lie along a straight line at a distance $\delta_0 = 6.9/T_R$ above the real frequency line (Fig. 3).

The poles distribute on the pole-line following a Poisson-like distribution as stated in the previous section; however, the zeros lie two dimensionally throughout the complex frequency plane. When the observer is in the reverberant field, the number of zeros on the pole-line is about half the number of poles[15, 16]. If the mode shape functions are real, and the pole-line is as shown in Fig.3, then by symmetry the remaining zeros are evenly distributed above and below the pole-line, which means that 1/4 of them are below the pole line. The portion of these zeros below the pole-line that are also below the real frequency axis are non-minimum phase zeros, and these zeros generate the reverberant phase part of the total phase delay between source and observer.

3.2 The Density Function for the Cloud of Zeros [10]

We will consider the TF for a reverberant field to be a random process in the complex frequency domain[3]. Following Rice's random noise theory[17] and Schroeder's "Frequency Auto-correlation Function" of a TF[18], if the real and imaginary parts of a TF can be considered statistically independent, then the density of the TF zeros should be proportional to the squared inverse of the distance δ_t from the pole-line in the complex-frequency domain. Such a hyperbolic type of density function, however, cannot give the total number of zeros, because such a distribution function will diverge close to the pole-line. We therefore postulate that the zeros are distributed in a cloud around the pole-line with a dependence on the distance normal to the line defined by

$$p(\beta) = \frac{4/\pi}{1 + 4\beta^2} \qquad (5)$$

where $\beta = \delta_t / D$, $D = 1/n_p(\omega)$ is the averaged pole spacing, and $n_p(\omega)$ is the modal density.

In order to test the ideas presented above, we have carried out a series of measurements of the TF of an 86 m^3 room with a reverberation time 1.8 sec. in the 500 Hz octave band. The measurements were performed at different distances of the microphone from the loudspeaker, and we have calculated the "averaged" number of zeros in 4TF's in the reverberant fields. The method for zero counting is explained in Ref.[10]. Figure 4 shows the experimental arrangements for the impulse response measurements. The averaged number of zeros below the test-frequency-line in the lower half plane is illustrated in Figure 5. The result clearly demonstrates that the distribution of zeros follows the solid line which decreases following Cauchy distribution by Eq.(5). The total number of non-minimum phase zeros below the real frequency axis is 48 at 500 Hz octave band following Eq.(5).

3.3 Accumulated Reverberant Phase[15, 16]

The accumulated phase can be determined by both the poles and zeros. Minimum phase zeros cancel the effects of the poles on the TF phase, while non-minimum phase zeros and the poles both increase the phase-lag of a TF. Thus, the reverberant phase is $\phi_{rev} = -2\pi N_Z^+$. The number of the non-minimum phase zeros N_Z^+ can be estimated following the Cauchy distribution. Figure 6 illustrates samples of TFs along different test frequency lines. The global phase trend is estimated (by ϕ_p in the graph) from the number of zeros. The accumulated phase, however, has a large variability from the theoretical trend[1]. Therefore, we investigate the local statistical properties of the phase in a frequency interval using the group delay.

4. POWER SPECTRUM AND VARIANCES OF THE GROUP DELAY FOR A TF[11]

We take the general form of the TF and the group delay as

$$H(\omega) = K\frac{(\omega-\omega_a)(\omega-\omega_b)\cdots}{(\omega-\omega_1)(\omega-\omega_2)\cdots} \qquad \phi = \arg(\omega-\omega_a)+\arg(\omega-\omega_b)+\cdots-\arg(\omega-\omega_1)-\arg(\omega-\omega_2)-\cdots$$

$$\arg(\omega-\omega_m) = \phi_m = -\tan^{-1}\frac{\delta_m}{\omega-\omega_m^r} \qquad \tau(\omega) = \frac{d\phi}{d\omega} = \sum_m \tau_m(\omega) = \sum_m \left(\frac{a_m}{\delta_m}\cdot\frac{1}{\zeta_m^2+1}\right) \qquad (6)$$

where the poles and zeros form a pattern in the complex frequency plane as shown in Fig. 3, $a_m = \pm 1$, $\omega_m = \omega_m^r + j\,\delta_m$ (complex singularities, poles and zeros of H), and $\zeta_m = (\omega-\omega_m^r)/\delta_m$. The values of a_m are determined from the steps in the phase of TF. The positive group delay pulses are due to zeros above the test frequency line, and the negative pulses are due to the zeros below the line.

Fig.7a shows a sample for the group delay of the reverberant TF. We produce a "power spectrum" of the "random pulse process" of the group delay $\tau = \sum_m \tau_m$ for each δ - strip(Fig.3). The Fourier transform of $\tau_m(\omega)$ ($\omega \to x$, $\delta_m = \delta$ on a δ - strip) is

$$T_m(x) = \frac{1}{2\pi}\int_{-\infty}^{+\infty} \tau_m(\omega)\exp(-j\,\omega x)\,d\omega = (a_m/2)\exp(-\delta x) \qquad (7)$$

According to the density of the zero cloud, the strip off the pole-line has a number of singularities per unit-frequency interval[15,16] (here, δ is a delta-function),

$$dn_{\text{(zero-cloud)}}(\omega) = \{n_p(\omega)/4\}\,p(\beta)\,d\beta\,, \quad dn_{\text{(pole-line)}}(\omega) = (3/2)\,n_p(\omega)\,\delta(\beta-\beta_0)\,d\beta \qquad (8)$$

since there are n_p singularities due to poles ($a_m = -1$) and $(1/2)n_p$ singularities ($a_m = +1$) due to the zeros on the pole-line. Consequently, using an integration over all the δ - strip with the density of singularities, the total power spectrum of the group delay due to all the singularities is approximately written at a test frequency line by,

$$P_{\text{S, total}}(x) = P_{\text{S, pole-line}}(x) + P_{\text{S, zero-cloud}}(x) \approx \left|\frac{3}{8}n_p\exp(-2x\,\delta_t) + \frac{1}{16\pi x\,\delta_t^2}\right| \qquad (9)$$

as $x\,\delta_t$ becomes large.

The power spectrum of the group delay has the trend of $1/(x\,\delta_t)^2$. Fig.7b demonstrates the power spectrum of the group delay. We can clearly see a tendency towards the "1/x" type of spectrum, as $x\,\delta_t$ becomes large. Fig.7c shows the variances of the group delay which is calculated by the total energy of the power spectrum density by Eq.(9) above. The variances decrease squared inversely, as δ_t becomes large; the phase fluctuations decrease independent of frequency, as the damping increases.

5. WAVEFORM RECOVERY IN A REVERBERANT SPACE

Inverse filtering and source waveform recovery are important issues for sound and vibration control[1]. Inverse filtering, however, is not a stable process, since the TF generally has non-minimum phase zeros[19]. We propose a method for the pulse-like source waveform recovery that takes the absolute value of the group delay and inversely filters the minimum phase components of a TF.

5.1 Minimum Phase Components Extraction and Inverse Filtering

A TF of a non-minimum phase system is always written as the product of a minimum-phase TF and an all-pass TF as shown by Fig.8 [1]. If the source waveform is itself minimum-phase, it is completely recovered by the inverse filtering only for the minimum phase part of the TF. The authors propose a new method for the minimum phase decomposition that takes the absolute value of the group delay of a TF.

The signal processing procedure is explained in the Appendix. We take a TF for a "reference" obtained from an impulse-response-like record having a finite data length. Thus, the TF has only zeros in the discrete frequency plane; all of the polynomial poles of the TF are located at the origin of the discrete frequency plane. When the source waveform is non-minimum phase, the non-minimum phase component is approximately recovered by "reversing the phase lag of the all-pass part" using a delayed process[20]. The inverse filtering for non-minimum phase TFs, however, becomes completely possible using the TF data obtained by multi-channel observation[21].

5.2 Samples of Recovered Waveforms in a Reverberant Space

We have carried out a series of measurements concerning the reverberant responses to a train of pulse waveform source signals(f_e : 500 Hz) in an 86 m^3 room under the similar conditions to those in Fig.4. Figure 9b shows the recovered waveform from the response data (Fig.9a) observed at M1. We can clearly see that a pulse-like source waveform is extracted from the reverberant response.

Figure 10 are examples of waveforms at M2a and M2b recovered by the inverse filter for M2 using an exponential time window[20, 22] and smoothing average in the frequency domain of the TF. The recovery process becomes more "robust" to the unpredictable changes of the TFs. This is partly because the density of the zeros closely located to the test frequency line decreases by the exponential windowing or the smoothing average[23] following the statistical properties of the rev- TFs.

6.CONCLUSION

We have investigated the distribution of zeros of TFs theoretically and numerically by using impulse response data obtained from measurements in a reverberant space. The distribution of zeros normal to the pole-line is the Cauchy distribution. The number of non-minimum phase zeros and the accumulated phase inversely decrease, as the damping (or the modal overlap) of the vibrating system increases. We have also formulated the fluctuations in the phase, and confirmed the results using measured TFs.

A source waveform recovery in a reverberant space has been demonstrated. A pulse-like waveform can be recovered by inverse filtering which uses the minimum phase part obtained from the reverberant TF by taking the absolute value of group delay. We recommend the exponential windowing and smoothing TFs for robust waveform recovery, since such the procedures make the recovery process less sensitive to changes of the reverberant conditions over time. The authors thank to the NTT Computing Center for consulting of inverse filtering calculation by CRAY-II.

REFERENCES

[1] R.Lyon, "*Machinery Noise and Diagnostics*," Butterworths (1987)
[2] R. Bolt, J. Acoust. Soc. Am. 19, 79-90 (1947)
[3] R.Lyon, J. Acoust. Soc. Am. 45, 545 - 565 (1969)
[4] M. Schroeder, Acustica 4, 594 - 600 (1954)
[5] M. Schroeder, J. Audio Eng. Soc., 37, 795-808 (1989)
[6] E. Wigner, *Statistical Theories of Spectra: Fluctuations* (Ed. C. Porter) Academic Press Inc., 188-198(1965)
[7] J. Davy, Inter-Noise '90, 159-164 (1990)
[8] R. Weaver, J. Acoust. Soc. Am. 85, 1005-1013 (1989)
[9] T. Brody et alli, Rev. Mod. Physics 53 385-479 (1981)
[10] M.Tohyama, R.Lyon, and T. Koike, J. Acoust. Soc. Am., 1701-1707 (1991)
[11] M.Tohyama, R.Lyon, and T. Koike, Int. Conf. Noise in Phy. Sys. and 1/f Fluctuations, 567-570 (1991)
[12] E. Wente, J. Acoust. Soc. Am. 7, 123-126 (1935)
[13] K.Sato and M.Koyasu, J. Acoust. Soc. Jpn 13 231-241 (1957)
[14] P. Morse and R. Bolt, Rev. Mod. Phy. 16, 69-150 (1944)
[15] R.Lyon, J. Acoust. Soc. Am. 73 1223-1228 (1983)
[16] R.Lyon, J. Acoust. Soc. Am. 76, 1433-1437 (1984)
[17] S. Rice, Bell Sys.Tech. J. 24, 46 - 108 (1945)
[18] M. Schroeder, J. Acoust. Soc. Am. 34, 1819 - 1823 (1962)
[19] S. Neely and J. Allen, J. Acoust. Soc. Am. 66, 165 - 169 (1979)
[20] J. Mourjopoulos, P.M. Clarkson, and J.K. Hammond, Proc. of ICASSP'82, 1858-1861 (1982)
[21] M. Miyoshi and Y. Kaneda, IEEE ASSP-36, 145-152 (1988)
[22] M.Tohyama and R. Lyon, J. Acoust. Soc. Am. 86, 2025 - 2029 (1989)
[23] J. Mourjopoulos, J. Sound & Vib. 102, 217-228 (1985)

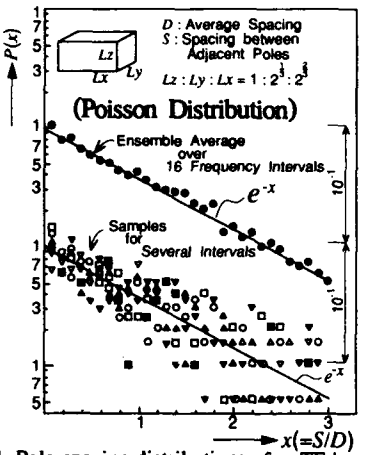

Fig.1 Pole-spacing distributions of a TF in a rectangular room

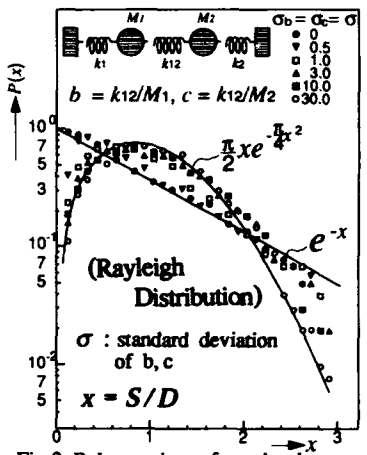

Fig.2 Pole-spacing of randomly coupled mechanical springs

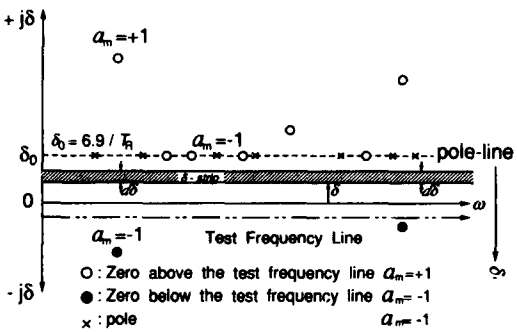

Fig.3 Pole-zero locations of a TF in the complex frequency plane and a δ-strip for the group delay singularities

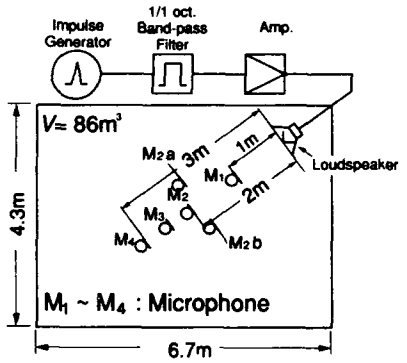

Fig.4 Exponential set-up in a reverberant space. The distance between M2a,b:0.68m

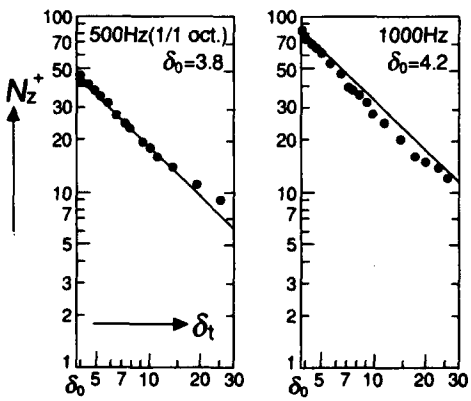

Fig.5 The number of zeros located below the test frequency line. The solid line is estimated from Eq.(5)

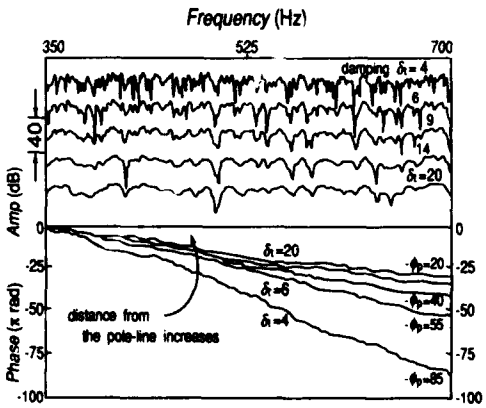

Fig.6 Amplitude and phase of the TFs at different test frequency lines

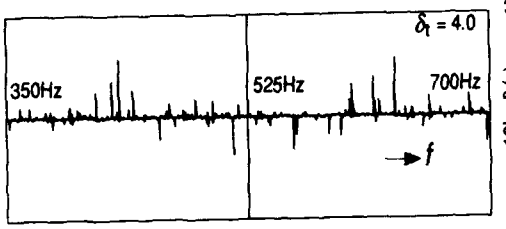

Fig.7a A group delay sample for the TF

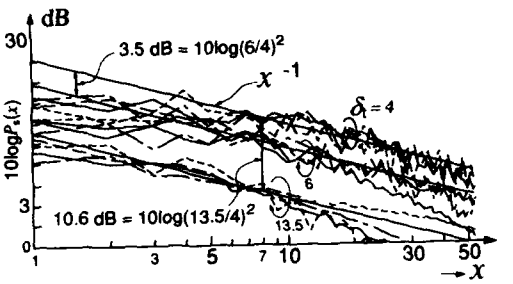

Fig.7b Power spectrum of the group delay at different test frequency lines

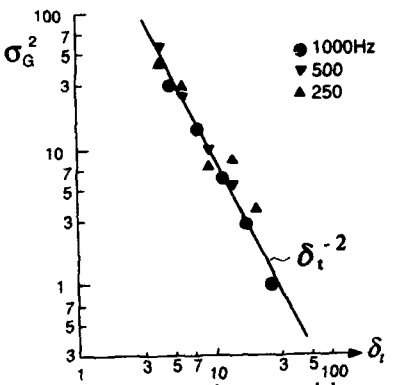

Fig.7c Variances of the group delay samples

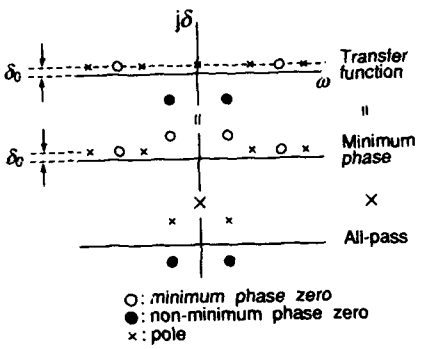

Fig.8 Decomposition of a TF into all-pass and minimum phase components

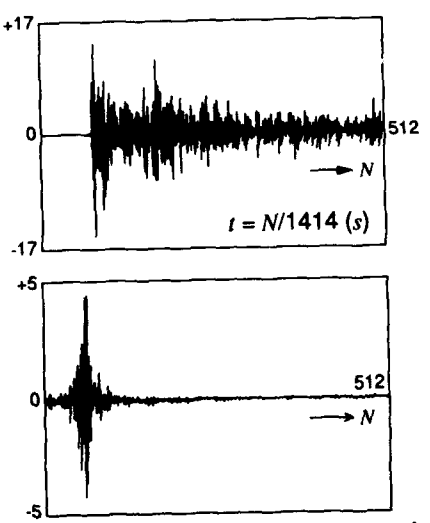

Fig.9 Reverberant response and recovered source waveform at M1

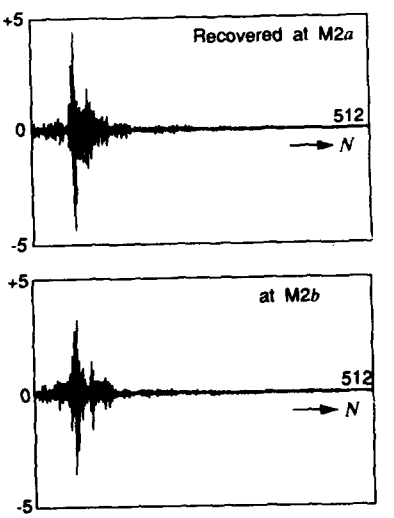

Fig.10 Recovery at M2a and M2b by the inverse filter for the TF at M2. A smoothing average (within 60 Hz) and an exponential window (reduced effective T_R:0.36s) is applied.

Appendix: Source Waveform Recovery Procedure

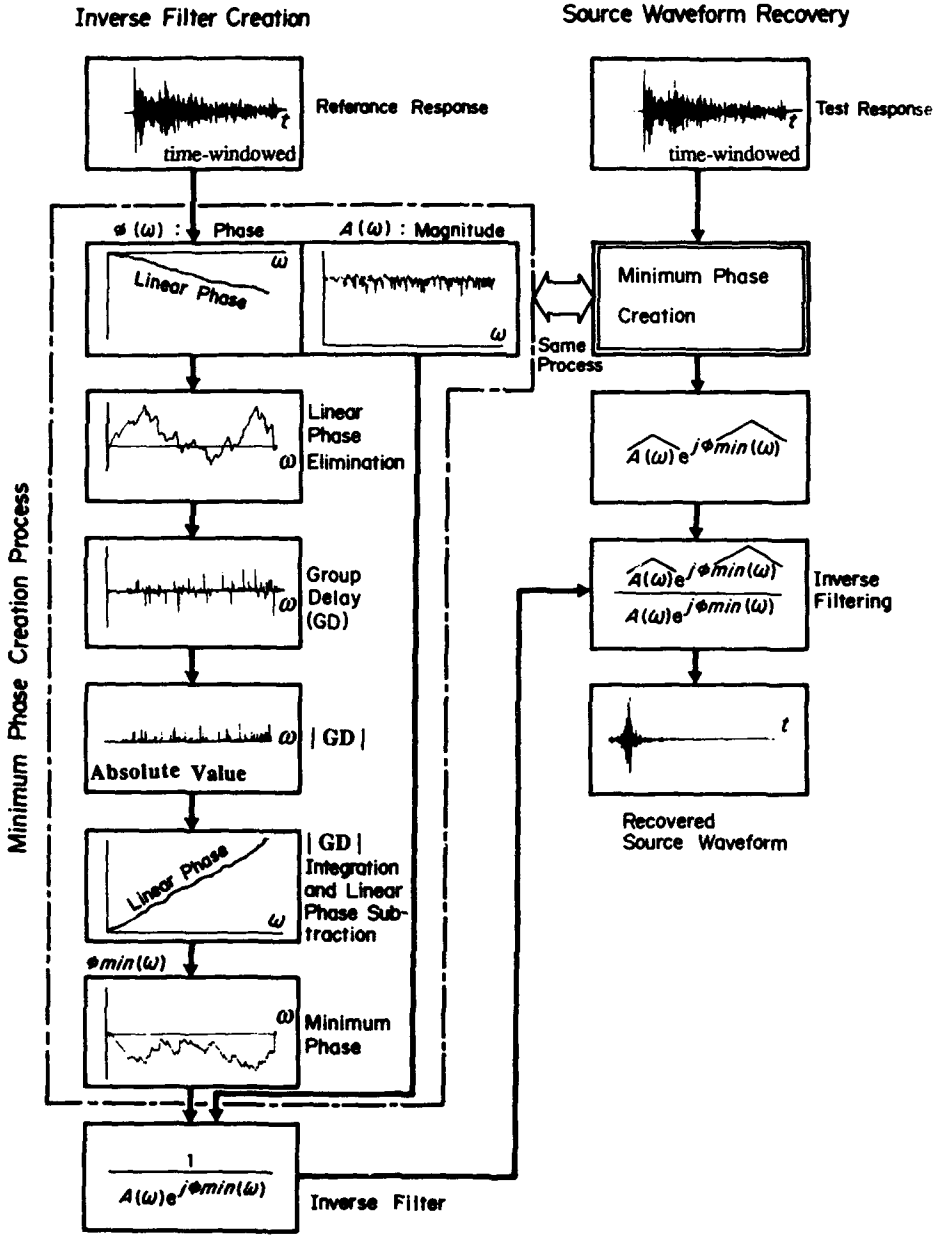

KEYNOTE ADDRESS

OVERVIEW OF ACOUSTICAL TECHNOLOGY FOR NONDESTRUCTIVE EVALUATION

Robert E. Green, Jr.

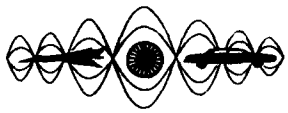

SECOND INTERNATIONAL CONGRESS ON
RECENT DEVELOPMENTS IN AIR- AND
STRUCTURE-BORNE SOUND AND VIBRATION
MARCH 4-6, 1992 AUBURN UNIVERSITY, USA

OVERVIEW OF ACOUSTICAL TECHNOLOGY FOR NONDESTRUCTIVE EVALUATION

Robert E. Green, Jr.
Center for Nondestructive Evaluation
The Johns Hopkins University
Baltimore, MD 21218
U.S.A.

ABSTRACT

A brief overview is presented of acoustical techniques for nondestructive evaluation of materials and structures. Among the general topics covered are modes of elastic wave propagation in solid materials, energy flux vector, and nonlinear effects. Included in the section on ultrasonic measurements are ultrasonic attenuation, laser ultrasonics, full-field imaging of acoustic displacements, optical detection of acoustic emission, acousto-ultrasonics, acoustic microscopy, ultrasonic tomographic imaging, thermal-wave and electron-acoustic waves, and the use of low-power ultrasound to probe the effect of high-power ultrasound on materials.

INTRODUCTION

Acoustical techniques, particularly ultrasonics play a prominent role in nondestructive testing because they afford very useful and versatile nondestructive methods for evaluating the microstructures, associated mechanical properties, as well as micro- and macroscopic flaws in solid materials. This offers definite advantages over other techniques which rely on surface measurements alone, since it is well known that many properties exhibited by the surface layer of a solid are not identical with the behavior of the bulk material. Surface ultrasonic waves may also be used to advantage, however, to probe the surface layer. Interrogation can be performed at various depths into the material, since the penetration depth of such waves increases with decreasing frequency. Moreover, a variety of guided waves are finding increased usefulness for probing interfaces between different materials.

Since in nondestructive evaluation applications it is not desirable for the ultrasonic waves to alter the material through which they pass, it is necessary to work with very low amplitude waves, which normally are regarded to obey linear elasticity theory. Although most practical uses of ultrasonics are applied to solid materials which are polycrystalline aggregates and therefore assumed to be isotropic, with real crystalline solids the condition of ideal isotropy is extremely difficult, if not impossible, to attain. In the case of composite materials the presence of anisotropy may be even more pronounced than in crystalline metals and ceramics because of the particular lay-up or filament placement processes involved. Since in the case of fairly thin composites panels as used in aerospace structures anisotropy exerts only a minor influence on ultrasonic wave propagation along the thickness direction, the effect of this anisotropy has also been generally ignored. However, as more applications are found for increasingly thicker composites there is an increased awareness of the need to

account for anisotropy effects in ultrasonic wave propagation and the associated nondestructive evaluation techniques.

MODES OF WAVE PROPAGATION

In order to determine precisely what type of waves will propagate in a given direction in a specific anisotropic material, the density and elastic moduli of the material must be known and the eigenvalues (wave speeds) and the eigenvectors (particle displacements) determined from solution of the equation of motion. Three different linear elastic waves may propagate along any given direction in an anisotropic material. These three waves are usually not pure modes since each wave generally has particle displacement components both parallel and perpendicular to the wave normal. However, one of these components is usually much larger than the other; the wave with a large parallel particle displacement component is called quasi-longitudinal, while the two waves with large perpendicular particle displacement components are called quasi-shear. In the event that the material is isotropic, then all modes become pure modes, i.e. the particle displacements are either parallel or perpendicular to the wave normal, and the two quasi-shear modes degenerate into one pure shear mode [1].

Energy Flux Vector

Also of great practical importance to elastic wave propagation in anisotropic materials is the fact that the direction of the flow of energy per unit time per unit area, the energy-flux vector, does not in general coincide with the wave normal as it does in the isotropic case, i.e. the ultrasonic beam exhibits refraction even for normal incidence [1]. An example as to how disregard for energy flux vector deviation in thick anisotropic materials can cause errors in nondestructive detection of cracks or delaminations is shown in Fig. 1. If the degree of energy flux vector deviation was not determined prior to this test and the assumption made that no deviation occurred, subsequent investigation would not reveal the crack in the calculated position beneath the transducer, while the real crack location would not be identified.

Nonlinear Effects

Nonlinear effects associated with ultrasonic wave propagation may also be used to advantage for nondestructive materials characterization. Nonlinear effects in elastic wave propagation may arise from several different causes. First, the amplitude of the elastic wave may be sufficiently large so that finite strains arise. Second, a material, which in its undeformed state behaves in a linear fashion, may behave in a nonlinear fashion when infinitesimal ultrasonic waves are propagated, provided that a sufficient amount of external static stress or internal residual stress is superimposed. Finally, the material itself may contain various energy absorbing mechanisms such that it is locally nonlinear, e.g. the defects enumerated previously [1].

ULTRASONIC MEASUREMENTS

Two features of ultrasonic waves are primarily used for obtaining information about the microstructure and associated mechanical properties of materials, namely, velocity and attenuation. Ultrasonic velocity measurements permit determination of thickness, crack location, and bulk residual stress (strain). Ultrasonic attenuation measurements serve as a very sensitive indicator of internal loss mechanisms arising from microstructure and microstructural alterations in the material.

Ultrasonic Attenuation

Although geometrical effects can cause energy to be lost from the ultrasonic beam, such losses are not indicative of intrinsic loss mechanisms associated with the microstructure. Once proper precautions are taken to either eliminate or control these geometrical effects, ultrasonic attenuation measurements serve as a very sensitive indicator of internal loss mechanisms in the material. This sensitivity derives from the ability of ultrasonic waves of the appropriate frequency to interact with a variety of defects including cracks, microcracks, foreign particles, precipitates, porosity, fiber breaks, delaminations, disbonds, voids, grain boundaries, interphase boundaries, magnetic domain walls, and even dislocations [2].

Laser Generation/Detection of Ultrasound

Although piezoelectric crystals have been predominantly used as ultrasonic transducer materials, a major problem associated with their use is the requirement that both the generating and receiving transducers be acoustically bonded to the test material with some sort of acoustical impedance matching coupling medium such as water, oil, or grease. In addition to modification of the ultrasonic signal and potential harm to the test structure by the coupling medium, the requirement of physical contact between transducer and test structure places additional limitations on ultrasonic testing. Although both capacitive pick-ups and electro-magnetic acoustic tranducers (EMAT's) are presently available, the only universally useful non-contact technique is laser beam generators and detectors. Laser beam probes afford the opportunity to make truly non-contact ultrasonic measurements in both electrically conducting and non-conducting materials, in materials at elevated temperatures, in corrosive and other hostile environments, in geometrically difficult to reach locations, in outer space, and do all of this at relatively large distances, i.e. meters, from the test structure surface. Incorporation of scanning techniques or full-field imaging greatly increase the capability of testing large structures without the present necessity of either immersing the test object in a water tank of using water squirter coupling [3-4].

Full-Field Holographic Imaging of Acoustic Displacements

Figure 2 shows the results of a holographic interferometry technique which permits full-field imaging of surface displacements due to ultrasonic wave propagation [5]. A laser pulse was used to record a holographic image of a graphite/epoxy composite plate. Subsequently, a second laser pulse was incident on the center of the plate (opposite side than shown in figure) and, after sufficient time for the resulting ultrasonic wave to travel to the opposite surface of the plate (side shown in figure), a third laser pulse was used to re-expose the holographic plate. The resulting interference pattern shows the ultrasonic wavefront traveling outward from the source with the influence of the anisotropic character of the plate clearly evident. An alteration in the holographic image is also evident in the left lobe of the figure probably caused by a delamination between one of the internal composite layers.

Optical Acoustic Emission Detection

The importance of acoustic emission monitoring is that proper detection and analysis of acoustic emission signals can permit remote identification of source mechanisms and the associated microstructural alteration of the material. Several non-contact optical interferometric detectors have been used to record acoustic emissions from a variety of metal specimens [6]. In several series of tensile tests, the dimensions of the specimens the gauge sections were chosen to be very small so that any microstructural alteration would be visible on the gauge section surface and could be examined in detail using both optical and scanning electron microscopy. Because of the large flat frequency bandwidth (0 - 60 MHz) of the optical probe, acoustic emission signals were obtained in a frequency regime not normally detected with conventional transducers. Tests run on a series of stainless steel specimens revealed a large number of acoustic emission signals at 9 - 10 MHz prior to fracture. Scanning electron microscopic examination of the fracture surface resulted in a one-to-one correspondence between these high frequency signals and the fracture of intermetallic particles in the steel.

Acousto-Ultrasonics

Originally, the acousto-ultrasonic method used a conventional ultrasonic transducer operating in the 1-10 MHz regime as a generator, while the receiver transducer was a conventional acoustic emission transducer operating in the 100-150 kHz regime. Acousto-ultrasonic tests are now run with various types of transducers, such as broadband ones, and the receiving transducers are no longer limited to the 100-150 kHz regime. In a few examples, through transmission has been reported, but the majority of acousto-ultrasonic tests are run with both the generating and receiving transducers coupled to the same side of the matrial under test. The received signals are more complex than those normally obtained with conventional pulse-echo testing, and, therefore, require more elaborate electronic processing. Recently pulsed lasers have been used for generating acousto-ultrasonic signals and laser interferometers have been used as detectors. A laser acousto-ultrasonic system has been recently used to obtain waveforms from composite materials [7].

Acoustic Microscopy

In recent years scanning acoustic microscopy has developed to the extent that it possesses spatial resolution comparable with optical microscopes. Instruments have operated at room temperature with frequencies as high as 3.5 GHz possessing wavelengths down to 400 nm. Cryogenic and high pressure instruments have worked with wavelengths less than 250 nm. Since the contrast mechanisms depend on the elastic properties of the materials under examination, these instruments provide a valuable tool for materials characterization not obtainable in any other manner. A particularly exciting acoustic microscope system permits evaluation of materials and processes on a practical scale [8]. Images are formed directly by displaying the amplitude of broadband acoustic pulses possessing center frequencies from 10 to 100 MHz. Figure 3 shows an example of the use of this system to investigate a solder bond between two silicon wafers. Note that not only are the voids in the solder bond easily detected, but the grains in the larger silicon wafer are visualized without the need for chemical etching.

Ultrasonic Tomographic Imaging

X-ray tomography has proven to be an extremely useful nondestructive evaluation technique. However, the experimental apparatus is sophisticated, expensive and poses an inherent radiation hazard. On the other hand, x-rays travel in straight lines or fan beams as desired and are not refracted by any anisotropy in the material through which they pass. The equipment for ultrasonic tomography is relatively simple, inexpensive, and extremely safe. However, ultrasonic tomography has only met with limited success, primarily with medical imaging, because the human body is very nearly isotropic as far as density and elastic properties are concerned. The complications introduced by anisotropic in industrially important metals has prevented successful implementation of ultrasonic tomography in these materials. Unfortunately, there is no simple nondestructive method of determining the texture of bulk metals a priori.

On the other hand, the anisotropy of composite materials can be determined a priori because the particular lay-up or fiber placement of composite materials is controlled during the manufacturing process. Moreover, the anisotropy of composite materials generally mimics that of single crystals for which the general ultrasonic propagation characteristics are well known. Therefore, it is highly probable that ultrasonic tomography will be easier to implement in composite materials than in metals. Research is currently underway to make full use of all information with regard to ultrasonic wave propagation in anisotropic materials in order to develop an ultrasonic tomography technique for defect imaging in anisotropic materials, particularly composites [9].

Thermal-Wave and Electron-Acoustic Wave Imaging

As initially developed thermal-wave imaging used laser beam scanning of a test object placed in a closed gas-filled container to cause changes in the gas pressure in direct proportion to thermal property changes in the surface layers of the test object. More recent developments have permitted elimination of the gas-filled container by use of a second probe laser beam which either detects surface displacements of the test object due to localized thermal expansion or changes in the refractive index of the air just above the sample surface. Thermal-acoustic imaging describes a modification where the laser beam introduces heat locally and periodically onto one surface of a specimen and the elastic wave resulting from local thermoelastic expansion of the sample is measured, usually with a piezoelectric transducer coupled to the other surface of the specimen.

Another modification uses a chopped electron beam in a scanning electron microscope to excite thermal and elastic waves at the top surface of a test object. The elastic waves are detected by either a piezoelectric transducer coupled to the bottom surface of the test object or an optical interferometric displacement probe. By displaying and recording the output of the detector as a function of position of the scanning electron beam an "electron-acoustic" image of the test object can be obtained, Fig. 4, [10].

High-Power Ultrasonic Waves

High-intensity ultrasound has found practical application in welding, machining, drawing, forming, grain refinement during solidification, diffusion enhancement, accelerated fatigue testing, and stress relieving. However, the mechanism by which high-intensity ultrasound influences the mechanical deformation of metals is still unknown. A multiparameter system which permitted simultaneous measurement of a number of quantities to test the proposed mechanisms for the influence of high-intensity ultrasound on the mechanical properties of metals [11]. An 8 MHz x-cut quartz transducer was acoustically coupled to the flat upper end of a test specimen, while a 20kHz ultrasonic horn was coupled to the lower end. The x-cut transducer was electrically connected through an impedance matching network to an ultrasonic pulse-echo system. The insonation period of the high-intensity ultrasonic unit was controlled by a timing circuit which permitted the insonation period to be continuously varied. Measurements of elastic wave velocity directly yielded information on the variation of the effective Young's modulus as a function of application of high-intensity ultrasound. The same system permitted simultaneous measurement of ultrasonic attenuation, which served as a monitor of dislocation motion.

CONCLUSIONS

In this paper, a brief overview has been presented of acoustical techniques for nondestructive evaluation of materials and structures. Unfortunately, because of space limitations all currently used and developing techniques have not been covered. There is still much work to be done in developing a complete understanding of ultrasonic wave propagation in anisotropic and inhomogeneous materials. Three-dimensional imaging of defects in industrially important metals and ceramics and in thick composites using ultrasonic techniques is not yet a reality. These developments will finally bring to fruition the ability of ultrasonics to successfully be classified as a quantitative NDE technique.

REFERENCES

[1] R.E. Green, Jr., Ultrasonic Investigation of Mechanical Properties, Treatise on Materials Science and Technology, Vol. III, Academic Press, New York (1973).

[2] R.E. Green, Jr., "Effect of Metallic Microstructure on Ultrasonic Attenuation in Nondestructive Evaluation: Microstructural Characterization and Reliability Strategies, Otto Buck and Stanley M. Wolf (eds.), Metallurgical Society of AIME, Warrendale, Pa, pp. 115-132, (1981).

[3] D.A. Hutchins, "Ultrasonic Generation by Pulsed Lasers", Physical Acoustics, W.P. Mason and R.N. Thurston (Eds.), Vol. 18, pp.21-123, Academic Press, NY (1988).

[4] J.W. Wagner, "Optical Detection of Ultrasound", Physical Acoustics, W.P. Mason and R.N. Thurston (Eds.), Vol. 19, pp.201-266 Academic Press, NY (1990).

Figure 3. Acoustic microscope image of solder bond between two silicon wafers [7].

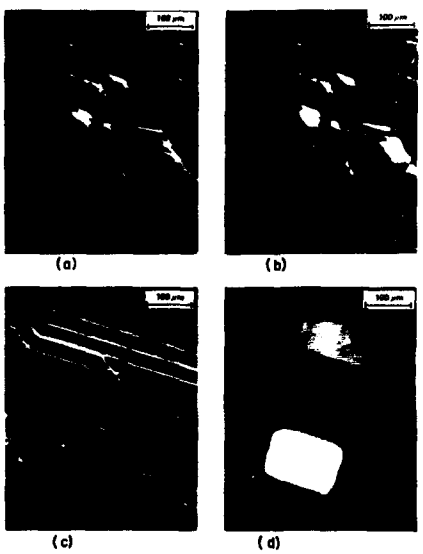

Figure 4. Scanning electron microscope and electron-acoustic images of integrated circuit [9]:
5 keV (a) SEM, (b) electron-acoustic
30 keV (c) SEM, (d) electron-acoustic

[5] M.J. Ehrlich and J.W. Wagner, "Anisotropy Measurements and Indication of Ply Orientations in Composite Materials Using Holographic Mapping of Large Amplitude Acoustic Waves", in Nondestructive Characterization of Materials, P. Holler et al.(Eds.), Springer-Verlag, New York, 99-106 (1989).

[6] J. Murphy, J.T. Glass, S. Majerowica, and R.E. Green, Jr., "Laser Interferometric Probe for Detection of Acoustic Emission", Materials Evaluation 48, 714-720 (1990).

[7] R.D. Huber and R.E. Green, Jr., "Noncontact Acousto-Ultrasonics Using Laser Generation and Laser Interferometric Detection", Materials Evaluation 49, 613-618 (1991).

[8] R.S. Gilmore, K.C. Tam, and D.R. Howard, "Acoustic Microscopy from 10 to 100 MHz for Industrial Applications", General Electric Report No. 86CRD015, General Electric Corporate Research and Development, Schenectady, NY (1986)

[9] X. Teng, E. Bolz and R.E. Green, Jr., "Ultrasonic Tomography of Anisotropic Materials", to be published in Proceedings of 14 th International Congress on Acoustics, September 3-10, 1992, Beijing, China.

[10] J.C. Murphy, J.W. Maclachlan, and L.C. Aamodt, "Image Contrast Processes in Thermal and Thermoacoustic Imaging", IEEE Transactions on Ultrasonics, Ferroelectrics, and Frequency Control, UFFC-33, 529-541 (1986).

[11] R.B. Mignogna and R.E. Green, Jr., "Multiparameter System for Investigation of the Effects of High-Power Ultrasound on Metals", Rev. Sci. Instrum. 50, 1274-1277 (1979).

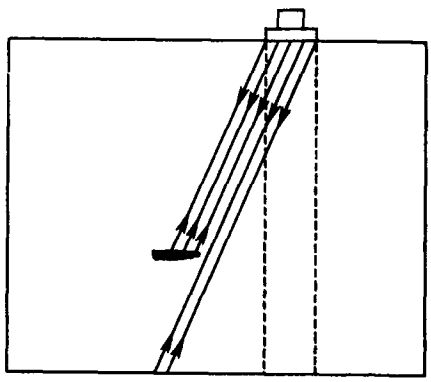

Fig. 1. Ilustration of energy-flux vector deviation (refraction) causing misjudgement of crack location in anisotropic solid.

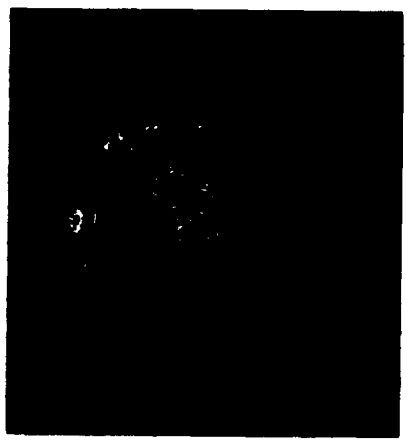

Figure 2. Holographic full-field imaging of ultrasonic waves on surface of graphite/epoxy composite [4].

MATERIAL CHARACTERIZATION AND NON-DESTRUCTIVE EVALUATION

SECOND INTERNATIONAL CONGRESS ON
RECENT DEVELOPMENTS IN AIR- AND
STRUCTURE-BORNE SOUND AND VIBRATION
MARCH 4-6, 1992 AUBURN UNIVERSITY, USA

ANALYTICAL DETERMINATION OF DYNAMIC STRESS ON PRACTICAL CEMENT MILLS USING RANDOM VIBRATION CONCEPT

V.Ramamurti
Distinguished Visiting Professor
Department of Mechanical Engineering
University of Toledo, U.S.A.

and

C.Sujatha
Senior Scientific Officer
Department of Applied Mechanics
Indian Institute of Technology
Madras, INDIA

ABSTRACT

The dynamic stresses experienced by the skin of cement mills is essentially due to the impact of the freely falling balls and cylpebs inside the rotating mill. The determination of the magnitude of the forces acting on the surface of the mill and consequently the associated stresses is a complicated exercise. Random vibration concept in conjunction with cyclic symmetry is used to present a method to handle such a problem in this paper.

KEYWORDS:- Stress analysis, Cement mill analysis, FEM technique, Random vibration analysis.

1. INTRODUCTION

Tumbling mills [1] are used for grinding in most of the plants where nonmetallic minerals are processed. The operation can be in a wet or dry medium. In the majority of tumbling mills the rotating container is a cylindrical shell mounted with axis horizontal, and provided with openings through the heads for feed and discharge of material respectively. The differences between various mills lie in the shell proportions, nature of tumbling bodies and the method of discharge. The mill is typically a combination of cylindrical and conical shells as can be seen in Fig.1. The end plates of the mill heads are bolted to the shell flanges. The inlet and outlet heads of the mill are generally of cast steel with integral hollow trunnions ; the trunnion corresponding to the gear end is provided with a collar, whereas the trunnion at the other end of the mill forms a plain journal.

1.1 Stresses due to dead load

Typical industrial mills vary in diameter from 1.2 to 3.6 m with lengths of the cylindrical portion varying from 5.4 to 16.2 m as shown in Table 1 [2]. Typical shell thicknesses are also indicated in the Table. Liner thicknesses are normally around 1.6 times the main shell thickness. The semi-cone angles (α) are typically 60, 72 or 85°. For the normal loading encountered (40% of the volume of the shell) stresses introduced by the asymmetric bending of the dead load due to the charge inside are normally less than 30 N/mm^2 with peak values around the junction of the cone and the cylinder even when the liner thickness is ignored [3]. But this sort of estimation of stress does not take into account the dynamic stress introduced by the freely falling steel balls/cylpebs when the mill is run. These mills generally run at speeds of about 60% of their critical speeds ensuring the free fall of these balls from a substantial height. This introduces a considerable magnitude of dynamic stress on the

shell and this has, hitherto, not been taken into account in reported literature [4].

The present investigation aims at determining the dynamic strains due to the random loading of the steel balls on the skin of the shell. The three parameters which influence the dynamic loading are the diameter of the shell, the speed of operation of the mill and the size and weight of the charge inside the mill.

1.2 Mechanism of Tumbling

The tumbling mill has overall variability not only in size but also in shape, in total weight and the motion of the tumbling media. It has been observed that the motion of these bodies within the cylinder comprises two distinct varieties (i) rotation of the rods around their own axes lying parallel to the mill axis and (ii) cascading (rolling down the surface of the load) or cataracting (parabolic free fall above the mass).

Fig.2 is an idealized representation of the action in a mill operating at a speed resulting in cataracting. Shown alongside is the actual flow pattern inside a tumbling mill. In the lower part of the mill, balls are in irregular layers concentric with the mill shell. The layer in contact with the shell itself is moving at substantially the same rate as the shell; the rougher the mill lining, the less the slip. Any ball in this layer between lines a-a and b-b, is subjected to two sets of forces, one applied at the point of contact with the mill shell, in a direction tangential to the shell (as shown in Fig.2) and clockwise; the other applied on the opposite side of the ball and oppositely directed. This pair of forces acting on any one ball constitutes a couple and since the ball is constrained by contact with the shell and its neighbours, it rotates about an axis. Thus every ball in the zone between a-a and b-b has similar rotation under the action of similar couple. The result is sliding of cataracting surfaces across each other under pressure. Particles nipped and passed between are ground by abrasion.

In the zone from b-b to a-a, reckoning clockwise, in a mill operating at cataracting speeds, there is substantial free fall of balls out of contact with each other and no grinding or breaking action whatever. At the surface c-c there is crushing by impact between the falling balls and the balls below the surface, which are supported by the mill shell. In the zone a-c, c-c, d-d, there is most intense and turbulent motion, consisting of violent tumbling in the region above the heavy dotted line and rapid shear of the mass along the dotted line with the portion of the balls below the line moving rapidly with the mill shell and those above appearing as a mass, to be stationary, although each individual in this mass is in rapid motion with respect to its neighbours.

2. DETERMINATION OF DYNAMIC STRESS

The freely falling cylpebs produce an enormous amount of dynamic load on the skin of the shell. The intensity of this loading is a function of the diameter of the ball, speed of the mill and height of fall (diameter of the shell). The centrifugal effect of the rotating shell is normally of small magnitude [5], since speeds encountered for typical mills are in the range 17-22 rpm [4].

From the experiments conducted [6] on an aluminium model of a mill (Fig.3), it is assumed that radial pressure varies as the square of the speed while the circumferential pressure varies linearly as the operating speed. It is also assumed that the rms pressures both in the radial and the circumferential directions are roughly proportional to the diameter of the ball. Based on these assumptions the rms pressures for typical ball mills have been predicted for 40% charge and are shown in Table 2.

3. FINITE ELEMENT IDEALIZATION

For the analytical solution of the problem, the ball mill (Figs.4 and 5) has been treated as a cyclic symmetric structure with asymmetric loading [7]. Though rotationally symmetric, the concept of cyclic symmetry has been adopted to allow for the introduction of ribs if necessary and to reduce the size of the problem. If one is interested in discretising the whole structure, the core and time needed would be enormous.

The ideal finite elements for solving problems under this category are triangular shell elements [8] with six degrees of freedom at each node. The stiffness and mass matrices formulated in Cartesian co-ordinates are to be transformed to polar form resulting in displacements along radial, circumferential and axial directions.

The mathematical modelling of a cyclic symmetric structure for static analysis under generalised loading is given by one of the authors [7]. Let us consider a cyclic symmetric structure with N identical repeating sectors. The force acting on the structure is expressed as a sum of several Fourier components. The number of such harmonics is finite (N). Thus for each harmonic, analysis of a single repeating sector is possible. This is in fact an extension of the standard practice of analysis for an axisymmetric structure under arbitrary loading. The forces and the corresponding displacements are expressed in terms of a corresponding Fourier series. The total response is obtained as a sum of the individual Fourier harmonic responses.

4. DYNAMIC ANALYSIS WITH ASYMMETRIC LOAD

The dynamic problem considered here involves computation of transfer function for unit load (varying harmonically with time) at frequencies in the range of excitation. The solution to the steady-state vibration problem with harmonic forcing function $\sin\omega t$ with maximum intensity unity involves modifying the principal diagonals of the stiffness matrix by adding appropriate $M\omega^2$ terms (inertia forces) and using the same solution technique as for static analysis. This is valid only when damping in the system is ignored. From the experimentally arrived at values of power spectral density of dynamic pressures [6], it is seen that the highest forcing frequency for which the power spectral density value is of measurable magnitude is around 10 Hz. From what follows in the next section, it is seen that the lowest natural frequencies of practical mills are much higher than the highest forcing frequencies. Hence, the chances of the mill getting excited at any of its natural frequencies is remote. Therefore, for the subsequent dynamic analysis, damping is ignored and the frequencies of excitation used for computing the transfer function vary from 0 Hz to the frequency corresponding to the tenth harmonic of the running speed. In subsequent computations, it is found that the contribution from $M\omega^2$ terms to the modified stiffness matrix is negligibly small.

Fig.6 shows the variation of displacement due to unit dynamic line load $\sin\omega t$ for a mill without liner. The displacements of the sector in which the load is applied and the adjoining sectors all around the circumference have been plotted. Fig.7 shows the corresponding variation of stresses around the circumference. It is observed that the decay rate around the circumference is not fast for mills with liners. Table 3 shows the computation time for the dynamic response due to load $\sin\omega t$. The computations were made on a computer which takes 6μs for multiplication.

5. NATURAL FREQUENCY DETERMINATION

The governing equation for free vibration can be written as

$$[K]\{\delta\} = \omega^2 [M]\{\delta\} \qquad (1)$$

where [K] is the stiffness matrix, $\{\delta\}$ the displacement vector and [M] the mass matrix. Since the eigen vector $\{u_i\}$ of a repeated sector is connected to the (i + 1)th vector by the relationship

$$\{u_{i+1}\} = e^{i\phi}\{u_i\} \qquad (2)$$

the stiffness matrix of any cyclically symmetric structure will be Hermitian [7]. Hence for N even, Eq.(1) has to be solved for (N/2 + 1) values of ϕ and N odd calls for solution of (N + 1)/2 values of ϕ to get all the eigen values of the entire structure.

Table 4 gives the lowest natural frequencies of typical industrial ball mills mentioned in Table 1. Also shown in the Table are recommended operating speeds for these mills. It is seen that the fundamental frequencies are much higher than the operating speeds (at least 20 times). These values are obtained for mills of the type shown in Fig.3. The forcing frequency (the dominant pressure frequency corresponding to the running speed) and its 10 harmonics thus lie in a range far below the natural

frequencies. Hence while doing the steady state analysis one is justified in neglecting the damping.

6. RANDOM VIBRATION CONCEPT

To determine the spectral density of the response of a system [9] to a single randomly varying force, it is only necessary to know the spectral density of the exciting force, and the relevant receptance of the system. In cases where a number of forces act together, complication arises not simply from the larger numbers, but from the possibility that the different forces are in some way related, so that their cross-correlations are to be taken into account. The response of a system to a single input is given by the equation

$$S_x(f) = |\alpha(if)|^2 S_p(f) \tag{3}$$

where $S_x(f)$ is the power spectral density of the output response, $S_p(f)$ the power spectral density of the input force and $\alpha(if)$ the transfer function.

Eq.3 has been extended to the case of multiple loads. It has also been assumed that the radial and circumferential pressure inputs are uncorrelated.

6.1 Response to multiple loads

When more than two random forces act together, the analysis may be extended without difficulty, although, of course, the number of cross-correlation terms is greatly increased, and equations get lengthier.

Consider, e.g., the response x(t), of a system, in a given direction, to three random loadings P(t), Q(t), R(t), acting simultaneously. We can obtain an expression giving the auto-correlation function $R(\tau)$ in terms of the auto-correlation functions $R_p(\tau)$, $R_Q(\tau)$, $R_R(\tau)$ and the cross-correlation functions $R_{PQ}(\tau)$, $R_{QP}(\tau)$, $R_{QR}(\tau)$, $R_{RQ}(\tau)$, $R_{RP}(\tau)$ and $R_{PR}(\tau)$ and this result can be used to express the spectral density S(f) of output x(t) in terms of the spectral densities and cross-spectral densities of the loadings. Proceeding in this way we obtain

$$S_x(f) = \begin{bmatrix} \alpha^*_{xP}\alpha_{xP}S_P(f) + \alpha^*_{xP}\alpha_{xQ}S_{PQ}(f) + \alpha^*_{xP}\alpha_{xR}S_{PR}(f) \\ + \alpha^*_{xQ}\alpha_{xQ}S_Q(f) + \alpha^*_{xQ}\alpha_{xR}S_{QR}(f) + \alpha^*_{xQ}\alpha_{xP}S_{QP}(f) \\ + \alpha^*_{xR}\alpha_{xR}S_R(f) + \alpha^*_{xR}\alpha_{xP}S_{RP}(f) + \alpha^*_{xR}\alpha_{xQ}S_{RQ}(f) \end{bmatrix} \tag{4}$$

Where there are n forces $P_1, P_2, \ldots P_n$ acting, a general result having the form

$$S_x(f) = \sum_{r=1}^{n} \sum_{s=1}^{n} \alpha_{xP_r}\alpha_{xP_s}S_{P_rP_s}(f) \tag{5}$$

obviously applies, where $S_{P_rP_r}(f)$ is to be interpreted as $S_{P_r}(f)$.

For the finite element model of the mill considered, there are 12 repeating sectors with 6 partitions per sector. Hence 72 line loads with a time lag of τ_o between successive loads have been considered. Hence in the present analysis n = 72.

Since adjacent forces P_r and P_s for the ball mill are such that

$$P_r(x,t) = P_s(x, t + \tau_o) \tag{6}$$

it follows that

$$S_{P_r P_s}(f) = e^{i2\pi f \tau_o} S_{P_r}(f) \tag{7}$$

Here $2\pi f \tau_o = 2\pi/72$ (8)

where f is the frequency corresponding to the operating speed of the mill. Hence Eq.5 may be simplified as

$$S_x(f) = \sum_{r=1}^{n} \sum_{s=1}^{n} \alpha_{xP_r}^{*} \alpha_{xP_s} e^{i2\pi(s-r)/72} S_{P_r}(f) \tag{9}$$

Since the effect of damping is ignored as mentioned earlier, the transfer functions of displacement and stress are real quantities. Besides, the contribution from $m\omega^2$ terms to the modified stiffness matrix being negligible, the simplification shown in Eq.10 could be made.

$$\sigma_x = \left[\sum_{r=1}^{n} \sum_{s=1}^{n} \alpha_{xP_r} \alpha_{xP_s} e^{i2\pi(s-r)/72} \right]^{\frac{1}{2}} \sigma_{P_r} \tag{10}$$

It is this equation which has been made use of to predict the rms values of stresses for actual mills from the predicted rms values of pressure.

7. COMPUTATIONAL PROCEDURE

The ball mill has been assumed to have 12 repeated structures each subtending 30^o at the centre. Let the first of such structures consist of 6 partitions, each subtending 5^o at the centre as shown in Fig.4. In the finite element model of the actual mill shown only one half-length of the mill has been considered assuming symmetry. Each structure consists of 112 nodes and 180 triangular plate elements. Each plate element has six degrees of freedom at each of its nodes. Since the mill can be thought of as being simply supported at both ends, all degrees of freedom corresponding to the three translational modes have been suppressed at all nodes at the support end. Since the mill has been assumed to be symmetric about the middle of the longitudinal axis, all degrees of freedom corresponding to the translatory motion z and the rotational motions corresponding to r and θ for all nodes at mid-span have been suppressed giving rise to a problem of size 540x108 for each structure.

For the finite element model of the mill 72 line loads have been considered. A line load with components of uniform intensity in the radial and circumferential directions has been assumed to act along a meridional line including the conical portion and the cylindrical portion of larger diameter. For the actual mills mentioned in Table 1, the analysis has been done considering a liner, the thickness of which is twice that of the shell. The output displacements and stresses have been computed on the basis that the radial and circumferential inputs are uncorrelated.

Many of the actual mills do not have diaphragms. But there are quite a few with diaphragms [2]. The diaphragms are annular circular plates typically at 20% and 50% of the length of the mill dividing it into three compartments. The first compartment has cylpebs of mean diameter 65 mm , the second 45 mm and the third 35 mm, so that the effective diameter works out to 45 mm. For the present analysis, a diaphragm has been assumed to exist at 1/3 span of the cylindrical portion and its effect has been simulated by arresting displacements in all three mutual perpendicular directions. This simplifying assumption need not necessarily be true.

Fig.8 show the variation of stress along the length of the mill for one of the actual mills mentioned in Table 1. Steel balls of 47 mm dia. have been assumed for the

calculations. These stress values have been plotted for the cases of diaphragm present and absent.

8. CONCLUSION

The circumferential and the meridional stresses computed by considering the static asymmetric loading of the grinding media are found not to exceed a maximum value of around 30 N/mm^2 even for the largest mill [3] assuming the main shell alone to take the load. Since the liner which is concentric with the shell also contributes to the strength, its thickness should also be accounted for in the analysis. If this is taken into account, it is likely that the maximum stress level may go down by about one-sixth of the original value (inversely proportional to the square of the effective thickness) and this will then be around 5 N/mm^2. This value gives an impression of the mill being grossly overdesigned. But from Fig.8 it is observed that the maximum dynamic stress computed due to the random loading when the mill does not have diaphragms can reach a value as high as 115 N/mm^2. However, many practical mills of large spans have diaphragms. The introduction of diaphragms as seen from the same figure brings down the values substantially (30 N/mm^2). However, introduction of the diaphragms has been assumed to result in zero deformation in all the three directions mutually at right angles. Probably this is an over simplification of what is really happening in practice. This, in the authors' opinion, is to be re-examined.

REFERENCES

1. Taggart, Handbook of Mineral Processing, John Wiley, New York, 1954.
2. Labahn, O., Cement Engineers' Handbook, 3rd Edn. Bauverlag, GmBH, Wiesbaden, 1971.
3. Ramamurti, V., Siva Prasad, N. and Rayudu G.V.N. Stress analysis of mill heads of large tube mills, Zement Kalk Gips, V 36, n 11, 1983, pp 633-638.
4. Ramamurti, V. and Alwar, R.S., Stress Analysis of a tube mill, Jl. Strain Analy. v.8, n 3, 1973, pp 200-208.
5. Ramamurti, V. and Omprakash, V., Failure analysis of semi-autogeneous grinding mills, Zement Kalk Gips, v 21, n 2, 1988, pp 87-90.
6. Ramamurti, V., Sujatha, C. and Irretier, H. Dynamic strain measurement on a model of a cement mill, Zement Kalk Gips, v 44, n 2, 1991, pp 123-126.
7. Ramamurti, V., Computer Aided Design in Mechanical Engineering, Tata McGraw Hill, New Delhi, 1985.
8. Zienkiewicz, O.C., The Finite Element Method in Engineering Science, McGraw Hill, New York, 1971.
9. Robson, J.D., An Introduction to Random Vibration, Elsevier Pub.Co., London, 1964.

TABLE 1

DIMENSIONS OF TYPICAL BALL MILLS (mm.)

Type	r_1	l_1	r_2	l_2	t
1	185	225	608	5400	16
2	295	330	910	8000	24
3	470	460	1217	10800	34
4	658	610	1522	13500	44
5	750	800	1825	16200	50

TABLE 2

PREDICTED PRESSURES FOR TYPICAL INDUSTRIAL MILLS

Type	Mill Span l_2(mm)	Recommended operating speed (rpm)	Predicted rms pressure for 47 mm balls (N/mm^2)	
			Radial	Circumferential
1	5400	29.8	0.0576	0.589
2	8000	24.4	0.0576	0.721
3	10800	21.1	0.0577	0.835
4	13500	18.9	0.0579	0.935
5	16200	17.2	0.0577	1.022

TABLE 3

COMPUTATION TIME FOR DYNAMIC RESPONSE TO UNIT LOAD SIN ωt

	Size of the problem	No. of sectors considered	Time (CPU sec)
Actual mill	540x108	6	420
Model mill	360x78	3	155

TABLE 4

NATURAL FREQUENCIES OF TYPICAL INDUSTRIAL BALL MILLS

Type	Span (mm)	Recommended Operating speed (rpm)	Natural freq. (Hz)	Operating freq./Natural freq.
1	5400	29.8	46.53	0.01067
2	8000	24.4	32.39	0.01256
3	10800	21.1	23.97	0.01467
4	13500	18.9	19.31	0.01631
5	16200	17.2	15.49	0.01851
5*	16200	17.2	22.39	0.01280
Model 225		65.3	435	0.00250

*Liner included

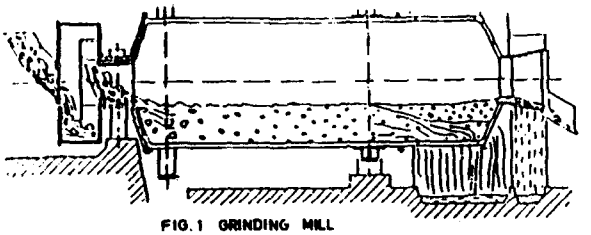

FIG. 1 GRINDING MILL

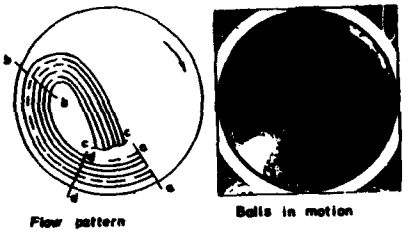

Flow pattern

Balls in motion

FIG. 2 MILL WITH BALLS INSIDE

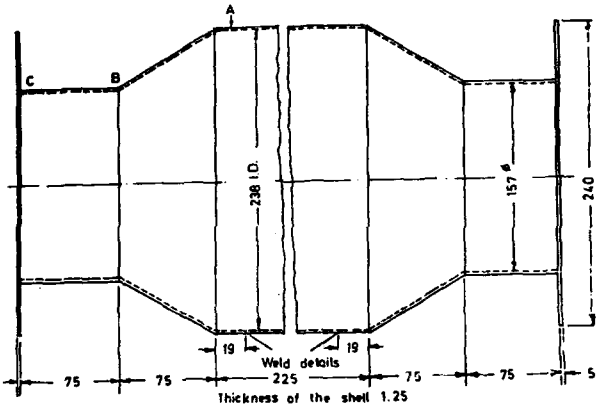

Thickness of the shell 1.25

All dimensions in mm

FIG.3 DETAILS OF THE ALUMINUM SHELL

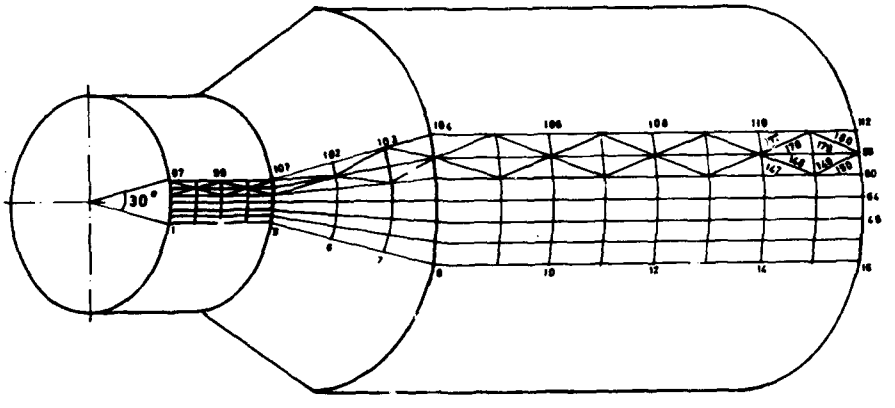

For one structure:

Partitions = 6, Nodes = 112, Elements = 180, Equations = 540, Bandwidth = 108

FIG.4 FINITE ELEMENT MODEL OF BALL MILL

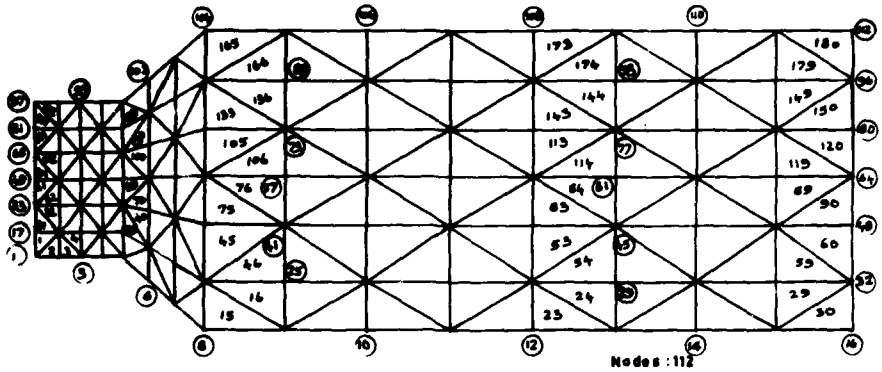

Nodes : 112
Elements : 180
Equations : 540
Band width : 108

FIG.5 FINITE ELEMENT MODEL OF ACTUAL MILL
(One repeating structure)

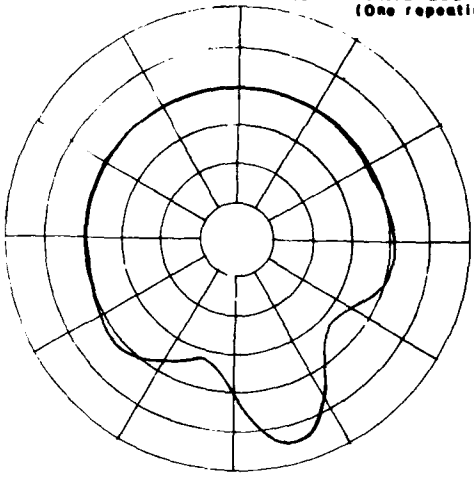

FIG.6 DISPLACEMENT VARIATION ALONG THE CIRCUMFERENCE OF THE SHELL FOR UNIT LINE LOAD.

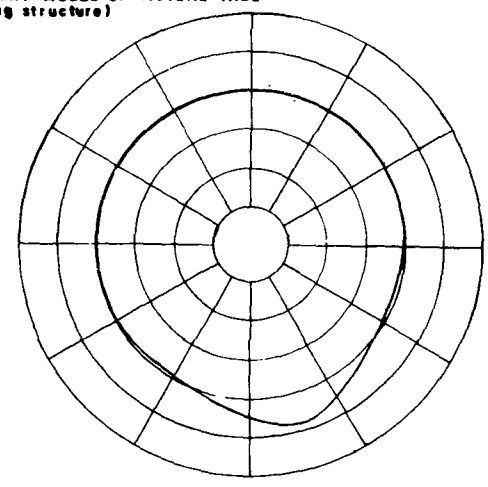

FIG.7 STRESS VARIATION ALONG THE CIRCUMFERENCE OF THE SHELL FOR UNIT LINE LOAD.

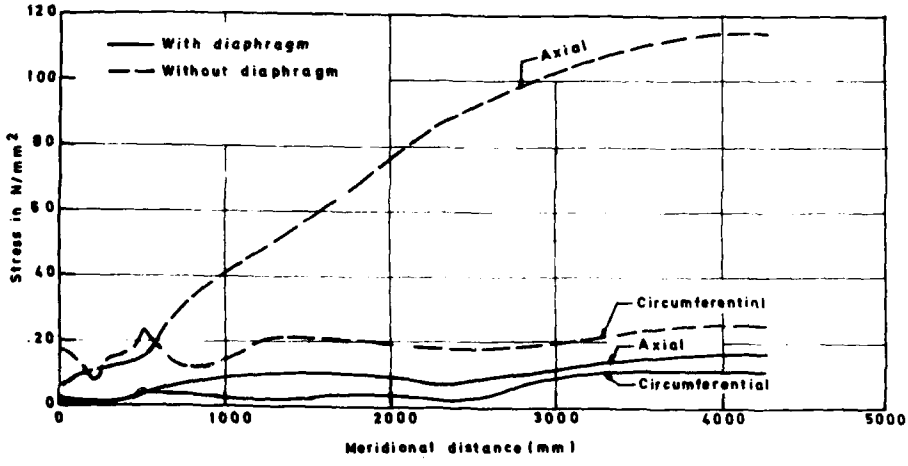

FIG. 8 STRESS VARIATION FOR MILL OF RADIUS 900 mm AND SPAN 8800mm.

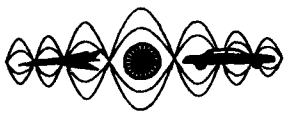

SECOND INTERNATIONAL CONGRESS ON
RECENT DEVELOPMENTS IN AIR- AND
STRUCTURE-BORNE SOUND AND VIBRATION
MARCH 4-6, 1992 AUBURN UNIVERSITY, USA

EVALUATION OF ACOUSTIC EMISSION SOURCE LOCATION FOR DIFFERENT THREE-SENSOR ARRAY CONFIGURATIONS

Vasisht Venkatesh and Professor J.R. Houghton
Department of Mechanical Engineering
Tennessee Technological University
Cookeville, TN 38505, U.S.A

ABSTRACT

A common method of detecting a discrete acoustic emission source is by computing the time difference between each sensor arrival time. A three sensor equilateral triangular array is often used to locate sources in two dimensional cases. However, this arrangement can create false source locations.

Experiments were carried out to find a possible sensor array configuration, that would reduce the ambiguity in source location. Various three sensor array configurations were used, while keeping the sampling rate, trigger level and gain constant.

Results indicated that a scalene (having unequal sides) triangular array configuration provided accurate locations with the least amount of ambiguity and no false source locations.

INTRODUCTION

The acoustic emission (AE) technique, of nondestructive testing, detects stress waves which have been emitted within or on the material surface. The AE technique has many advantages , since it is capable of detecting dynamic processes[1]. The source of energy released is within the test object and does not need to be supplied. Acoustic emission sensor arrays can also detect sources from any direction on the test object without depending on prior knowledge of probable location.

In order to be able to locate acoustic emission sources an array of sensors are placed on the surface of the test object to form a monitoring region. The arrival times of stress waves at each sensor is noted, and the source is located by the difference in arrival times. At least three sensors are required to locate sources in a two dimensional case. Additional sensors can be added to reduce the ambiguity in source location, however increasing part and instrumentation costs. Only the three-sensor array is discussed in this paper.

The ability to accurately locate acoustic emission sources is an important area of nondestructive evaluation. The NDE methods need to be improved to lower the margin of error and the false locations. The major additional problem today is source location in non-isotropic materials such as engineering composites structures. This paper provides results to experiments, with three sensor array configurations as shown in Fig. 1, which were conducted to find configurations that provide the least number false source locations.

THEORY

Consider three sensors on a plate as shown in Fig.2. Assume isotropic conditions where the shear wave from an acoustic emission source travels at a constant velocity, $\sqrt{\frac{G}{\rho}}$. Where G is the shear modulus of elasticity and ρ is the mass density. The sensor arrival sequence is marked 1,2,3 as shown in Fig.2. The respective distances between sensors and sources, and the angles are also noted. The time difference measurements would be between second and first sensors and third and first sensors (Eqs.1 and 2). Figure 3 shows typical signals and the respective arrival times.

$$\Delta t_1 = t_2 - t_1 \tag{1}$$

$$\Delta t_2 = t_3 - t_1 \tag{2}$$

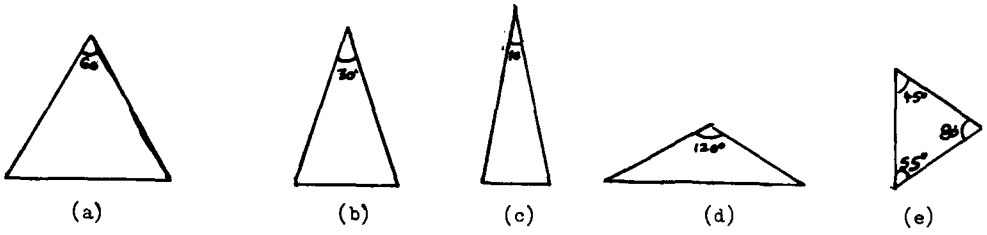

(a) (b) (c) (d) (e)

Fig.1 Triangular sensor configurations used, (a) equilateral, (b) 30° isosceles, (c) 10° isosceles, (d) 120° isosceles, (e) scalene.

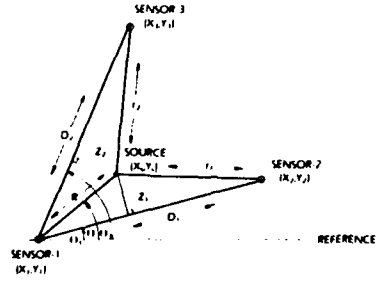

Fig.2 Generic sensor configuration.[1]

The distance from source to reference sensor, S_1, is given by the following equations [1]

$$L(source\,to\,S_1)_{1\text{-}2} = \frac{D_1^2 - \Delta t_1^2 V^2}{2\,(\Delta t_1 V + D_1\,COSINE\,(\Theta - \Theta_1))} \qquad (3)$$

$$L(source\,to\,S_1)_{1\text{-}3} = \frac{D_2^2 - \Delta t_2^2 V^2}{2\,(\Delta t_2 V + D_2\,COSINE\,(\Theta_3 - \Theta))} \qquad (4)$$

where, V is the velocity of the shear wave, determined experimentally.

Equations(3) and (4) are equations of a hyperbola and can be solved simultaneously to find the source location from the first hit sensor. The solutions to these equations very often provides two solutions (Fig. 4), both of which satisfy the input conditions. It is not possible to distinguish the true source from the false source without further information.

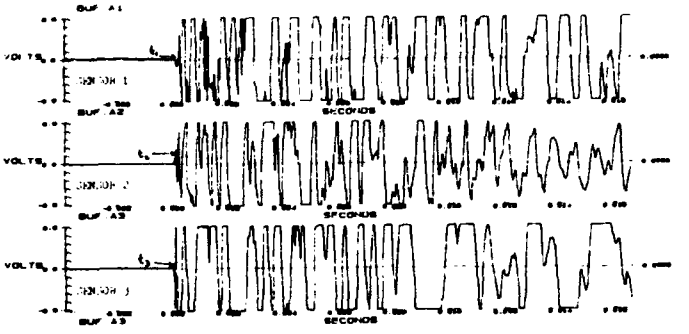

Fig.3 Typical signals showing arrival times.

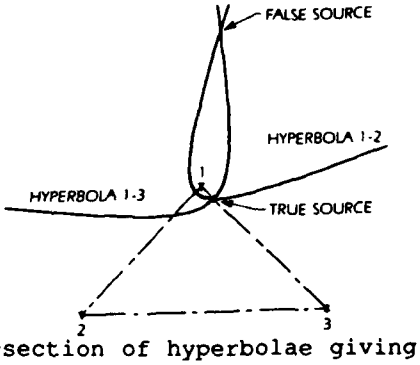

Fig.4. Intersection of hyperbolae giving rise to two source locations.

In determining the time difference measurements in Eqs.(1) and (2) it is possible to use sensors 2 and 3 as the first hit sensors instead of sensor 1. This would require changing the input data (angles and distances) in equations (3) and (4). For example by using sensor 2 as the reference sensor Eqs.(1) and (2) become

$$\Delta t_1 = t_1 - t_2 \tag{5}$$

$$\Delta t_2 = t_3 - t_2 \tag{6}$$

The arrival times used in these equations are the same as those used Eqs.(1) and (2). It can, therefore, be seen that for a given acoustic emission (3 arrival times) Eqs.(3) and (4) can be solved three separate times, yielding three possible source locations. This method, as wil be seen, improves the accuracy of source location for scalene sensor array configurations.

EXPERIMENT

Experiments were carried out on a 1219.2 X 457.2 mm aluminum plate. Four Valpey-Fisher, VP-1093, pinducers were used in the experiments. One was located next to the AE source as a trigger sensor to activate the signal analyzer. The pinducers used were broadband transducers with a flat frequency response to 1.4 MHz. These transducers were mounted on the aluminum plate by coupling wax. A 4-channel Data Precision, Data 6100, waveform analyzer was set at 25,000 samples per second sampling rate. A Tektronix, model AM 502, amplifier was set at a 23 dB gain. See Fig.5 for experimental set-up.

An artificial acoustic emission source was used to carry out the source location tests. A brittle fracture or pencil lead (Hsu-Nielson)[3] source was used with a 0.3 mm diameter, and HB hardness lead. This pencil lead source was usd because it provided an easily reproducable signal.

The various sensor array configurations, in Fig.1, were set up and pencil lead breaks were performed at different points on the aluminum plate. These lead break points were mapped and the arrival times at the three sensors were recorded. These arrival times along with the angle and distance data are input into an iterative computer program, that iterates Eqs.(3) and (4) until the absolute difference between them is under a tolerance of 1.0 mm. If this tolerance limit is not satisfied, then no solution is found for the input arrival times. The output data is then mapped to determine the accuracy of the solutions

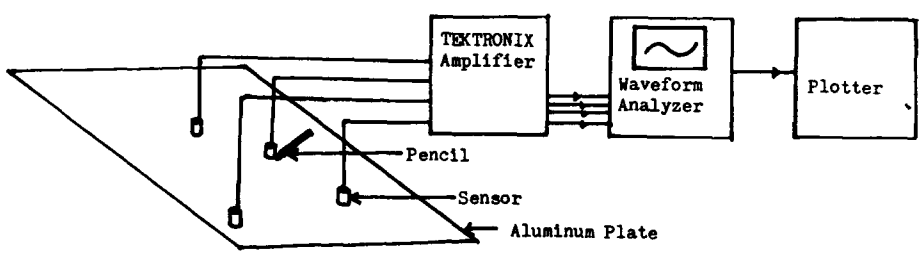

Fig.5 Experimental setup

RESULTS AND CONCLUSION

As can be seen from Fig.3 the arrival times of the signals are fairly easy to find, however with a sampling rate of only 25 KS/s the possible error is 40 us[1]. This error is rather large and could produce upto a 90 mm error. It is interesting to note that the experimental errors were much less than 90 mm for the scalene triangle. This error should be reduced by using systems with higher sampling rates.

The results of some of the experiments are shown in Table 1. and Fig.6. These results show that the equilateral, 10°and 30° isoceles triangluar arrays located two sources within 4 mm, however these same good results produced false sources. All initial source locations for the equilateral, 10° and 30° isosceles triangular arrays, were found using sensor 1 as the reference sensor as shown in Fig.6. When the reference sensor was changed to sensor 2 and 3 very few solutions were achieved, for the isosceles triangular configuration, by the iterative program. The solutions were mapped and the area where source locations were within 50 mm from the actual source were found. This area as shown in Fig.7 is the effective source location area. As the arrays were changed from the equilateral to the 30° and 10° isoceles configurations the effective source location area got thinner, but streched further away from sensor 1 as shown in Fig. 7.

Table 1. A few of the actual and calculated sources with an equilateral sensor array configuration. This table shows the two hyperbolae intersections as source 1 and source 2. Refer to Fig.6.

Sample No.	Actual values from REF at Sensor A		Source 1		Source 2 (False Source)	
	Distance, mm	Angles, degrees	Distance, mm	Angles, degrees	Distance, mm	Angles, degrees
1.	129.40	90	107.44	104.85	113.23	107.71
2.	219.96	90	219.71	90.52	96.77	270.31
3.	279.40	90	283.46	90.01	157.73	270.01
4.	127.0	35	183.64	44.11	-	-
5.	203.20	70	275.60	79.64	-	-

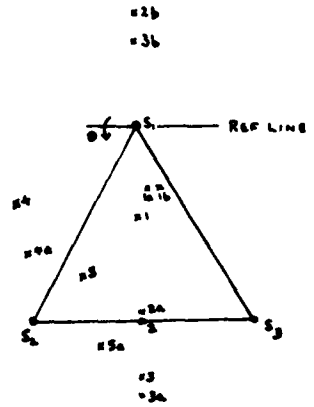

Fig.6 Source location of equilateral sensor array from Table 1. True and false sources are shown for the solutions.

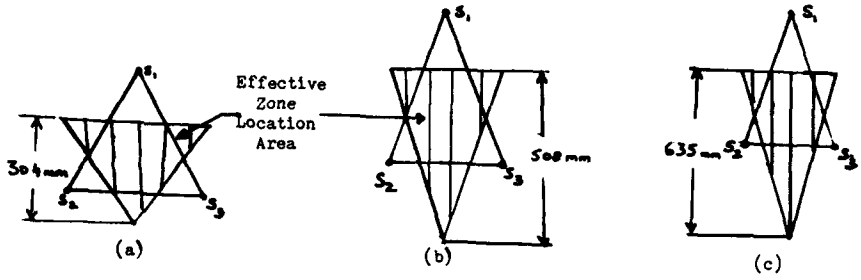

Fig.7 Effective source location area for (a) equilateral, (b) 30 isosceles and (c) 10 isosceles triangular configurations.

The scalene triangular array provided different results from the equilateral or the isoceles arrays. Although the scalene configuration located sources from 20 to 70 mm of the actual source, it **did not produce any false sources** (see Table 2. and Fig.8). The scalene array configuration also provided three sets of solutions (A,B,C) for every source by changing the reference sensor, as seen in Table 2. It can be seen from Fig.8 that the three solutions generally formed close groups. The actual source would generally be close to the average distance of the three solutions. There are, however, places of uncertainity where the three solutions are widely seperated (5a,5b,5c).

Table 2. This table shows some of the actual and calculated source locations calculated for the scalene configuration with reference sensor A. Refer to Fig.8.

Sample No.	Actual values from REF sensor A		Experimental values from REF A		Absolute error in source location	
	Distance, R_A mm	Angle, Deg	Distance, R_E mm	Angle, Deg	$R_A - R_E$	$\theta_A - \theta_E$
1A	152.4	120.0	180.09	146.7	27.7	26.7
1B	152.4	120.0	185.4	150.0	33.0	30.0
1C	152.4	120.0	190.5	146.0	38.1	26.0
2A	203.2	110.0	271.8	104.8	68.6	5.2
2B	203.2	110.0	236.2	118.0	33.0	8.0
2C	203.2	110.0	279.4	109.0	76.2	1.0
3A	304.8	110.0	271.8	104.8	33.0	5.2
3B	304.8	110.0	266.7	108.0	38.1	2.0
3C	304.8	110.0	279.4	109.0	25.4	1.0
4A	431.8	110.0	455.9	113.4	24.1	3.4
4B	431.8	110.0	457.2	114.0	25.4	4.0
4C	431.8	110.0	477.5	114.0	45.7	4.0
5A	254.0	60.0	272.8	104.8	18.8	44.8
5B	254.0	60.0	261.6	107.0	7.6	47.0
5C	254.0	60.0	279.4	109.0	25.4	49.0

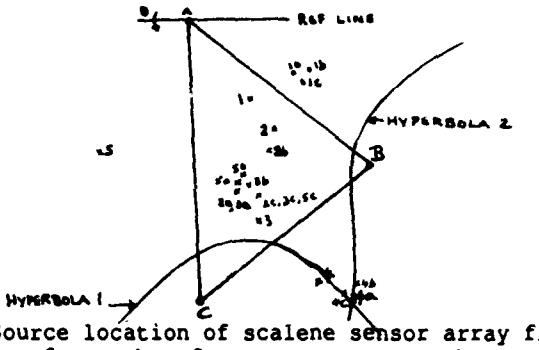

Fig.8 Source location of scalene sensor array from Table 2. Solutions for each reference sensor are shown.

The 120° isosceles array configuration tests provided ambiguous results, since the configuration approaches a linear configuration. It was also noted that all configurations produce ambiguous results when the sources were within 70 mm from any sensor.

In summary although, the equilateral 30° and 10° isosceles arrays produced accurate results within the zone location area, false sources are also located. The scalene triangular array on the other hand, had source locations that were not very accurate, but did not produce false sources. The source location can, however be improved by using an analyzer with a faster sampling rate. A sampling rate around 100 KHz could significantly improve the accuracy of the scalene configuration to within a 10 mm circle of uncertainity.

REFERENCES

[1] Ronnie K. Miller and Paul McIntire, "Nondestructive Testing Handbook", American Society for Nondestructive Testing, Vol.5, 1987.

[2] Dong-Jin Yoon, Young H. Kim and Oh-Yang Kwon, "New Algorithm for Acoustic Emission Source Location in Cylindrical Structures", Journal of Acoustic Emission, Vol.9,No.4/October 1990.

[3] Michael R. Gorman and William H. Prosser, "AE Source Orientation by Plate Wave Analysis", Journal of Acoustic Emission, Vol.9,No.4/October 1990.

SECOND INTERNATIONAL CONGRESS ON
RECENT DEVELOPMENTS IN AIR- AND
STRUCTURE-BORNE SOUND AND VIBRATION
MARCH 4-6, 1992 AUBURN UNIVERSITY, USA

DEFECTS DETECTION IN STRUCTURES AND CONSTRUCTIONS BY NOISE SIGNALS DIAGNOSTICS METHODS

Vadim A. Robsman
Union "Electronics of Russia"
2 Krasnopresnenskaya nab.
Moscow, 103274, USSR

ABSTRACT

In the course of engineering structures maintenance noise signals may occur as a consequence of technological equipment loading, or signals, emitted by special generators -gauges. Generation and propagation of microdefects in the form of cracks and disruption of elements connecting contacts in structural units are possible in the caurse of dynamic loading.

Identification algorithms are based on usage of noise signals multiparametric analysis. The signals could be classified into 2 groups: signals, generated by outer noise sources, and signals, emitted by defects and damages themselves. The experiments proved, that various non-linear effects and transformations of noise signals and their spectrum, detected in separate space and time points, are very important.

Irreversible structure modifications processes and brittle failure in structurl materials take place as a result of local defects accumulation. Such processes generate at the starting stage of plastic deformation and develope together with micro- and macrocracks complex propagation, ending abruptly by catastrophic failure. Such phenomena investigation is of some interest from the acoustic point of view, as various structural defects in material produce different nonlinear effects in acoustic waves propagation in solid deformed medium. Besides, defects generation and accumulation zones in medium also demonstrate themselves as inner sources of acoustic noise - acoustic emission (AE). Defected zones generation and propagation in material, produced by outer loads, have stochastic nature, which is correspondingly reflected in statistical regularities of acoustic detection and ranging signals parametric changes. Both statistical parameters and acoustic non-linearity effects are identification features for margins between faults development stages.

The performed investigations contain methods and results for the following problems solution:

- spectrum distortion degree comparsion for active detection and

ranging of deformed media by regular and noise acoustic signals;

- interaction of acoustic waves with various spectral characteristics alongside with non-linear deformation propagation;
- cracks acoustic emission probabalistic characteristics at deformed medium failure stages;
- acoustic emission signals spectrum change analysis at vaious stages of non-linear deformation and failure propagation;
- defects detection in structures for failure conditions prevention.

The experimental researches have been carried out using special laboratory testing beds, as well as in situ. The insitu experiments have been carried out on soil masses and engineering structures and structural elements, failed in the course of the Spitak earthquake in Armenia. Diagnostics of structures, failed during the earthquake, covered masonry dwellings and industrial buildings made of precast reinforced concrete and metal elements.

The first experimental series contains materials investigation under the conditions of rather low level of non-linear deformation; it was connected with non-linear acoustic effects analysis in plastically deformed materials. These researches allowed to ascertain that in the course of plastic deformation propagation advancing dislocations stimulate generation of AE signals stationary flow in the form of narrow -band noise pulses complex, parameters of which do not have considerable fluctuations. And by the AE signals appearance moment discreteness it could be concluded that dislocational movement is abrupt, but not in the form of smooth continuous displasement. The other experimental series was dedicated to the investigation of additional ultrasonic action influence effect on non-linearly deformed material. This stimulated dislocational movement activization. The abnormal acoustic phenomena investigations were carried out under the conditions of various spectral characteristics of outer ultrasonic transducers and non-linear deformation levels. So, for example, considerably powerfull narrow -banded noise pulses action on plastically deformed materials produced non-linear spectrum distortion in the form of its maximum displacement to the region of lower frequencies and irregular power redistribution to both spectrum wings. The influence of outer static loading and acoustic influence were studied within dislocation model of Frenkel-Kontorova. At the beginning so far as outer acoustic action oscillation is increased, oscillators networks undergo non-linear distortions, the spectrum is enriched by the highest harmonics, but the process remains periodical. Then the periodicity is disturbed by atoms migration from one potential field into another; new spectrum components are generated. At last subharmonics mass generation takes place, as well as all possible heterodyne frequencies, that is a transition into the random frequencies mode is observed.

Acoustic phenomena investigations in metal and reinforced concrete structures were carried out under static and dynamic loading applied up to complete failure stage. The experiments provided for organization of multichannel monitoring of acoustic signals in tensile and compressive stressed zone, as well as for differences definition of acoustic spectra non -linear transformation zones.

Even at the starting stages of non-linear deformations, corresponding to not less than 15 % of breaking load, narrowbanded noise signals of active detection and grading were monitored, which had the amplitude and spectral lines width of high-frequency harmonics higher, than of the first one. But such widening was limited by the distance to the transducer of no

more than 1 m. With further increase of non -linear deformation the similar effect was observed in the compressed zone at 0, 5 - 0,7 m distance, and there was a 20 - 25 % increase of the second harmonics power in the limited frequency band. But in tensile zone the second harmonics power increase did not exceed 17 - 20 %. When the loading reached 60 - 65 % of the breaking one, the second harmonics power increased 2,7 - 3 times compared to 10 - 15 % of breaking load power level.

In the course of reinforced concrete beam detection and ranging by wide -band noise there is irregular power redistribution from the central part of the spectrum to the region of low and high frequences depending on the sign and non-linear deformation obsolute value, as well as distance to the transducer. When the distance to the transducer is increased, there is decrease and redistribution of power in spectrum high- and low-frequency zones. On compressed parts of the material the power of the spectrum high -frequency wing is 1,6 - 1,8 times greater than of signal spectrum in the tensile part. Besides, some frequency range narrowing of wide-band noise signals spectrum was observed in material's parts under tensile stresses.

The experiments on non-linearly deformed reinforced concrete beam also showed that under interaction of regular waves and noise, generated in one direction by two parallel transducers, power redistribution to the higher-frequency zone takes place simultaneously with new spectrum zones formation and power decrease in monoharmonic component of the spectrum. In noise component there is also power redistribution to low-frequency and high -frequency zones when the distance to the transducer increases. The increase of the distance to the transducer is accompanied by power dispersion in the spectrum with high-frequency component increase only in compressed zone. In tensile stress zone there is a spectrum maximum shift to the lower frequencies zone together with power decrease, which also depends on relative deformation level.

Non-linearly deformed solid media evolution could be represented as successive stages of irreversible destructive processes, with acoustic emission (AE) signals as indications of their development. Such process and margins between its separate stages could be analized by the appearance of characteristic non-linear transformations in emission signals spectra. In AE signals spectra there are non-linear distortions in the form of local extremes on subharmonic frequencies with their doubling effect and the following spectrum reorganization into the noise one in the low-frequency wing before abrupt failure. In all cases extremes appearance on new frequencies was connected with the beginning of the local defects interaction stage, and the noise spectrum formation identified the abrupt failure start. Non-linear spectra transformations, found in the course of experiments, allowed to suppose that in the emission process development there is a certain analogy with bifurcational transition to random stage accourding to Feigenbaum pattern or combinatorial subharmonic components formation in the spectrum. The AE pulses flow could be simulated as random transition process complex in connected non-linear oscillations. The computer-aided experiments using this model proved random transition mode in the form of bifurcations stage.

The investigations allowed to establish acoustic spectra nonlinear transformations not only by active medium detection and ranging, but also AE signals, emitted by growing defects. Non-linear spectral distortions observed in the course of physical experiments and computeraided simulations recognize quantitative differences in failure stages. This provides for identification of destructive processes separate stages in order to prevent failure catastrophic stages.

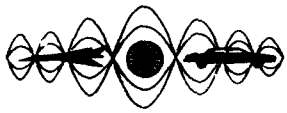

SECOND INTERNATIONAL CONGRESS ON
RECENT DEVELOPMENTS IN AIR- AND
STRUCTURE-BORNE SOUND AND VIBRATION
MARCH 4-6, 1992 AUBURN UNIVERSITY, USA

TOOL FAILURE DETECTION USING VIBRATION DATA

T.N. Moore
Associate Professor
Department of Mechanical Engineering
Queen's University
Kingston, Ontario, CANADA

J. Pei
Research Engineer
Technical Services Division
Stelco
Hamilton, Ontario, CANADA

ABSTRACT

This paper investigates the possibility of using vibration signals to detect failure of a multi-insert face mill. Tests were performed using a three-insert face mill to machine a standard workpiece. Cutting inserts with known amounts of edge fracture or wear were used, in various combinations, during the milling process. The resulting vibration signals, obtained both on the workpiece and the clamping fixture, were analysed to determine both the type and severity of insert failure that can be recognized using various signal analysis methods. It is shown that both edge fracture and wear can be detected, albeit with varying degrees of confidence.

INTRODUCTION

A major component of any effort to develop intelligent and flexible automation systems must be the concurrent development of automated, diagnostic systems to handle machinery maintenance and process control functions. In the short term such systems promise major gains in productivity and product quality. In the longer term, such diagnostic systems are one of the enabling technologies for the "lights out" factory.

An important element of the automated process control function is the real-time detection of cutting tool failure, including both wear and fracture mechanisms. The ability to detect such failures "on-line" would allow remedial action to be undertaken in a timely fashion, thus ensuring consistently high product quality and preventing potential damage to the process machinery. Of all the metal removal processes employed in industry, by far the most prevelant are those of drilling and milling.

A number of researchers [1,2] have investigated the potential for on-line diagnosis of drill failure (particularly drill breakage) and several commercial systems are, in fact, presently available.

However, far less emphasis has been placed on the real-time detection of milling cutter failure. For this reason the present study will focus on milling operations, particularly that of face-milling.

The basic premise of any automated, real-time tool condition monitoring system is that there exists either a directly measurable, or a derived parameter, which can be related to advancing tool wear and/or breakage. Obviously the most desirable monitoring system would be capable of detecting both types of failure successfully.

In the ideal case, the system should be able to detect levels of wear well below those at which the tool would have to be replaced, and should also be sensitive to relatively small changes in the level of wear. The latter characteristic would provide the system with the potential to "trend" the

wear pattern and predict the amount of useful life left in the tool (allowable wear limit reached).

With respect to tool fracture, the system should be able to detect both small fractures, "chipping" phenomena, and catastrophic failure of a tool. Although prediction of such failures would be desirable, it is problematic whether this is a practical goal, at least in the near future. The number of variables which determine the actual occurrence of tool fracture together with their complex interactions, and in many instances their underlying stochastic nature, make reliable prediction capabilities, at best, a long-term prospect in tool monitoring systems.

A number of parameters have been studied to determine their suitability as indicators of cutting tool failure including cutting forces [3,4], spindle motor current [5], acoustic emissions [6], and noise [7]. These methods have achieved varying degrees of success.

An additional parameter which has a number of practical advantages is vibration. Accelerometers, the transducers most often used for the vibration measuring task, are small, rugged, reasonably inexpensive, and easily mounted near the cutting process. In addition, they are available with various sensitivities and frequency response ranges.

Research carried out by Mehta, Pandey and Chakravarti [8] and Grieshaber, Ramalingam and Frohrib [9] has indicated that vibration signals certainly could form the basis of a tool condition monitoring system for face-milling operations. However, this work was carried out for a single-tooth mill which is not particularly representative of the multi-insert face-mills actually employed in industry.

OBJECTIVE

The objective of the present study, then, is to investigate the possibility of using vibration signals generated during interrupted face-milling to detect tool failure on multi-insert milling cutters.

This paper will report on the methodology and initial results of cutting tests employing inserts with known degrees of wear or breakage. Preliminary analyses of these signals in the time and frequency domains will also be presented. The results of more involved analyses and the development of strategies for automated recognition of these failure signals will be presented in future work.

METHODOLOGY

The experimental studies were carried out using a 3hp vertical milling machine. The cutting tool was a 3.81cm diameter, three insert, face-mill employing Carboloy TPG-322E grade 370 tungsten carbide cutting inserts. The "standard" workpiece was a mild steel plate with a length of 30.5cm, a height of 15.2cm, and a width of 1.3cm.

While cutting, the mill traversed the length of the workpiece performing an interrupted, symmetric cut. See Figure 1. The actual cutting conditions used are shown in Table 1.

The vibration generated during milling was measured at two locations: on the workpiece itself, and on the workpiece clamp (the more practical location from an industrial application point of view). The location of each accelerometer and its measurement axis is shown in Figure 2. The vibration signals were tape recorded for later analysis in the laboratory.

Recognizing that changes in the structural dynamic characteristics of the machine-tool-workpiece system (MTWS) would also result in changes to the vibration signal generated during milling, it was decided to minimize this effect as much as possible during the cutting experiments. This was done by fixing the three dimensions shown in Figure 3. Thus the tool-spindle projection, H1, the height of the table above the machine base, H2, and the height of the workpiece above the clamp, H3, were kept fixed during each cut. This approach is consistent with the "real life", high volume, production machining situation since, in this instance, the structural dynamic characteristics of the MTWS would not be expected to change significantly during the milling cycle on each new (nominally identical) workpiece.

Since it was desired to determine the potential for recognizing both wear and fracture failures of the milling inserts, two sets of tests were run.

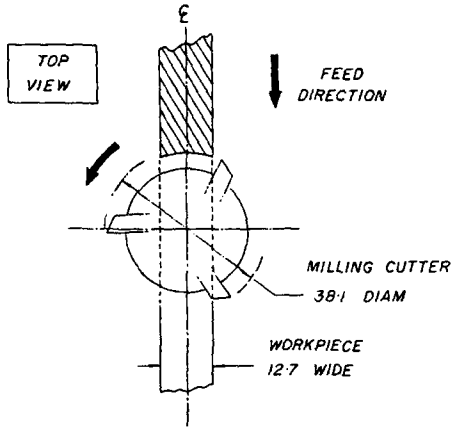

Figure 1. Schematic of interrupted symmetric milling cut.

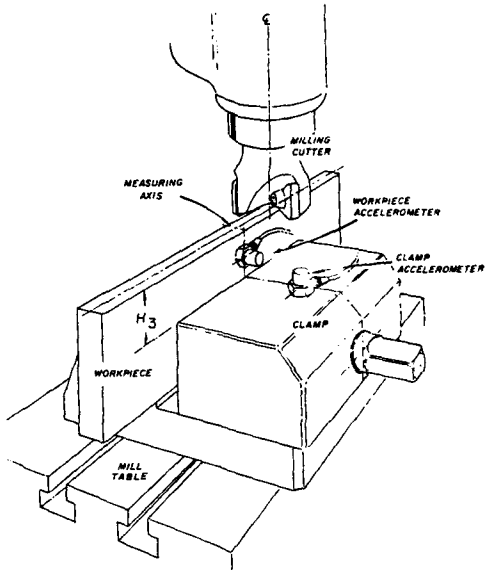

Figure 2. Test set-up

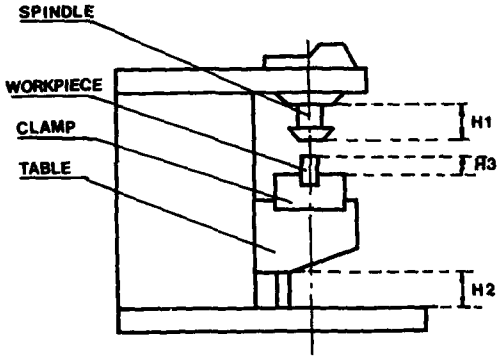

Figure 3. Dimensions fixed during all milling tests.

Table 1. Cutting conditions used in milling tests.

Depth of Cut:	1.0mm
Fee Rate:	0.18mm/tooth
Cutting Speed:	180m/min.
Engagement Angle:	39.8°

The first series of tests consisted of milling cuts made using various combinations of worn and sharp inserts in the three-insert cutter. The worn inserts were obtained by machining a "wear block" under very light, and non-interrupted, machining conditions, thus achieving a slowly increasing amount of wear (flank wear on the insert) with minimal chance for edge chipping. If chipping did occur on an insert it was discarded. Once the desired flank wear had been obtained, the insert was put aside to be used subsequently in the actual interrupted face-milling tests performed on the standard workpiece.

In the second series of tests milling cuts were made using various combinations of "fractured" and sharp inserts in the three-insert cutter. Due to the difficulty in obtaining controlled amounts of edge fracture during normal machining operations, it was decided to simulate fracture of the insert using electrical discharge machining to remove a controlled amount of the insert cutting edge. This is shown in Figure 4. The dimension, L, is used in this study to quantify the magnitude of the edge fracture.

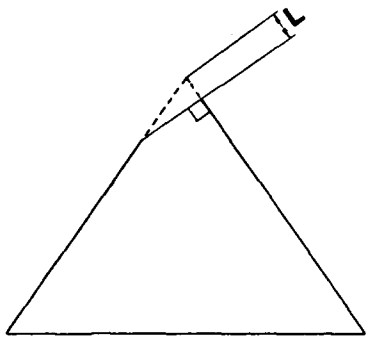

Figure 4. Simulation of insert fracture.

Table 2. Summary of failure dimensions.

mm / Insert	A	B	C	D	E	F	G	H
Dimension of Fractured Inserts	0.13	0.26	0.39	0.52	0.65	0.78	0.91	1.04
Dimension of Worn Inserts	0.13	0.26	0.39	0.52	0.65	0.78	-	-

Table 3. Milling cutter configurations.

Insert / Configuration	No. 1	No. 2	No. 3
G1	Sharp	Sharp	Sharp
G2	Failed	Sharp	Sharp
G3	Failed	Sharp	Failed
G4	Failed	Failed	Failed
"Failed" indicates either worn or fractured, as appropriate			

Table 2 summarizes the magnitudes of wear and fracture used in the experiments. For each of these values, four cutter configurations were used, as shown in Table 3. It should be noted that for those tests in which more than one "failed" insert was used (i.e., G3 and G4), the inserts always had the same failure dimensions.

To keep track of a particular insert, individual insert pockets on the milling cutter body were permanently identified as "1", "2", and "3", in sequential order. Thus the insert mounted in pocket 1 was subsequently identified as Insert No. 1, etc. In those tests where only one "failed" insert was used, it was always placed in pocket 2. In those tests where two "failed" inserts were present, they were always mounted in pockets 1 and 2.

RESULTS

Although measurements were made both on the workpiece and on the clamp, only the latter will be presented in this paper. The measurements made on the workpiece were generally of greater magnitude and of slightly different spectral character, but indicated the same trends as those from the clamp location. For this study the analyses were always undertaken using that portion of the vibration signal generated during the middle third of the cutting cycle.

Time Domain Analysis

Fractured Inserts. Figure 5 shows typical acceleration level versus time histories. The notation along the time axis indicates the instant at which the designated insert engages the workpiece.

Figure 5(a) is for the case of three sharp inserts. Note that the engagement of each insert in the workpiece is clearly evident and that all engagements share similar characteristics, although they are by no means identical. This is consistent with recent work published by Johnston, Richter and Spiewak [10] which provided strong evidence that individual inserts on multi-insert cutters can have significantly diverse properties. Generally, however, the case of three sharp inserts would be easily recognizable from the data shown in Figure 5(a).

Figure 5(b) shows the resultant acceleration signal for the combination of two sharp inserts and one insert with a 0.26mm fracture. The sharp inserts produce signals consistent with those shown in Figure 5(a) while the fractured insert produces a significantly different output. The reduced output level for the fractured insert is a result of the much smaller depth of cut associated with this insert. Also, the rather higher vibration levels

associated with the insert following the fractured insert is apparent. The much higher vibration level associated with the insert's disengagement from the workpiece is particularly noticeable. These features are due to the increased "effective" depth of cut associated with this insert.

The results for other magnitudes of fracture and numbers of fractured inserts are basically the same. The presence of a fracture is readily detectable. It would seem from the time domain data available, that the use of either an "envelope detection" or a "threshold crossing" scheme would provide the ability to automate the detection of tool fracture in a multi-insert milling operation. However, it is not yet clear whether the time domain signal, on its own, can be used to reliably classify the actual magnitude of the fracture. This work remains to be done.

Worn Inserts. The acceleration-time histories for the worn inserts do not, in general, produce the noticeably different engagement signals evident in the case of fracture. However, by processing the data in a slightly different manner it is possible to detect evidence of tool wear.

Figure 6 shows the amplitude probability density (APD) for several tool conditions. This distribution shows the percent of time a given level was present within the sample period. The data shown is for eight ensemble averages.

Figure 6(a) is for three sharp inserts. Note the essentially symmetrid distribution. For the combination of two sharp inserts and one with 0.65mm flank wear, see Figure 6(b), the APD is skewed to the left and its peak value is also shifted noticeably from its position for three sharp inserts. Figure 6(c) shows the results for three inserts with 0.65mm flank wear. In this case the peak has decreased and shifted to the left and broadened significantly.

It thus seems possible that insert wear could be detected using such features as the location of the peak in the APD, the magnitude of the peak, and the area under specific segments of the distribution. This technique would also seem to hold promise for fractured inserts.

Frequency Domain Analysis

Frequency spectra were obtained for the various tool conditions. All spectra were generated using eight ensemble averages and were calculated over a bandwidth of 0 to 20kHz using 800 lines of resolution.

In many cases it was observed that the level of the spectral peaks within the the frequency range 12 to 18kHz was affected by the tool condition. However a review of all the available spectra data indicated that this change in spectral level did not always occur and that the change which did occur was not consistently related to the known change in insert condition. That is, an increase in fracture dimension, or wear, did not always result in a consistent increase (or decrease) in a particular frequency band. Thus, although such frequency spectra may well provide some indication of tool failure under most conditions, it seems very unlikely that

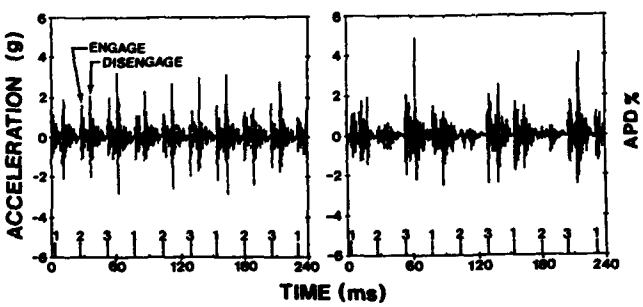

Figure 5. Time domain data - insert fracture.

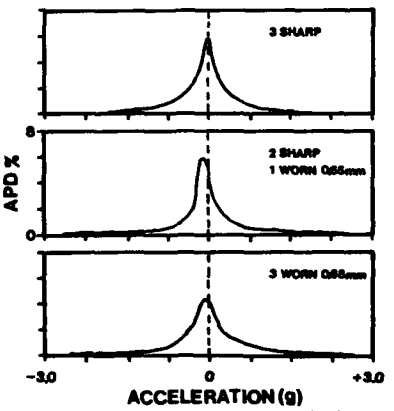

Figure 6. Amplitude probability density - insert wear.

they would ever be able to provide a reliable indication of the particular magnitude of the failure.

It was recognized that one reason for such inconsistent results could be the lack of synchronous averaging when acquiring the data signal to be frequency transformed.

To circumvent this problem an external trigger system was built. It generated trigger pulses which were keyed to the engagement of each of the three inserts with the workpiece. The trigger pulses generated for each insert were recorded on separate tape tracks. In this manner a given pulse track could be used to acquire the vibration data associated with a specific insert engagement and to ensure that the vibration signal was completely and consistently captured within the data window of the FFT analyzer. All the frequency spectra discussed in this section employ the synchronous averaging technique.

Fractured Inserts. Figure 7 presents an example of the synchronously averaged spectra obtained for the combination of one fractured and two sharp inserts. In this case Insert 2 was fractured and the figure presents the spectra obtained for each of the eight fracture magnitudes tested, ranging from 0.13 mm to 1.04 mm. Recall that due to the use of synchronous averaging, the spectra shown in Figure 7(a) (triggered on Insert 1 engagement) are obtained from the vibration signal generated only by Insert 1 engagement. In the same manner, Figure 7(b) represents only the Insert 2 vibration signal and Figure 7(c) represents only the Insert 3 vibration signal.

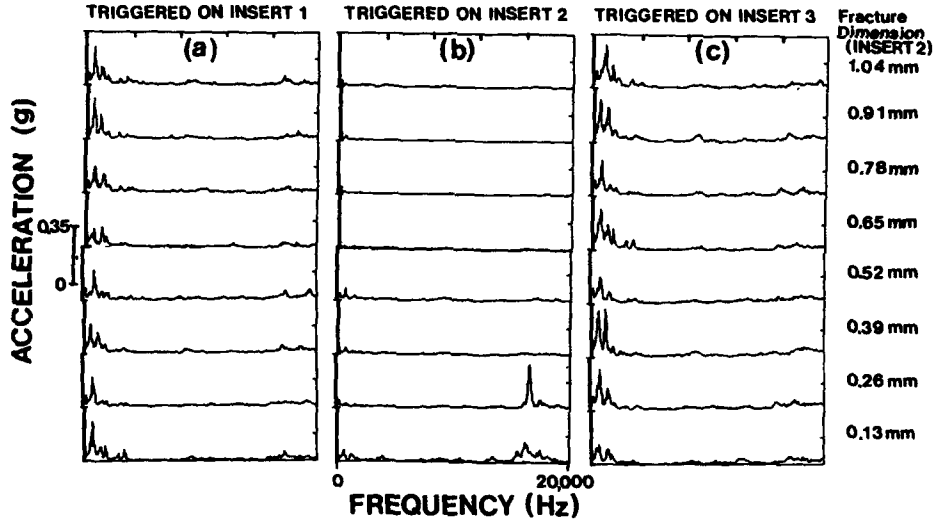

Figure 7. Frequency domain data - insert fracture.

Comparing the results presented in these figures, the presence of insert fracture is readily apparent. The spectra associated with the fractured insert are significantly different from those obtained from the two sharp inserts.

Interestingly, for small fracture dimension (0.13mm and 0.26mm) the spectral magnitude increases in the range 15 to 18kHz. This is likely the result of the specific insert geometry causing significantly more energy to be generated in the cutting zone at these high frequencies. Such frequencies are known to be associated with metal deformation/shearing processes. The combination of an increase in energy a these high frequencies and a reduction in energy level at lower frequencies, could serve as a very sensitive indicator of insert "chipping" (loss of a small amount of the cutting edge).

The spectra for Insert 1 and Insert 3 (both sharp) share the same general characteristics. However since Insert 3 follows Insert 2 (the

fractured Insert) in the cutting cycle (see Figure 5), and thus has a greater effective depth of cut than Insert 1, the spectra associated with Insert 3 have generally greater magnitude than for Insert 1.

The results for the combination of two fractured and one sharp insert are similar, with the fracture condition readily apparent. The distinct differences between the "sharp" and "fractured" spectra leave little doubt that the presence of fracture can be reliably detected. However, the question remains whether a method can be found to use this data to reliably quantify the magnitude (determine the severity) of the fracture.

Worn Inserts. Figure 8 presents the results obtained for the combination of two worn and one sharp insert. To begin, notice that the frequency spectra associated with the sharp insert, Figure 8(c), remain consistent with those seen earlier during the fracture tests (see for example Figures 7(a) and (c)). The sharp insert spectra are also basically unchanged for increasing wear dimensions on Inserts 1 and 2.

The worn insert spectra are noticeably different from the sharp insert spectra. The worn insert spectra decrease in magnitude at lower frequencies (0 to 4 kHz) with increasing flank wear, and tend to increase in magnitude at the higher frequencies (15 to 18kHz) with increasing wear. Thus it would seem likely that such spectral data could be used not only to provide an indication that flank wear is present, but also the relative magnitude of that wear.

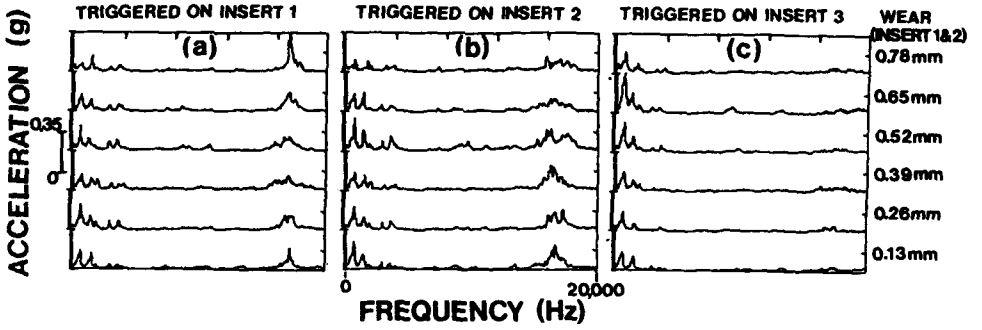

Figure 8. Frequency domain data - insert wear.

Quantitative Fault Features. The results presented earlier indicate that both insert fracture and wear could be recognized from changes in the spectral data associated with insert engagement vibration signals. If such a technique were to be applied in an automated (computer controlled) diagnostic system it would be necessary to obtain quantifiable "features" associated with these spectra, that could then be manipulated by the computer in such a manner as to provide a decision making mechanism.

One such "feature" might be the area under the spectrum within a particular range of frequencies. The change in this area (or areas, if more than one range of frequencies is employed) could then be related to the wear (or fracture) dimension on the insert.

For this particular exercise it was decided to limit the features obtained to the area under the spectrum within the 15 to 18 kHz frequency range. This was called the Wear Identification Area (Fracture Identification Area for the case of fracture). Figure 9 shows the Wear Identification Area (WIA) curve that results when using the average of the WIA values obtained for the wear test series described in this study.

The average WIA curve shows a relatively rapid increase in value until approximately 0.5mm flank wear (at which point the WIA has reached approximately three times the value for a sharp insert) after which it begins to decrease. This type of relationship could be used by an automated diagnostic system to quantify the magnitude of flank wear present on a given insert.

Of course it may well be possible to enhance the reliabiliity of such a

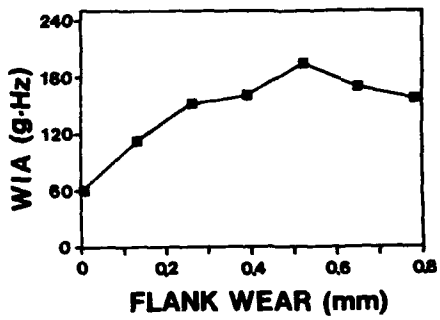

Figure 9. Average WIA as a function of insert wear.

system by employing WIA values based on additional frequency ranges (such as 0 to 4 kHz). The Fracture Identification Area (FIA) curve could be generated and used in a similar manner.

CONCLUSIONS

This paper has presented preliminary results from a study undertaken to determine if vibration signals could be used to detect the failure (edge wear and fracture) of cutting inserts on a multi-insert face milling cutter.

It was shown that evidence of both tool fracture and flank wear can be found in both time and frequency domain analyses. However, it is also noted that when employing the simple analysis methods described in this paper, it is not possible to reliably determine the actual magnitude of the tool failure nor to distinguish between the type of failure (wear or fracture) that has occurred.

Future work will attempt to identify processing methods which produce feature vectors capable of providing both quantitative measures of tool failure and unambiguous indication of the type of failure.

REFERENCES

1. Braun, S. et. al., "Signature Analysis Applied to Drilling", ASME J. of Mechanical Design, Vol. 104, pp. 258-276, 1982.
2. Moore, T.N. and Reif, Z.F., "Detection of Tool Breakage Using Vibration Data", Society of Manufacturing Engineers, Manufacturing Engineering Transactions, pp. 45-50, 1985.
3. Altintas, Y., Yellowley, I. and Tlusty, J., "The Detection of Tool Breakage in Milling Operations", Journal of Engineering for Industry, Vol. 110, pp. 271-277, 1988.
4. Richter, F. and Spiewak, S.A., "A System for On-Line Detection and Prediction of Catastrophic Tool Failure in Milling", Proceedings of NAMRC XVII, pp. 137-143, 1989.
5. Matsushima, K., Bertok, P. and Sata, T., "In-Process Detection of Tool Breakage by Monitoring the Spindle Current of a Machine Tool", ASME Winter Annual Meeting, Measurement and Control for Batch Manufacturing, pp. 145-154, 1982.
6. Diei, E.N. and Dornfeld, D.A., "Acoustic Emission Sensing of Tool Wear in Face Milling", ASME J. of Engineering for Industry, Vol. 109, pp. 227-233, 1987.
7. Lee, L.C., "A Study of Noise Emission for Tool Failure Prediction", J. Machine Tool Design and Research, Vol. 26, No. 2, pp. 205-215, 1986.
8. Mehta, N.K., Pandey, P.C. and Chakravarti, G., "An Investigation of Tool Wear and the Vibration Spectrum in Milling", Wear, Vol.91, pp. 219-234, 1983.
9. Grieshaber, D., Ramalingam, S. and Frohrib, D., "On Real-Time Tool Fracture Monitoring in Milling", Proceedings of NAMRC XV, pp. 477-484, 1987.
10. Johnston, C.M., Richter, F. and Spiewak, S.A., " A Comprehensive Model of the Milling Process for On-Line Tool Condition Monitoring", Proceedings of NAMRC XVI, pp. 178-197, 1988.

SECOND INTERNATIONAL CONGRESS ON
RECENT DEVELOPMENTS IN AIR- AND
STRUCTURE-BORNE SOUND AND VIBRATION
MARCH 4-6, 1992 AUBURN UNIVERSITY, USA

PHOTOACOUSTIC METHOD APPLICATION QUALITY CONTROL OF ULTRACLEAN WATER

Aleksei M. Brodnikovskii, Vladimir A. Sivovolov
R&D Center "Praktik"
Institute of Electronic Machinery
Moscow 103498, Russia

ABSTRACT

The report is about laser photoacoustic device development and testing for ultraclean water organic pollutants used in microelectronics. The fourth harmonic Nd:YAG laser (energy in pulse 2 mJ) is used as a radiation source for optoacoustic signal excitation. The detection limit is about 20 ppb. Also the device can detect microparticles in liquids (one micron size and larger).

Organic pollutants water control is the very important problem from microelectronic technique point of view. Laser UV excitation fluorescent spectroscopy is one of the most sensitive method of control. But there is the whole number of organic compounds which have the low quantum fluorescent efficiency.

The laser device based on photoacoustic effect was developed for non-fluorescent pollutants control. When part of the laser radiation energy is selectively absorbed by pollutants the acoustic pulses are appeared in control medium registered by sensitive piezoceramic sensor. The fourth harmonic Nd:YAG laser is used as a radiation source. Pulse radiation energy is 2 mJ, wavelength is 266 nm, pulse duration — 15 - 20 ns.

The radiation is directed to thermostabilized photoacoustic cell through which tested water pumped.

The cell's construction permits to register photoacoustic and fluorescence signals simultaneously (set-up is shown on Fig. 1). Acoustic pulses are detected by sensitive piezoelement ceramic PZT-19 cylinder. Further the electric signal is amplified by low noise preamplifier and amplifier (the total amplifier coefficient K = 2000). The boxcar integrator permits to suppress the outside acoustic noise and parasitic signal noise due to radiation absorption in cells windows.

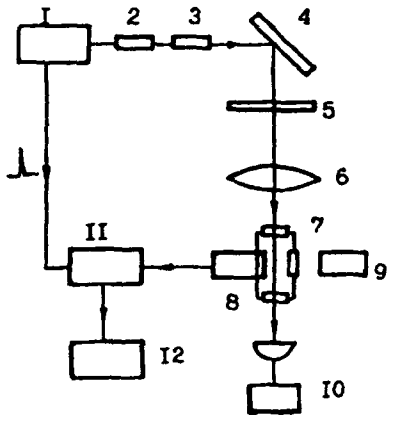

Fig. 1. Experimental set-up. 1 — Nd:YAG laser; 2, 3 — doubling crystals; 4 — selective mirror; 5 — filter; 6 — focusing lens; 7 — photoacoustic cell; 8 — piezoelectric element and preamplifier; 9 — fluorescense channel; 10 — power meter; 11 — boxcar integrator; 12 — plotter.

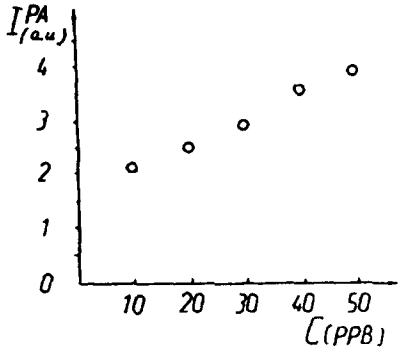

Fig. 2. Experimental results. PA signal vs concentration of added pollutant — KHP (dissolved in water). Zero level of PA signal corresponds with absorption of laser radiation in water.

This set-up can register the energy absorbed inside the cell as small us 2×10^{-7} J. To determine the limits for device analytic possibilities the measurements of PA signal dependance on KHP concentration were made.

The test results show the minimum detectable concentration of organic pollutants (KHP) is about 5 ppb with S/N=3 (Fig. 2). This set-up permits to detect the presence of microparticles (size more than 1 μm) in liquids and to conduct the photochemical dynamics reactions research work also.

SECOND INTERNATIONAL CONGRESS ON
RECENT DEVELOPMENTS IN AIR- AND
STRUCTURE-BORNE SOUND AND VIBRATION
MARCH 4-6, 1992 AUBURN UNIVERSITY, USA

ULTRASONIC MEASUREMENTS

Vinay Dayal

Assistant Professor, Aerospace Eng. and Eng. Mechanics Dept., and
Faculty Associate, Center for Non-Destructive Evaluation,
Iowa State University, Ames, Iowa, 50011.
USA

ABSTRACT

A travelling wave can basically be defined by two basic ultrasonic parameters: Wave Velocity, and Attenuation. The measurement of these parameters has been done by the conventional time-of-flight techniques. These techniques breakdown when the medium in which the waves are travelling are thin, or, the wave velocity is dependent on the signal frequency. All the limitations of the time-of-flight method can be eliminated by the use of Fourier transformation techniques. The development of a frequency based measurement and it's automation are described here, and results are presented to show the accuracy and precision of the method applied to metallic and composite materials of various thickness.

INTRODUCTION

The measurement of wave speed of an ultrasonic wave in materials has been performed for a very long time. The purpose, in general, has been Non-destructive Testing, and material properties evaluation. The velocity of the wave can be related to the stiffness of the sample [1]. There are many excellent techniques developed for the measurement of wave velocity and attenuation. Very briefly, the technique can be described as follows. An ultrasonic wave is passed through the material and the time taken for the wave to travel through the specimen is measured using an accurate oscilloscope. A series of pulses are obtained and the time interval between the two received pulses is twice the time taken for the wave to travel across the width of the specimen. An observer measures the time between any two peaks in the received signal and if the thickness of the specimen is known the wavespeed can be calculated by v = 2*(thickness)/time. The attenuation is measured by measuring the decreasing amplitude of a series of pulses. The limitations of this technique are: (1) the thickness of the specimen should be accurately known before the can be reliably measured, (2) though each and every point in the signal has gone through the specimen and hence obviously contains the information about the wave speed, only one point is picked disregarding the information contained at all other points, (3) human judgement is required so as to identify the exact location of the peak of the signal which introduces some subjectivity to the measurement. McSkimin[2] improved this technique by using a copy of the same wave translated in time so that the two pulses could be overlapped and a better match of the signals could be achieved. Papadakis[3] used pulse echo overlap for increasing the accuracy of measurements. But again this was more of a judgement measurement and works very well if the material is non dispersive and the pulse is not distorted as it passes through the specimen. If the material is dispersive, or the attenuation is dependent on the signal frequency, then a variation of the time-of-flight method, called tone-burst method, could be used. Here a burst of signal, about ten cycles long of a single frequency is used, but the measurement technique remains the same. This helps in identifying the frequency at which the wave velocity and attenuation are measured. The measurement of time-of-flight is possible only if the reflections from the two surfaces of the specimen can be clearly separated in time domain. This is obviously a big draw back and restricts the use of the ultrasonic methods to relatively thick samples.

Kinra and Dayal[4] developed a new technique for the measurement based on the Fourier transformation of the signal from time domain to frequency domain. The Fourier transformation of the first and the second pulse in the signal is obtained and the slope of the phase vs. frequency curve is calculated. Now, if the thickness of the specimen is known, the wave speed can be calculated and if the wavespeed is known then the thickness can be calculated. This technique can be used for automation if the thickness of the plate is constant and the changes in wave speed are to be measured. In cases where there the thickness is not known very accurately or if there is local variation in thickness, then the results will be in error. This technique, with a slight variation could be applied to samples where the individual pulses could not be separated, which has increased the range of measurement of the ultrasonic method.

The above mentioned methods worked if the thickness of the samples was measured beforehand. Now for the purpose of Non-Destructive Evaluation, where a large number of measurements are required, the above techniques become extremely slow. First, the thickness has to be measured at all the points where the velocity is required and then the ultrasonic measurement could be made. Dayal[5] has developed a new computer controlled variation of the Frequency domain technique where both the wave velocity and the thickness of the sample can be measured. The technique is based on the transformation of the signal from time domain to frequency domain and the whole process is possible only with the help of computers.

The development of the ultrasonic measurement of wave velocity by the Fourier Transformation technique and the automation are outlined here. These methods make the measurement precise and automated.

ULTRASONIC MEASUREMENT METHODS

Time of Flight method

A typical signal as reflected from an aluminum plate is shown in Fig.(1). The time, t, for a complete travel of the signal from the front surface to the rear surface and back is show on the figure. If the sample thickness, h, is known, then the wave velocity, v, can be written as,

$$v = 2*h/t \qquad (1)$$

Attenuation coefficient, k_2, is defined as the decrease in the signal amplitude as the wave travels through the sample. This decay is exponential and hence the signal amplitude is measured over a number of pulses and fitted to $\exp(-k_2 x)$ curve and an average value of k_2 is obtained.

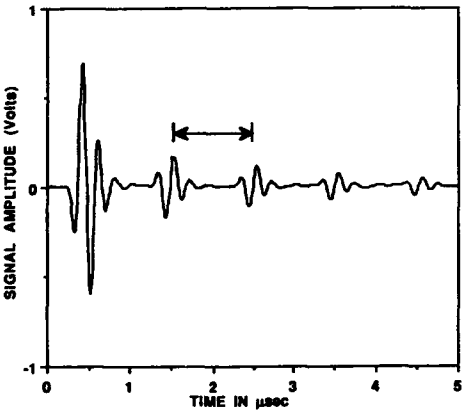

Fig. 1 Various pulses reflected from an aluminum plate of thickness 4.7 mm.

Frequency Domain method for thick samples

The technique works both for the reflection and transmission mode of wave propagation. Due to paucity of space, only the reflection mode of measurement will be described. Interested reader is referred to[4] for the transmission mode of measurement. In this mode of wave propagation, only one transducer

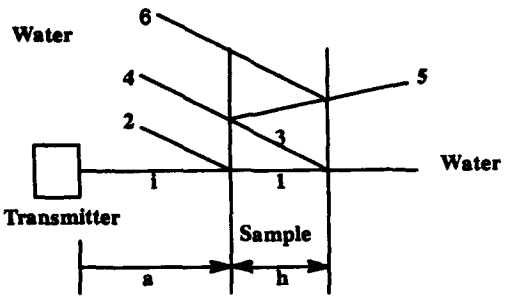

Fig. 2. Wave propagation through the specimen in reflection mode.

acts both as the transmitter and receiver. A typical experimental setup is as shown in Fig. (2).

Let $U_1(t) = f_0(\omega t - k_0 x)$ be the wave produced by the transmitter. If a is the distance of the front surface from the transducer, the reflection from the front surface of the specimen is,

$$U_2(t) = R_{01} f_0(\omega t - 2ak_0), \tag{2}$$

where ω is the circular frequency of the signal, $k_0 = \omega/c_0$ is the wave number in water, and c_0 is the wave velocity in water.

The reflection from the back surface is,

$$U_4(t) = T_{01}R_{10}T_{10} f_0(\omega t - 2ak_0 - 2hk), \tag{3}$$

where h is the plate thickness and k is the wavenumber in water.

In the above equations, the reflection coefficients R_{ij} and transmission coefficients T_{ij} are defined as,

$R_{ij} = (\rho_i c_i - \rho_j c_j)/(\rho_i c_i + \rho_j c_j)$, and

$$T_{ij} = 2\rho_i c_i /(\rho_i c_i + \rho_j c_j), \tag{4}$$

where subscript i defines the medium from which the wave is incoming and hitting the interface between medium i and medium j.

The Fourier transform is defined as,

$$F^*(\omega) = \mathrm{FFT}[f(t)] = \frac{1}{\sqrt{2\pi}} \int_{-\infty}^{\infty} f(t) e^{-i\omega t} dt \quad , -\infty < \omega < \infty , \tag{5}$$

Using the Fourier transformation, Eq.(2&3) give,

$$F_2^*(\omega) = R_{01}\ e^{-i2k_0 a}\ F_0^*(\omega), \tag{6}$$

$$F_4^*(\omega) = T_{01}R_{10}T_{10}\ e^{-i2k_0 a} e^{-i2kh}\ F_0^*(\omega), \tag{7}$$

Now a combination of Eq.(6) and Eq.(7) gives,

$$\left(F_2^*/F_4^*\right) = \frac{R_{01}}{T_{01}R_{10}T_{10}} e^{2ikh} \tag{8}$$

It should be noted that in the above equation the wave number k for the material can be real for

elastic materials and complex for linear viscoelastic materials. Thus Eq.(8) is valid for linear viscoelastic materials if the damping is small. Then k can be written as, $k = k_1 + i\,k_2$, and $k_2 / k_1 << 1$.

Now, equating the real and imaginary parts on the two sides of Eq.(8) one obtains,

$k_1(\omega) = -\phi/2h$, and

$$k_2(\omega) = \ln\left(F_2^*/F_4^*\right)/2h \tag{9}$$

here k_2 is the attenuation coefficient for the material.

These equations are useful if various pulses can be separated in time domain. The advantage over the time of flight is that the wave velocity and attenuation can be determined as a function of frequency. They breakdown if the sample width is such that the pulses cannot be separated in time domain. In that case following analysis can be performed.

Frequency domain method for thin composites

Referring to Fig.(2) the Fourier transform of pulses labeled (6) can be written as

$$F_6^* = T_{01}R_{10}^3T_{10}\, e^{-i2k_0a}e^{-i4kh}\, F_0^*(\omega), \tag{10}$$

Since pulse (2) cannot be separated a new reference pulse is obtained. This is done by replacing the thin sample by a thick coupon with the front surface precisely at x=a. The Fourier transform of this reference signal then is,

$$F^*(\omega) = R_{01}\, e^{-i2k_0a}\, F_0^*(\omega), \tag{11}$$

The series of pulses 2,4,6,.... are added as follows,

$$G^*(\omega) = F^*(\omega) + T_{01}R_{10}T_{10}\sum_{m=1}^{\infty} R_{10}^{2(m-1)}F_0^*(\omega).e^{-i[2k_0a+m2kh]} \tag{12}$$

Now if

$$Z = R_{10}^2e^{-2ikh} \qquad \text{with} \qquad |Z| < 1 \tag{13}$$

$$\text{Then} \quad \frac{G^*}{F^*} - 1 = \frac{T_{01}T_{10}}{R_{01}R_{10}}\sum_{m=1}^{\infty} Z^m \tag{14}$$

Since $|Z| < 1$ and $(1-Z)^{-1} = 1 + Z + Z^2 + Z^4 \ldots \infty$, and if

$$\beta = \frac{R_{01}R_{10}}{T_{01}T_{10}}\left(\frac{G^*(\omega)}{F^*(\omega)} - 1\right) \tag{15}$$

one obtains $Z = \beta / (1 + \beta)$. The complex valued wave number, k, can easily be obtained from Z. This summation of the infinite series is easier done for the transmitted field and in that case the problem of the replacement of the block does not arise. In this case one can derive the following relation,

$$\frac{G^*(\omega)}{F^*(\omega)} = \frac{T_{01}T_{01}e^{-ih(k-k_o)}}{1 - R_{01}^2e^{-i2kh}} \tag{16}$$

This equation can be reduced to,

$$Z^2 + ZY - D_0 = 0, \tag{17}$$

where $Y = \dfrac{T_{01}T_{10}}{R_{10}Z_0}\dfrac{F^*(\omega)}{G^*(\omega)}$, $Z_0 = \exp(-ihk_0)$ and $D_0 = 1/R_{10}^2$

For the details of the solution of these equations the interested reader is referred to [4].

Simultaneous measurement of wave speed and Attenuation

The set up for this method is shown in Fig. 3. Here a reflector is placed at some distance at the back of the sample.

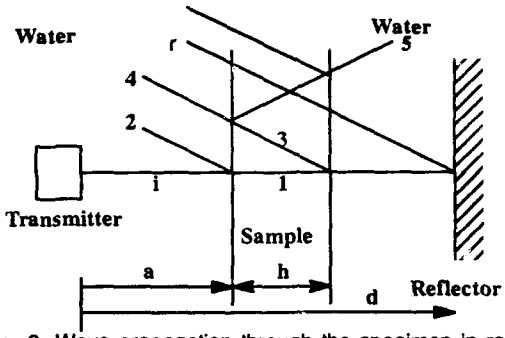

Fig. 3. Wave propagation through the specimen in reflection mode.

The Fourier Transform of the pulse reflected from the reflector surface and received by the transducer, when no specimen is present, is

$$F_d^*(\omega) = R_{02}\ e^{-i2k_0d}\ F_0^*(\omega), \tag{18}$$

The transform of the front surface reflection (2) , the back surface reflection (4) and the wave (r) which is transmitted through the specimen, reflected from the reflector and again travelling through the specimen is received by the transducer, are

$$F_2^*(\omega) = R_{01}\ e^{-i2k_0a}\ F_0^*(\omega), \tag{19}$$

$$F_4^*(\omega) = T_{01}R_{10}T_{10}\ e^{-i2k_0a}e^{-i2k_1h}\ F_0^*(\omega), \text{ and} \tag{20}$$

$$F_r^*(\omega) = R_{02}T_{01}^2T_{10}^2\ e^{-i2k_0(d-h)}e^{-i2hk_1}\ F_0^*(\omega). \tag{21}$$

A combination of Eqs. 18,19,20 and 21 gives,

$$\left(\frac{F_r^*}{F_d^*}\right)\left(\frac{F_2^*}{F_4^*}\right) = \frac{T_{01}T_{10}R_{01}}{R_{10}}e^{-2ihk_0} \tag{22}$$

Comparing the phase of both sides of Eq.22, the following relation is obtained,

$$\text{phase}\left[\left(\frac{F_r^*}{F_d^*}\right)\left(\frac{F_2^*}{F_4^*}\right)\right] = \phi_r = 2k_0h, \text{ or}$$

$$h = \frac{c_w}{4\pi}(\phi_r/f). \tag{23}$$

Now,

$$\left(\frac{F_4^*}{F_2^*}\right) = \frac{T_{01}T_{10}R_{10}}{R_{01}}e^{-2ihk_1} \tag{24}$$

The phase of both sides of Eq. 24 is compared and the wave speed can be calculated from.

$$c = \frac{4\pi h}{(\phi/f)} \tag{25}$$

RESULTS AND DISCUSSION

A special test specimen is prepared for implementing the various methods for thick composites for comparison purposes. The sample is as shown in Fig. 4.

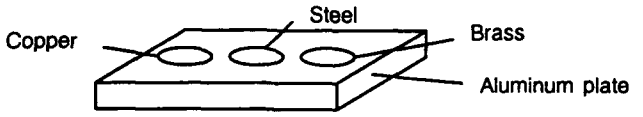

Fig.4 Test sample.

A 9.4 mm aluminum plate is prepared with holes drilled at three locations. These holes were then filled with three inserts of copper, brass, and steel. Thus, we have a sample with roughly the same thickness but very different materials. Various results obtained are shown in the Table.

Table I : *Comparison of three measurement methods.*

Technique *	Aluminum		Brass		Steel		Copper	
	c	d	c	d	c	d	c	d
1.	6.375	9.5	4.234	9.4	5.732	9.4	4.696	9.3
2.	6.372	9.5	4.241	9.4	5.713	9.4	4.704	9.3
3.	6.347	9.423	4.218	9.357	5.702	9.363	4.363	9.352

* 1. Time of Flight / physical measurement of thickness.
2. Frequency domain method / physical measurement of thickness.
3. Simultaneous measurement reflection mode
c: wave velocity in mm/μsec
d: specimen thickness in mm.

In this table the results are in the following order. First, the physical dimensions of the sample and the wave velocity as measured by the time of flight method, are recorded. Next, the wave velocities as obtained by the technique developed by Kinra and Dayal[3] and outlined above as the Frequency domain method for thick samples. The schematic of the method is as shown in Fig. 2. Note here that in this technique the experimenter has to provide the thickness of the sample and hence thickness is physically measured and wave speed is calculated by computer. Next, we present the results obtained by the reflection mode. The schematic of this setup is shown in Fig. 3. Here both the wave speed and thickness are estimated by the computer. The input for this technique is the wave speed in water which is accurately determined. The results for the computerized tests are averaged over 25 points and the standard deviation of the measurement for all the values was less than 0.1 %. It is seen that the technique developed here is capable of measuring the thickness and wave speed of the material quickly and precisely.

The technique described under the method for thin specimen, is applied to an aluminum plate. The wave speed was measured in an aluminum plate and the plate was gradually machined to reduce the thickness. The results are shown in Table II. In this table the first measurement is for an aluminum plate 2.807 mm thick with the tone-burst method. Then the same plate is analyzed by the method for the thin plates and the results are shown. Next, the plate is gradually machined to 0.258 mm and the results are presented. For comparison purposes the ratio of the sample thickness to the signal wavelength, λ, is also listed. It can be observed that even when the plate thickness is less than half of the wave length the method provides with an accurate wave speed. All the measurements were made ten times and the standard deviation of $\pm$.14 % shows the repeatability of the measurement.

Table II Results for a thin aluminum sample.

h mm	h/λ	c $mm/\mu sec$	σ/c %	Technique
2.807	4.4	6.3572	0.013	Tone Burst
2.807	4.4	6.3275	0.010	Thin sample
1.686	2.7	6.3461	0.040	Thin sample
1.001	1.6	6.3538	0.030	Thin sample
.613	0.96	6.3594	0.130	Thin sample
.258	0.40	6.3231	0.140	Thin sam{le

Sample : Aluminum Frequency : 10 MHz. Mode : Transmission

Now some results from the automation of the simultaneous measurement technique will be presented. A Stepped plexi-glass sample was prepared for testing and a line scan of the wave velocity and thickness is made. The results are as shown in Fig. 4. It is observed that the thickness of the sample is very precisely measured and the wave velocity remains constant over the entire measurement range.

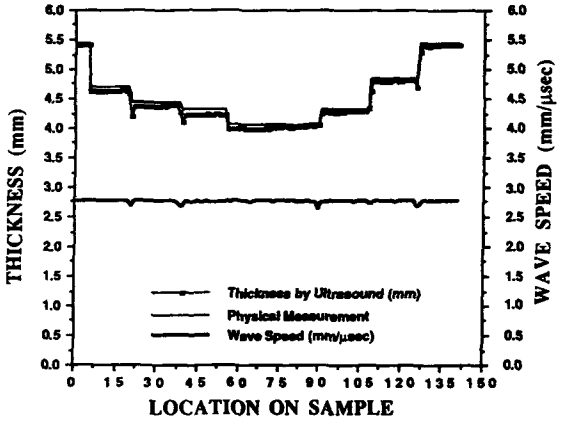

Fig. 4 Wave velocity and thickness scan of a stepped plexi-glass sample.

Next, a Graphite/Epoxy composite specimen was specially made for proving the usefulness of the technique. The specimen has a step variation in thickness in the middle. The specimen is as shown in Fig. 5, and was subjected to the computerized thickness-velocity scan. The results show that the technique presented here very efficiently measures the change in thickness while the wave velocity remains essentially constant. Notice also that the thickness scan shows some scatter of values at the edge. This is because when the transducer is on the step, part of the wave is reflected from the upper surface and part from the lower surface. This obviously cannot be differentiated and results in wrong values.

The limitation of the automated technique is that both the sides of the specimen should be accessible. In the reflection mode though only one transducer is needed on one side of the specimen, a reflection plate has to be provided. In transmission mode transducers have to be placed on both sides of the specimen. The advantages are the precision of measurement, speed of data collection and very specially, if the specimen has varying thickness, the technique will provide with the thickness and wave speed automatically.

CONCLUSIONS

The conventional time-of-flight method of measuring the acoustic parameters is good if the sample is thick and thickness is accurately known. Transformation of signal into frequency domain improves

the precision of the technique. If the sample is thin and the individual signal pulses cannot be separated then the frequency domain analysis is the only method of measurement. For a large number of measurements over a sample which is not accurately measured, the automated method of simultaneous measurement of wave velocity and thickness can be used. The use of computational methods increase the reliability and precision of the measurement.

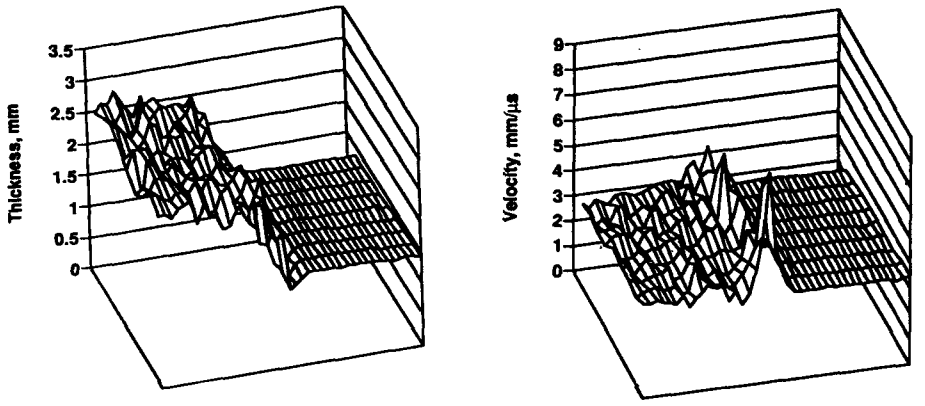

Fig. 5 Wave velocity and thickness scan of a stepped Gr.Ep composite sample.

REFERENCES

1. V.K. Kinra and V. Dayal, " Acoustic Methods of Evaluating Elastic Properties, or, Will the Real Youngs Modulus Please stand up ?" Manual on Experimental Methods for Mechanical Testing of Composites, Ed. R.L. Pendleton and M.E. Tuttle, published by the Society of Experimental Mechanics.
2. M.J. McSkimin, " Pulse Superposition method for measuring Ultrasonic Wave Velocity in Solids,"J. Acoust. Soc. Am. 33(1),12 (1961).
3. E.P. Papadakis, "Ultrasonic Phase Velocity by the Pulse-Echo overlap method incorporating Diffraction Phase Correction," J. Acoust. Soc. Am., 42(5), (1967).
4. V.K.Kinra, and V. Dayal, "A New Technique for Ultrasonic-Nondestructive Evaluation of Thin Specimens," Expt. Mech., 28(3), (1988).

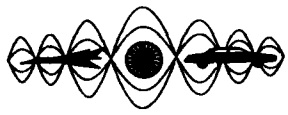

SECOND INTERNATIONAL CONGRESS ON RECENT DEVELOPMENTS IN AIR- AND STRUCTURE-BORNE SOUND AND VIBRATION
MARCH 4-6, 1992 AUBURN UNIVERSITY, USA

EVALUATION OF LAMINATED COMPOSITE STRUCTURES USING ULTRASONIC ATTENUATION MEASUREMENT

Peitao Shen and J. Richard Houghton
Department of Mechanical Engineering
Tennessee Technological University
Cookeville, TN 38505

ABSTRACT

The existence of delamination and porosity in laminated composite structures will degrade the strength of the structures. The detection of delamination can be easily obtained using ultrasonic C-scan or A-scan methods. But, the detection of porosity in laminated structures has been a difficult task for years, especially in production condition. This paper will analytically evaluate the current techniques used in industry, and develop accurate attenuation measurement methods for the evaluation of porosity. The test samples, which are used in the laminated structures of the German airbus by Textron Aerostructures, Inc, will be tested using ultrasonic C-scan and grid-based A-scan methods. The digitized waveforms are stored and analyzed using different attenuation measurement algorithms. The volume of porosity are calculated using digital imaging analysis. Finally, the correlation between ultrasonic attenuation and the volume fraction of porosity are calculated and analyzed.

INTRODUCTION

The existence of delamination and porosity in graphite-epoxy composite materials will degrade the strength of structures. The ultrasonic nondestructive inspection in aircraft wing structures made by graphite-epoxy composite materials is a required quality assurance procedure in the aircraft industry. The regular procedure is first to inspect the parts using ultrasonic C-scan through-transmission testing method. From the C-scan results, it is usually quite easy to locate the regions with delamination according to some recommended industrial C-scan testing standards. But, however, the detection and quantization of porosity is a difficult task. The difficulties of evaluating porosity come mainly from the following factors: (i) The lack of theoretical results about sound property in porous laminated composite materials; (ii) The lack of acceptable measurement techniques for porosity evaluations.

According to some reported literatures, the early study on the relationship between porosity and ultrasonic attenuation coefficient in isotropic materials was carried out by Gubernatis and Domany [1,2]. They developed approximate expressions for ultrasonic attenuation in porous media with finite-sized pores. Adler et al. successfully applied Gubernatis and Domany's results to the characterization of the porosity in aluminum alloy castings [3]. The porosities in aluminum castings are dominated by spherical pores with a Gaussian type of peak size distribution in the diameter of the pores. On the basis of Adler's experimental results and Gubernatis and Domany's theory, Nair and Hsu et al. made a study on the estimation of porosities using frequency-dependent attenuation measurements [4,5]. Instead of directly using Gubernatis and Domany's approximation, they developed an attenuation slope algorithm which was felt to be more suitable for the cylindrical pores which typically exist in composite materials.

Although laboratorial research has been applied to evaluation of porosity in graphite-epoxy composites, the understanding and testing techniques are still inadequate for application in industry. Based on the testing techniques currently used in industry, this paper will present practical ultrasonic attenuation measurement

algorithms, conduct ultrasonic attenuation measurement and porosity analysis experiments, and correlate the volume of porosity with ultrasonic attenuation coefficients.

ULTRASONIC ATTENUATION MEASUREMENT METHODS

The attenuation of sound in test materials may not have many direct interests to engineers. But, the change of attenuation is often a result of some physical or chemical change related to the property of the test materials. Thus, the use of ultrasonic attenuation measurement technique to characterize material property has become an important subject for NDE engineers. Papadakis did a series of research work on absolute attenuation measurement which focused on the beam diffraction correction [6]. Other research on quantitative attenuation measurement has been reported by Simpson et al. [7]. In this study, the investigation of attenuation measurement will be based on current measurement techniques used in industry. The equations for the calculation of ultrasonic attenuation using contact pulse-echo and through transmission testing methods will be introduced.

Ultrasonic attenuation can be defined as the rate of decay of mechanical radiation at ultrasonic frequency as it propagates through a material. For a plane wave, which should be the case in the far field measurement, the attenuated wave in space is expressed as

$$P=P_0e^{(-\alpha z)}, \tag{1}$$

where P_0 and P are the amplitudes of wave pressures at the beginning and the end respectively, and α is the attenuation of the wave travelling in the z-direction of the test materials. The attenuation α is measured in nepers per unit length or in decibels per unit length.

Figure 1 is a diagram of wave propagation indicating both pulse-echo testing and through transmission testing methods. The ultrasonic transducer first sends the longitudinal waves to medium 1 (delay line or water path), and then the waves propagate through medium 2 and medium 3. For through transmission testing method, medium 2 is usually the test specimen, medium 3 is usually the same as medium 1. Water is usually the couplant medium. In the case of contact pulse-echo testing with a solid delay line, medium 1 is the delay line and medium 3 is air which would not transmit ultrasonic wave.

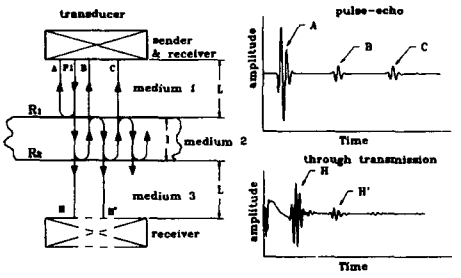

Figure 1. Diagram of wave propagation and A-scan presentation

Methods available for calculation of the ultrasonic attenuation based on the A-scan presentation is very diversified. One method used in industry only makes use of the echo B from the back-wall. In this method, the echo B_g is initially set at 80% of full scale on the display at some reference location which is assumed by the operator to be a good area without porosity. The attenuation at another location is calculated by comparing a new B_b value with the B_g value obtained at the reference location. For through transmission testing method, only the wave pressure H is used for attenuation measurement. In this section, equations for ultrasonic attenuation measurement using contact pulse-echo and through transmission testing methods will be introduced. The testing methods used in industry can then be evaluated analytically.

Ultrasonic Attenuation Measured by Pulse-echo Method

From the wave propagation relationship shown in Figure 1, the following equations are derived [6,8],

$$\alpha_2 = \frac{1}{2l} \ln\left[\frac{(1-R_1^2)}{R_1}\frac{A}{B}\right], \tag{2}$$

and

$$R_1 = \left(\frac{AC}{AC-B^2}\right)^{\frac{1}{2}}, \tag{3}$$

or

$$R_1 = \frac{A}{A_0}, \tag{4}$$

where α_2 is the attenuation coefficient in medium 2, A, B, and C are echoes defined in Figure 1, R_1 is the reflection coefficient between medium 1 and medium 2, and A_0 is the echo from the delay line bottom surface when it is not coupled to the test specimen. For normal attenuation measurements, Equation (3) is recommended to measure R_1. But in the case that the echo C is not visible, which is very possible in areas with the existence of porosity, Equation (4) is an alternative measure of R_1. Determining the experimental R_1 is extremely important for accurate attenuation measurement. In using the above equations, one must consider the possibility of a phase inversion at the reflection surface.

The attenuation given by Equation (2) is in nepers per unit length. It is common to transfer nepers into decibel (*1 nepers = 8.686 dB*). In the measurement of porosity vs. attenuation, one first calculates the attenuation in good areas (without porosity) α_g, and then the attenuation in bad areas (with porosity) α_b. The attenuation caused by porosity will be the difference of these attenuations.

Considering the change of reflection coefficient because of good and bad areas, the attenuation coefficients for good and bad areas are

$$\alpha_{2_g} = \frac{1}{2l} \ln\left[\frac{(1-R_{1_g}^2)}{R_{1_g}}\frac{A_g}{B_g}\right], \tag{5}$$

and

$$\alpha_{2_b} = \frac{1}{2l} \ln\left[\frac{(1-R_{1_b}^2)}{R_{1_b}}\frac{A_b}{B_b}\right]. \tag{6}$$

The difference between these is

$$\alpha_{2_b} - \alpha_{2_g} = \frac{1}{2l} \ln\left[\frac{(1-R_{1_b}^2)R_{1_g}}{(1-R_{1_g}^2)R_{1_b}}\frac{A_b B_g}{B_b A_g}\right]. \tag{7}$$

Equation (7) is an accurate expression for relative attenuation measurement. If one assumes that $R_{1b} = R_{1g}$ and $A_b = A_g$, then one has

$$\alpha_{2_b}-\alpha_{2_g}=\frac{1}{2l}\ln\frac{B_g}{B_b}. \tag{8}$$

Equation (8) is the expression for attenuation measurement only using the echo B, and is the approximate attenuation measurement method used in industry. It is obviously the most convenient method for the ultrasonic inspector.

Ultrasonic Attenuation Measured by Through Transmission Method

Similarly, from the wave propagation relationship shown in Figure 1, one can find [9],

$$H=P_1(1-R_1^2)e^{-\alpha_2 l}e^{-2\alpha_1 L}. \tag{9}$$

where α_2 is the attenuation coefficient in medium 2, R_1 is the reflection coefficient between medium 1 and medium 2.

Next, the question is to find the actual attenuation caused by porosity. From Equation (9), one can find the amplitudes for both good and bad areas

$$H_g=P_1(1-R_{1_g}^2)e^{-\alpha_{2_g} l}e^{-2\alpha_1 L}, \tag{10}$$

and

$$H_b=P_1(1-R_{1_b}^2)e^{-\alpha_{2_b} l}e^{-2\alpha_1 L}. \tag{13}$$

The difference of attenuation between bad and good areas is

$$\alpha_{2_b}-\alpha_{2_g}=\frac{1}{l}\ln\frac{H_g}{H_b}-\frac{1}{l}\ln\left(\frac{1-R_{1_g}^2}{1-R_{1_b}^2}\right). \tag{12}$$

In this equation, the first term on the right side of the equation is the measured attenuation using H, the $(\alpha_{2b}-\alpha_{2g})$ is the actual attenuation caused by porosity, and the second term on the right side is the error caused by changes in the reflection coefficient at different surfaces. In reality, the reflection coefficients change from specimen to specimen, the error caused by the reflection coefficients can be very significant. One solution is to determine an H_g measurement on each new surface before searching that surface. From Equations (7) and (12), one can see that the measured attenuation using contact pulse-echo and through transmission methods are theoretically not correlated.

If surface conditions are assumed to be the same for the both sides of the test specimen, from Equation (12), one can get

$$\alpha_{2_b}-\alpha_{2_g}=\frac{1}{l}\ln\frac{H_g}{H_b}. \tag{13}$$

This is really the equation for attenuation measurement using through transmission method. Thus, by referring to Figure 1, the procedure to calculate attenuation is: (i) measure H at good areas (without porosity), H_g; (ii) measure H at any other areas H_b; (iii) calculate attenuation using Equation (13). Under the condition of above simplification, the attenuation measured by through transmission method is half of that measured by pulse-echo method.

ULTRASONIC ATTENUATION MEASUREMENT AND POROSITY ANALYSIS

The ultrasonic A-scan tests using both contact pulse-echo and through transmission testing methods were carried out on some graphite-epoxy composite test specimens with different thickness. These specimens are constructed from one to four books. While, each book has a lay-up configuration of (0/45/-45/90/-45/45/0). The attenuation coefficients were calculated using both the developed accurate method and the industrial approximate method (only use the echo B). The ultrasonic C-scan testing was also conducted. The areas with indications of porosity were marked with grid patterns. The A-scan waveforms were digitized on each grid, and stored for attenuation analysis. The size and volume of porosity were analyzed by destructive cutting and imaging analysis. These results will then be correlated with ultrasonic attenuation coefficients.

Comparison of two ultrasonic attenuation measurement methods

In this test, the test specimens are those with different thicknesses but the same book lay-up. Because of the manufacturing process, the surface roughness of these specimen is different. Table 1 lists the surface roughness and specimen thicknesses of the test specimens.

Table 1. Test Specimens

No.	Thickness(mm)	Ra(um)
1	3.454	9.47
2	5.055	8.51
3	3.759	0.94
4	5.004	5.51
5	2.972	10.24
6	4.902	2.24
7	0.914	---

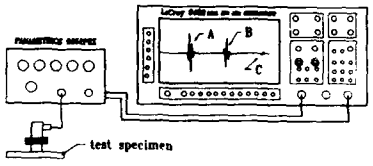

Figure 2. A-scan testing system

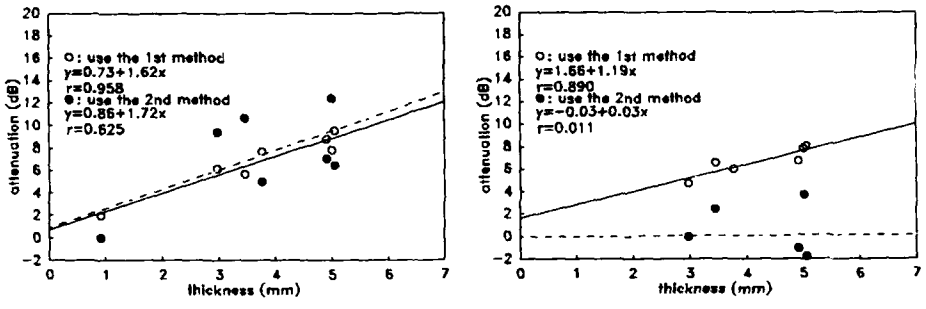

(a) 5 MHz transducer (b) 2.25 MHz transducer

Figure 3. Attenuation results from specimens with different thickness and surface roughness

Figure 2 is the testing system for ultrasonic attenuation measurement using the two methods. The RF waveform from the ultrasonic pulse/receiver (Panametrics 5052PRX) is displayed on the LeCroy digital oscilloscope. The echoes A, B and C shown in Figure 1 are recorded for ultrasonic attenuation measurement. Because the test areas selected for the comparison of attenuation measurement methods are defects-free, the echo C is possible to measure. Thus, Equation (3) can be employed in calculating reflection coefficients. In this test, because the attenuation is only caused by the change of specimen thickness, thus the attenuation for

good area is marked on the specimen with smallest thickness. Figure 3 is the attenuation measurement results from the test specimens with different surface conditions. The first method is an exact attenuation measurement method shown in Equation (7), and the second is an approximate method expressed by Equations (8). The first method provides good correlation results using ultrasonic transducers of 5 and 2.25 MHz. The correlation between attenuation and thickness using the second method is not good at all. One can conclude that the second method is very sensitive to the surface and coupling conditions, while the first method is more applicable to the different surface condition.

Ultrasonic C-scan Testing

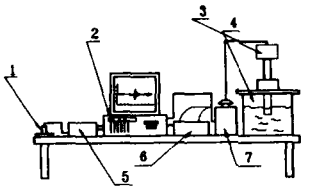

1. Transducer: Panametrics M201 5.0/0.25
2. PC-386 computer with C-scan and attenuation calculation program
3. X,Y,Z-axis Manipulator
4. Immersion tank
5. Panametrics 5052PRX50 Pulser/Receiver
6. HP Paintjet XL color printer
7. Motor controller

Figure 4. PC-based ultrasonic testing system

In a manufacturing environment quality assurance procedure of composite structure, the C-scan through transmission testing is first carried out covering all the accessible sections of the structures. The areas with delamination indications are first sorted out. Then for some suspicious areas, mostly the areas with existence of porosity, the A-scan testing is further manually conducted. The areas with porosity are marked. The final decision will be made according to the industry accept/reject criterion. So far, the identification of porosity is mainly made based on the attenuation corresponding to the echo B. The manufacturers' objective is to determine what the relationship is between ultrasonic attenuation and porosity.

In this laboratory study, the C-scan testing was performed to show the flaw distribution on the test specimens using a laboratorial PC-based ultrasonic testing system as shown in Figure 4. This system was consisted of a 100 MHz A/D board, Panametrics 5052X pulse/receiver, and Sonix ultrasonic testing software. Figure 5 shows the C-scan image of test specimen No.5.

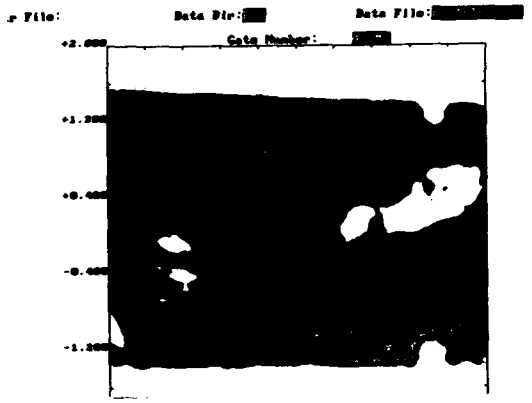

Figure 5. C-scan of test specimen No.5

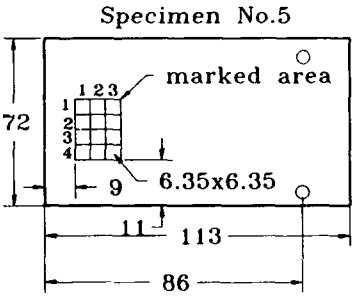

Figure 6. Marked area for porosity analysis

From the image shown in Figure 5, the darker regions indicate defects. The information about the defects in the transition region was not well defined. For this study, the area which shows porosity were verified by manual A-scan testing method, and marked as shown in Figure 6.

Ultrasonic A-scan Testing

The RF waveforms were digitized and stored from each grid of the marked area. As rule of thumb, if there exist echoes between the front and the back wall echoes, and also with the existence of the back wall echo, this indicates the existence of porosity. If the back wall echo disappears, this indicates the existence of delamination. Thus, the selection of the area for porosity analysis follows this rule. The contact through transmission testing were also conducted in the marked area. The ultrasonic attenuation measurement was calculated using the two methods for contact pulse-echo testing and through transmission method expressed by Equation (13).

Porosity Analysis

After the A-scan testing, the marked area shown in Figure 6 was first cut by a diamond blade, the area was cut into thin slices by a diamond wafer blade. These thin slices were first photographed at 5x magnification, and the resulting pictures were processed with a digital-imaging analysis system. The contour for each individual porosity cross section was traced automatically by the software, and then the area of each porosity was calculated. The volume fraction of porosity was obtained considering the volume of porosity in each slice and the volume of each grid. Figure 7 shows an example of porosity analysis.

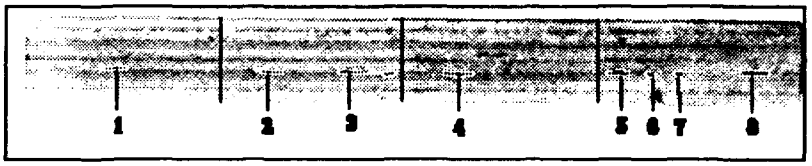

Porosity size (mm^2)			
1. 0.106	2. 0.080 3. 0.184	4. 0.082	5. 0.095 6. 0.045 7. 0.039 8. 0.132

Figure 7. An example of porosity analysis

Correlation between Ultrasonic Attenuation and Porosity

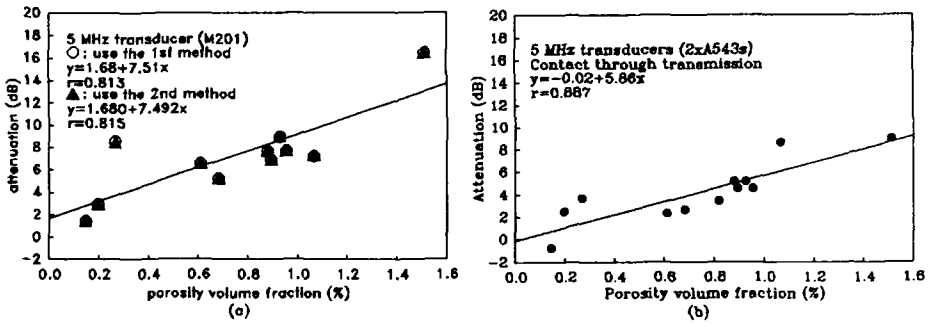

Figure 8. Ultrasonic attenuation vs. porosity volume fraction

The correlation between ultrasonic attenuation and porosity volume fraction was calculated using linear least square fit analysis. Figure 8 shows the results using contact pulse-echo and through transmission testing methods. In Figure 8(a), the results obtained from the two methods using Equations (7) and (8) are seen to be quite similar. The reason for this is that the reflection coefficient R_1 was calculated from Equation (4), and the good area for attenuation calculation was measured on the same test specimen. Thus, the surface conditions between the good and the bad areas are the same. This also indicates that the approximate method can produce good results if the test specimens have nearly the same surface condition. The correlation coefficients are shown in the figures as 0.815 and 0.887 respectively for the pulse-echo method Figure 8(a) and through transmission method Figure 8(b).

CONCLUSIONS

As a result of this study, the following conclusions can be made.

(i). The exact equations of attenuation measurement for pulse-echo and through transmission testing methods are derived. The result indicates that the conventional equations for attenuation measurement are approximations, and the relative attenuation measurements have a higher reliability using Equation (7) or (12).

(ii). The method expressed by Equation (8) is an approximate attenuation measurement method. Analytical investigation shows that it can provide good approximate if the reflection coefficients between the test point and the reference point are similar.

(iii). There exists a linear relationship between ultrasonic attenuation and porosity volume fraction. In using contact testing methods, the correlation coefficients obtained in this study are 0.815 and 0.887 using pulse-echo and through transmission testing methods respectively.

REFERENCES

[1] Gubernatis, J. E., E. Domany and J. A. Krumhansl, 1977, " Formal Aspects of the Theory of the Scattering of Ultrasound by Flaws in Elastic Materials", *Journal of Applied Physics*, Vol.48, No.7, pp. 2048-2811.

[2] Gubernatis, J. E. and E. Domany, 1983, " Effects of Microstructure on the Speed and Attenuation of Elastic waves: Formal Theory and Simple Approximation", *Review of Progress in Quantitative Nondestructive Evaluation*, D. O. Thompson and D. E. Chimenti, eds (Plennum, New York, 1983), Vol.2A, pp. 833-850.

[3] Adler, L., J. H. Rose and C. Mobley, 1986, " Ultrasonic Method to Determine Gas Porosity in Aluminum Alloy Castings: Theory and Experiment", *Journal of Applied Physics*, Vol.59, pp. 336-347.

[4] Nair, S. M., D. H. Hsu and J. H. Rose, 1989, " Porosity Estimation Using the Frequency Dependence of the Ultrasonic Attenuation", *Journal of Nondestructive Evaluation*, Vol.8, No.1, pp. 13-26.

[5] Hsu, D. K. and K. M. Uhl, 1987, "A Morphological Study Of Porosity in Graphite-Epoxy Composites," *Review of Progress in Quantitative Nondestructive Evaluation*, Vol.6B, pp. 1175-84.

[6] Papadakis, Emmanuel P., 1990, "The Measurement of Ultrasonic Attenuation," Ultrasonic Measurement Methods," *Ultrasonic Measurement Methods, Physical Acoustics XIX*, edited by R. N. Thurston and Allan D. Pierce, Academic Press, Inc., 1990, pp. 108-154.

[7] Simpson, W. A. and R. W. McClung, " Quantitative Attenuation Technique for Materials Characterization," Materials Evaluations, Vol.49, pp1409-1413.

[8] Lynnworth, L. C., 1973, "Attenuation Measurements Using the Pulse-Echo AB method, Without Multiple Echo Reverberations in Specimen," *Materials Evaluations*, Vol.30, pp. 6-16.

[9] Houghton, J. R. and P. Shen, "A Study on Porosity Content of Laminate Structures of German Airbus Using Ultrasonic Attenuation Measurement Method," *Technical Report: No. MCTR1191-02, to Textron Aerostructures, Inc, Tennessee Technological University*, October, 1991.

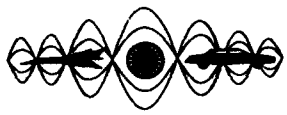

SECOND INTERNATIONAL CONGRESS ON
RECENT DEVELOPMENTS IN AIR- AND
STRUCTURE-BORNE SOUND AND VIBRATION
MARCH 4-6, 1992 AUBURN UNIVERSITY, USA

EXPERT SYSTEM FOR ULTRASONIC FLAW DETECTOR

A.N.Agarwal, S.C.Suri, M.S.Bageshwar
Central Scientific Instruments Organisation
S&M Centre, CSIR Complex, NPL Campus, Hillside Road
New Delhi-110 012
INDIA

ABSTRACT

Ultrasonic flaw detectors are being increasingly employed for non-destructive testing and inspection of materials, in wide ranging fields. Due to paucity of suitable expertise and infrastructure, instruments remain unattended, and become faulty, resulting in shut-downs, causing a drain on national economy. Effecient utilisation of instrumentation resources in a country is basic requirement for development of advanced techniques so as to contribute substantially for its technical, industrial, and economic growth. With latest research techniques being incorporated in design of sophisticated instruments, challanges of installation, operation, and repair can be met by adopting recent techniques like Artificial Intelligence/ Expert System, for equipment diagnosis and maintenance management. The paper discusses design of expert system which shall prove beneficial in enhancing equipment utilisation, substantially reducing shut-downs besides contributing towards development of human resources.

INTRODUCTION

Ultrasonic equipment are being extensively employed in non-destructive testing, study of material properties besides medical diagnosis and therapy. Due to rapid industrialisation of developing countries, there has been even more rapid increase in their applications in diverse fields of research, education, health care, and industry. Ultrasonic flaw detector is a sophisticated equipment, which permits wide coverage of non-destructive tests and thickness gauging in materials with the help of different types of probes. It is generally used to detect blows in castings, cracks caused by fatigue and flaws in metallic materials. It can also be utilised for assessing the physical and metallurgical characteristics of a material through measurements of velocity and its attenuation properties. Depending upon use, storage, environment, handling, stability of line voltage and life of components, instruments may go out of order during their normal operation. These instruments also need recalibration at regular intervals, so that their working do not deviate from set standards and uses. The techniques of installation, operation, maintenance and calibration of such instruments being relatively complex, skilled, and trained personnel are not available in sufficient numbers, especailly, in developing countries. As these instruments represent sizable investment, it is important to develop precision instrumentation techniques, so that wastage of limited national resources and draining of foreign exchange are avoided.

Computers have affected profoundly our life and their applications [1] are becoming indispensable in development of instrumentation techniques. For computer scientists, artificial intelligence (AI) represents an attempt to set up algorithmic principles for simulating thinking process of the brain, to develop some sort of general problem solving or human like intelligence behaviour. Expert system (ES) and knowledge engineering are

amongst the most important areas of application of AI. Applications of expert system include non-destructive testing and inspection, manufacturing, and optimal routing to fault-diagnosis. At various UNIDO workshops discussing instrument related problems, one of the important recommendations include development of expert system for fault-diagnosis, repair, and maintenance, so that suitable maintenance facilities and related human resources are available to meet challanges of advancing technology. The concepts of expert system act as a modern tool for efficient operation, maintenance, and fault-diagnosis of ultrasonic equipment [2]. Development of expert system is also helpful to have computer aided instruction packages for training of instrument operators and repair personnel.

EXPERT SYSTEM

The expert system is a branch of AI that makes extensive use of specialised knowledge to solve problems at the level of a human expert. An expert system is regarded as a computer programme that embodies the expertise of one or more experts in some domain and applies this knowledge to make useful inferences for user of the system [3]. It makes extensive use of specialised knowledge available from books, magazines, journals, instrumets manuals, and knowledgeable persons to solve problems, much more effecientiy, at the level of a human expert. An expert is a person who has expertise in a certain area, that is not known or avialable to most people. ES is often applied today to any system which uses expert system technology. This may include special expert system languages, programmes, and hardware designed to aid in the development and execution of expert system.

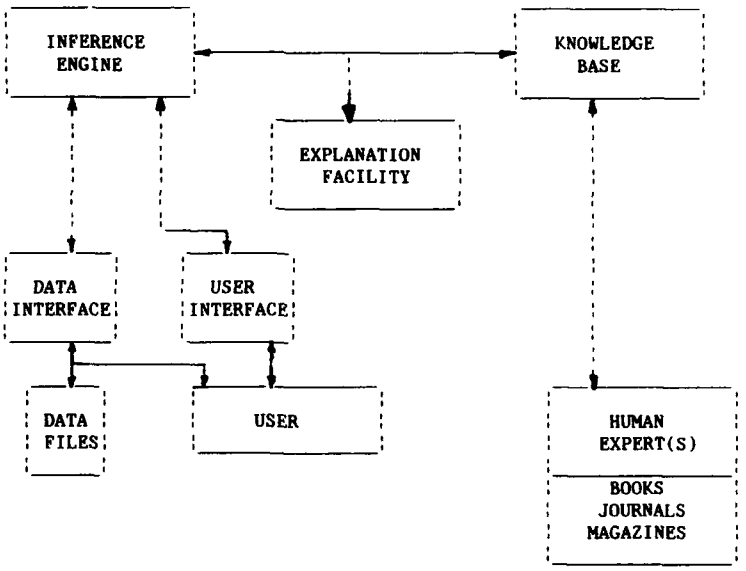

Figure 1--Expert system block diagram

The expert system consists of four main elements called ES-Shells :i) Knowledge base; ii) Inference engine; iii) Data interface; and iv) User interface. The basic concepts of a knowledge based expert system are shown in figure 1. The expert's knowledge about solving specific problems is called the knowledge domain and is entirely included within the problem domain. The knowledge of an ES may be represented in a number of ways. One commonly used method of representing knowledge is in the form IF, THEN type rules. A wide range of knowledge based ES have been built, now a days. The process of building an ES is called knowledge engineering, which refers to the acquisition of knowledge from a human expert or other sources and its coding in the expert system. Rule based system has

been preferred for our problem because rules and facts are input directly into the expert system. The procedural programming relates to a conventional programme starting at a point 'x1', and then a series of sequential procedures are defined, which upon completion give the answer at point 'x2'. The expert system starts by asking what is the answer at point 'x2' and then by examining the facts and rules in the knowledge base, it determines which data is required to derive the answer. The means by which the system carries out these operations is called the Inference engine.

As in most of expert sytems, in our case also, both data and user interface are one and same thing, since the user is required to input data after inspecting the sub-system/ equipment into expert system by answering its questions. This is termed fully Interactive system. However, sophisticated expert system is able to determine answers to many of their questions by accessing data stored on computer. Some of the important features [2] are i) increased availability; ii) multiple expertise; iii) reduced cost; iv) permanence; v) increased reliability; vi) explanation facility; vii) fast response; viii) steady, unemotional, and complete response at all times; ix) intelligent guide; and x) intelligent data-base. There is also indirect advantage as the knowledge being explicitly known, it can be examined for correctness, consistency, and completeness.

For development of an expert system, knowledge engineer first establishes contacts with the human expert(s) in order to explicit the expert knowledge, and then codes it explicitly in the knowledge base. The expert after evaluation gives a critique to knowledge engineer and process iterates until system's performance is judged to be satisfactory by the expert(s). It must be of high quality otherwise it may become prone to bugs. It is generally designed very different from conventional programmes, because the problem usually has no algorithmic solution but relies only on inferences and it must be able to explain its reasoning so that same can be checked. An explanation facility is an integral part of sophisticated expert system and may be designed to allow the user to explore multiple lines of WHAT, IF... type questions, called hypothetical reasoning and even translate natural languages into rules. Expert system has been very successful in dealing with real-world problems that conventional programming methodologies have been unable to solve, especially those dealing with uncertain or incomplete information. It is designed to have general charateristics [2] like i) high performance; ii) adequate response time; iii) good reliability; iv) understandable; v) flexibility; and vi) simple explanation facility. In a rule based system, knowledge can easily grow incrementally, so that its performance and correctness can be continually checked. Expert system has been applied to almost every field of knowledge and hundreds have been built and reported in computer journals, books, and conferences.

Basically, depending upon whether the problem is knowledge or intelligence intensive, suitable language can be choosen. Expert system rely, to a great extent, on specialised knowledge or expertise, to solve a problem and on a pattern matching within a restricted knowledge domain to guide. Now a days, dozens of languages are available and terminology includes tools, shells or integrated environments. Expert system language, in addition to its being a translator of commands written in a specific syntax, also provides an inference engine to execute statements of language. Primary considerations for selecting a language are portability, running time, convenience of access, ease of reading, ease of maintaining and updating, flexibility, interfacing with other languages, familiarity of the programmer with the language. The most commonly used languages in writing of expert system are LISP and PROLOG. These languages are symbolically oriented i.e., designed particularly to work with word symbols rather than numerical calculations and analytical algorithms. Other features are recursion and facility of dynamic memory allocation [4]. PROLOG, especially has a number of advantages for diagnostic systems because it is specially designed for logic expressions (IF/THEN), contains a special procedure for solving systems of logic expressions, and built-in backward chaining. It is more convenient and effecient to built large expert system with shells and utility programmes, specifically designed for their building.

We feel that scientists and engineers should write their own expert system i.e., special knowledge engineers are not required. The commercially available software packages (shells) and special languages LISP and PROLOG are unnecessary and even undesirable [4]. Most of us are conversant with a procedural high level language, such as FORTRAN, BASIC, PASCAL, or C. All of these do an excellent job on codifying expert systems. Features like recursion and dynamic memory allocation are available in PASCAL but for FORTRAN 77, these can be done quite easily by indirect means and using data management in the coding using linked list. Also, the engineer is an expert on the engineering procedure, as well as being specialist, or near specialist, in some phase of engineering. The engineer has an almost unique training and experience in intuitive decision making, which is the whole basis of expert system. Finally, engineers are highly

creative, and can cope with the creativity requirements of designing expert systems. The expertise, combined with the rigorous training in logical thinking that all engineers possess, make them uniquely well qualified to develop expert systems.

ULTFD EXPERT SYSTEM

The designed expert system is equipped with following four main knowledge base utilities:

1. Equipment knowledge utility (EK-Utility)
2. Test & auxillary equipment utility (TAE-Utility)
3. Equipment maintenance utility (EM-Utility)
4. Equipment fault-diagnosis utility (FD-Utility)

While entering ULTFD expert system, computer will display:

Utility	Code	Page No. *
Equipment Knowledge	1	
Maintenance	2	
Fault-diagnosis	3	
EXIT	4	

PLEASE ENTER DESIRE CODE @

and ask now to enter a desired code. On entering code 1, expert system starts displaying EK-text, page by page, on user intervention. One may quit a sub-utility or utility by using control commands. On completion or quit, page No. * will be again displayed on monitor. On entering code 2, the expert system asks user regarding availability of tools, test and measuring equipment, and chemicals required for maintenance of equipment with him. On positive response, expert system starts describing, step by step procedure for maintenance of the equipment. On pressing code 3, expert system first asks availability of items required for fault-diagnosis using TAE-utility. On positive response, a block diagram of electronic circuit of equipment will be displayed on video display unit (VDU). Expert system then asks user to measure various technical parameters at various test points of equipment. In response utilising internal knowledge base contained in FD-utility, it will suggest fault(s) on VDU. Again, expert system will instruct user to measure the parameters at various test points. On user feed-back, expert system will display the faulty components(s).

EK-utility

The utility of expert system provides user, detailed general operating instructions with video presentations, examples, precautions, and warnings, about working of the equipment. It consists of following fifteen EK-sub-utilities:

EK-1: General layout of the equipment
EK-2: Specifications/ technical data of equipment
EK-3: Accessories supplied with the equipment
EK-4: Operating controls, their function & location
EK-5: Installation procedure near test spot
EK-6: Adjustment of operating voltage at-site
EK-7: Fuses and their locations
EK-8: Connection of probes in various modes
EK-9: Principle of operation
EK-10: Adjustment of operating controls
EK-11: Preparation of test surface and precautions for optimum results
EK-12: Selection of probe for a particular application
EK-13: Operating procedure depending upon specific problem, preliminary controls setting and checks for optimum operation
EK-14: Flaw alarm, adjustment of gate position and width
EK-15: Inspection techniques

For example, EK-2 Sub-utility describes detailed knowledge about equipment parameters and functions viz., operating mode, measurement range, test frequency, accuracy, pulse repetition rate, sweep linearity, dead zone, pulse delay, calibrated attenuation, selective scale expansion, receiver gain, monitor gate position, monitor width, monitor level/ sensitivity, alarm indications, CRT, operating tempertaure range, dimensions and weight of the equipment. EK-4 Sub-utility describes function of equipment, monitor operating controls on front panel (25 Nos.) and side panels (left-2Nos. and

Figure 2--Flow chart for fault-diagnosis of ultrasonic flaw detector

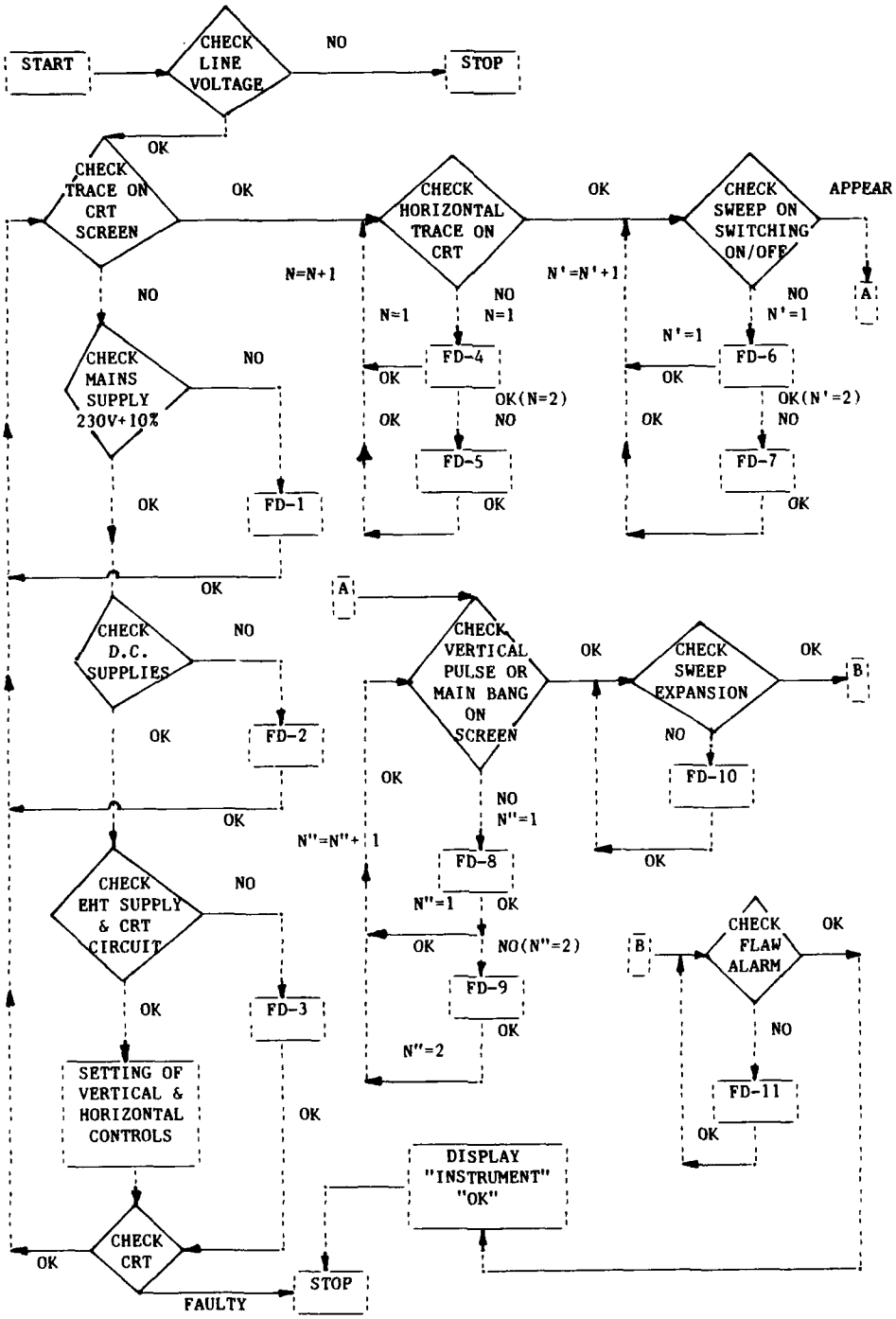

right-4Nos.). It also shows the broad view of each control knob individually and their location on the equipment. EK-8 Sub-utility describes connections of probes in single and double transducer mode. EK-12 Sub-utility describes efficient utilisation of straight, angular, and surface wave probes for particular application. It also instructs about availability of probe for immersion techniques used for testing of material of peculiar shape which otherwise is difficult to detect using either a straight or angular probe, or where test surface is rough and gritty. EK-15 Sub-utility explains inspection techniques for detection and thickness gauging of flaw, employing single and double transducer approach.

TAE-utility

This utility of expert system provides users, list of test and auxiliary equipment, tools, and chemicals with complete specifications/ technical details required for maintenance, as well as, fault-diagnosis of flaw detector. The list mainly includes digital and analog multimeters, two channel oscilloscope (20MHz), high tension test set, adjustable transformer (5V.....250V, 1A), signal generators, sine wave generator (0....12MHz), adapter board amplifier and trigger, recorder and amplifier dummy, steel references, stepped reference steel blocks, probes, screw driver set, pliers, and carbon tetrachloride.

EM-utility

This utility of expert system consists of five packages and provides detailed instructions alongwith video presentations regarding:

EM-1: Checking of cables, operating voltage, fuses, movement of controls, cleaning of joints, and removal of dust from equipment
EM-2: Preventive maintenance programmes
EM-3: List and location of PCB's
EM-4: Dismounting and assembly of PCB's
EM-5: Calibration of equipment

These packages describe step by step procedure by intervention with user, by asking questions from him. It also instructs him about various warnings and precautions to be observed at respective stages. As an example, EM-3 Sub-utility describes the most effective way of reducing the number of failures and increasing instrument useful life. It reduces breakdowns during operation by repairing minor faults before they give rise to serious troubles. It also stresses the advantage in maintenance of history sheets and maintenance schedules. EM-4 Sub-utility describes for the users, the systematic way of assembly and disassembly of various PCB's from chasis by using required tool(s) in a proper manner by observing instructions on monitor. Calibration of the equipment by taking measurements of standard samples with flaws at specified distances by using various control knobs is described in EM-5 Sub-utility.

FD-utility

For fault-diagnosis [5], the user should have good grasp of basic electronics, test and measuring equipment, and should be well conversant with the localising and pin-pointing the source of trouble. There may be many reasons for the trouble and to localise the fault, it is essential to eliminate the other sources in proper sequence by scientific experimentation and proper checks. It is known that faults due to component deterioration, dry solder, and intermittent contacts are difficult to diagnose and repair. By using test points voltage data and principle of operation of circuits, fault-diagnosis can be systematically carried out. FD-Utility helps users in fault-finding of the instruments. Brief flow-chart for fault-diagnosis is given in figure 2. It is mainly associated with following eleven sub-utilities:

FD-1: Fault-diagnosis of main supply
FD-2: Fault-diagnosis of power supplies (±100V, ±20V & 400V)
FD-3: Fault-diagnosis of EHT supply & CRT circuits
FD-4: Fault-diagnosis of clock circuit
FD-5: Fault-diagnosis of sweep amplification circuit
FD-6: Fault-diagnosis of unblanking circuit
FD-7: Fault-diagnosis of Z-axis amplification circuit
FD-8: Fault-diagnosis of main bang delay circuit
FD-9: Fault-diagnosis of transmitter, receiver, & TCG circuits
FD-10: Fault-diagnosis of selective/ sweep expansion circuit
FD-11: Fault-diagnosis of flaw alarm circuit

From flow chart, it is observed that if horizontal trace and sweep appear on CRT on switching ON/OFF, FD-utility bypasses sub-utilities FD-1 to FD-7. If, however, slope of

the sweep is not varying, but vertical pulse/main bang appear on screen, then fault lies in selective/ sweep expansion circuit and can be rectified by application of fault-diagnosis FD-10 sub-utility. Each FD-sub-utility, describes the detailed principle of operation of the specified circuit before proceeding to related fault-diagnosis.

These utilities based on block diagram of the equipment, cover following electronic circuits:

1) Power supply circuits (±10V, ±20V, ±100V & 400V)
2) EHT supply and CRT circuits
3) Horizontal and vertical shift circuits
4) Clock circuit
5) Sweep and unblanking circuit
6) Sweep amplification circuit
7) Z-axis amplification circuit
8) Main bang delay circuit
9) Transmitter circuit
10) Receiver circuits (I & II)
11) Time compensated gain circuit
12) Selective expansion circuit
13) Flaw alarm monitor circuits (I & II)

Here, the trouble-shooting hints and test point sets are stored with their respective tolerance limits. It is further associated with four mini-packages: COMPONENT, CONNECTOR, OSCGRAM, and TECHDATA. Test points in most of the circuits are selected at terminals of transistors, zener diodes, potentiometers, and switches.

Sub-utility : COMPONENT. Each component/ element of a circuit is specified with its respective code. For example, figure 3 shows z-axis amplification circuit. This utility contains the list of all PCBwise electronic components alongwith their detailed specifications , remarks/ tolerances as shown below:

Resistance	R	Part No.	Value	Wattage	%tolerance	Type
Potentiometer	P	Part No.	Value	Wattage	%tolernace	Type
Capacitor	C	Part No.	Value	Working-Voltage	%tolernace	Dielectric
Transistor	Q	Part No.	Type	Make	Special remarks	
Diode	D	Part No.	Type	Make	Special remarks	
Zener-diode	ZD	Part No.	Type	Make	Special remarks	
Misc. Component	V	Part No.	Description	Make	Special remarks	
Switch	SW	Part No.	Description	Make	Special remarks	
Transformer	T	Part No.	Description	Make	Special remarks	
Fuse	F	Part No.	Description	Make	Special remarks	
Coil	L	Part No.	Description	Make	Special remarks	
Panel Receptacle	AM	Part No.	Description	Make	Special remarks	

There are total seven PCB's in the instrument. The first numerical digit specified for component stands for its PCB number.

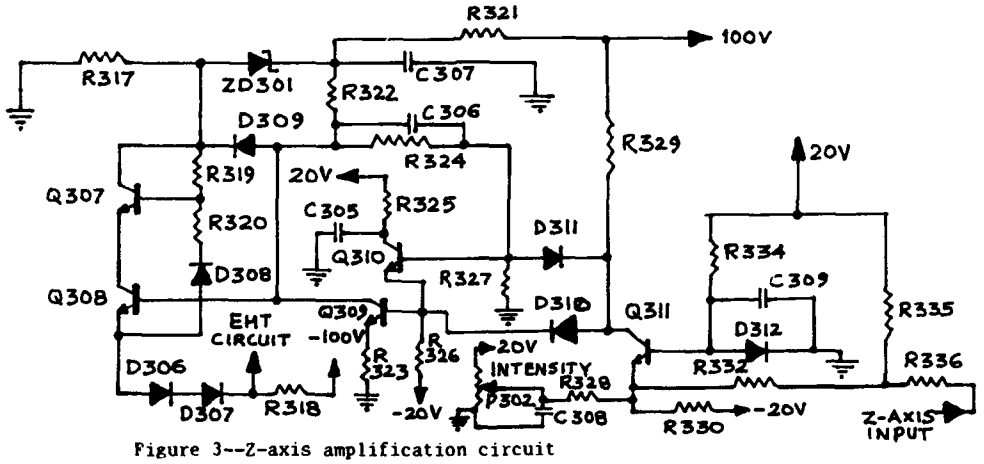

Figure 3--Z-axis amplification circuit

Sub-utility : CONNECTOR. This utility describes the connector-wiring plan and semiconductor elements connections.

Sub-utility : OSCGRAM. This utility contains the part-numberwise oscillograms at various test points at base, emitter and/or collector of transistors. For example, figure 4 shows oscillograms observed at collector of transistors used in z-axis amplification circuit. The oscillogram at any test point may be displayed at any stage of fault-diagnosis by user intervention.

Sub-utility : TECHDATA. This utility contains the part-numberwise voltage levels at various test points at transistors (emitter, base and collector); and voltage across zener-diodes. Table 1 shows voltage data at various test levels in z-axis amplification circuit for reference. The data may be recalled at any stage during fault-diagnosis by user intervention. Volatge data at various test points in flaw alarm circuit are given, both, with and without Alarm ON & off position.

Table 1--Voltage levels at various test points in z-axis amplification circuit for ready reference

Transistor Code	Emitter	Base	Collector
Q307	72	72	73
Q308	32	33	72
Q309	.2	.8	33
Q310	.8	1.5	3
Q311	-.1	.5	2 at inter min or max

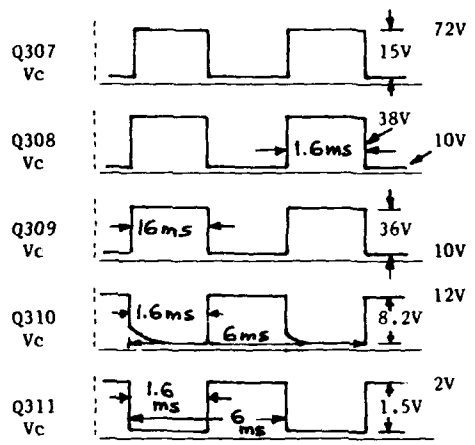

Figure 4--Oscillograms at different test points in z-axis amplification circuit

CONCLUSION

The expert system designed is expected to be highly advantageous for instrument users for proper installation, efficient operation, and calibration. It shall also help to curtail down-time of the instruments by providing expertise in preventive maintenance; fault-diagnosis; and repair, even when experts or relevent technical literature, or material are not easily accessible. The expert system designed and being developed shall not only open new vistas of creating expert human resources in developing countries, in this specialised field but also save valuable national resources, and foreign exchange involved in procurement of equipment. It will also contribute towards increasing industrial and economic progress of the country. The authors are thankful to Dr. K.R. Sharma, Director, CSIO, Chandigarh for kind permission to express our views.

REFERENCES

1. A.N. Agarwal, S.C. Suri, M.S. Bageshwar; Use of computer in management and maintenance of ultrasonic equipment; Proceedings of national symposium on ultrasonics; 1989.
2. A.N. Agarwal, S.C. Suri, M.S. Bageshwar; Expert system for maintenance and fault-diagnosis of ultrasonic equipment; Proceedings of international congress on ultrasonics; 1990; A30-35.
3. R. Jackson; Introduction to expert systems; Addision-Wesley, Reading, Mass; 1986.
4. James N. Siddal; Expert system for engineers; Marcel Dekker, Inc., New York; 1990.
5. S. C. Suri; Expert system for maintenance of ultrasonic flaw detector; M.S. Thesis, BITS, Pilani; 1991

BOUNDARY ELEMENTS AND FINITE ELEMENTS

SECOND INTERNATIONAL CONGRESS ON
RECENT DEVELOPMENTS IN AIR- AND
STRUCTURE-BORNE SOUND AND VIBRATION
MARCH 4-6, 1992 AUBURN UNIVERSITY, USA

RECENT APPLICATIONS OF BOUNDARY ELEMENT MODELING IN ACOUSTICS

A. F. Seybert, T. W. Wu and G. C. Wan

Department of Mechanical Engineering
University of Kentucky
Lexington, KY 40506-0046
U. S. A.

ABSTRACT

This paper discusses recent applications and advances in using the boundary element method (BEM) in acoustics. A brief review of the BEM theory is followed by several illustrative examples in various areas of application. These include: radiation and scattering of sound from elastic structures, muffler and silencer performance prediction, evaluation of partial enclosures for noise control, and prediction of sound radiation efficiency. The paper also reports some recent progress in overcoming the nonuniqueness problem, thin-body radiation and scattering, and frequency interpolation.

REVIEW OF THE BEM THEORY

Consider a body with boundary surface S submerged in an infinite acoustic medium Ω of mean density ρ_0 and speed of sound c. The body may be either set in vibration in a radiation problem or subject to an incident wave velocity potential ϕ_I in a scattering problem. In linear acoustics with time-harmonic excitations of angular frequency ω, the particle velocity v and the sound pressure p are related to the velocity potential ϕ by $v = -\nabla\phi$, and $p = ikz_0\phi$, respectively, where $i = \sqrt{-1}$, $k=\omega/c$, and $z_0=\rho_0 c$. The normal vector n is defined as the unit normal on S directed away from the acoustic medium Ω. The boundary value problem can be reformulated in terms of the Helmholtz integral equation as follows [1]:

$$C(P)\phi(P) = \int_S \left[\psi(P,Q)\frac{\partial\phi}{\partial n}(Q) - \frac{\partial\psi}{\partial n}(P,Q)\,\phi(Q)\right] dS(Q) + 4\pi\phi_I(P) \qquad (1)$$

where $\psi = e^{-ikr}/r$ ($r = |Q - P|$) is the free-space Green function due to a time-harmonic point source at P. C(P) is a constant that depends on the location of P.

A numerical solution to the Helmholtz integral equation [Eq. (1)] can be achieved by discretizing the boundary surface S into a number of surface elements and nodes. Quadratic isoparametric elements (six-node triangles and eight-node quads) have been widely used in recent years so that both the acoustic variables and the boundary geometry can be more accurately modeled. The global Cartesian coordinates X_i (i=1, 2, 3) of any point on an element are assumed to be related to the nodal coordinates $X_{i\alpha}$ by

$$X_i(\xi) = \sum_\alpha N_\alpha(\xi) X_{i\alpha} \quad , \alpha = 1, ..., 6 \text{ or } 8 \qquad (2)$$

in which N_α are second-order shape functions of the local coordinates (ξ,η). The same set of quadratic shape functions is used to interpolate the velocity potential ϕ on each element, that is,

$$\phi = \sum_{\alpha} N_{\alpha} \phi_{\alpha} \quad . \tag{3}$$

where ϕ_α are the nodal values of the velocity potential. The normal velocity $\partial\phi/\partial n$ on each element is also obtained by the same interpolation of the nodal values of $\partial\phi/\partial n$.

Discretizing Eq. (1) and putting point P at each node result in a system of equations as follows [1]:

$$[C]\{x\} = \{b\} \tag{4}$$

where [C] is a square coefficient matrix, {b} is the right hand side vector and {x} contains the unknowns (ϕ or $\partial\phi/\partial n$) on the boundary S.

COUPLED FEM/BEM FOR FLUID-SOLID INTERACTION PROBLEMS

When an elastic structure is submerged in a heavy fluid such as sea water, the vibration of the structure will be affected by the surrounding fluid, and the whole system becomes a coupled structural acoustic problem. A coupled technique, using the finite element method (FEM) for the structure and the BEM for the fluid, is a natural choice for numerical solution of fluid-structure interaction problems. Combining the FEM and the BEM equations and enforcing continuity conditions on the fluid-solid interface (the "wet" surface) lead to the following coupled structure acoustic equations [2]:

$$\begin{bmatrix} K-\omega^2 M & L \\ -B & A \end{bmatrix} \begin{bmatrix} u \\ p \end{bmatrix} = \begin{bmatrix} f^m \\ 4\pi p_I \end{bmatrix} \tag{5}$$

where p, u, and p_I are the nodal value vectors of the sound pressure, displacement, and incident sound pressure, respectively, and f^m is the mechanical load vector. The top part of Eq. (5) is from the FEM and the acoustic load is represented by -[L]{p}. The bottom part of Eq. (5) is from the BEM. Equation (5) can be solved for both the displacement and pressure simultaneously. The dimension of the final system of equations may be reduced by expressing the structural displacement as a linear combination of either Ritz vectors or eigenvectors [3].

An example problem is given to demonstrate the coupled FEM/BEM approach. Consider an aluminum cylindrical shell with both ends being excited internally by a uniform pressure p_0. The length of the cylinder is $4a$ and the thickness is $a/4$ where a is the mean radius. Figure 1 shows the pressure directivity for $ka = 1$ at a radius $50a$ from the cylinder. It is also shown that for this example the Ritz vector synthesis converges faster than the modal synthesis.

BEM FORMULATION FOR MULTIPLE DOMAINS

In many industrial noise problems, the domains and boundaries are quite complex. In an industrial silencer, for example, the interior domain may be partially subdivided by baffles and other surfaces. In such cases, the single-domain BEM formulation is cumbersome to use and may not be computationally attractive. However, by subdividing the original domain into subdomains and matching appropriate continuity conditions at interfaces, it is possible to solve the problems by using the BEM [4]. To illustrate the application of the multi-domain BEM, two problems in industrial noise control are shown in the following: transmission loss of silencers [4] and radiation from a source within a partial enclosure [5, 6].

Transmission loss of silencers

A simple expansion chamber with an extended inlet tube is shown in Fig. 2a. From the modeling standpoint, the extended tube is viewed as a thin projecting surface extending into the acoustic field for which a singularity arises when the single-domain BEM is used. Using the multi-domain BEM, the interior region of the expansion chamber is divided into two subdomains, as shown in Fig. 2a. Figure 3 shows the comparison of the transmission loss (TL) calculated by the BEM and an axisymmetric FEM for the case in Fig. 2a. The FEM model consisted of 166 four-node linear elements with a total of 206 nodes, whereas the BEM model consisted of only 17 quadratic line elements with a total of 36 nodes. As shown in Fig. 3, the TL varies considerably with frequency kL. In addition to the classic expansion humps at odd multiples of quarter-wavelength, the very narrow peaks which increase the TL values abruptly are the results of resonance and side-branch effects due to the extension tube. Excellent agreement between the boundary element solution and the finite element solution is observed.

As a second example, consider the double-expansion chamber with an internal connecting tube shown in Fig. 2b. The BEM solution and the axisymmetric FEM solution are compared in Fig. 4. The FEM mesh consisted of 318 four-node linear quadrilateral elements with 388 nodes. The BEM mesh consisted of 30 quadratic line elements with 63 nodes. Good agreement between the BEM and the FEM solutions is obtained.

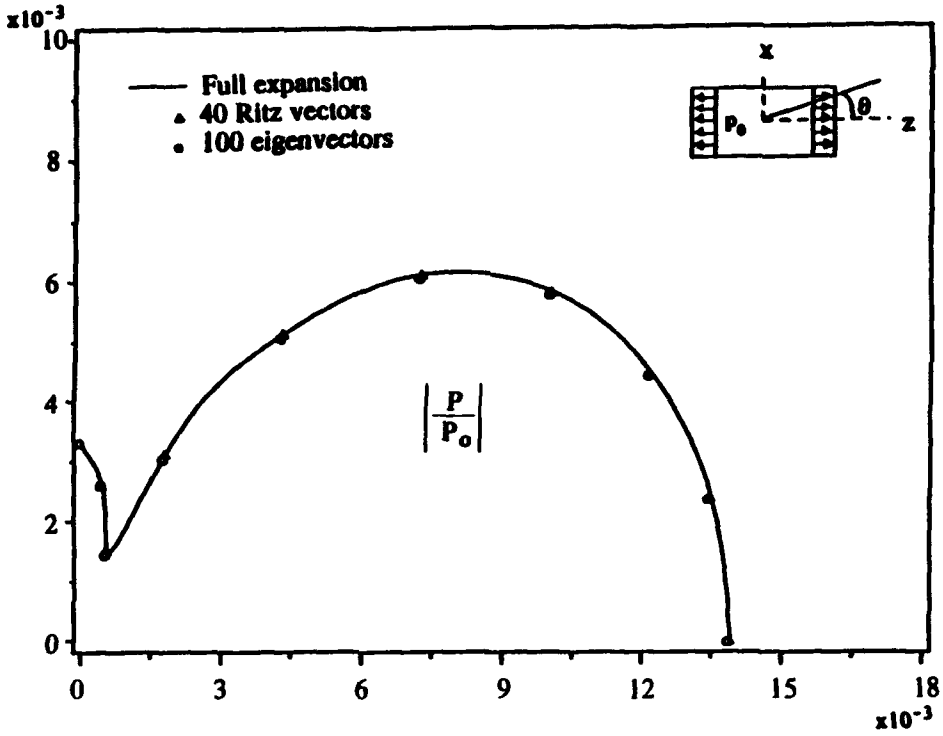

Figure 1. Normalized pressure magnitude at a distance of 50a from the center of the cylindrical shell.

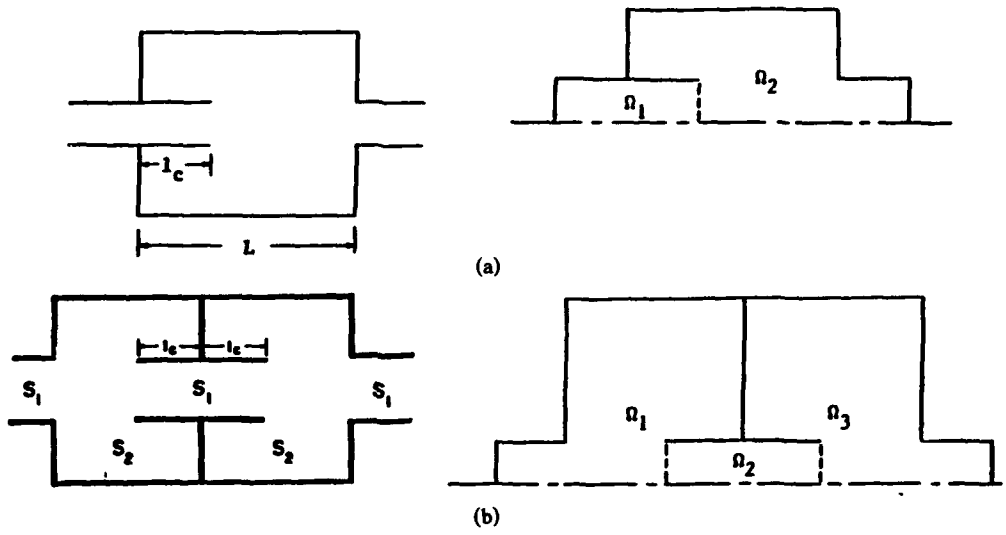

Figure 2. Silencer geometry and multi-domain BEM model of each: (a) expansion chamber with extended inlet, (b) double expansion chamber with internal connecting tube.

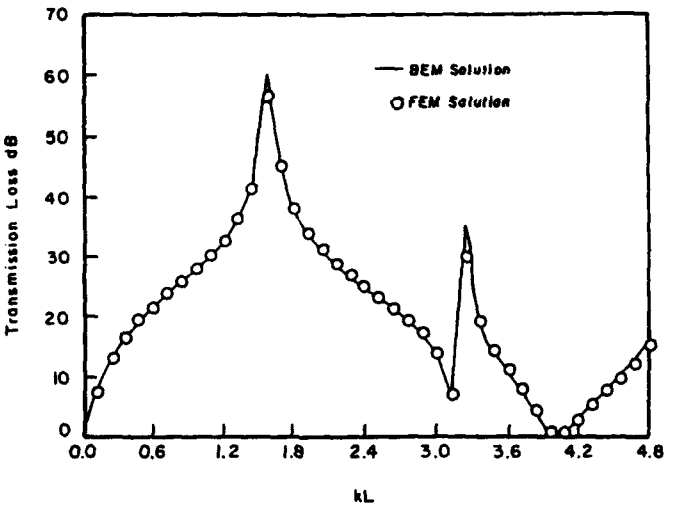

Figure 3. Transmission loss versus kL for the silencer in Fig. 2a.

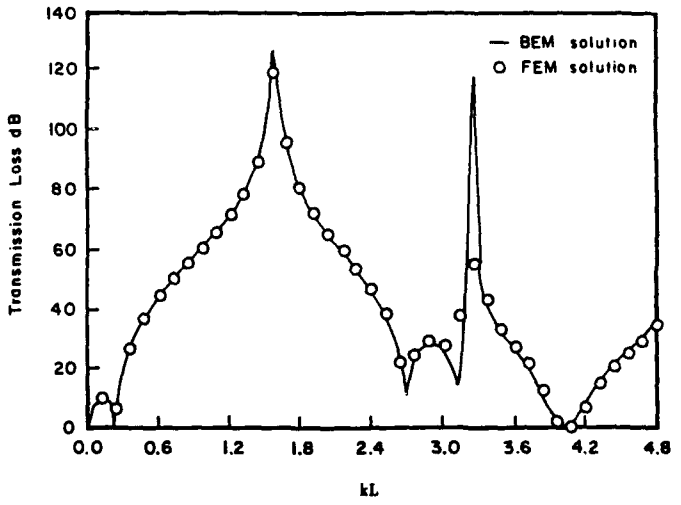

Figure 4. Transmission loss versus kL for the silencer in Fig. 2b.

Radiation from a source within a partial enclosure

Figure 5 shows a spherical source at the center of a cubical enclosure with two square openings. The radius of the source is 0.1 m, the length of each edge of the enclosure is 0.5 m and the size of the openings is 0.1 m square. The enclosure is rigid. The boundary condition on the spherical source is a uniform normal velocity of 0.2 m/s, and the boundary condition on both the inside and outside surfaces of the enclosure is normal velocity of zero.

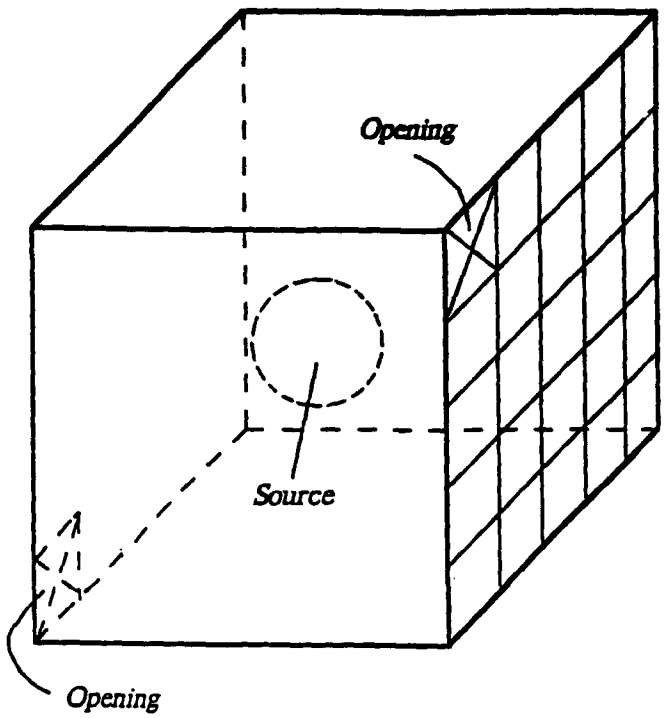

Figure 5. Radiation from a spherical source within a partial enclosure. The grid on the right side of the enclosure is the BEM mesh used on the inside and outside surfaces of the enclosure.

Two approaches are used. In the first approach, the multi-domain (coupled interior/exterior) BEM is used to determine the sound field inside and outside of the enclosure simultaneously. The mesh used is shown in Fig. 5. The second approach is an approximate "two-step" method used for comparison purpose only. In this approach, the interior and exterior sound fields are decoupled by assuming a radiation impedance z_r at the openings. If the frequency range is sufficiently low such that the sound pressure and particle velocity at the openings are approximately uniform, a reasonable approximation of the radiation impedance is

$$z_r = 0.5\,(ka)^2\rho_0 c + j\,(0.85\,ka)\,\rho_0 c\,, \tag{6}$$

where a is the radius of an equivalent circular, baffled piston. Using the radiation impedance boundary condition on the openings, the interior sound field may be determined using the interior BEM. The exterior sound field is then found by solving the exterior problem using the exterior BEM. The boundary condition on the openings for the exterior problem is the normal velocity (or sound pressure) determined from solving the interior sound field.

Figure 6 shows the sound pressure level (dB re 20μPa) as a function of frequency at the center of the opening, as calculated by both methods. The frequency range in Fig. 6 has been restricted to less than 1000 Hz where the approximate solution is valid. Figure 7 shows the sound pressure level at 790 Hz (a resonance frequency of the interior of the enclosure) at a distance of 5m from the center of a plane parallel to the side of the enclosure and passing through the openings. The two sets of data in Fig. 7 correspond to the case in which the enclosure is rigid, and the case in which the interior surfaces of the enclosure are lined with a sound absorbing material having a normal acoustical impedance $z = 208 + j208$, i.e., a normal incidence absorption coefficient of 0.8. Also shown for reference in Fig. 7 is the sound pressure level that would be present when the enclosure is absent.

The multi-domain BEM can help a noise control engineer determine the effect of the size and location of openings and select the best absorbing material for a partial enclosure design.

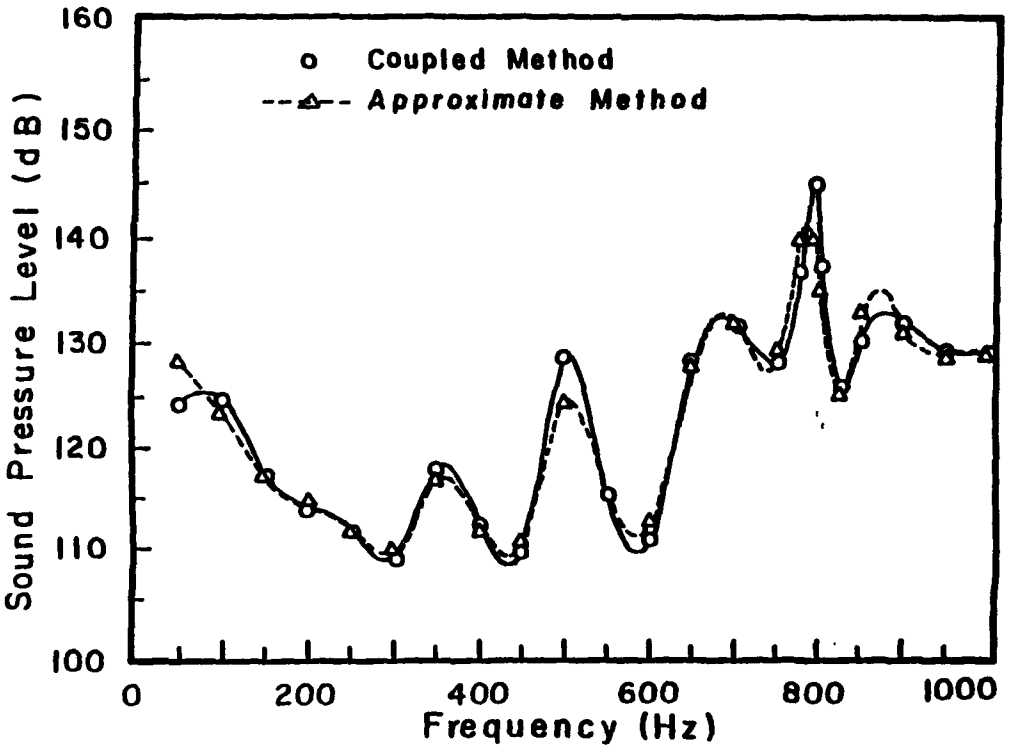

Figure 6. Sound pressure level at the center of the opening.

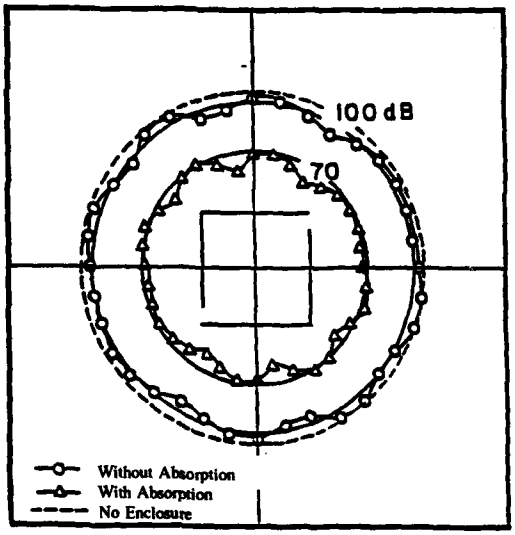

Figure 7. Sound pressure level at a distance of 5m from center of a plane passing through the openings of the enclosure.

PREDICTION OF SOUND RADIATION EFFICIENCY

Direct sound radiation from a vibrating structure is a function of the exciting force applied to the structure, the structural properties, and the sound radiation efficiency of the structure. The vibrational response of a structure may be described by a superposition of its vibrational modes. It is, therefore, important to know the modes of vibration and the radiation efficiency of these modes. The radiation efficiency is a function of the mode shape and the frequency of vibration. Although a mode shape is a normalized vibration, the radiation efficiency is an absolute value; it is a property of the mode. Therefore, the radiation efficiency can be used to compare the sound radiating characteristics of different structural modes.

After applying the BEM to solve for the unknown (sound pressure or normal velocity) at every node on the surface of a structure, the sound intensity at each node can be calculated. By integrating the sound intensity over the whole surface, the total sound power W radiated by the structure is determined. The radiation efficiency σ is the ratio of the sound power radiated by a vibrating structure, to the sound power that would be radiated by an equivalent flat piston vibrating in an infinite baffle:

$$\sigma = \frac{W}{\rho_0 c S \langle v^2 \rangle} \tag{7}$$

where $\langle v^2 \rangle$ is the mean square velocity of the surface S.

The following is an example to illustrate how the analysis of the radiation efficiency can be accomplished by the BEM [7]. Figure 8 shows a gearbox with its BEM mesh. The vibration data of the gearbox, including eight modes in the frequency range from 500 to 3,000 Hz, was obtained from modal analysis experiments. The vibration of the gearbox (normal velocity on the surface) is used as the boundary condition in the BEM. The radiation efficiencies of the eight modes are calculated by the BEM and shown in Fig. 9. As seen in Fig. 9, all of the modes are very efficient radiators of sound. These results can be checked by using Wallace's plate radiation theory [8] to make an approximate analysis. This theory is strictly valid only for simply supported plates in an infinite baffle, and is based on k/k_b, the ratio of the acoustic-to-bending wave numbers. In Fig. 10 the radiation efficiencies of the seven of the eight modes are compared to the radiation efficiencies of a rectangular plate having the same dimensions as the top surface of the box, as determined by Wallace's theory. The mode at 2000 Hz is not shown since it does not exhibit a dominant plate mode on the top surface. The discrepancies observed in Fig. 10 are due to that the top surface of the box is not baffled and there is radiation from the other surfaces.

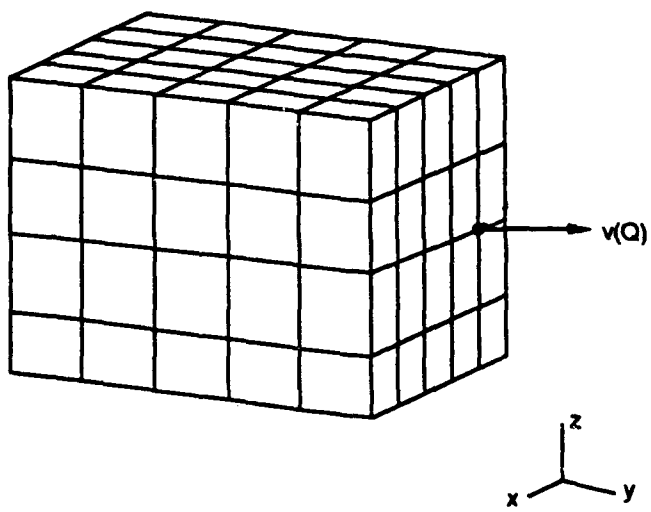

Figure 8. BEM mesh of the gearbox.

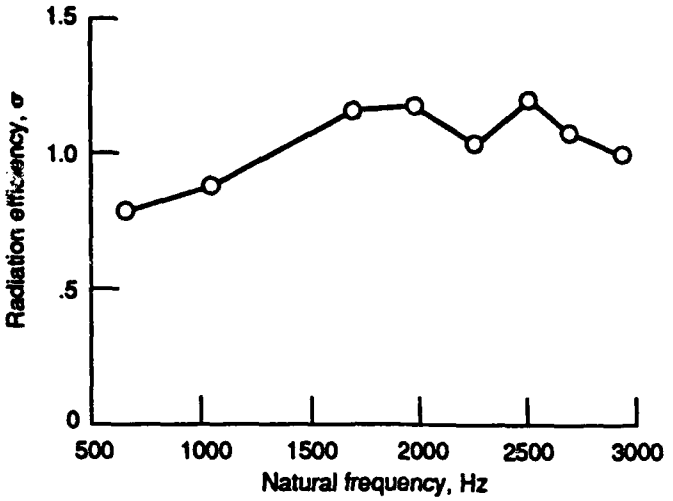

Figure 9. Radiation efficiencies of the eight transmission housing modes.

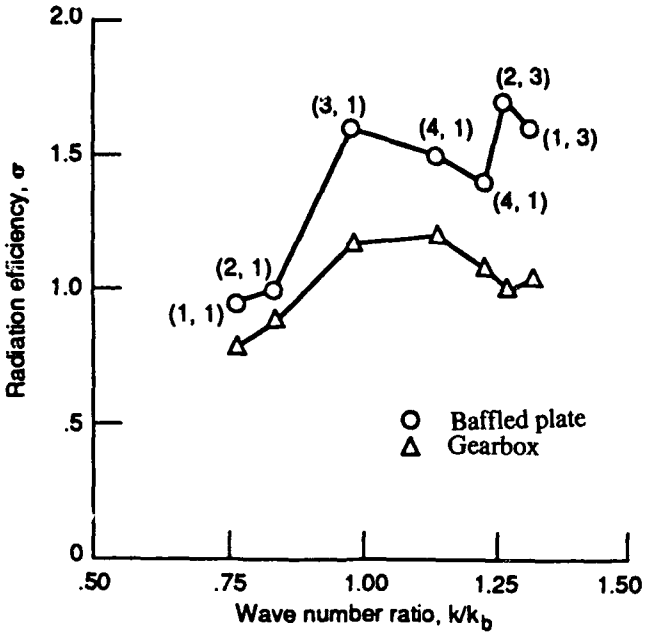

Figure 10. Radiation efficiencies calculated by the BEM and plate theory, respectively.

Structural modification of the gearbox is a logical method to control its sound radiation. In general, the spectrum of the forces which excite a structure is dominated by relatively low frequency components. Modifications which stiffen a structure tend to push the vibrational modes to higher frequencies where these forces are weaker-an effect that reduces vibration. However, this simplistic approach ignores the effect of radiation efficiency on the radiation of sound. Equation (7) shows that the sound power is directly proportional to the radiation efficiency. Thus, while modification of the structure may reduce the mean-square vibration, it may also increase the radiation efficiency.

Consider the effect of a straightforward modification to the thickness of the gearbox's surface plates. This alternation would change the natural frequencies of the modes without materially altering the mode shapes. To see the effect of such a modification, the radiation efficiency of each mode was determined at frequencies above and below the measured value. These data are plotted in Figs. 11 and 12 for the 658- and 2722-Hz modes, respectively. The actual measured natural frequency of each mode is represented by the filled data symbol.

The radiation efficiency of the 658-Hz mode increases with frequency, as shown in Fig. 11. Thus, a thicker gearbox will radiate more noise if the reduction in vibration does not offset the increase in radiation efficiency. It is also possible that making the gearbox thicker may cause a mode with a high radiation efficiency to move from a frequency where it is not excited to a new frequency (e.g. a gear mesh frequency) where it radiates considerably more sound energy.

By contrast, the radiation efficiency of the 2722-Hz mode is almost independent of frequency, as see in Fig. 12. Thickening of the box will not increase the radiation efficiency of this mode, and unless the new frequency coincides with a gear mesh frequency, the sound energy radiated by this mode will decrease.

THE NONUNIQUENESS PROBLEM

One potential shortcoming of the BEM in acoustics is that the exterior boundary integral formulation shares the difficulty of nonuniqueness of solution at resonance frequencies of the associated interior problem [9]. Several modified integral formulations have been proposed to overcome the nonuniqueness problem. The most commonly used one is the Combined Helmholtz Integral Equation Formulation (CHIEF) proposed by Schenck [9]. This formulation uses the Helmholtz integral equation with points (CHIEF points) inside of the body (where C(P) = 0) as a constraint that must be satisfied along with the usual Helmholtz integral equation on the surface. The resulting over-determined system may then be solved by a least-squares procedure. If a CHIEF point falls on any nodal surface of the related (auxiliary) interior problem, it becomes useless. Recently, Wu and Seybert proposed two different enhanced CHIEF formulations, the "Enhanced" CHIEF method [10] and the "Weighted Residual" CHIEF [11] method, to partially remedy this difficulty. The "Enhanced" CHIEF method includes the derivatives of the CHIEF equations in three coordinate directions as three additional constraint equations that must be satisfied along with the original CHIEF system. Therefore, there will be a total of four constraint equations at each CHIEF point. To further improve the CHIEF method, the "Weighted Residual" CHIEF method in which the "Enhanced" CHIEF equations are weakly satisfied in a volume, instead of CHIEF points, inside of the body.

Another formulation to overcome the nonuniqueness problem is the method proposed by Burton and Miller [12]. This approach consists of a linear combination of the Helmholtz integral equation and its normal derivative equation. It has been proved that the linear combination of these two equations will yield a unique solution for all frequencies if the multiplicative constant of the derivative equation is appropriately chosen. However, the major difficulty in this formulation is that the normal derivative of the Helmholtz integral equation contains a hyper-singular integral. Procedures to integrate the hypersingular integrals for three-dimensional problems with curved boundary surfaces have recently been reported [13, 14, 15].

FREQUENCY INTERPOLATION TECHNIQUE

Although the BEM is a very efficient numerical technique for acoustic analysis at a few frequencies, it may be impractical for multi-frequency applications. The main reason is that the integral in the Helmholtz integral equation is frequency dependent. For each frequency, all of the components in the coefficient matrix [C] and the right-hand side vector {b} in Eq. (4) need to be recalculated. The procedure is very time consuming if solutions for a wide frequency spectrum are required.

A frequency interpolation technique has been successfully applied to multi-frequency analysis by Schenck and Benthien using constant elements [16]. The concept has been extended to quadratic isoparametric elements [17, 18] and will be described briefly here. It is known that the integral of the Helmhotz integral equation may vary rapidly with frequency due to the fluctuating term e^{-ikr} in the Green's function. The rapid variation with frequency can be neutralized by multiplying the integral by a "counteracting" wave. Neutralized integrals can be calculated at a set of reasonably spaced "key" frequencies. The integral at a certain frequency can then be formulated by interpolating the integrals at adjacent "key" frequencies.

An example of the use of frequency interpolation is shown in the following problem. Consider the rectangular duct shown in Fig. 13. The left end of the duct is driven by a piston with a velocity equal to 1 m/sec. The right end of the duct is rigid. Figure 14 shows the sound pressure level on the middle cross section of the duct (X = L/2) in a frequency range up to kL = 14. Note the good agreement between the analytical solution and the values predicted by the BEM with and without frequency interpolation. Two key frequencies at kL = 0.458 and 11.9 were used for this frequency interpolation run. This test case was run on the IBM3090

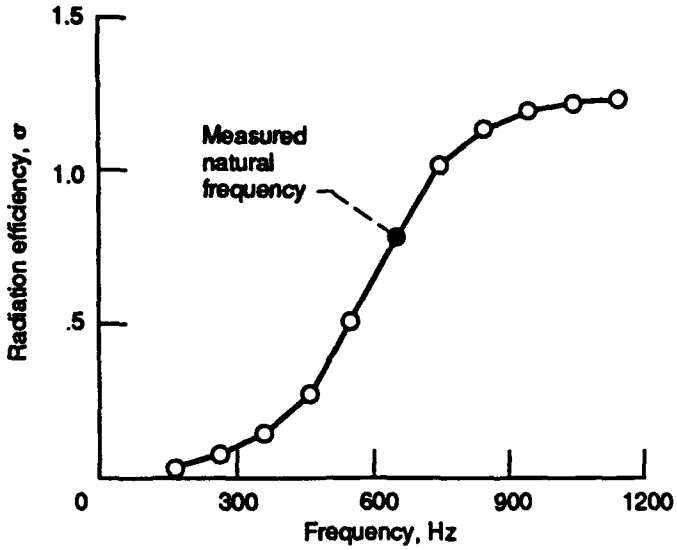

Figure 11. Radiation efficiencies of the 658-Hz vibration mode as a function of natural frequency.

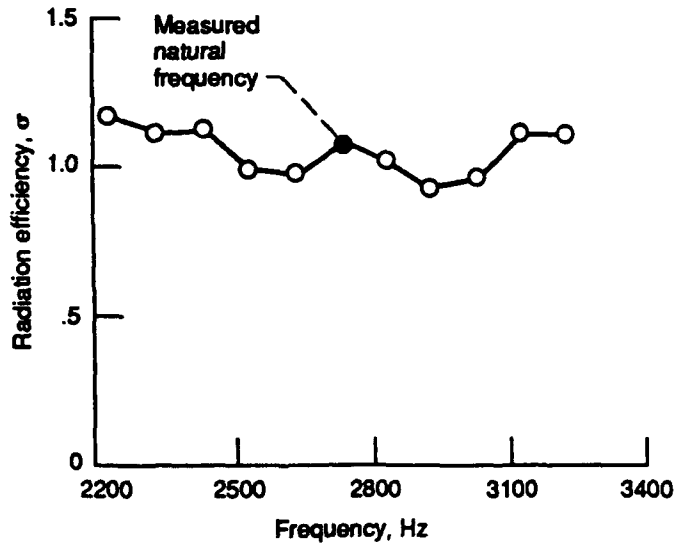

Figure 12. Radiation efficiencies of the 2722-Hz vibration mode as a function of natural frequency.

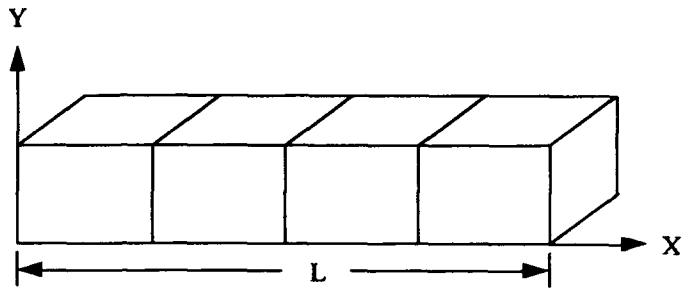

Figure 13. BEM mesh of the rectangular duct.

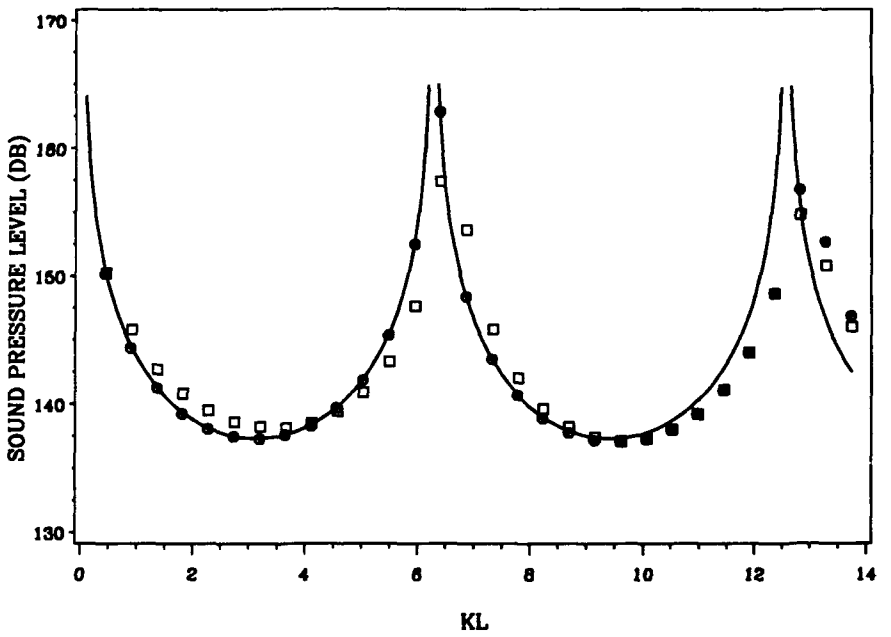

Figure 14. Sound pressure level on the middle cross section of the duct: solid line, analytical solution; circles, direct BEM solution; squares, BEM solution with frequency interpolation technique.

supercomputer under vector mode[17]. The CPU time for this frequency interpolation run is slightly less than 50% of the CPU time for the corresponding direct solution run.

THIN-BODY RADIATION AND SCATTERING

Sound radiation and scattering from thin bodies has many important applications (such as transducers and fins) in acoustics. It has been known that the conventional boundary element method (BEM) using the Helmholtz integral equation is not suitable for problems involving thin bodies. The major difficulty is due to the fact that the mesh on one side of a thin body is too close to the mesh on the opposite side. Therefore, extremely fine meshes have to be used and nearly singular behavior may occur in the integral equation. Recently, a normal derivative integral equation that converges in the Cauchy principal value sense has been successfully implemented in a quadratic isoparametric element environment to solve the thin-body problem [19, 20].

SUMMARY

This paper briefly reviews recent progress in the BEM research in acoustics and noise control at the University of Kentucky. Detailed discussion of each of the individual topics can be found in the references. The results have shown promising future of the application of the BEM to practical engineering problems.

REFERENCES

1. A. F. Seybert, B. Soenarko, F. J. Rizzo and D. J. Shippy, "An Advanced Computational Method for Radiation and Scattering of Acoustic Waves in Three Dimensions," J. Acoust. Soc. Am., Vol. 77, No. 2, pp. 362-368, 1985.
2. T. W. Wu, A. F. Seybert and W. L. Li, "Applications of the Coupled FEM/BEM Technique to Structural Acoustics Using Consistent Isoparametric Elements," ASME Vibration Control Mechanical, Structural, and Fluid-Structural Systems, K. W. Matta and M. K. Au-Yang (Eds.), PVP-Vol. 202, pp. 25-30, 1990.
3. A. F. Seybert, T. W. Wu and W. L. Li, "A Coupled FEM/BEM Solution for Structural Acoustic Problems Using Ritz Vectors and Eigenvectors," ASME Structural Acoustics, R. F. Keltie, et al. (Eds.) , NCA-Vol. 12/AMD-Vol. 128, pp. 171-178, 1991; also to appear in ASME Transactions J. Vib. Acoust.
4. C. Y. R. Cheng, A. F. Seybert and T. W. Wu, "A Multi-domain Boundary Element Solution for Silencer and Muffler Performance Prediction," J. Sound Vib., Vol. 151, pp. 119-129, 1991.
5. A. F. Seybert, C. Y. R. Cheng and T. W. Wu, "The Solution of Coupled Interior/Exterior Problems Using the Boundary Element Method, J. Acoust. Soc. Am., Vol. 88, pp. 1612-1618, 1990.
6. A. F. Seybert, T. W. Wu and W. L. Li, "Analysis of Noise Radiated by a Source within a Partial Enclosure Using the Boundary Element Method", Proceedings of the Inter-Noise 89, pp. 1225-1228, Newport Beach, California, 1989.
7. A. F. Seybert, T. W. Wu, X. F. Wu and F. B. Oswald, "Acoustical Analysis of Gear Housing Vibration," NASA Technical Memorandum 103691, 1991.
8. C. E. Wallace, "Radiation Resistance of a Rectangular Panel," J. Acoust. Soc. Am., Vol. 51, No. 3, pp. 946-952, 1972.
9. H. A. Schenck, "Improved Integral Formulation for Acoustic Radiation Problems," J. Acoust. Soc. Am., Vol. 44, pp. 41-58, 1968.
10. T. W. Wu and A. F. Seybert, "Acoustic Radiation and Scattering," Boundary Element Methods in Acoustics, Chap. 3, R. D. Ciskowski and C. A. Brebbia (Eds.), Computational Mechanics Publications, Southampton, UK, 1991.
11. T. W. Wu and A. F. Seybert, "A Weighted Residual Formulation for the CHIEF method in acoustics," J. Acoust. Soc. Am., Vol. 90, No. 3, pp. 1608-1614, 1991.
12. A. J. Burton and G. F. Miller, "The Application of Integral Equation Methods to the Numerical Solutions of Some Exterior Boundary Value Problems," Proc. Roy. Soc. Lond., A 323, 201-210, 1971.
13. G. Krishnasamy, L. W. Schmerr, T. J. Rudolphi and F. J. Rizzo, "Hypersingular Boundary Integral Equations: Some Applications in Acoustic and Elastic Wave Scattering," ASME J. App. Mech. 57, 404-414, 1990.
14. T. W. Wu, A. F. Seybert and G. C. Wan, "On the Numerical Implementation of a Cauchy Principal Value Integral to Insure a Unique Solution for Acoustic Radiation and Scattering," J. Acoust. Soc. Am. Vol. 90, 554-560, 1990.
15. C. C. Chien, H. Rajiyah and S. N. Atluri, "An Effective Method for Solving the Hypersingular Integral Equations in 3-D Acoustics," J. Acoust. Soc. Am., Vol. 88, pp. 918-937, 1990.
16. H. A. Schenck and G. W. Benthien, "The Application of a Coupled Finite-Element Boundary-Element Technique to Large-Scale Structural Acoustic Problems," Advances in Boundary Elements, Vol. 2, pp. 309-319, C. A. Brebbia and J. J. Connor (Eds.), Computational Mechanics Publications, Southampton, UK, 1989.
17. T. W. Wu, A. F. Seybert, G. C. Wan and R. Ciscowski, "Vectorization and Parallelization of the BEMAP program on the IBM 3090," Proceedings of International Congress on Recent Developments in Air and Structure Borne Sound and Vibration, pp. 489-498, Auburn University, Auburn, Alabama, 1990.
18. A. F. Seybert and T. W. Wu, "Application in Industrial Noise Control," Boundary Element Methods in Acoustics, Chap. 9, R. D. Ciskowski and C. A. Brebbia (Eds.), Computational Mechanics Publications, Southampton, UK, 1991.
19. T. W. Wu and G. C. Wan, "Numerical Modeling of Acoustic Radiation and Scattering from Thin Bodies Using a Cauchy Principal Integral Equation," submitted to J. Acoust. Soc. Am., 1991.
20. T. W. Wu and G. C. Wan, "Isoparametric Boundary Element Modeling of Acoustical Cracks," to be presented at the Second International Congress on Recent Developments in Air- & Structure-Borne Sound & Vibration, Auburn University, Alabama, March 4-6, 1992.

SECOND INTERNATIONAL CONGRESS ON
RECENT DEVELOPMENTS IN AIR- AND
STRUCTURE-BORNE SOUND AND VIBRATION
MARCH 4-6, 1992 AUBURN UNIVERSITY, USA

NUMERICAL MODELING OF PERFORATED REACTIVE MUFFLERS

Z. H. Jia, A. R. Mohanty and A. F. Seybert
Department of Mechanical Engineering
University of Kentucky
Lexington, Kentucky 40506

ABSTRACT

In this work, a multidomain boundary element approach is used to model both three-dimensional and axisymmetric perforated structures and solve for the acoustical parameters. Impedance on the perforated plate is assumed known and equals the ratio of pressure drop across the perforation to particle velocity there. Three numerical examples are considered. The first two involve simple geometry and boundary conditions, and the numerical results obtained are accurate in comparison with exact solutions. The third example treats a plug muffler. Transmission loss from several different porosities are obtained and are seen to agree favorably with available experimental results.

INTRODUCTION

Mufflers are an important noise control device used in the automotive and other industries. One effective strategy in reactive muffler design to obtain maximum sound attenuation at relatively high frequencies is to use perforated components. The introduction of perforated baffle plates, tubes and other perforated structures enhances the performance of a muffler in a desired frequency range.

A number of researchers in the past have developed various prototypes for experimental and analytical verifications. A state-of-art review of muffler design has been given by Munjal [1]. Using a one-dimensional model, Igarashi and Toyama [2] demonstrated the effect of perforation in mufflers both analytically and experimentally. Sullivan and Crocker [3] derived a one-dimensional model for a perforated concentric-tube muffler with mean flow. Sullivan [4,5] improved their method by including a varying perforation impedance along the axial direction. Nonlinear effects due to the changing impedance and high sound-pressures were also considered. A numerical decoupling technique was presented by Krishnamurthy and Yam [6] and Peat [7], but their approach may not be applied to

nonlinear cases such as treated by sullivan [4,5], although it works well in linear cases. A time domain approach for perforated mufflers was presented by Chang and Cummings [8]; the extra computational time required in their study remains a question. The aforementioned work are all analytical or experimental in nature, and deal with somewhat simplified geometry.

For problems involving complex geometry, numerical results are also available. Ross [9], for instance, presented a finite element solution to a complex three-dimensional muffler with perforated structures. He treated the perforated tube as a flexible membrane, and assumed that the acoustical particle velocity to be the same on both sides of the membrane. Another powerful and perhaps a more effective numerical method for acoustic problems, the boundary element method (BEM), has been used extensively in modeling acoustic radiation and scattering problems, including muffler problems. Seybert and Cheng [10] presented results for transmission loss of simple mufflers, using the BEM. Work by Tanaka *et al.* [11] and Kipp and Bernhard [12] also used the boundary element technique.

Despite numerous work in solving acoustic problems using the BEM, modeling of the perforated structures with the BEM has not been done. In this study, we present a boundary element approach to solve problems involving three-dimensional perforated structures. In our analysis, a complex muffler is partitioned into subdomains between which impedance boundary conditions [3]

$$p_1 - p_2 = \rho_o c \zeta u_n \tag{1}$$

are specified, where p_1, and p_2 are the acoustic pressures at each side of a perforated interface. ρ_o and c are density and the speed of sound, respectively, u_n is the normal particle velocity and ζ is the nondimensional specific acoustic impedance which may be obtained by experiments [4,5].

An arbitrary-shaped muffler with complex internal structures can be modeled using the current method by modifying the existing multidomain boundary element formulation [13,14] into one which considers perforation at interfaces of subdomains. Unlike the existing formulation [13,14] in which the interfaces are artificial, the perforated interfaces are physically real. This requires that the interface conditions (1) be included in the integral equations. One may also view Eq. (1) as an extra constraint. The current formulation considers only zero-mean-flow cases. For cases involving mean flow, further modifications are required and such problems will be considered in future studies.

Three numerical examples are presented. The first two are simple problems with exact solutions. In the third problem, the transmission loss of a plug muffler is compared to the experimental result by Sullivan [5].

FORMULATION

Considering a structure with internal perforated partitions shown in Fig.1, the entire acoustic volume enclosed by boundary S_E can be treated as a group of subdomains B_j connected by a common interface S_I (For convenience, only two domains are shown). For

a typical subdomain B_j, the governing differential equation in a time-harmonic acoustic wave field is the Helmholtz equation

$$\nabla^2 p^{(j)} + k^2 p^{(j)} = 0. \tag{2}$$

In Eq. (2), $p^{(j)}$ is the acoustic pressure in domain B_j, $k = \omega/c$ is the wave number, ω is the angular frequency, and c is the speed of sound.

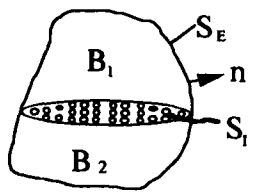

Fig. 1 - A structure with internal perforated partitions.

The boundary integral formulation of the Helmholtz equation governing the acoustic field in subdomain B_j [i.e. Eq. (2)] can be expressed as

$$C^o(\mathbf{x})p^{(j)}(\mathbf{x}) = \int_{\partial B_j} \left(\psi(\mathbf{x},\mathbf{y})\frac{\partial p^{(j)}}{\partial n}(\mathbf{y}) - p^{(j)}(\mathbf{y})\frac{\partial \psi}{\partial n}(\mathbf{x},\mathbf{y})\right) ds(\mathbf{y}), \tag{3}$$

where $\psi = e^{-ikR}/R$ is the free-space Green's function in which $R = |\mathbf{x} - \mathbf{y}|$, $\mathbf{x}$ and $\mathbf{y}$ are position vectors of a collocation point and the integration point, respectively, and n is the unit outward normal on the boundary ∂B_j of domain B_j, (∂B_j consists of both external boundary S_E and interfaces S_I), and $i = \sqrt{-1}$ The leading coefficient $C^o(\mathbf{x})$ is given by

$$C^o(\mathbf{x}) = -\int_{\partial B_j} \frac{\partial}{\partial n}\left(\frac{1}{R}\right) ds(\mathbf{y}). \tag{4}$$

In Eq. (3), the normal derivative of $p^{(j)}$ with respect to n is related the normal particle velocity $u^{(j)}$ by

$$\frac{\partial p^{(j)}}{\partial n} = -i\omega\rho_o u^{(j)}, \tag{5}$$

where ρ_o is the fluid density at equilibrium.

Substituting Eq. (5) into (3) and performing discretization via boundary elements, we convert Eq. (3) into a set of linear algebraic equations. In matrix form, the equations for subdomain B_j may be expressed as

$$\begin{bmatrix} \mathbf{A}_{11}^{(j)} & \mathbf{A}_{12}^{(j)} \\ \mathbf{A}_{21}^{(j)} & \mathbf{A}_{22}^{(j)} \end{bmatrix} \begin{Bmatrix} \mathbf{p}_E^{(j)} \\ \mathbf{p}_I^{(j)} \end{Bmatrix} + \begin{bmatrix} \mathbf{B}_{11}^{(j)} & \mathbf{B}_{12}^{(j)} \\ \mathbf{B}_{21}^{(j)} & \mathbf{B}_{22}^{(j)} \end{bmatrix} \begin{Bmatrix} \mathbf{u}_E^{(j)} \\ \mathbf{u}_I^{(j)} \end{Bmatrix} = \begin{Bmatrix} \mathbf{0} \\ \mathbf{0} \end{Bmatrix}, \tag{6}$$

where $\mathbf{A}_{nm}^{(j)}$ and $\mathbf{B}_{nm}^{(j)}$ are submatrices generated by numerically integrating the kernels of the integral equations. $\mathbf{p}_E^{(j)}$ and $\mathbf{p}_I^{(j)}$ are the sound pressure at S_E and S_I, respectively, and $\mathbf{u}_E^{(j)}$ and $\mathbf{u}_I^{(j)}$ are the particle velocity at the corresponding boundaries. Bold letters are used here because both quantities contain multiple discretized values.

Without loss of generality, we assume that $\mathbf{u}_E^{(1)}$ and $\mathbf{u}_E^{(2)}$ are known at S_E for a two-domain structure as in Fig.1. By moving the known quantities to the right-hand-side of Eq. (6), the equations for domain B_1 and B_2 become

$$\begin{bmatrix} \mathbf{A}_{11}^{(1)} & \mathbf{A}_{12}^{(1)} & \mathbf{B}_{12}^{(1)} \\ \mathbf{A}_{21}^{(1)} & \mathbf{A}_{22}^{(1)} & \mathbf{B}_{22}^{(1)} \end{bmatrix} \begin{Bmatrix} \mathbf{p}_E^{(1)} \\ \mathbf{p}_I^{(1)} \\ \mathbf{u}_I^{(1)} \end{Bmatrix} = - \begin{bmatrix} \mathbf{B}_{11}^{(1)} \\ \mathbf{B}_{21}^{(1)} \end{bmatrix} \{ \mathbf{u}_E^{(1)} \}, \tag{7}$$

and

$$\begin{bmatrix} \mathbf{A}_{11}^{(2)} & \mathbf{A}_{12}^{(2)} & \mathbf{B}_{12}^{(2)} \\ \mathbf{A}_{21}^{(2)} & \mathbf{A}_{22}^{(2)} & \mathbf{B}_{22}^{(2)} \end{bmatrix} \begin{Bmatrix} \mathbf{p}_E^{(2)} \\ \mathbf{p}_I^{(2)} \\ \mathbf{u}_I^{(2)} \end{Bmatrix} = - \begin{bmatrix} \mathbf{B}_{11}^{(2)} \\ \mathbf{B}_{21}^{(2)} \end{bmatrix} \{ \mathbf{u}_E^{(2)} \}. \tag{8}$$

It is obvious that neither Eq. (7) nor (8) can be solved independently since the number of unknowns is greater than that of the equations. However, by considering the continuity of velocity across the interface S_I expressible as

$$\mathbf{u}_I^{(1)} = -\mathbf{u}_I^{(2)}. \tag{9}$$

and using Eq. (1), $\mathbf{p}_I^{(2)}$ and $\mathbf{u}_I^{(2)}$ can be eliminated from Eq. (8). A combined system of equations involving the entire structure is expressed as:

$$\begin{bmatrix} \mathbf{A}_{11}^{(1)} & \mathbf{A}_{12}^{(1)} & \mathbf{B}_{12}^{(1)} & \mathbf{0} \\ \mathbf{A}_{21}^{(1)} & \mathbf{A}_{22}^{(1)} & \mathbf{B}_{22}^{(1)} & \mathbf{0} \\ \mathbf{0} & \mathbf{A}_{12}^{(2)} & \mathbf{D}_{12}^{(2)} & \mathbf{A}_{11}^{(2)} \\ \mathbf{0} & \mathbf{A}_{22}^{(2)} & \mathbf{D}_{22}^{(2)} & \mathbf{A}_{21}^{(2)} \end{bmatrix} \begin{Bmatrix} \mathbf{p}_E^{(1)} \\ \mathbf{p}_I^{(1)} \\ \mathbf{u}_I^{(1)} \\ \mathbf{p}_E^{(2)} \end{Bmatrix} = - \begin{Bmatrix} \mathbf{B}_{11}^{(1)} \mathbf{u}_E^{(1)} \\ \mathbf{B}_{21}^{(1)} \mathbf{u}_E^{(1)} \\ \mathbf{B}_{11}^{(2)} \mathbf{u}_E^{(2)} \\ \mathbf{B}_{21}^{(2)} \mathbf{u}_E^{(2)} \end{Bmatrix}, \tag{10}$$

where $\mathbf{D}_{mn}^{(2)} = -\mathbf{B}_{mn}^{(2)} - \rho_o c \zeta \mathbf{A}_{mn}^{(2)}$.

Gaussian elimination is employed to solve the system simultaneously for the unknowns at both S_E and S_I. Values of $\mathbf{p}_I^{(2)}$ and $\mathbf{u}_I^{(2)}$ can be recovered from Eq. (1) and (9), respectively.

NUMERICAL EXAMPLES

The first example is a perforated sphere with a point source at its center (Fig.2). The interface impedance on the perforation is assumed known. Four different three-dimensional meshes are used to model this interior/exterior coupling problem. Exact solution for this problem is derived for comparison. The results of boundary pressure p_1 (inside) and p_2 (outside) are listed in Table 1.

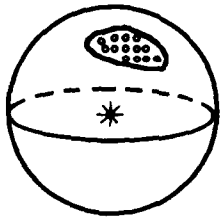

Fig. 2 - A perforated sphere with a point source at the center.

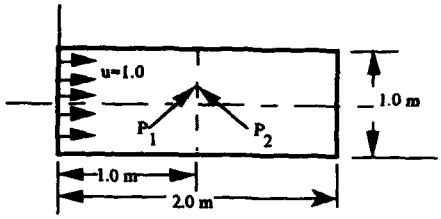

Fig. 3 - Circular duct with a perforated partition at the center.

Table 1. Boundary pressure for perforated sphere ($\zeta = 1$, $k = 1$)

# of ele.	$p_1/(i\rho_o\omega)$(BEM)	$p_1/(i\rho_o\omega)$(exact)	$p_2/(i\rho_o\omega)$(BEM)	$p_2/(i\rho_o\omega)$(exact)
8	-0.466 -1.944	-0.488 -1.852	0.215 -0.856	0.171 -0.838
24	-0.486 -1.862	-0.488 -1.852	0.179 -0.840	0.171 -0.838
96	-0.488 -1.853	-0.488 -1.852	0.176 -0.838	0.171 -0.838
128	-0.488 -1.853	-0.488 -1.852	0.175 -0.838	0.171 -0.838

It is clear that the numerical results in Table 1 converge rapidly with mesh refinement. Different values of ζ (from 1 to 100) and k (from 1 to 10) were also considered. The results are similar to those in Table 1 and hence are not presented here.

The second example involves a circular-cross-section duct with a perforated plate as a partition in the middle (Fig.3). The particle velocity at one end is specified as $u = 1m/s$. Numerical results are shown in Table 2, where p_1 and p_2 are sound pressures on each side of the partition.

Table 2. Boundary pressure for circular duct ($\zeta = 1$, $k = 1$)

# of ele.	$p_1/(i\rho_o\omega)$(BEM)	$p_1/(i\rho_o\omega)$(exact)	$p_2/(i\rho_o\omega)$(BEM)	$p_2/(i\rho_o\omega)$(exact)
16	0.817 0.267	0.818 0.288	0.381 -0.358	0.370 -0.288
32	0.816 0.255	0.818 0.288	0.369 -0.335	0.370 -0.288
58	0.821 0.264	0.818 0.288	0.365 -0.330	0.370 -0.288
100	0.821 0.275	0.818 0.288	0.364 -0.319	0.370 -0.288

As with the first example, the numerical results converge to the exact solution with an increasing mesh refinement, although with a somewhat slower rate.

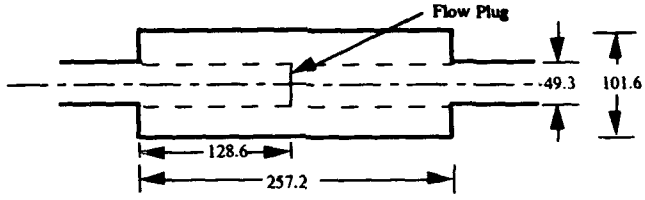

Fig. 4 - Schematic of the Plug Muffler
(all dimensions in mm)

In the third example, a plug muffler analyzed by Sullivan [5] and Krishnamurthy and Yam [6] is considered. A schematic plot of the muffler and its dimensions are given in Fig.4. For the perforated interface, a nondimensional specific impedance obtained by Sullivan [5] is used:

$$\zeta = (6.0 \times 10^{-3} + i4.8 \times 10^{-5} f)/\sigma, \tag{11}$$

where f is frequency in Hz and σ is the porosity of the perforated tube. An axisymmetric model with 156 elements (not shown) is used for this problem. For $\sigma = 0.039$ and temperature at $22°C$, the transmission loss is calculated from $f = 0$ to 3500 Hz. The computed transmission loss (dB) is presented in Fig.5, together with the experimental results by Sullivan [5]. A good agreement between these results can be seen in Fig.5.

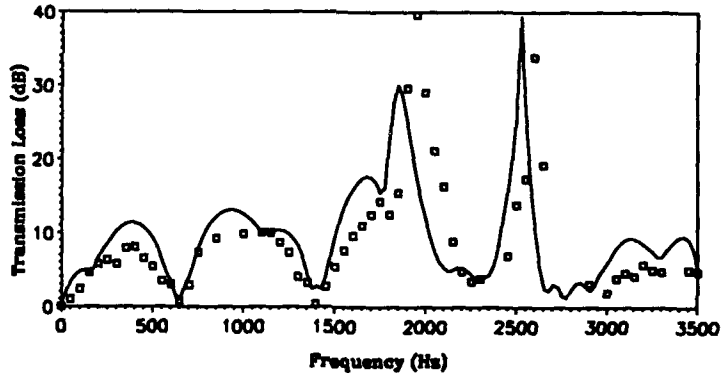

Fig. 5 - Transmission loss for Plug Muffler in fig. 4,
____ present method, ▫ experimental ref [5].

In order to see the effect of changing the porosity, values of porosity ranging from 0.03 to 0.07 are used to compute the transmission loss. The computed results are presented in Fig.6. By examining the curves associated with different porosity, it becomes clear that the porosity does play an important role in noise reduction.

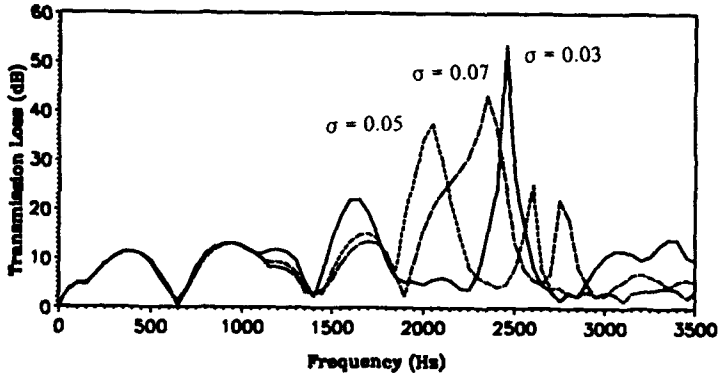

Fig. 6 - Transmission loss for varying porosities from 0.03 to 0.07

DISCUSSION

A boundary element formulation for acoustic structures with perforations was presented. Satisfactory results were obtained. The current study does not include mean flow. The influence of the mean flow on the Transmission Loss of a muffler is an important subject which will be discussed in future studies, although at low Mach numbers (< 0.3, as in the case of automobile exhaust), its effect is limited. Dissipative mufflers can also be modeled with the current approach. Experimental work involving both mean flow and dissipative effects is under way.

ACKNOWLEDGMENT

This work was supported by NSF grant MSM-8810909.

REFERENCES

1. M. L. Munjal, "State of the Art of Acoustics of Active and Passive Mufflers", *Shock and Vibration Digest*, **22**, No. 2, (1990), 3 - 12.

2. J. Igarashi and M. Toyama, "Fundamentals of Acoustical Silencers (I)", *Report No. 339, Aeronaut. Res. Inst., Univ. of Tokyo*, (1958), 223 - 241.

3. J. W. Sullivan and M. J. Crocker, "Analysis of Concentric-tube Resonators having unpartitioned Cavities", *J. Acoust. Soc. Am.* **64**, (1978), 207 - 215.

4. J. W. Sullivan, "A Method for Modeling Perforated Tube Muffler Components. I. Theory", *J. Acoust. Soc. Am.* **66**, (1979), 772 - 778.

5. J. W. Sullivan, "A Method for Modeling Perforated Tube Muffler Components. II. Applications", *J. Acoust. Soc. Am.* **66**, (1979), 779 - 788.

6. J. Krishnamurthy and K. Yam, "Decoupling Approach to Modeling Perforated Tube Muffler Components," *J. Acoust. Soc. Am.*, **69**, (1981), 390 - 396.

7. K. S. Peat, "A Numerical Decoupling Analysis of Perforated Pipe Silencer Elements," *J. Sound Vib.*, **123**, (1988), 199 - 212.

8. I. J. Chang and A. Cummings, "A Time Domain Solution for the Attenuation, at High Amplitudes, of Perforated Tube Silencers and Comparison with Experiment," *J. Sound and Vib.*, **122**, (1988), 243 - 259.

9. D. F. Ross, "A Finite Element Analysis of Perforated Component Acoustic Systems", *J. Sound Vib.* **79**, (1981), 133 - 143.

10. A. F. Seybert and C. Y. R. Cheng, "Application of the Boundary Element Method to Acoustic Cavity Response and Muffler Analysis", *ASME J. Vib. Acoust. Stress Rel. Dsgn.* **109**, (1987), 15 - 21.

11. T. Tanaka, T. Fujikawa, T. Abe and H. Utsuno, "A Method for the Analytical Prediction of Insertion Loss of a Two-dimensional Muffler Model Based on the Transfer Matrix Method Derived from the Boundary Element Method", *ASME J. Vib. Acoust. Stress Rel. Dsgn.*, **107**, (1985), 86 - 91.

12. C. R. Kipp and R. J. Bernhard, "Prediction of Acoustic Behavior in Cavities Using an Indirect Boundary Element Method", *ASME J. Vib. Acoust. Stress Rel. Dsgn.*, **109**, (1987), 22 - 28.

13. A. F. Seybert, C. Y. R. Cheng, and T. W. Wu, "The Solution of Coupled Interior/exterior Acoustic Problems using the Boundary Element Method," *J. Acoust. Soc. Am.*, **88**, (1990), 1612 - 1618.

14. A. F. Seybert, Z. H. Jia and T. W. Wu, "Solving Knife-edge Scattering Problems using Singular Boundary Elements," *J. Acoust. Soc. Am.*, Accepted for publication.

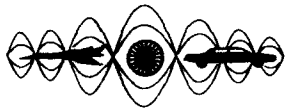

SECOND INTERNATIONAL CONGRESS ON
RECENT DEVELOPMENTS IN AIR- AND
STRUCTURE-BORNE SOUND AND VIBRATION
MARCH 4-6 1992 AUBURN UNIVERSITY USA

ON SELECTING CHIEF POINTS TO OVERCOME THE NONUNIQUENESS PROBLEM IN BOUNDARY ELEMENT METHODS

Peter M. Juhl
The Acoustics Laboratory
Technical University of Denmark
Building 352, DK-2800 Lyngby
Denmark

ABSTRACT

In this paper the problem of fictitious eigenfrequencies in acoustic radiation and scattering problems is considered. A simple method to overcome the nonuniqueness problem is the Combined Helmholtz Integral Equation Formulation (CHIEF) proposed by Schenck[1]. However, CHIEF points placed on or near a nodal surface of the corresponding interior problem do not provide a linearly independent constraint. The problem of selecting 'good' CHIEF points is therefore still a major topic using CHIEF.

By using a rank revealing factorization of the BEM coefficient matrix it is shown that the necessary number of 'good' CHIEF points may be determined; furthermore one may decide whether a CHIEF point is 'good' or not.

This new approach is successfully tested on an axisymmetric BEM formulation using one or several CHIEF points.

INTRODUCTION

Boundary Element Methods (BEM) have successfully been used for solving radiation and scattering problems in acoustics for some years. One of the most significant advantages of BEM compared to the Finite Element Method (FEM) is that a three-dimensional problem may be described by a two-dimensional integral equation so that only the boundary of the (e.g. exterior) domain has to be discretized. Not only does this solve the problem of handling domains of infinite extent, which obviously are difficult to deal with with FEM, but the work of discretizing a problem to obtain a numerical solution is reduced significantly.

One of the frequently addressed problems in BEM is the problem of fictitious eigenfrequencies (or characteristic frequencies) in exterior boundary integral formulations. These fictitious eigenfrequencies are a result of the formulation into an integral equation (Fredholm integral equation of the second kind), and are the eigenfrequencies of a corresponding interior problem, but they have no physical meaning for the exterior problem under consideration.

The nonuniqueness problem is numerically manifested in a rank deficiency of the BEM coefficient matrix, and in order to obtain the unique solution that is known to exist several modified integral equation formulations that provide additional constraints to the system of equations have been proposed. As the space given here does not allow for a summary of the different formulations and their advantages/disadvantages (such a summary is given in a recent article by Wu and Seybert [2]), suffice it to say that a theoretically robust formulation suffers from being complicated and/or computationally inefficient. On the other hand, a simple formulation easy to implement, like the CHIEF proposed by Schenck [1], leaves the user without the insurance of having obtained the correct solution.

The CHIEF formulation proposed by Schenck [1] uses the Helmholtz Integral Equation for exterior problems with interior points (CHIEF points) to produce the necessary constraint

to obtain an unique solution, when the constraint is satisfied along with the Helmholtz Integral Equation with points on the surface. This formulation has the drawback that points placed on a nodal surface of the corresponding interior problem do not provide a linearly independent constraint and are therefore useless ('bad' CHIEF points). The term 'good' CHIEF points is used for points that do provide a linearly independent constraint. Another problem using CHIEF is how to determine how many 'good' CHIEF points that are needed to obtain the correct solution - recently it has been reported [2] that the use of only one 'good' CHIEF point is not in general sufficient at higher characteristic frequencies.

The problem of characteristic frequencies and interior nodal surfaces is of practical importance due to the numerical treatment: When dicretizing the problem bad solutions occur not only at the characteristic frequencies but in a range of frequencies near the characteristic frequencies - likewise are CHIEF points placed near (and not only on) the interior nodal surfaces 'bad' CHIEF points. The 'bandwidth' of the zone leading to false solutions depends on: the frequency, the sophistication of the method (the order of the polynomials used to approximate the geometry and the acoustic variables), and of the used 'fineness' of the mesh. Since it is unlikely that one should chose a frequency exactly equal to a characteristic frequency it is always (at least in theory) possible to circumvent the non-uniqueness problem by making the mesh finer. However, this is a strategy that leads to an enormous amount of computational work and storage required. According to this point of view the use of CHIEF and other methods to circumvent nonuniqueness may be regarded as methods to enable the user to maintain a mesh as coarse as possible to obtain a given accuracy when the problem of nonuniqueness is neglected (a rule of thumb is to chose the mesh size to be half a wavelength). The computational work of a formulation to circumvent nonuniqueness is therefore an important parameter to be considered.

FORMULATION

Assuming time-harmonic waves and omitting the time factor $e^{i\omega t}$ the general Helmholtz integral formula [3] can be expressed in terms of the complex pressure p:

$$C(P)\,p(P) = \int_S \left(p(Q)\,\frac{\partial G(R)}{\partial n} + ikz_0 v(Q)\,G(R) \right) dS + 4\pi p^I(P)\,. \qquad (1)$$

This formula is valid in an infinite homogeneous medium (e.g. air) outside a closed body B with a surface S. In the medium p satisfies $\nabla^2 p + k^2 p = 0$. Q is a point on the surface S, and P is a point either inside, on the surface of, or outside the body B. $R = |P-Q|$ is the distance between P and Q, and $G(R) = e^{-ikR}/R$ is the free-space Green's function; $k = \omega/c$ is the wavenumber, where ω is the circular frequency and c is the speed of sound; i is the imaginary unit and z_0 is the characteristic impedance of the medium; n is the unit normal to the surface S at the point Q directed away from the body, and v is the (complex) surface velocity normal to the body. The quantity $C(P)$ has the value 0 for P inside B and 4π for P outside B. In the case of P on the surface S, $C(P)$ equals the solid angle measured from the medium ($=2\pi$ for a smooth surface) [4]. In order to solve Eq.(1) numerically a mesh is used to discretizise the body B. The acoustic variables p and v are then supposed to follow a specific shape (e.g. quadratic) between then nodes of the mesh. In this way the geometry and the acoustic variables of the problem are defined by the values on a finite number (N) of nodes. In most problems the values of v are known or may be expressed in terms of p by an impedance relation: $p(Q) = z(Q)v(Q)$ (note however that this formula is valid only for a locally reacting surface). In order to obtain N equations matching the N unknown values of the pressure p the point P is placed on the N nodes of the surface S. The resulting equations may then be expressed in matrix form:

$$\boldsymbol{D}\boldsymbol{p} = \boldsymbol{M}\boldsymbol{v} + \boldsymbol{p}^I\,, \qquad (2)$$

where capital bold letters denote matrices and minor bold letters denote vectors. Using the boundary conditions with Eq.(2) reduces Eq.(2) to:

$$\boldsymbol{C}\boldsymbol{x} = \boldsymbol{y}\,, \qquad (3)$$

where $\boldsymbol{x}$ is the unknown vector and $\boldsymbol{y}$ is the known vector. For the problem of scattering from a rigid surface $\boldsymbol{C}$ equals $\boldsymbol{D}$ and $\boldsymbol{y}$ equals $\boldsymbol{p}^I$, and for a radiation problem where $\boldsymbol{v}$ is known $\boldsymbol{C}$ equals $\boldsymbol{D}$ and $\boldsymbol{y}$ equals $\boldsymbol{M}\boldsymbol{v}$.

SINGULAR VALUE DECOMPOSITION

As the frequency approaches a characteristic frequency the matrix $\boldsymbol{C}$ becomes ill-conditioned. The condition number κ may roughly be described as the factor a disturbance of

an element in the matrix C or the righthand-side y is multiplied with in the solution vector x. As the elements of C are a result of approximations (discretization and numerical integration) the uncertainty of these elements are usually larger than the machine epsilon (the accuracy in which the numbers are represented internally in the computer). The problem of characteristic frequencies is reflected in a large condition number.

In handling singular matrices the Singular Value Decomposition (SVD) often is considered the ultimate tool (see e.g. Press et al.[5]). The Singular Value Decomposition of a square NxN matrix A is defined as

$$A = UWV^T \ , \tag{4}$$

where V^T denotes the transposed of the matrix V. This decomposition is always possible[5], and programs to preform the SVD are available both for main-frames and for PC's (routines are listed e.g. in Press et al.[5]). The matrices U and V are each orthogonal i.e.:

$$\sum_{i=1}^{N} u_{ik} u_{in} = \delta_{kn} \ , \quad \begin{matrix} 1 \le k \le N \\ 1 \le n \le N \end{matrix} \tag{5a}$$

$$\sum_{j=1}^{N} v_{jk} v_{jn} = \delta_{kn} \ , \quad \begin{matrix} 1 \le k \le N \\ 1 \le n \le N \end{matrix} \tag{5b}$$

where u_{ik} denotes the element in row i column k, and δ is the Kronecker delta. W is a diagonal matrix, and the values w_j in the diagonal of W are called the singular values. Without loss of generality the columns of the matrices U, V, and W may be arranged in order of descending w_j's so that w_1 is the largest element and w_N is the smallest. Since U and V are orthogonal their inverses equal their transposes, and the inverse of A is

$$A^{-1} = V \cdot [\mathrm{diag}(1/w_j)] \cdot U^T \ . \tag{6}$$

Analytically this formula behaves well if none of the w_j's are zero, but numerical problems arise if one or several of the w_j's are small compared to the accuracy of the elements of A. The condition number κ of a matrix is defined as the ratio w_1/w_N, and the matrix is said to be ill-conditioned/singular if this ratio is large/infinite.

In order to investigate the properties of the SVD further it is convenient to regard A as the matrix of a linear mapping:

$$y = Ax \ , \tag{7}$$

i.e. the vector x is mapped onto the vector y by Eq.(7). The columns in U and V calculated by a SVD are connected by the simple relation:

$$Av_j = w_j u_j \ . \tag{8}$$

Any vector $x \in \mathbb{R}^N$ may be expressed by the columns of V:

$$x = \xi_1 v_1 + \xi_2 v_2 + \ldots + \xi_N v_N \tag{9}$$

and the vector y onto which x is mapped by Eq.(7) may be expressed using Eq.(8) and Eq.(9):

$$y = \sum_{j=1}^{N} \xi_j w_j u_j \ . \tag{10}$$

In this way (considering Eq.(8)) the w_j's may be regarded as the magnification of the v_j's when mapped onto the corresponding u_j's (in some sense similar to a 'transfer-function'). If A is regular (non-singular) then when x goes through all possible combinations of the columns of V (by Eq.(9)) y will go through all possible combinations of the columns of U. Consequently the columns in V spans a orthogonal basis for the solution space of A, and the columns of U spans a orthogonal basis for the range of A (range refers to 'what may be 'reached' by A').

If A is singular then one or several of the w_j's are zero (say the last N-R ones, R<N) and the corresponding last column(s) of V are called singular vectors and are by Eq.(8) mapped into the zero-vector:

$$Av_j = 0 \ . \tag{11}$$

In this case A is said to be rank deficient (the rank of A is R), and two additional subspaces are needed in the discussion of the mapping: The last N-R columns of V are called the null space of A (since they are mapped into the zero vector), and the corresponding (last N-R) columns of U are called the orthogonal complement of A (since this vector space may not be 'reached' by A). The solution space of A is then spanned by the first R columns of V, and the range of A by the first R columns of U. These properties are summarized in table 1:

Table 1: The connection between the four fundamental subspaces and the SVD.

name	basis vectors	dimension
range	$u_1, u_2, \ldots, u_R$	R
orthog. compl.	$u_{R+1}, \ldots, u_N$	N-R
solution space	$v_1, v_2, \ldots, v_R$	R
null space	$v_{R+1}, \ldots, v_N$	N-R

If A is the coefficient matrix of a system of equations to be solved for a known right-hand side b i.e.:

$$Ax = b \ , \tag{12}$$

a singular matrix corresponds to one of two alternatives: Either the system of equations has no solution (b is not in the range of A) or the system of equations has one or several infinities of solutions (b is in the range of A, and may be expressed as a linear combination of the first R columns of A), since in this case any combination of the zero-vectors ($v_{R+1}, \ldots, v_N$) may be added to a specific solution. In contrast to e.g. the simple source formulation[1] a solution is known to exist at characteristic frequencies, and the latter alternative is therefore the actual one. The number of zero w_j elements is as previously stated the rank deficiency of the matrix A and is the number of missing linearly independent equations that must be added in order to maintain a system where the number of equations equals the number of unknowns. The problem is therefore to add additional constraints to the system of equations in order to obtain an unique solution (or in other words in order to pick out the correct combination of the singular vector(s)).

Numerically an exact singular matrix seldom occurs, but the situation described above is manifested in an ill-conditioned matrix. The numerical rank of a matrix may be defined as the number of w_j's under a certain value (corresponding to a maximal condition number κ_{max} chosen with regard to the approximations made or with regard to experience). If Eq.(6) is used without modifications at a characteristic frequency the solution vector may be drawn towards infinity in a direction that is almost a singular vector or in the case of a rank deficiency higher than one: a combination of the singular vectors (the solution is polluted with a constant times the singular vector(s)) due to approximations made and/or round-off errors. (As previously stated round-off errors are mostly negligible compared to the approximations made.)

USING SVD IN BEM

The CHIEF approach uses the Helmholtz integral equation with interior points in order to produce these linearly independent equations [1]. However, a CHIEF point placed on or near a nodal surface of the corresponding interior problem does not provide a linearly independent constraint and is useless [2] (or sometimes even more corrupting to the solution than doing nothing). An approach is to distribute a number of CHIEF points hoping that a sufficient number of CHIEF points do not fall on or near a nodal surface. The resulting overdetermined system of equations is then solved by means of a least-squares procedure. Note that the SVD may also be used in the case of a MxN matrix (M>N). In this case U is a MxN column-orthogonal matrix, and the matrices V and W are both NxN. The (generalized) condition number is still defined as the ratio w_1/w_N. In terms of accuracy the SVD is more favourable than the normal least-squares procedure using A^TA since the matrix A^TA has the condition number κ^2, if the rectangular matrix A has the condition number κ.

The theory in the last paragraph was discussed for the case of a real matrix A. Handling the complex BEM coefficient matrix in Eq.(3) may be done either by a complex SVD routine or by rewriting the complex system of equations in Eq.(3) to a real system of equations: With $C=A+iB$, $x=x^R+ix^I$, and $y=y^R+iy^I$ one may rewrite Eq.(3):

$$\begin{bmatrix} A & -B \\ B & A \end{bmatrix} \begin{Bmatrix} x^R \\ x^I \end{Bmatrix} = \begin{Bmatrix} y^R \\ y^I \end{Bmatrix} . \tag{13}$$

If $x_0=x_0^R+ix_0^I$ is a singular vector:

$$\begin{bmatrix} A & -B \\ B & A \end{bmatrix} \begin{Bmatrix} x_0^R \\ x_0^I \end{Bmatrix} = 0 \ , \tag{14}$$

then it immediately follows that $-x_0^I+ix_0^R$ is a singular vector as well, and this vector is evidently orthogonal to $x_0=x_0^R+ix_0^I$. It can be shown that the singular values of the matrix

in Eq.(12) always are pairs of same value due to the special structure of the 2Nx2N matrix, and that the two columns in U and V corresponding to the two identical w_j's have the above mentioned property. In the following examples only one value of the pair of w_j's is shown. In order to investigate the behaviour of the singular values (the w_j's) near a fictitious eigenfrequency, SVD has been preformed on the square BEM coefficient matrix in the case of a rigid sphere. The axisymmetry of the geometries in the presented examples has been made use of, and hence the test case is made on an axisymmetric BEM formulation where only the generator of the bodies is discretizied. The generator of the sphere was divided into 19 line segments and 20 nodes, and p was assumed to follow a linear variation between the nodal values (v is zero).

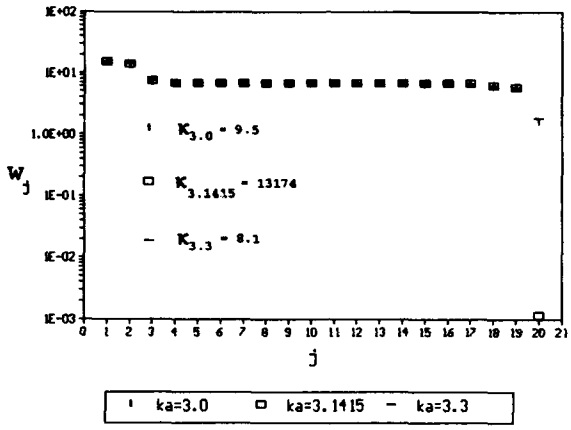

Figure 1: The singular values at three frequencies near the first fictitious eigenfrequency $ka=\pi$. The last singular value becomes very small at $ka=\pi$, whereas the other singular values are practically identical in the range $3<ka<3.3$. This behaviour is directly reflected in the condition number $\kappa=w_1/w_N$, which becomes large at $ka=3.1415$.

One of the important properties of the SVD can be deduced from figure 1, which shows the singular values of the BEM coefficient matrix at the frequencies $ka=3$, 3.1415, and 3.3. In the cases $ka=3$ and $ka=3.3$ all the singular values are of same magnitude, and the condition number κ is small and the solution produced by the normal BEM formulation is good. In the case $ka=3.1415$ (very close at $ka=\pi$) the last singular value becomes very small, and therefore the condition number becomes large. Hence the solution produced by solving the square system of equations is bad (useless). Since only one singular value becomes small at $ka=3.1415$ only one good CHIEF point is needed to add sufficient constraint to the system of equations, and the condition number calculated by the SVD for the overdetermined system of equations produced by the BEM coefficient matrix with a CHIEF point in the centre of the sphere is $\kappa=2.6$. Note that the condition number for the overdetermined system at the first fictitious eigenfrequency is less than the condition number at the two nearby frequencies ($ka=3$ and $ka=3.3$); this indicates that at these frequencies the problem of fictitious eigenfrequencies is already detected by the SVD due to the 'bandwidth' of the fictitious eigenfrequencies, but is not at this distance to the fictitious eigenfrequency so severe that a bad solution is obtained.

ADDING A CHIEF POINT

Once one by inspecting the singular values of the BEM coefficient matrix has decided the number of good CHIEF points needed to pick out the correct solution to the problem it becomes important to be able to estimate the quality of the CHIEF point. Note that if the complex system of equations has been translated to a real system by Eq.(13) a CHIEF point provides two independent equations to be satisfied along with the normal BEM coefficient matrix corresponding to the two singular vectors shown to exist in the previous section for the two identical singular values.

The SVD provides a very good tool for deciding whether a CHIEF point is good: The singular vectors. When a matrix A is rank-one deficient any constant times the singular

vector may be added to a specific solution without altering the righthand side. Consider the system of equations:

$$Ax = y \quad (=A(x+t\,x_0)) \; . \tag{15}$$

Normally the solution x found by the SVD or any other equation solver is encumbered with a wrong constant times the singular vector, and the problem is now to obtain an extra equation to determine the constant t_1 giving the correct solution $x_1=x+t_1x_0$. If an extra equation is added to Eq.(14) then the following system is obtained:

$$\begin{bmatrix} A \\ a_{ex}^T \end{bmatrix}(x+t_1x_0) = \begin{bmatrix} y \\ y_{ex} \end{bmatrix} \tag{16a}$$

$$\Updownarrow$$

$$Ax = y \;\wedge\; (a_{ex}^T)(x+t_1x_0) = y_{ex} \; . \tag{16b}$$

Here the first statement in Eq.(16b) obviously is correct since x is a solution to Eq.(15), and since x_0 is a singular vector. If the extra equation contains further information than Eq.(15) then x_0 must not be a singular vector to the overdetermined system, and by using the last statement in Eq.(16b) this implies that:

$$a_{ex}^T \; x_0 \neq 0 \; . \tag{17}$$

If Eq.(17) is true (in practice the lefthand side must be greater than a certain threshold) then may Eq.(16) be solved for the unknown t_1, and the correct solution is thereby found. The lefthand side of Eq.(17) may be used as a quality control of the extra equation, since a small product implies that no additional constraint has been obtained. A good choice for the particular solution x is the least squares solution produced by the SVD by zeroing $1/w_j$ if w_j is small [5]; this corresponds to eliminating the influence of the singular vector by zeroing the constant with which they are encumbered in a normal solution obtained by a SVD with unchanged $(1/w_j)$'s or any other method to solve linear equations.

The theory described above is also valid for the case of the 2Nx2N real system translated from the complex BEM coefficient matrix. Here the combination of two singular vectors corresponding to two identical singular values is to be found from the two extra equations added by a CHIEF point. Due to the special symmetry of the equations the largest of the dot products of an extra equation and the singular vector (like Eq.(17)) may be used as a quality control. In order to test this formulation the case of a rigid sphere is considered at ka=6.2832. The condition number of the BEM coefficient matrix in this case is 12161, and a 30 node discretization is used. The residual is calculated as the vector containing the difference between the analytical magnitude of the nodal pressures and the magnitude of the nodal pressures calculated by the above described method. At $ka=2\pi$ the interior nodal surface is a sphere with the same centre and the radius a/2. Figure 2 shows the error calculated as the length of the residual vector and the value of the quality control calculated by Eq.(17) as functions of the ρ-coordinate of the CHIEF point the z-coordinate being zero. It is evident that the quality control is very well correlated with the solution error.

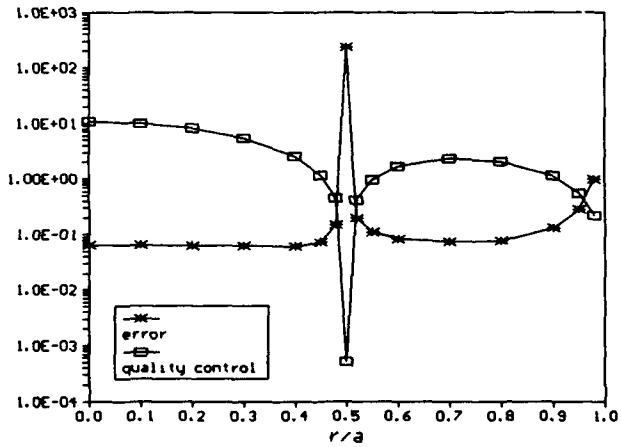

Figure 2: The error and the quality control as functions of the ρ-coordinate (z=0) of the CHIEF point for the case of a rigid sphere at ka=6.2832.

SVD AT HIGHER FREQUENCIES

At higher frequencies the nonuniqueness problem becomes more severe due to the close spacing and to the 'bandwidth' of the characteristic frequencies. One may very well encounter the situation where the bands of bad solutions no longer are disjunct and the solution is corrupted by two or more characteristic frequencies near any chosen frequency. This situation is reflected in two or more small singular values calculated by the SVD with corresponding singular vectors, and the (numerical) rank deficiency of the BEM coefficient matrix is greater than one. The number of required good CHIEF points equals the number of small singular values, and they must be chosen so that the quality control is fulfilled for all singular vectors for at least one CHIEF point (but a single CHIEF point does not need to fulfil the quality control for all singular vectors). Note that the method of quality control and finding the right combination of singular vectors are valid also when the w_j's are not exactly zero but less than a threshold decided by the user. In this way one may at any higher frequency benefit from adding CHIEF points selected by inspection of the quality control indicators.

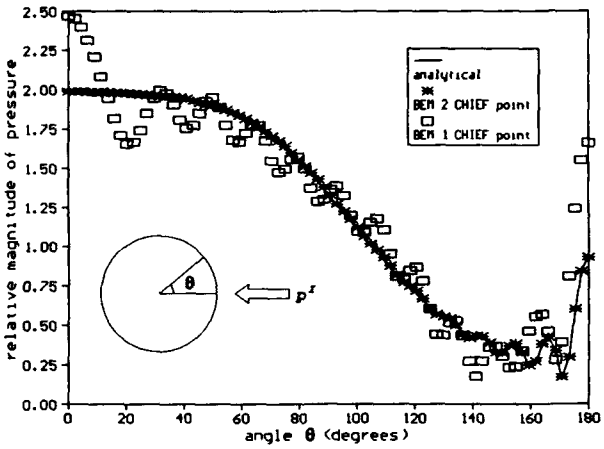

Figure 3: Scattering by a sphere for ka=15.0397. Two CHIEF points are needed to obtain an accurate solution.

In order to provoke a higher rank deficiency, scattering of a plane wave with magnitude one from a rigid sphere for ka=15.0397 is considered. The generator of the sphere is discretizied in 79 elements and 80 nodes. In this case two singular values become very small due to the presence of another fictitious eigenfrequency at ka=15.0335 ($\kappa=w_1/w_N$=2466; w_1/w_{N-1}=310; w_1/w_{N-2}=9.7), and the rank deficiency of the BEM coefficient matrix is two. Figure 3 shows the magnitude of the pressure on the surface as a function of the angle defined in the small inset in the figure. It is evident that in this case two 'good' CHIEF points are required to obtain an accurate solution. The CHIEF points are selected with respect to the quality control.

DISCUSSION

The two important features of the SVD are:

1) The singular values, which allow the user to decide how many CHIEF points are needed (if any).
2) The singular vectors, which provide an excellent tool to check the quality of the CHIEF points.

The main disadvantages of the SVD are its great complexity and the fact that calculating the SVD is quite time consuming compared to other methods. However, in BEM the time consumed by setting up the equations is in most cases still much larger than the time used to solve the system of equations.

Recently another method to estimate the singular values and the singular vectors -the rank revealing QR factorization (RRQR)- has been discovered[6]. The RRQR is far more efficient (in terms of consumed time and storage) than the SVD.

In many cases it would be more advantageous to solve the overdetermined system of

equations arising from the BEM coefficient matrix and from the CHIEF points rather than finding the right combination of singular vectors (by solving a small system of equations for the unknown t_1's). Using the SVD this probably means that a new SVD must be calculated for the resulting overdetermined system of equations, but using the RRQR factorization it is possible to update the factorization when extra equations are added to the original system[7].

Note that the attempt described in this paper is valid for any kind of extra equations one may wish to add to the original BEM coefficient matrix. This attempt may therefore be used in more advanced formulations to circumvent the nonuniqueness problem like SuperCHIEF or CHIEF-block (see [2] and the references therein). The extra equations obtained by any of these advanced CHIEF methods may be checked in the same way as the ordinary CHIEF points. Since these formulations often offer more equations than the rank deficiency of the BEM coefficient matrix, the resulting overdetermined set of equations must be solved in least squares since - e.g. by the use of a RRQR factorization.

It must be emphasized that the test cases presented in this paper concerns an axisymmetric model where the rank deficiency problem is less severe than in a general three-dimensional formulation, but this method is valid for general three-dimensional formulations as well.

Finally it should be mentioned that the approach proposed by Burton and Miller and used in [4] also can be expected to fail when the frequency get so high that the bands of bad solutions from the Helmholtz Integral Equation and its normal derivative no longer are disjunct.

CONCLUSIONS

In this paper it has been shown that the rank deficiency of the BEM coefficient matrix at characteristic frequencies may be revealed by a singular value decomposition (SVD).

It has been shown that due to the 'bandwidth' of the characteristic frequencies the rank deficiency of the BEM coefficient matrix may be greater than one when two or several characteristic frequencies are near the frequency in interest.

The number of 'good' CHIEF points needed to obtain an unique solution equals the rank deficiency of the BEM coefficient matrix, and it has been shown that by making use of the singular vectors obtained by the SVD the quality of the CHIEF points can be evaluated reliably.

This formulation may also be applied to more advanced methods to overcome the non-uniqueness problem.

The author believes that this formulation provides a useful tool not only for solving the nonuniqueness problem, but also for maintaining a mesh as coarse as possible for a given accuracy. This latter feature becomes very significant when modelling complex structures at higher frequencies, and the author believes that by the use of this formulation it is possible to apply BEM to a larger category of problems than up to the present.

REFERENCES

1. H.A.Schenck, "Improved Integral Formulation for Acoustic Radiation Problems", J. Acoust. Soc. Am. 44,41-58 (1968).

2. T.W.Wu and A.F.Seybert, "A weighted residual formulation for the CHIEF method in acoustics", J. Acoust. Soc. Am. 90,1608-1614 (1991).

3. B.B.Baker and E.T.Copson "The mathematical Theory of Huygens' Principle", 2nd Edition Oxford University Press, 1-32 (1953).

4. C.C.Chien,H.Rajiyah and S.N.Atluri,"An Effective Method for Solving the Hypersingular Integral Equations in 3-D Acoustics", J. Acoust. Soc. Am. 88, 918-937 (1991).

5. W.H.Press et al. "Numerical Recipes", Cambridge University Press, 52-64 (1986).

6. T.F.Chan, "Rank revealing QR factorizations", Lin.Alg.Appl. 88/89 (1987), 67-82.

7. G.H.Golub and C.F.Van Loan, "Matrix Computations", 2nd Edition, The John Hopkins University Press 592-600 (1989).

SECOND INTERNATIONAL CONGRESS ON RECENT DEVELOPMENTS IN AIR- AND STRUCTURE-BORNE SOUND AND VIBRATION
MARCH 4-6, 1992 AUBURN UNIVERSITY, USA

Implementation of Boundary Element Method for Solving Acoustic Problems on a Massively Parallel Machine

A. Dubey*, M. Zubair†, and U.S. Shirahatti‡

Abstract

Boundary Element Method (BEM) has found increasing use in the solution and analysis of acoustic field problems. The BEM requires less grid generation and is ideal for solving infinite domain problems. The BEM is computationally intensive and is suitable for parallel implementation. The three major tasks in the implementation of BEM are:

- Computation of H and G action matrices using numerical integration. The elements of these matrices can be computed in parallel.
- Rearrangement of H and G matrices into [A] {X} = {B} form. On a parallel machine this essentially means redistribution of data. To minimize redistribution cost it is desirable to map the problem intelligently on the parallel machine.
- Solving for the unknown X on the boundaries and at the required field points in the interior of the domain. Here, parallelism can be exploited both for computing X at the boundaries and in the interior.

In this paper we look at the implementation of BEM on a hypercube based parallel machine, the Intel iPSC-860. The example problem which we consider is the solution of Helmholtz equation inside a three-dimensional rectangular acoustic duct.

*Department of Computer Science, Old Dominion University, Norfolk, VA
†Department of Computer Science, Old Dominion University, Norfolk, VA
‡Department of Mechanical Engineering and Mechanics, Old Dominion University, Norfolk, VA

1 Introduction

The numerical solution of acoustic field problems has attracted considerable attention in recent years. The numerical solutions have been proposed using the finite difference, the finite element or the boundary element method (BEM) [1]. The BEM is computationally intensive and is suitable for parallel implementation. In implementing BEM one can exploit parallelism at two phases. One while computing the unknown quantities at the boundary elements and the second while computing the field values inside the domain. Major part of computations in both the phases involve evaluation of mutually independent surface integrals which is ideally suited for parallel environment. The other major computation is parallel solution of a system of linear equations, which has been extensively studied by researchers in past, e.g. [2, 3]

In this paper we look at the implementation of BEM on a hypercube based parallel machine, the Intel iPSC-860. The example problem is the computation of acoustic field inside a three-dimensional rectangular duct with various boundary conditions prescribed on the surface. The equation governing the acoustic field quantities is the three-dimensional wave equation.

2 Boundary Element Formulation

The acoustic field in a duct is governed by the wave equation,

$$\nabla^2 p = \left(\frac{1}{c^2}\right)\left(\frac{\partial^2 p}{\partial t^2}\right) \quad , \tag{1}$$

where, c represents the speed of sound in the fluid. The Laplacian, ∇^2, in cartesian coordinates for three-dimensions, is

$$\nabla^2 = \frac{\partial^2}{\partial x^2} + \frac{\partial^2}{\partial y^2} + \frac{\partial^2}{\partial z^2} \tag{2}$$

By assuming the pressure in the form,

$$(px, y, z, t) = p(x, y, z)e^{-i\omega t}, \tag{3}$$

the wave equation is reduced to the Helmholtz equation,

$$\nabla^2 p + k^2 p = 0, \quad \textit{in the domain } \Omega \tag{4}$$

where k is defined as the wave number ($k = \omega/c$). The symbol p represents the pressure distribution and q is defined by,

$$q = \frac{\partial p}{\partial n} \tag{5}$$

where n is the unit normal on the boundary.

Now consider the following boundary conditions,

$$\begin{aligned} &p = \bar{p} \text{ on } \Gamma_1 \quad \textit{Essential Condition} \\ &q = \bar{q} \text{ on } \Gamma_2 \quad \textit{Natural Condition} \end{aligned} \tag{6}$$

where the total boundary of the domain Ω is $\Gamma = \Gamma_1 + \Gamma_2$.

The boundary conditions basically consist of two types of known values. Either the pressure or the normal derivative of the pressure is known at the boundary as seen in Eq(6).

The method of weighted residuals statement of the Helmholtz equation is

$$\int_\Omega \left(\nabla^2 p + k^2 p\right) p^* d\Omega = 0 \tag{7}$$

where the fundamental solution,p^*, or Green's function for the Helmholtz equation satisfies

$$\nabla^2 p^* + k^2 p^* + \Delta_i = 0, \tag{8}$$

and Δ_i is the Dirac delta function. The fundamental solution in three-dimensional space is

$$p^* = \frac{i}{4\pi r} e^{ikr}, \tag{9}$$

and

$$q^* = \frac{1}{4\pi r}\left(\frac{-1}{r} + ik\right) e^{ikr} \tag{10}$$

where r is the distance between the source point and the observation point.

Integrating Eq.(7) by parts twice, we get

$$\int_\Omega \left(\nabla^2 p^* + k^2 p^*\right) p \, d\Omega = -\int_\Gamma q p^* d\Gamma + \int_\Gamma p q^* d\Gamma. \tag{11}$$

The term, $\int_\Omega (\nabla^2 p^* + k^2 p^*)\, p\, d\Omega$ in Eq.(10) can be shown to reduce to $-c_i p_i$. The expression c_i is considered constant for each boundary element and is defined as

$$\begin{aligned} c_i &= 0 \;\; \textit{outside the boundary} \\ c_i &= \frac{1}{2} \;\; \textit{on a smooth boundary} \;\; (\Gamma) \\ c_i &= 1 \;\; \textit{inside the boundary} \, (\Omega) \end{aligned} \tag{12}$$

The boundary element governing equation becomes

$$c_i p_i + \sum_{j=1}^{N} \int_{\Gamma_j} q^* p d\Gamma = \sum_{j=1}^{N} \int_{\Gamma_j} p^* q d\Gamma, \tag{13}$$

where N is the total number of elements. Eq.(13) is applied to each element to form a set of equations with p or q unknown in each element. Substituting the fundamental solution, Eq.(9), into the boundary element governing equation, Eq.(13), gives

$$c_i p_i + \sum_{j=1}^{N} \int_{\Gamma_j} p \left[(i/4\pi r)(-1/r + ik)\, e^{ikr} \right] d\Gamma = \sum_{j=1}^{N} \int_{\Gamma_j} q \left[(i/4\pi r)\, e^{ikr} \right] d\Gamma. \tag{14}$$

If constant elements are used, p and q are assumed constant over each element. Therefore, p and q can be extracted from the integrals in Eq.(14).

System of equations.

By applying the governing equation to each element, a set of equations is formed which can be represented in matrix form. The integrals in Equations (13) and (14) can be written as

$$\hat{H}_{ij} = \int_{\Gamma_j} q^* d\Gamma, \quad G_{ij} = \int_{\Gamma_j} p^* d\Gamma \tag{15}$$

for constant elements. The integrals in Eq.(15) are solved using a four-point Gauss quadrature technique. The system of equations becomes

$$c_i p_i + \hat{H}_{ij} p_i = G_{ij} q_i. \tag{16}$$

The $c_i p_i$ term can be combined with the $\hat{H}_{ij}$ term to form a new matrix H_{ij}

$$H_{ij} = \begin{cases} \hat{H}_{ij} + c_i & i = j \\ \hat{H}ij & i \neq j \end{cases}. \tag{17}$$

Therefore, the system of equations in matrix form is

$$[H]\{P\} = [G]\{Q\} \tag{18}$$

Both $\{P\}$ and $\{Q\}$ vectors contain known and unknown values of p and q. To solve Eq.(18), the matrices will be transformed into a new matrix equation

$$[A]\{X\} = \{B\}; \tag{19}$$

where all the unknowns are in $\{X\}$. After solving the system of equations, all the p and q terms are known at the boundary. If any values of internal points are required, they can be found only after the boundary values have been calculated.

3 Parallel Implementation

3.1 Intel iPSC-860

The Intel iPSC-860 is a large-scale parallel supercomputer with a Multiple Instruction Multiple Data distributed memory architecture. Computation is carried out in physically independent processors referred to as nodes. The nodes are physically connected in a multidimensional hypercube topology. A hypercube of dimension d has 2^d processors labeled 0 to $2^d - 1$, with a connection between two processors if and only if the binary representations of the labels of these processors differ in exactly one bit. The interconnection network of a 16 node hypercube is shown in Figure 1.

A single node of an Intel iPSC-860 is a fully functional computer system containing an i860 microprocessor with I/O facilities. The Intel i860 microprocessor uses an advanced architecture to deliver balanced integer and floating-point performance. The iPSC-860 systems are scalable from 8 processors to 128 processors, with peak performance ranging from 480 MFLOPS for an 8 processor system to 7.6 GFLOPS for a system with 128 processors. Each processing node can have 8 to 64 MBytes providing total system memory ranging from 64 MBytes to 8 GBytes. Communication among nodes is a critical performance element for parallel processing computers. The Intel iPSC-860 nodes communicate via Intel's proprietary Direct-connect internal network, a message passing system that dynamically creates communication circuits between communication nodes. When two nodes wish to communicate, the network builds a communication channel between them for as long

as the communication lasts and transmits the message at a bi-directional rate of 5.6 MBytes/sec. Total communication bandwidth scales with the number of computing nodes.

3.2 Parallel Implementation of BEM

An informal description of a parallel implementation of BEM on the Intel iPSC-860 is as follows.

Step 1. Distribute geometry information about the physical domain including the elements details to all the p nodes of the iPSC-860 system.

Step2. Assign $k = N/p$ distinct elements to each node, where n is the total number of elements. Each node then computes $2k(n-1)$ integral expressions using gauss quadrature. After this step we have all the elements of action matrices H and G distributed over various nodes of the system.

Step 3. Redistribute and combine the elements of H, G, P, and Q so as to get the $AX = B$ form. The redistribution is such that contiguous columns of A are mapped to a node. We have opted for this distribution because we intend to use the system solver package developed by Dongarra and Ostrouchov [2].

Step 4. Solve for X using an the package described in [2]. After this step we have all the information about the boundary points which is distributed to all the nodes of the system.

Step 5. Let N_d be the total number of points of interest in the interior domain. Assign N_d/p points to a node of the iPSC-860 system. Each node then computes field values for N_d/P points by evaluating surface integrals using Gauss quadrature.

To illustrate these steps in some detail, let us consider an example where the problem domain is divided into 24 boundary elements, as shown in Figures 2-3 (four elements per face of the duct). The hypercube chosen for this example has a dimension 2. In the first step we distribute the geometry information (consisting of the coordinates of end points and mid point of each element) of the entire domain to all four nodes of the hypercube. Figure 4 shows the distribution of these 24 elements to the nodes of the hypercube. Figure 5 indicates the generation of the columns of G and H matrices corresponding to the elements mapped onto each node. For example, node PE_0 generates first six columns of G and H. Generation of a column of G or H involves 23 surface integrals (Note that the diagonal element which corresponds to the singularity is analytically obtained.). The rearrangement step basically involves (i) a local sub-matrix into vector operation resulting

in b^i's, and (ii) movement of b^i's across the nodes. This is illustrated in Figures 6-8. The implementation of Step 5 is similar to that of Step 2.

4 Preliminary Study

Our preliminary study is for a rectangular duct, the surface of which has been modeled using constant quadrilateral elements. The boundary conditions on the rectangular duct would be as rigid walls on four of longer faces. We will incorporate a harmonic time dependent forcing function on one of the smaller faces. The boundary condition on the opposite small face will consist of (i) rigid wall, (ii) ρc termination, and (iii) impedance termination. Preliminary results will be presented.

References

[1] C.A. Brebbia, J.C.F. Telles, and L.C. Wrobel, *Boundary Element Techniques*, Springer Verlag, 1984.

[2] J. Dongarra and S. Ostrouchov, *LAPACK block factorization algorithms on the Intel iPSC-860*, LAPACK Working Note 24, Technical Report CS-90-115, University of Tennessee, Oct.1990.

[3] K.A. Gallivan et al., *Parallel algorithms for matrix computations* , SIAM, 1990.

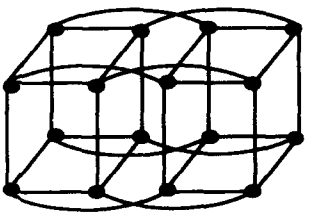

Figure 1. Interconnection network for a sixteen node hypercube.

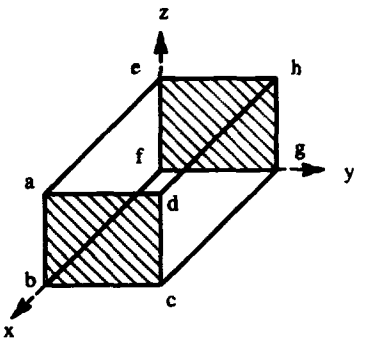

Figure 2. A rectangular duct.

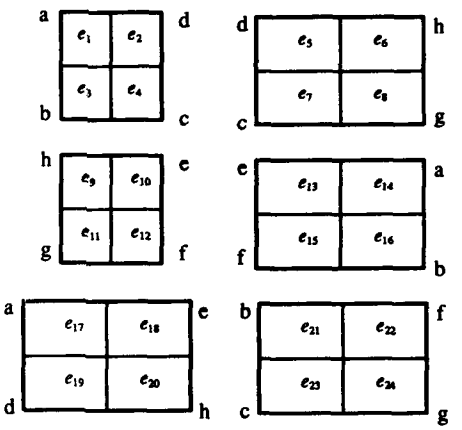

Figure 3. Division of the six faces of the rectangular duct into boundary elements.

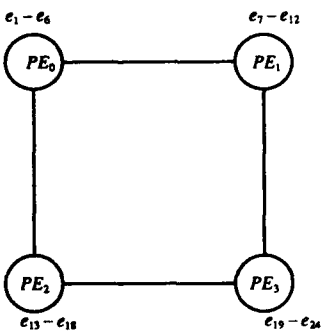

Figure 4. Boundary elements mapping on a 2-dimensional hypercube.

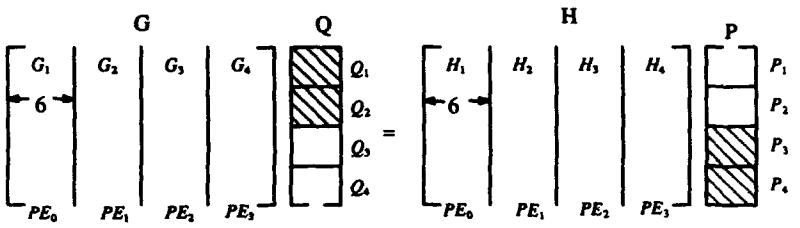

Figure 5. Assignment of Processors for computing matrix coefficients. (the shaded regions indicate known values and the unshaded regions indicate unknown values).

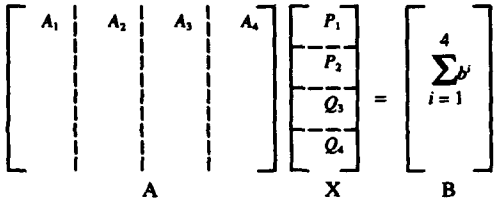

Figure 6. Rearrangement of G and H matrices. (Note that $b^1 = G_1Q_1$, $b^2 = G_2Q_2$, $b^3 = H_3P_3$, $b^4 = H_4P_4$)

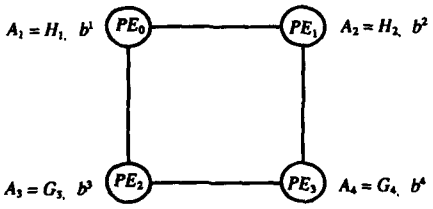

Figure 7. Distribution of matrix–A, and vector–b–partial–sum on a 2–dimensional hypercube.

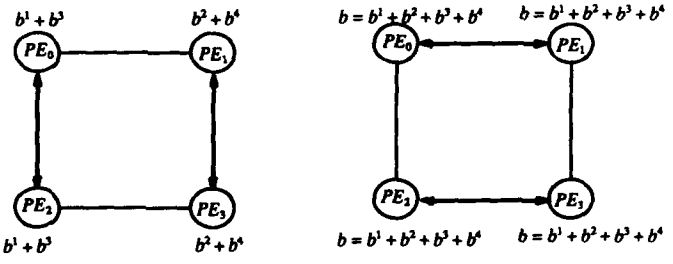

Figure 8. Algorithm for computing partial sums of b and its distribution to all the nodes.

SECOND INTERNATIONAL CONGRESS ON
RECENT DEVELOPMENTS IN AIR- AND
STRUCTURE-BORNE SOUND AND VIBRATION
MARCH 4-6, 1992 AUBURN UNIVERSITY, USA

SOUND RADIATION OF HEAVY-LOADED COMPLEX VIBRATORY STRUCTURES USING BOUNDARY INTEGRAL EQUATION METHOD

Michael V. Bernblit
Department of Electronics and Controls.
St.-Petersburg Ocean Technology University.
St.-Petersburg, 190008.
U.S.S.R.

The computational method for calculating of Complex Vibratory structures' Sound Radiation into an infinite acoustical medium is developed using a modified Boundary Integral Equation (BIE) technique. The two-level procedure is presented as the computational shell for Sound Radiation of heavy-loaded structures when their vibration in air is numerically predicted. The method is compared to the conventional modal analysis approach. Numerical results are presented for the normal point-force driven free-free beam in water.

The radiation field of a complex structure vibrating with a speciefied distribution of the normal velocity $Vn(\vec{x})$ at its surface S can be calculated using Boundary Integral Equation [1-3]

$$0.5\ p(\vec{z}) + \int p(\vec{x}) \cdot g_v(\vec{z},\vec{x}) dS = -j\omega\rho \int Vn(\vec{x}) \cdot g_p(\vec{z},\vec{x})\ dS\ , \quad (1)$$

where $p(\vec{z})$ is a surface pressure to be computed; $\vec{x},\vec{z}$ are the source and surface field points; ρ is the density of the acoustic medium; $\omega = 2 \cdot \pi \cdot f$; $g_p(z,x)=\exp(jkr)/4\pi r$ is a free-space Green function for the infinite acoustic medium; $k=\omega/c$-wavenumber; $g_v = \partial g_p/\partial n$ is the Green function's normal derivative. After $p(\vec{z})$ is calculated from Eq.1 Sound Field at any arbitrary point can be computed using Helmholz integral. More over, Sound Intensity mapping can be added to observe acoustic energy distribution. Total radiated power and radiation efficiency also can be derived numerically. So using BIE technique the compete solution of the Sound Radiation Problem can be obtained.

Unfortunatly, when the normal component of the surface velocity $Vn(\vec{x})$ is not specified, it should be derived from the matrix equation of the body-motion

$$[M]\ \{\ddot{x}\} + [R]\ \{\dot{x}\} + [k]\ \{x\} = \{Q\} - \{P\}\ , \quad (2)$$

where [M], [R], [k] are the mass, damping and stiffness matrices; {x} and {Q} are the vectors of the surface displacements and the intensity of the applied forces; $\{P\}^T = \{0,0,p\}$ is the acoustic radiation loading. In case of "light" acoustic medium (in air) the surface pressure loading {P} in Eq.2 can be ignored and $Vn(\vec{x})$ is easily computed (any commercial Finite

Element or Modal Analysis software can be used). But when the acoustic loading is heavy (in liquids) Eq.1 and 2 must be treated simultaneously, because $Vn(\vec{x})$ depends on the unknown distribution of the surface pressure. Many efforts has been done to combine BIE with the conventional eigenvalue analysis, but all of them couldn't provide the exact solution, because of the Modal Coupling problem in Sound-Structure's Interaction.

Nevertheless such a solution can be obtained using a definition of the displacement vector {x} as a convolution of the structural Green function $G(\vec{x},\vec{y})$ with the intensity of the applied forces [4]:

$$\{x\} = \int [\ G(\vec{x},\vec{y})\ ] \cdot (\{Q(\vec{y})\} + \{P(\vec{y})\}\ )\ dS.$$

Thus the displasement of a fluid-loaded surface is presented as a sum of that one $\{x\}_0$ for the unloaded structure and a convolution of its Green function and the surface presure p(y)

$$\{x\} = \{x\}_0 + \int G_3(\vec{x},\vec{y}) \cdot p(\vec{y})\ dS \qquad (3)$$

where $G_3(\vec{x},\vec{y}) = \sum_{i=1}^{N} G_{i3}$ is the normal component of the N-dimensioned compliant matrix.

Substituting Eq.3 into Eq.1 one can obtain the modified BIE

$$0.5\ p(\vec{z}) + \int p(\vec{y}) \cdot g_{pv}(\vec{y},\vec{z})\ dS = \rho \int a_n^{(0)} g_p(\vec{y},\vec{z})\ dS, \qquad (4)$$

where $a_n^{(0)} = -\omega^2 \cdot \{x\}_3$ is the normal surface acceleration; the kernel

$$g_{pv}(\vec{z},\vec{y}) = g_v(\vec{z},\vec{y}) - \rho \int g_p(\vec{z},\vec{x})\ G_3^{(a)}(\vec{x},\vec{y})\ dS$$

contains the additional member which is the convolution of the structural $G_3^{(a)} = -\omega^2 G_3$ and medium g_p Green functions.

Thus the two-level procedure of BIE method is presented for the acoustically loaded structures. At first the fluid loading is ignored and the in-vacuo acceleration $a_n^{(0)}$ and the Structural Green function is calculated using any available software. Then the surface pressure distribution is computed from Eq.4. At second the vibration of the loaded structure is derived from Eq.3. As a result, Helmholz integral formula predicts the pressure at any arbitrary field point.

The numerical solution of 3d Helmholz integral eqation and the problem of its uniqueness were discussed in various publications.The Combined Helmholz Integral Equation Formulation (CHIEF) [3] was prefered. The body surface S was devided into N planar elements assuming that the velocity and pressure distribution were iniform over each of the surface element ΔS. For this case Eq.4 can be rewritten in the matrix form

$$\{\ [I] + [D]\ \}\ \{p\} = [Q]\ \{a_n^{(0)}\}\ , \qquad (5)$$

where $D_{qs} = 2 \int g_{pv}(r_{qs}) \cdot dS$ and $Q_{qs} = 2\rho \int g_p(r_{qs}) \cdot dS$ are coefficients, related the contribution of the dipole and monopole elementary sources. This coefficients are calculated numerically [5]; [I] is the Unit matrix.

It is interesting to compare the modified BIE procedure with the approach, based on the conventional modal analysis, previously developed in Sound-Structure's interaction problem. For this purpose the in-vacuo $a_n^{(0)}(y)$ and fluid-loaded $a_n(\vec{y})$ surface acceleration can be given in series

$$a_n(\vec{y}) = \sum A_\nu \Psi_\nu(\vec{y}); \qquad a_n^{(0)}(\vec{y}) = \sum A_\nu^{(0)} \Psi_\nu(\vec{y})\ , \qquad (6)$$

where A_ν and $A_\nu^{(0)}$ are modal complex amplitudes, $\Psi_\nu(\vec{y})$ is the in-vacuo

orthonormal modal functions.

The structural in-vacuo Green function has a well known representation [6]

$$G_s^{(\omega)}(\vec{x},\vec{y}) = \sum_{\nu} \Psi_\nu(\vec{x}) \cdot \Psi_\nu(\vec{y}) \; / \; m_\nu(1- \bar{\omega}_\nu^2/\omega^2) \; , \qquad (7)$$

where m_ν is the modal (per unit area) mass; $\bar{\omega}_\nu^2 = \omega_\nu^2 \cdot (1-j\eta_\nu)$; ω_ν is the natural frequency of the ν-mode; η_ν is the corresponding in-vacuo loss factor. Neglecting the influence of the surface dipole sources, $p(\vec{x})$ is represented by

$$p(x) = 2\rho \int a_n^{(\omega)}(\vec{y}) \; g_p(\vec{x},\vec{y}) \; dS \; . \qquad (8)$$

Substituting (6-8) into Eq.4 one can derive the infinite system

$$A_\nu + \sum_{\mu} A_\mu (\bar{m}_{\nu\mu} / [m_\mu(1- \omega_\mu^2/\omega^2)] = A_\nu^{(0)} \; , \qquad (9)$$

where $\bar{m}_{\nu\mu} = -2\rho \int_{S_y} \Psi_\nu(\vec{y}) \cdot \int_{S_x} \Psi_\nu(\vec{x}) g_p(\vec{x},\vec{y}) \; dS_x dS_y$ is the complex modal entrained mass.

If the modal coupling is not considered, then from Eq.9

$$\frac{A_\nu}{A_\nu^{(\omega)}} = \frac{1- \omega^2/\omega_\nu^2 - j\eta_\nu}{1- \omega^2/\Omega_\nu^2 - j(\eta_\nu + \eta_\nu^r \omega^2/\omega_\nu^2)} \; , \qquad (10)$$

where $\Omega_\nu = \omega_\nu / \sqrt{1+\gamma_\nu}$ is the resonant frequency of the fluid loaded structure; γ_ν is the entrained mass coefficient for the ν-mode; $\eta_\nu^r = \rho c \sigma_\nu / \omega m_\nu$ is the sound radiation loss factor; $\bar{m}_{\nu\nu} = m_\nu(\gamma_\nu + j\eta_\nu^r)$ is the complex entrained mass of the ν-mode which radiation efficiency is σ_ν.

Thus one can notice that the eigenvalue approach can be derived from the BIE method which provides the most efficient instrumentation to solve the modal coupling interaction problem for the fluid-loaded structures.

The numerical results were recieved for a normal point force driven free-free thin beam. The exact solution for the Structural Green function is given in [7], using Krilov's functions $V_i(\mu x/L)$, i=1,...,4

$$G(x/x', \varphi/\varphi') = -\frac{M}{\mu}\{ \frac{\Delta_1}{\Delta} V_1(\mu x/L) + \frac{\Delta_2}{\Delta} V_2(\mu x/L) + V_4[\mu(x-x')/L]H\}\cos(\varphi-\varphi') \; ,$$

where $\mu = k_B L(1-j\eta/4)$; k_B is the in-vacuo bending wave-number; L is the beam's length; M is it's in-vacuo total mass; $\{x,\varphi\}$ -cylindrical coordinates; H=1, if x > x', else H=0;

$$\Delta = V_3^2(\mu) - V_2(\mu) \; V_4(\mu); \qquad \Delta_1 = V_1(\tilde{\mu}) V_4(\mu) - V_2(\tilde{\mu}) V_3(\mu);$$

$$\Delta_2 = V_2(\tilde{\mu}) V_2(\mu) - V_1(\tilde{\mu}) V_3(\mu); \qquad \tilde{\mu} = \mu \cdot (1 - x'/L).$$

The modified BIE method was used in the low frequency band $kr_0 < 1$, where kr_0 is the beam's wave-radius. The in-vacuo loss factor $\eta = 0.01$.

Fig.1 shows the frequency response at the excitation point $x=L/2$, $\varphi=0$ of the beam in air (solid line) and in water (dashed line) when the unit force is applied normally. The acceleration level La is plotted in decibels re. a =1/M. The chosen beam parameters provided the first bending in -vacuo resonance $k_B L=4.73$, when $kr_0=0.18$. The second natural frequency can't be observed because of the exitation point at x=L/2. The third resonance $k_B L=11$ is out of span $kr_0 < 1$. The resonant maximum of La and the frequency shift were compared with the results of modal analysis and were in a good agreement when $kr_0 < 1$. The cylindrical surface of the beam was covered with planar elements $\Delta S = (2\pi r_0/N_\varphi)\, L/N_x$. The two flat covers of the cylinder were broken onto $N_L \cdot N_\varphi$ sectors by N_L circles ($N_\varphi=9$; $N_x=15$; $N_L=2$).

Fig.2 shows the pressure distribution along the line $|x| < 1.5$ L, partly coinsiding with the beam surface $r=r_0$ at $\varphi=0$. The solid line curve 1 shows the pressure distribution at the first resonant frequency in water ($kr_0=0.13$). The pressure is plotted in decibels re. p =1/S, where S is the surface area of the beam. The dashed-line curve 2 corresponds to the normal acceleration at this frequency. It is interesting to notice that the surface pressure follows the normal acceleration in the limits of the beam except the edges of the aperture, where the pressure field decays very rapidly when $|x| > L/2$. This fact was noticed in [8] using the Generalised Nearfield Acoustical Holography (GENAH) approach. The same result is noticed at a non resonant frequency. Solid-line curve 3 shows the pressure distribution at $kr_0=0.2$ in water. One can see that it still corresponds to the first mode of the beam, but the level is much lower. To compare to the beam curve 4 shows the surface pressure distribution over the solid body of the same form and weight at $kr_0=0.2$. Now it has nothing in common with the beam distribution. Besides the surface pressure far field was calculated. When the distance $R/L > 1.5$ the pressure level was tipical for the equivalent dipole source.

For the more complex heavy-loaded vibratory systems the developed approach on a base of modified BIE method can be used as a computational shell for sound radiation calculations, when their vibtation in air is numerically predicted.

ACKNOWLEDGMENTS

It is a pleasure to thank the Rector of St.-Petersburg Ocean Technology University Professor D.M.Rostovtsev for valuable discussions, advice and Professor M.J.Crocker-for support.

REFERENCES

1. G. Chertock. "Sound radiation from vibrating Surfaces". J. Acoust. Soc. Am. 36,(7),1964,1305-1313.
2. L.G. Copley. "Integral Equation Method for Radiaton from Vibrating Bodies". J.Acoust.Soc.Am.41,(4),1966,807-816.
3. H.A. Schenck. "Improved Integral formulation for Acoustic Radiation Problems". J.Acoust.Soc.Am.44,(1),1967,41-58.
4. E.G. Williams, H.D. Dardy. "Nearfield acoustical holography using underwater automated scanner". J.Acoust.Soc.Am.78,(2),1985,789-798.
5. S. Suzuki, S.Maruyma, H.Ido. "Boundary element analysis of cavity noise problems with complicated boundary conditions". J.Sound and Vib.130,(1),1989,79-91.
6. E. Skudrzik. "Simple and Complex Vibratory Systems". The Pennsylvania State University Press, 1968.
7. M.V. Bernblit, U.A. Gonchar."The intensity mapping of simple and complex sources". Acoust. J. (U.S.S.R.),35,(5),1989,940-942.
8. E.G. Williams,H.D. Dardy."Generalized nearfield acoustical holography for cylindrical geometry: Theory and experiment". J.Acoust. Soc.Am. 81,(2),1987,389-407.

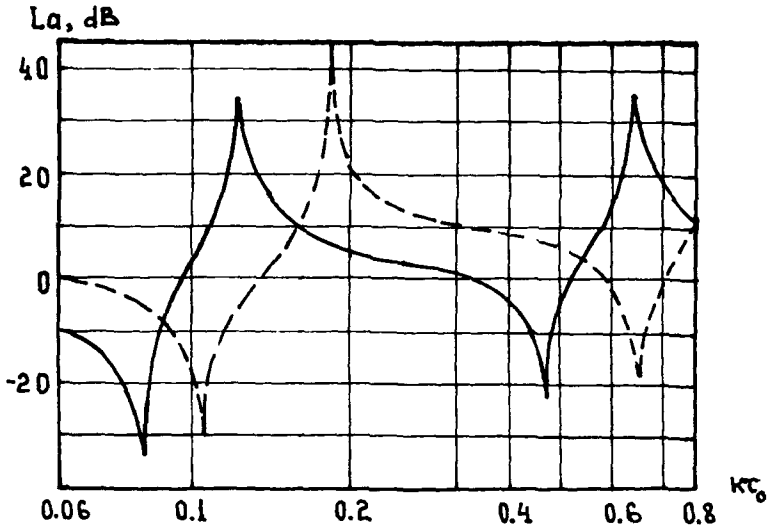

Figure 1--Beam normal surface acceleration distribution in air and in water

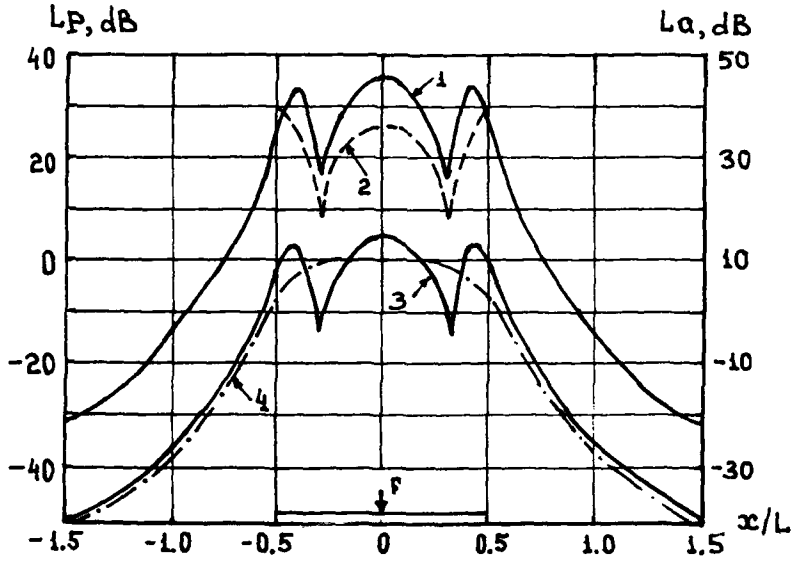

Figure 2-- Beam surface pressure distribution

SECOND INTERNATIONAL CONGRESS ON RECENT DEVELOPMENTS IN AIR- AND STRUCTURE-BORNE SOUND AND VIBRATION
MARCH 4-6, 1992 AUBURN UNIVERSITY, USA

OBTAINING OF UNIQUE SOLUTION OF A SOUND RADIATION AND SCATTERING PROBLEM USING A BEM BASED OF THE HERMHOLTZ'S INTEGRAL

I.E. Tsukernikov
Scientific and Industry Amalgamation "Mir"
Moscow
USSR

A version of the boundary element method is considered. The external boundary – value problem is brought to surface integral of the first kind for an unknown surface characteristic of sound field: pressure if the Neumann's problem is considered or normal velosity for the Dirichlet's problem. It is shown that the fundamental solutions of the integral equation are the boundary values of standing waves existing in the interior region at the characteristic frequencies and so the nonunique solvability of the integral equation is not transfered to the external problem solution writted by the Helmholtz's integral. The merit of the method is illustrated on the example of calculating the sound field of the pulsating sphere.

A method of boundary elements is widely used for numerical solution of sound radiation and scattering problems. The solution is presented in an integral form and the problem comes to an integral equation relatively to an unknown field characteristic (sound pressure or normal component of vibrating velocity) on the boundary surface.

The most difficult is the task of selecting and solving an integral equation because it is connected with nonunique solvability of equations at Dirichlet's or Neumann's eigenfrequences of the interior region determined by the boundary surface [1]. To overcome the obstacle at present the most widely used are two methods [2, 3]: the method offered by Schenk [4] in which the problem is brought to an overdetermined system of equations and the method of Burton and Miller [5] in which a combined integral equation is used. Under certain constraints both methods make it possible to attain unique solution of the equations and problem.

If the final task is calculating of field characteristics outside of the boundary surface, there exists a version of the method of boundary elements which does not require a unique solution of the integral equation. The problem is brought to an integral equation of the first kind nonunique solvability of which due to specific properties of eigenfunctions of a homogenious equation does not transfer to the solution of the exterior problem expressed by the Helmholtz's integral. In the case of the Dirichlet's problem that result was obtained in the work [6]. In the present article it is transfered on the case of the Neumann's exterior problem. It makes it true for all problems of sound radiation and scattering in which the question of nonunique solvability is present.

Let us consider a problem of determining a radiation field of a body vibrating with a predetermined velocity v on its surface S. In a mathematical sense this problem is equivalent to a problem of sound scattering on a stiff obstacle and is formulated for harmonic time dependence as the Neumann's exterior problem for the homogenious equation of Helmholtz. Let us put down a solution in the form of the Helmholtz's integral [7]

$$p(x) = \int_S \left\{ p(y) \frac{\partial}{\partial n_y} - ik\rho cv(y) \right\} g(x, y)\, dS, \qquad (1)$$

where $p(x)$ and $p(y)$ are sound pressures in the point x of the exterior region and in the point y located on the surface S of the body; $(\partial/\partial n_y)$ is the derivative with respect to external normal to the surface S in the point y; $g(x, y) = \exp(ik|x-y|)/(4\pi|x-y|)$ is the free space Green's function ; k is the wave number; ρ and c are the medium density and the sound velocity in it.

Taking the derivative of Eq.(1) with respect to the exterior normal to S in the point y_0 on S and tending the point x to $S(x \to y_0 + 0)$ due to the boundary condition $\partial p/\partial n = ik\rho cv$ we obtain an integral equation of the first kind relatively to unknown distribution of pressure $p(y)$ on S:

$$\frac{\partial}{\partial n_{y_0}} \int_S p(y) \frac{\partial g(y_0, y)}{\partial n_y} dS = ik\rho c \left[\frac{v(y_0)}{2} + \int_S v(y) \frac{\partial g(y_0, y)}{\partial n_{y_0}} dS \right]. \qquad (2)$$

The integral in the left-hand side of Eq.(2) should be understood in the sense of the Caushy's principal value . Some methods of its regulation are examined in the works [2, 5].

It is known [1] that the Eq.(2) has not a unique solution if the wave number coincides with an eigen value $k_i (i = 1, 2, \ldots)$ of the interior Neumann's problem.

Let us determine the physical sense of characteristic solutions of the homogenious integral equation.

The solution p^i of the homogenious interior Neumann's problem (with the boundary condition $v^i(y)=0$ on S) written down with the Helmholtz's integral lookes iike as follows:

$$p^i(x) = -\int_S p^i(y) \frac{\partial g(x, y)}{\partial n_y} dS \qquad \text{for } x \text{ inside } S \qquad (3)$$

Let us differentiate Eq. (3) with respect to the exterior normal to the surface S in the point y_0 and tend the point x to S: $x \to y_0 - 0$. As the function $p^i(y)$ is continuous on S the potential of the double layer (3) has continuous normal derivative on S [1]. As a result satisfying the boundary condition of the problem we obtain the equality

$$\frac{\partial}{\partial n_{y_0}} \int_S p^i(y) \frac{\partial g(y_0, y)}{\partial n_y} dS = 0,$$

which coincides with the homogenious equation for Eq.(2) and shows that the solution of that equation is the boundary value of the Neumann's interior problem solution.

Using the way identical to that applied in the work [6] it becomes possible to show that if the eigen value k_i is degenerate of order n the boundary values $p_j^i(y)$ $(j = 1, 2, \ldots, n)$ of principal solutions of the Neumann's interior problem form the basis of the eigen functions of Eq.(2), that is they are the only set of linearly independent fundamental solutions of homogenious integral equation.

General solution of Eq.(2) should be written down as follows:

$$p(y) = p^0(y) + \sum_{j=1}^{n} c_j p_j^i(y), \qquad (4)$$

where p^0 is the particular solution depending on the right-hand side part of the equation and constants c_j may have any values.

From the mathematical property of the Helmholtz's integral it follows that for $p_j^i(y)$ the next equality is true:

$$\int_S p_j^i(y) \frac{\partial g(x, y)}{\partial n_y} dS = 0 \qquad \text{for } x \quad \text{outside } S.$$

In a physical sense it reflects the fact that the fundamental solutions of the integral equation, being the boundary values of standing waves which exist inside S upon eigen values of the wave number, do not give

any contribute to the exterior field.

As a result, substituting Eq.(4) in Eq.(1) we see that the required solution p(x) of the exterior problem depends only on a particular solution of the integral equation. So, despite the fact that the solution of the integral equation is not a unique one found out with the help of the Helmholtz's integral (1) solution of the exterior problem is a unique one. The considered method of boundary elements has an advantage over the version based on an integral equation of the second kind [8] a nonunique solution of which is completely transfered to the pressure of the exterior field written down with the help of Eq.(1).

As an illustration, curves of dependence of the maximum relative error δ, % (in comparison with an analitic solution) versus wave radius ka, obtained by calculation of the radiation field of a pulsating sphere with the radius a using the above-mentioned method are shown in Fig. 1(a). The calculations were carried out for the range of wave numbers including the first two eigen values of the Neumann's interior problem for which ka=4.49 and ka = 7.25. The dash line corresponds to the error which appeared in the solution of the integral equation (2). The solid line corresponds to the error of pressure in the radiation field in points of the sphere with the R=10a calculated with the help of Eq.(1). Increasing of the error up to 100% in the solution of the integral equation in the visinity of the characteristic frequences does not influence on the results of the radiation field calculation. For comparison the analogues curves corresponding to the error appearing when the integral equation of the second kind is used [8] are represented in Fig. 1(b). The error in the solution of the integral equation is fully transfered to the results of the radiation field calculation.

REFERENCES

1. Kolton D., Kress R. Integral equations methods in scattering theory. – New York. Chichester· Bricbane· Toronto· Singapore: Wiley & Sons, 1983.
2. Akyol T.P. Schallabstrahlung von Rotationskorpern. – Acustica, b.61, No. 3, 1986, s. 200–212.
3. Tobocman W. Extention of the Helmholtz integral equation method to shorter wavelengths. – J. Acoust. Soc. Am., v. 80, No. 6, 1986, p. 1826–1837.
4. Schenck H.A. Improved integral formulation for acoustic radiation problems. – J. Acoust. Soc. Am., v. 44, No. 1, 1968, p. 41–58.
5. Burton A.J., Miller G.F. The application integral equation methods to the numerical solution of some interior boundary-value problems. – Proc. Royal Soc. London, v. A323, 1971, p. 201–220.
6. Tsukernikov I.E. Numerical solution of the exterior Dirichlet problem by means of an integral equation of the first kind. – U.S.S.R. Computational Mathematics and Mathematical Physics, v. 16, N 5, 1976, p. 267–273.
7. B.B.Backer, E.I.Copson. The mathematical theory of Huigens' principle. – Oxford, 1953.
8. Chertock G. Sound radiation from vibrating surfaces. – J. Acoust. Soc. Am., v. 36, 1964, p. 1306–1313.

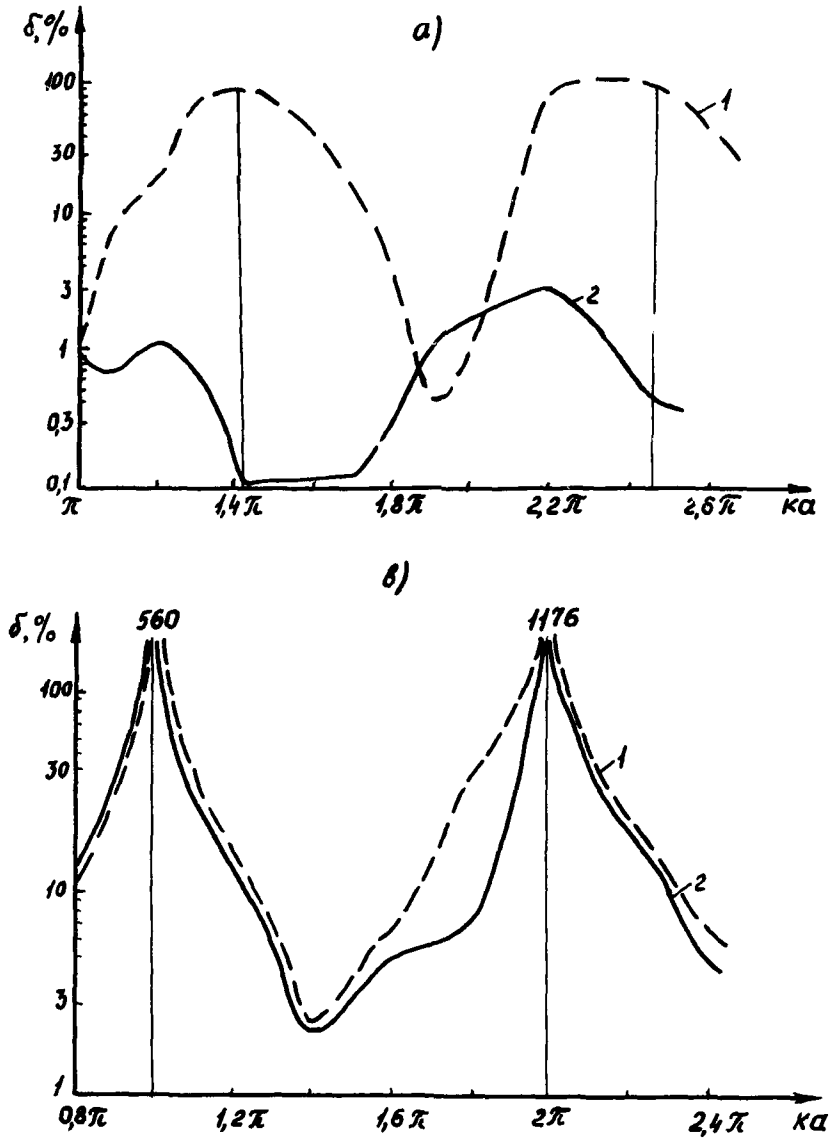

Figure 1 – – Errors of the calculation results of the pulsating phere radiation field obtained with using the integral equation of the first (a) and second (b) kind

1 – in the solution amplitude of the integral equation; 2 – in the pressure amplitude of the far field.

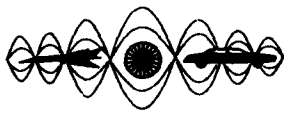

SECOND INTERNATIONAL CONGRESS ON
RECENT DEVELOPMENTS IN AIR- AND
STRUCTURE-BORNE SOUND AND VIBRATION
MARCH 4-6, 1992 AUBURN UNIVERSITY, USA

ISOPARAMETRIC BOUNDARY ELEMENT MODELING OF ACOUSTICAL CRACKS

T. W. Wu and G. C. Wan

Department of Mechanical Engineering,
University of Kentucky, Lexington, KY 40506,
U. S. A.

ABSTRACT

When a thin structure of infinitesimal thickness is submerged in an infinite acoustic medium, the acoustic velocity field contains a singularity at the knife edge of the thin structure. This problem resembles a crack problem in fracture mechanics. In this paper, a boundary element formulation using a Cauchy principal integral equation is used to model this acoustical crack problem. Quadratic isoparametric elements are used in the formulation so that the knife-edge singularity can be easily modeled by the quarter-point technique.

INTRODUCTION

Sound radiation and scattering from thin bodies has many important applications (such as transducers and fins) in acoustics. It has been known that the conventional boundary element method (BEM) using the Helmholtz integral equation is not suitable for problems involving thin bodies. The major difficulty is due to the fact that the mesh on one side of a thin body is too close to the mesh on the opposite side. Therefore, extremely fine meshes have to be used and nearly singular behavior may occur in the integral equation. This problem is very similar to the crack problem in fracture mechanics. One way to solve a thin-body problem is to use the multi-domain BEM formulation [1]. However, it requires a lot of preprocessing efforts and may also result in a very large system of equations because an imaginary interface surface has to be constructed and discretized.

A more elegant way to solve the thin-body problem is to use the normal derivative integral equation. However, it involves the evaluation of a hypersingular integral in the order of $1/r^3$, which is integrable only in the finite-part sense. Several techniques have been proposed to regularize this hyper-singular integral [2-5]. In this paper, we briefly review a recent BEM formulation to solve the thin-body problem [6]. This formulation uses a less-singular normal derivative integral equation, originally derived by Maue [7] and later by Mitzner [8] using a different approach. The normal derivative integral equation by Maue is less singular because the singularity is in the order of $1/r^2$ only and it converges in the Cauchy principal value sense rather than only in the finite-part sense. Numerical integration of the Cauchy principal singularity in Maue's equation can be achieved by subtracting a term at the singular point and then adding the term back [9].

It should be noted that the convergence of Maue's equation requires two continuity conditions [6,9]. The first condition is that the sound pressure must be continuous everywhere. This requires the use of at least the C^0 continuous elements. The second condition is that the tangential derivatives of the sound pressure must be continuous at collocation points. This is the C^1 continuity condition. The simplest way to satisfy both of the C^0 and C^1 continuity conditions simultaneously is to use the regular C^0 isoparametric elements and put collocation points inside each element. One important feature of using the C^0 isoparametric elements is that the resulting numerical model will be compatible with other analysis tools, such as the finite element method. In addition, the quadratic C^0 isoparametric elements will allow the use of the quarter-point technique [10,11] to model the $1/\sqrt{r}$ singularity of the tangential velocities at the knife edge of a thin body [12].

Through a systematic collocation point generation scheme, the number of collocation points will be always greater than the number of nodal-points. In other words, there will be more equations than unknowns. The overdetermined system is then solved by a least-squares procedure. Numerical examples are given to verify

this formulation.

I. INTEGRAL FORMULATION AND NUMERICAL IMPLEMENTATION

Consider a thin body submerged in an infinite acoustic medium of mean density ρ_0 and speed of sound c. The neutral surface of the thin body is denoted by S. The thin body may be either set in vibration in a radiation problem or subject to an incident wave velocity potential ϕ_I in a scattering problem. The first thin-body integral equation is [6]

$$\int_S \frac{\partial \psi}{\partial n}(\phi^+ - \phi^-)\, dS = \begin{cases} 4\pi\phi(P) & P \text{ not on } S \\ C^0(P)\phi^+(P) + C(P)\phi^-(P) & P \text{ on } S \end{cases}, \tag{1}$$

where $r = |Q - P|$. $\psi = e^{-ikr}/r$ is the free-space Green function due to a time-harmonic point source at P. C(P) and $C^0(P)$ are constants that depend on the location of P.

It should be noted that Eq. (1) itself is not sufficient to solve the problem because it contains two unknowns (ϕ^+ and ϕ^-). In addition, the normal velocity of the thin body, which is usually the boundary condition in a radiation or scattering problem, is not included in the equation. Hence, another integral equation containing the normal velocity of the thin body is needed to supplement Eq. (1). The equation is [6]

$$\int_S \{(\mathbf{n}_P \times \nabla_P \psi)\cdot[\mathbf{n}\times\nabla(\phi^+ - \phi^-)] + k^2(\mathbf{n}_P\cdot\mathbf{n})\,\psi\,(\phi^+ - \phi^-)\}dS + 4\pi\frac{\partial\phi_I}{\partial n_P}(P) = 4\pi\frac{\partial\phi}{\partial n_P}(P) \quad . \tag{2}$$

where n_P is the normal at P, and the differentiation in both ∇_P and $\partial/\partial n_P$ is taken with respect to the coordinates of P.

For a radiation or scattering problem, $\partial\phi/\partial n$ is specified on S and Eq. (2) can be solved for the velocity potential jump $\phi^+ - \phi^-$. Equation (1) is then integrated to get ϕ at any field point in the acoustic medium or the velocity potential sum $C\phi^- + C^0\phi^+$ on the thin body. Once $\phi^+ - \phi^-$ and $C\phi^- + C^0\phi^+$ are both known on the thin body, ϕ^+ and ϕ^- can be easily obtained.

It should be noted that there is no velocity potential jump along the knife edge of a thin body because the acoustic medium is continuous there. In other words,

$$\phi^+(Q) - \phi^-(Q) = 0 \quad , \qquad \text{for Q along the knife edge.} \tag{3}$$

A numerical solution to Eq. (2) can be achieved by discretizing the thin-body neutral surface S into a number of elements. The regular 8-node quadrilateral and 6-node triangular isoparametric elements are used in the numerical study. However, collocation points are placed inside the elements to satisfy the C^1 continuity condition at P. The numerical procedure used here to solve Eq. (2) is similar to that used in Ref. [9] to overcome the nonuniqueness problem. Figure 1 shows the configuration of the master elements and the positions of nodal points and collocation points. The global Cartesian coordinates X_i (i=1, 2, 3) of any point on an element are assumed to be related to the nodal coordinates $X_{i\alpha}$ by

$$X_i(\xi) = \sum_\alpha N_\alpha(\xi) X_{i\alpha} \quad , \alpha = 1, \ldots, 6 \text{ or } 8 \tag{4}$$

in which N_α are second-order shape functions of the local coordinates (ξ,η). The same set of quadratic shape functions is used to interpolate the velocity potential jump $(\phi^+ - \phi^-)$ on each element, that is,

$$(\phi^+ - \phi^-) = \sum_\alpha N_\alpha\,(\phi^+ - \phi^-)_\alpha \quad , \tag{5}$$

where $(\phi^+ - \phi^-)_\alpha$ are the nodal values of the velocity potential jump. The normal velocity $\partial\phi/\partial n_P$ at the collocation point P [used on the right hand of Eq. (2)] is also obtained by the same interpolation of the nodal values of $\partial\phi/\partial n$.

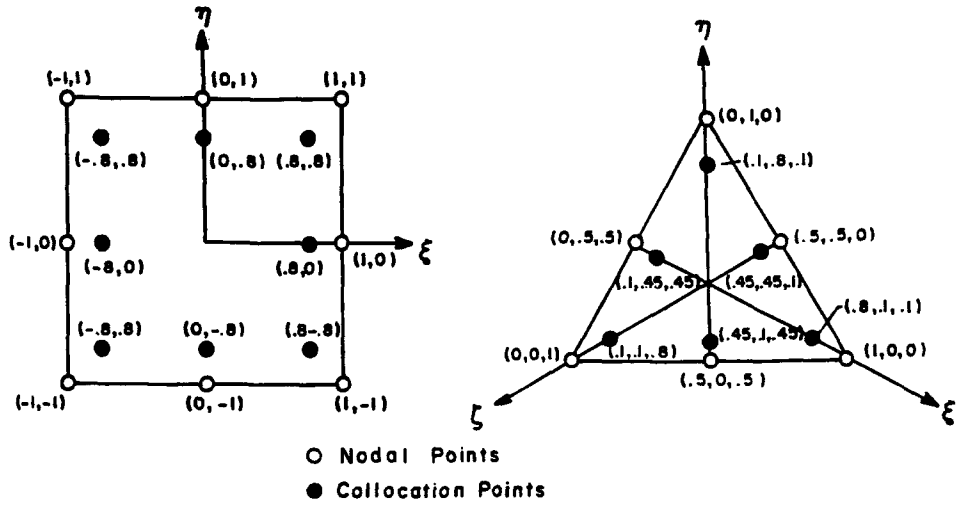

Figure 1. Configuration of the master elements.

The integration of the kernel $(n_P \times \nabla_P \psi) \cdot [n \times \nabla(\phi^+ - \phi^-)]$ in Eq. (2) should be performed in the Cauchy principal value sense. For each collocation position of P, there is only one element that contains the singular point P. This element is denoted by S_e. Numerical integration on all the other elements are nonsingular and can be carried out in the usual way. For integration on the singular element S_e, a polar coordinate system (ρ,θ) is used on the corresponding master element S_m as shown in Fig. 2. Numerical integration of $(n_P \times \nabla_P \psi) \cdot [n \times \nabla (\phi^+ - \phi^-)]$ on S_e can be achieved by subtracting a term at the singular point and then adding the term back. Detailed discussion of this procedure can be found in Ref. [9]. The result is

$$\int_{S_e} (n_P \times \nabla_P \psi) \cdot [n \times \nabla(\phi^+ - \phi^-)]\, dS = \int_0^{2\pi} \int_0^{R(\theta)} \frac{F(\rho,\theta) - F(0,\theta)}{\rho}\, d\rho\, d\theta + \int_0^{2\pi} F(0,\theta) \ln R(\theta)\, d\theta \quad , \tag{6}$$

where $R(\theta)$ is distance from P to the element boundary measured on the master element plane as shown in Fig. 2 and

$$F(\rho,\theta) = \rho^2 (n_P \times \nabla_P \psi) \cdot [n \times \nabla(\phi^+ - \phi^-)]\, |J| \quad , \tag{7}$$

in which $|J|$ is the Jacobian between S_e and S_m.

For the collocation scheme suggested in Fig. 1, the total number of collocation points is always greater than the total number of nodal points. The overdetermined system is then solved by a least-squares procedure. In addition, $\phi^+ - \phi^-$ is also forced to be zero at all of the knife-edge nodes. This will reduce the total number of unknowns in Eq. (2) even further. It is well known that the acoustic velocity field at the knife edge has a singularity in the order of $1/\sqrt{r}$, where r is measured from the knife edge [12]. Unlike the multi-domain BEM approach [1], the thin-body integral formulation does not require modeling of an imaginary interface, and hence, eliminates the need to model the singularity of the velocity field on the fluid side of the knife edge. In addition, since the normal velocity on the thin body is always given as a boundary condition, the $1/\sqrt{r}$ singularity exists only in the tangential derivatives of $\phi^+ - \phi^-$. As will be shown in the example problems, this singularity can be easily modeled by moving the midside nodes of the elements adjacent to the knife edge to their quarter-point

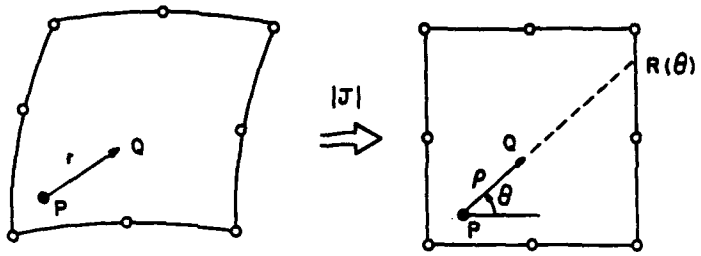

Figure 2. Polar coordinate transformation.

positions [10, 11]. After Eq. (2) is solved for $\phi^+ - \phi^-$ at every nodal point, Eq. (1) is then integrated to obtain $C\phi^- + C^0\phi^+$. Note that Eq. (1) is only weakly singular and is integrable in the normal sense. Therefore, the singular point P is collocated directly at each nodal point to get $C\phi^- + C^0\phi^+$ there.

II. EXAMPLE PROBLEMS

The first example problem is the radiation from a vibrating circular plate of radius *a*. The plate is clamped around its boundary and vibrating at its first axisymmetric mode with $ka = 1$. The vibrating velocity is normalized by setting the maximum velocity at the center to be *1*. The neutral surface of the disk is discretized by 24 eight-node quadrilateral elements and eight six-node triangular elements as shown in Fig. 3. Note that for all of the 8 quadrilateral elements adjacent to the knife edge, their midside nodes on the elements' sides in the radial direction are moved from the regular middle-point positions to the quarter-point positions. This will implicitly incorporate the $\sqrt{r}$ behavior in the quadratic shape functions and consequently the $1/\sqrt{r}$ singularity in the derivatives of the shape functions. Since this problem may not have an analytical solution, an axisymmetric multi-domain BEM solution is used to verify the thin-body BEM solution. Therefore, also shown in Fig. 3 is the axisymmetric multi-domain BEM mesh used for this problem. In the axisymmetric multi-domain BEM model, the circular plate is modeled by four line elements and six additional line elements are used to form an interface. In addition, special singular elements [13] are used to model the knife-edge singularity. To verify the BEM solution, variation of the magnitude of the velocity potential ϕ^- in the radial direction on one side of the circular plate is compared to an axisymmetric multi-domain BEM solution in Fig. 4. Excellent agreement is observed between the two BEM solutions. The importance of the $1/\sqrt{r}$ singularity is also shown in Figs. 4 by the solutions obtained when the quarter points are intentionally moved back to their regular middle-point positions. It is obvious that the quarter-point technique is very important to the accuracy of the solution.

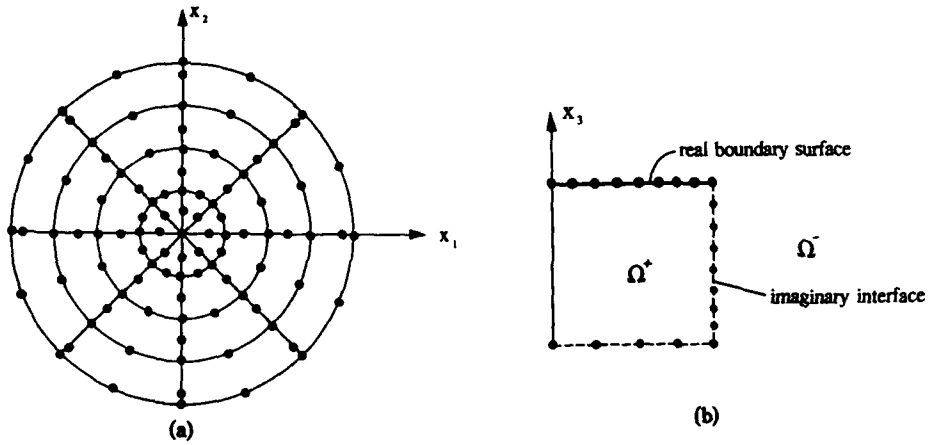

Figure 3. BEM meshes for the circular plate: (a) the thin-body approach; (b) the axisymmetric multi-domain approach.

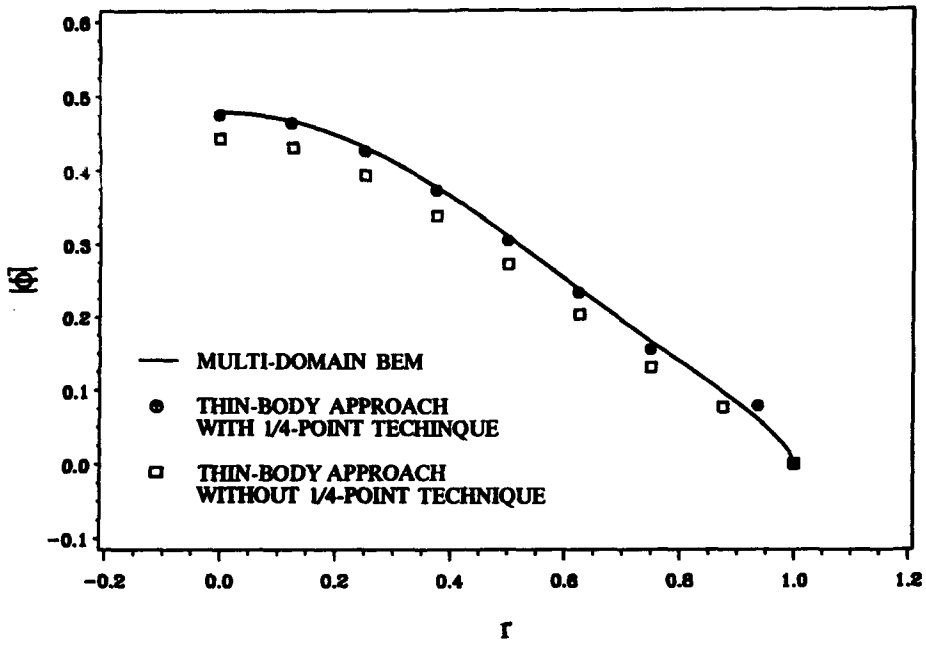

Figure 4. Magnitude of the velocity potential on one side of the circular plate as a function of the distance from the center.

The second example problem is the scattering of an incident plane wave from a rigid thin-walled hemisphere with radius a. Two BEM meshes used to model this hemisphere are shown in Fig. 5. Note that quarter points rather than middle points are used for the elements adjacent to the knife edge. The incident plane wave has a velocity potential of unit amplitude and is traveling in the $-X_3$ direction. Again, this problem is also solved by the axisymmetric multi-domain BEM with special singular elements being used to model the knife-edge singularity. The comparison between these two BEM solutions for the scattered velocity potentials on both sides (exterior and interior) of the cylindrical surface is given in Figs. 6 and 7. Figure 6 shows the real part of the scattered velocity potentials and Fig. 7 shows the corresponding imaginary part. Again, very good agreement is observed.

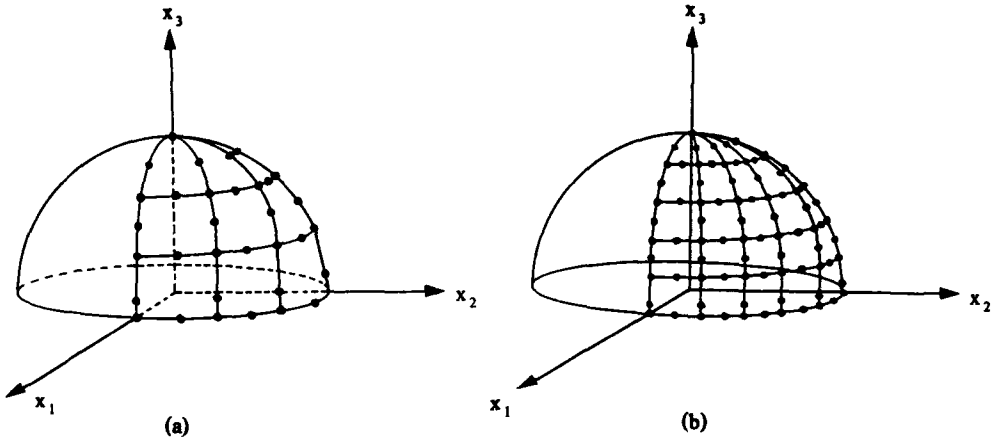

Figure 5. BEM meshes for the hemisphere: (a) 109-node mesh; (b) 301-node mesh.

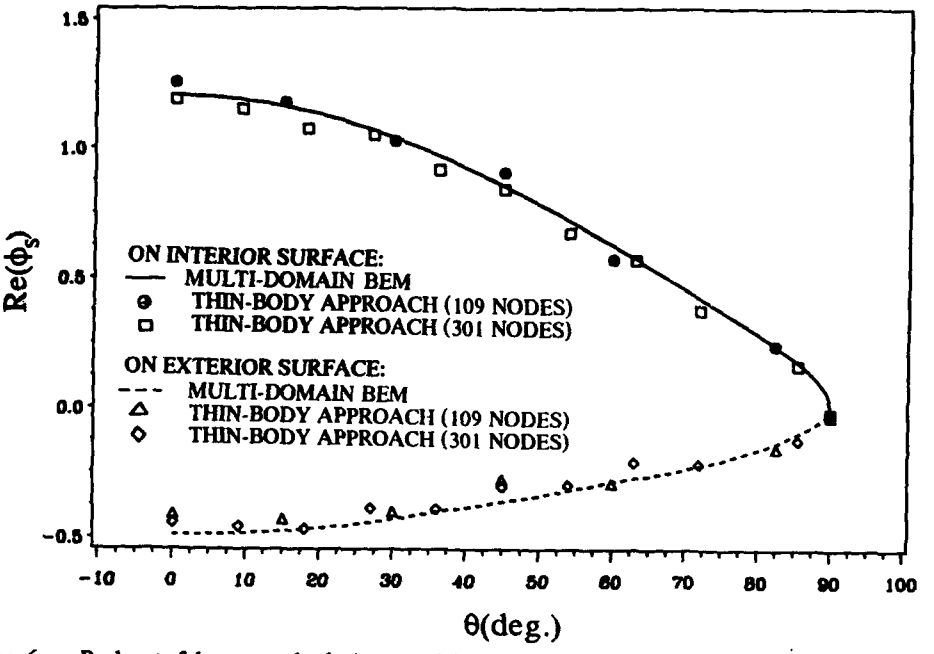

Figure 6. Real part of the scattered velocity potentials on the interior and exterior surfaces of the hemisphere as a function of the angle measured from the X_3-axis.

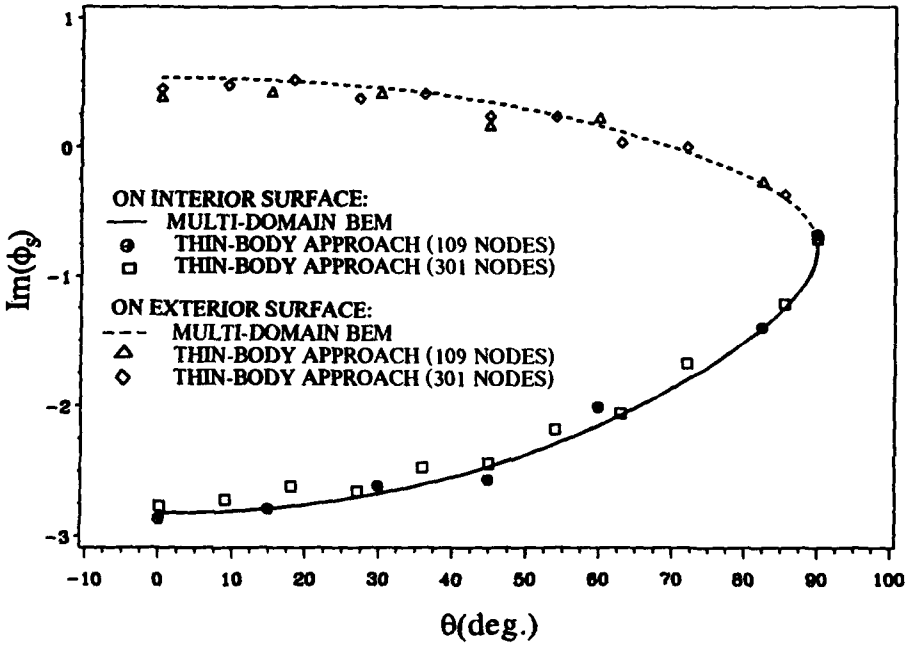

Figure 7. Imaginary part of the scattered velocity potentials on the interior and exterior surfaces of the hemisphere as a function of the angle measured from the X_3-axis.

III. CONCLUSIONS

The normal derivative integral equation originally derived by Maue is applied to the BEM solution of thin bodies (or acoustic cracks). This normal derivative integral equation converges in the Cauchy principal value sense rather than only in the finite-part sense. The formulation is implemented in an isoparametric element environment. The quarter-point technique is used to model the $1/\sqrt{r}$ singularity associated with the tangential velocities at the knife edge. The BEM results compare very well with axisymmetric multi-domain BEM solutions.

REFERENCES

1. A. F. Seybert, C. Y. R. Cheng and T. W. Wu, "The Solution of Coupled Interior/Exterior Acoustic Problems Using the Boundary Element Method," J. Acoust. Soc. Am. 88, 1612-1618 (1990).

2. A. J. Burton and G. F. Miller, "The Application of Integral Equation Methods to the Numerical Solutions of Some Exterior Boundary Value Problems," Proc. Roy. Soc. Lond. A 323, 201-210 (1971).

3. T. Terai, "On Calculation of Sound Fields Around Three-Dimensional Objects by Integral Equation Methods," J. Sound Vib. 69, 71-100 (1980).

4. J. B. Mariem and M. A. Hamdi, "A New Boundary Finite Element Method for Fluid-Structure Interaction Problems," Int. J. Num. Methods Eng. 24, 1251-1267 (1987).

5. G. Krishnasamy, L. W. Schmerr, T. J. Rudolphi and F. J. Rizzo, "Hypersingular Boundary Integral Equations: Some Applications in Acoustic and Elastic Wave Scattering," ASME J. App. Mech. 57, 404-414 (1990).

6. T. W. Wu and G. C. Wan, "Numerical Modeling of Acoustic Radiation and Scattering from Thin Bodies Using a Cauchy Principal Integral Equation," submitted to J. Acoust. Soc. Am. (1991).

7. A. W. Maue, "Zur Formulierung eines allgemeinen Beugungsproblems durch eine Integralgleichung," Z. Phys. 126, 601-618 (1949).

8. K. M. Mitzner, "Acoustic Scattering from an Interface Between Media of Greatly Different Density," J. Math. Phys. 7, 2053-2060 (1966).

9. T. W. Wu, A. F. Seybert and G. C. Wan, "On the Numerical Implementation of a Cauchy Principal Value Integral to Insure a Unique Solution for Acoustic Radiation and Scattering," J. Acoust. Soc. Am. 90, 554-560 (1990).

10. D. Henshell, "Crack Tip Finite Elements Are Unnecessary," Int. J. Num. Methods Eng. 9, 495-507 (1975).

11. R. Barsoum, "On the Use of Isoparametric Finite Elements in Linear Fracture Mechanics," Int. J. Num. Methods Eng. 10, 25-37 (1976).

12. P. M. Morse and K. U. Ingard, Theoretical Acoustics (McGraw-Hill, New York, 1968), Chap. 8.

13. A. F. Seybert, Z. H. Jia and T. W. Wu, "Solving Knife-edge Scattering Problems Using Singular Boundary Elements," to appear in J. Acoust. Soc. Am.

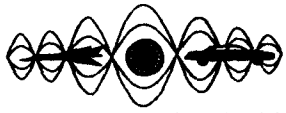

SECOND INTERNATIONAL CONGRESS ON
RECENT DEVELOPMENTS IN AIR- AND
STRUCTURE-BORNE SOUND AND VIBRATION
MARCH 4-6, 1992 AUBURN UNIVERSITY, USA

A SOLUTION METHOD FOR ACOUSTIC BOUNDARY ELEMENT EIGENPROBLEM WITH SOUND ABSORPTION USING LANCZOS ALGORITHM

by
C. Rajakumar and Ashraf Ali
Swanson Analysis Systems, Inc.
Houston, PA 15342

ABSTRACT

A damped system eigenvalue analysis of acoustical cavities using the boundary element method is presented. The acoustic boundary element eigenproblem formulation presented by Banerjee et al. [1] is extended to include sound absorption in acoustical cavities. A dissipative term is included in the eigenvalue matrix equation to account for boundary absorption. The resulting damped system eigenvalue problem is solved using a new approach of applying the Lanczos subspace algorithm to quadratic eigenproblems. Since the boundary element matrices are unsymmetric, the Lanczos algorithm presented is in its most general form for unsymmetric quadratic eigenproblems. Examples are presented to show the application of the method to find the eigenfrequencies of acoustic cavities with sound absorption.

INTRODUCTION

Computation of the acoustic cavity resonant frequencies is an essential part in the design of automobile passenger cabins. Finite element modeling of the acoustical problem is routinely carried out where the discretized wave equation is set up as an eigenvalue problem and the resonant frequencies and mode shapes computed. Employing the boundary element method, the acoustical cavity resonance problem was set up as an algebraic eigenvalue problem by Banerjee et al. [1]. Although the boundary element matrices are smaller in size than the finite element matrices, they are unsymmetric. Therefore, the use of boundary element eigenvalue analysis requires an efficient eigenvalue extraction method for unsymmetric matrices. In the paper by Rajakumar et al. [2] the Lanczos solution algorithm for the unsymmetric generalized eigenvalue problem was applied to the acoustic boundary element eigenanalysis.

In the present work, the Lanczos algorithm is applied to the damped system eigenvalue problem formulated by the boundary element discretization of acoustic cavities with sound absorption. The algorithm presented is unique, in that, it does not use the method of matrix augmentation to linearize the quadratic eigenvalue problem arising in damped dynamic systems. In order to treat unsymmetric stiffness, mass, and damping matrices, the algorithm is kept general enough and therefore is quite suitable for the absorptive acoustic boundary element eigenproblem.

A brief outline of the paper is as follows: first, we set up the acoustic boundary element eigenproblem as shown in the paper by Banerjee et al. [1]. Then, a simple method of incorporating the boundary absorption into the boundary element formulation is shown. Finally, the resulting quadratic eigenvalue problem is solved using a new approach of applying the Lanczos algorithm, which eliminates the need for dealing with doubled size matrices of the matrix augmentation method. The Lanczos algorithm and its implementation details are included.

ACOUSTIC BOUNDARY ELEMENT EIGENPROBLEM

The acoustic wave equation governing the acoustic pressure p in a fluid is given by:

$$\nabla^2 p = \frac{1}{c^2} \frac{\partial^2 p}{\partial t^2} \tag{1}$$

c is the speed of sound and t is the time. For the harmonic oscillations of pressure in the sound pressure wave problem considered, $p = Pe^{j\omega t}$. P is the pressure amplitude, and ω is the circular frequency. Substituting for p in Eq. (1), the Helmholtz equation governing the amplitude of pressure oscillations is obtained.

$$\nabla^2 P = -(\omega/c)^2 P \tag{2}$$

To find the acoustic resonant frequencies of an enclosed acoustic domain, this equation needs to be discretized and solved for the free response. In the boundary element discretization process, the fundamental solution used for the Helmholtz equation consists of the wave number $k = \omega/c$ as a parameter. Therefore, the boundary element matrices obtained are a function of ω and the free response problem cannot be cast as an algebraic eigenvalue problem. Banerjee et al. [1] presented an alternative way of discretizing Eq. (2) which leads to an algebraic eigenvalue problem. In the present analysis, we shall use their approach and extend it to include dissipation of energy for the sound absorbing acoustic cavity problem.

For the sake of completeness, we shall briefly outline the method of Banerjee et al. [1] here. First, P in Eq. (2) is represented as a sum of two pressures, $P = P_c + P_I$. The complimentary function P_c satisfies the homogeneous equation

$$\nabla^2 P_c = 0 \tag{3}$$

Substituting $P = P_c + P_I$ in Eq. (2), and in view of Eq. (3), the equation governing the particular solution P_I is given by:

$$\nabla^2 P_I = -(\omega/c)^2 P \tag{4}$$

Considering 2-D problems, the fundamental solution to the Laplace equation $g(x,\xi) = (1/2\pi) \ln (1/r)$ is used to discretize Eq. (3), leading to the following boundary integral equation:

$$\alpha P_c(\xi) + \int_\Gamma \frac{\partial g(x,\xi)}{\partial n} P_c(x)\, d\Gamma(x) = \int_\Gamma g(x,\xi) \frac{\partial P_c(x)}{\partial n}\, d\Gamma(x) \tag{5}$$

r is the distance between the source point ξ and the field point x, α is a geometric coefficient at the source point, and n is the outward normal to the boundary Γ of the acoustic domain Ω (Fig. 1). Note that $g(x,\xi)$ is independent of the frequency ω. Using the polynomial shape functions to approximate $P_c(x)$ and $\partial P_c(x)/\partial n$ on the discretized boundary segments Γ_e, the resulting boundary element matrix equation is given by:

$$[G]\left\{\frac{\partial P_c}{\partial n}\right\} = [H]\{P_c\} \tag{6}$$

Substituting for $\{P_c\} = \{P\} - \{P_I\}$, Eq. (6) is rewritten as:

$$[G]\left\{\frac{\partial P}{\partial n}\right\} - [H]\{P\} = [G]\left\{\frac{\partial P_I}{\partial n}\right\} - [H]\{P_I\} \tag{7}$$

Now considering Eq. (4), the pressure P is represented as $P = \sum_{m=1}^{\infty} (R_o - r)\, \phi(\xi_m)$, where R_o is a constant, r is the distance between a point in the domain x and a source point ξ_m at the boundary, and ϕ is a fictitious function at the boundary. With this approximation of P, the solution to Eq. (4) is obtained as $P_I = \sum_{m=1}^{\infty} -\left(r^3/9 - R_o r^2/4\right) \phi(\xi_m)$. Instead of the infinite series, using finite number of fictitious functions ϕ_i (i=1, 2...n) at the boundary nodes, the following matrix equations can be written down:

$$\{P\} = [A]\{\phi\}, \quad \{P_I\} = [D]\{\phi\}, \quad \left\{\frac{\partial P_I}{\partial n}\right\} = [B]\{\phi\} \tag{8}$$

Substituting for $\{P_I\}$ and $\{\partial P_I/\partial n\}$ into Eq. (7), and defining $[M] = ([G][B] - [H][D])$ and

$$\{Q\} = \left\{\frac{\partial P}{\partial n}\right\} \tag{9}$$

the boundary element equation for the acoustic problem is obtained.

$$[G]\{Q\} - [H]\{P\} = (\omega/c)^2 [M]\{\phi\} \tag{10}$$

Banerjee et al. [1] used $\{\phi\} = [A]^{-1}\{P\}$ in Eq. (10) to formulate the algebraic eigenproblem. In the reference by Ali et al. [3], $\{P\}$ was replaced by $[A]\{\phi\}$ to form the eigenproblem with $\{\phi\}$ as the eigenvector, thereby avoiding the inversion of [A]. When the boundary of the acoustic domain is hard, $\{Q\}=0$, and the algebraic eigenproblem can be written as:

$$[K]\{\phi_i\} = \lambda_i [M]\{\phi_i\} \tag{11}$$

where, $[K] = -[H][A]$, $\lambda_i = (\omega_i/c)^2$

The boundary element matrices [K] and [M] are independent of the frequency ω and Eq. (11) is a generalized eigenvalue problem. The eigenpairs λ_i, $\{\phi_i\}$ represent the resonant frequencies and mode shapes of a non–absorbing acoustic cavity. Starting from Eq. (10), a method of incorporating a dissipation term to account for sound absorption at the boundaries of an acoustic cavity is shown next.

SOUND ABSORPTION AT THE BOUNDARY

Invariably, some amount of energy is dissipated due to the absorption of sound at the boundaries of an acoustic domain. In order to account for the dissipated energy, Craggs [4] has presented a damped form of Helmholtz Eq. (2). For the absorption of sound at the boundaries of an acoustic cavity, we employ a similar approach by considering the linear momentum equation that relates the fluid pressure gradient and the velocity at the boundary

$$\frac{\partial p}{\partial n} = -\varrho \frac{\partial \mathbf{v}}{\partial t} \cdot \mathbf{n} \tag{12}$$

where, ϱ is the fluid density, $\mathbf{v}$ is the velocity vector, and $\mathbf{n}$ is the outward normal. To account for the energy dissipated at the boundaries, an absorption term is introduced on the right–hand side of Eq. (12):

$$\frac{\partial p}{\partial n} = -\varrho \frac{\partial \mathbf{v}}{\partial t} \cdot \mathbf{n} + R\mathbf{v} \cdot \mathbf{v} \tag{13}$$

In the absorption term, the reason for using the velocity divergence $\nabla \cdot \mathbf{v}$ as opposed to $\mathbf{v}$ as in Cragg's paper comes from the consideration of the consistency of units, where the acoustic resistance R is in rayl (n–s/m^3). Furthermore, Zienkiewicz and Newton [5] have shown the relationship $\partial p/\partial n = -(1/c)\,\partial p/\partial t$ to account for the energy loss due to the out bound pressure waves at an open boundary for plane wave situations. Since $\partial p/\partial t$ is related to $\nabla \cdot \mathbf{v}$ via the conservation of mass equation

$$\nabla \cdot \mathbf{v} = -\frac{1}{\varrho c^2} \frac{\partial p}{\partial t} \tag{14}$$

of a compressible fluid, the boundary absorption term used in Eq. (13) would be appropriate. So, substituting for $\nabla \cdot \mathbf{v}$ from Eq. (14) into Eq. (13) the pressure gradient at an absorbing boundary is written as

$$\frac{\partial p}{\partial n} = -\varrho \frac{\partial \mathbf{v}}{\partial t} \cdot \mathbf{n} - \beta \left(\frac{1}{c} \frac{\partial p}{\partial t}\right) \tag{15}$$

$\beta = R/\rho c$ is the nondimensional absorption coefficient of the sound absorbing material at the boundary. The acoustic resistance R for foam and fibrous type material are given as a function of frequency by Craggs [4].

For the harmonic oscillations in acoustical problems, the boundary pressure and velocity in Eq. (15) are represented in complex exponential form as $p = Pe^{j\omega t}$ and $v = Ve^{j\omega t}$, respectively. In the present paper, the boundary velocity is not used since the fluid–structure interface boundary is assumed to be stationary. The boundary pressure gradient at a sound absorbing boundary is, then, obtained from Eq. (15) as:

$$\frac{\partial P}{\partial n} = -j\frac{\omega}{c}\beta P \tag{16}$$

ABSORPTION TERM IN THE BOUNDARY ELEMENT MATRIX EQUATION

Using the relationship in Eq. (16), the absorption in an acoustic cavity can be incorporated in the discretized boundary element Eq. (10). Eq. (16) is rewritten in terms of the nodal pressure gradients as follows:

$$\{Q\} = -j(\omega/c)\beta\{P\} \tag{17}$$

When absorption material is used on a part of the boundary Γ_1, Eq. (10) is written down in partitioned form as:

$$\left[\begin{array}{c|c} G_{11} & G_{12} \\ \hline G_{21} & G_{22} \end{array}\right] \left\{\begin{array}{c} Q_1 \\ \hline Q_2 \end{array}\right\} - [H]\{P\} = (\omega/c)^2[M]\{\phi\} \tag{18}$$

Pressure gradients at the absorbing and non–absorbing boundary nodes are denoted by $\{Q_1\}$ and $\{Q_2\}$, respectively. Then, substituting from Eq. (17) into Eq. (18)

$$\left[\begin{array}{c|c} -j(\omega/c)\beta G_{11} & G_{12} \\ \hline -j(\omega/c)\beta G_{21} & G_{22} \end{array}\right] \left\{\begin{array}{c} P_1 \\ \hline Q_2 \end{array}\right\} - [H]\{P\} = (\omega/c)^2[M]\{\phi\} \tag{19}$$

For the part of the boundary where there is no absorption, we assume acoustically hard boundary condition $\{Q_2\}=0$. Partitioning the matrix [A] in Eq. (8), we substitute for $\{P_1\} = [A_{11}]\{\phi_1\} + [A_{12}]\{\phi_2\}$ in Eq. (19).

$$-j(\omega/c)\beta\left[\begin{array}{c|c} G_{11}A_{11} & G_{11}A_{12} \\ \hline G_{21}A_{11} & G_{21}A_{12} \end{array}\right] \left\{\begin{array}{c} \phi_1 \\ \hline \phi_2 \end{array}\right\} - [H][A]\{\phi\} = (\omega/c)^2[M]\{\phi\} \tag{20}$$

Taking the coefficient $-\beta$ into the matrix, and denoting the absorption matrix as [C] and $[K] = -[H][A]$, Eq. (20) is rewritten as:

$$j(\omega/c)[C]\{\phi\} + [K]\{\phi\} = (\omega/c)^2[M]\{\phi\} \tag{21}$$

Eq. (21) is the eigenvalue problem for the acoustic cavity with sound absorption. Defining the eigenvalues as $\lambda_i = j(\omega/c)$, and the eigenvectors $\{x_i\} = \{\phi\}$, the quadratic eigenproblem to be solved is

$$[K]\{x_i\} + [\lambda_i][C]\{x_i\} + \lambda_i^2[M]\{x_i\} = 0 \tag{22}$$

LANCZOS ALGORITHM FOR QUADRATIC EIGENVALUE PROBLEMS

The successful implementation of the boundary element acoustic eigenproblem formulation presented depends upon the availability of an efficient method of solving the quadratic eigenproblem posed in Eq. (22).

The system stiffness, damping, and mass matrices [K], [C], and [M], respectively, are unsymmetric and fully populated and are of size n x n. For large acoustic cavity resonance problems, usually only the first few eigenfrequencies are of interest, out of the 2n eigenfrequencies of the eigenproblem. Therefore, we choose a subspace technique. Further, the Lanczos subspace method is specifically chosen because the Lanczos subspace matrix is tridiagonal whose eigenpair can be extracted very efficiently.

In order to solve Eq. (22), the usual approach is the method of matrix augmentation, leading to a linear eigenvalue problem. This method doubles the size of system matrices to 2n and is undesirable from the point of computer storage requirements. In the present approach, the Lanczos algorithm is applied to the quadratic eigenproblem directly, eliminating the need for matrix augmentation. In reference [6], Zheng et al. presented an inverse iteration method of solving quadratic eigenproblems without augmentation. Pursuing along their approach, here we seek to set up the Lanczos algorithm to solve Eq. (22). For the quadratic eigenproblem, matrix R of size n x m and matrix T of size m x m are defined as the characteristic matrix and eigenvalue square matrix, respectively, if they satisfy

$$[M][R] + [C][R][T] + [K][R][T]^2 = 0 \tag{23}$$

and rank (T)=m. Then the eigenvalues of the standard eigenproblem

$$[T]\{y_i\} = \mu_i \{y_i\} \tag{24}$$

will approximate the eigenvalues of the original problem in Eq. (22), $\lambda_i = 1/\mu_i$. A recursion scheme that generates the Lanczos vectors $\{r_j\}$, j=1, 2...m ($m \leq 2n$), which are the columns of the characteristic matrix [R], needs to be set up in order to transform Eq. (22) into Eq. (24) in the subspace $\mathcal{S}$ m x m. The Lanczos recursion for the unsymmetric generalized eigenvalue problem, given by [M] = 0 in Eq. (22), was presented by Rajakumar and Rogers [7]. Extending this work, a complete derivation of the Lanczos algorithm for the quadratic eigenproblem, along with proofs are shown in the reference by Rajakumar [8]. Here we shall present the Lanczos recursion without the detailed derivations and proofs.

For symmetric matrices, the single–sided Lanczos recursion scheme for the generalized eigenvalue problem is well known [9]. Since the matrices in Eq. (22) are unsymmetric, we seek to formulate the Lanczos two–sided recursion where the transposed eigenproblem

$$[K]^T\{z_i\} + \{\lambda_i\}[C]^T\{z_i\} + \lambda_i^2 [M]^T\{z_i\} = 0 \tag{25}$$

is considered, along with the original problem. It can be shown that the eigenvalues of Eq. (25) are the same as that of Eq. (22) $\{x_i\}$ and $\{z_i\}$ are called the right and left–hand eigenvectors, respectively. They are biorthogonal since they satisfy the generalized biorthogonality condition

$$\{z_j\}^T[C]\{x_i\} + \{\bar{z}_j\}^T[M]\{x_i\} + \{z_j\}^T[M]\{\bar{x}_i\} = 0 \tag{26}$$

when $i \neq j$. $\{\bar{x}_i\} = \lambda_i \{x_i\}$ and $\{\bar{z}_j\} = \lambda_j \{z_j\}$ are defined as the dependent right and left–hand eigenvectors, respectively. In the Lanczos two–sided recursion given below, two primary and two secondary sequence of vectors $[V] = [v_1\ v_2 \dots v_m]$, $[W] = [w_1\ w_2 \dots w_m]$ and $[R] = [r_1\ r_2 \dots r_m]$, $[S] = [s_1\ s_2 \dots s_m]$, respectively are generated. The primary and secondary Lanczos vectors will map the independent and dependent eigenvectors, respectively.

Two sets of arbitrarily chosen vectors $\{\hat{v}_1\}$, $\{\hat{w}_1\}$ and $\{\hat{r}_1\}$, $\{\hat{s}_1\}$ are normalized such that $\{w_1\}^T[C]\{v_1\} + \{s_1\}^T[M]\{v_1\} + \{w_1\}^T[M]\{r_1\} = 1$ to get the starting set of primary and secondary Lanczos vectors $\{v_1\}$, $\{w_1\}$ and $\{r_1\}$, $\{s_1\}$. We set $\{\hat{v}_1\} = \{\hat{w}_1\}$ and $\{\hat{r}_1\} = \{\hat{s}_1\}$ in our implementation since these vectors are arbitrarily chosen. For j=1, 2...m, ($m \leq 2n$)

$$\{v_{j+1}\} = -[K]^{-1}\left([C]\{v_j\} + [M]\{r_j\}\right) - \alpha_j\{v_j\} - \beta_j\{v_{j-1}\} \tag{27}$$

$$\{\bar{w}_{j+1}\} = -[K]^{-T}\left([C]^T\{w_j\} + [M]^T\{s_j\}\right) - \alpha_j\{w_j\} - \delta_j\{w_{j-1}\} \tag{28}$$

$$\{\bar{r}_{j+1}\} = \{v_j\} - \alpha_j\{r_j\} - \beta_j\{r_{j-1}\} \tag{29}$$

$$\{\bar{s}_{j+1}\} = \{w_j\} - \alpha_j\{s_j\} - \delta_j\{s_{j-1}\} \tag{30}$$

(when $j = 1$, $\beta_1 v_0 = \beta_1 r_0 = \delta_1 w_0 = \delta_1 s_0 = 0$)

$$\alpha_j = -\left(\{w_j\}^T[C] + \{s_j\}^T[M]\right)[K]^{-1}\left([C]\{v_j\} + [M]\{r_j\}\right) + \{w_j\}^T[M]\{v_j\} \tag{31}$$

$$\Delta_{j+1} = \{\bar{w}_{j+1}\}^T[C]\{\bar{v}_{j+1}\} + \{\bar{s}_{j+1}\}^T[M]\{\bar{v}_{j+1}\} + \{\bar{w}_{j+1}\}^T[M]\{\bar{r}_{j+1}\} \tag{32}$$

$$\delta_{j+1} = |\Delta_{j+1}|^{1/2} \tag{33}$$

$$\beta_{j+1} = \delta_{j+1}\ \text{sign}\ (\Delta_{j+1}) \tag{34}$$

$$\{v_{j+1}\} = \frac{1}{\delta_{j+1}}\{\bar{v}_{j+1}\} \tag{35}$$

$$\{w_{j+1}\} = \frac{1}{\beta_{j+1}}\{\bar{w}_{j+1}\} \tag{36}$$

$$\{r_{j+1}\} = \frac{1}{\delta_{j+1}}\{\bar{r}_{j+1}\} \tag{37}$$

$$\{s_{j+1}\} = \frac{1}{\beta_{j+1}}\{\bar{s}_{j+1}\} \tag{38}$$

The Lanczos vectors generated in the recursion presented above satisfy the generalized biorthogonality condition given by

$$[W]^T[C][V] + [S]^T[M][V] + [W]^T[M][R] = [I] \tag{39}$$

In finite precision computations, they loose their biorthogonality [9], and the following reorthogonalization scheme is used in our implementation.

The (j+1)st vectors computed in Eqs. (35) thru (38) are checked for their biorthogonality with respect to each of the j vectors by computing the coefficients θ_i and ϕ_i as follows:

$$\theta_i = \{w_i\}^T[C]\{v_{j+1}\} + \{s_i\}^T[M]\{v_{j+1}\} + \{w_i\}^T[M]\{r_{j+1}\} \tag{40}$$

$$\phi_i = \{w_{j+1}\}^T[C]\{v_i\} + \{s_{j+1}\}^T[M]\{v_i\} + \{w_{j+1}\}^T[M]\{r_i\} \tag{41}$$

If the magnitude of any of the coefficients, say the k th coefficient, is greater than a predetermined small number, ε_o, then the reorthogonalizing steps are given by

$$\{v_{j+1}\} \rightarrow \{v_{j+1}\} - \theta_k \, v_k \tag{42}$$

$$\{w_{j+1}\} \rightarrow \{w_{j+1}\} - \phi_k \, w_k \tag{43}$$

$$\{r_{j+1}\} \rightarrow \{r_{j+1}\} - \theta_k \, r_k \tag{44}$$

$$\{s_{j+1}\} \rightarrow \{s_{j+1}\} - \phi_k \, q_k \tag{45}$$

In the present implementation, $\varepsilon_o = 10^{-8}$ is used.

The two–sided Lanczos recursion presented in Eqs. (27) thru (38) results in a biorthogonal transformation of the quadratic eigenproblem into the standard eigenvalue problem given in Eq. (24). The eigenvectors are related by

$$\{x_i\} = [V]\{y_i\}, \; \{\bar{x}_i\} = [R]\{y_i\} \tag{46}$$

Using the recursion equations (27) and (29), it can be shown that [8] matrices [R] and [T] satisfy the characteristic equation (23), and that [T] is a tridiagonal matrix formed by the Lanczos recursion coefficients.

$$[T] = \begin{bmatrix} \alpha_1 & \beta_2 & & 0 \\ \delta_2 & \alpha_2 & \ddots & \\ & \ddots & \ddots & \beta_m \\ 0 & & \delta_m & \alpha_m \end{bmatrix} \tag{47}$$

The eigenvalues $\mu_i = (1/\lambda_i)$ of the standard eigenvalue problem in Eq. (24) are extracted by a QR algorithm [10] designed to extract complex eigenvalues. With an increasing number of recursion steps, the subspace size m increases and the eigenvalues at the lower end of the eigenvalue magnitude spectrum quickly converge to yield the λ_i's of the original problem. In the present application , the first k eigenvalues converged usually within a subspace size of m = k + 16. To compute the eigenvectors of the original problem, Eq. (46) is used. Eigenvectors $\{y_i\}$ are computed by inverse iterations of the [T] matrix.

EXAMPLES

Three simple examples are shown to validate the incorporation of sound absorption in the acoustic boundary element eigenproblem. The boundary absorption method presented has also been implemented in the acoustic finite element eigenproblem in the ANSYS® general purpose program [11]. Therefore, the boundary element results are compared with the finite element results in these examples.

Example 1

A square cavity shown in Fig. 2 is considered. The absorption free eigenfrequencies for this problem are $f_i = (c/2)\left[(\ell_x/L_x)^2 + (\ell_y/L_y)^2\right]^{1/2}$, $\ell_x, \ell_y = 0, 1, 2 \ldots \infty$. L_x and L_y are the length and width of the domain, respectively. We use this example to validate the Lanczos eigenvalue computation algorithm presented. The absorption coefficients at the absorption layer and at the walls β_a and β_b, respectively, are set to zero. For the boundary element discretization, 36 boundary nodes and 14 internal nodes are used. The need for internal nodes to improve the accuracy of computed frequencies was pointed out in reference [3]. The frequencies shown in Table 1 include the theoretical and a 10 x 10 mesh finite element [11] results for comparison with the boundary element solution. The acoustic resonant frequencies are the positive imaginary parts of the conjugate pair of

eigenvalues computed. The five eigenmode frequencies from the boundary element method compare favorably with the finite element solution in coming close to the theoretical frequencies.

Example 2

The square cavity problem is solved with uniform boundary absorption by taking $\beta_a = \beta_b = 0.2$. Table 2 shows the frequencies computed by the boundary and finite element methods using the same discretization as in Example 1. The eigenvalues $\lambda_i = \sigma_i \pm j\,\omega_i$, now have a nonzero real part. The imaginary part gives the damped resonant frequency $f_i = \omega_i / 2\pi$. Compared to the nonabsorption case, the frequencies have slightly reduced for modes 3–8. Mode 2 shows a nonoscillatory exponential decay response. The boundary element results compare well with the finite element results at the lower modes. With an increasing number of internal points, the boundary element results will improve. The mode shapes 2 and 4 obtained from the finite element results are plotted in Fig. 3.

Example 3

Here the absorption is nonuniform, $\beta_a = 0.9$ and $\beta_b = 0$. Table 3 shows the frequency results. Modes 3–10 show an increase from the undamped frequencies. Mode 2 again shows a nonoscillating decay. The plot of mode shapes 2 and 4 obtained from the finite element analysis are shown in Fig. 4. It is interesting to note the concentration of contours near the absorption layer in these plots.

CONCLUSIONS

A method of incorporating boundary absorption in the eigenvalue analysis of acoustic cavities using the boundary element technique has been validated. Since the damping matrix is obtained from the discretized boundary element matrix, the implementation of the method is simple. Using the experimentally correlated absorption coefficients of fibrous and foam type material found in reference [4], the damped system resonant modes of acoustic cavities, such as the automobile passenger cabin, can be computed. The Lanczos algorithm for quadratic eigenproblem employed is found to be quite efficient since it does not require augmentation of the system matrices. When only a few eigenvalues of a large dynamic system is needed the Lanczos subspace method is quite effective, both in speed of computation and in accuracy. However, when the number of eigenvalues needed is large, say >50, the total reorthogonalization scheme used will slow down the computation and a selective reorthogonalization [9] would improve the situation. Finally, the absorption in cavities affect the eigenmode pressure distribution quite appreciably, even though the damped system frequencies are not very far away from the undamped frequencies.

ACKNOWLEDGEMENTS

The authors thank Swanson Analysis Systems, Inc. for the support of this work. Contributions of Jackie Williamson and Charmaine Grunick in the preparation of the manuscript is acknowledged.

REFERENCES

1. P. K. Banerjee, S. Ahmad and H. C. Wang, 'A new BEM formulation for acoustic eigenfrequency analysis', Int. J. Numer. Methods Eng., 26, 1988, 1299–1309.

2. C. Rajakumar, A. Ali and S. M. Yunus, 'Lanczos algorithm for acoustic boundary element eigenvalue problems', J. Acoust. Soc. Am., to appear, 1992.

3. A. Ali, C. Rajakumar and S. M. Yunus, 'On the formulation of the acoustic boundary element eigenvalue problems', Int. J. Numer. Methods Eng., 31, 1991, 1271–1282.

4. A. Craggs, 'A finite element model for acoustically lined small rooms', J. Sound Vib., 108(2), 1986, 327–337.

5. O. C. Zienkiewicz and R. E. Newton, 'Coupled vibrations of a structure submerged in a compressible fluid', Proc. Int. Symp. on Finite Element Techniques, Stuttgart, 1969, pp. 359–379.

6. T–S Zheng, W. M. Liu and Z. B. Cai, 'A generalized inverse iteration method for solution of quadratic eigenvalue problems in structural dynamic analysis', Computers & Structures, 33, 1989, 1139–1143.

7. C. Rajakumar and C. R. Rogers, 'The Lanczos algorithm applied to unsymmetric generalized eigenvalue problem', Int. J. Numer. Method Eng., 32, 1991, 1009–1026.

8. C. Rajakumar, 'Lanczos algorithm for the quadratic eigenvalue problem in engineering applications', Computer Meth. App. Mech. and Eng., submitted for possible publication.

9. B. Nour–Omid, 'The Lanczos algorithm for solution of large generalized eigenproblems', in T. J. R. Hughes, The Finite Element Method, Prentice–Hall, Englewood Cliffs, NJ, 1987.

10. J. H. Wilkinson, The Algebraic Eigenvalue Problem, Clarendon Press, Oxford, 1988.

11. G. J. DeSalvo and R. W. Gorman, ANSYS® Engineering Analysis Systems User's Manual, Revision 4.4, Swanson Analysis Systems, Inc., Houston, PA, 1989.

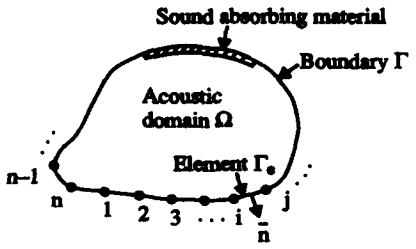

Figure 1 Acoustic cavity

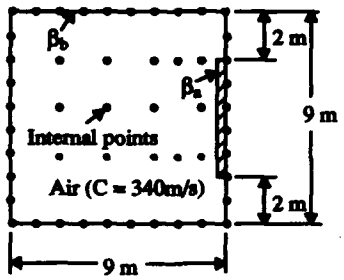

Figure 2 Boundary element mesh of square cavity (Absorption coefficient : β_a = at the absorption layer, β_b = at the walls).

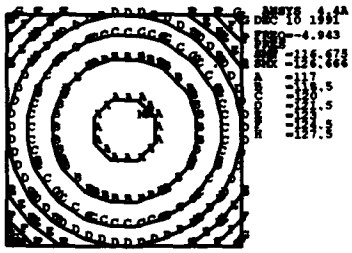

Mode 2

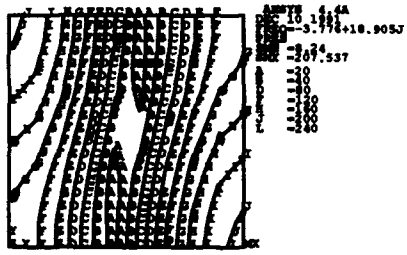

Mode 4

Figure 3 Square cavity mode shapes for uniform absorption ($\beta_a = \beta_b = .2$)

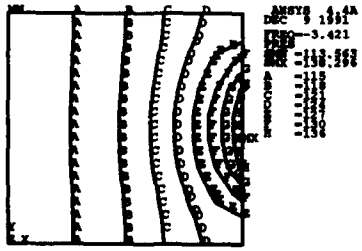

Mode 2

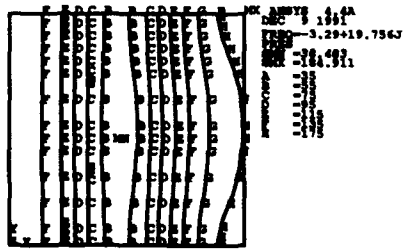

Mode 4

Figure 4 Square cavity mode shapes for non–uniform absorption ($\beta_a = .9$, $\beta_b = 0$)

Table 1 Acoustic resonance frequencies of cavity with zero absorption ($\beta_a = \beta_b = 0$)

No.	Theoretical Frequencies (Hz)	Computed Frequencies			
		Boundary Element		Finite Element	
1		0.90094705E-05	-0.16054364E-05 J	-0.73030743E-04	-0.98103609E-06 J
2	0	-0.90096915E-05	0.16051918E-05 J	0.73051942E-04	0.98157164E-06 J
3	-	0.00000000E+00	-19.031585 J	0.00000000E+00	-18.984927 J
4	18.8889	0.00000000E+00	19.031585 J	0.23827455E-06	18.984927 J
5	-	-0.19916942E-06	-19.127708 J	0.29067474E-06	-18.984928 J
6	18.8889	0.00000000E+00	19.127708 J	0.29076915E-06	18.984928 J
7	-	0.00000000E+00	-26.972142 J	0.00000000E+00	-26.848742 J
8	26.7129	0.00000000E+00	26.972142 J	0.00000000E+00	26.848742 J
9	-	0.00000000E+00	-39.214077 J	0.00000000E+00	-38.548881 J
10	37.7778	0.00000000E+00	39.214077 J	0.00000000E+00	38.548881 J

Table 2 Acoustic resonance frequencies of cavity with uniform absorption ($\beta_a = \beta_b = 0.2$)

No.	Computed Frequencies			
	Boundary Element		Finite Element	
1	-0.69521872E-10	-0.32956126E-09 J	0.53712161E-09	0.51497840E-09 J
2	-4.8788198	0.00000000E+00 J	-4.9431474	0.00000000E+00 J
3	-3.8496925	-18.905690 J	-3.7763896	-18.905246 J
4	-3.8496920	18.905690 J	-3.7763896	18.905246 J
5	-3.9248480	-18.973677 J	-3.7763897	-18.905247 J
6	-3.9248480	18.973678 J	-3.7763897	18.905247 J
7	-5.3478454	-26.783942 J	-5.1516059	-26.823973 J
8	-5.3478454	26.783942 J	-5.1516060	26.823973 J
9	-4.5679968	-39.211240 J	-3.9654993	-38.695024 J
10	-4.5679969	39.211240 J	-3.9654994	38.695024 J

Table 3 Acoustic resonance frequencies of cavity with non-uniform absorption ($\beta_a = 0.9$, $\beta_b = 0$)

No.	Computed Frequencies			
	Boundary Element		Finite Element	
1	-0.32277792E-07	-0.31245974E-07 J	0.70742767E-08	-0.37968327E-08 J
2	-3.3779687	0.00000000E+00 J	-3.4207326	0.00000000E+00 J
3	-0.61991593	-19.372290 J	-0.61317013	-19.236889 J
4	-0.61991592	19.372290 J	-0.61317014	19.236889 J
5	-3.3924172	-19.793552 J	-3.2898905	-19.755583 J
6	-3.3924172	19.793552 J	-3.2898902	19.755583 J
7	-1.3665337	-27.344634 J	-1.3564097	-27.252889 J
8	-1.3665337	27.344634 J	-1.3564100	27.252889 J
9	-0.39190014	-39.427160 J	-0.32248800	-38.721521 J
10	-0.39190016	39.427160 J	-0.32248844	38.721522 J

SECOND INTERNATIONAL CONGRESS ON
RECENT DEVELOPMENTS IN AIR- AND
STRUCTURE-BORNE SOUND AND VIBRATION
MARCH 4-6, 1992 AUBURN UNIVERSITY, USA

THEORETICAL AND PRACTICAL CONSTRAINTS ON THE IMPLEMENTATION OF ACTIVE ACOUSTIC BOUNDARY ELEMENTS

P. Darlington G.C. Nicholson

Department of Applied Acoustics
University of Salford
Salford M5 4WT UK

ABSTRACT

The reflection of normally incident plane acoustic waves from a plane impervious boundary can be controlled by actively modifying the mechanical impedance of the boundary suspension. This application of active control techniques motivates the study of active absorbers. The performance of such active boundaries is limited by both physical constraints on the transducers and controlling filters and by the behaviour of adaptive signal processing algorithms which are used to design the controllers. This paper details some operational constraints imposed by the properties of the suspension and forcing actuator used in the device and by the practical requirements of stability and causality in the system. The constraints are illustrated in the context of an attempt to implement a broadband active acoustic absorber.

NOMENCLATURE

c	speed of sound	(m/s)	z_E	voice coil blocked impedance	(Ω)
d	distance (cone to microphone)	(m)	z_d	desired spec. acoustic impedance	(Ns/m^3)
F	total force on cone	(N)			
i	voice coil current	(A)	z_m	mechanical impedance	(Ns/m)
j	$\sqrt{-1}$				
m	moving mass	(kg)	Φ	transformation factor	(N/A)
p	acoustic pressure	(Pa)	ρ_0	equilibrium mass density	(kg/m^3)
P	power	(Watts)	τ	delay	(s)
R	mechanical damping	(Ns/m)	ω	angular velocity	(rad/s)
S	cone area	(m^2)			
T	controller delay	(s)	Subscripts..		
u	cone velocity	(m/s)			
V	controller output voltage	(V)	c	at surface of cone	
W	control filter		i	incident component	
X	cone displacement	(m)	r	reflected component	

1 INTRODUCTION

If a plane impervious rigid plate, suspended with respect to mechanical ground by linear springs and damping elements, is excited by a normally incident plane wave, it will be forced into motion. The suspension elements can be arranged so as to allow uniform motion over the entire surface. Under

this condition, the analysis of the reflection of the incident acoustic wave, absorption of incident acoustic energy by the surface and transmission of the acoustic disturbance into a compressible medium backing the plate is a simple problem found in many acoustics textbooks. The behaviour of the system can be characterized in terms of the ratio of the characteristic impedance(s) of the fluid(s) on either side of the plate and the mechanical impedance of the suspended plate, this mechanical impedance being determined by the plate's surface mass density and the parameters of the suspension elements. If an additional forcing term is added to the equation of motion of the plate, it is possible to actively modify the mechanical impedance of the structure and so modify the reflection, absorbtion or transmission of sound.

Such an "Active Acoustic Boundary" has been the subject of considerable research effort, including work performed at Gottingen [1,2] and considerable research at Virginia Polytechnic Institute [3,4]. The German work has focussed upon the control of the reflection and absorbtion of an actively controlled boundary element, whilst much of the American work has concentrated upon the control of transmission of acoustic energy over a partition. This paper describes some fundamental limits which define an operating envelope for practical active boundary elements, presented in the simplified context of a small active boundary element forming the termination of an acoustic waveguide, operating at frequencies below the plane wave "cut-off" frequency.

2 MODEL PROBLEM - THE ELECTRODYNAMIC ACTIVE ACOUSTIC ABSORBER

The discussions and experimental results presented in this paper are based upon an implementation of the "Active Acoustic Boundary Element" concept built around a conventional direct radiating electrodynamic loudspeaker. Using a loudspeaker as the boundary element has several advantages - it has an (approximately) plane impervious surface (the cone) which is linearly suspended with respect to mechanical ground (the frame) by a suspension designed to permit uniform "piston-like" displacement of the cone. The loudspeaker also has a motor system via which controlling forces can be applied to the cone. To instrument the surface impedance, a miniature pressure microphone was fixed on the moving cone, in such an orientation as to minimise the transducer's acceleration response. The cone velocity can be transduced by several means - the results presented in this paper use velocity measures derived from a miniature accelerometer fixed on the cone, the output of which was integrated electronically.

The control required to force the surface impedance to some prespecified value is obtained by a linear filtering operation on measures of an acoustic variable in the waveguide. In the system studied in this paper, the pressure at the cone of the loudspeaker, or at a point in the waveguide some distance from the active termination, is the variable used as the input to the controlling filter.

2.1 Optimal Controller Configuration

If the active impedance device illustrated in Fig. 1 is achieving a desired impedance:

$$\frac{p_c}{u} = z_d \qquad (1)$$

then it is possible to identify the optimal configuration of the controlling filter, W_{opt}, by solving the equation of motion of the cone. The total force on the cone is a sum of the force due to the motor system, the acoustic reaction, and the stiffness and damping of the suspension:

$$F = \phi\,(V - \frac{\phi u}{z_E}) - p_c S - Ru - \frac{ku}{j\omega} \qquad (2)$$

Substituting the total force defined in equation 2 into the equation of motion of the cone gives:

Figure 1 Experimental Electrodynamic Active Absorber

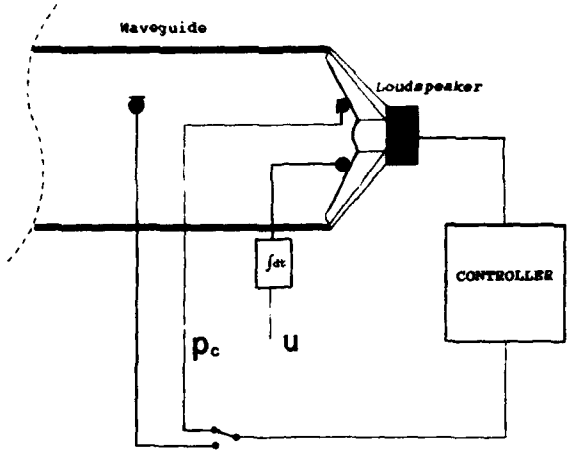

$$\phi\frac{(V-\phi u)}{z_E} - p_c S - Ru - \frac{ku}{j\omega} = mj\omega u \qquad (3)$$

which, recalling that the loudspeaker voltage is obtained by passing the pressure at the cone through the controller (see Fig. 1):

$$V = p_c.W_{opt}$$

and substituting for p_c from equation 1, gives the optimum filter:

$$W_{opt} = z_d^{-1}\left(\frac{z_m z_E}{\phi} + \phi\right) + \frac{S z_E}{\phi} \qquad (4)$$

Equation 4 shows that the filter required to force the surface acoustic impedance at the cone of the loudspeaker to the desired value of z_d has two additive terms. The first term is proportional to the inverse of the desired impedance, whilst the second term, Sz_E/ϕ, is independent of the required impedance. (This second term is actually the filter required to hold the cone of the loudspeaker perfectly still, implementing an infinite impedance, $z_d = \infty$). In order for the optimum filter to be realizable, the desired surface impedance should have a causally stable inverse (as z_d^{-1} is a factor of the first term of the right hand side of (4)). The only other potential problem in specifying the filter W_{opt} are the singularities in the mechanical impedance of the loudspeaker, z_m, at zero and infinite frequencies. Z_m has infinite magnitude at d.c. due to the suspension stiffness - this would require that W_{opt} should have infinite d.c. gain, which is, clearly, impractical. Fortunately, practical implementations of active impedances are bandpass limited (at low frequencies by the linear excursion of the suspension, see section 3.1, and at high frequencies by the plane wave "cut-off" of the wave guide) so the singularities in the ideal filter solution, (4), are never required.

2.2 Optimum Controller Using Upstream Pressure Signal.

If the input to the controlling filter is derived from a microphone located in the waveguide some distance from the surface of the cone (changing the position of the switch in Fig. 1) then the optimum controller solution becomes significantly more complicated. If the waveguide is lossless, such that the transfer function between the component of pressure due to rightwards propagating waves at the upstream microphone location and the cone can be described by a pure delay,

the optimal controller is given by:

$$W_{OPT} = \frac{\left[\frac{S}{Z_T} + Z_d^{-1}\right]\left[1 + \left(\frac{Z_d / \rho_0 c - S}{Z_d / \rho_0 c + S}\right)\right]}{\frac{\Phi}{Z_E Z_T}\left[\frac{1}{F} + F\left(\frac{Z_d / \rho_0 c - S}{Z_d / \rho_0 c + S}\right)\right]} \qquad (5)$$

where Z_T is the effective mechanical impedance and F is the delay term:

$$Z_T = Z_m + \phi^2 / Z_E \qquad F = e^{j\omega d/c}$$

Equation (5) reduces to equation (4) when F=1.

3 OPERATIONAL CONSTRAINTS OF PRACTICAL ELECTRODYNAMIC ACTUATORS

The optimal solutions developed above assume that the loudspeaker system used as the basis of the active termination has ideal behaviour, characterized fully by a linear equation of motion, such as (3). Real loudspeakers depart from this ideal in two important respects; they have nonlinear suspensions and motor systems and the voice coil can handle only a finite power. Both of these non-ideal properties define edges of the operational envelope of adaptive impedances built around electrodynamic actuators, which are discussed below.

3.1 Suspension Nonlinearity

The suspension of a practical electrodynamic actuator does not have a linear compliance (and damping) term, rather the compliance reduces as the cone is displaced further from equilibrium - the suspension stiffness hardens. There is, therefore, an absolute limit on the cone excursion. Well before this fracture limit is reached, the suspension will become significantly nonlinear and it is appropriate to define an limit of (approximately) linear cone excursion. This limit of linear excursion, $|X|_{max}$, defines a frequency dependant limit of maximum linear velocity, $|u|_{max}$:

$$|u|_{max} = \omega |X|_{max} \qquad (6)$$

Note that the transducer has a velocity zero at d.c., as a consequence of the displacement limit. Given this zero in the practical transducer's response, it is never necessary to attempt to implement the d.c. pole in the ideal optimal filter solution, (4). If, as shown in equation (6), the velocity of the cone of an actively controlled impedance is limited, then it is possible to define a maximum pressure that can exist at the cone when the system is implementing a desired impedance:

$$|p|_{max} = |u|_{max} |Z_d| \qquad (7)$$

An example of this limitation on the pressure at the cone is presented in section 3.3.

3.2 Actuator Power Handling

The motor system of an electrodynamic loudspeaker has a finite electrical power handling capacity, which limits the voice coil current and resulting electrical force applied to the cone. This force imposes a second limit to the cone velocity, when the impedance at the cone is held by the controller to the desired value of Z_d. If the maximum power handling of the voice coil is P Watts, then the maximum voice coil current is :

$$I_{RMS} = \sqrt{P / \Re e(Z_E)}$$

which, assuming the active impedance is successfully implementing the desired impedance

(equation 1) can be substituted into the equation of motion (3) to define the maximum velocity:

$$u_{max} = \left| \frac{\phi}{(z_{ar}+Sz_d)} \right| \sqrt{P/\Re e\{z_s\}} \qquad (8)$$

As described for equation (6), the velocity limit defined by (8) can be used either to specify the the maximum pressure permissible for a given z_d (see section 3.3), or minimum z_d for a specified maximum pressure.

3.3 Example

The cone velocity limits imposed by the maximum cone linear excursion and the motor voice coil power handling can be evaluated given the desired impedance, and the specifications of the actuator used. The experimental rig developed at the University of Salford uses B200A drive units, manufactured by KEF Electronics Limited, Tovil, Maidstone, England, having a 6.3mm (peak to peak) linear cone excursion, 50 Watts (programme) power handling and 8 Ohm nominal impedance. If this loudspeaker is controlled, such that the specific acoustic impedance at its cone is 415 Rayls, then the velocity limits are shown in Figure 2.

Figure 2 Velocity and Pressure Limits for the Electrodynamic Active Absorber(z_d = 415 Rayls.)

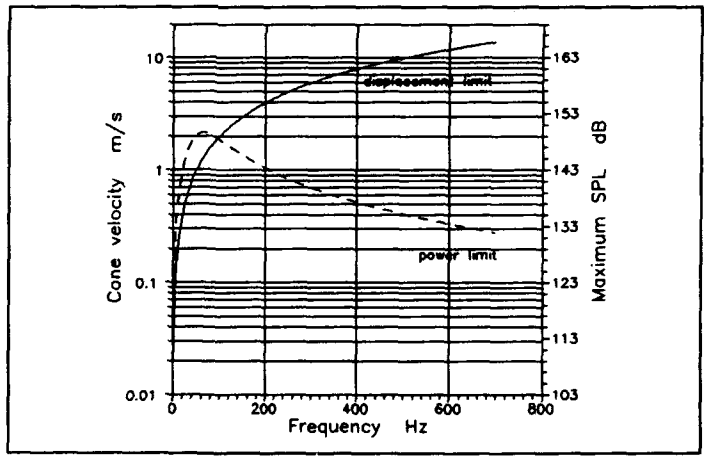

The actual velocity limit is defined by the smallest of equations (6 & 8) at any frequency - the cone displacement limit dominates at low frequencies, whilst at frequencies above approximately 100 Hz. the velocity of the cone is limited by the power handling capability of the coil. As the impedance at the surface of the cone is known to be z_d = 415 Rayls, the maximum velocity data can be easily scaled to give the maximum pressure which can be sustained at the cone of this active absorber - this maximum pressure is also shown in Figure 2.

4 CONSTRAINTS INTRODUCED BY THE 'FEEDBACK' CONTROL TOPOLOGY

Most of the previous work on the active control of surface acoustic impedance (for example [1-4]) has been characterized by the use of a "feedforward" controller architecture. That is to say the controlling filter senses the input acoustic pressure incident on the active termination and uses this signal to derive the control force required to drive the active boundary. The work described in this paper uses a fundamentally different architecture, in which the controller observes one component of the system response (the cone pressure) and uses this signal to derive the control force. This approach is (almost) a "feedback" control topology, in which, as the name suggests, a feedback

path exists from the plant response to the controller input. In the active termination system described in this paper, the feedback path is from the cone velocity (system output) to the pressure at the cone (controller input) - any component of cone velocity caused by the electrical forcing term in the equation of motion (3) changes the pressure at the cone.

Using this feedback control approach introduces several complications, including the potential for loop instability, which must be avoided if the system is to be practically useful. The incident and reflected pressure components at the cone may be related through an equation derived from continuity of velocity:

$$p_r = p_i - \rho_0 c . u_c$$

which allows the system to be represented in terms of the block diagram of Figure 3 The figure clearly shows a feedback path around the controlled termination, generating the reflected pressure component of the acoustic pressure at the cone, pc. In order for the loop to be stable, its magnitude transfer function should be smaller than unity :

$$| z_d^{-1} . \rho_0 c | < 1$$

which can be rearranged to give a lower limit on the impedance which can be implemented by a controller in the presence of the feedback path:

$$| z_d | > \rho_0 c \qquad (9)$$

Note that a further potential feedback path exists, in which the reflected pressure propagates away from the actively controlled termination and is again reflected, to form a component of the incident pressure. In a practical duct this feedback path has magnitude gain equal to or smaller than the direct path described above and does not usually significantly alter the stable bound (9).

Equation (9) shows that it is impossible to implement an active ideal absorber ($z_d = \rho_0 c$) using a pure feedback architecture. The system studied at the University of Salford includes an electrical "feedback cancelling" path which subtracts an estimate of the feedback components of p_c from the input of the controlling filter. The transfer function of the feedback cancelling filter is automatically estimated before the system is operated, and attempts to cancel both the "direct" reflected pressure component and any component of the incident pressure due to feedback. Using this feedback

Figure 3 Block Diagram of the Feedback Controlled Active Absorber

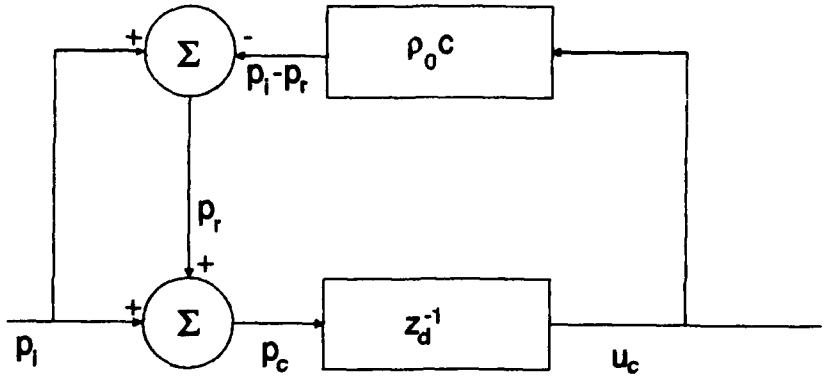

cancelling approach, the system is able to implement surface acoustic impedances well below the limit suggested in Equation (9), such that an anechoic load can be implemented.

If the controlling filter uses the total acoustic pressure some distance upstream of the active termination as its input, as discussed in section 2.1, there is a different loop stability condition, involving the transfer function representing the propagation path between the upstream microphone and the cone. As this transfer function is a pure delay in a lossless uniform duct, the limit of impedances which can be implemented (9) applies when the control signal is derived from an upstream pressure measurement, unless steps are taken to avoid the feedback path.

5 CAUSAL CONSTRAINTS ON THE IMPLEMENTATION OF ACTIVE TERMINATIONS

The controlling filter generating the forcing signal to drive the surface impedance of an active acoustic boundary to a desired value will usually be implemented using digital signal processing technology. This enables an appropriate estimate of the required filter to be derived automatically "on-line" using adaptive signal processing algorithms [5]. Using digital filters has the disadvantage of introducing pure delay components into the controller response associated with the finite instruction rate of the processing element, sampling delays associated with the data converter systems and large group delays through high order anti-aliasing and reconstituting filters. If the control path includes such pure delays, then the controlling filter must act as both a filter and *predictor* if the active impedance concept is to be useful. In order for the controlling filter to be realizable, it must have an impulse response which is causal - it is not able to compensate for the delays by introducing an equal advance component. The presence of pure delays in the control loop of the system introduces therefore a causal constraint on the performance of the active impedance illustrated in Fig. 1.

The implication of causality in the context of conventional active control of sound is well understood and has been reported in the literature [6]. Causal constraints on the operation of the feedback active impedance device can be analysed by solving a Wiener-Hopf integral equation for the optimum causally constrained controller, using techniques found in standard automatic control texts [7]. The current paper presents some experimental results which illustrate the causal constraint and further illustrate a practically useful relationship between an easily measured property of the incident pressure's autocorrelation function and the expected performance of the actively controlled impedance.

Although it is not possible to introduce an advance into the response of a physical filter, it is possible to derive the input signal to the controller from a point in the duct d metres upstream of the active termination. The incident pressure component of this upstream pressure is advanced by d/c seconds (the controller has adopted a partially feedforward structure). If the delay inherent in the control loop is T seconds then the total equivalent delay in the system with upstream pressure sensing is (T - d/c) seconds - it is possible to eliminate all of the delay if the upstream microphone is far enough away from the cone.

Figure 4 shows a plot of the normalized mean square (velocity) error when a loudspeaker is actively controlled to present a specific acoustic impedance of 415 Rayls, as a function of the spacing from the cone to the upstream microphone. The incident pressure wave was a one octave band of noise, centered on 200 Hz., and generated 115dB SPL at the controlled cone. The data is an average of the converged solutions of thirty two, 45 second evolutions of a simple adaptive controller for each distance reported and the error bars show +/- one standard deviation. The error in implementing the anechoic termination is seen to hold roughly constant value until the distance increases to approximately 25 cm, after which point the error decreases. The delay in the control path was measured as 1.3 msec (corresponding to the time taken for an acoustic signal to propagate across a distance of approximately 45 cm.).

Figure 4 Converged Normalized MS Velocity Error and Max $\{|r_{xx}(\tau)|\}_{\tau > (T-d/c)}$ for the Adaptive Absorber (z_s=415) with Upstream Pressure Detection. (Error bars show +/- σ)

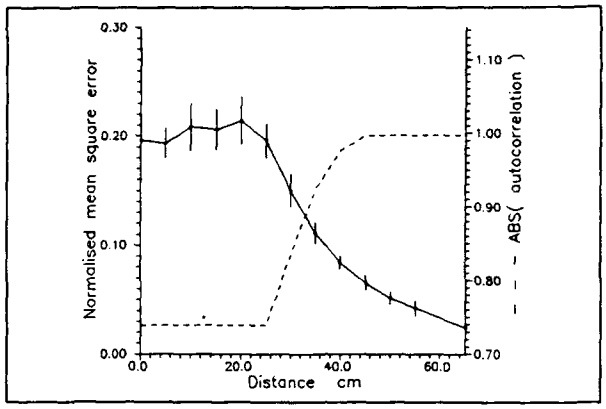

Also shown in Fig. 4 is the maximum absolute value of the incident pressure's autocorrelation function for lag greater than the effective delay (T-d/c). Experience has shown this parameter to be reasonably well correlated with the norm of the optimum controller's impulse response vector and, consequently, with the coherence between the actual and predicted cone velocities. According to this empirically observed relationship, the optimum mean squared error in the implementation of a desired impedance is proportional to:

$$E[e^2] \propto 1 - (\text{Max}\{|r_{xx}(\tau)|\})^2 \qquad (10)$$
$$\tau > (T-d/c)$$

Equation 10 shows that the causal constraint can be effectively removed by increasing d, when the system becomes a pure feedforward controller. Equation 10 also reveals that a pure feedback system (d=0) can estimate a desired impedance to an accuracy which can be predicted if the autocorrelation function of the incident pressure signal is known.

CONCLUDING REMARKS

This paper has demonstrated that physical properties of a conventional electrodynamic loudspeaker used as the basis of an active acoustic boundary element impose limits upon the range of specific acoustic impedances which can be implemented. Further constraints are imposed by the physical requirements of controller stability and causality. Despite these constraints it is possible to construct active acoustic loads using feedback control which will approximate desired surface specific acoustic impedances to a predictable degree of accuracy for a defined incident pressure signal.

REFERENCES

[1] Guicking, D., Karcher,K. & Rollwage, M. **"Coherent Active Methods for use in Room Acoustics"**, JASA v78(4) 1985 pp1426 - 1434

[2] Wenzel, M. & Guicking, D **"Simulationen und Experimente zur Adaption einer aktiven Schallwand auf eine breitbandig vorgegebene Wandimpedanz"**, Fortschritte der Akustik, DAGA '90, 1990 pp 899 - 902

[3] Fuller, C. **"Active Control of Sound Transmission / Radiation from Elastic Plates by Vibration Inputs : I. Analysis"** J.Sound Vib. v136 1990 pp 1-15

[4] Fuller, C. **"Active Control of Sound Radiation from a Vibrating Rectangular Panel by Sound Sources and Vibration Inputs : An Experimental Comparison"** J.Sound Vib. v145(2) pp 196 - 215

[5] Nicholson, G.C. & Darlington, P. **"Smart Surfaces for Building Acoustics"**, Proc. IOA, v13, pt8,1991,pp 155-164

[6] Nelson, P.A., Hammond, J.K. & Elliott, S.J. **"Causal Constraints on the Active Control of Sound"**, Proc. ICASSP'87, 1987, pp 145-148

[7]Laning, J.H. & Battin, R.H. **"Random Processes in Automatic Control"**, McGraw-Hill, 1956, (Chapter 7)

SECOND INTERNATIONAL CONGRESS ON
RECENT DEVELOPMENTS IN AIR- AND
STRUCTURE-BORNE SOUND AND VIBRATION
MARCH 4-6, 1992 AUBURN UNIVERSITY, USA

BOUNDARY ELEMENT FORMULATIONS FOR ACOUSTIC SENSITIVITIES WITH RESPECT TO STRUCTURAL DESIGN VARIABLES, AND ACOUSTIC IMPEDANCE

Nickolas Vlahopoulos
Automated Analysis Corporation
2805 South Industrial, Suite 100, Ann Arbor, MI

ABSTRACT

The concept of acoustic optimization for structure - borne noise (i.e. modifying the vibrating structure in order to reduce the emitted noise) is closely related with the derivation of acoustic sensitivities. In this paper the principles of acoustic optimization are discussed initially, and two algorithms for acoustic sensitivities are developed. (i) Acoustic sensitivities with respect to structural sizing design variables, where physical properties of the structure are used as design variables. These can be readily used in an automated optimization process. This methodology is applicable to both interior and exterior problems. (ii) Acoustic sensitivities with respect to acoustic impedance. The property of the absorbing material used as treatment is the design variable in this formulation. These sensitivities can indicate the optimum distribution of absorbing material.

I. INTRODUCTION

Two type of analyses are associated with analytical structure - borne noise prediction (Figure 1). The Finite Element Method (FEM) is commonly used to compute the vibration of the structure emitting noise [1], [2], and the Boundary Element Method (BEM) can be used to predict the generated noise [3]. Therefore, the structural analysis is performed by FEM and the acoustic analysis by BEM. Other methods for acoustic prediction are also available (finite element method [4], statistical energy analysis [5]) but in this paper the focus will be on the BEM. The scope of an acoustic optimization process is to reduce the structure - borne noise by modifying the noise source, i.e. the structure. Design iterations can be performed by the designer based on practical experience, but this is not the most efficient method. An automated optimization process can be developed (Figure 2) with the structural and the acoustic analysis as integral parts of the optimization. Within each loop the FEM analysis computes the response of the structure, and the BEM analysis predicts the generated sound. The optimizer changes the values of the structural design variables, the finite element structural model is updated, and the next optimization loop begins. The process is continued until convergence, or an acceptable noise reduction is achieved. In an optimization scheme it is important to have available the gradients (sensitivities) of the objective function and the constraints with respect to the design variables in order to guide the solution [6]. Formulation of acoustic sensitivities is the first step in creating an acoustic optimization process, and the scope of this paper is to develop formulations that can readily be used within an automated process. Two algorithms for acoustic sensitivities are developed in this paper:

(i) Acoustic sensitivities with respect to sizing design variables.
The physical properties of the structure are used as design variables. This methodology can be applied to both interior and exterior problems for noise reduction.

(ii) Acoustic sensitivities with respect to acoustic impedance.
The acoustic impedance of the absorbing material used as treatment is the design variable in this formulation.

Previous work has been done in deriving shape sensitivities in the BEM [7], [8]. However, there are two problems associated with actually implementing them in an automated optimization process:

(i) It is expensive to obtain good shape sensitivities, and general purpose finite element programs do not in general have available such a feature.

(ii) It is difficult to update the finite element model within an automated process at the beginning of each iteration, when shape modifications must be implemented [9]. Simple modification rules for deforming the initial mesh often run into problems, and general purpose software packages performing adaptive mesh refinement are not yet available.

In this paper the effort is concentrated on formulating sensitivities with respect to sizing design variables, that can be used in an automated process.

Efforts have also been made to use sensitivity analysis and optimization concepts with other acoustic prediction methods. Specifically a finite element procedure for design of cavity acoustical treatments was developed [10]. Acoustic optimization using the finite element method for acoustic prediction was performed for a car interior [11], and an optimization method selecting the damping treatment was developed [12] using the statistical energy analysis method.

In Section II of this paper the formulation of acoustic sensitivities with respect to sizing design variables is derived, and areas of applicability are identified. Section III contains the formulation with respect to acoustic impedance and the potential applications. Finally, Section IV contains the plans for utilization of this research, and further developments.

II. ACOUSTIC SENSITIVITIES WITH RESPECT TO STRUCTURAL SIZING DESIGN VARIABLES

The numerical implementation of the Boundary Element Method in acoustics is a two step process. First the system of equations:

$$[A]\{p\} - [B]\{u_n\} = \{0\} \tag{1}$$

is solved on the boundary surface. $\{p\}$ = vector of acoustic pressure on the surface, $\{u_n\}$ = the vector of normal velocities on the structural boundary, [A] and [B] = full matrices depending only on the geometry of the surface and the frequency of excitation. Once $\{p\}$ and $\{u_n\}$ are computed the acoustic pressure at any field point can be computed :

$$p_o = \{A_o\}^T\{p\} - \{B_o\}^T\{u_n\} \tag{2}$$

where subscript "$_o$" indicates a field point and the vectors $\{A_O\}$, $\{B_O\}$ depend only on the geometry of the problem and the frequency of excitation.

The scope of this formulation is to derive the acoustic sensitivity $\frac{\partial p_o}{\partial h}$ where p_O = acoustic pressure at the field point, and h = structural sizing design variable. The term sizing indicates that the change in the physical property h does not influence the shape and the geometry of the structure. The design variable h can be for example the thickness of a plate, the stiffness of a spring, the cross sectional area of a beam, a material property etc. In this formulation we will consider only velocity boundary conditions for the acoustic problem. This, however, does not impose any restriction in the formulation, since condensation can be used to reduce the system in the section with only velocities as boundary conditions. The algebra involved, however, is more tedious and therefore not presented in this paper.

By using the chain rule, $\frac{\partial p_o}{\partial h}$ can be written:

$$\frac{\partial p_o}{\partial h} = \sum_{i=1}^{I} \frac{\partial p_o}{\partial u_{ni}} \frac{\partial u_{ni}}{\partial h} \tag{3}$$

where u_{ni} = normal velocity of the i^{th} element, and I = total number of boundary elements used in the model.

In this manner the acoustic sensitivity is decomposed in two parts, $\frac{\partial p_o}{\partial u_{ni}}$ which can be calculated from the BEM acoustic analysis, and $\frac{\partial u_{ni}}{\partial h}$ which can be calculated by the FEM structural analysis. The first part indicates how the acoustic pressure changes with respect to the boundary conditions (acoustic part), and the second how the boundary conditions change with respect to the design variables (structural part). By differentiating Eq. (1) with respect to the i^{th} element normal velocity u_{ni} :

$$\frac{\partial [A]}{\partial u_{n_i}} \{p\} + [A] \frac{\partial \{p\}}{\partial u_{n_i}} - \frac{\partial [B]}{\partial u_{n_i}} \{u_n\} - [B] \frac{\partial \{u_n\}}{\partial u_{n_i}} = \{0\} \tag{4}$$

In this equation $\frac{\partial [A]}{\partial u_{n_i}}$, $\frac{\partial [B]}{\partial u_{n_i}} = 0$, because [A] and [B] are only geometry dependant, and change of the velocity u_{ni} does not imply changes in the geometry, since only sizing variables are considered in this formulation. Therefore from Eq. (4):

$$\frac{\partial \{p\}}{\partial u_{n_i}} = [A]^{-1} [B] \{I_i\} \tag{5}$$

where $\{I_i\}$ = unit vector with only one non - zero component in the i^{th} position. For a field point differentiating Eq. (2) with respect to u_{ni} results in:

$$\frac{\partial p_o}{\partial u_{n_i}} = \{A_o\}^T \frac{\partial \{p\}}{\partial u_{n_i}} - \{B_o\}^T \{I_i\} \tag{6}$$

where zero terms $\frac{\partial \{A_o\}^T}{\partial u_{n_i}}$, $\frac{\partial \{B_o\}^T}{\partial u_{n_i}}$ are neglected. Substituting Eq. (5) into (6) results in:

$$\frac{\partial p_o}{\partial u_{n_i}} = \left(\{A_o\}^T [A]^{-1} [B] - \{B_o\}^T \right) \{I_i\} \tag{7}$$

This constitutes the derivation of the acoustic part of the acoustic sensitivity $\frac{\partial p_o}{\partial h}$. The terms in the right hand side of Eq. (7) can be readily available from the solution of the BEM analysis for the acoustic pressure. The additional computational effort in solving Eq. (7) is negligible if a solution for the acoustic problem exists. For all the optimization iterations $\frac{\partial p_o}{\partial u_{ni}}$ will not change since all the terms in the right hand side of Eq. (7) depend on the geometry only. Therefore, in an acoustic optimization process with structural sizing design variables $\frac{\partial p_o}{\partial u_{ni}}$ need to be calculated only during the first iteration. $\frac{\partial p_o}{\partial u_{ni}}$ constitutes the acoustic part of the acoustic sensitivities.

The second part of the acoustic sensitivities is $\frac{\partial u_{ni}}{\partial h}$ and can be calculated during the finite element analysis of the structure. When the frequency response analysis is performed using the direct approach the solution is computed in the frequency domain by:

$$-\omega^2[M]\{x_o\} + i\omega[CS]\{x_o\} + [K]\{x_o\} = \{F_o\} \tag{8}$$

where [M], [CS], [K] = mass, damping, and stiffness matrix, $\{F_O\}$ = forcing vector, $\{x_O\}$ = response displacement, and ω = frequency of excitation. Eq. (8) can be written as:

$$[S]\{x_o\} = \{F_o\} \tag{9}$$

where $[S] = [-\omega^2[M] + i\omega[C] + [K]]$. By differentiating Eq. (9) with respect to a sizing design variable h results in:

$$\frac{\partial[S]}{\partial h}\{x_o\} + [S]\frac{\partial\{x_o\}}{\partial h} = \{0\} \qquad \Rightarrow$$

$$\frac{\partial\{x_o\}}{\partial h} = -[S]^{-1}\frac{\partial[S]}{\partial h}\{x_o\} \tag{10}$$

where $\frac{\partial[S]}{\partial h} \approx \left[-\omega^2\frac{\Delta[M]}{\Delta h} + i\omega\frac{\Delta[C]}{\Delta h} + \frac{\Delta[K]}{\Delta h}\right]$. From Eq. (10), considering that the solution is obtained in the frequency domain, $\frac{\partial\{u\}}{\partial h}$ can be derived from $\frac{\partial\{x_o\}}{\partial h}$ and accounting for the geometry $\frac{\partial u_{ni}}{\partial h}$ can be computed. This is the structural part, of the acoustic sensitivities and it can be computed within the structural analysis. Unlike the acoustic part it must be computed within each iteration loop. If the modal method is used for frequency analysis the structural part of the acoustic sensitivities can be computed using information from the eigenvalue and eigenvector derivatives.

In this section the acoustic sensitivities with respect to structural sizing design variables are derived. The formulation for the acoustic part can be readily implemented in an acoustic code based on the BEM, and it is intended to be implemented in SYSNOISE, a general purpose acoustic code [13]. The structural part can be computed either externally from a general purpose finite element code using data extracted from the code, or internally if the code has a capability for the user to modify the solution sequence (for example DMAP programming in MSC/NASTRAN). The developed methodology can be used in all the areas where acoustic prediction through the BEM is applicable. It can be used for both interior and exterior noise problems. In the automotive and the construction equipment industry it can be used in reducing the interior passenger cabin noise (see Figure 3), or the exterior noise emitted from vibrating components (engine blocks, transmission etc). Aerospace application can be the reduction of the passenger cabin noise. Finally, it can have significant military applications, contributing in reducing the noise emitted from structural components of military vehicles. This is important because their survivability depends on the acoustic signature they emit.

III. ACOUSTIC SENSITIVITIES WITH RESPECT TO ACOUSTIC IMPEDANCE

For this development Eq. (1) and (2) of the two step BEM solution process are used. By considering either velocity or impedance boundary condition, and denoting them with subscript "1" and "2" respectively, Eq. (1) and (2) become:

$$\begin{bmatrix} A_{11} A_{12} \\ A_{21} A_{22} \end{bmatrix} \begin{Bmatrix} p_1 \\ p_2 \end{Bmatrix} - \begin{bmatrix} B_{11} B_{12} \\ B_{21} B_{22} \end{bmatrix} \begin{Bmatrix} u_{n1} \\ u_{n2} \end{Bmatrix} = \{0\} \tag{11}$$

and

$$p_o = \begin{Bmatrix} A_{o1} \\ A_{o2} \end{Bmatrix}^T \begin{Bmatrix} p_1 \\ p_2 \end{Bmatrix} - \begin{Bmatrix} B_{o1} \\ B_{o2} \end{Bmatrix}^T \begin{Bmatrix} u_{n1} \\ u_{n2} \end{Bmatrix} = \{0\} \tag{12}$$

For area "2", $\{p_2\} = [C]\{u_{n2}\}$, where [C] = diagonal acoustic impedance matrix. Substituting in Eq. (11) results:

$$\begin{bmatrix} A_{11}A_{12} \\ A_{21}A_{22} \end{bmatrix} \begin{Bmatrix} p_1 \\ [C]\{u_{n2}\} \end{Bmatrix} - \begin{bmatrix} B_{11}B_{12} \\ B_{21}B_{22} \end{bmatrix} \begin{Bmatrix} u_{n1} \\ u_{n2} \end{Bmatrix} = \{0\} \quad \begin{matrix} (a) \\ (b) \end{matrix} \tag{13}$$

In order to condense this equation to variables of the area "1" only, first $\{u_{n2}\}$ is expressed in terms of $\{p_1\}$ and $\{u_{n1}\}$ from Eq. (13b), and then it is substituted in Eq. (13a). This results in:

$$\{u_{n2}\} = [D]\left[[B_{21}]\{u_{n1}\} - [A_{21}]\{p_1\}\right] \tag{14}$$

and

$$[AC]\{p_1\} - [BC]\{u_{n1}\} = \{0\} \tag{15}$$

where $[D] = \left[[A_{22}][C] - [B_{22}]\right]^{-1}$, and

$$[AC] = \left[[A_{11}] - [A_{12}][C][D][A_{21}] + [B_{12}][D][A_{21}]\right] \tag{16}$$

$$[BC] = \left[[B_{11}] - [A_{12}][C][D][B_{21}] + [B_{12}][D][B_{21}]\right] \tag{17}$$

By considering the impedance value of an element as design variable, or an entire area of elements with a common value for acoustic impedance and denoting it by c_i, differentiation of Eq. (15) results in:

$$[AC]\frac{\partial\{p_1\}}{\partial c_i} + [DAC]\{p_1\} - [BC]\frac{\partial\{u_{n1}\}}{\partial c_i} + [DBC]\{u_{n1}\} = \{0\} \tag{18}$$

where

$$\frac{\partial[C]}{\partial c_i} \approx \frac{\Delta[C]}{\Delta c_i} \qquad \frac{\partial[D]}{\partial c_i} \approx \frac{\Delta[D]}{\Delta c_i} \tag{19}$$

$$[DAC] = \frac{\partial[AC]}{\partial c_i} \qquad [DBC] = \frac{\partial[BC]}{\partial c_i} \tag{20}$$

In deriving Eq. (18), (19) and (20) matrices [A] and [B] are independent from the acoustic impedance used as design variable. In Eq. (18) $\{u_{n1}\}$ is independent of c_i, therefore:

$$[AC]\frac{\partial\{p_1\}}{\partial c_i} = -[DAC]\{p_1\} - [DBC]\{u_{n1}\} = \{DF\} \tag{21}$$

$\frac{\partial\{p_1\}}{\partial c_i}$ can be computed from Eq. (21), and $\frac{\partial\{u_{n2}\}}{\partial c_i}$ from Eq. (14) as:

$$\frac{\partial\{u_{n2}\}}{\partial c_i} = \frac{\partial[D]}{\partial c_i}\Big[[B_{21}]\{u_{n1}\} - [A_{21}]\{p_1\}\Big] - [D][A_{21}]\frac{\partial\{p_1\}}{\partial c_i} \tag{22}$$

Then for a field point Eq. (12) results in:

$$\frac{\partial p_o}{\partial c_i} = \begin{Bmatrix} A_{o1} \\ A_{o2} \end{Bmatrix}^T \begin{Bmatrix} \dfrac{\partial p_1}{\partial c_i} \\ \dfrac{\partial[C]}{\partial c_i}\{u_{n2}\} + [C]\dfrac{\partial u_{n2}}{\partial c_i} \end{Bmatrix} - \begin{Bmatrix} B_{o1} \\ B_{o2} \end{Bmatrix}^T \begin{Bmatrix} 0 \\ \dfrac{\partial u_{n2}}{\partial c_i} \end{Bmatrix} \tag{23}$$

In this type of acoustic optimization the structural analysis determining the velocities $\{u_{n1}\}$ need to be performed only during the first iteration, since the structural vibration is not considered to be affected from the absorbing material used as acoustic treatment. Only the acoustic analysis will be performed within each iteration (see Figure 2). This methodology can be applied in the automotive and aerospace industry to optimize the distribution of the absorbing material used as treatment in passenger compartments.

IV. FUTURE APPLICATIONS

The two formulations for acoustic sensitivities, developed in this paper, can be implemented in the general purpose acoustic code SYSNOISE. They are based on the collocation boundary element method, uncoupled solution (i.e. only the effect of the structure on the fluid is considered). Since SYSNOISE also includes the variational formulation and a coupled solution sequence, effort will be made to further expand the algorithms developed in this paper for the variational BEM method, and for coupled problems.

V. ACKNOWLEDGEMENTS

I would like to express my gratitude to Automated Analysis Corporation for the availability of the sources that allowed completion of this research effort, and to Numerical Integration Technologies for their encouragement in pursuing this development.

REFERENCES

1. Hughes, T.J.R., "The Finite Element Method, Linear Static and Dynamic Finite Element Analysis," Prentice - Hall, 1987.

2. Meirovitch, L., "Computational Methods in Structural Dynamics," Sijthoff and Nordhoff, 1980.

3. Fyfe, K.R., and Coyette, J.P., "Acoustical Design Using the Boundary Element Method," Second International Conference on Methodology and Innovations in Automotive Experimentation, Florence, Italy, November 22 - 25, 1988, pp. 102 - 116.

4. Coyette, J.P., and Guisset, P., "Finite Element Methods for Interior Acoustics," Second International Conference Methodology and Innovations in Automotive Experimentations, Florence, November 22 - 25, 1988, pp. 138 - 154.

5. Lyon, R.H., "Statistical Energy Analysis of Dynamical Systems: Theory and Applications," The MIT Press, 1975.

6. Haftka, R.T., and Kamal, M.P., "Elements of Structural Optimization," Martinus Nijhoff Publishers, 1985.

7. Smith, D.C., and Bernhard, R.J., "Computation of Acoustic Shape Design Sensitivity Using a Boundary Element Method," Numerical Techniques in Acoustic Radiation, Winter Annual Meeting of ASME, San Francisco, California, December 10-15, 1989, pp. 109 -116.

8. Kane, J.H., Mao, S., and Everstine, G.C., "A Boundary Element Formulation for Acoustic Shape Sensitivity Analysis," Journal of the Acoustical Society of America, Vol.90, July 1991, pp. 561 - 573.

9. Haftka, R.T., and Grandhi, R.V., "Structural Shape Optimization - A Survey," Computer Methods in Applied Mechanics and Engineering, vol. 57, 1986, pp. 91 - 106.

10. Bernhard, R.J., and Takeo, S., "A Finite Element Procedure for Design of Cavity Acoustical Treatments," Journal of the Acoustical Society of America, Vol 83, June 1988, pp. 2224 - 2232.

11. Nagabuchi, K., Hagiwara, I., and Arai, A., "Application of MSC/NASTRAN Sensitivity Analysis at Nissan Motor Company," 1989 MSC World Users Conference Proceedings, March 15 - 17, 1989.

12. Lu, L.K.H., "Optimum Damping Selection by Statistical Energy Analysis," Statistical Energy Analysis, Winter Annual ASME Meeting, December 13 - 18, 1987, Boston, Mass, pp. 9 - 14.

13. Coyette, J.P., "Numerical Acoustic Analysis in Automotive Design Using SYSNOISE," NAG Nederlands Akoestisch Genootschap, Journal 99, September 1990, pp.29 -42.

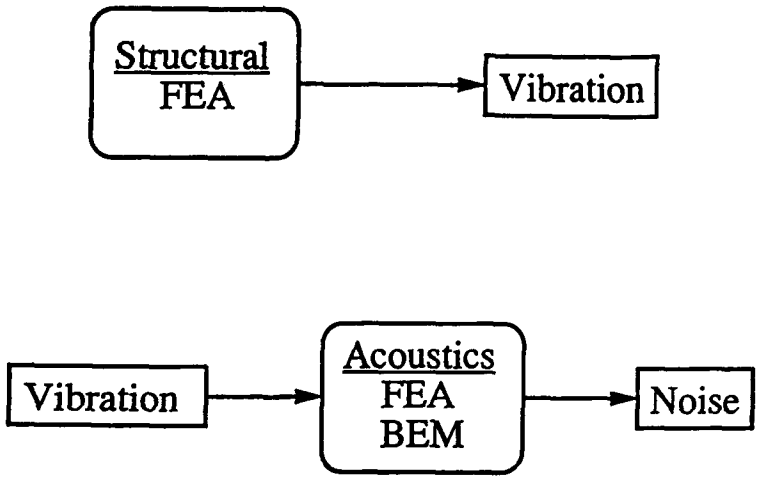

Figure 1. Analyses associated with noise prediction

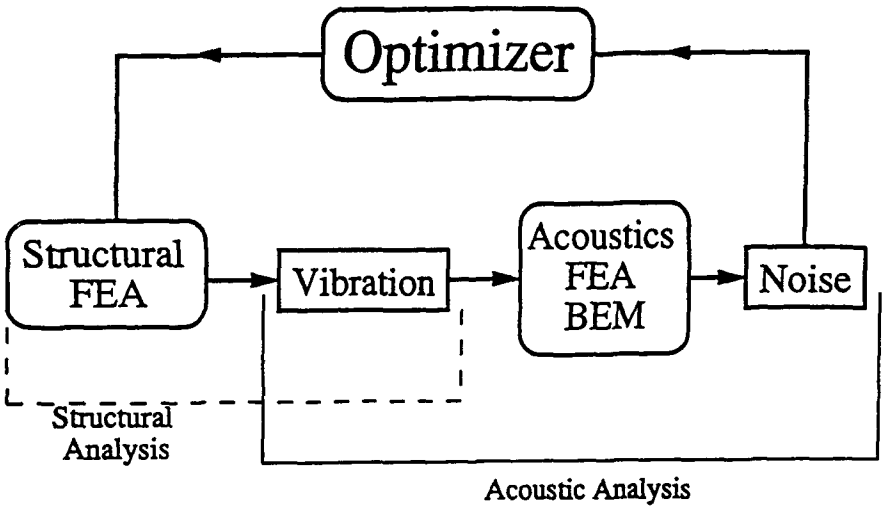

Figure 2. Flowchart of an acoustic optimization process

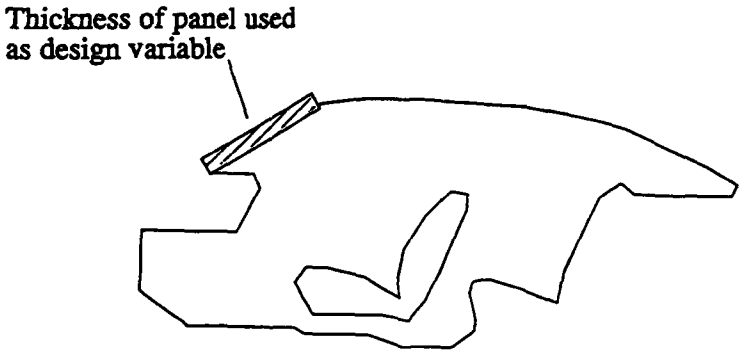

Figure 3. Example of a sizing design variable for an automobile compartment

SECOND INTERNATIONAL CONGRESS ON
RECENT DEVELOPMENTS IN AIR- AND
STRUCTURE-BORNE SOUND AND VIBRATION
MARCH 4-6, 1992 AUBURN UNIVERSITY, USA

MODELLING RADIATION FROM SUBMERGED STRUCTURES A COMPARISON OF BOUNDARY ELEMENT AND FINITE ELEMENT TECHNIQUES

Jean-Pierre G. Coyette
Numerical Integration Technologies N.V.
Ambachtenlaan, 29
B3001 Heverlee
(Belgium)

ABSTRACT

Various computational strategies are available for modelling radiation from submerged structures. The most usual way consists to use a coupled procedure where the unbounded acoustic medium is modelled using boundary elements while finite elements are selected for the structure.

An alternative is offered by selecting both acoustic and structural finite elements. In this case, the near field is modelled using conventional acoustic finite elements while the far field is dicretized into infinite elements. These infinite elements contain appropriate interpolation functions in order to describe the far field behaviour. The so-called 'wave envelope' approach can be selected in order to speed up the generation of element matrices.

These two approaches are reviewed and compared in this paper. Both formal aspects are described but also specific application to radiation from submerged structures.

INTRODUCTION

Modelling of radiation from submerged structure usually involve coupled models where reciprocical fluid-structure interaction effects are taken into account : structural displacements act as boundary conditions for the fluid while fluid pressures generate additional loads on the structure.

The effective consideration of these effects require selection of appropriate models. The unbounded character of the fluid domain is a difficulty which can be overcome using a boundary integral formulation. The dimensionality of the problem is reduced so that only a boundary discretization is required. The direct boundary integral representation usually selected involves surface pressures and normal velocities.

Reciprocical effects can easily be handled using a coupling procedure converting, on one hand, structural displacements into boundary normal velocities and, on the other hand, fluid pressures into mechanical loads. This approach has been described by WILTON [8] and will be summarized below.

An alternative procedure consists to use both acoustic and structural finite elements. The unbounded character of the fluid domain is not well suited for a finite element approach. The problem can however be handled by defining some radiation impedance boundary condition on a fictive surface located at a finite distance from the structure. Difficulties of locating this fictive boundary and assigning suitable boundary condition can be overcome by using acoustic infinite elements for the far field. These elements allow to map a region of infinite extension and use appropriate interpolation functions in order to reproduce the expected far field behaviour.

These elements have been introduced by BETTESS [1] some years ago and have been successfully refined recently by ASTLEY and COYETTE [4,5] through application of a 'wave envelope' process allowing to simplify generation of related element matrices.

These two concurrent approaches are presented below. Application to a submerged structure is then described.

MIXED FINITE ELEMENT/BOUNDARY ELEMENT APPROACH

As stated before, this approach relies on the use of a conventional finite element model for the structure while a direct boundary integral representation sustains the development of the acoustic boundary element model.

Acoustic boundary element representation. In the frequency domain (assuming a time dependence like $\exp(+i\omega t)$), the basis for such an approach is the Helmholtz surface integral equation linking surface pressure p and normal velocity v_n :

$$c(x)p(x) = p_i(x) + \int_S \left(p(y)\frac{\partial G(x,y)}{\partial n_y} + i\rho\omega v_n(y)G(x,y) \right) dS(y) \quad (1)$$

where x and y are points located on boundary surface S, n_y is the local normal to S at boundary point y (assumed to be directed into the fluid medium) and p_i is the incident field pressure.

In the above expression, G(x,y) is the usual Green function (fundamental solution of 3-D Helmholtz equation for a point source located at y point) given by

$$G(x,y) = \frac{\exp(-ikR(x,y))}{4\Pi R(x,y)} \quad (2)$$

where R is the distance between x and y points while k is the wavenumber.

The numerical procedure relies on discretization of boundary surface S and selection of interpolation functions for both surface pressure and normal velocity.

Collocation of the discrete form of Eq. (1) at each boundary node in turn allows to set up a relation between nodal pressure vector P and nodal normal velocity vector V :

$$[A](P) = (P_i) + [B](V) \qquad (3)$$

where A and B are frequency dependent matrices while P_i is the vector of nodal incident pressures.

In a coupled model, the normal velocity vector V is related to the structural displacement vector U through :

$$(V) = i\omega[T](U) \qquad (4)$$

where the matrix T contains normal components at boundary nodes.

Structural finite element model. The structural model is based on a displacement finite element model and is characterized, in the frequency domain, by :

$$[Z_s](U) = (F_s) - [C^T](P) \qquad (5)$$

where C is the geometrical coupling matrix allowing to convert fluid pressures into mechanical loads while Z_S is the structural impedance matrix given by :

$$[Z_s] = [K_s] + i\omega[D_s] - \omega^2[M_s] \qquad (6)$$

where K_S, M_S and D_S are the usual stiffness, mass and damping matrices.

Coupled model and solution strategy. The coupled model results from merging Eq. (5) and (3) using the kinematical continuity requirement expressed by Eq. (4). The resulting coupled system appears as

$$\begin{bmatrix} Z_s & C^T \\ -i\omega BT & A \end{bmatrix} \begin{pmatrix} U \\ P \end{pmatrix} = \begin{pmatrix} F_s \\ P_i \end{pmatrix} \qquad (7)$$

Alternatively this system can be written using a modal description for the structure. In this case, the structural displacement vector U is expressed as a combination of structural modes through

$$(U) = [\Phi](X) \qquad (8)$$

where Φ is the modal matrix while X is the vector of modal participation factors.

System (7) can be rewritten as

$$\begin{bmatrix} \hat{Z}_s & \hat{C}^T \\ -i\omega\hat{BT} & A \end{bmatrix} \begin{pmatrix} X \\ P \end{pmatrix} = \begin{pmatrix} \hat{F}_s \\ P_i \end{pmatrix} \qquad (9)$$

where

$$\left[\hat{Z}_s\right] = [\Phi^T][Z_s][\Phi]$$

$$\left(\hat{F}_s\right) = \left[\Phi^T\right](F_s)$$

$$\left[\hat{C}\right] = [C][\Phi]$$

$$\left[\hat{T}\right] = [T][\Phi] \qquad (10)$$

are the so-called modal impedance matrix, modal load vector, modal coupling matrix and modal normal matrix, respectively.

Solution of either system (7) or (9) is performed using an efficient fluid methodology where structural unknowns are first eliminated (taking into account sparseness and symmetry of structural matrices and specific properties of C and T matrices). The resulting updated fluid set of equations is then solved for nodal pressures. Recovery of structural displacements results from solution of system (5).

It must be stressed that the direct boundary integral formulation suffers from non-uniqueness of the solution at critical frequencies (eigenfrequencies of related Dirichlet interior problem). The so-called 'CHIEF' procedure [10] has been selected to remove this problem.

The above procedure has been implemented in *SYSNOISE* 4.4 [6] which allows to import either structural matrices or a modal basis from structural packages in order to set up the structural model and to solve the coupled problem.

FINITE ELEMENT/INFINITE 'WAVE ENVELOPE' ELEMENT APPROACH

This alternative procedure makes use of structural finite elements comobined with (volumic) acoustic finite elements for the near field while infinite 'wave envelope' acoustic elements are selected for the far field.

Acoustic finite elements are iso-parametric elements with unknown nodal pressures. Infinite 'wave envelope' elements are based on mapped infinite elements (as described in [2]) and make use of special interpolation functions combining polynomial and harmonic expansions.

Weighted residual statement. Solution of Helmholtz equation in an infinite domain V is based on application of a weighted residual statement incorporating field and boundary residuals.

Considering only velocity boundary conditions on surface S :

$$\partial p/\partial n = -i\rho\omega v_n \text{ on } S \qquad (11)$$

and the equivalent finite approximation for the radiation condition on a far field boundary S_∞ :

$$\partial p/\partial n = -ikp \text{ on } S_\infty \qquad (12)$$

the weighted residual statement is formulated as

$$\int_V \left(\nabla W_i \cdot \nabla p + k^2 W_i p\right) dV + \int_S i\rho\omega\, W_i\, v_n\, dS - \int_{S_\infty} ik\, W_i\, p\, dS = 0 \qquad (13)$$

where W_i are weighting functions.

If acoustic pressure p(x) is written as a trial expansion of known basis functions $N_i(x)$ and unknown coefficients q_i, corresponding stiffness, mass and damping matrices are

$$K_{a,ij} = \int_v \left(\nabla W_i \cdot \nabla N_j\right) dV$$

$$M_{a,ij} = \int_v \left(W_i N_j\right) dV \qquad (14)$$

$$D_{a,ij} = \int_{S_\infty} \left(W_i N_j\right) dS$$

and the acoustical loading vector is

$$F_{a,i} = i\rho\omega \int_S \left(W_i v_n\right) dS \qquad (15)$$

The unknown coefficient vector Q (containing nodal pressures q_i) is given by solution of equations

$$\left[K_a + ikD_a - k^2 M_a\right](Q) = \left(F_a\right) \qquad (16)$$

Infinite element mapping. The existence of the infinite domain requires to subdivide exterior region into inner and outer subregions. The inner region lies close to the radiating surface while the outer region extends to S_∞ .

A conventional finite element mesh is constructed within the inner region and usual shape functions are selected for both N_i and W_i functions.

The outer region is subdivided into a single layer of infinite wave envelope elements matched to the conventional mesh at an arbitrary interface.

The mapping and interpolation functions related to these three-dimensional elements are based on reference [2] :

$$N_i(\zeta, \eta, \xi) = F_i(\zeta, \eta, \xi)\, e^{-ik(r(\xi) - a(\xi))} \qquad (17)$$

Polynomial expansions F_i in local coordinates (ζ,η,ξ) are selected such that the expected far field behaviour (1/r for 3-D problems) is well reproduced along local infinite direction ξ

The wavelike behaviour of the solution is also approximated by the exponential factor. Moreever since the near field/far field interface is located at r=a, compatibility with conventional acoustic finite elements is ensured.

Wave envelope weighting scheme. The wave envelope approach introduced by ASTLEY [3] for large but finite elements has been extended to infinite elments by ASTLEY and COYETTE [4,5] and involves weighting functions defined as the complex conjugates of the basis functions N_i multiplied by a factor $(a/r)^2$ ensuring that mass and stiffness integrals are finite and that radiation integral vanishes as the outer boundary approaches infinity

$$W_i = (a/r)^2 N_i^* \qquad (18)$$

The use of above interpolation and weighting functions allows to set up element mass and stiffness matrices which can be assembled in the usual way to form global mass and stiffness matrices.

A key feature of these element matrices is the cancellation of the exponential factors within each integrand and the boundedness of all resulting integrals as the element volume becomes infinite. All integrands can therefore be transformed to a finite region of the parent space and integrated numerically using standard Gauss-Legendre quadratures.

This is a major advantage over conventional infinite elements which require the more complex Gauss-Laguerre quadrature scheme. An additional interest results from the fact that related element matrices are frequency independent so that far field mesh usually doesn't need to be refined as frequency increases.

Extension to coupled problem. Extension of above approach to coupled problems is straightforward. The discrete structural model based on finite elements can easily be coupled to the above acoustic finite element/infinite 'wave envelope' element model following the procedure described for coupling structural finite elements and acoustic boundary elements. This operation leads to the system :

$$\begin{bmatrix} K_s - \omega^2 M_s & C^T \\ C & \dfrac{K_a - K^2 M_a}{\rho\omega^2} \end{bmatrix} \begin{pmatrix} U \\ Q \end{pmatrix} = \begin{pmatrix} F_s \\ \dfrac{F_a}{\rho\omega^2} \end{pmatrix} \qquad (19)$$

Various solution strategies can be selected for solving Eq. (19). The fluid methodology is based on elimination of structural degrees of freedom and solution of related (updated) fluid problem. Conventional modal approach can also be used for the structural model while Ritz vector approach [7] appears as a promising tool for this kind of problem.

APPLICATION

The problem of a submerged spherical shell is considered [9]. In this problem, a thin-walled spherical shell is submerged in a liquid and driven internally with a point load. The shell has a radius a = 5m, a uniform thickness h = 0.15m while the constitutive material has a Young's modulus of 2.07×10^{11} Pa, a Poisson's ratio of 0.3 and a density of 7669 kg/m^3. The fluid is water with a density of 1000 kg/m^3 and a sound speed of 1524 m/sec. A load of 1 N is applied at one pole and solution is computed at ka=1 and 1.5 .

Due to symmetry, only one fourth of the actual structure has been modelled. The structural finite element mesh is shown at Figure 1 (241 nodes, 216 elements). This mesh is also the boundary element mesh used for coupled FEM/BEM computations. The acoustic finite element mesh used for the near field is represented at Figure 2 (864 brick elements). Far field is modelled using 241 infinite wave envelope elements with linear interpolation functions F_i along infinite direction.

Surface pressures along a meridian line are represented at Figures 3 and 4 for ka=1 and 1.5, respectively.

From these surface results, far field pressures can be computed using the discrete form of Eq. (1). Directivity diagram in symmetry plane x = 0, at a distance d=20a from shell's center has been computed using surface pressures and normal velocities obtained from the two models. Magnitude of far field pressures is represented at Figures 5 and 6 for ka=1 and 1.5, respectively.

As it can be seen from these figures, the two models give similar results.

CONCLUSIONS

Two alternative procedures for handling acousto-structural problems have been presented.

The mixed boundary element/finite element technique allows to reduce the dimensionality of the problem. Acoustic matrices A and B are however full, complex, unsymmetric matrices.

The number of degrees of freedom involved in the wave envelope solution is generally much large than an equivalent boundary element solution and mesh generation is more time consuming but the resulting equations are more sparse so that the solution time is not necessarly much greater than for the boundary element solution. Additionally the non-uniqueness problems which cause difficulty with some boundary element formulations are entirely absent.

REFERENCES

[1] P. BETTESS and O.C. ZIENKIEWICZ, 'Diffraction and refraction of surface waves using finite and infinite elements', Int. J. Num. Meth. Eng., 11, 1271-1290, 1977.

[2] O.C. ZIENKIEWICZ, K. BANDO, P. BETTESS and T.C. CHIAM, 'Mapped infinite elements for exterior wave problems', Int. J. Num. Meth. Eng., 21, 1229-1251, 1985.

[3] R.J. ASTLEY and W. EVERSMAN, 'A note on the utility of a wave envelope approach in finite element duct transmission studies', Journal of Sound and Vibration, 76, 595-601, 1981.

[4] R.J. ASTLEY and J.P. COYETTE, 'Mapped wave envelope elements of infinite extent : applications to acousto-structural scattering', International Conference on Recent Advances in Structural Dynamics, Southampton, July 15-18, 1991 (Additional Papers Volume, 1-10).

[5] R.J. ASTLEY, J.P. COYETTE and G.J. MACAULAY, 'Mapped wave envelope elements for acoustical radiation and scattering', submitted to Journal of Sound and Vibration, 1991.

[6] SYSNOISE User's Manual Version 4.4, Numerical Integration Technologies, 1991.

[7] J.P. COYETTE, 'Ritz vectors synthesis versus modal synthesis for fluid-structure interaction modeling', Proceedings Int. Conference on Recent Developments in Air- and Structure-Borne Sound and Vibration, Auburn, Eds. M.J. CROCKER, Vol. 1, 115-126, 1990.

[8] D.T. WILTON, 'Acoustic radiation and scattering from elastic structures', Int. J. Num. Meth. Eng., 13, 123-138, 1978.

[9] G.C. EVERSTINE and F.M. HENDERSON, 'Coupled finite element/boundary element approach for fluid-structure interaction', J. Acoust. Soc. Am., 87, 1938-1947, 1990.

[10] H.A. SCHENCK, 'Improved integral formulation for acoustic radiation problems', J. Acoust. Soc. Am., 44, 41-58, 1968.

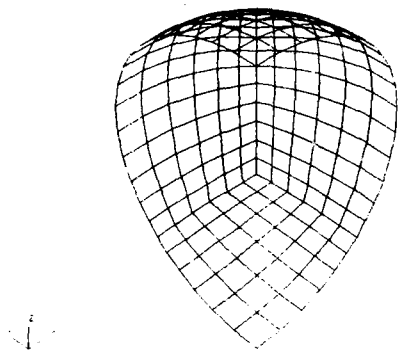

Figure 1 Structural FE Mesh.

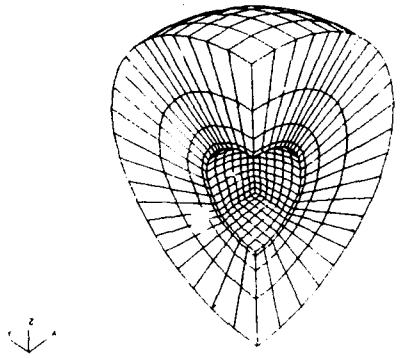

Figure 2 Acoustic FE Mesh for the Near Field.

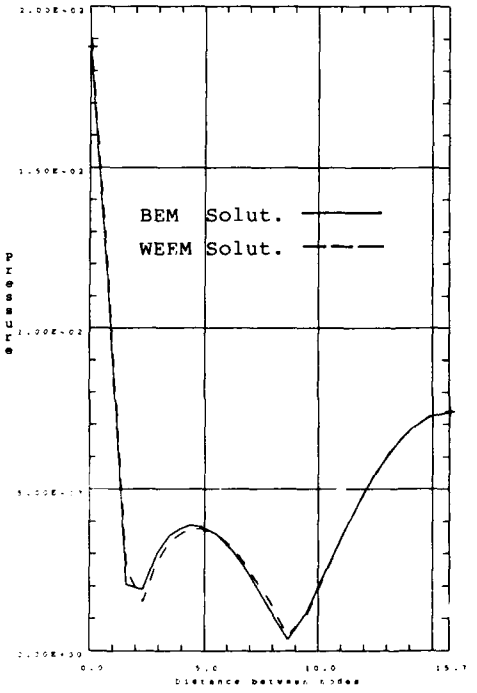

Figure 3 Surface Pressure along a meridian line at ka=1.

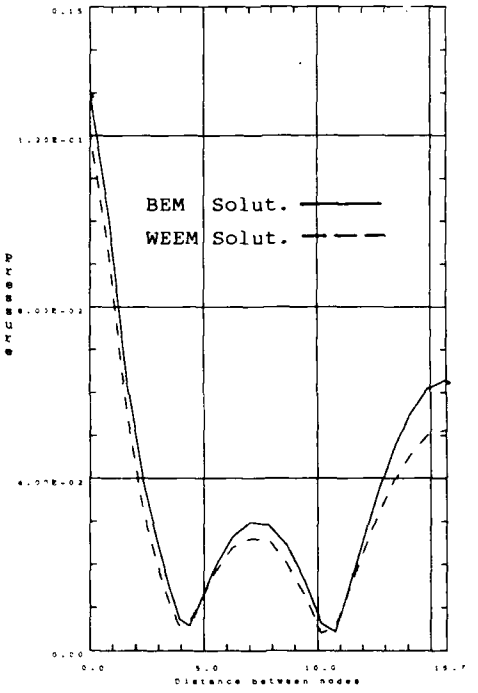

Figure 4 Surface Pressure along a meridian line at ka=1.5.

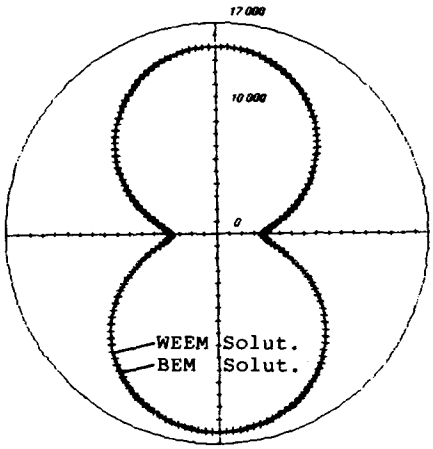

Figure 5 Directivity Diagrams for Pressure at d=20a for ka=1 (dB value, reference 2.10-5 Pa).

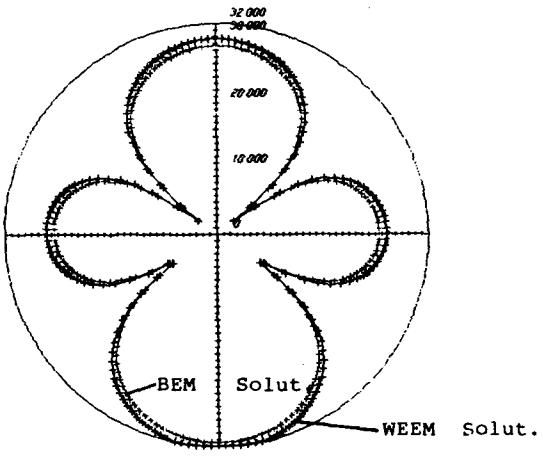

Figure 6 Directivity Diagrams for Pressure at d=20a for ka=1.5 (dB value, reference 2.10-5 Pa).

SECOND INTERNATIONAL CONGRESS ON
RECENT DEVELOPMENTS IN AIR- AND
STRUCTURE-BORNE SOUND AND VIBRATION
MARCH 4-6, 1992 AUBURN UNIVERSITY USA

FINITE ELEMENT MODELING OF VISCOELASTIC DAMPERS

A. Gupta, M.J. Kim, and A.H. Marchertas
Department of Mechanical Engineering
Northern Illinois University
DeKalb, Illinois 60115

ABSTRACT

Behavior of isolation bearings used for supports of nuclear reactors is studied in this paper. These seismic isolation bearings have very high vertical stiffness to support the weight of the structure while having very low horizontal stiffness for isolation purpose. The passive damping provided by these bearings is of interest. A finite element model of 3-D constitutive relation of these viscoelastic materials is developed. Hysteresis loops are drawn for different maximum strains at a particular frequency, and the process is repeated for various frequencies. The area under the hysteresis loop is computed in order to obtain damping properties.

INTRODUCTION

Environmental safety of nuclear reactors is always of concern and present global environmental consciousness makes it even more important. Isolation bearings placed between the structure and the ground would greatly enhance the safety of the reactors from seismic effects. These bearings have many desirable properties such as a very high vertical stiffness and very low horizontal stiffness, durability, corrosion resistance, and relatively high damping capacity.

A 3-D constitutive model predicting the behavior of such material is essential for reliable design. Sufficient internal damping of these bearings would eliminate the need for an active vibration control system. In this paper damping properties of materials used for such bearings are studied.

THEORY FORMULATION

The following outline describes the computational steps performed in order to evaluate stresses from given nodal displacements. The constitutive relations are based on work by Simo and Taylor [1-3]. For given nodal displacements at time s, the deformation gradient $\underline{F}$ is first computed, then the right Cauchy Green tensor is evaluated as

$$\underline{C} = \underline{F}^T \underline{F}$$

Next,

$$\overline{\underline{C}} = J^{-2/3}\, \underline{C} \qquad \text{where } J = \det \underline{F}$$

making $\det \overline{\underline{C}} = 1$. The deviatoric stress becomes

$$dev\ \overline{\underline{C}}\ (s) = \overline{\underline{C}}\ (s) - \frac{1}{3}\ [tr\ \underline{C}\ (s)]\ \underline{G}$$

where $\underline{G}$ is metric tensor in the reference configuration. If rectangular Cartesian coordinates are used, $\underline{G} = \underline{I}$ (second order unit tensor). The Euclidian norm

$$\| \, dev \, \underline{C} \, (s) \, \| = [\underline{C} \, (s) : \underline{C} \, (s)]^{\frac{1}{2}}$$

is used to evaluate the damage function which is assumed [2]

$$\Psi_t = \max \| \, dev \, \underline{C} \, (s) \, \| \, , \quad s \in (- \infty , t)$$

The effective deviatoric Lagrangian strain is

$$\underline{\pi} \, (s) = \bar{I} \, (\Psi_t) \, dev \, \underline{C} \, (s) \, ,$$

where $\bar{I} \, (\Psi_t)$ *is a function of damage variable* Ψ_t *, defined as*

$$\bar{I} \, (\chi) = \beta + (1 - \beta) \frac{1 - e^{-\chi/\alpha}}{\chi/\alpha}, \; \alpha \in [0 , \infty] \; and \; \beta \in [0 , 1]$$

Here α and β are input parameters, α being the damage exponent and β being the damage limit.

The stress tensor is taken as:

$$\underline{\sigma} = K \ln J \, \underline{I} + \int_{-\infty}^{t_n} [G_\infty + (G_0 - G_\infty) \, e^{-(t-s)/\upsilon}] \, \dot{\underline{\pi}} \, (s) ds$$

where K is the bulk modulus, υ is the relaxation time constant, G_0 corresponds to the short term shear modulus, and G_∞ to the long germ shear modulus. The dot denotes the derivative with respect to time.

The stress tensor is updated through incremental steps based on the following derivation:

$$\underline{\sigma}_{n+1} = \underline{\sigma}_{n+1} + \int_{-\infty}^{t_n} [G_\infty + (G_0 - G_\infty) e^{-(t_n - s)/\upsilon}] \dot{\underline{\pi}} \, (s) \, ds - \int_{-\infty}^{t_n} [G_\infty + (G_0 \, G_\infty) e^{-(t_n - s) \, /\upsilon}] \dot{\underline{\pi}}(s) \, ds$$

$$= K \ln J_{n+1} \underline{I} + \int_{-\infty}^{t_{n+1}} [G_\infty + (G_0 - G_\infty) e^{-(t_{n+1} - s)/\upsilon}] \dot{\underline{\pi}}(s) \, ds$$

$$+ \int_{-\infty}^{t_n} [G_\infty + (G_0 - G_\infty) e^{-(t_n - s)/\upsilon}] \dot{\underline{\pi}}(s) ds - \int_{-\infty}^{t_n} [G_\infty + (G_0 - G_\infty) e^{-(t_n - s)/\upsilon}] \dot{\underline{\pi}}(s) ds$$

$$= K \ln J_n \, \underline{I} + K \frac{\Delta J_{n+1}}{J_n} \underline{I} + \int_{-\infty}^{t_{n+1}} [G_\infty + (G_0 - G_\infty) e^{-(t_{n+1} - s)/\upsilon} \,] \dot{\underline{\pi}}(s) ds$$

$$+ \int_{-\infty}^{t_n} [G_\infty + (G_0 - G_\infty) e^{-(t_n - s)/\upsilon}] \dot{\underline{\pi}}(s) ds - \int_{-\infty}^{t_n} [G_\infty + (G_0 - G_\infty) e^{-(t_n - s)/\upsilon} \dot{\underline{\pi}}(s) \, ds]$$

$$= K \ln J_n \, \underline{I} + \int_{-\infty}^{t_n} [G_\infty + (G_c - G_\infty) e^{-(t_n - s) \, /\upsilon}] \dot{\underline{\pi}}(s) ds + K \frac{\Delta J_n + 1}{J_n} \underline{I}$$

$$+\int_{-\infty}^{t_n}[G_\infty+(G_0-G_\infty)e^{-(t_n-\Delta t-s)/\theta}]\dot{\varepsilon}(s)ds+\int_{t_n}^{t_{n+1}}[G_\infty+(G_0-G_\infty)e^{-(t_{n+1}-s)/\theta}]\dot{\varepsilon}(s)ds$$

$$-\int_{-\infty}^{t_n}[G_\infty+(G_0-G_\infty)e^{-(t_n-s)/\theta}]\dot{\varepsilon}(s)ds$$

$$=\underline{\sigma}_n+K\frac{\Delta J_{n+1}}{J_n}\underline{I}+\int_{t_n}^{t_{n+1}}G_\infty\dot{\varepsilon}(s)ds+\int_{t_n}^{t_{n+1}}[G_0-G_\infty)e^{-(t_{n+1}-s)/\theta}]\dot{\varepsilon}(s)ds$$

$$+(e^{-\Delta t/\theta}-1)\int_{-\infty}^{t_n}(G_0-G_\infty)e^{-(t_n-s)/\theta}\dot{\varepsilon}(s)ds$$

$$=\underline{\sigma}_n+K\frac{\Delta J_{n+1}}{J_n}\underline{I}+G_\infty\Delta\varepsilon(\hat{t})+(G_0-G_\infty)\frac{(1-e^{-\Delta t/\theta})}{\Delta t/v}\Delta\varepsilon(\hat{t})$$

$$+(e^{-\Delta t/\theta}-1)\int_{-\infty}^{t_n}(G_0-G_\infty)e^{-(t_n-s)/\theta}\dot{\varepsilon}(s)ds \text{ for } t_n\le\hat{t}\le t_{n+1}$$

The fourth term in the above equation was evaluated by using the mid-point rule and the mean value theorem as follows:

$$\int_{-\infty}^{t_{n+1}}(G_0-G_\infty)e^{-(t_{n+1}-s)/\theta}\dot{\varepsilon}(s)ds$$

$$=[\int_{t_n}^{t_{n+1}}(G_0-G_\infty)e^{-(t_{n+1}-s)/\theta}ds]\dot{\varepsilon}(\hat{t}),t_n\le\hat{t}\le t_{n+1}$$

$$=(G_0-G_\infty)v(1-e^{-\Delta t/v})\dot{\varepsilon}(\hat{t})$$

$$=(G_0-G_\infty)\frac{(1-e^{-\Delta t/v})}{\Delta t/v}\Delta t\,\dot{\varepsilon}(\hat{t})$$

$$=(G_0-G_\infty)\frac{(1-e^{-\Delta t/\theta})}{\Delta t/v}\Delta\varepsilon(\hat{t})$$

$$=(G_0-G_\infty)\frac{(1-e^{\Delta t/\theta})}{\Delta t/v}\Delta\varepsilon_{n+1}$$

$$\text{Thus } \underline{\sigma}_{n+1}=\underline{\sigma}_n+K\frac{\Delta J}{J_{n+1}}\underline{I}+G_\infty\Delta\varepsilon_{n+1}+(G_0-G_\infty)\frac{1-e^{-\Delta t/\theta}}{\Delta t/v}\Delta\varepsilon_{n+1}+(e^{-\Delta t/\theta}-1)H_n$$

where the history variable H_n and $\Delta\varepsilon_{n+1}$ are defined as

$$H_n=\int_{-\infty}^{t_n}(G_0-G_\infty)e^{-(t_n-s)/\theta}\dot{\varepsilon}(s)ds$$

$$\Delta\varepsilon_{n+1}=\varepsilon(t_{n+1})-\varepsilon(t_n)$$

Finally the stress can be expressed in incremental form as

$$\underline{\sigma}_{n+1} = \underline{\sigma}_n + K\frac{\Delta J}{J_{n+1}}\underline{I} + G_\infty \Delta \underline{\varepsilon}_{n+1} + \Delta \underline{H}_{n+1}$$

where

$$\Delta \underline{H}_{n+1} = (e^{-\Delta t/\upsilon} - 1)\underline{H}_n + (G_0 - G_\infty)\frac{1 - e^{-\Delta t/\upsilon}}{\Delta t/\upsilon}\Delta \underline{\varepsilon}_{n+1}$$

RESULTS

Since these isolation bearings are used to protect the reactors from earthquakes, the frequency range that is of interest is usually very low. First the bearing is subjected to a loading frequency of 0.05 Hz. Maximum strains of 30, 60, 90, 120, 150, 120, 90, 60, and 30%, three cycles each, are specified for the input. The loading history is shown in Figure 1. The corresponding stress-strain plots are plotted in Figure 2, the traces of decreasing amplitude being indicated in dotted lines. The next loading input is similar to the previous one except that the new frequency is 0.5 Hz.

The damping ratio ξ is measured from the definition $\xi = A_h/2\pi A_e$ where A_h is the area of the hysteresis loop and A_e is the elastic strain energy or the hysteresis loop. The numerical values of damping ratios for the two loading histories are presented in Table 1.

Next the speciman is subjected to an offset cyclic loading as shown in Figure 3. The shear speciman was loaded to 100% straining (3 1/2 cycles) followed by two full cycles from 50% to 100% strain and then back to the previous loading of 100% strain. The response of the speciman is shown in Figure 4. Dotted lines indicate the receding amplitude loading.

The speciman is subjected to some more loading histories with maximum strain ranging from 25% to 150%. The variation of damping ratio on frequency is plotted in Figure 5. Similarly Figure 6 displays variation of damping ratio with maximum strains for frequencies ranging from 0.05 Hz to 1 Hz.

CONCLUDING REMARKS

The results show that damping decreases with increasing frequency. This is in agreement with Steidel [4] but not with Tarjlan [5]. Damping decreases slightly with increasing strain if only 1st cycle is considered but 2nd cycle onwards damping is independent of maximum strain. Further investigation is needed to correlate the analytical and experimental results.

REFERENCES

1. Simo, J.C., and Taylor, R.L., "A Simple Three-Dimensional Viscoelastic Model Accounting for Damage Effects".

2. Simo, J.C., and Taylor, R.L., "A Three-Dimensional Finite Deformation Viscoelastic Model Accounting for Damage Effects," UCB/SESM/85-02. SESM, V.C. Berkeley, 1985.

3. Simo, J.C., "On a Fully Three-Dimensional Finite-Strain Viscoelastic Damage Model: Formulation and Computational Aspects". Comp. Meths. Appl. Mech. Engr., 60. 1987, Pp. 153-173.

4. Steidel, R.E., An Introduction to Mechanical Vibrations, 3rd Edition, John Wiley & Sons, 1989.

5. Tajirian, F.F., and Kelly, T.M., "Testing of Seismic Isolation Bearings for Advanced Liquid Metal Reactor Prism," Seismic. Shock and Vibration Isolation, ASME PVP - Vol. 147, 1988.

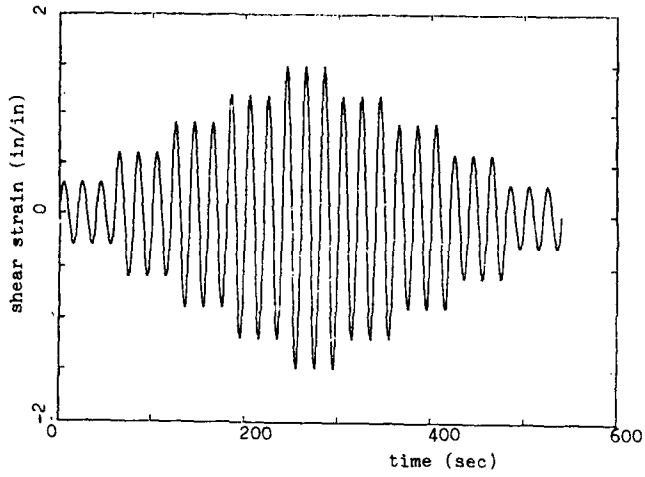

Figure 1. Time History of 0.05 Hz Loading

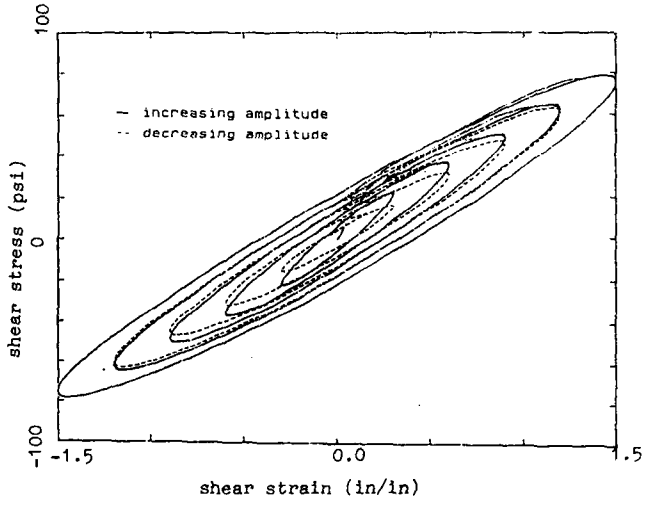

Figure 2. Sequence of Hysteresis Plots due to Loading in Figure 1

Table 1. Damping in Hysteresis Loops with Increasing & Decreasing Strain

Cycles	Maximum Strain in/in	Damping at Loading Frequencies	
		0.05 Hz	0.5 Hz
1st	0.3	0.1517	0.1198
2nd		0.1429	0.1068
3rd		0.1429	0.1074
1st	0.6	0.1500	0.1155
2nd		0.1429	0.1072
3rd		0.1429	0.1074
1st	0.9	0.1460	0.1111
2nd		0.1429	0.1073
3rd		0.1429	0.1074
1st	1.2	0.1444	0.1093
2nd		0.1429	0.1073
3rd		0.1429	0.1074
1st	1.5	0.1436	0.1086
2nd		0.1429	0.1073
3rd		0.1429	0.1074
1st	1.2	0.1456	0.1091
2nd		0.1429	0.1076
3rd		0.1429	0.1074
1st	0.9	0.1465	0.1096
2nd		0.1429	0.1076
3rd		0.1429	0.1074
1st	0.6	0.1483	0.1106
2nd		0.1429	0.1077
3rd		0.1429	0.1074
1st	0.3	0.1538	0.1137
2nd		0.1429	0.1079
3rd		0.1429	0.1075

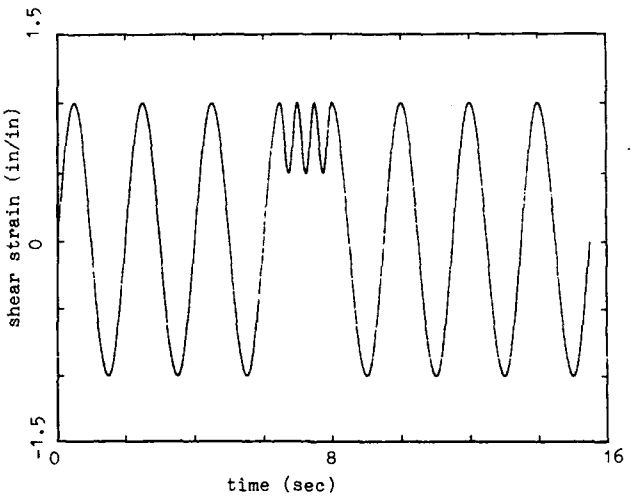

Figure 3. Time History of Offset Loading

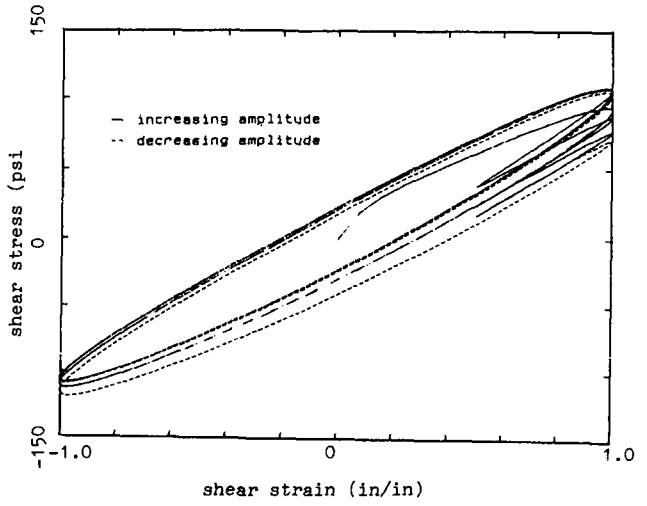

Figure 4. Sequence of Hysteresis Plots due to Loading in Figure 3

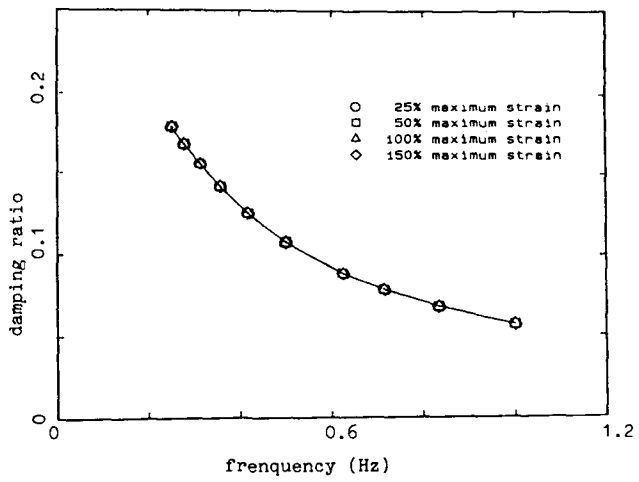

Figure 5. Variation of Damping with Frequency for Different Values of Strain

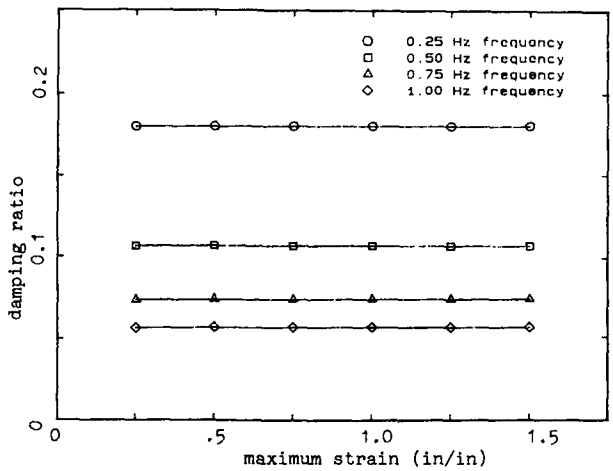

Figure 6. Variation of Damping with Maximum Strain for Different Values of Frequency

SECOND INTERNATIONAL CONGRESS ON
RECENT DEVELOPMENTS IN AIR- AND
STRUCTURE-BORNE SOUND AND VIBRATION
MARCH 4-6, 1992 AUBURN UNIVERSITY, USA

THE METHOD OF MODAL PARAMETERS TO DETERMINE THE BOUNDARY CONDITION OF FINITE ELEMENT MODEL

Wang Fengquan, Chen Shiyu, Professor
Department of Mathematics Mechanics
Southeast University, Nanjing, P.R.China

ABSTRACT

In this paper, a method used to determine the boundary condition of Finite Element Model with structure modal parameters is presented. On deriving the method, the theory of Finite Element Model for dynamic calculating is used. Combined with the modal parameters got from experiment, a FEM–Modal Parameter equation to determine the boundary condition is put forward. For solving the equation, three methods are given. The first is the accurate method. The second is the full mode computation method by means of generlized inverse matrix. The third is the interpolation method of frequency. An applied example is given and the results of calculation fully verify the effectiveness of the method offered.

NOMENCLATURE

$[K_A]$ = Stiffness matrix of the FEM
$[K^*]$ = Unknown bound stiffness matrix
L = The mumber of unknown bound
$[M_A]$ = Mass matrix of the FEM
$\{x\}$ = Displacement vector
$\{\ddot{x}^*\}$ = Acceleration vector
$\{\Phi_A\}$ = The i–th eigenvector
$\{\Phi_e\}_i$ = The i–th tested modal vector
ω_{Ai} = The i–th eigenfrequency
ω_i = The i–th tested natural frequency

INTRODUCTION

Before the structure dynamic calculation of Finite Element Model, it is very important to determine the boundary condition accurately. In fact, the boundary condition of a large number of structures cann't be simplified as ideal boundary condition. For example, the bearing supporter of rotor machine, the joint of machine element, and the installing and fixing point of a structure, cann't be described as a ideal boundary condition. Because of this, it is very significant to determine the boundary condition of a structure before the structure dynamic computation.

Based on the Finite Element Model and structure modal parameters got from experiment, a method

used to determine the boundary condition of Finite Element Model is presented.

FEM–MODAL PATAMETER EQUATION

For a undamped structure, the equation of motion for the structure Finite Element Model is

$$[M_A]\{\ddot{x}\} + [K_A]\{x\} = 0 \tag{1}$$

Where: $[M_A]$is the mass matrix of the FEM of order N by N, $[K_A]$ is the stiffness matrix of the FEM of order N by N, and $\{x\}$ and $\{\ddot{x}\}$ are the displacement (including the translational displacement and the rotational displacement) and acceleration vectors of order N.

The eigenfrequency and eigenvector of equation (1) are obtained from the solution of

$$([K_A] - \omega_A^2[M_A])\{\Phi_A\} = 0 \tag{2}$$

For each i, we have a vector $(\omega_{Ai},\{\Phi_A\}_i, i = 1,2,\cdots,n)$, and these vectors constitute a full mode group.

In fact, the boundary condition of a large number of structures cann't be simplified as ideal boundary condition and it is called unideal boundary condition. Suppose there are some unknown elastic bounds in some given FEM nodes in some given direction. Then, all of the bound stiffness of the unknown elastic bound constitute a bound stiffness matrix $[K^*]$, and the matrix $[K^*]$ is a diagonal matrix. Therefore, the unknown elastic bounds supply a bound force $-[K^*]\{x\}$, which is opposite to the displacement.

In that case, equation (1) changes into

$$[M_A]\{\ddot{x}\} + [K_A]\{x\} = -[K^*]\{x\} \tag{3}$$

Equation (3) is called the dynamic equation of the Finite Element Model with unideal boundary bound.

If the accurate modal parameters ω_i and $\{\Phi_e\}_i$ $(i = 1,2,\cdots,m)$ are got from modal testing, for the r–th eigenfrequency,we have

$$-\omega_i^2[M_A]\{\Phi\}_i + [K_A]\{\Phi\}_i = -[K^*]\{\Phi\}_i \qquad i = 1,2,\cdots,m \tag{4}$$

where $\{\Phi\}_i = \begin{Bmatrix}\Phi_e\\ \Phi_f\end{Bmatrix}_i (i = 1,2,\cdots,m)$, containing the tested modal vector and the untested modal vector.

Equation (4) is called the FEM–Modal Parameter equation used to determine the boundary condition of structure Finite Element Model.

By solving equation (4), we can get the unknown boundary bound stiffness $K_1, K_2,\cdots, K_L$(L is defined as the numder of unknown bound).

THE ACCURATE METHOD

If all the tested mode on the node of the FEM of a structure are full mode (containing the mode branch of rotational direction of order N, and $\{\Phi_e\}_i$ is the i–th column of the tested modal matrix. Substitute $\{\Phi_e\}_i$into equation (4). For each i, a set of $K_{1i},K_{2i},\cdots,K_{Li}(L < n)$ can be got $(i = 1,2,\cdots,m)$. So, we get m sets of unknown boundary bound stiffness solution.

By using the method of the least squares, a solution of unknown boundary condition with minimum variance can be got, that is:

$$K_i = \frac{1}{m}\sum_{i=1}^{m} K_{ii},$$

$$K_2 = \frac{1}{m}\sum_{i=1}^{m} K_{2i}$$
$$\cdots\cdots\cdots\cdots, \tag{5}$$
$$K_L = \frac{1}{m}\sum_{i=1}^{m} K_{Li}$$

The accurate method is used only in the case that the measured mode is a full mode.

The solution of this method is accurate and satisfying, but, as all known, it is difficulty to test rotational modal branch.

FULL MODE COMPUTATION METHOD BY MEANS OF GENERLIZED INVERSE MATRIX

The eigenfrequency and eigenvector of equation (3) can be got from

$$\left([K_A + K^*] - \omega^2[M_A]\right)\{\Phi\} = 0 \tag{6}$$

For the i–th. eigenvaluc, equation (6) can be written into

$$\left(-\omega_i^2\begin{bmatrix} M_{cc} & M_{cf} \\ M_{cf}^T & M_{ff} \end{bmatrix} + \begin{bmatrix} K_{cc} & K_{cf} \\ K_{cf}^T & K_{ff} \end{bmatrix}\right)\begin{bmatrix} \Phi_c \\ \Phi_f \end{bmatrix}_i = 0$$
$$i = 1,2,\cdots,m \tag{7}$$

where $[K_{ff}]$ contains $[K^*]$, subscript c and f is regard as testing degree and untesting degree. From equation (7), we get

$$\left([K_{cf}] - \omega_i^2[M_{cf}]\right)\{\Phi_f\}_i = -\left([K_{cc}] - \omega_i^2[M_{cc}]\right)\{\Phi_c\}_i$$
$$i = 1,2,\cdots,m \tag{8}$$

There are a lot of solution to equation (8), By leading in an additional constrain condition.

$$\|\{\Phi_f\}_i\|_F = \min \tag{9}$$

then, only a solution of equation (8) which has the minimum Frobenius norm can be got

$$\{\Phi_f\}_i = -\left([K_{cf}] - \omega_i^2[M_{cf}]\right)^+\left([K_{cc}] - \omega_i^2[M_{cc}]\right)\{\Phi_c\}_i$$
$$i = 1,2,\cdots,m \tag{10}$$

From equation (10), we get the i–th eigenvector

$$\{\Phi\}_i = \begin{Bmatrix} \Phi_c \\ \Phi_f \end{Bmatrix}_i, \qquad i = 1,2,\cdots,m \tag{11}$$

Equation (10), (11) is called the full mode computation method by means of generlized inverse matrix. When the rotational mode branch has not been tested, the rotational mode branch can be got from the translational mode with this method. Substituting the full mode into equation (4), we can get an approximate solution of $[K_1^*]$. A computation example can be seen later in this paper.

THE INTERPOLATION METHOD OF FREQUENCY

Before solving equation (4), two sets of modal parameter are ealculated with finite element model in

two cases. First, let all the unknown boundary bound be free. (i.e, all equal to zero). Second. let all the unknown boundary bound be fixed end.

For solving equation (4), there are two interpolation method. One method use the restrained stiffness, the other use the restrained mode branch.

1.THE INTERPOLATION METHOD WITH RESTRAINED STIFFNESS

If the eigenfrequency of the finite element model of the structure when all the unknown boundary bound be let free is $\omega_i^F(i=1,2,\cdots,m)$, and the eigenvector are $\left\{\begin{matrix}\Phi^F \\ nF\times 1\end{matrix}\right\}_i$ $(i=1,2,\cdots,m)$. The eigenfrequency of the finite element model of the structure when all the unknown boundary bound be fixed end is $\omega_i^S(i=1,2,\cdots,m)$, and the eigenvector are $\left\{\begin{matrix}\Phi^S \\ nS\times 1\end{matrix}\right\}_i$ $(i=1,2,\cdots,m)$. $\omega_i(i=1,2,\cdots,m)$ is the tested modal parameter of the structure. Suppose $\omega_i^0(i=1,2,\cdots,m)$ is the calculated modal parameter when the boundary bound stiffness are $K_1^0,K_2^0,\cdots,K_L^0$, and

$$\omega_i^F < \omega_i^0 < \omega_i^S, \qquad i=1,2,\cdots,m \tag{12}$$

Then, the boundary bound stiffness can be got with interpolation method, it is

$$\begin{aligned} K_1^1 &= \frac{\omega_i-\omega_i^F}{\omega_i^0-\omega_i^F}K_1^0, \\ K_2^1 &= \frac{\omega_i-\omega_i^F}{\omega_i^0-\omega_i^F}K_2^0, \\ &\cdots\cdots\cdots, \\ K_L^1 &= \frac{\omega_i-\omega_i^F}{\omega_i^0-\omega_i^F}K_L^0, \end{aligned} \tag{13}$$

where i may be anyone of 1,2,···,m.

As a general rule, the unknown boundary bound stiffness affect the lower eigenfrequency most. So, for the interpolating of equation (13), the first eiger frequency will often be used, we have

$$K_j^1 = \frac{\omega_1-\omega_1^F}{\omega_1^0-\omega_1^F}K_j^0, \qquad j=1,2,\cdots,L \tag{14}$$

After the bound stiffness $K_j^1(j=1,2,\cdots,L)$ *is got from equation (14), we calculate the eigenfrequency* ω_1^1 and eigenvector in that case. Then, we continue to interpolate with the calculated eigenfrequency and bound stiffness until the satisfying result of eigenfrequency and eigenvector which are equal to the tested modal parameters are got.

2. THE INTERPOLATION METHOD OF BOUNDARY BOUND MODE BRANCH

If $\{\Phi_j^F\}_i$ is the j–th branch of the i–th eigenvector of the finite element model of the structure when all the unknown boundary bound be let free, and $\{\Phi_j^S\}_i$ is the j–th branch of the i–th eigenvector of the finite element model of the structure when all the unknown boundary bound be fixed end. Then, the inter-

polation result of the j–th branch of the i–th eigenvector is

$$\{\Phi_j\}_i = \frac{\omega_i - \omega_i^F}{\omega_i^S - \omega_i^F}\left(\{\Phi_j^S\}_i - \{\Phi_j^F\}_i\right) + \{\Phi_j^F\}_i$$

$$(j = 1,2,\cdots,L;\ \ i = 1,2,\cdots,m) \tag{15}$$

Generally, the first order eigenvector was taken for interpolating calculation (i = 1). After the full moder was got with full mode computation method Presented by Peng Xiaohong, et al. [1], the unknown boundary bound stiffnes could be got by substituting $\{\Phi\}_1$ into equation (4). Again, we calculate the eigenfrequency and eigenvector of this bound stiffness case. we continue to calculate until the satisfying result of eigenfrequency and eigenvector which are equal to the tested modal parameters are got.

AN APPLIED EXAMPLE

Now, we applied the method to determine the boundary condition of a Multi–disk system. For a Multi–disk Rotor system of Figure 1, the diameter of its shaft is 6mm, the length of the shaft is 290mm, and the shaft is fixed in two bearings at both ends with a thin 502 glue. The Rotor system have three diskes. one disk weighs 608 grams, the other two diskes weigh 559 grams each. These three diskes are fixed in the shaft evenly.

The boundary condition of the Rotor system is not an ideal boundary condition of simple support. Figure 3. is the mechanics model of the Multi–disk Rotor system.

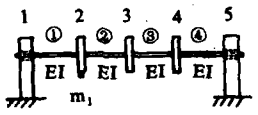

Figure 1. Multi–disk Rotor System

At both ends of the shaft, the displacement in the vertical direction is equal to zero (i,e. be fixed). K_1 and K_2 represent the rotational bound stiffness on the end, and $K_1 = K_2 = K$.

Mode(f) / Point	f_1 = 47.43Hz 1	f_2 = 123.52Hz 2	f_3 = 224.86Hz 3
1	0	0	0
2	0.1245	0.3550	0.2442
3	0.2150	0.0357	−0.2082
4	0.1315	−0.3534	0.2068
5	0	0	0

Table 1. Tested Modal Parameters

Mode	Simple Support at Both Ends		Fixed End at Both Ends	
	Consider The Rotational Inertia of The Diskes	Do Not Consider The Rotational Inertia	Consider The Rotational Inertia of The Diskes	Do Not Consider The Rotational Inertia
1	23.47Hz	23.73Hz	52.95Hz	54.26Hz
2	90.59Hz	94.17Hz	134.11Hz	142.68Hz
3	191.42Hz	202.93Hz	232.72Hz	237.58Hz

Table 2. The Eigenfrequency of FEM of The Multi-disk Rotor System in Two Boundary Condition Case

The mode of the Multi-disk Rotor system was excited with random excitation method (by using an untounched BJ-II type broad band electric exciter). After modal analysis and parameter identification, the tested modal parameters are got as table 1. The synthesized amplitude-frequency characteristic and first 3 mode are shown in Figure 2. The unknown boundary condition need to be determined with the method we put forward.

All the eigenfrequency of the two Finite Element Models are listed in Table 2. The first Finite Element Model has an assumed boundary condition of simple support at both ends, the other has an assumed *boundary condition of fixed end* at both ends. (I_p: The rotational inertia of the diskes) The unknown boundary bound stiffness K_1,K_2 was determined with the method we presentd. Figure 3 is the Mechanics Model of the Multi-disk Rotor System.

First, with the interpolation method of frequency, the unknown bound stiffness is determined to be:

$$K_1 = K_2 = 1472.41 N \cdot m$$

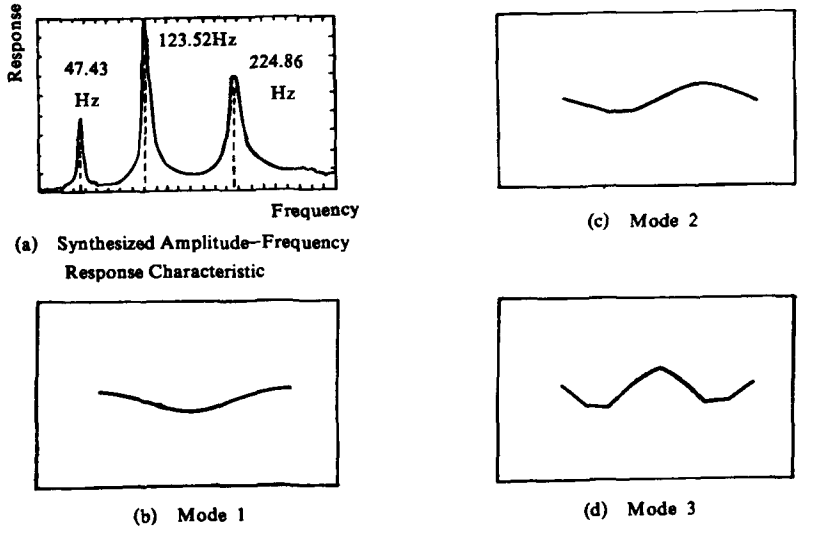

Figure 2. Synthesized Frequency Response Function of The Multi-disk Rotor System

In this case, the eigenfrequencyes of the Finite Element Model are:

$f_1 = 47.72Hz,$

$f_2 = 123.31Hz,$

$f_3 = 220.40Hz,$

Then, with the Full Mode computation Method By means of Generlized Inverse Matrix, the unknown bound stiffness is determined

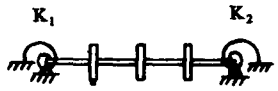

Figure 3. The Mechanics Model of The Rotor System

as listed in Table 3. It is an approximate

Bound Stiffness	*Determined* With $\{\Phi\}_1$	Determined With $\{\Phi\}_2$	Determined With $\{\Phi\}_3$
K_1	1119.22N · m	1411.59N · m	22977.63N · m
K_2	933.43N · m	377.03N · m	4062.56N · m

Table 3. The Results of Bound Stiffness With Full Mode Computation Method By Means of Generlized Inverse Matrix

solution of the bound stiffness. Because in the computation of Finite Element Model, the result of lower eigenfrequency is more accurate than the result of higher eigenfrequency. So, the bound stiffness determined with lower order of eigenvector is more correct. Here, the result of K_1,K_2 determined with $\{\Phi\}_1$ is more trustworthy. So, $K_1 = K_2 = 1472.41N \cdot m$ is taken as the solution of the unknown boundary bound stiffness, and a Finite Element Model of the real structure is got. With the Finite Element Model, the error of eigenfrequency is less than 2%.

To verify the rightness of the boundary condition which has just been determined, three pieces of added mass were attached to the three diskes of the Rotor system. The added mass weighs 54 grams each. After Modal testing and analysis, the modal parameters of the modifyed structure were got as:

$f_1 = 45.70Hz,$

$f_2 = 115.30Hz$

$f_3 = 212.20Hz$

By using the structure Finite Element Model which has the determined boundary bound stiffness K_1 and K_2, and the additional mass matrix was taken as:

$$\Delta m = \begin{bmatrix} 0 & & & & & & \\ & 0.054 & & & & & \\ & & 0 & & & & \\ & & & 0.054 & & & \\ & & & & 0 & & \\ & & & & & 0.054 & \\ & & & & & & 0 \\ & & & & & & & 0 \end{bmatrix}$$

three eigenfrequency of FEM of the modifyed structure were calculated as:

$$f_1 = 45.73\text{Hz},$$
$$f_2 = 118.64\text{Hz},$$
$$f_3 = 211.54\text{Hz},$$

The value of eigenfrequency calculated with the FEM of the modifyed structure is consistent with the tested modal parameters of the modifyed structure. From this result, it clearly shows the boundary bound stiffness determened with the method we presented can be taken as the real boundary bound stiffness which are used for the dynamic computation and analysis of the structure.

ACKNOWLEDGEMENT:

The author would like to thank the research associate Wu Xuixing for hers support and assistence in doing experiment.

REFERENCES:

1. Peng Xiaohong. "To Correct the Finite Element Model of a Structure With Tested Modal Parameter", Vibration and Shock, No. 3, 1984.
2. Xu Wanli; Xia Yilin, "Mass Matrix and Stiffness Matrix Correction Using Generlized Inverse Matrix", Proceedings of the 5rd National Modal Analysis and vibration testing conferere, P. R.China, 1988, pp. 858–866.
3. Baruch, M. "Optimazation Procedure to Correct Stiffness and Flexibility Matrix Using Vibration Tests" AIAA J. Vol. 16. No. 11, Nov. 1978, pp. 1208–1210.
4. Berman, A. "Mass Matrix Correction Using an Incomplete Set of Measured Modes". AIAA J. Vol. 17, No. 10, Oct. 1979, pp. 1147–1148.
5. Lu Zhenhua, Feng Zhendong, "The Optimal Structural Modification Principle for the Maximum Shifts of Natural Vibration Frequencies" Proceedings of the 6rd International Modal Analysis Conference, 1988, pp. 1107–1111.

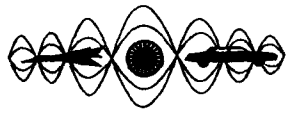

SECOND INTERNATIONAL CONGRESS ON
RECENT DEVELOPMENTS IN AIR- AND
STRUCTURE-BORNE SOUND AND VIBRATION
MARCH 4-6, 1992 AUBURN UNIVERSITY, USA

VIBRATION AND EIGENVALUE ANALYSIS USING FINITE ELEMENTS

Tirupathi R. Chandrupatla
Mechanical Engineering Department
GMI Engineering and Management Institute
Flint, MI 48504
U.S.A.

and

Ashok D. Belegundu
Mechanical Engineering Department
The Pennsylvania State University
University Park, PA 16802
U.S.A.

ABSTRACT

The paper presents the steps involved in the use of finite elements for the analysis of vibration problems. Formation of stiffness and mass matrices is followed by discussion of techniques of reducing the size of the matrices. Characteristic polynomial, vector iteration, and transformation methods of eigenvalue and eigenvector evaluation for free vibrations of structures are presented. Damping aspects are discussed for the special case of Raleigh damping.

INTRODUCTION

A structure vibrates when forces of variable nature are applied on it. Sudden application or sudden release of forces also cause the structure to oscillate in a cyclic manner about its equilibrium position. If an elastically deformed structure is suddenly released, the resulting oscillations are referred to as natural vibration. A structure modeled as a mass-spring system tends to oscillate indefinitely. The frequency of oscillation is called the natural frequency. For variable forces, if the disturbing frequency is less than one third of the lowest natural frequency, the structure may be treated as static and mass effects need not be considered [1]. Vibration in real structures subsides with time due to damping action. Damping in structures may be due to internal material condition, friction in joints, or external dampers introduced to absorb vibration.

It is clear from the discussion above that evaluation of the lowest natural frequencies is necessary to predict the dynamic behavior of the structure. This is accomplished by considering the stiffness and mass effects using finite elements. The vibration control aspects require consideration of damping in the system. The purpose of this paper is to give an overview of the use of finite elements for the analyses. First, the formation of stiffness and mass matrices is considered. Techniques of matrix size reduction are discussed. Methods of evaluating natural frequencies or

equivalently the eigenvalues are presented. Strategies for considering damping effects are developed.

STIFFNESS, MASS, AND MATRIX REDUCTION

In the finite element analysis, a structure is divided into elements which are connected at nodes. Consider the structure shown in Fig. 1. The nodal displacements referred to as *global degrees of freedom* are denoted Q_1, Q_2, Q_3, ... It is convenient to consider the energy in the structure by considering the energy contributed by each element. A typical element is illustrated in Fig. 2. The nodal displacements of the element are denoted q_1, q_2, q_3, ... These may be referred to as the *local degrees of freedom*. The finite element model expresses the displacement field in the element in terms of the nodal displacements of the element.

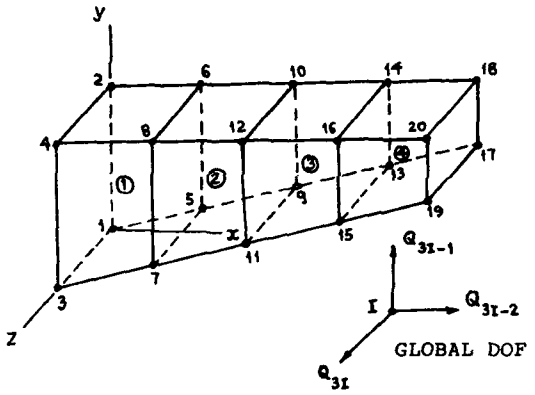

Figure 1 Structure

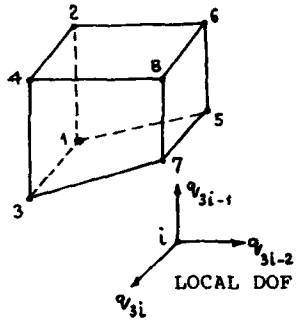

Figure 2 Element

The total strain energy in the structure is obtained as the summation of strain energy in the elements. The result of these steps is represented as follows:

$$S.E. = \sum_e \frac{1}{2} q^T k^e q = \frac{1}{2} Q^T K Q \qquad (1)$$

Noting that in dynamic problems, the nodal displacements are functions of time, the total kinetic energy is also obtained through element kinetic energy.

$$K.E. = \sum_e \frac{1}{2} \dot{q}^T m^e \dot{q} = \frac{1}{2} \dot{Q}^T M \dot{Q} \qquad (2)$$

On developing the Lagrange's equations of motion, the finite element representation becomes:

$$M\ddot{Q} + KQ = 0 \tag{3}$$

On setting

$$Q = U \sin\omega t \tag{4}$$

where ω is the circular frequency ($= 2\pi f$, f Hz) and U is called the *eigenvector* representing the corresponding mode shape. Denoting $\lambda = \omega^2$, where λ is called the *eigenvalue*, we have,

$$KU = \lambda MU \tag{5}$$

Stiffness and mass matrices for various structural elements are presented in [2, 3].

Stiffness and mass matrices formed above are square matrices of size given by the number of degrees of freedom. Generally these matrices are banded. Some techniques of eigenvalue analysis make use of the banded nature of the matrices. There are other methods which work with full size matrices. In these cases, it will be of interest to reduce the size of the matrices. This helps in handling large scale problems while retaining the possibility of calculating significant modes of vibration. A technique commonly used is called Guyan Reduction [4].

Guyan Reduction

The key here is to identify master and slave degrees of freedom [1]. The master degrees of freedom control the eigenvalues and modes desired and slave degrees of freedom are those which have minimal inertia contribution. In a beam bending problem, the rotational degrees of freedom are typical slave degrees of freedom. If U_m and U_s are identified as master and slave degrees of freedom respectively, we partition the stiffness and mass matrices as follows:

$$\begin{bmatrix} K_{mm} & K_{ms} \\ K_{ms}^T & K_{ss} \end{bmatrix} \begin{bmatrix} U_m \\ U_s \end{bmatrix} = \lambda \begin{bmatrix} M_{mm} & M_{ms} \\ M_{ms}^T & M_{ss} \end{bmatrix} \begin{bmatrix} U_m \\ U_s \end{bmatrix} \tag{6}$$

The slave degrees of freedom are eliminated using

$$U_s = -K_{ss}^{-1} K_{ms}^T U_m \tag{7}$$

In the computations, the inversion need not be explicitly carried out. The product $T = K_{ss}^{-1} K_{ms}^T$ can be obtained by applying Gauss elimination on K_{ss}

together with each column of K_{ms} as the right hand side, and then backsubstituting for each column. Denoting the reduced matrices as K_r and M_r respectively, we get

$$\begin{aligned} T &= K_{ss}^{-1} K_{ms}^T \\ K_r &= K_{mm} - K_{ms} T \\ M_r &= M_{mm} - M_{ms} T - T^T M_{ms}^T + T^T M_{ss} T \end{aligned} \tag{8}$$

The reduced problem is given by

$$K_r U_m = \lambda M_r U_m \tag{9}$$

Various strategies can be used for identifying the slave degrees of freedom. The idea is to look for the ratio of diagonal element of K and the corresponding diagonal element of M. The degrees of freedom with largest ratios are candidates for slave DOF. For a detailed account see [1, 5, 6]. We also note here that if elements of M_{ss} and M_{ss} are all zero, the Guyan reduction is precisely *static condensation*. A bound algorithm for the reduction has been presented by Wright and Miles [6]. The stage is now set for discussing the techniques of finding the eigenvalues and eigenvectors.

EIGENVALUES AND EIGENVECTORS

The eigenvalue-eigenvector evaluation procedures fall into the broad categories of characteristic polynomial, vector iteration, and transformation methods. Main characteristics of these techniques are discussed below.

Characteristic Polynomial Technique

Solution of the problem posed by (5) or (9) is equivalent to determining zeroes of the polynomial in λ given by

$$\det(K - \lambda M) = 0 \tag{10}$$

The eigenvector corresponding to each eigenvalue is then evaluated. This technique is quite efficient for small problems. The technique is also referred to as *determinant search method* [8].

Vector Iteration Methods

Chief among the vector iteration methods is the *inverse iteration method*. The method uses properties of the *Rayleigh quotient*. We start with a trial vector u_1. Then for steps k = 1,2,..., we determine u_2, u_3,...

$$\begin{aligned} K\bar{u}_{k+1} &= Mu_k \\ u_{k+1} &= \frac{\bar{u}_{k+1}}{\left(\bar{u}_{k+1}^T M \bar{u}_{k+1}\right)^{\frac{1}{2}}} \end{aligned} \tag{11}$$

The inverse iteration converges to the lowest eigenvalue. It is necessary here that the boundary conditions are applied to modify the stiffness to make it positive definite. We alao note that the banded nature of the stiffness and mass matrices can be effectively used in this method. Higher eigenvalues are obtained efficiently by excluding the space spanned by the eigenvectors already evaluated using the *Gram-Schmidt Orthogonalization*. Subspace iteration algorithm proposed by Bathe [9] involves iteration in a subspace of dimension determined by the number of eigenvalues desired.

Transformation Methods

A transformation method that is quite efficient for small scale problems is the *Generalized Jacobi Method*. A series of transformations P_1, P_2,...,P_s are used such that if P represents the product

$$P = P_1 P_2 \ldots P_m \tag{12}$$

then the off diagonal terms of $P^T K P$ and $P^T M P$ are simultaneously zero. In practice, the *limits on off* diagonal terms may be set as 10^{-6}x(smallest diagonal stiffness element) for stiffness matrix, and 10^{-6}x(largest diagonal mass element) for mass matrix. The zero check is more efficiently performed by checking elements farthest from the diagonal to the diagonal in the order (1,n), (1,n-1), (2,n), (1,n-2),... . Since initial matrices are banded, this approach saves computational effort. In this approach, full matrices are used. Both stiffness and mass matrices need not be positive definite.

There are other transformation methods where the generalized eigenvalue problem is first turned into a standard form

$$K^{-1}MU = \frac{1}{\lambda}U \tag{13}$$

The matrix $K^{-1}M$ is then tridiagonalized using various transformation methods such as Householder method or Lanczos method. Required eigenvalues are then determined using inverse iteration. QR iteration may be used to determine all eigenvalues. Lanczos method is becoming popular for large scale systems.

Lanczos Method. In the tridiagonalization process, matrix X of Lanczos vectors x_1, x_2, x_3,... represented by

$$X = [x_1, x_2, \ldots, x_n] \tag{14}$$

is chosen such that

$$\begin{aligned} X^T M X &= I \\ X^T M K^{-1} M X &= T \end{aligned} \tag{15}$$

where I is the identity matrix and T is a tridiagonal matrix. The eigenvalue problem in the tridiagonal form is represented by

$$\begin{aligned} U &= X\hat{U} \\ T\hat{U} &= \frac{1}{\lambda}\hat{U} \end{aligned} \tag{16}$$

For details of computations for the formation of Lanczos vectors refer to [5,8,9]. Recently considerable research has been devoted to the development of the Lanczos method. Several FEA software vendors have implemented this method in their codes. The main problems involved are in overcoming the rounding off errors in computations.

DAMPING CONSIDERATIONS

With damping, the equations of motions for free response are

$$M\ddot{Q} + C\dot{Q} + KQ = 0 \tag{17}$$

The damping matrix C is rarely developed from element level. A common approach is to assume that C is a linear combination of K and M. Thus

$$C = \alpha K + \beta M \tag{18}$$

where α and β are scalars. This case is referred to as *Raleigh damping* [9,10]. We now assume the steady state solution to (17) is of the form

$$Q = Ue^{st} \tag{19}$$

Where U is a mode shape. Substituting int (17), and noting Eq.(18), we have

$$KU = \left(-\frac{\beta s + s^2}{1 + \alpha s}\right) MU \tag{20}$$

Comparing the above equation to Eq.(5), we see that the mode shapes of the undamped and the proportionally damped system are the same. Further the quantity within brackets is simply equal to square os the undamped natural frequency ω. Thus

$$\omega^2 = -\frac{\beta s + s^2}{1 + \alpha s} \tag{21}$$

Solving for s, we get

$$\begin{aligned} s &= -\omega\zeta + i\omega_d \\ 2\omega\zeta &= \alpha\omega^2 + \beta \\ \omega_d &= \omega\sqrt{1 - \zeta^2} \end{aligned} \tag{22}$$

where ζ is the damping ratio and ω_d is the damped circular frequency for the mode corresponding to natural frequency ω. Above equation helps in determining the α and β experimentally for a given dynamic structure or in the determination of their values for given damping ratios [11].

DISCUSSION AND CONCLUSIONS

Several aspects of vibration analysis have been presented in this paper. Finite element formulation of stiffness and mass matrices is followed by eigenvalue and mode shape determination. Forced vibrations have not been considered in this presentation. We have discussed Raleigh damping, but there are several other aspects of general damping have not been considered here. Hysteritic damping and damping considerations in viscoelastic materials [12] pose challenging problems.

BIBLIOGRAPHIC REFERENCES

1. COOK, R.D., *Concepts and Applications of Finite Element Analysis*, John Wiley & Sons, New York, 1981

2. PRZMIENIECKI, J.S., *Theory of Matrix Structural Analysis*, McGraw-Hill, New York, 1968

3. CHANDRUPATLA, T.R., and A.D. BELEGUNDU, *Introduction to Finite Elements in Engineering*, Prentice Hall, Englewood Cliffs, New Jersey, 1991

4. GUYAN, R.J., "Reduction of Stiffness and Mass Matrices," *AIAA Journal*, 3 (1965), 380.

5. HUGHES, T.J.R., *The Finite Element Method - Linear Static and Dynamic Finite Element Analysis*, Prentice Hall, Englewood Cliffs, New Jersey, 1987

6. HENSHELL, R.D., and J.H. Ong, "Automatic Masters for Eigenvalue Economization," *Earthquake Engineering and Structural Dynamics*, 3 (1975), 375-383

7. WRIGHT, G.C., and G.A. MILES, "An Economical Method for Determining the Smallest Eigenvalues of Large Linear Systems," *Int. J. for Numerical Methods in Engineering*, 3 (1971), 25-33

8. HUMAR, J.L., *Dynamics of Structures*, Prentice Hall, Englewood Cliffs, New Jersey, 1990

9. BATHE, K.J., *Finite Element Procedures in Engineering analysis*, Prentice Hall, Englewood Cliffs, New Jersey, 1982

10. INMAN, D.J., *Vibration with Control, Measurement, and Stability*, Prentice Hall, Englewood Cliffs, New Jersey, 1989

11. EWINS, D.J., *Modal Testing : Theory and Practice*, Research Studies Press, 1984

12. SEGALMAN, D.J., "Calculation of Damping Matrices for Linearly Viscoelastic structures", *Journal of Applied Mechanics*, 54 (1987), 585-588

SECOND INTERNATIONAL CONGRESS ON
RECENT DEVELOPMENTS IN AIR- AND
STRUCTURE-BORNE SOUND AND VIBRATION
MARCH 4-6, 1992 AUBURN UNIVERSITY, USA

DYNAMIC ANALYSIS OF PRACTICAL BLADED DISKS USING FEM AND CYCLIC SYMMETRY TECHNIQUES

A.S.Panwalkar*
V.Ramamurti**
A.Rajamani*

*Vibration Laboratory,
Corporate Research and Development Division,
Bharat Heavy Electricals Limited,
Vikasnagar, Hyderabad, 500593, India

**Department of Applied Mechanics,
Indian Institute of Technology, Madras, 600036, India

ABSTRACT

Coupled free vibration characteristics of practical bladed disks are computed using triangular shell element and cyclic symmetry. Potters' method is used for solution of the eigenvalue problem. Blade-disk joint constraints are applied based on Love-Kirchhoff hypothesis. Blade to blade variation of looseness at the blade-disk joint is also considered. Results of three practical bladed disks with different blade aspect ratios and having approximately the same disk radii ratio are presented. For large aspect ratio of blades, the bladed disk vibration behaviour is simple. For the medium and small aspect ratio blades, complex mode behaviour is observed.

INTRODUCTION

The bladed disk assemblies in general are flexible and have to withstand severe operating conditions such as large centrifugal force loading, higher operating temperatures, flow induced dynamic loads etc. Therefore, it is very essential to determine the vibration behaviour pattern of the bladed disk from design point of view for long time trouble free operation of the machine [1]. A typical turbine bladed disk constitutes a dynamic system in which different flexibilities of its components such as disk, blades, shrouds etc., dynamically interact with each other. Kuo [2] illustrated the influence of blades and shrouds upon the natural frequencies. Omprakash and Ramamurti [3] made a parametric study of the coupled free vibration characteristics of rotating bladed disks. Irretier and Schmidt [4] used receptance techniques and component mode synthesis. They emphasized the use of component mode synthesis to solve the problem of mistuning. Ewins [5,6] has done a detailed study to understand vibration behaviour of bladed disks and addressed to the problem of mistuning. Ewins and Imregun [7] made studies on the bladed disks with packeted blades. Griffin and Hoosac [8] considered mistuning using spring and mass constants as the random variables for blades. Pierre and Cha [9] and Wei and Pierre [10] used perturbation approach to explain mode localization phenomena in a mistuned bladed disk. Afolabi [11] uses eigenvalue spectrum method as suggested by Ewins [6] and he classifies [12] the vibration behaviour of mistuned bladed disk. Finbow and Watson [13] presented practical experiences on the working bladed disks.

The aim of this paper is to study the vibration behaviour pattern of practical cases of steam turbine bladed disks which are in operation. A triangular shell element is used for both disk and blades. The attachment of blades to the disk is maintained by a set of constraint equations derived from Love-Kirchhoff's hypothesis. Potters' scheme and cyclic symmetry [14] are used to solve the equations. The bladed disks which are considered for the analysis have blade aspect ratios of 2.23, 3.1 and 4.4 with disk

radii ratio (ratio of disk inside radius to outside radius) 'ε' of 0.43, 0.49 and 0.45 respectively. For blade aspect ratio of 2.23 and 4.4, the results are given for three conditions viz. (i) Analysis of a sector of bladed disk containing single blade: The vibration behaviour thus determined will represent the one for tuned bladed disk. (ii) Analysis of a sector containing two blades: Here, deviation between blade to blade for root looseness has been studied. (iii) Analysis of a sector containing four blades: Here different conditions of variation in root looseness are studied.

FORMULATION

Constraint Equation

Disk and blades both are represented by shell elements owing to their structural sizes and shapes. A three noded triangular shell element with six degrees of freedom (DOF) i.e. $\{\delta\} = [u, v, w, \theta_x, \theta_y, \theta_z]^t$ per node is used for the analysis. Here u,v are the inplane displacements and w is the bending displacement. θ_x, θ_y, θ_z are the rotations of the normal.

Midsurfaces of disk and blade do not lie in the same plane (Fig. 1). For the rigid root fixity conditions perfect matching of blade and disk displacement at the blade-disk joint nodes is to be assured. This is done by Love-Kirchhoff hypothesis as

$$w_b = w_d \;,\; u_b = u_d + z\left(\frac{\partial w}{\partial x}\right)_d \;,\; v_b = v_d + z\left(\frac{\partial w}{\partial y}\right)_d$$

$$\theta_{x_b} = \theta_{x_d} \;,\; \theta_{y_b} = \theta_{y_d} \;,\; \theta_{z_b} = \theta_{z_d} \qquad (1)$$

where subscripts 'b' and 'd' refer to blade and disk and 'z' is the distance between the two points A_b and A_d(shown in Fig. 1) in undeformed condition.

The disk is divided into N identical sectors of which one sector is analyzed by incorporating proper constraints from its adjoining sectors using cyclic symmetry. One sector of the disk containing one blade is shown in Fig. 2. To apply Potters' method the sector is shown divided into a number of partitions. From this figure it can be seen that in partition No. 2, there is one blade node whose displacement is to be related to its corresponding disk node represented by b' and d'. This is called one joint node. Whereas, for partition No. 3, there are two joint nodes 'b_1' and 'b_2', corresponding to 'd' as the disk node. This is called two joint node. It is required to eliminate the blade displacement at the joint nodes, as per Eq. (1), from the unknown displacement vector for a partition in which joint node occurs. The resulting displacement vector (modified displacement vector) is only solved from equilibrium equations. The process of elimination of blade displacements is illustrated here for two joint node partition. The details for one joint node is given in Ref. [3].

Let

$$\{\delta\}_i = [\delta_1, \delta_2 \ldots \delta_{m_1}, \delta_d, \delta_{b_1}, \delta_{m_2} \ldots \delta_{m_3}, \delta_{b_2}, \delta_{m_4} \ldots \delta_m]_i^t$$

be the displacement vector of the i^{th} partition in which suffixes 1, 2, m_1, d,b, etc. are the node numbers in that partition as shown in Fig. 2. δ_{b_1} and δ_{b_2} are the two blade node displacements which are to be eliminated by relating them to δ_d, a corresponding disk node displacement. The modified displacement vector $\{\delta'\}_i = [\delta_1, \delta_2 \ldots \delta_{m_1}, \delta_d, \delta_{m_2} \ldots \delta_{m_3}, \delta_{m_4}, \ldots \delta_m]^t$ and the relation is given by

$$\{\delta\}_i = [T_c]_i \{\delta'\}_i \qquad (2)$$

where $[T_c]_i$ is the transformation matrix which is given by

$$\left[T_c\right]_i = \begin{bmatrix} \begin{bmatrix} R_1 \\ [Q_1] \end{bmatrix} & 0 & \\ & \begin{bmatrix} R_2 \\ [Q_2] \end{bmatrix} & \\ 0 & & \left[R_3\right] \end{bmatrix} \tag{2a}$$

where, $[R_1]$, $[R_2]$ and $[R_3]$ are the unit matrices of sizes $[6(m_1+1),\ 6(m_1+1)]$, $[6(m_3-m_2+1),\ 6(m_3-m_2+1)]$ and $[6(m-m_4+1),\ 6(m-m_4+1)]$ respectively. $[Q_1]$ and $[Q_2]$ are of size (6, 6) and the terms of these matrices are obtained by using the constraint Eq. (1) for blade nodes b_1 and b_2 and disk node d. It may be noted that for one joint node partition $[T_c]$ will contain the above matrices excluding $[Q_2]$ and $[R_3]$; the resulting matrix $[T_c]$ will be same as that derived in Ref. [3].

Stiffness And Mass Matrices

The element stiffness is determined by triangular shell elements. Masses are lumped for translational degrees of freedom equally at the three nodes. In Potters' scheme element matrices are assembled partition-wise and hence the matrix equation for the eigen value 'ω' is written as (Ref. [14]).

$$\begin{bmatrix} B_1 & A_1 & 0 & 0 & \ldots & 0 & 0 & A_n^t k_1 \\ A_1^t & B_2 & A_2 & 0 & \ldots & 0 & 0 & 0 \\ 0 & A_2^t & B_3 & A_3 & \ldots & 0 & 0 & 0 \\ & \cdot\cdot & \cdot\cdot & \cdot\cdot & & \cdot\cdot & \cdot\cdot & \cdot \\ 0 & 0 & 0 & 0 & \ldots & A_{n-2}^t & B_{n-1} & A_{n-1} \\ A_n k_2 & 0 & 0 & 0 & \ldots & 0 & A_{n-1}^t & B_n \end{bmatrix} \begin{Bmatrix} z_1 \\ z_2 \\ z_3 \\ \cdot\cdot \\ z_{n-1} \\ z_n \end{Bmatrix} = \omega^2 \left[M\right] \begin{Bmatrix} z_1 \\ z_2 \\ z_3 \\ \cdot\cdot \\ z_{n-1} \\ z_n \end{Bmatrix} \tag{3}$$

where $[B_i]$, $[A_i]$ etc. are the elements of partitioned stiffness matrix, $\{z_i\}$ is the partitioned eigenvector and [M] is dia $[M_1, M_2, M_3 \ \ldots \ M_{n-1}, M_n]$ with M_i as the partitioned mass. Suffix 'i' represents partition number and there are (n+1) partitions present in one sector. It may be pointed out that the matrices [B], [A] are required to be transformed using transformation matrix given by Eq. (2). This transformation is explained in Ref. [3]. In Eq. (3), $k_1 = e^{-i\mu}$ and $k_2 = \frac{1}{k_1}$; $i = \sqrt{-1}$ and μ is the wave propagation constant which relates displacement vectors of k^{th} sector and its previous sector i.e. (k-1) by the equation $\Delta_k = e^{-i\mu}\ (\Delta_{k-1})$. The value of '$\mu$' depends upon the wave number or the number of nodal diametral mode 'n' to be analyzed such that

$$\mu = \frac{2\pi n}{N} \tag{4}$$

where N is the total number of sectors; 'n' can take following values

$n = 0, 1, 2 \quad \ldots\ (N/2) \quad$ for N even
$n = 0, 1, 2 \quad \ldots\ (N - 1)/2$ for N odd

The solution of Eq. (3) yields modified displacement vector. The recovery of actual displacement vector can be made by Eq. (2).

CONDITIONS OF BLADE ROOT FIXITY

In analyzing the bladed disk assemblies three root conditions which pertain to different blade root looseness are studied. Looseness is modeled as follows. There are six nodes at the blade root which join with the disk nodes. Out of these six nodes, two nodes which appear in the third partition are released and the displacements are treated as DOF's without any joint constraint. Whereas for a tight blade, joint constraints are applied for all the nodes as described earlier. This way the difference between a loose blade and a tight blade is incorporated. The conditions considered are: 1) Single blade in a sector without releasing the nodes. This is the case of tuned bladed disk with all blades attached tightly. 2) Two blades in a sector with first blade tight and the second blade let loose. This means that there are alternate loose and tight blades attached to the disk. 3) Four blades in a sector with first and fourth blades tight whereas second and third blades have looseness. This means that every two tight blades are followed by two loose blades in succession.

ANALYSIS OF BLADED DISKS

The results obtained by the present method are compared for a circular disk considered by Salama [15] and for a typical Low Pressure (LP) turbine blade for which results have been obtained by using commercial packages PAFEC and VIPACK and by experiments [16] for checking the computer program developed. The comparison is found to be excellent. Three bladed disk assemblies which are in operation are considered. These assemblies have blade aspect ratios (i.e. ratio of blade length to chordwise width at the blade root profile) of 2.23, 4.4 and 3.1 with corresponding disk radii ratios of 0.43, 0.45 and 0.49.

Case 1- Intermediate Pressure (IP) Turbine Stage

This is a case of an IP stage of 110 MW steam turbine with 168 blades on the disk and a blade aspect ratio of 2.23. Three conditions (as described above) are considered for analysis.

Condition 1. This condition represents a tuned bladed disk. A plot of natural frequency versus nodal diameter for the first three modes is given in Fig. 3. Vibration modes of cantilever blade corresponding to first flapwise bending (1B - tangential) and first edgewise bending (1EB - axial) are also shown in this figure. From this figure it is observed that 0 nodal circle axial mode frequency rises as nodal diameter increases. This curve crosses the frequency curve for tangential vibration around 10 nodal diameters. Similarly 1 nodal circle axial mode frequency curve also crosses the frequency curve for tangential vibration around 5 nodal diameter. At the cross over region the mode shapes are highly coupled with tangential and axial displacements. Similar findings have been experimentally observed by Finbow and Watson [13]. The tangential vibration frequency curve has distortion in the cross over region. However, finally it settles down to a lower value and fairly remains unaffected by increase in nodal diameter after 12. Omprakash and Ramamurti [3] have also reported severe coupling of blade and disk modes for small aspect ratio blades for a given ε. It may be pointed out that the parameter ε determines the flexibility of the disk. This flexibility can be compared with the flexibility of the blades.

Condition 2. In this condition the second blade is deviated in its looseness at the root. This is similar to a bladed disk with alternate blade having looseness. It may be noted that such kind of looseness may be prevailing in the bladed disk at the time of assembling. The results under this condition are given in Fig. 4. It is observed from the figure that the tangential mode splits into two curves. The lower curve gives predominantly second blade tangential mode. Whereas upper curve is for the first blade. Again the tangential mode frequencies distort due to the cross over by 0 nodal circle axial mode and 1 nodal circle axial mode. It is also observed that for 0

nodal diameter the tangential modes are not split corresponding to first blade vibration or second blade vibration. Instead both blades vibrate tangentially in phase with each other and also with disk (1117.97 Hz) or out of phase with each other (1431.21 Hz) or both blades tangential in phase with each other and out of phase with disk (1917.96 Hz). This behaviour is quite peculiar. It is likely that severe coupling between disk and blades causes this behaviour. Hence it may be realized that simple spring and mass models are inadequate to bring out this type of behaviour. It may also be noted that deviation in the blade's root looseness has clearly isolated the frequencies and, therefore it represents the practical case. Experimentally, quite varied frequencies are observed for a practical case for which all blades may not get excited for a given resonance frequency [17].

Condition 3. This condition represents a bladed disk for which after every two blades there are two consecutive loose blades. The mode shapes for this condition are highly complex and it is difficult to categorize. Plotting of frequency curves give confusing trend if modes have not been correctly identified. Therefore, instead of plotting, a table is given in which modes are approximately identified. Table - 4 shows various modes and their frequencies. The tangential mode frequencies are split. The in phase and out of phase motions with respect to each other are mentioned in the table.

Case 2- Low Pressure (LP) Turbine Stage

This is a case of an LP stage of 110 MW steam turbine where there are 132 blades on the disk with blade aspect ratio of 4.4. These blades are long and twisted. The analysis is done upto 10 nodal diameters for the three conditions.

Condition 1. A plot of natural frequencies for the first three modes versus diameter is given in Fig. 5. Vibration modes of cantilever blade corresponding to flapwise bending (1B - tangential), first edgewise bending (1EB - axial) and torsional (1T) are also shown in this figure. Frequencies for axial vibrations increase with nodal diameter and the rise is controlled by the cantilever blade frequency as blades vibrate along with disk. Thus for higher nodal diameters there is no appreciable rise in frequency. For 0 nodal circle mode the frequency is below the edgewise bending mode of the cantilever blade. One nodal circle mode is here combined with torsional mode of the blade. This suggests that spring and mass models without admitting modal stiffness and modal masses for torsional modes will be inadequate to explain this behaviour. The 1 nodal circle mode at 10 nodal diameter is below the torsion mode of cantilever blade.

Condition 2. The results of the analysis are given in Fig. 6. It is observed that 0 nodal circle axial frequency behaves as in the previous case. The tangential frequency splits into two and both are marginally affected by increase in nodal diameter. Whereas, combined torsion and 1 nodal circle mode frequency splits into two, one of which is for blade torsion alone. This frequency is considerably low in magnitude and it is marginally affected by increase in nodal diameter. The second one which is similar to combined torsion and 1 nodal circle mode shows a similar trend as observed in Fig. 5. The split in frequencies for the tangential and torsional mode is due to the looseness created in the second blade.

Condition 3. The results of the analysis are given in Fig. 7. Here also the 0 nodal circle axial mode frequency shows similar trend as observed in Figs. 5, 6. Tangential vibration mode splits into four frequencies - two for the tight blade and other two for the loose blades. So it forms two groups. In each group the two frequencies are very close and at times it is very difficult to distinguish them on the graph. In case of torsion mode also two groups are formed. The first group in which only one frequency is present is for combined blade torsion and 1 nodal circle mode. Whereas the second group has 3 close frequencies corresponding to blade torsion mode only. The trend of these curves is very similar to those in Figs. 5 and 6.

The general observation from this analysis is that the axial mode of 0 nodal circle does not split in spite of the root looseness. This mode crosses over tangential vibration mode. There is little coupling between these two modes. This phenomena is also seen for the long blades in Ref. [3]. Therefore, large aspect ratio blades which behave like beams can be represented by spring and mass models for bladed disk analysis.

Case 3- High Pressure (HP) Turbine Stage

This is a case of a HP stage of 236 MW steam turbine where there are 94 blades on the disk with blade aspect ratio of 3.10. In this case only condition no. 1 (i.e. the sector containing one blade) is considered. Conditions 2 and 3 have not been considered as the trend due to blade root looseness variation has been obtained for the extreme cases of blade aspect ratios given above. The analysis was done upto 45 nodal diameters. For each diametral mode first three modes are obtained. The natural frequencies for these modes are plotted against nodal diameter as shown in Fig. 8. These modes depict both axial and tangential vibrations of blades. The coupled modes are observed around fifth nodal diameter. All these modes show general tendency of increase in frequency value with respect to nodal diameter from 0 to (approximately) 10 and thereafter less significant change is observed with increase in nodal diameter.

CONCLUSIONS

The above analysis shows behaviour of both axial and tangential modes of vibration for practical bladed disks. From the behaviour pattern of these bladed disks following points have been concluded -

1. For small aspect ratio blades, the bladed disk modal behaviour is highly coupled. Therefore, it is desirable to perform detailed analysis using FEM instead of lumped spring and mass models.

2. For large aspect ratio blades, the bladed disk behaviour is simple and insignificant coupling of blades and disk is observed. Therefore, the lumped spring and mass models can be used adequately.

3. For large aspect ratio blades, the torsional mode is observed to be combined with one nodal circle mode.

4. The root looseness has no influence on the zero nodal circle mode for all the cases considered.

5. For medium aspect ratio of blades, the blades and disk modes tend to couple.

REFERENCES

1. A.S.PANWALKAR, A.RAJAMANI and V.RAMAMURTI 'Turbomachinery blade dynamics - a review' Shock and Vibration Digest vol. 22, no. 12, 1990, pp 3-9.

2. P.S.KUO 'On the formulation of coupled /uncoupled dynamic analysis of bladed - disc assemblies' American Society of Mechanical Engineers, Paper No. 81-DET-126, 1981.

3. V.OMPRAKASH and V.RAMAMURTI 'Coupled free vibration characteristics of rotating tuned bladed disk systems' Journal of Sound and Vibration, vol. 140, no. 3, 1990, pp 413-435

4. H.IRRETIER and K.J.SCHMIDT 'Mistuned bladed disks - dynamical behaviour and computation' International conference on Rotor Dynamic Problems in Power Plants, Rome, Italy, 1982, pp 215-226.

5. D.J.EWINS 'Vibration characteristics of bladed disk assemblies' Journal of Mechanical Engineering Science vol. 15, no. 3, 1973, pp 165-186.

6. D.J.EWINS 'Vibration modes of mistuned bladed disks' Transactions of the American Society of Mechanical Engineers, Journal of Engineering for Power, vol. 98, no. 3, 1976, pp 349-355.

7. D.J.EWINS and M.IMREGUN 'Vibration modes of packeted bladed discs' Vibration of Bladed Disk Assemblies, American Society of Mechanical Engineers, 1983, pp 25-33.

8. J.H.GRIFFIN and T.M.HOOSAC 'Model development and statistical investigation of turbine blade mistuning' Transactions of the American Society of Mechanical Engineers, Journal of Vibration, Acoustics, Stress and Reliability in Design, vol. 106, no. 2, 1984, pp 204-210.

9. C.PIERRE and P.D.CHA 'Strong mode localization in nearly periodic disordered structures' AIAA Journal, vol. 27, no. 2, 1989, pp 227-241.

10. S.T.WEI and C.PIERRE 'Localization phenomena in mistuned assemblies with cyclic symmetry part I: free vibrations' Transactions of the American Society of Mechanical Engineers, Journal of Vibration, Acoustics, Stress and Reliability in Design, vol. 110, no. 4, 1988, pp 429-438.

11. D.AFOLABI 'The eigenvalue spectrum of a mistuned bladed disk' Vibrations of Blades and Bladed Disk Assemblies, American Society of Mechanical Engineers, 1985, pp 23-30.

12. D.AFOLABI 'The frequency response of mistuned bladed disk assemblies' Vibrations of Blades and Bladed Disk Assemblies, American Society of Mechanical Engineers, 1985, pp 15-21.

13. I.FINBOW and S.J.WATSON 'Experimental verification of turbine blade vibration characteristics' IMechE paper C 196/79, 1979, pp 163-172.

14. V.RAMAMURTI 'Computer Aided Design in Mechanical Engineering' New Delhi: Tata McGraw-Hill, 1989.

15. A.M.SALAMA 'Finite Element Dynamic Analysis of Blade Packets and Bladed Disc Assemblies' Ph.D. Thesis, Institute of Sound and Vibration Research, The University of Southampton, 1976.

16. O.P.SHARMA 'Generation of Campbell diagram for last stage LP moving blades of 500 MW steam turbines' Steam Turbine Engineering and Development Centre, Bharat Heavy Electricals Limited, Hardwar, India, Rep. No. TB-002-0-DL, 1989.

17. A.S.PANWALKAR, A.RAJAMANI AND V.RAMAMURTI 'Free vibration studies on turbine stage using cyclic symmetry' Presented at the International Conference on Engineering Software held at IIT New Delhi, India Dec. 4-7 1989, Engineering Software, Narosa Publishing House, Editors C.V.Ramakrishnan et. al., 1989, pp 459-466.

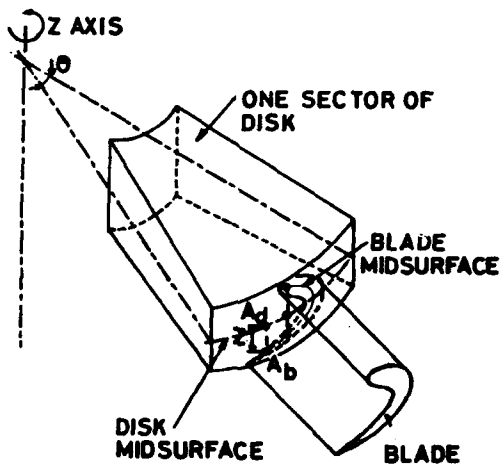

FIG 1. A SECTOR OF BLADED DISK CONTAINING ONE BLADE

TABLE 1 NATURAL FREQUENCIES IN Hz FOR CASE NO.1, CONDITION NO. 3

Nodal Dia.	0 Nodal Circle	Tangential motion for 2nd and 3rd blades		Tangential motion for 1st and 4th blades		1 Nodal circle
		In phase	Out of phase	In phase	Out of phase	
0	242.33					
2	269.26	1287.11	1285.15	1622.23	1644.53	1370.20
5	557.94	1291.91	1288.01	1703.14	1707.71	1731.68
7	931.34	1296.46	1288.09	1647.30	1646.57	2398.27
8	1190.48	1304.53	1288.40	1649.37	1646.58	2687.31
9	1275.79*	1382.03	1293.48	1652.27	1647.27	-
10	1433.14*	1285.37	1391.66	1666.09	1649.65	-
15	2345.41	1290.41	1384.93 1489.91	1645.97**	-	-
20	2615.13	1290.93	1408.12 1462.77	1646.47**	-	-

For 0 nodal diameter following frequencies are observed which could not be put in the categories mentioned above:

1) 1113.58 Hz - All blades tangential motion in phase with disk
2) 1277.74 Hz - 1st and 4th blades axial with 1 nodal circle and 2nd and 3rd blades strong tangential motion
3) 1282.34 Hz - 1st and 4th blades axial with 1 nodal circle and 2nd blade strong tangential motion
4) 1643.83 Hz - 1st and 4th blade tangential out of phase with each other
5) 1434.50 Hz - 2nd and 3rd blade strong tangential motion
6) 1920.88 Hz - All blades tangential motion out of phase with disk

* This mode is mixed with 2nd and 3rd blade in tangential motion

** This mode gives tangential motion for 1st blade only

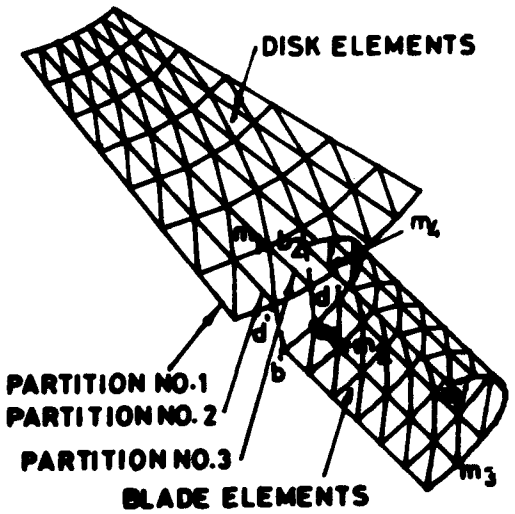

FIG 2. PARTITIONED SECTOR OF BLADED DISK

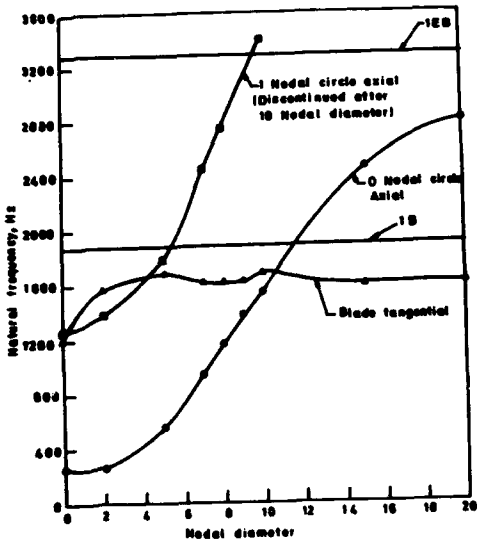

FIG.3. NATURAL FREQUENCIES FOR CASE 1, CONDITION NO 1

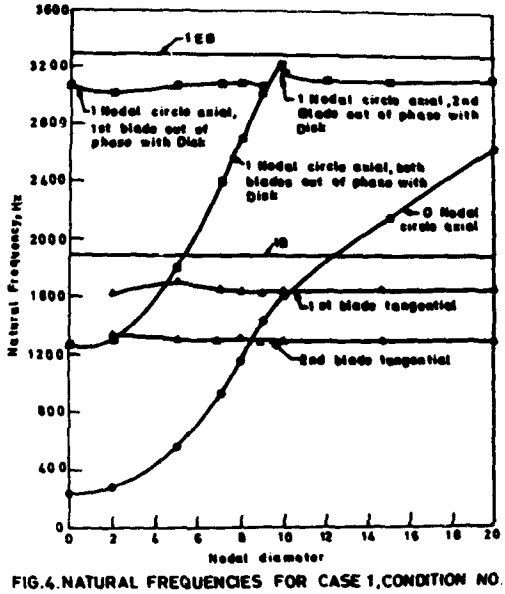

FIG.4. NATURAL FREQUENCIES FOR CASE 1, CONDITION NO.2

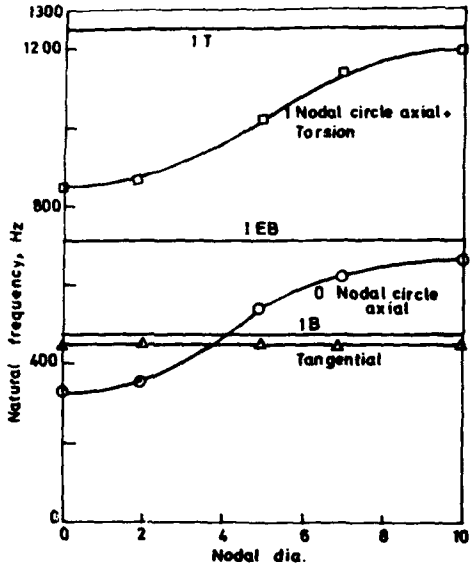

FIG. 5 NATURAL FREQUENCIES FOR CASE-2, CONDITION-1

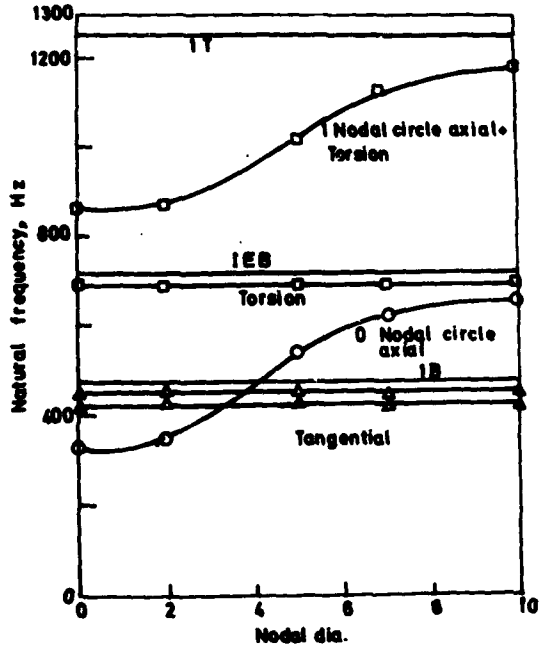

FIG. 6 NATURAL FREQUENCIES FOR CASE-2, CONDITION-2

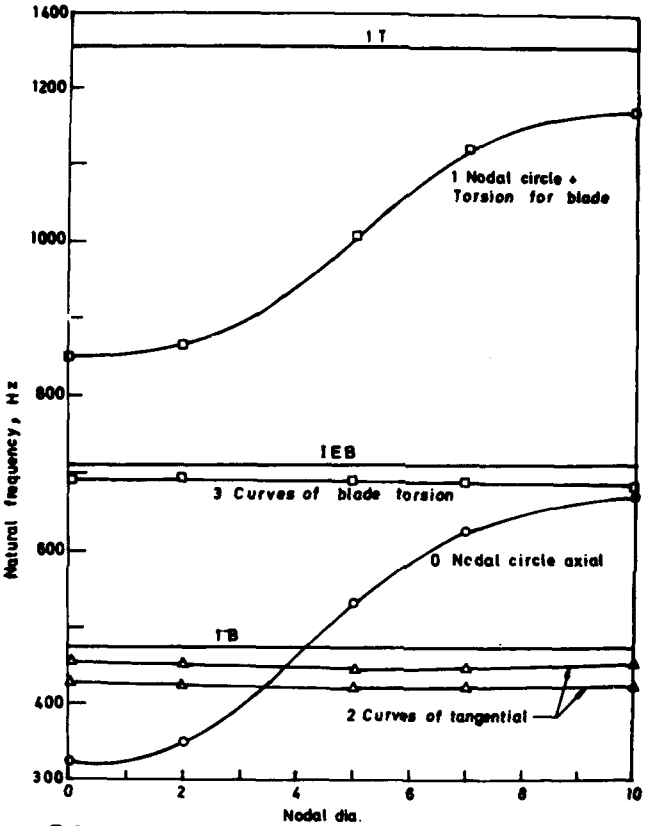

FIG. 7 NATURAL FREQUENCIES FOR CASE-2 CONDITION-3

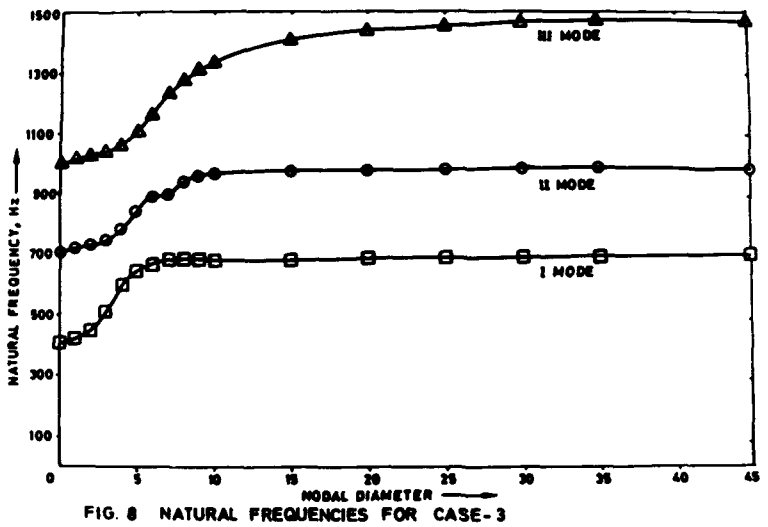

FIG. 8 NATURAL FREQUENCIES FOR CASE-3

AUTHOR INDEX

Adhikari, Rajesh, 271
Afonina, Olga A., 1455
Agarwal, A.N., 935
Agneni, A., 237
Ahuja, K.K., 1093, 1627, 1637
Akay, Adnan, 633
Ali, Ashraf, 1001
Alim, O.A., 1459
Allaei, Daryoush, 1611
Allard, Jean F., 759
Antonov, A.I., 1669
Asminin, Victor F., 165
Austin, Eric M., 181
Avilova, G.M., 533
Badilla, Gloria A., 543
Bageshwar, M.S., 935
Bagley, Ronald L., 169
Baklanov, V.S., 143
Ball, James F., 1125
Banks-Lee, Pamela, 1527
Bao, W., 157
Bao, X.L., 1195
Barrett, David John, 257
Belegundu, Ashok D., 1053
Bergen, Thomas F., 543
Bernblit, Michael V., 983
Bhat, R.B., 461
Biron, D., 1353
Blake, William K., 1647
Blakemore, M., 561
Bobrovnitskii, Yurii I., 847
Bockhoff, Michael, 1293
Bokil, Vijay B., 1595
Boone, Marinus M., 1261
Borthwick, W.K.D., 821
Botros, K.K., 717
Boulter, Nicholas J., 435
Bremner, Paul G., 569, 1673
Brévart, B., 413
Briscoe, A., 829
Brodnikovskii, Aleksei M., 917, 1525
Brown, David, 1555
Browning, Douglas R., 395
Budrin, Sergei V., 555
Caimi, Raoul, 97
Çalişkan, Mehmet, 651, 1475
Callister, John R., 1535
Carletti, E., 1429
Castellani, A., 237
Chander, R., 739
Chandrupatla, Tirupathi R., 1053
Chang-Su, Hahn, 405
Chen, Q., 1603
Chepulsky, Yury P., 165
Chistiakov, A.J., 803
Chon, J.T., 551
Chotelev, Sergey I., 165
Cleghorn, W.L., 729
Clerc, C., 499, 1235
Cody, George, 753
Coelho, J.L. Bento, 711
Collier, Robert).., 197
Comănescu, L., 1521
Constantine, Paris, 1673
Cottle, Eugene T., 279
Coyette, Jean-Pierre G., 1027
Cray, Benjamin A., 1141
Creamer, N.G., 369
Crema, L. Balis, 237
Crocker, Malcolm J., 659, 1543, 1681
Cŭdina, Mirko, 1661
Cummings, Alan 689
Cuschieri, J.M., 1361
D'Ambrogio, W., 1567
Dalmatova, Natalya V., 1455
Darlington, P., 1011
Dayal, Vinay, 919
de la Croix, D. Vaucher, 499, 1235
de Jong, C.A.F., 577
Dean, Cleon E., 675
Dickey, J., 541
Didkovsky, V., 1413
Doucet, Anne B., 217
Dowling, Ann, 37

Dragan, S.P., 1327
Dragonette, Louis R., 1075
Drakatos, P.A., 821
Drozdova, Ludmila Ph., 485
Dubbelday, Pieter S., 151
Dubey, A., 973
Efron, A.J., 321
Ekimov, A.E., 859
Eversman, Wlater, 121
Fahy, F.J., 611
Faustov, A.S., 811
Feit, David, 1647
Fengquan, Wang, 1045
Fessina, Micahel I., 1465
Finn, Brian M., 345
Fisher, M.J., 305
Flatau, Alison B., 1243
Flavitsky, Yu V., 1425
Fleeter, Sanford, 113
Fraiman, B.J., 811
Fujiwara, Kyoji, 1285
Fukumizu, Kenji, 329
Fuller, C.R., 377, 413
Galaktionova, T.I., 807
Ganeriwala, Surendra N., 1379
Gao, Jianjun, 1527
Garrison, M.R., 157
Gaudreault, Michele L.D., 169
Gaul, Lothar, 445
Gaumond, Charles F., 1103, 1179
Gaunaurd, Guillermo C., 1117
George, Albert R., 1535
Gibbs, Max A., 217
Ginsberg, Jerry H., 1587
Goncharenko, B.I., 1387
Gönenç, Arzu, 651
Gordienko, V.A., 1387
Govindswamy, Kiran M., 177
Graupe, D., 321
Green, Robert E., 879
Guicking, D., 313
Guo, Y.P., 507
Gupta, A., 1037
Guzhas, Danielius, 1219
Hald, Jørgen, 1331
Hammoud, Chafic M., 1171
Hanagud, S., 739
Harari, A., 1253
Hardin, Jay C., 51
He, Shulin, 249, 265
Hetenyi, Gyula, 1497
Hickling, Robert, 1125
Hoenes, Eric, 1371
Holodova, S.V., 1345
Hong, Westwood K.W., 435
Houghton, J.R., 897, 927
Houston, Brian H., 1103
Hughes, David H., 1203
Ibrahim, S.R., 1567
Ih, Jeong-Guon, 645
Ivakin, Anatoly N., 1087
Ivannikov, A.N., 811, 815, 1345
Ivanov, Nickolay I., 1437
Jacobsen, Finn, 1299
Jia, S.H., 957
Jian, Pang, 795
Jiricek, Ondreij, 1293
Johnson, Conor D., 181
Jones, H.W., 1489
Joon, Shin, 405
Juang, Ten-Bin, 1243
Juhl, Peter M., 965
Kaduchak, Greg, 1203
Karadgi, V.G., 863
Kazarov, V.M., 863
Kergomard, Jean, 697
Kerkyras, S.C., 821
Kharin, Oleg A., 1111
Khomenko, Villen P., 641
Kim, Bong-Ki, 645
Kim, Jeung-tae, 1581
Kim, M.J., 1037
Kim, Jin-Yeon, 645
Kim, W.S., 1307
Kinra, Vikram K., 223
Kitagawa, Hiroo, 329
Klauson, Aleksander, 1227
Klimov, Boris I., 1449
Kljachko, L.N., 725, 1395
Klusman, Steven A., 425
Kohoutek, Richard, 295
Koike, Tsunehiko, 869
Kolodieva, I.I., 859
Koropchenko, A.A., 1387
Korotin, P.I., 859
Korotin, P.I., 1151
Kumar, PVS Ganesh, 1505
Kuo, Sen M., 345, 851
Kurtzev, Georgiy M., 1437
Lafarge, Denis, 759
Lahti, Tapio, 1337
Larsson, Conny, 1269

Larucow, Alexander S., 667
Latcha, Michael A., 633
Lauchle, Gerald C., 137
Lebedev, A.V., 1151, 1163
Lebedeva, I.V., 1327
Ledenyov, V.I., 1669
Lee, Gilbert F., 763
Lesieutre, George A., 177
Levenson, M., 369
Levraea, Vincent J., 287
Levy, C., 1603
Li, Chengde, 1527
Liebst, Brad S., 169
Lighthill, Sir James, 5
Ljunggren, Sten, 1481
Lu, Jiawei, 1543
Lucas, Michael J., 1315
Lyon, Richard H., 869
Maidanik, G., 541
Makeev, S.V., 815
Mann, J. Adin, 771
Marchertas, A.H., 1037
Margasahayam, Ravi, 97
Markelov, P., 1413
Marston, Philip L., 1203
Martin, J.T., 1637
Mathur, Gopal P., 81
McInerny, S.A., 59
Medaugh, Raymond S., 395
Metsaveer, Jaan, 1227
Meyyappa, M., 739
Miccoli, G., 1429
Miles, R.N., 157
Miller, Russel D., 1195
Mirskov, A.S., 863
Mitjavila, A., 1353
Mityurich, G.S., 845
Mohanty, A.R., 957
Moore, T.N., 909
Mundkur, G., 461
Murti, PV Ramana, 1505
Murty, R.L., 837
Muzychenko, Vadim V., 1211
Myers, R.J.M., 561
Nale, Tim A., 425
Nashif, Ahid D. 189
Nashif, Peter J., 361
Nataraj, C., 599
Navaneethakrishnan, P.V., 1405
Nelson, P.A., 305
Newland, David E., 779
Ng, Kam W., 67
Nicholson, G.C., 1011
Nikiforov, Alexei S., 555
Njunin, Boris N., 667
Norris, Andrew, 753
Norton, M.P., 621
Novikov, I.I., 725, 1395
Ochmann, Martin, 1187
Oh, Jae-Eung, 405, 1419
Önsay, T., 787
Otsuru, Toru, 477
Otte, Dirk, 129
Panwalkar, A.S., 1061
Parot, J.M., 499
Pate, Anna L., 1243
Patel, J.R., 1681
Pauzin, S., 1353
Pavelyev, V.B., 1425
Pavlov, V.I., 811, 815, 1111, 1345
Pei, J., 909
Perry, Lori Ann, 137
Pinnington, R.J., 829
Plenge, Michael, 445
Plotkin, Kenneth J., 105
Powell, Robert E., 89
Prasad, M.G., 1307
Qunli, Wu, 585
Rajakumar, C., 1001
Rajamani, A., 1061
Raju, P.K., 599, 1543, 1681
Ramamurti, V., 889, 1061
Rao, Mohan D., 217, 249, 265
Rao, V Bhujanga, 1505
Ravinder, D., 745
Reinhall, Per G., 1171
Rennison, David C., 569, 1673
Reuben, R.L., 821
Rioual, J.-L., 305
Robsman, Vadim A., 905
Rogers, Lynn C., 287
Rongying, Shen, 795
Rosenhouse, G., 1513
Rosenthal, Felix, 337
Rotz, Christopher A., 257
Ruckman, C.E., 377
Rybak, Samual A., 1149
Salvini, P., 1567
Sandman, B.E., 1253
Sarkissian, A., 1103, 1179
Schanz, Martin, 445
Scharton, Terry D., 543

Schmidt, Laszlo, 1497
Seliverstov, B.A., 1445
Sepcenko, Valentin, 97
Serdyukov, A.N., 845
Sestieri, A., 1567
Seybert, A.F., 945, 957
Shaw, Richard P., 1133
Shen, Qun, 353
Shen, Peitao, 927
Sheng, Ping, 753
Shin, Joon, 1419
Shirahatti, U.S., 973, 1595
Shiyu, Chen, 1045
Simpson, Myles A., 81
Sivovolov, Vladimir A., 917
Sizova, Natalia V., 1449
Sommerfeldt, Scott D., 361
Sorensen, Alan, 1371
Spanias, Andreas, 353
Sridhara, B.S., 659
St-Cyr, L.K., 551
Stan, A., 1521
Starobinsky, Rudolf N., 1465, 1619
Stech, Daniel J., 387
Stevens, J.C., 1627
Strifors, Hans C., 1117
Stusnick, Eric, 1315
Subbarao, A., 369
Suhanov, N.L., 803
Sujatha, C., 889
Sun, Naihua, 1203
Sun, Fangning, 1527
Sun, J.Q., 157
Suri, S.C., 935
Sutherland, Louis C., 1255
Sviridova, V.V., 845
Szabó, Kalman, 1497
Szwerc, Richard P., 205
Terao, Michihito, 703
Tohyama, Mikio, 869
Tomilina, T.M., 1157
Trakhtenbroit, Moissei A., 493
Tso, Yan, 523
Tsukernikov, I.E., 989, 1445
Tulchinsky, Leonid N., 641
Turcotte, Jeffrey S., 387
Tzanetos, K.L., 821
Überall, Herbert, 1195, 1653
Ünlüsoy, Y. Samim, 1475
Ustelencev, L.I., 725
Vaidya, U.K., 1681
Van der Auweraer, Herman, 129
Venkatesh, Vasisht, 897, 1399
Verheij, J.W., 577, 591
Vinokur, Roman Y., 515
Vlahopouios, Nickolas, 1019
Vul, V.M., 143
Wan, G.C., 945, 993
Webb, Steven G., 387
Werby, Michael F., 1195, 1653
Weyer, Richard M., 205
Williams, Earl G., 683, 771, 1103
Wilson, D. Keith, 1277
Woodhouse, J., 561
Wren, Graeme G., 223
Wu, T.W., 945, 993
Xue, W., 1399
Yamaguchi, Hiroki, 271
Yan, Yong, 851
Ye, Ling, 753
Yoneyama, Masahide, 329
Yoshimura, Junichi, 469
Yu, S.D., 729
Zaki, N.A., 1459
Zaldonis, J.A., 1253
Zelyony, V.P., 845
Zhang, Ligang, 1203
Zhou, Minyao, 753
Zubair, M., 973